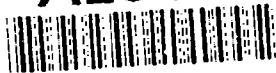
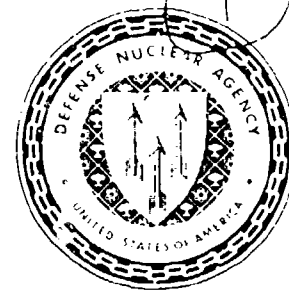


AD-A281 668



Defense Nuclear Agency  
Alexandria, VA 22310-3398



DNA-TR-93-63

# Laboratory Investigation and Analysis of the Strength and Deformation of Joints and Fluid Flow in Salem Limestone

Daniel E. Chitty, et al.  
Applied Research Associates, Inc.  
New England Division  
RFD #1 Box 120A  
Waterman Road  
South Royalton, VT 05068

DTIC  
ELECTE  
JUL 15 1994  
S F D

June 1994

Technical Report

CONTRACT No. DNA 001-90-C-0132

94-22176



Approved for public release;  
distribution is unlimited.

94 7 14 062

**Best  
Available  
Copy**

Destroy this report when it is no longer needed. Do not return to sender.

PLEASE NOTIFY THE DEFENSE NUCLEAR AGENCY,  
ATTN: CS11, 6801 TELEGRAPH ROAD, ALEXANDRIA, VA  
22310-3398, IF YOUR ADDRESS IS INCORRECT, IF YOU  
WISH IT DELETED FROM THE DISTRIBUTION LIST, OR  
IF THE ADDRESSEE IS NO LONGER EMPLOYED BY YOUR  
ORGANIZATION.



## DISTRIBUTION LIST UPDATE

This mailer is provided to enable DNA to maintain current distribution lists for reports. (We would appreciate your providing the requested information.)

- ☐ Add the individual listed to your distribution list.
- ☐ Delete the cited organization/individual.
- ☐ Change of address.

### NOTE:

Please return the mailing label from the document at any additions, changes, corrections or deletions can be made easily.

NAME: \_\_\_\_\_

ORGANIZATION: \_\_\_\_\_

### OLD ADDRESS

### CURRENT ADDRESS

\_\_\_\_\_  
\_\_\_\_\_  
\_\_\_\_\_

\_\_\_\_\_  
\_\_\_\_\_  
\_\_\_\_\_

TELEPHONE NUMBER: (    ) \_\_\_\_\_

### DNA PUBLICATION NUMBER/TITLE

### CHANGES/DELETIONS/ADDITIONS, etc.) (Attach Sheet if more Space is Required)

\_\_\_\_\_  
\_\_\_\_\_  
\_\_\_\_\_

\_\_\_\_\_  
\_\_\_\_\_  
\_\_\_\_\_

DNA OR OTHER GOVERNMENT CONTRACT NUMBER: \_\_\_\_\_

CERTIFICATION OF NEED-TO-KNOW BY GOVERNMENT SPONSOR (if other than DNA): \_\_\_\_\_

SPONSORING ORGANIZATION: \_\_\_\_\_

CONTRACTING OFFICER OR REPRESENTATIVE: \_\_\_\_\_

SIGNATURE: \_\_\_\_\_

CUT HERE AND RETURN





DEFENSE NUCLEAR AGENCY  
ATTN: TITL  
6801 TELEGRAPH ROAD  
ALEXANDRIA, VA 22310-3398

DEFENSE NUCLEAR AGENCY  
ATTN: TITL  
6801 TELEGRAPH ROAD  
ALEXANDRIA, VA 22310-3398

REPORT DOCUMENTATION PAGE			Form Approved OMB No. 0704-0188	
<small>Public reporting burden for this collection of information is estimated to average 1 hour per response, including the time for reviewing instructions, searching existing data sources, gathering and maintaining the data needed, and completing and reviewing the collection of information. Send comments regarding this burden estimate or any other aspect of this collection of information, including suggestions for reducing this burden to Washington Headquarters Services, Directorate for Information Operations and Reports, 1215 Jefferson Davis Highway, Suite 1204, Arlington, VA 22202-4302, and to the Office of Management and Budget, Paperwork Reduction Project (0704-0188), Washington, DC 20503.</small>				
1. AGENCY USE ONLY (Leave blank)	2. REPORT DATE 940601	3. REPORT TYPE AND DATES COVERED Technical 900801 - 930630		
4. TITLE AND SUBTITLE Laboratory Investigation and Analysis of the Strength and Deformation of Joints and Fluid Flow in Salem Limestone		5. FUNDING NUMBERS C - DNA 001-90-C-0132 PE - 62715H PR - RS TA - RH WU - DH303150		
6. AUTHOR(S) Daniel E. Chitty, Scott E. Blouin, Xiaoqing Sun, and Kwang J. Kim				
7. PERFORMING ORGANIZATION NAME(S) AND ADDRESS(ES) Applied Research Associates, Inc. New England Division RtD #1 Box 120A Waterman Road South Royalton, VT 05068		8. PERFORMING ORGANIZATION REPORT NUMBER  5634		
9. SPONSORING/MONITORING AGENCY NAME(S) AND ADDRESS(ES) Defense Nuclear Agency 6801 Telegraph Road Alexandria, VA 22310-3398 SPSD/Senseny		10. SPONSORING/MONITORING AGENCY REPORT NUMBER  DNA-TR-93-63		
11. SUPPLEMENTARY NOTES This work was sponsored by the Defense Nuclear Agency under RDT&E RMC Code B4662D RS RH 00018 SPSP 4300A 25904D.				
12a. DISTRIBUTION/AVAILABILITY STATEMENT  Approved for public release; distribution is unlimited.			12b. DISTRIBUTION CODE	
13. ABSTRACT (Maximum 200 words) As part of the Underground Technology Program, fundamental mechanisms that influence the mechanical response of jointed, saturated rock masses were investigated with laboratory tests performed on Salem (Indiana) limestone. Mating joint surfaces were created by 1) tensile splitting, 2) sawing and grinding, and 3) cutting to a specified fractal dimension using numerically controlled machine tools. Triaxial tests on specimens with inclined joints were performed to measure joint strength and deformation, and a constitutive model for joints was developed, including the observed strain softening. Permeability of the intact limestone was measured at various stress states including deviator stresses, and joint flow was measured under a range of normal stress conditions. Other aspects of the project included an investigation of strain rate effects, and measurement of the saturated undrained compressibility and specific storage of the limestone.  This contract also sponsored ARA's participation in an interlaboratory test program sponsored by the Institute for Standards Research of the American Society for Testing and Materials to develop statements of precision and bias for four standard rock test methods.				
14. SUBJECT TERMS Rock Mechanics      Fractals      Limestone Rock Joints      Constitutive Modeling      Permeability			15. NUMBER OF PAGES 378	
			16. PRICE CODE	
17. SECURITY CLASSIFICATION OF REPORT UNCLASSIFIED	18. SECURITY CLASSIFICATION OF THIS PAGE UNCLASSIFIED	19. SECURITY CLASSIFICATION OF ABSTRACT UNCLASSIFIED	20. LIMITATION OF ABSTRACT SAR	

UNCLASSIFIED

SECURITY CLASSIFICATION OF THIS PAGE

CLASSIFIED BY:

N/A since unclassified.

DECLASSIFY ON

N/A since Unclassified.

Accession For	
NTIS CRASH	<input checked="" type="checkbox"/>
DTIC TAB	<input type="checkbox"/>
Unannounced	<input type="checkbox"/>
Justification	
By	
Distribution	
Availability Codes	
Dist	Avail and/or Special
A-1	

SECURITY CLASSIFICATION OF THIS PAGE

UNCLASSIFIED

# CONVERSION TABLE

Conversion factors for U.S. customary to metric (SI) units of measurement

To Convert From	To	Multiply
angstrom	meters (m)	1.000 000 X E-10
atmosphere (normal)	kilo pascal (kPa)	1.013 25 X E+2
bar	kilo pascal (kPa)	1.000 000 X E+2
barn	meter <sup>2</sup> (m <sup>2</sup> )	1.000 000 X E-28
British Thermal unit (thermochemical)	joule (J)	1.054 350 X E+3
calorie (thermochemical)	joule (J)	4.184 000
cal (thermochemical)/cm <sup>2</sup>	mega joule/m <sup>2</sup> (MJ/m <sup>2</sup> )	4.184 000 X E-2
curie	giga becquerel (GBq)*	3.700 000 X E+1
degree (angle)	radian (rad)	1.745 329 X E-2
degree Fahrenheit	degree kelvin (K)	$t_K = (t_F + 459.67) \div 1.8$
electron volt	joule (J)	1.602 19 X E-19
erg	joule (J)	1.000 000 X E-7
erg/second	watt (W)	1.000 000 X E-7
foot	meter (m)	3.048 000 X E-1
foot-pound-force	joule (J)	1.355 818
gallon (U.S. liquid)	meter <sup>3</sup> (m <sup>3</sup> )	3.785 412 X E-3
inch	meter (m)	2.540 000 X E-2
jerk	joule (J)	1.000 000 X E+9
joule/kilogram (J/Kg) (radiation dose absorbed)	Gray (Gy)	1.000 000
kilotons	terajoules	4.183
kip (1000 lbf)	newton (N)	4.448 222 X E+3
kip/inch <sup>2</sup> (ksi)	kilo pascal (kPa)	6.894 757 X E+3
ktop	newton-second/m <sup>2</sup> (N-s/m <sup>2</sup> )	1.000 000 X E+2
micron	meter (m)	1.000 000 X E-6
mil	meter (m)	2.540 000 X E-5
mile (international)	meter (m)	1.609 344 X E+3
ounce	kilogram (kg)	2.834 952 X E-2
pound-force (lbf avoirdupois)	newton (N)	4.448 222
pound-force inch	newton-meter (N-m)	1.129 848 X E-1
pound-force/inch	newton/meter (N/m)	1.751 268 X E+2
pound-force/foot <sup>2</sup>	kilo pascal (kPa)	4.788 026 X E-2
pound-force/inch <sup>2</sup> (psi)	kilo pascal (kPa)	6.894 757
pound-mass (lbm avoirdupois)	kilogram (kg)	4.535 924 X E-1
pound-mass-foot <sup>2</sup> (moment of inertia)	kilogram-meter <sup>2</sup> (kg-m <sup>2</sup> )	4.214 011 X E-2
pound-mass/foot <sup>3</sup>	kilogram/meter <sup>3</sup> (kg/m <sup>3</sup> )	1.601 846 X E+1
rad (radiation dose absorbed)	Gray (Gy)**	1.000 000 X E-2
roentgen	coulomb/kilogram (C/kg)	2.579 760 X E-4
shake	second (s)	1.000 000 X E-6
slug	kilogram (kg)	1.459 390 X E+1
torr (mm Hg, 0°C)	kilo pascal (kPa)	1.333 22 X E-1

\*The becquerel (Bq) is the SI unit of radioactivity: Bq = 1 event/s.

\*\*The Gray (Gy) is the SI unit of absorbed radiation.

# TABLE OF CONTENTS

Section	Page
CONVERSION TABLE .....	iii
FIGURES .....	vii
TABLES .....	xvi
1 INTRODUCTION .....	1
1.1 BACKGROUND. ....	1
1.2 OBJECTIVES. ....	1
1.3 SCOPE. ....	2
2 SALEM LIMESTONE ORIGIN, DESCRIPTION, AND PHYSICAL PROPERTIES .....	4
2.1 ORIGIN AND DESCRIPTION. ....	4
2.2 PHYSICAL PROPERTIES. ....	5
3 JOINT SURFACE PREPARATION .....	8
3.1 JOINT SURFACE FABRICATION .....	8
3.1.1 Smooth Ground Joint Surfaces .....	8
3.1.2 Tensile Fracture Joint Surfaces .....	9
3.1.3 Synthetic Joint Surfaces .....	9
3.2 SURFACE GEOMETRY MEASUREMENT .....	11
4 TEST PROCEDURES .....	21
4.1 SPECIMEN PREPARATION. ....	21
4.2 MOISTURE CONTENT PREPARATION. ....	22
4.2.1 Unsaturated Specimens. ....	22
4.2.2 Saturated Specimens. ....	22
4.3 LOADING. ....	23
4.3.1 Triaxial Compression. ....	23
4.3.2 Hydrostatic Compression. ....	24
4.3.3 Uniaxial Strain. ....	24
4.4 INSTRUMENTATION. ....	24
4.5 DATA RECORDING AND REDUCTION. ....	25
5 MECHANICAL PROPERTIES OF INTACT LIMESTONE .....	30
5.1 UNCONFINED COMPRESSION TESTS. ....	31
5.1.1 Unconfined Compression Tests at Various Water Contents .....	31
5.1.2 Post-Failure Response of Limestone in Unconfined Compression. ....	32
5.2 TRIAXIAL COMPRESSION TESTS. ....	33
5.2.1 Intact Strength Determination. ....	34
5.2.2 Investigation of Specimen Aspect Ratio and End Conditions. ....	34
5.3 HYDROSTATIC COMPRESSION TESTS. ....	37
5.5 UNIAXIAL STRAIN TESTS. ....	38

## TABLE OF CONTENTS (Continued)

Section	Page
6 MECHANICAL PROPERTY TESTS ON JOINTED LIMESTONE SPECIMENS . . . . .	58
6.1 TEST PROCEDURES. . . . .	58
6.2 STRENGTH TEST RESULTS. . . . .	59
6.3 JOINT DEFORMATION. . . . .	63
7 EFFECTS OF VARIATIONS IN DEFORMATION RATE . . . . .	83
7.1 STRAIN RATE TESTS ON INTACT SALEM LIMESTONE . . . . .	83
7.1.1 Numerical Simulations of Intact Tests . . . . .	84
7.2 STRAIN RATE TESTS ON JOINTED SALEM LIMESTONE . . . . .	86
8 SATURATED UNDRAINED HYDROSTATIC COMPRESSION TEST AND SPECIFIC STORAGE MEASUREMENT . . . . .	103
8.1 TEST PROCEDURES. . . . .	103
8.2 TEST RESULTS. . . . .	104
8.3 RATIO BETWEEN PORE PRESSURE AND HYDROSTATIC STRESS . . . . .	104
8.4 SPECIFIC STORAGE. . . . .	106
9 PERMEABILITY OF INTACT AND JOINTED LIMESTONE . . . . .	116
9.1 DESCRIPTION OF EXPERIMENT. . . . .	116
9.1.1 Test Specimens, Equipment, and Instrumentation. . . . .	117
9.1.2 Test Procedures. . . . .	118
9.1.3 Fluid Flow Equations. . . . .	119
9.2 PERMEABILITY OF INTACT SALEM LIMESTONE. . . . .	122
9.2.1 Flow Tests with Hydrostatic Skeleton Loading. . . . .	122
9.2.2 Flow Tests with Triaxial Skeleton Loading. . . . .	124
9.3 PERMEABILITY OF JOINTED SALEM LIMESTONE SPECIMENS . . . . .	125
9.3.1 Joint Permeability Formulations. . . . .	126
9.3.2 Tensile Fracture Joint Permeability Test Results . . . . .	127
9.3.3 Smooth Ground Joint Permeability Test Results . . . . .	132
9.3.4 Synthetic Joint Permeability Test Results . . . . .	133
10 NUMERICAL SIMULATION OF ROCK JOINT RESPONSE . . . . .	181
10.1 THEORETICAL DERIVATION OF ELASTOPLASTIC RESPONSE OF JOINTS . . . . .	181
10.1.1 Notations . . . . .	181
10.1.2 Total Strain Increment . . . . .	183
10.1.3 Elastic Stress-Strain Relationship . . . . .	183
10.1.4 Yield Equation . . . . .	184
10.1.5 Flow Rule . . . . .	185
10.1.6 Normal to the Yield Function . . . . .	186
10.1.7 Consistency Equation . . . . .	186
10.1.8 Formulation of Elastoplastic Stress-Strain Matrix . . . . .	187

## TABLE OF CONTENTS (Continued)

Section	Page
10.2 EVALUATION OF MODEL PARAMETERS FOR TENSILE FRACTURE JOINTS OF SALEM LIMESTONE . . . . .	188
10.2.1 Elastic Constants . . . . .	189
10.2.2 Joint Compressibility . . . . .	189
10.2.3 Peak and Residual Shear Strength Parameter . . . . .	191
10.2.4 Strain Softening Parameter . . . . .	192
10.2.5 Plastic Potential Parameters . . . . .	192
10.3 VERIFICATION PROBLEM . . . . .	193
10.4 CONCLUSIONS RELATED TO JOINT SIMULATION . . . . .	194
11 ASTM/ISR INTERLABORATORY TEST PROGRAM . . . . .	207
11.1 SPECIMEN PREPARATION AND MEASUREMENT . . . . .	207
11.1.1 Phase 1 Specimen Preparation . . . . .	208
11.1.2 Phase 2 Specimen Preparation . . . . .	208
11.2 ULTRASONIC WAVESPEED MEASUREMENTS . . . . .	209
11.3 UNCONFINED COMPRESSION TESTS . . . . .	209
11.4 SPLITTING TENSILE STRENGTH TESTS . . . . .	210
11.5 TRIAXIAL COMPRESSION TESTS . . . . .	210
12 SUMMARY AND CONCLUSIONS . . . . .	228
13 REFERENCES . . . . .	232
 Appendix	 Page
A PROFILES OF JOINT SURFACES . . . . .	A-1
B UNCONFINED COMPRESSIVE TESTS WITH POST FAILURE RESPONSE . . . . .	B-1
C TRIAXIAL COMPRESSION TESTS ON INTACT SPECIMENS . . . . .	C-1
D HYDROSTATIC COMPRESSION TESTS . . . . .	D-1
E UNIAXIAL STRAIN TESTS . . . . .	E-1
F ASTM/ISR INTERLABORATORY COMPARISON TESTS . . . . .	F-1

## FIGURES

Figure		Page
3-1	Photographs of the three types of surfaces used in joint testing . . . . .	14
3-2	Layout of the profile lines for characterization of joint surfaces on shear test specimens . . . . .	15
3-3	Typical profiles of a tensile fracture joint . . . . .	16
3-4	Typical profiles of a synthetic joint . . . . .	17
3-5	FFT amplitudes of three typical tensile fracture joint profiles . . . . .	18
3-6	FFT amplitudes of three typical synthetic joint profiles . . . . .	19
3-7	Comparison of the average FFT amplitudes of ten profiles each on a tensile fracture joint and a synthetic joint . . . . .	20
4-1	Schematic of preparation and instrumentation of triaxial specimens . . . . .	28
4-2	Schematic of system for saturation of porous triaxial test specimens . . . . .	29
5-1	Illustration of the relationship between water content and unconfined strengths in Salem limestone . . . . .	42
5-2	Schematic of the stiffener ring used in tests to determine post-failure response of Salem limestone in unconfined compression . . . . .	43
5-3	Overlay of six axial stress-strain curves including post-failure response of Salem limestone in unconfined compression . . . . .	44
5-4	Comparison of axial stress-strain curves for Salem limestone tested in triaxial compression at a range of confining pressure in the brittle regime . . . . .	45
5-5	Strength data from triaxial compression tests on intact Salem limestone specimens at confining pressures ranging from zero to 400 MPa . . . . .	46
5-6	Strength data from triaxial compression tests on intact Salem limestone specimens at confining pressures ranging from zero to 25 MPa . . . . .	47
5-7	Comparison of pre-failure response of Salem limestone tested in triaxial compression at 25 MPa confining pressure under three different test conditions . . . . .	48



## FIGURES (Continued)

Figure	Page
5-8 Relationship between average axial strain and radial strains measured in a 25-MPa triaxial compression test at three different heights on a test specimen with $L/D = 2$ and unlubricated ends . . . . .	49
5-9 Relationship between average axial strain and radial strains measured in a 25-MPa triaxial compression test at three different heights on a test specimen with $L/D = 2$ and lubricated ends . . . . .	50
5-10 Relationship between average axial strain and radial strain measured in a 25-MPa triaxial compression test on a test specimen with $L/D = 1$ and lubricated ends . . . . .	51
5-11 Comparison of volumetric strains computed from 25-MPa triaxial compression under three different test conditions . . . . .	52
5-12 Typical relationship between confining pressure and volumetric strain for intact Salem limestone loaded in hydrostatic compression . . . . .	53
5-13 Typical relationship between axial and radial strain for intact Salem limestone loaded in hydrostatic compression . . . . .	54
5-14 Typical relationship between axial stress and axial strain for intact Salem limestone loaded in uniaxial strain . . . . .	55
5-15 Typical relationship between axial stress and confining pressure for intact Salem limestone loaded in uniaxial strain . . . . .	56
5-16 Typical relationship between mean stress and volumetric (axial) strain for intact Salem limestone loaded in uniaxial strain . . . . .	57
6-1 The relationships between stress difference and gross specimen deformations for specimens of Salem limestone with $\sim 30^\circ$ smooth ground joints tested in triaxial compression at various confining pressures . . . . .	66
6-2 The relationships between stress difference and gross specimen deformations for specimens of Salem limestone with $\sim 30^\circ$ tensile fracture joints tested in triaxial compression at various confining pressures . . . . .	67

## FIGURES (Continued)

Figure		Page
6-3	The relationships between stress difference and gross specimen deformations for specimens of Salem limestone with $\sim 30^\circ$ synthetic joints tested in triaxial compression at various confining pressures . . . . .	68
6-4	The relationships between stress difference and gross specimen deformations for specimens of Salem limestone, both intact and with three types of $\sim 30^\circ$ smooth ground joints, tested in triaxial compression at 1 MPa confining pressure . . . . .	69
6-5	The relationships between stress difference and gross specimen deformations for specimens of Salem limestone, both intact and with three types of $\sim 30^\circ$ smooth ground joints, tested in triaxial compression at 2 MPa confining pressure . . . . .	70
6-6	The relationships between stress difference and gross specimen deformations for specimens of Salem limestone, both intact and with three types of $\sim 30^\circ$ smooth ground joints, tested in triaxial compression at 5 MPa confining pressure . . . . .	71
6-7	The relationships between stress difference and gross specimen deformations for specimens of Salem limestone, both intact and with three types of $\sim 30^\circ$ smooth ground joints, tested in triaxial compression at 10 MPa confining pressure . . . . .	72
6-8	The relationships between stress difference and gross specimen deformations for specimens of Salem limestone, both intact and with three types of $\sim 30^\circ$ smooth ground joints, tested in triaxial compression at 20 MPa confining pressure . . . . .	73
6-9	The relationships between stress difference and gross specimen deformations for specimens of Salem limestone, both intact and with three types of $\sim 30^\circ$ smooth ground joints, tested in triaxial compression at 35 MPa confining pressure . . . . .	74
6-10	Peak strength data for three types of joints in Salem limestone with the strength envelope for intact rock shown for comparison . . . . .	75
6-11	Residual strength data for three types of joints and intact Salem limestone with the peak strength envelopes shown for comparison . . . . .	76

## FIGURES (Continued)

Figure		Page
6-12	Normal and tangential deformations of smooth ground joints in Salem limestone plotted against normal and tangential deformations, respectively, for a range of confining pressure conditions . . . . .	77
6-13	Normal and tangential deformations of tensile fracture joints in Salem limestone plotted against normal and tangential deformations, respectively, for a range of confining pressure conditions . . . . .	78
6-14	Normal and tangential deformations of synthetic joints in Salem limestone plotted against normal and tangential deformations, respectively, for a range of confining pressure conditions . . . . .	79
6-15	Relationship between normal and tangential deformation of smooth ground joints in Salem limestone under a range of confining pressure conditions . .	80
6-16	Relationship between normal and tangential deformation of tensile fracture joints in Salem limestone under a range of confining pressure conditions . .	81
6-17	Relationship between normal and tangential deformation of synthetic joints in Salem limestone under a range of confining pressure conditions . .	82
7-1	Comparison of stress-strain curves from intact unsaturated (2-5% water content) Salem limestone specimens tested in triaxial compression with 20 MPa confining pressure at strain rates of $10^5$ , $10^4$ , and $10^3 \text{ s}^{-1}$ . . . . .	89
7-2	Comparison of stress-strain curves from intact saturated Salem limestone specimens tested in drained triaxial compression with 20 MPa confining pressure at strain rates of $10^5$ and $10^3 \text{ s}^{-1}$ . . . . .	90
7-3	Comparison of stress-strain curves from intact unsaturated (2-5% water content) Salem limestone specimens tested in triaxial compression with 25 MPa confining pressure at strain rates of $10^5$ , $10^4$ , $10^2$ , $\text{s}^{-1}$ . . . . .	91
7-4	Summary of the relationship between strength and strain rate for the test data presented in Figure 7-1 through 7-3 . . . . .	92
7-5	Comparison of mean stress-volume strain curves from intact unsaturated (2-5% water content) Salem limestone specimens tested in triaxial compression with 20 MPa confining pressure at strain rates of $10^5$ and $10^3 \text{ s}^{-1}$ . . . . .	93

## FIGURES (Continued)

Figure		Page
7-6	Illustration of the finite element mesh used to simulate the saturated drained tests on intact limestone specimens . . . . .	94
7-7	Mean stress and pore pressure as functions of volume strain from a numerical simulation of the saturated drained 20-MPa triaxial compression test at $10^{-5}$ s $^{-1}$ strain rate, showing the measured mean stress for comparison . . . . .	95
7-8	Mean stress and pore pressure as functions of volume strain from a numerical simulation of the saturated drained 20-MPa triaxial compression test at $10^{-3}$ s $^{-1}$ strain rate, showing the measured mean stress for comparison . . . . .	96
7-9	Comparison of stress-strain curves from 30° tensile fracture jointed Salem limestone specimens tested in triaxial compression with 20 MPa confining pressure at strain rates of $10^{-5}$ and $10^{-3}$ s $^{-1}$ and different initial saturation conditions . . . . .	97
7-10	Comparison of stress-strain curves from 30° smooth ground jointed Salem limestone specimens tested in triaxial compression with 20 MPa confining pressure at strain rates of $10^{-5}$ and $10^{-3}$ s $^{-1}$ and different initial saturation conditions . . . . .	98
7-11	Comparison of stress-strain curves from 30° synthetic jointed Salem limestone specimens tested in triaxial compression with 20 MPa confining pressure at strain rates of $10^{-5}$ and $10^{-3}$ s $^{-1}$ and different initial saturation conditions . . . . .	99
7-12	Comparison of the strengths of tensile fracture joints tested at various strain rates and initial saturation conditions with the strength envelope for the same type joints tested unsaturated at $10^{-4}$ s $^{-1}$ strain rate . . . . .	100
7-13	Comparison of the strengths of smooth ground joints tested at various strain rates and initial saturation conditions with the strength envelope for the same type joints tested unsaturated at $10^{-4}$ s $^{-1}$ strain rate . . . . .	101
7-14	Comparison of the strengths of synthetic joints tested at various strain rates and initial saturation conditions with the strength envelope for the same type joints tested unsaturated at $10^{-4}$ s $^{-1}$ strain rate . . . . .	102

## FIGURES (Continued)

Figure	Page
8-1 Results of test in which a saturated specimen of Salem limestone was loaded hydrostatically to 138 MPa without drainage and then allowed to drain, showing total stress, effective stress, and pore pressure . . . . .	109
8-2 Relationship between axial and radial skeleton strain from the test shown in Figure 8-1 . . . . .	110
8-3 The relationship between pore pressure and the volume of drained water for a Salem limestone specimen that were first saturated and loaded hydrostatically to 138 MPa without drainage . . . . .	111
8-4 Comparison between the results of a saturated undrained hydrostatic compression test on Salem limestone with a numerical simulation based on drained rock skeleton properties . . . . .	112
8-5 Comparison of the pore to confining pressure ratios from two tests with the results of a numerical simulation based on drained rock skeleton properties . . . . .	113
8-6 Comparison of the pore to confining pressure ratios resulting from numerical simulations with different initial pressure ratios . . . . .	114
8-7 The relationship between specific storage and effective stress resulting from two tests and a numerical simulation based on drained rock skeleton properties . . . . .	115
9-1 Schematic section of permeability test apparatus . . . . .	151
9-2 Typical upstream pore pressure time history . . . . .	152
9-3 Typical intensifier displacement time history, which is proportional to pore fluid displacement . . . . .	153
9-4 High-pressure permeability measurements on intact limestone under hydrostatic loading illustrating the linear and quadratic dependence of pressure gradient on apparent fluid velocity . . . . .	154
9-5 The linear flow coefficient, $a$ , for Forchheimer's equation as a function of effective stress in the rock skeleton . . . . .	155

## FIGURES (Continued)

Figure		Page
9-6	The quadratic flow coefficient, $b$ , for Forchheimer's equation as a function of effective stress in the rock skeleton . . . . .	156
9-7	High-pressure permeability measurements on intact limestone under hydrostatic loading illustrating the linear approximation of the dependence of pressure gradient on apparent fluid velocity . . . . .	157
9-8	Absolute permeability of intact limestone under hydrostatic loading as a function of effective stress in the rock skeleton . . . . .	158
9-9	Absolute permeability of intact limestone under hydrostatic loading as a function of volumetric strain in the rock skeleton . . . . .	159
9-10	Absolute permeability of intact limestone under hydrostatic loading as a function of effective stress in the rock skeleton . . . . .	160
9-11	Illustration of the relationship between the mechanical response and permeability of limestone subjected to triaxial compression at 5 MPa . . . .	161
9-12	Illustration of the relationship between the mechanical response and permeability of limestone subjected to triaxial compression at 10 MPa . . .	162
9-13	Illustration of the relationship between the mechanical response and permeability of limestone subjected to triaxial compression at 20 MPa . . .	163
9-14	Typical set of permeability measurements on a limestone specimen with a tensile fracture joint under hydrostatic loading illustrating the linear approximation of the dependence of pressure gradient on apparent fluid velocity . . . . .	164
9-15	Measured variation in permeability with confining pressure for two different intact limestone specimens showing fits each test and the average of the two fits . . . . .	165
9-16	Equivalent permeability measurements from a limestone specimen with a tensile fracture joint (G5A2) compared with the fits to the two intact permeability tests shown in Figure 9-15 . . . . .	166
9-17	Data used in the derivation of joint permeabilities for a tensile fracture joint, Test G5A2 . . . . .	167

## FIGURES (Continued)

Figure	Page
9-18 Data used in the derivation of joint permeabilities for a tensile fracture joint, Test U30A2 . . . . .	168
9-19 Data used in the derivation of joint permeabilities for a tensile fracture joint, Test A15A2 . . . . .	169
9-20 Data used in the derivation of joint permeabilities for a tensile fracture joint, Test OAA282 . . . . .	170
9-21 Data used in the derivation of joint permeabilities for a tensile fracture joint, Test OAA302 . . . . .	171
9-22 Summary of the relationships between joint permeability, $\kappa_j$ , and confining pressure for five tensile fracture joint tests . . . . .	172
9-23 Measured normal deformations of two tensile fracture joints and the derived joint aperture values . . . . .	173
9-24 Relationship between joint permeability and joint aperture to two tensile fracture joints . . . . .	174
9-25 Set of permeability measurements on a limestone specimen with a smooth ground joint under hydrostatic loading illustrating the linear approximation of the dependence of pressure gradient on apparent fluid velocity . . . . .	175
9-26 Data used in the derivation of joint permeabilities for a smooth ground joint, Test L15A2 . . . . .	176
9-27 Relationship between joint permeability, $\kappa_j$ , and confining pressure for a smooth ground joint test . . . . .	177
9-28 Set of permeability measurements on a limestone specimen with a synthetic joint under hydrostatic loading illustrating the dependence of pressure gradient on apparent fluid velocity . . . . .	178
9-29 Data used in the derivation of joint permeabilities for a synthetic joint, Test L20A2 . . . . .	179

## FIGURES (Continued)

Figure		Page
9-30	Relationship between joint permeability, $\kappa_j$ , and confining pressure for a synthetic joint test . . . . .	180
10-1	Illustration of the yield and strength envelopes for the joint model . . . . .	196
10-2	Measured joint roughness profile that was used to derive the joint thickness . . . . .	197
10-3a	Axial deformation measurements from an unconfined normal compressibility test on a tensile fracture joint . . . . .	198
10-3b	Joint compressibility curve derived from the data shown in Figure 10-3a . . . . .	198
10-4	Nonlinear elastic modulus curve derived from the data shown in Figure 10-3a, assuming a joint thickness of 0-74 mm . . . . .	199
10-5	Strength data from triaxial compression tests on 30° jointed Salem limestone specimens (Ref. Chitty and Blouin, 1992) with fits used to derive the strength parameters for the joint model . . . . .	200
10-6	Relationships between joint shear stress and plastic work derived from triaxial compression tests at various confining pressures on 30° tensile fracture jointed specimens of Salem limestone . . . . .	201
10-7	Definition of strain softening parameters during joint shear . . . . .	202
10-8	The relationship between normal and tangential joint displacement for tensile fracture joints in Salem limestone loaded in triaxial compression at a range of confining pressures . . . . .	203
10-9	Direction of the plastic strain vector as a function of confining pressure . . . . .	204
10-10	Stress paths computed from a specified strain loading for tensile fracture joints by the model . . . . .	205
10-11	Relationships between joint shear stress and plastic work computed for tensile fracture joints by the model . . . . .	206



## TABLES

Table		Page
2-1	Physical properties of Salem limestone blocks from which specimens were prepared . . . . .	7
2-2	Ultrasonic wavespeeds of Salem limestone specimens from the various blocks . . . . .	7
6-1	Summary of mechanical property tests on jointed Salem limestone specimens . . . . .	65
9-1	Summary of high-pressure permeability tests on intact Salem limestone under hydrostatic loading . . . . .	135
9-2	Summary of low-pressure permeability tests on intact Salem limestone under hydrostatic loading . . . . .	136
9-3	Summary of low-pressure permeability tests on intact Salem limestone under hydrostatic loading (second specimen) . . . . .	137
9-4	Summary of permeability tests on intact Salem limestone loaded in triaxial compression at 5 MPa confining pressure . . . . .	138
9-5	Summary of permeability tests on intact Salem limestone loaded in triaxial compression at 10 MPa confining pressure . . . . .	139
9-6	Summary of permeability tests on intact Salem limestone loaded in triaxial compression at 10 MPa confining pressure (repeat test) . . . . .	140
9-7	Summary of permeability tests on intact Salem limestone loaded in triaxial compression at 20 MPa confining pressure . . . . .	141
9-8	Summary of permeability tests on intact Salem limestone loaded in triaxial compression at 50 MPa confining pressure . . . . .	142
9-9	Summary of permeability tests on intact Salem limestone loaded in triaxial compression at 90 MPa confining pressure . . . . .	143
9-10	Summary of permeability tests on a tensile fracture jointed Salem limestone specimen (A15A2) . . . . .	144
9-11	Summary of permeability tests on a tensile fracture jointed Salem limestone specimen (U30A2) . . . . .	145

## TABLES (Continued)

Table	Page
9-12 Summary of permeability tests on a tensile fracture jointed Salem limestone specimen (G5A2) . . . . .	146
9-13 Summary of permeability tests on a tensile fracture jointed Salem limestone specimen (OAA282) . . . . .	147
9-14 Summary of permeability tests on a tensile fracture jointed Salem limestone specimen (OAA302) . . . . .	148
9-15 Summary of permeability tests on a smooth ground jointed Salem limestone specimen . . . . .	149
9-16 Summary of permeability tests on a synthetic jointed Salem limestone specimen with synthetic fracture . . . . .	150
10-1 Plastic work at $s=0.5$ tabulated as a function of normal stress . . . . .	195
11-1 Summary of ultrasonic wavespeed measurements on Barre granite . . . . .	213
11-2 Summary of ultrasonic wavespeed measurements on Berea sandstone . . . . .	214
11-3 Summary of ultrasonic wavespeed measurements on Salem limestone . . . . .	215
11-4 Summary of ultrasonic wavespeed measurements on Tennessee marble . . . . .	216
11-5 Summary of unconfined compression test data for Barre granite . . . . .	217
11-6 Summary of unconfined compression test data for Berea sandstone . . . . .	218
11-7 Summary of unconfined compression test data for Salem limestone . . . . .	219
11-8 Summary of unconfined compression test data for Tennessee marble . . . . .	220
11-9 Splitting tensile strength data for Barre granite . . . . .	221
11-10 Splitting tensile strength data for Berea sandstone . . . . .	222
11-11 Splitting tensile strength data for Salem limestone . . . . .	223
11-12 Splitting tensile strength data for Tennessee marble . . . . .	224
11-13 Summary of triaxial compression test results on Barre granite . . . . .	225

## TABLES (Continued)

Table		Page
11-14	Summary of triaxial compression test results on Berea sandstone . . . . .	226
11-15	Summary of triaxial compression test results on Tennessee marble . . . . .	227

## **SECTION 1**

### **INTRODUCTION**

This report presents the results of a research project that included laboratory testing and analysis of the response of porous limestone to various load conditions, including high-pressure loading of intact rock, shear loading of man-made rock joints, and fluid flow through intact and jointed rock. This research was conducted by Applied Research Associates, Inc. (ARA) under Contract No. DNA001-90-C-0132 with the Defense Nuclear Agency (DNA). The tests were conducted by the Materials Testing Laboratory of the New England Division of ARA in South Royalton, Vermont during the period August 1990 through September 1992.

#### **1.1 BACKGROUND.**

DNA has a requirement to develop a high-confidence method for predicting structural hardness for use in the assessment of survivability and vulnerability of deep underground facilities. The DNA Underground Technology Program (UTP) will develop such a methodology through combined theoretical, analytical, and experimental activities. This method will be embodied in a mathematical model for structural deformation and failure that accounts for parameters such as ground shock waveform (e.g. rise time, peak stress, duration, and flow field), facility depth, rock mass properties, and rock opening dimensions and reinforcement. A credible weapons attack on a deep underground facility cannot be simulated at full scale because of environmental and treaty limitations. Therefore, the method will be developed on the basis of data from field tests performed at several scales and a fundamental understanding of scaling of structural response in rock masses.

#### **1.2 OBJECTIVES.**

The objectives of the research effort reported herein were to:

- 1) measure rock joint stiffness and strength under normal and shear loading;

- 2) measure fluid flow along joints and through pore space under high pressure gradients;
- 3) develop mathematical models based on these measurements,
- 4) assess the influence of deformation rate on the mechanical properties of limestone; and
- 5) develop a database that will contribute to the development of statements of precision and bias for standard rock test methods.

### 1.3 SCOPE.

In order to satisfy the stated objectives, rock specimens were prepared and an extensive series of laboratory tests was performed, including a variety of specimen and loading configurations.

The body of the report contains descriptions of the laboratory work performed along with summarized results and analyses of the resulting data. Section 2 describes the porous limestone used for the majority of the test work, including its physical properties. A general discussion of test equipment and methods is given in Section 3. Since many different types of tests were performed in the course of this effort, details of specific testing are included in the individual sections where the test results are reported. Section 4 presents the techniques used to prepare the test specimens with man-made joint surfaces. Tests conducted for the purpose of mechanical characterization of the intact material are described in Section 5. The results of the mechanical property tests that were performed on jointed specimens are presented in Section 6, and the investigation of the influence of deformation rate is documented in Section 7. Section 8 presents the results of a series of tests and numerical simulations of compressibility of saturated undrained Salem limestone. The results of the high-pressure fluid flow measurements are presented in Section 9. Numerical modeling of the various tests is described in Section 10. Section 11 describes ARA's participation in an interlaboratory test program conducted under the direction of the American Society for Testing and Materials, Institute for Standards Research (ASTM/ISR)

for the purpose of developing precision and bias statements for standard rock test methods. Conclusions and recommendations are presented in Section 12, followed by references in Section 13. Plots of selected response quantities from the individual tests are included in the various appendices.

## SECTION 2

### SALEM LIMESTONE ORIGIN, DESCRIPTION, AND PHYSICAL PROPERTIES

With the exception of the test work conducted for the ASTM/ISR interlaboratory test program which is documented in Section 8, all of the laboratory experiments were performed on specimens made of Salem limestone, a porous material from Indiana. This Section documents the origin and physical properties of the material and presents the results of tests performed to characterize the mechanical properties of the intact material.

#### 2.1 ORIGIN AND DESCRIPTION.

The rock used in this test program was a porous limestone from the Salem formation in Indiana. The limestone was originally purchased by ARA for the US Army Engineer Waterways Experiment Station (WES) from the Elliot Stone Company in Bedford, Indiana. The particular block from which the specimen material was derived was designated EEC58 by Elliot. Quarry block EEC58 was sawn into approximately 72 smaller blocks having dimensions of approximately 228 mm x 356 mm x 406 mm, with the 356 mm x 406 mm face parallel with the natural horizontal bedding. The small blocks were shipped directly from the quarry to WES in Vicksburg, Mississippi for distribution to the various laboratories involved in the UTP and the interlaboratory test program. ARA received a total of four of the smaller (228 mm x 356 mm x 406 mm) blocks of Salem limestone from WES. At ARA, three of the four were split into two sub-blocks for easier handling, and those six sub-blocks were assigned ARA laboratory identifiers of SL-20 through SL-25. The fourth was assigned the identifier SL-26 and cut into pieces from which individual specimens were prepared.

The Salem limestone is a fine-grained porous material of very light gray color (Goddard, et al., 1948). The four blocks received were very homogeneous in appearance with no noticeable cracks, voids or other imperfections. All of the cylindrical test specimens were cut with their axes perpendicular to the bedding planes.

## 2.2 PHYSICAL PROPERTIES.

The grain density of the solid mineral portion of the rock, excluding all pore spaces was measured using a variation of the procedure presented in ASTM D854-83, which is briefly described as follows. A sample of rock was crushed into particles small enough to pass a No. 70 U.S. Standard sieve (0.210 mm). The resulting powder was oven dried, weighed, and its volume was then determined by the mass of de-aired distilled water it displaced. The volume measurement was made using a precision indexed flask, and corrected for temperature. At least one grain density determination was made on each of the four blocks that were used for testing. The results are presented in Table 2.1. The average measured grain density was 2.71 Mg/m<sup>3</sup> for blocks SL-20/21 and SL-22/23, and for blocks SL-24/25 and SL-26, the grain density was slightly lower at 2.70 Mg/m<sup>3</sup>.

In order to determine the porosities of the sample materials, oven dry bulk densities were determined by measuring the gross dimensions and oven-dry masses of right cylindrical specimens with flat ground ends. The dry bulk density values reported in Table 2.1 are averages of measurements on ten specimens from each block. The standard deviations on dry bulk density are of the order of 0.005 Mg/m<sup>3</sup>.

The porosity,  $n$ , was then computed as follows:

$$n = \frac{\rho_g - \rho_b}{\rho_g} \quad (2.1)$$

where:  $\rho_g$  = grain density  
 $\rho_b$  = dry bulk density

The values of porosity presented in Table 2.1 were computed individually by block from the measured grain density and the average value of dry bulk density. The porosities of the materials tested ranged from 0.162 to 0.171.



Ultrasonic wavespeeds were determined on representative specimens from each block. An ultrasonic transducer was placed on either side of the specimen. One transducer was excited by a step function generator and the other was used to detect the arriving pulse. A 20-MHz digital storage oscilloscope was used to measure the transit time. The transducer frequencies were 670 kHz and 2.25 MHz for the compression and shear wavespeed determinations, respectively. Compressional wavespeed measurements were made both perpendicular and parallel to the bedding planes of the limestone. Since the measurements were made on the prepared cylindrical specimens, it was not possible to make good shear wave measurements on the cylindrical surface parallel to the bedding planes, and shear wavespeeds were measured only in the parallel direction. The average measured compressional wavespeeds were 4.14 and 4.10 km/s in the directions perpendicular and parallel to the bedding planes, respectively. The average measured shear wavespeed was 2.38 km/s. Table 2.2 presents details of the wavespeed results.

**Table 2-1. Physical properties of Salem limestone blocks from which specimens were prepared.**

Block	ARA Lab ID	Grain Density (Mg/m <sup>3</sup> )	Dry Bulk Density (Mg/m <sup>3</sup> )	Porosity
EEC58	SL-20/21	2.709	2.252	0.169
EEC58	SL-22/23	2.708	2.246	0.171
EEC58	SL-24/25	2.701	2.264	0.162
EEC58	SL-26	2.701	2.26	0.163

**Table 2-2. Ultrasonic wavespeeds of Salem limestone specimens from the various blocks.**

ARA Lab ID	Compressional Wavespeed (km/s)		Shear Wavespeed (km/s) Perpendicular
	Perpendicular	Parallel	
SL-20/21	4.16	4.12	2.43
SL-22/23	4.16	4.07	2.43
SL-24/25	4.14	4.20	2.34
SL-26	4.08	4.01	2.33

**NOTE:** Parallel and Perpendicular designations are relative to the limestone bedding planes.

## SECTION 3

### JOINT SURFACE PREPARATION

For the joint tests, rock surfaces were prepared using three different techniques, as described in the following paragraphs. Shear test specimens were prepared with a single joint oriented  $30^\circ$  to the cylinder axis. For fluid flow tests, the specimens were prepared with a single joint parallel to the specimen axis, approximately along the diameter of the specimen. This section describes the fabrication of the man-made joint surfaces and the characterization of those surfaces using measurements made with a laser profilometer.

#### 3.1 JOINT SURFACE FABRICATION.

Three types of joint surfaces were fabricated for testing under this program, smooth ground, tensile fracture surfaces, and surfaces machined to specified fractal dimensions. This subsection describes the techniques used to create the three different surface types. Photographs of the three surface types are presented in Figure 3-1.

##### 3.1.1 Smooth Ground Joint Surfaces.

The simplest of the three joint surface types was ground smooth, but not polished. Initially, a block of limestone was cut slightly larger than the intended specimen dimensions. While still in the form of a block, a joint was sawn at the required angle. Each half, in turn, was fixtured on a surface grinder where the joint surface was ground using a 170 grit diamond wheel. The two ground surfaces were then glued together with a water soluble adhesive (common white glue diluted with water). After the glue had set, the cylindrical specimen was cut from the glued block using a diamond coring bit. The specimen thus formed was cut to length and its ends ground on the surface grinder. The final step in the process was to dissolve the glue in water and clean any glue residue from the rock surface.

### 3.1.2 Tensile Fracture Joint Surfaces.

As with the fabrication of jointed specimens, this procedure began with preparation of a block of limestone slightly larger than the specimen dimensions. Instead of cutting the block in two, it was lightly scored (approx. 3 mm deep) with a diamond blade where the joint to be formed intersected the surfaces of the block. The block was then split between knife edges seated in the saw cuts on opposite sides of the block. The rest of the procedure consisted of gluing, coring, cutting, grinding, and dissolving the glue as was done for the smooth ground joints and described in Section 3.1.1.

### 3.1.3 Synthetic Joint Surfaces.

We have used the term *synthetic joint* to refer to a surface manufactured using numerically controlled machine tools in accordance with a numerical map derived from a spectral representation of a fractal surface. Various authors (Brown and Scholz, 1985; Brown, 1987; Power and Tullis, 1991) have proposed the use of fractals to describe rock surface roughness. To our knowledge, fabrication of such a joint has not previously been attempted.

A modified version of a computer program by Brown (1991) was used to numerically define the synthetic joint surfaces. That program implements an algorithm presented by Saupe (1988) in which discrete Fourier coefficients are defined in two dimensions and then transformed using a two dimensional inverse discrete Fourier transform. The relative amplitudes of the Fourier coefficients,  $a_{ij}$ , were defined in terms of one quantity, the fractal dimension,  $D_f$  by:

$$|a_{ij}| = (i^2 + j^2)^{-(4-D_f)/2} \quad (3.1)$$

where  $i$  and  $j$  are the indices of the frequencies in two orthogonal directions in the plane of the surface. The phases of the Fourier coefficients were assigned random numbers uniformly distributed between 0 and  $2\pi$  radians, and the necessary symmetry conditions were applied in formulating the Fourier coefficients to assure that the resulting surface function is real (i.e., no imaginary component). The multi-dimensional Fast Fourier Transform subroutine, FOURN, presented by Press, et al. (1986) was used to compute the surface map from the Fourier coefficients.

After the shape of the surface was computed, its amplitude was scaled by a multiplicative scale factor. In the literature, the amplitude of a rough surface is often specified in terms of its standard deviation, which is simply the standard deviation of the data set consisting of the surface height at each point on a square grid of fine enough spacing to represent the frequency content of the surface. This measure of surface roughness can be somewhat deceptive because its value for a given fractal surface is dependent on the in-plane extent of the area considered. To understand this, consider the two-dimensional problem of roughness imposed on a straight line. If the roughness is simply sinusoidal with constant frequency and amplitude, then the standard deviation of the height of roughness is independent of sample size as long as a large enough sample is taken to average over several cycles. However, if the surface is fractal, there is some amplitude at all frequencies (obviously, this has some limits in representing real surfaces) and the amplitude increases with decreasing frequency. For a given fractal dimension and amplitude, a larger sample will contain lower frequencies and thus larger amplitudes.

The specific surfaces reported here were generated from a  $1024 \times 1024$  matrix of complex Fourier coefficients derived using  $D_f = 2.5$ , resulting in a  $1024 \times 1024$  surface function. It was scaled to have a standard deviation of 1.58 mm and then truncated to  $320 \times 640$  points and assigned a point spacing of 0.20 mm, corresponding to a 64-mm  $\times$  128-mm surface.

Once the numerical surface map was computed, a second program was used to generate instructions for a numerically controlled three-axis milling machine. This involves consideration in three dimensions, of the shape of the cutter relative to the rough surface. The frequency content of the surface map generated with 0.20-mm point spacing includes concave regions with radii too small to be cut with the available tooling. Thus, for each cutter movement, all map points within the radius of the cutter were checked to compute the new cutter position based on the criterion that no extra material be removed. As a result, some material that the numerical map specified for removal was left in the bottoms of the small-radius concave regions because the tool was too large to reach it. This results in imperfect mating of the portions of the surface that could be cut by the tool. In hindsight, some other criterion might have given better results.

The surfaces used in this work were machined in two passes. On the first, a 1/8-inch (approx. 3 mm) diameter solid carbide ball end mill was used with the geometry specified at points spaced 0.80 mm each way while ensuring that no extra material was removed at the intermediate positions. On the second pass, points were specified at the original 0.20-mm spacing and a 1/32-inch (approx. 0.8-mm) cutter of the same type was used. The overall procedure for fabrication of the synthetic joints closely follows the procedure for smooth ground joints described above, except that the surface machining is done in place of grinding.

### **3.2 SURFACE GEOMETRY MEASUREMENT.**

A laser profilometer was assembled for the purpose of measuring the topography of the various rock surfaces. The rock to be profiled is first attached to a fixture on an X-Y table which can be positioned by stepper motors under computer control. The table can be positioned with a resolution of 0.01 mm anywhere in its range. Attached to a static frame above the table is a non-contacting position sensor that measures the height of the rock surface relative to a reference plane. The position sensor is a commercially available unit that works on the principal of laser triangulation. It projects a laser spot downward on the vertical and receives the reflected light at a different angle. Depending on the height of the point where the light is reflected, it is focused on a different portion of the detector. The detector circuit converts the measurement to an analog voltage which is input to a 16-bit analog to digital conversion card in the computer. The system has a vertical resolution of 0.001 mm over a range of 20 mm. The size of the laser spot projected by the non-contacting position sensor is of the order of 0.1 mm. Thus, the spectral amplitudes at frequencies in excess of 10 cycles/mm are probably not accurate.

In order to fully characterize the geometry of a joint surface of the type used for mechanical property and fluid flow testing, it would be necessary to make a large number (of order  $10^6$ ) of height measurements. This was judged to be cost prohibitive. As an alternative, the profiling pattern illustrated in Figure 3-2 was defined. It includes profiles in two perpendicular directions, and consists of ten 2048-point traces, with 0.01-mm spacing between points, arranged in four lines. Figure 3-3 presents measured profiles of a tensile fracture joint.

The profiles are arranged on the plot to suggest the way they were measured, an 82-mm pass along the axis of the specimen and 20.5-mm passes on either side of center, and a 41-mm pass across the narrow dimension of the surface and 20.5 mm passes on either side. Corresponding data are presented for a synthetic joint in Figure 3-4. The profiles shown in Figures 3-3 and 3-4 were processed to determine their spectral characteristics. The data in each figure were separated into six 2048 point (20.5 mm) traces, and the mean was subtracted from each. A Fast Fourier Transform (FFT) was then computed from each 2048 point trace. The FFT computation was performed with the subroutine, FOUR1, from Press, et al. (1986). The values plotted in the figures labeled FFT amplitude are the magnitudes of the complex array,  $H_n$ , defined by:

$$H_n = \sum_{k=0}^{N-1} h_k e^{2\pi i k n / N} \quad (3.2)$$

where:  $h_k$  =  $k^{\text{th}}$  element of surface height array for one line  
 $i$  = the square root of -1  
 $k$  = index of the roughness array  
 $n$  = index of the FFT array  
 $N$  = number of points in profile array (here,  $N = 2048$ )

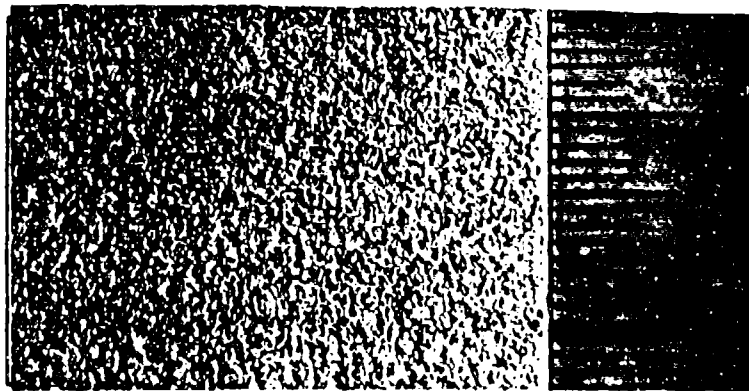
To avoid confusion, the computed FFT amplitudes have not been normalized, and thus their units are mm, the same as the input array. As with the standard deviations of a surface, caution must be exercised in comparing FFT amplitudes as their value for a given surface depends on the size of the input array. The amplitude spectra of three representative transforms are presented in Figures 3-5 and 3-6 for the tensile fracture and synthetic joints, respectively. In those figures, successive traces are offset horizontally by a factor of ten for clarity. There is clearly significant variation between individual traces from the same surface, and many of them would be impossible to fit unambiguously with a straight line. In order to obtain a more representative and useful characterization of the surfaces, all ten FFTs for each surface were averaged at each frequency point. The resulting average spectra are plotted for comparison without shifting in Figure 3-7. The slopes, and thus fractal dimensions, of the two different types of joint surfaces are very similar, but the synthetic joint has higher amplitude by approximately 60%.

Power and Tullis [1991] present the following relationship between the slope of the FFT amplitude spectrum,  $\beta$ , and the fractal dimension:

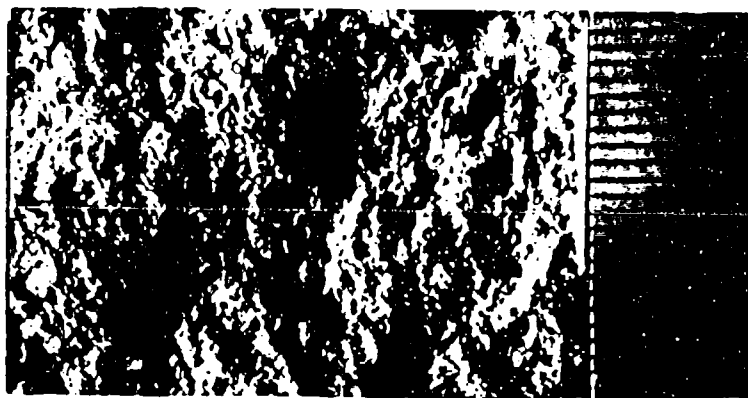
$$D_f = \beta/2 + 2 \quad (3.3)$$

From Figure 3-7, the synthetic surface has a slope of 1.0, corresponding to fractal dimension of 2.5 as specified in construction of the numerical map for machining the surface.

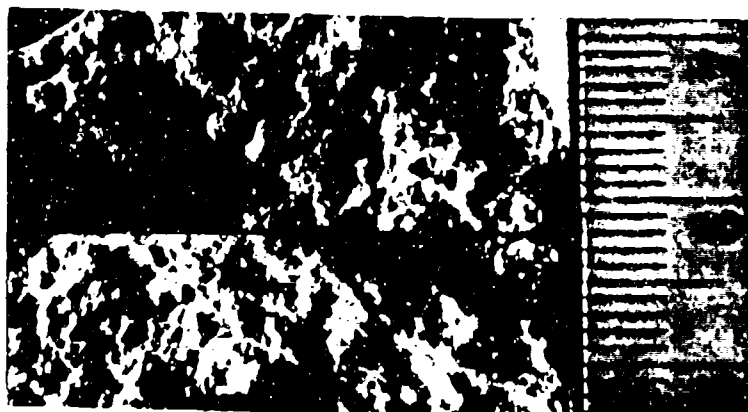




S m o o t h  
Ground



T e n s i l e  
Fracture



Synthetic

Figure 3-1. Photographs of the three types of surfaces used in joint testing.  
The smallest divisions on the rulers are mm.

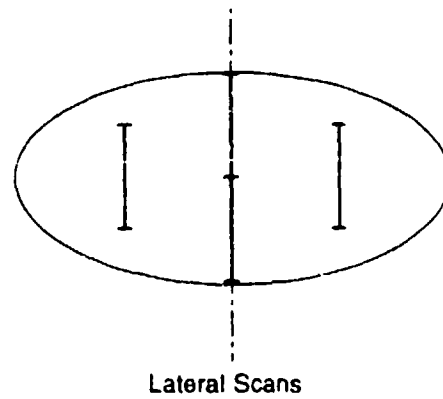
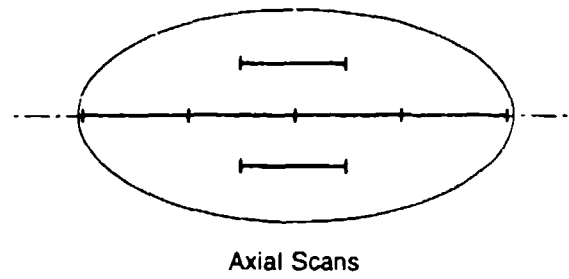
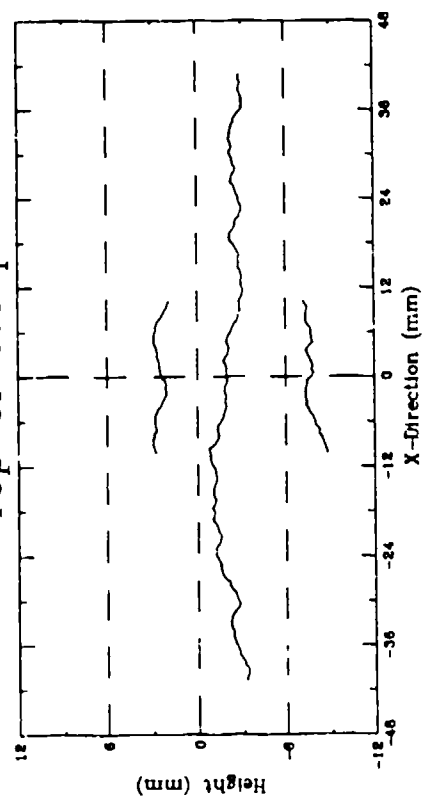


Figure 3-2. Layout of the profile lines for characterization of joint surfaces on shear test specimens.

# Salem Limestone -- M6A2

Top of Sample



Bottom of Sample

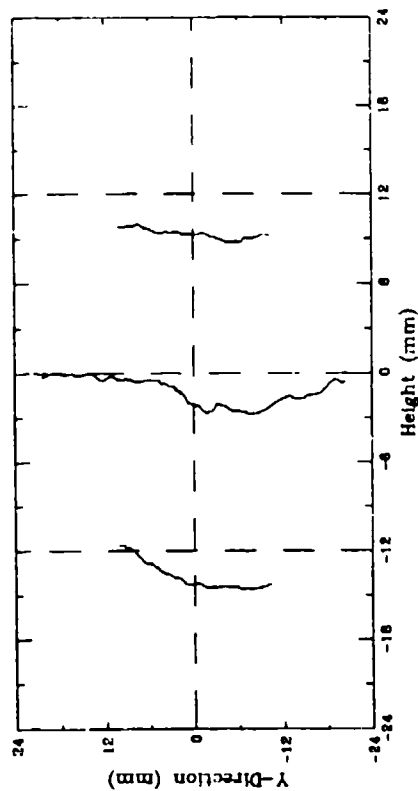
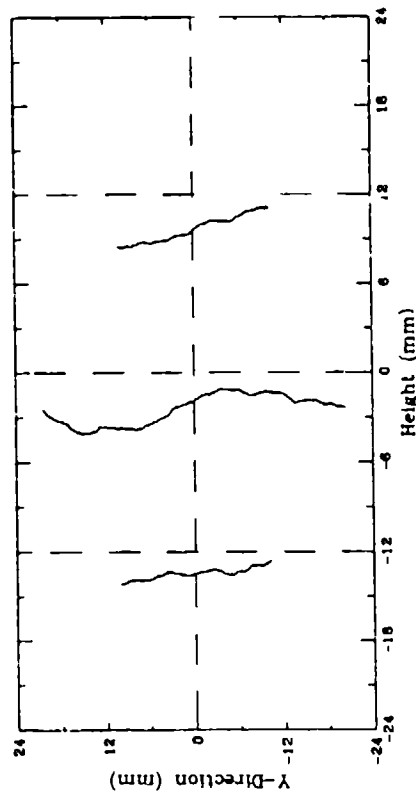
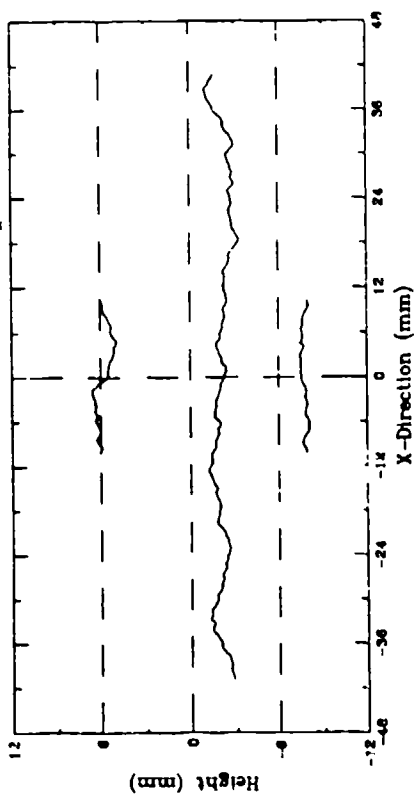
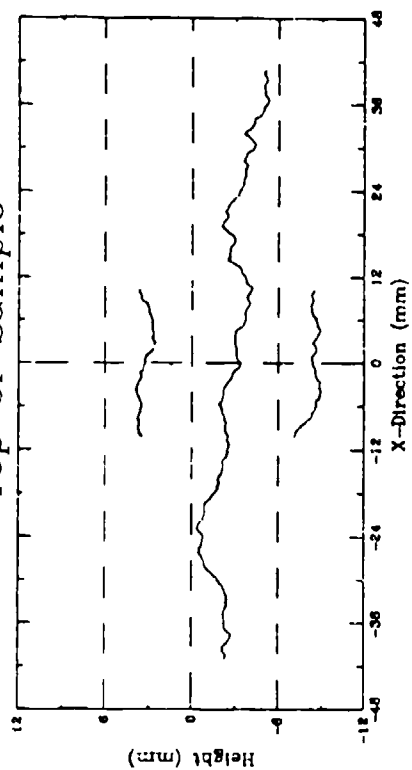


Figure 3-3. Typical profiles of a tensile fracture joint.

# Salem Limestone - M10B2

Top of Sample



Bottom of Sample

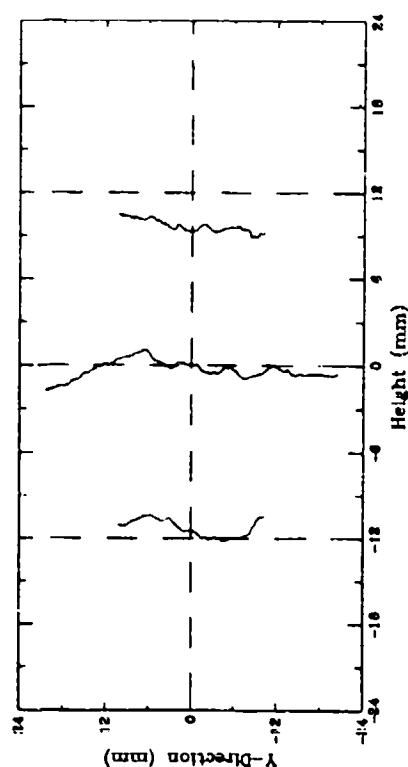
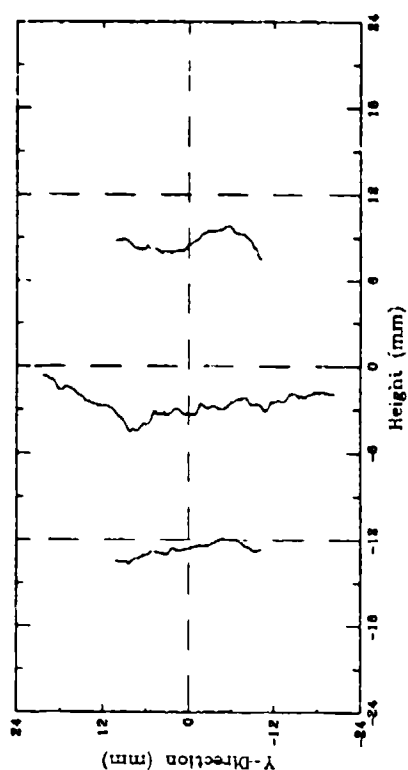
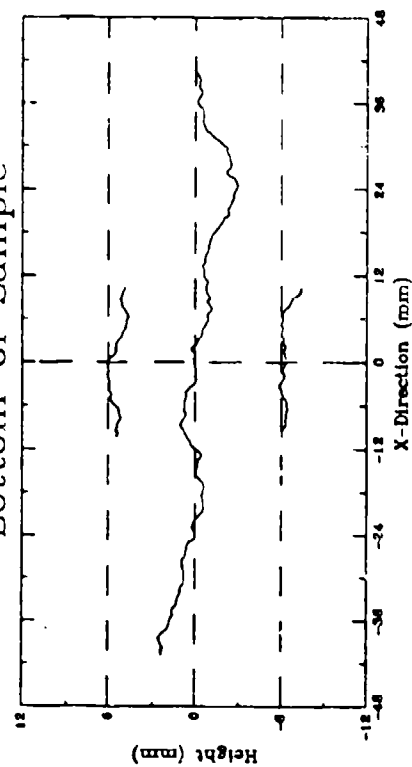


Figure 3-4. Typical profiles of a synthetic joint.

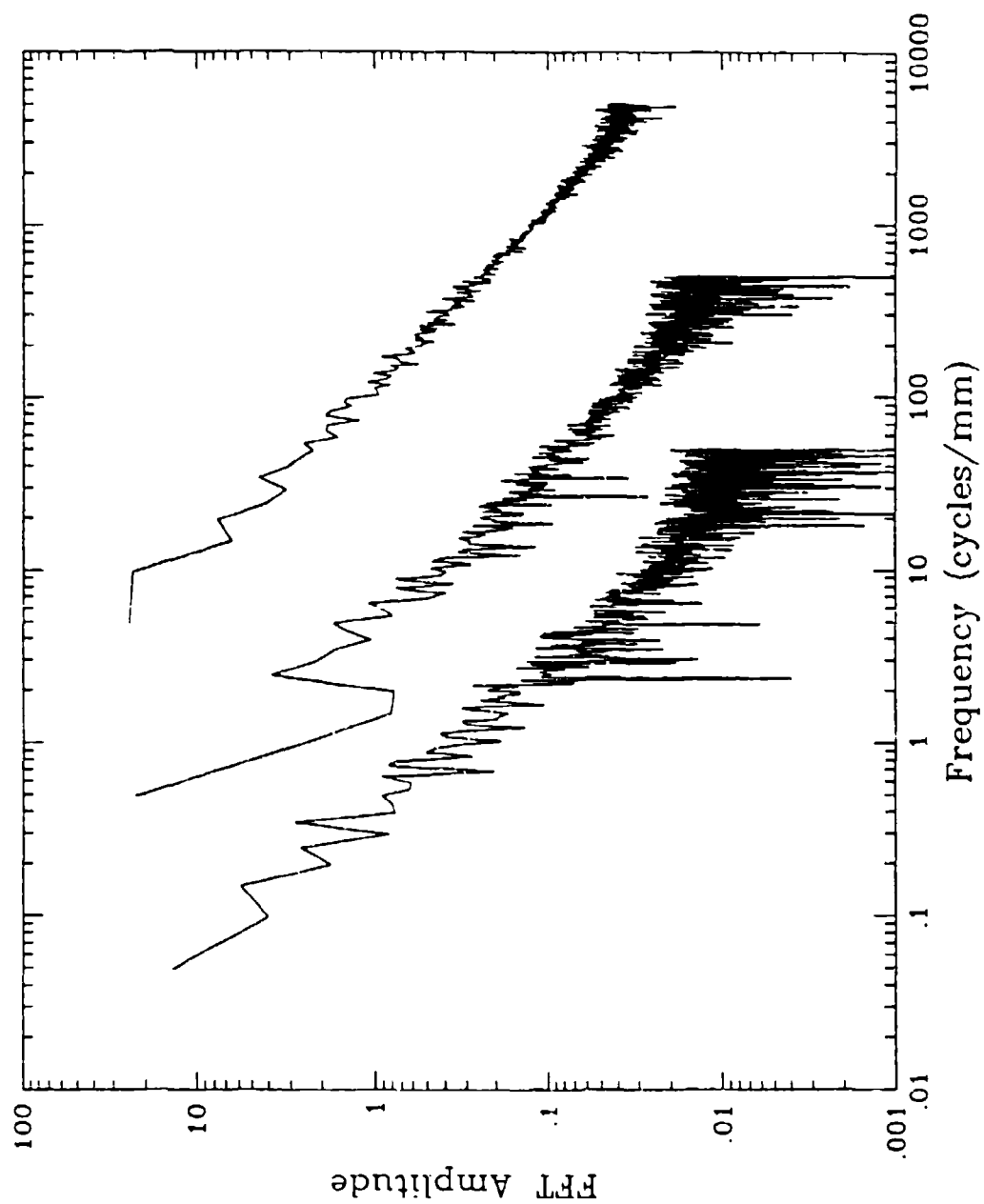


Figure 3-5. FFT amplitudes of three typical tensile fracture joint profiles.

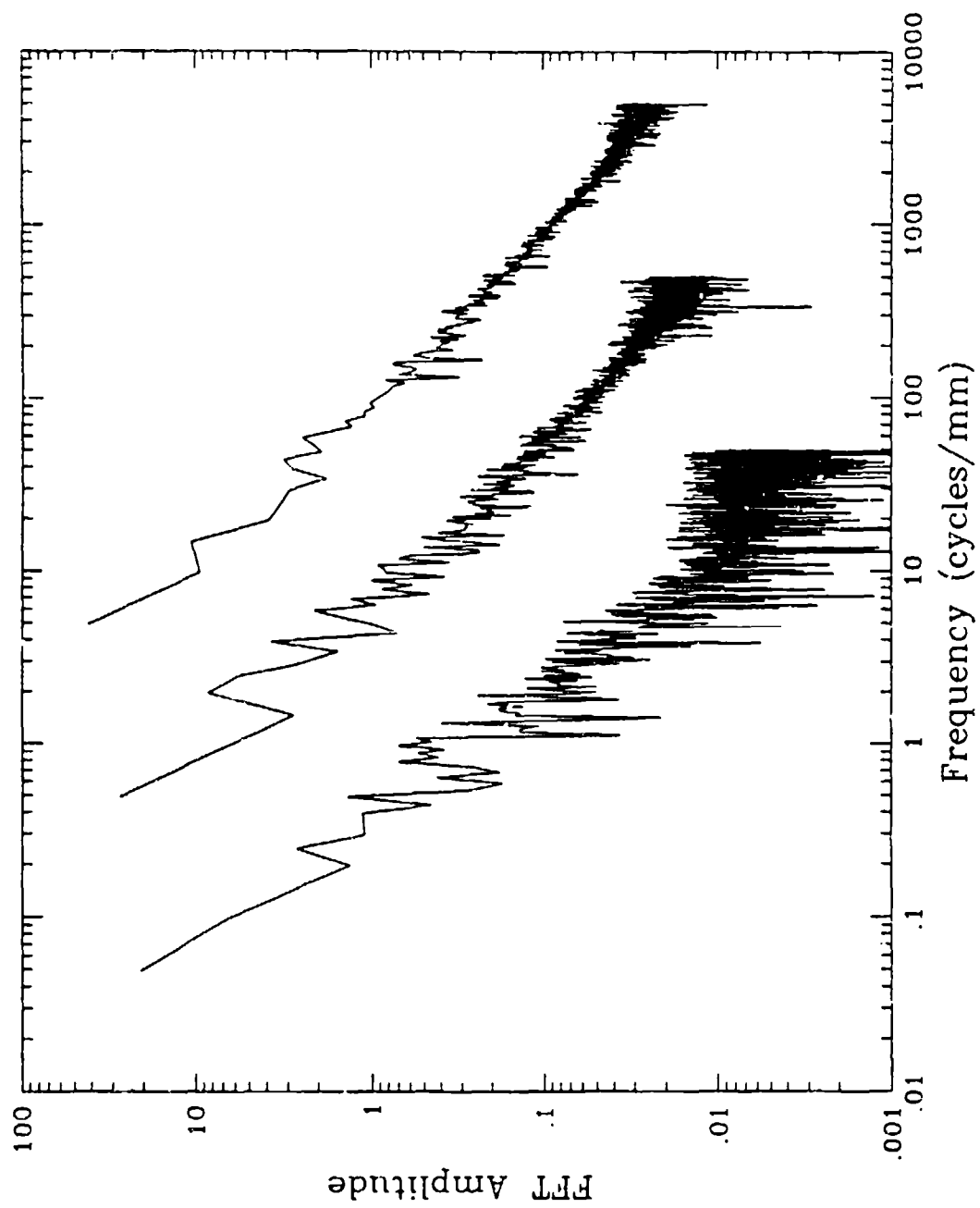


Figure 3-6. FFT amplitudes of three typical synthetic joint profiles.

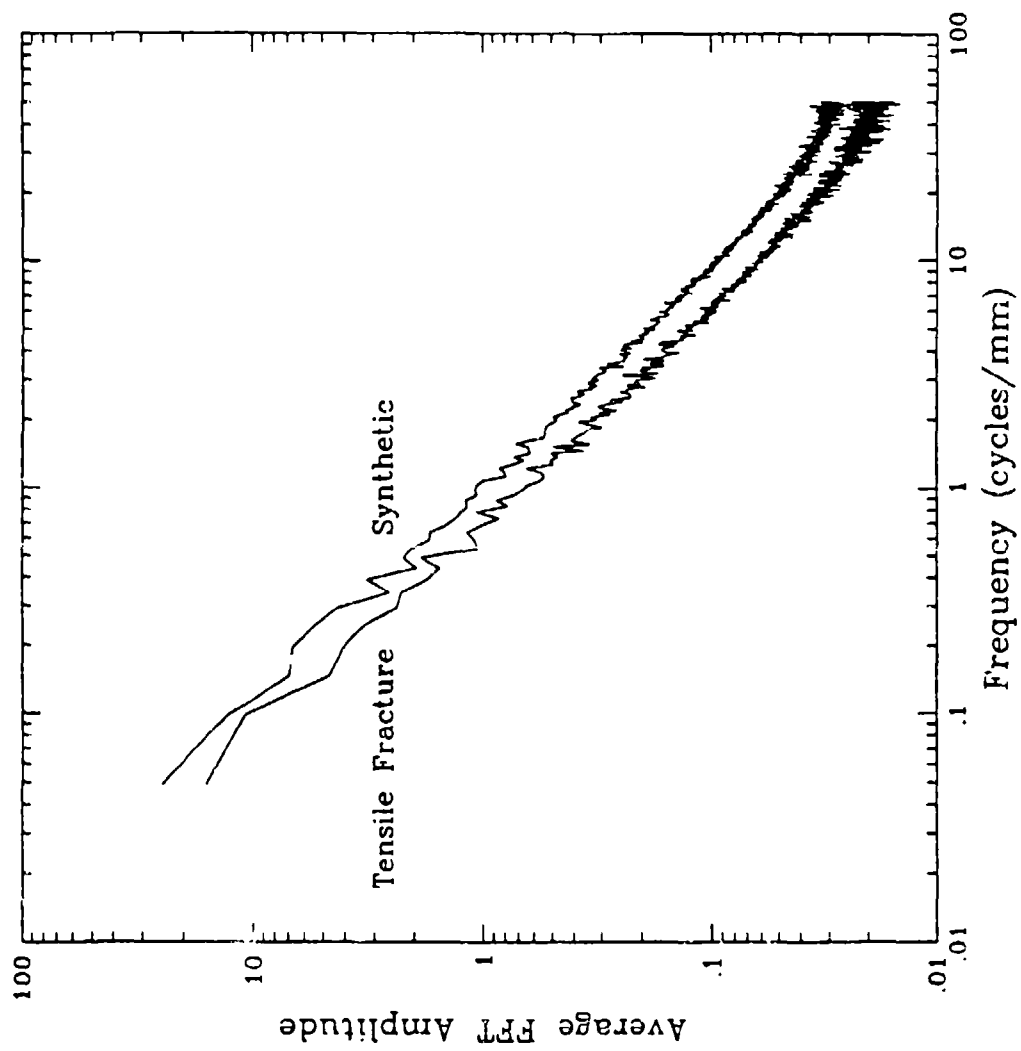


Figure 3-7. Comparison of the average FFT amplitudes of ten profiles each on a tensile fracture joint and a synthetic joint.

## SECTION 4

### TEST PROCEDURES

This section of the report describes the procedures used to prepare and instrument test specimens, loading methods for the various types of tests, and data recording and processing techniques.

#### 4.1 SPECIMEN PREPARATION.

The test specimens were prepared from the blocks of Salem limestone described in Section 2. A water-cooled diamond coring bit was used to cut cylindrical samples 48 mm in diameter with their axes perpendicular to the bedding planes of the limestone. For intact specimens, the cores were cut to length on a diamond saw, and their ends were ground flat and parallel on a machinist's surface grinder with a 170 grit diamond wheel. The finished specimen lengths were in the range of 96-100 mm. The jointed specimens, which were the same size as the intact ones, were prepared as described in Section 3. In all tests, the specimen was sealed inside a membrane, or jacket, to separate it from the confining fluid. At pressures of 10 MPa and above, a jacket of heat-shrinkable polyolefin tubing was used for this purpose. Tests performed on the polyolefin jacketing material indicate that it can add a maximum of approximately 0.2 MPa of additional confinement under large radial expansion. For confining pressures of 20 MPa and larger, this error of 1% or less was considered acceptable. A less stiff latex membrane was employed in its place at lower pressures. In either case, the jacket was sealed to the hardened steel endcaps at both ends using epoxy adhesive and wire clamps, as shown in Figure 4-1.

For joint testing in this configuration, it is essential to minimize the friction between the ends of the specimen and the steel endcaps. This is accomplished through the use of lubricating materials as shown in Figure 4-1. The endcap lubrication system consists of a 0.013-mm layer of copper against the specimen and two 0.05-mm layers of teflon lubricated with a drop of kerosene. Evaluations made under simulated test conditions, have shown that the coefficient of friction across the specimen-endcap interface is less than 0.05.



## **4.2 MOISTURE CONTENT PREPARATION.**

In the course of this work, tests were conducted on specimens having moisture conditions ranging from dry to fully saturated. The following subsections describe the procedures for preparing rock test specimens for those conditions.

### **4.2.1 Unsaturated Specimens.**

In preparation for testing in the dry or unsaturated conditions, specimens were held in a laboratory oven at 105°C for at least 24 hours. Upon completion of this step, the rock was considered to have zero moisture content. At that point the specimen was weighed and measured. As discussed in Section 5.1, the oven dry specimens have been shown to exhibit higher unconfined strengths than mechanically identical specimens with a few percent water content. Since the in situ structures that motivate this study are nearly always wet, the strengths of interest are those of the wet material. Thus, the majority of tests were run with approximately 2% water content by weight. For the limestone with 0.169 porosity, this corresponds to a degree of saturation of approximately 0.3, i.e. 30% of the void space of the rock was filled with water. To achieve this condition, the oven dry specimen was sealed in a plastic bag with the necessary quantity of water for approximately 2 hours.

### **4.2.2 Saturated Specimens.**

The equipment used to saturate the porous limestone specimens is shown schematically in Figure 4-2. The entire procedure was performed with the specimen mounted on the pedestal of the triaxial apparatus where it was to be tested. In preparation for testing, the specimen was sealed between endcaps with a jacket, as described in Section 4.1. The saturation was accomplished through a valved port in the base cap which forms a conduit between the pore space of the specimen and the atmosphere external to the pressure vessel. The specimen was first evacuated and then filled with de-aired deionized water under a low pressure. This pressure was sufficient to slightly oversaturate the specimen, i.e. there was a larger volume of fluid inside the jacket than required to fill the pore space of the specimen. Therefore, some of the fluid was allowed to collect between the specimen and the jacket. The valve was then closed and the

pressure vessel filled with oil and pressurized to approximately 4 MPa. Because of the excess fluid under the jacket, the pore pressure in the specimen at that point in the procedure was the same as the confining pressure. During this pressure soak phase, any minute amounts of air remaining in the pore space of the rock went into solution in the water. Prior to beginning the test, a small amount of water was released from the specimen, resulting in a drop in pore pressure to approximately 1.6 MPa. The ratio of pore pressure to confining pressure of 0.4 was selected as the starting condition because it approximates the stress ratio that would exist if a fully saturated but unstressed specimen was loaded hydrostatically without drainage. This is discussed further in Section 8. Since the valve that controls the pore fluid flow is located in the base cap, approximately 5 mm from the base of the specimen, the dead volume of fluid is approximately 1% of the pore volume of the specimen, and the compliance of the saturation system is negligible.

#### **4.3 LOADING.**

The triaxial test apparatus used to conduct these tests can apply two independently controllable components of load. The specimen is surrounded by a pressure vessel. When confining fluid is pumped into the vessel, the resulting pressure acts uniformly over the entire surface of the test specimen. There is also an axial loading piston that penetrates the vessel through a seal and bears on the top cap of the prepared specimen. The loading piston imposes an axial deformation on the specimen, resulting in an incremental axial stress.

In this program, two different loading schemes were employed, as described in the following subsections.

##### **4.3.1 Triaxial Compression.**

The majority of testing was done under conventional triaxial compression test conditions, i.e. the confining pressure was held constant while a compressive axial deformation was imposed. Where possible, loading continued until an axial deformation of at least 5% of the specimen length was reached. Axial strain rates ranging from  $10^{-5}$  to  $10^{-2} \text{ s}^{-1}$  were used.

#### **4.3.2 Hydrostatic Compression.**

In the hydrostatic compression tests, the jacketed specimens were simply loaded by fluid pressure with no additional loading from the piston.

#### **4.3.3 Uniaxial Strain.**

In a uniaxial strain test, the specimen is compressed axially while controlling the confining pressure such that no specimen deformation is allowed in the radial direction. The loading was controlled based on real-time feedback from the deformation instruments to achieve a specified deformation history.

### **4.4 INSTRUMENTATION.**

Electronic instruments were used to measure the confining stress and axial load applied to the specimen, and the resulting pore pressure and specimen deformation.

Confining pressure measurements were made with a commercial pressure transducer with the sensing element consisting of a strain gaged diaphragm. A load cell inside the pressure vessel, located between the top cap of the specimen and the loading piston was used to measure the axial load. Since it was inside the pressure vessel, it was not subject to errors due to seal friction. It was, however, subjected to the confining pressure. Its design, consisting of a full strain gage bridge, makes the internal load cell, in the ideal case, insensitive to the confining pressure. Since it is not ideal, there is a slight sensitivity which has been quantified and a correction was applied during data reduction.

The pore pressure was measured by a piezoresistive pressure transducer located in the basecap as illustrated in Figure 4-1. The pore pressure transducer was located immediately adjacent to the base of the specimen, minimizing the dead volume of fluid, and hence minimizing extraneous compliance.

Specimen deformations were measured with Linear Variable Differential Transformers (LVDTs). Each specimen was instrumented with three LVDTs as shown in Figure 4-1. Two LVDTs were attached to the base caps on diametrically opposite sides of the specimen to measure axial deformation. Since the axial LVDTs were mounted to the endcaps, the resulting displacement measurement included the deformation of the endcaps and lubricating materials in addition to the intended axial deformation of the rock specimen. A correction was applied during data reduction to eliminate the effect of endcap and lubricating membrane deformation from the measurements.

The third LVDT, used to monitor radial deformation of the test specimen, was mounted in a reference ring at the specimen's mid-height. In the conventional triaxial compression tests, all of loading and measurements take place at a constant confining pressure. Thus, there should be negligible change in the thickness of the jacket as the test progresses, and the radial deformation measurements are made on the outside of the jacket. In contrast, the strain path tests require that the confining pressure change throughout the test, resulting in variations in jacket compression during the test. In those tests the radial deformation measurements were made using studs glued to the specimen through holes in the jacket and sealed to the jacket with o-rings. In this manner, error due to jacket compression was eliminated.

#### **4.5 DATA RECORDING AND REDUCTION.**

All channels of instrumentation were digitally recorded using a 12-bit analog-to-digital converter. Since the strain rates in the various tests varied over orders of magnitude, sampling rates were adjusted to provide the necessary resolution in each test. The digitized data were then multiplied by the appropriate calibration factors to convert to engineering units and, where necessary, corrected for pressure effects.

The axial stress was computed by dividing the measured axial load by the original cross sectional area of the test specimen. The triaxial compression tests performed at pressures of 50 MPa and greater are presented in terms of true axial stress (or stress difference) which is computed by dividing the axial force (or load difference) by the current cross sectional area at

each time point. The reported axial deformation was computed as the average of the results of the two axial LVDT measurements. It was corrected for endcap deformation and thus represents the change in length of the entire specimen. When sliding occurs along a joint, the reference ring holding the radial LVDT rotates away from the horizontal, resulting in error in the radial deformation measurement. A correction based on the amount of axial deformation was applied to the radial measurement to correct for the rotation error.

For undrained tests, the effective stress was computed by subtracting the measured pore pressure from the total stress.

Additional processing was required to compute the joint response quantities. The shear and normal stresses on the joints were computed as follows:

$$\sigma_n = \frac{\sigma_a + \sigma_r}{2} - \frac{\sigma_a - \sigma_r}{2} \cos 2\theta \quad (4.1)$$

$$\tau = \frac{\sigma_a - \sigma_r}{2} \sin 2\theta \quad (4.2)$$

where:

$\sigma_n$  = normal stress on joint (+ is compressive)

$\sigma_a$  = axial stress on the specimen

$\sigma_r$  = radial stress on the specimen = confining pressure

$\theta$  = joint angle with respect to the core axis

$\tau$  = shear stress on the joint

The normal and tangential deformation of a joint were computed by first finding the difference between the overall deformations of a specimen containing a joint and the corresponding deformations of an intact specimen from an adjacent location in the same horizon. This computation was made only for those jointed specimens that failed by joint sliding. Since the stress supported by the jointed specimen was limited by the joint failure mode, the intact portions above and below the joint did not fail. Therefore, only the pre-failure portion of the intact test data was used to make the correction for deformation of the intact material. In

making this calculation, the intact deformation record was interpolated to the same stress levels as in the jointed test data. Once the response of the joint was isolated in terms of axial and radial deformation, the following transformation was made to arrive at deformations normal and tangential to the joint:

$$\Delta_n = \Delta_a \sin \theta + \Delta_r \cos \theta \quad (4.3)$$

$$\Delta_t = \Delta_a \cos \theta - \Delta_r \sin \theta \quad (4.4)$$

- where:
- $\Delta_n$  = joint normal deformation; positive implies joint compaction
  - $\Delta_a$  = axial deformation due to joint; positive implies the ends of the specimen move toward each other
  - $\Delta_r$  = radial deformation due to joint; positive implies opposite sides of the specimen move toward each other
  - $\Delta_t$  = joint tangential deformation; positive implies sliding of the joint such that the ends of the specimen move toward each other

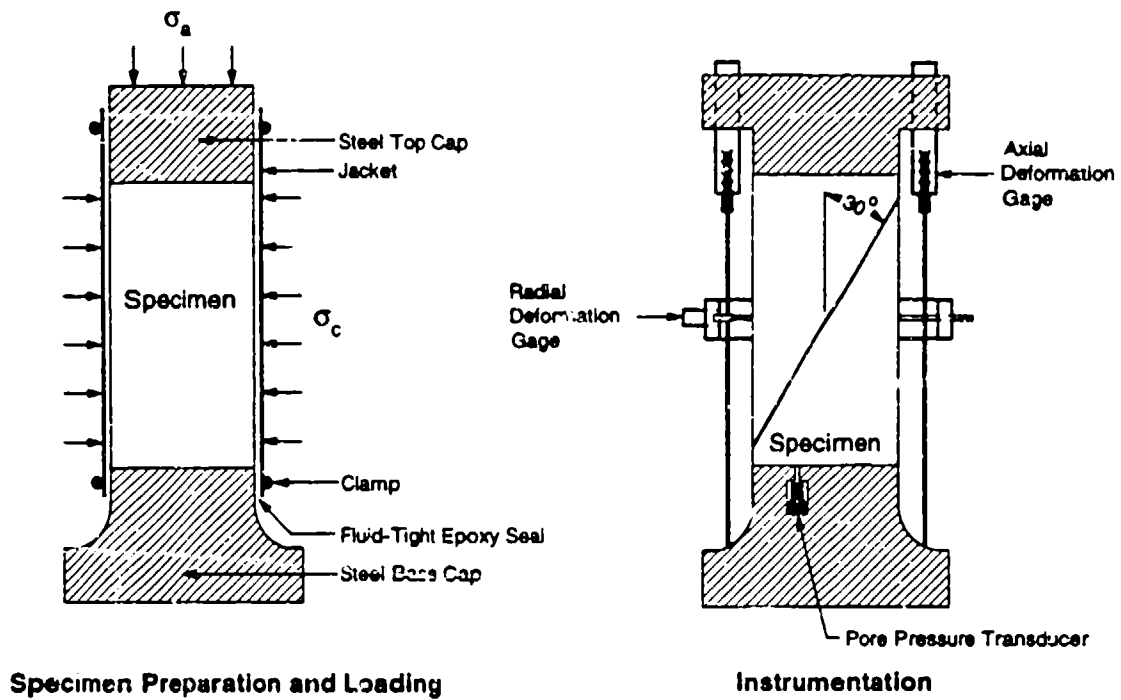


Figure 4-1. Schematic of preparation and instrumentation of triaxial test specimens.

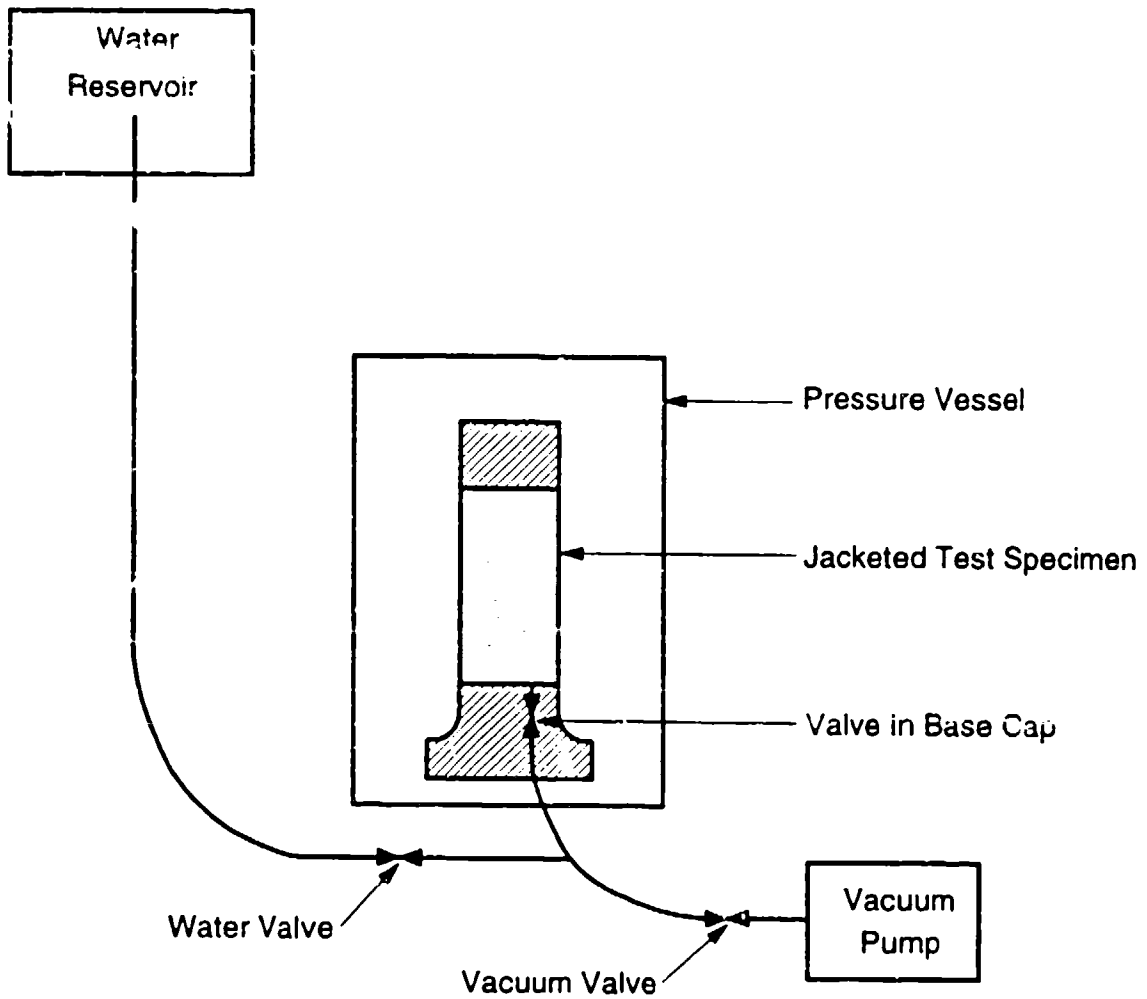


Figure 4-2. Schematic of system for saturation of porous triaxial test specimens.



## **SECTION 5**

### **MECHANICAL PROPERTIES OF INTACT LIMESTONE**

The mechanical properties of Salem limestone have been studied extensively under various DNA-sponsored contracts (Chitty and Blouin, 1990, 1992, 1993; Cummings, 1991). In spite of the fact that it is locally a very uniform material, values of porosity ranging from 0.12 to 0.17 have been observed. Since a complete set of mechanical property data was not available for Salem limestone with the same porosity as the specimen material ( $n = 0.17$ ), a limited series of standard and special tests was run to provide a characterization of the intact material. This includes unconfined compression tests at various water contents, unconfined compression tests in which the test machine was specially modified and controlled to measure the post-failure behavior of the material, triaxial compression tests at a range of confining pressures up to 400 MPa, hydrostatic compression tests, and uniaxial strain tests. This subsection presents the results of those tests.

#### **5.1 UNCONFINED COMPRESSION TESTS.**

Two sets of unconfined compression tests were performed for different purposes. Near the beginning of the project, a series of tests was performed to investigate the influence of water content on the mechanical response of the limestone. Those tests are documented in Section 5.1.1. A second set of unconfined compression tests, described in Section 5.1.2, was performed to determine the post-failure response of the material.

##### **5.1.1 Unconfined Compression Tests at Various Water Contents.**

In previous work, (Chitty and Blouin, 1993), it was found that the unconfined strengths measured for limestones exhibited a strong dependence on water content, with oven dry specimens having significantly higher strength than those with higher water contents. In order to quantify that effect for Salem limestone, a series of 14 unconfined compression tests was performed on specimens from the same block of limestone. These tests were done at water contents (mass of water divided by mass of dry rock) ranging from 0 to 0.055, corresponding

to degrees of saturation (volume of water divided by volume of void space) of 0 to 0.72. The results of those tests are summarized in Table 5-1 and plotted in Figure 5-1. The values for elastic modulus and Poisson's ratio presented in Table 5-5 were computed by least squares fits to the test data over a range of 25-65% of the unconfined strength. Consistent with the previous results, the three oven dry specimens had strengths averaging 58.2 MPa while the eight with water contents in excess of 0.01 had strengths averaging only 48.3 MPa. The elastic moduli were also higher for the dry specimens.

It is sometimes reported in the literature that rocks are tested in the "air dry" or "lab dry" condition. In order to quantify those expressions, an experiment was performed on a group of 27 specimens that had been exposed to ambient conditions in the ARA laboratory for at least two weeks since coring (using water as coolant) and grinding. They were weighed, oven dried at 105 C for 48 hours, and then reweighed. The moisture contents thus determined averaged 0.00042 with standard deviation of 0.00006. Based on the data presented in Table 5-1, the air dry specimens clearly have moisture contents in a range that would be expected to exhibit unconfined strengths significantly higher than moist specimens.

As a result of this study, we performed all tests on unsaturated specimens at a water content in excess of 0.01 in order to eliminate any influence of an over-dry condition on test results.

#### **5.1.2 Post-Failure Response of Limestone in Unconfined Compression.**

In a typical unconfined compression test, the objectives are to measure the strength of the material and possibly the elastic modulus and Poisson's ratio on initial loading. With these as objectives, it is only necessary to impose increasing axial strain (shortening) on the specimen until the load supported by the specimen peaks and begins to decrease. In such a test, strain energy increases in the test machine as the load in the specimen increases. Under typical circumstances, that energy is released into the specimen as it fails, causing a sudden dynamic axial deformation, and making it impossible to measure the post-failure response of the specimen. The tests reported here were conducted using procedures specially developed to

prevent the release of energy into the specimen upon failure and make it possible to record post-failure response.

Two modifications to the usual test techniques were implemented to accomplish this. First, an aluminum alloy stiffener ring was installed concentric with the test specimen and loaded in parallel with it. This is illustrated in Figure 5-2. Thus, when the specimen failed, the load in the test machine was transferred to the stiffener ring. Since the ring was stiffer than the test specimen, even before failure, it significantly limited the elastic rebound of the test machine upon specimen failure. A small load cell was placed atop the specimen within the ring so that it measured only that portion of the load applied to the specimen. In order to stay within the elastic range of the stiffener ring, the components of the system were sized such that approximately half of the rock specimen's elastic deformation was imposed before the stiffener began to be loaded.

The second modification was a special configuration of the test machine's servo-control system. In the usual control mode, a displacement transducer attached to the loading piston is used as feedback for the control system. While this is adequate under most circumstances, the control requirement for this type of test was very rigorous and the deformation of the load frame made it impossible to achieve the necessary precision in control. Thus, it was necessary take the feedback signal from the displacement transducers mounted directly to the steel endcaps on either end of the test specimen. Because the transducers were mounted to the endcaps and not directly to the specimen, they also measured some amount of endcap deformation. It is usual practice to correct for this in post-test processing. However, for these tests, it was necessary to include a correction for endcap deformation in the computation of the control signal. An attempt was made to avoid this complication by attaching the axial deformation transducers directly to the specimen. While this worked well during the elastic portion of the test, the attachment points tended to slip upon failure of the specimen, making subsequent control impossible. The criterion used to control the test was to move the ends of the specimen closer together at a constant rate.

Figure 5-3 presents an overlay of stress-strain curves from six nominally identical tests. Of the six, four fall very close together while one is significantly stronger and one is significantly weaker. In all of these unconfined tests, the softer portion of the stress-strain curve on initial loading is attributable to seating of the endcaps against the ends of the specimen. Appendix B presents individual plots of these tests, including radial strains measured at two locations 90° apart.

## **5.2 TRIAXIAL COMPRESSION TESTS.**

A series of triaxial compression tests at pressures ranging up to 400 MPa was performed to define the strength envelope of the Salem limestone in the intact condition. Those tests are documented in Section 5.2.1. Some of those test results were used along with tests on jointed specimens to derive the joint deformation data presented in Section 6. A brief test series, described in Section 5.2.2, was also conducted to investigate the effects of specimen aspect ratio and end conditions on the measured strength and deformations. Additional triaxial compression tests on intact specimens were performed to investigate the influence of strain rate, and those are described in Section 7.

### **5.2.1 Intact Strength Determination.**

The strength of the intact Salem limestone was determined through a series of triaxial compression tests at pressures ranging from zero (unconfined) to 400 MPa, as summarized in Table 5-2. The triaxial compression testing emphasized the pressure regime of interest to joints, i.e. confining pressures of less than 50 MPa. Figure 5-4 presents axial stress-strain curves from triaxial compression tests at confining pressures ranging from 0 to 35 MPa. For those tests in which the stress difference reached a maximum and then decreased, the state of stress at that maximum was taken as a point on the strength envelope. Above the brittle-ductile transition (~35 MPa confining pressure), where the stress did not peak during the tests, the stress state (in terms of true stress) corresponding to 15% axial strain was assumed to define the strength envelope. In the low pressure (brittle) regime, where failure occurs at strains less than 1%, the difference between true and engineering stress is insignificant. Strength data for the full range

of pressures are presented in Figure 5-5, and Figure 5-6 shows more detail in the low pressure range. Data from the triaxial compression tests that were not used for computation of joint deformations are presented in Appendix C. The data from joint-related triaxial compression tests on intact specimens are included with the joint tests in Section 6 and related appendices.

### **5.2.2 Investigation of Specimen Aspect Ratio and End Conditions.**

In previous work (Chitty and Blouin, 1992), the techniques described in Section 4 were developed to reduce the friction between the ends of the rock specimen and the steel endcaps through which the axial load is applied. For a triaxial compression test in the ductile regime, this lubrication technique produces uniform radial expansion over the height of the specimen rather than the barrel shape that typically results when the specimen-endcap interface is not lubricated. This approach has also worked well to reduce friction for shear testing of jointed specimens. For tests on intact specimens in the brittle regime and around the brittle-ductile transition, the reduced effective confinement at the ends of the specimen resulting from the reduction in end friction apparently makes it possible for failure to be initiated at locations other than at specimen mid-height. If radial deformation gages are only installed at or near the center of the specimen and failure is initiated near one of the ends, then the radial expansion in the failure zone will not be measured. This effect has been observed in many triaxial compression tests on intact specimens at confining pressures of interest to joint strength investigation. Measurements of the permanent volume change of a material following loss of strength are important for constitutive modeling of rocks and soils to support explosive effects calculations, and accurate axial and radial deformation measurements are essential for definition of the volume change of the specimen under load. Further, Chitty and Blouin (1990) demonstrated that the non-uniform radial deformation of a triaxial compression specimen is accompanied by a non-uniform axial strain field, making accurate computation of the volumetric behavior of the specimen impossible.

In order to investigate techniques for measurement of post failure volume change behavior, a brief series of triaxial compression tests was performed in the brittle-ductile transition pressure range (25 MPa confining pressure). Included were a "standard" test with

unlubricated endcaps and a 2:1 length to diameter ( $L/D$ ) ratio, a test with 2:1  $L/D$  and lubricated endcaps, and one with 1:1  $L/D$  and lubricated endcaps. Figure 5-7 presents the initial portions of the curves of stress difference plotted against axial and radial strains. From that figure it is apparent that there were no significant differences in either strength or deformation among the three test results. It is only in the post-failure portion of the tests that the differences become apparent. At this confining pressure (25 MPa) there is very little change in stress difference with increasing axial deformation after the peak strength has been reached. Thus, plots of strains against stress difference are not a good basis for comparisons among the tests in the post-failure region. As an alternative, consider the radial strain plotted as a function of axial strain. Figures 5.8 through 5-10 present such plots for the three tests described in this paragraph. In all cases, the plotted axial strain is the average over the entire specimen length, i.e. the change in length of the specimen divided by its original length. From the test measurements, there is no way of knowing whether the axial strain is uniform over the specimen length. Further, Figures 5.8 and 5.9 include multiple radial deformation measurements, representing different heights on the specimens. In all three tests, the radial gages give consistent readings for the initial approximately linear portions of the tests represented by the first half percent of axial strain

In the case of the specimen with unlubricated endcaps, shown in Figure 5.8, the three radial gage readings diverge, and never rejoin, indicating nonuniform radial deformation developing throughout the post-failure portion of the test. By the time the average axial strain reached 11%, two of the radial gages had gone off scale at over 10% radial strain while the third was indicating only about 4% radial strain. The test with lubricated endcaps presents a very different picture. Following failure of the specimen, the upper half of the specimen underwent a significant radial strain while the radial strain in the lower half remained essentially constant at the level of the initial failure until the axial strain reached approximately 5%. At this point, the lower half of the specimen began expanding radially while the radial strain in the upper part remained relatively constant. By about 12% axial strain, the two radial readings were essentially identical, indicating a nearly uniform strain field over the entire specimen. The specimen with unlubricated ends never reached that condition, and exhibited very nonuniform radial deformations at the conclusion of the test.

The results of the test with lubricated ends can be interpreted in the following way. Initially, there are uniform axial and radial strain fields throughout the specimen. At the peak of the stress-strain curve, where the strength of the material is reached, there is a localized failure somewhere in the specimen. In tests with lubricated ends, this has been observed to occur toward one end of the specimen. Possibly, this is a result of the relatively soft lubricating materials deforming more than the rock and applying a slight outward radial traction to the ends of the specimen. In general, we have observed that failures, wherever they occur in the specimen, to be localized over a length of specimen equal to roughly one specimen diameter. Once this localized failure is initiated, the stress in the specimen drops below the failure level, and the rest of the specimen remains intact. Eventually, the radial expansion in the localized region increases the cross sectional area to the point that it will support slightly more load than was required to initiate failure, resulting in sequential failure of the previously intact material in the opposite half of the specimen. With enough axial deformation, the conditions of the material in the two halves of the specimen become nearly the same. For the portion of the test between initiation of failure and the time the radial strain records from either half rejoin, the material in the un-failed half is elastic while the failed half undergoes significant plastic deformations. Thus, it seems reasonable to assume that the large increase in indicated axial strain is largely a result of deformation in the failed half of the specimen, and neither of the two curves shown in Figure 5.9 correctly represents the strain condition in either half of the specimen. This is a serious drawback for constitutive modeling where the post failure volumetric behavior of the material is very important.

For defining the post-failure deformation, it would be very desirable to conduct a test in which the specimen deforms uniformly over its entire volume. Since the failed zone appears to naturally occur over about one diameter of specimen length, it was hypothesized that this could be accomplished by testing a specimen with  $L/D$  equal to approximately one. Traditionally, an  $L/D$  of two has been used in an effort to avoid end effects. However, if lubrication of the ends can alleviate that problem, then the test may provide more representative post-failure deformation information. The relationship between radial and axial strains presented in Figure 5-10 is the result of such a test. The curve lies between the two shown in Figure 5.9 for the test with  $L/D = 2$ , and has a slope over the entire post-failure range that is approximately equal

to the equivalent slope in the part of the test on the long specimen where both radial gages were reading the same. The short specimen exhibits more radial strain than the long one at equal axial strains, the reason for which is unknown. However, we judge results from the short ( $L/D = 1$ ) specimen to be more representative of the actual material behavior than either of the other two tests. Figure 5-11 compares volumetric strains computed using the radial and axial deformation measurements from the three tests and plotted against average axial strain. Where multiple radial deformation measurements were made, the figure indicates which was used in the volume strain computation. There are very significant differences among the volume strains derived from the three tests. We believe that information derived from the test on the short ( $L/D = 1$ ) specimen with lubricated ends best represents the material's actual response. This approach is only applicable at confining pressures near the brittle-ductile transition where the failure is localized but the specimen does not fracture into multiple pieces.

While the study described here is far from an exhaustive investigation of the subject, we believe that most accepted test approaches result in non uniform specimen deformations, which in turn result in errors in volumetric strain determination. In view of the importance of the post-failure volumetric behavior in constitutive modeling, this subject deserves further investigation. A test on a specimen with  $L/D = 1$  and a lubricated end does appear to be a useful technique for obtaining more nearly uniform strain fields. A similar suite of tests were performed at 50 MPa confining pressure. Those tests exhibit the same trends and are included in Appendix C.

### 5.3 HYDROSTATIC COMPRESSION TESTS.

Six Salem limestone specimens were tested in hydrostatic compression to a maximum pressure of 400 MPa. One test was performed on a specimen in the oven dry condition and rest had 2.5% water content. The hydrostatic compression tests are summarized in Table 5-3. Figure 5-12 presents a typical pressure - volume strain curve. The relationship between radial and axial strain for the same test is shown in Figure 5-13, which clearly illustrates the lack of isotropy under hydrostatic loading. Once the hydrostatically loaded specimens begin to exhibit plastic deformation, the specimens compact significantly faster in the radial direction. Also shown in Figure 5-13 is a point indicating the permanent strain at the conclusion of the test as



determined from post-test measurements of the specimen. The post-test measurement validates at least the final instrument readings, and confirms the anisotropy. The complete set of test data is presented in Appendix C.

## **5.5 UNIAXIAL STRAIN TESTS.**

Specimens of Salem limestone were loaded in uniaxial strain up to the point where the confining pressure reached the ARA system's capacity of 400 MPa, as summarized in Table 5-4. All were tested with approximately 2.5% water content. A typical axial stress-strain curve is presented in Figure 5-14, the corresponding relationship between axial and radial stress is shown in Figure 5-15, and the mean stress-volume (axial) strain relationship is illustrated by Figure 5-16. Appendix D presents a complete set of uniaxial strain test data.

Table 5-1. Summary of unconfined compression tests performed to investigate the influence of moisture content.

Test ID	Specimen ID	Dry Density (kg/m <sup>3</sup> )	Porosity	Water Content	Degree of Saturation	Unconfined Strength (MPa)	Elastic Modulus (GPa)	Poisson's Ratio
O8E0	SL20-T5	2249	0.170	0.000	0.000	58.5	29.6	0.197
O8D0	SL20-B4	2254	0.168	0.000	0.000	59.3	29.3	0.204
O8C0	SL20-T4	2255	0.167	0.000	0.000	57.1	29.0	0.180
O8F0	SL20-T1	2247	0.170	0.004	0.049	53.0	27.3	0.218
J18A1	SL21-T3	2254	0.168	0.004	0.056	51.1	26.3	0.282
O9A0	SL20-B1	2242	0.172	0.008	0.109	49.0	26.0	0.229
O23C0	SL20-B5	2253	0.168	0.018	0.239	46.0	25.6	0.219
O23D0	SL20-T6	2259	0.166	0.018	0.245	50.6	26.5	0.245
O9B0	SL20-T2	2253	0.168	0.020	0.262	51.3	27.4	0.234
O9C0	SL20-B2	2254	0.168	0.036	0.482	48.2	26.8	0.216
O23E0	SL20-B6	2249	0.170	0.038	0.501	47.1	25.5	0.215
O24A0	SL20-T7	2256	0.167	0.038	0.506	49.4	26.6	0.242
O24B0	SL20-B7	2248	0.170	0.055	0.718	47.2	25.4	0.220
O24C0	SL20-B8	2252	0.169	0.054	0.720	47.8	25.2	0.222
Average		2253	0.168			48.45	26.1	0.227
Standard Deviation		5	0.002			1.6	0.72	0.011
Grain Density		2709kg/m <sup>3</sup>						

Note: Statistics are for those specimens with water content greater than 0.01.

Table 5-2. Summary of triaxial compression tests on intact material (not including intact tests performed for joint deformation determination).

Test ID	Specimen ID	Dry Density (kg/m <sup>3</sup> )	Moisture Content	L/D	Lub End Cap	Radial Measurements	Confining Pressure (MPa)	Stress @ Peak (MPa)	
								Stress Diff.	Mean Stress
D6D/C0	SL20-T18	2250	0.025	2	no	3	25	87.0	54.8
D20B0	SL20-B14	2244	0.025	2	yes	2	25	86.5	53.8
D4B0	SL20-T21B	2255	0.025	1	yes	1	25	88.0	54.3
D6B0	SL20-T18	2240	0.025	2	no	3	50	134	95
D5B0	SL20-B21	2252	0.025	2	yes	2	50	128	93
D3B0	SL20-T16A	2252	0.025	1	yes	1	50	135	95
O24E0	SL20-T9	2252	0	2	yes	1	100	224	175
D7B0	SL20-T19	2251	0.025	2	yes	1	100	218	173
O25B0	SL20-B9	2251	0	2	yes	1	200	353	318
D7D0	SL20-T13	2262	0.025	2	yes	1	200	356	319
O26B0	SL20-T10	2254	0	2	yes	1	400	544	581

**Table 5-3. Summary of hydrostatic compression tests on intact Salem limestone.**

Test ID	Specimen ID	Dry Density (kg/m <sup>3</sup> )	Water Content
Y20A1	SL21-T22	2258	0.025
Y17A1	SL21-B19	2251	0.025
Y16A1	SL21-B12	2247	0.025
Y15B1	SL21-T10	2251	0.025
Y15A1	SL21-T17	2258	0.025
N1A0	SL20-B11	2253	0

**Table 5-4. Summary of uniaxial strain tests on intact Salem limestone.**

Test ID	Specimen ID	Dry Density (kg/m <sup>3</sup> )	Moisture Content
U19A1	SL21-T20	2249	0.025
U18A1	SL21-B14	2247	0.025
Y23A1	SL21-T19	2255	0.025

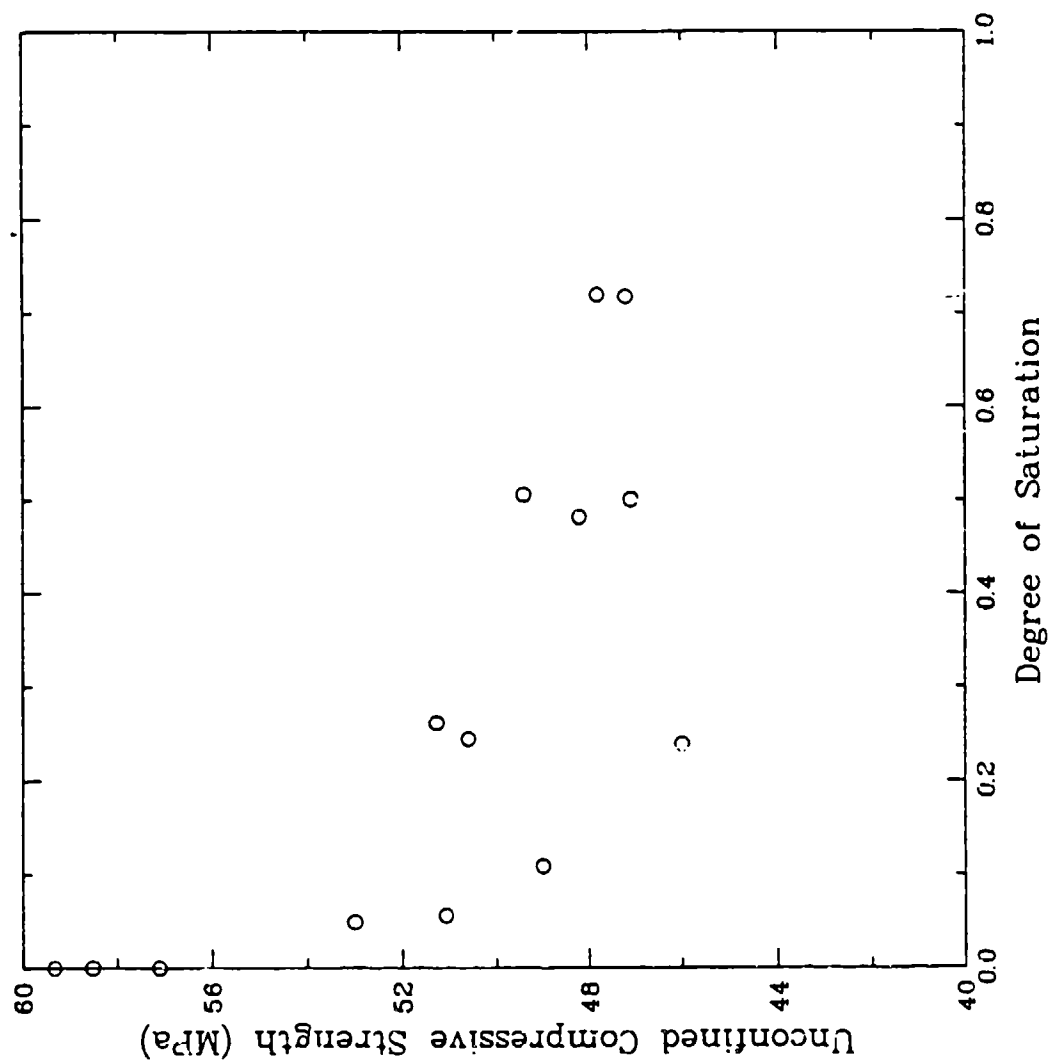


Figure 5-1. Illustration of the relationship between water content and unconfined strengths in Salem limestone.

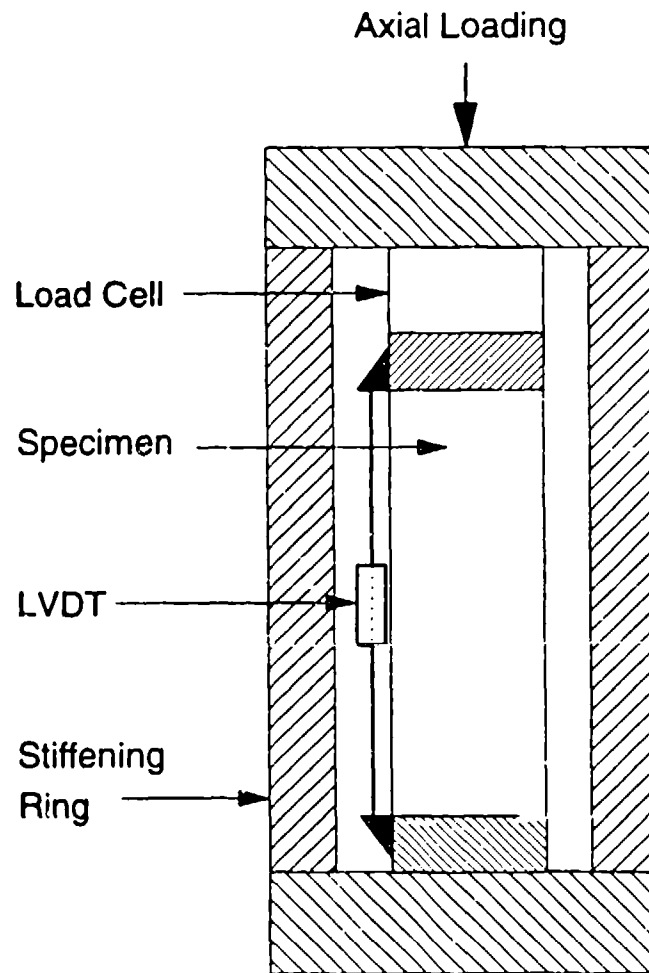


Figure 5-2. Schematic of the stiffener ring used in tests to determine post-failure response of Salem limestone in unconfined compression.

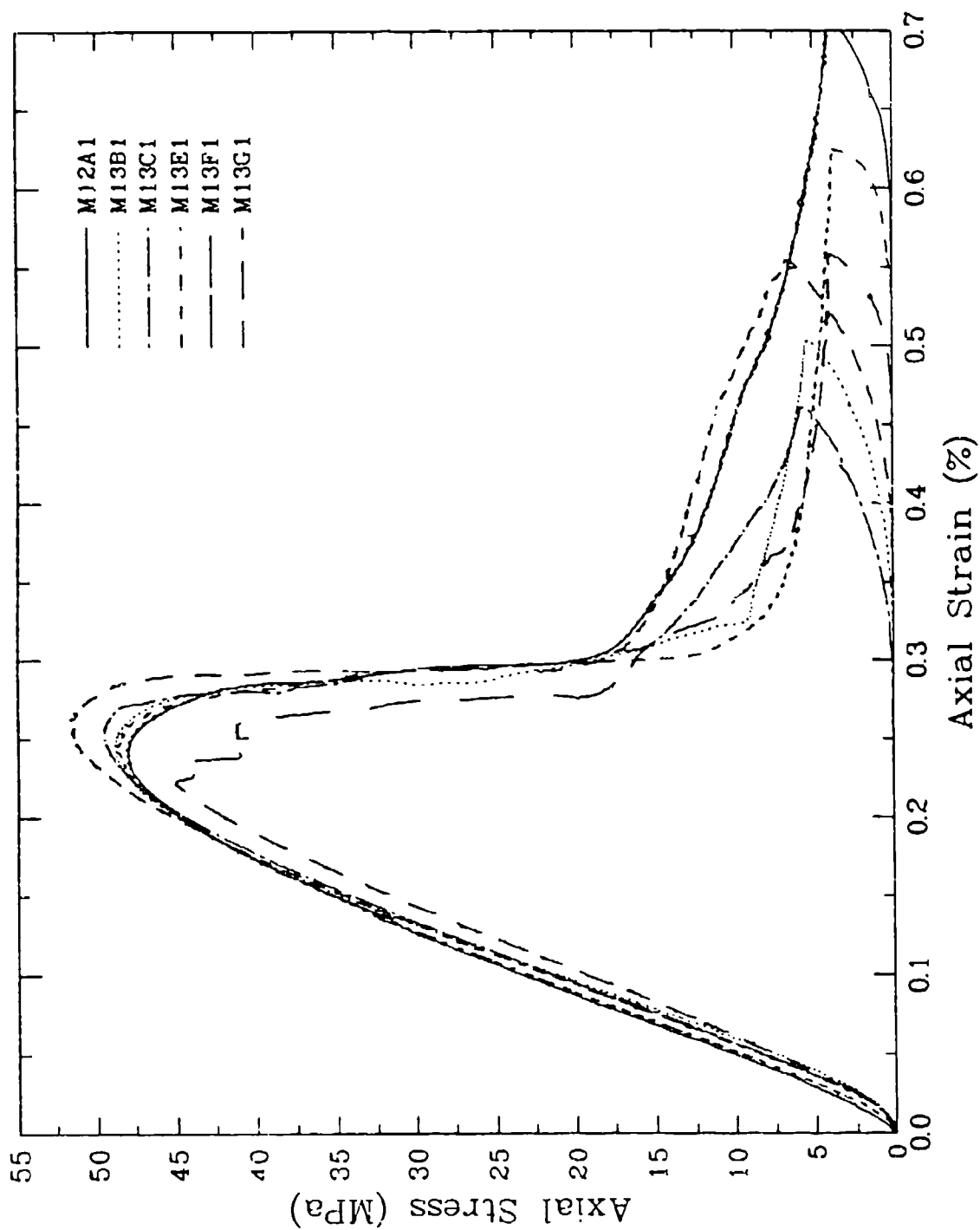


Figure 5-3. Overlay of six axial stress-strain curves including post-failure response of Salem limestone in unconfined compression.

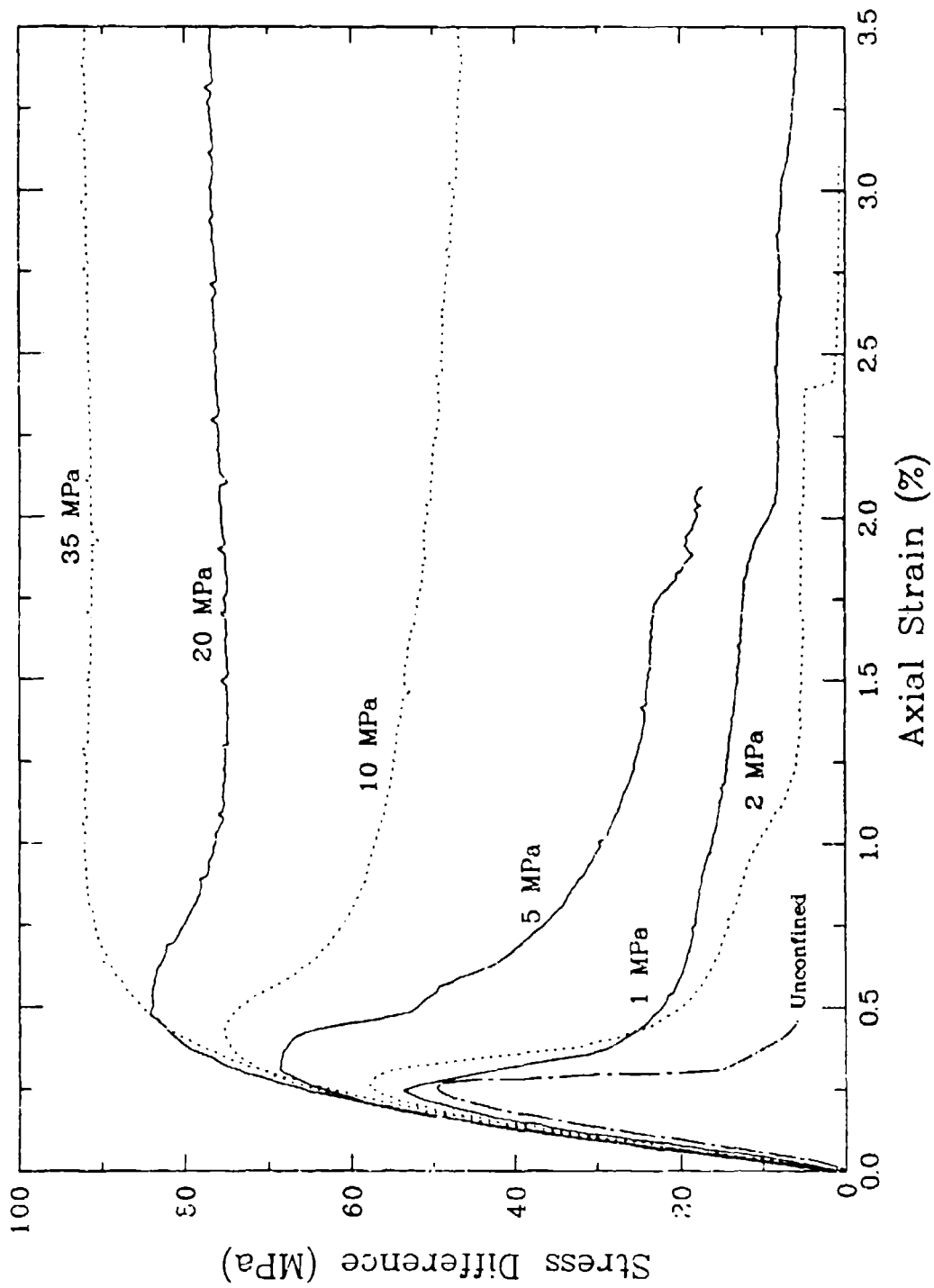


Figure 5-4. Comparison of axial stress-strain curves for Salem limestone tested in triaxial compression at a range of confining pressure in the brittle regime.



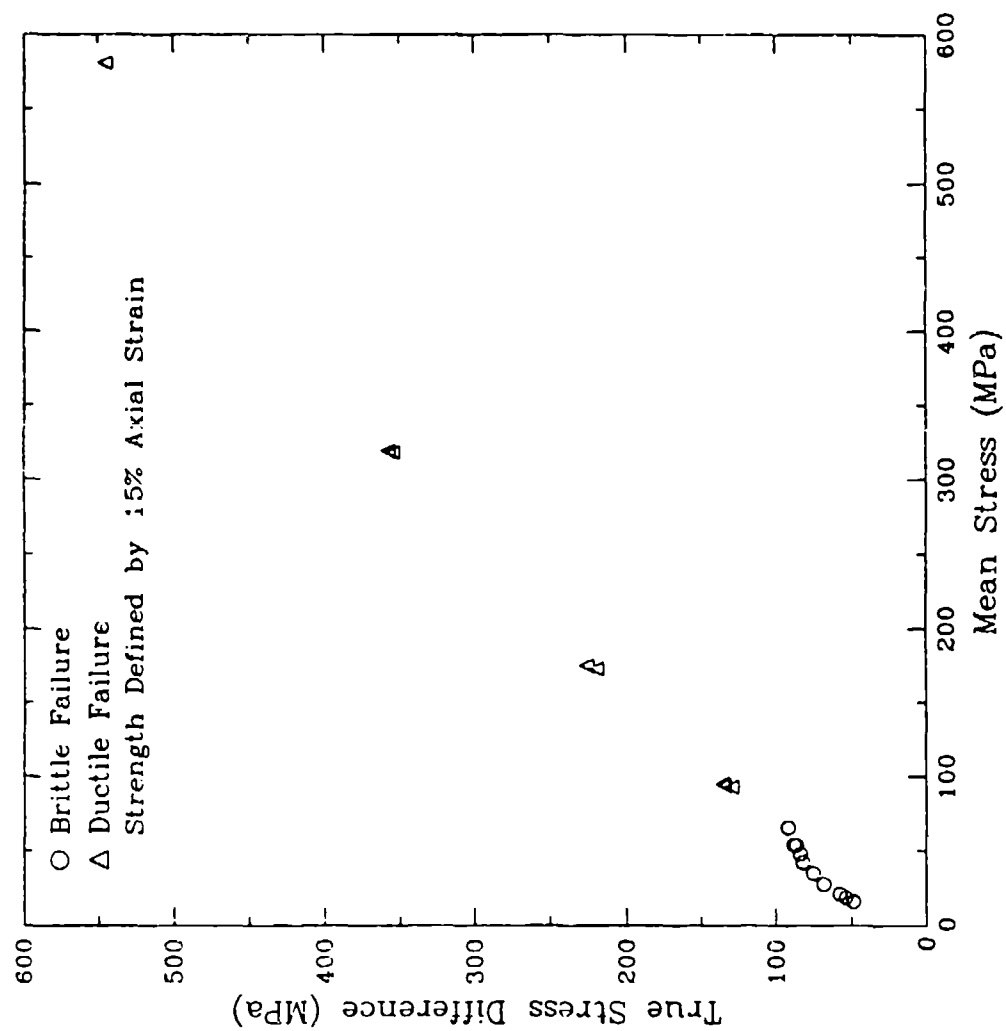


Figure 5-5. Strength data from triaxial compression tests on intact Salem limestone specimens at confining pressures ranging from zero to 400 MPa.

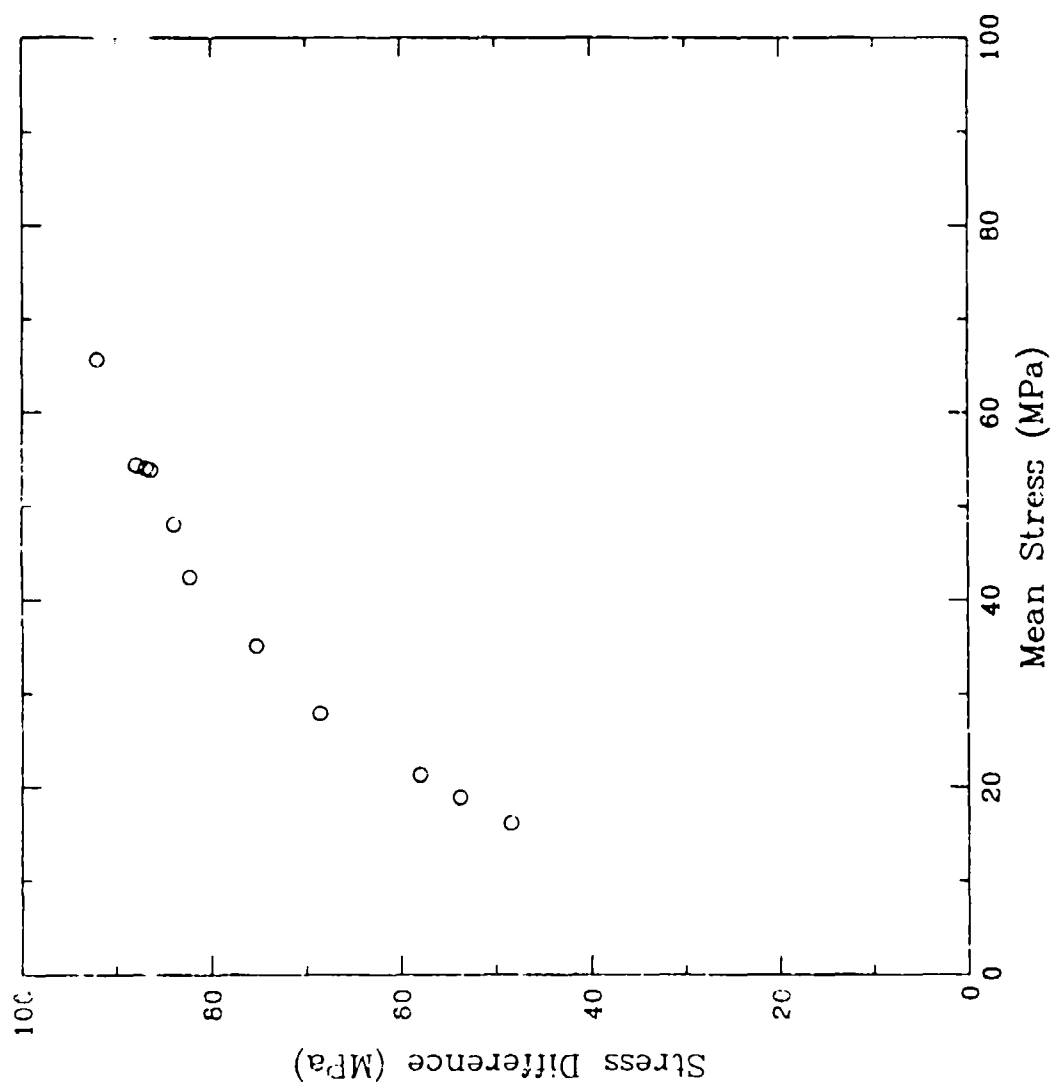


Figure 5-6. Strength data from triaxial compression tests on intact Salem limestone specimens at confining pressures ranging from zero to 35 MPa.

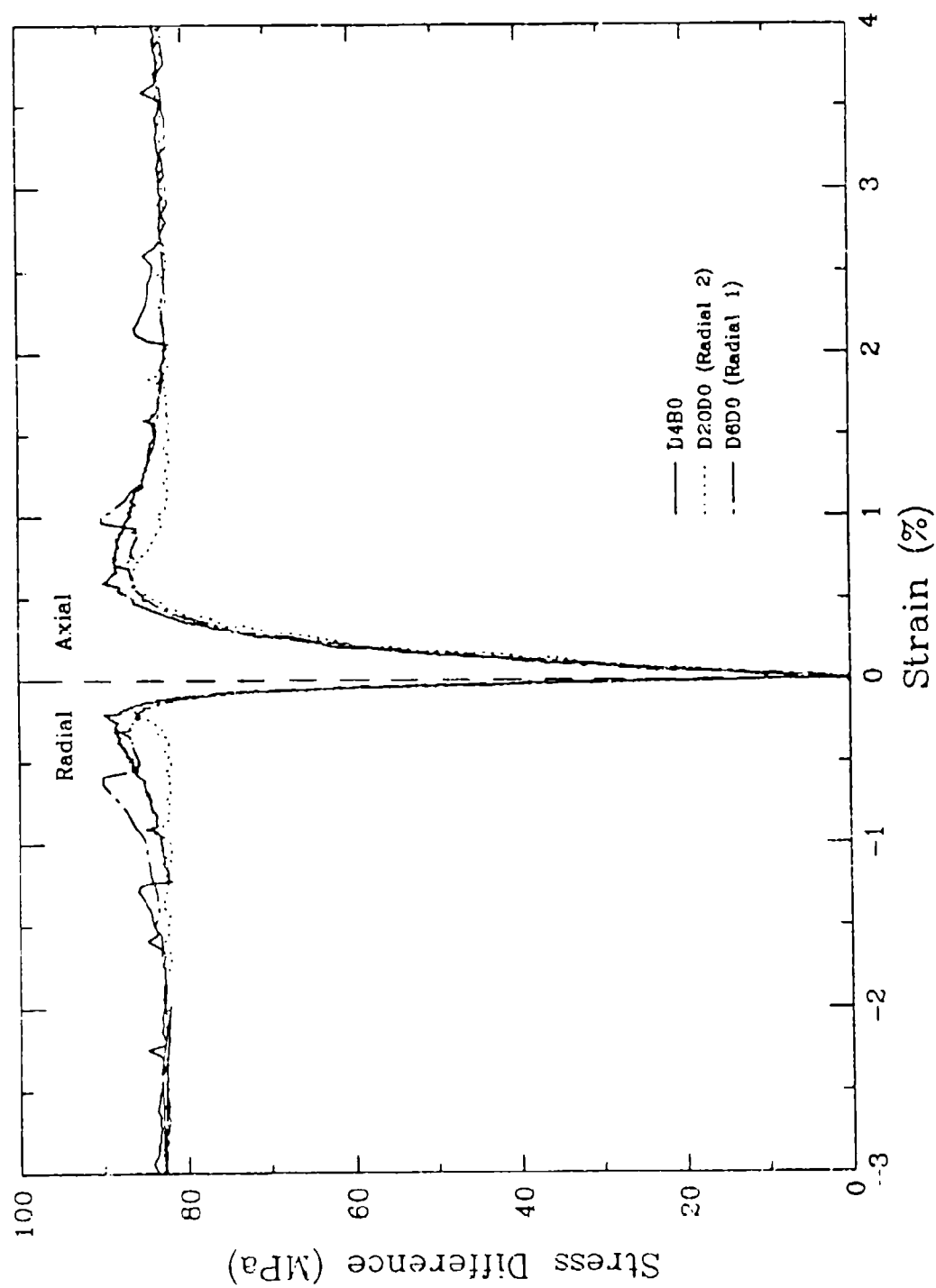


Figure 5-7. Comparison of pre-failure response of Salem limestone tested in triaxial compression at 25 MPa confining pressure under three different test conditions.

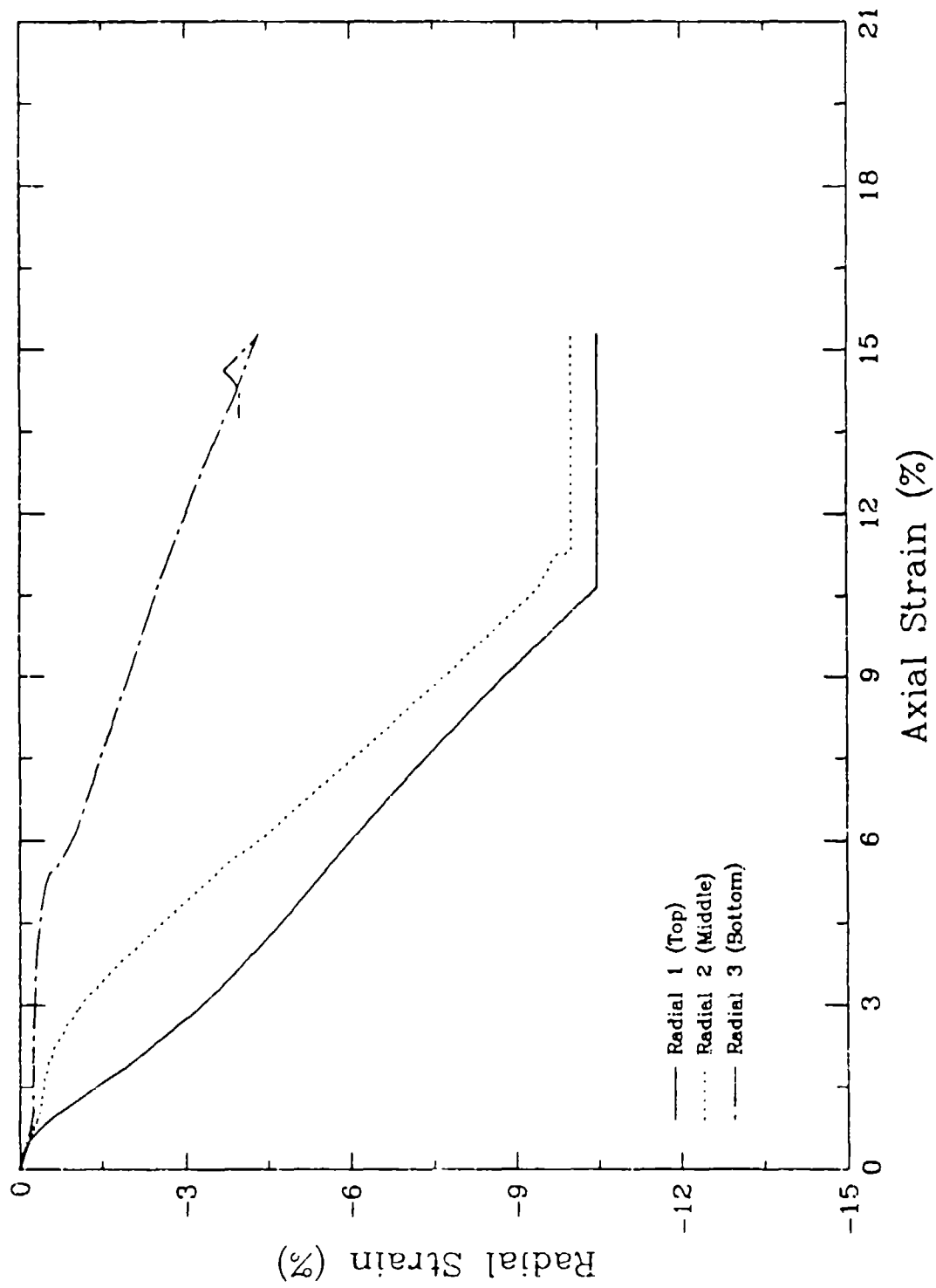


Figure 5-8. Relationship between average axial strain and radial strains measured in a 25-MPa triaxial compression test at three different heights on a test specimen with  $L/D = 2$  and unlubricated ends.

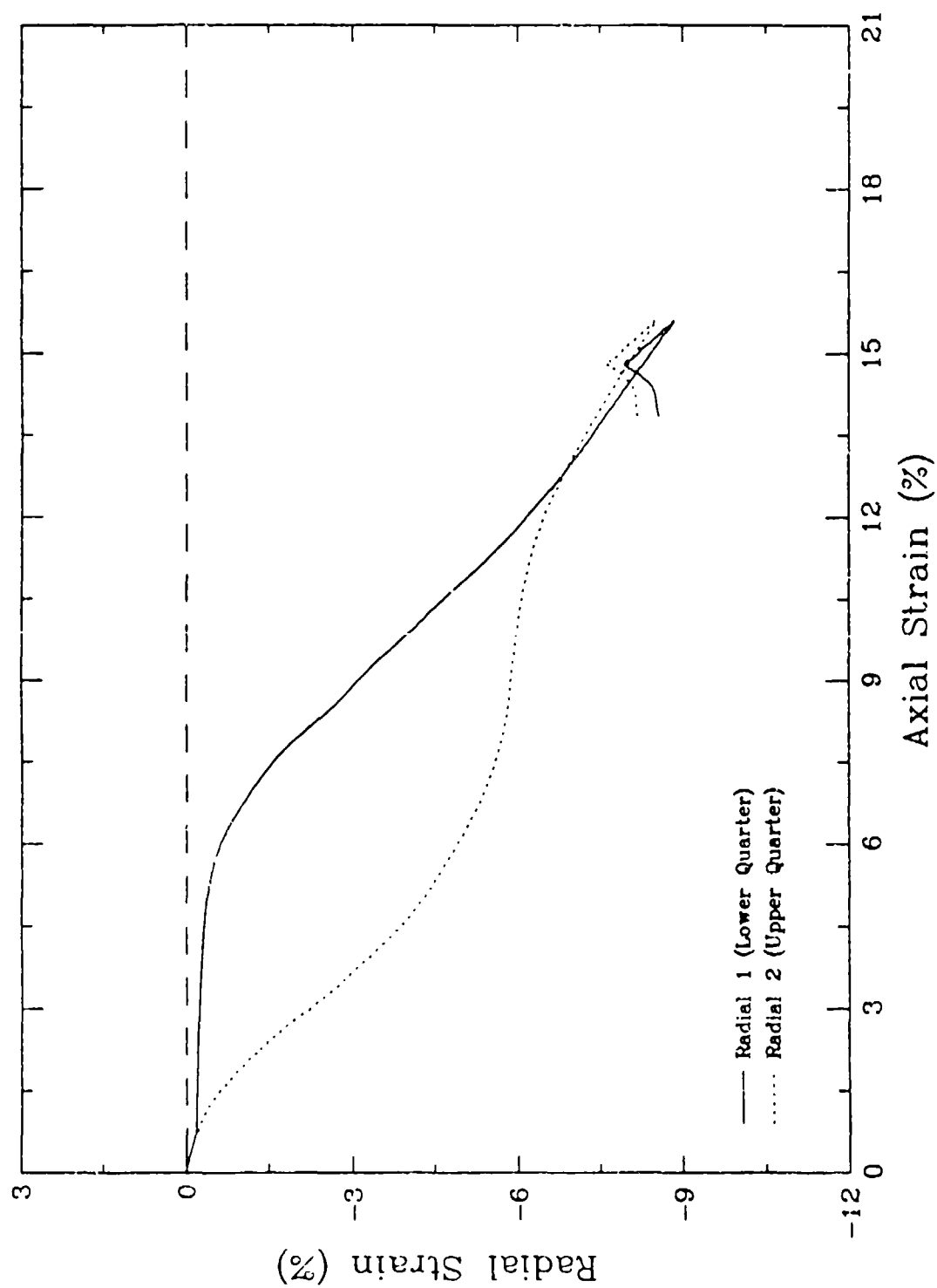


Figure 5-9. Relationship between average axial strain and radial strains measured in a 25-MPa triaxial compression test at three different heights on a test specimen with  $L/D = 2$  and lubricated ends.

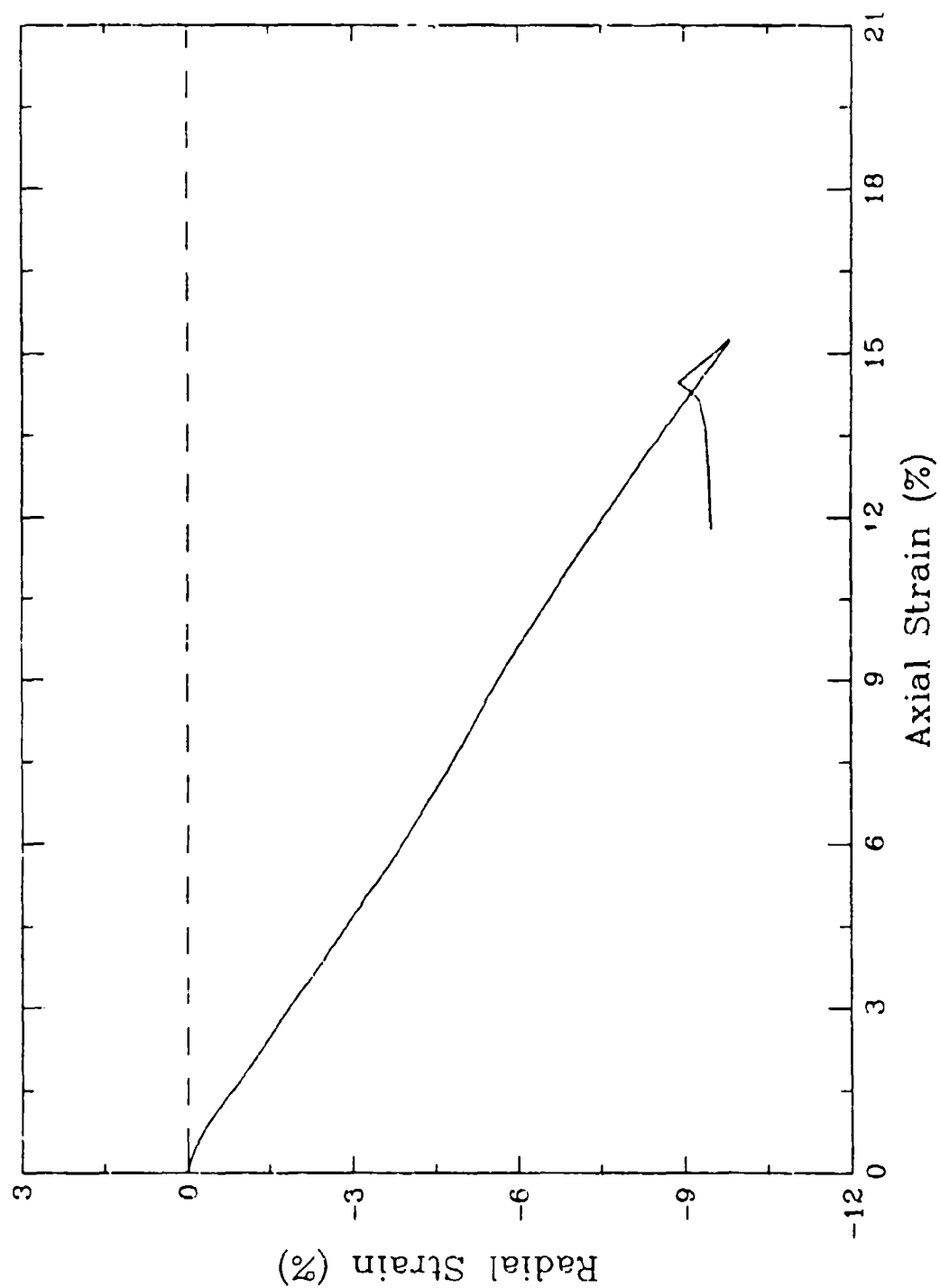


Figure 5-10. Relationship between average axial strain and radial strain measured in a 25-MPa triaxial compression test on a test specimen with  $L/D = 1$  and lubricated ends.

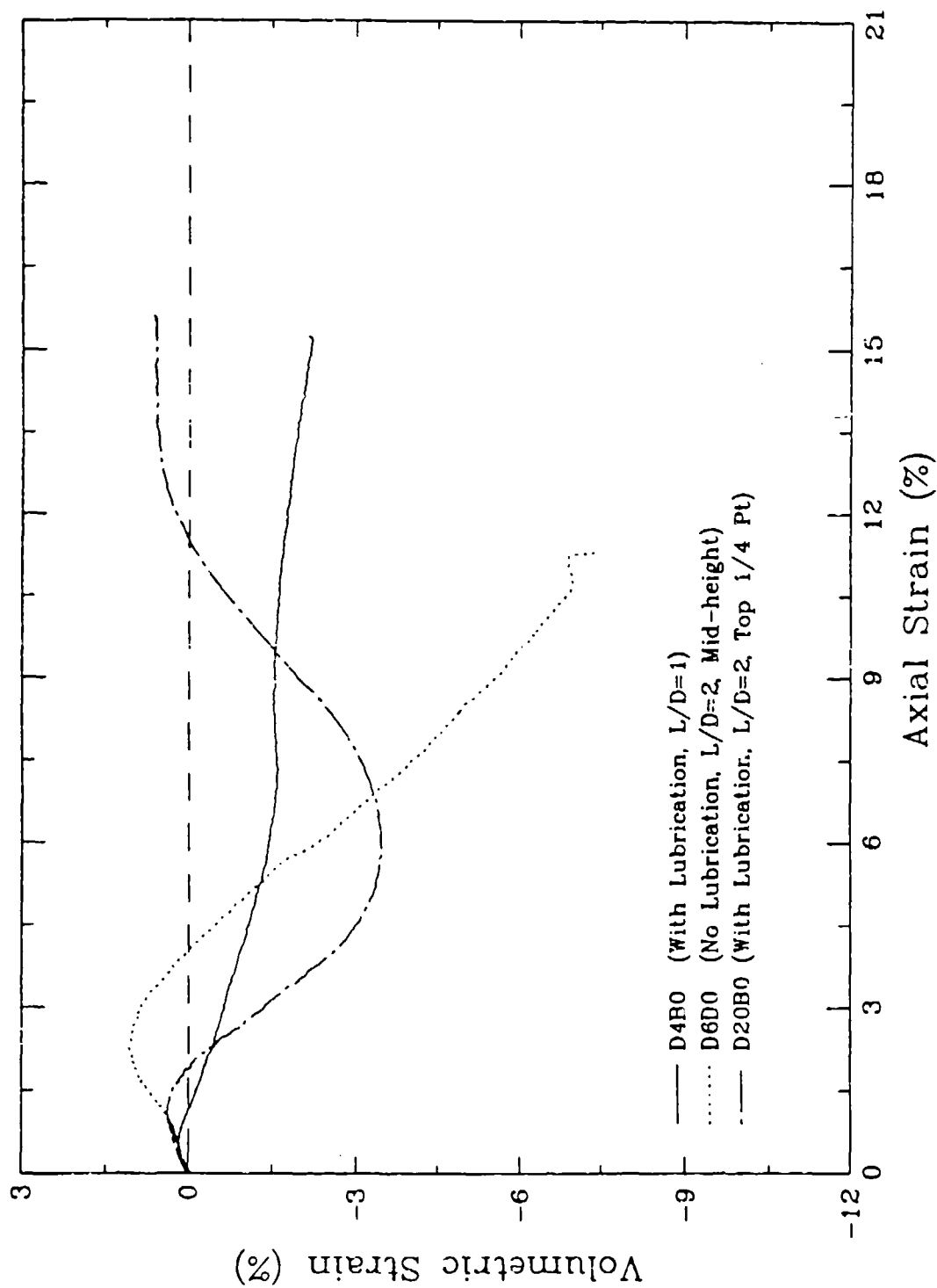


Figure 5-11. Comparison of volumetric strains computed from 25-MPa triaxial compression under three different test conditions.

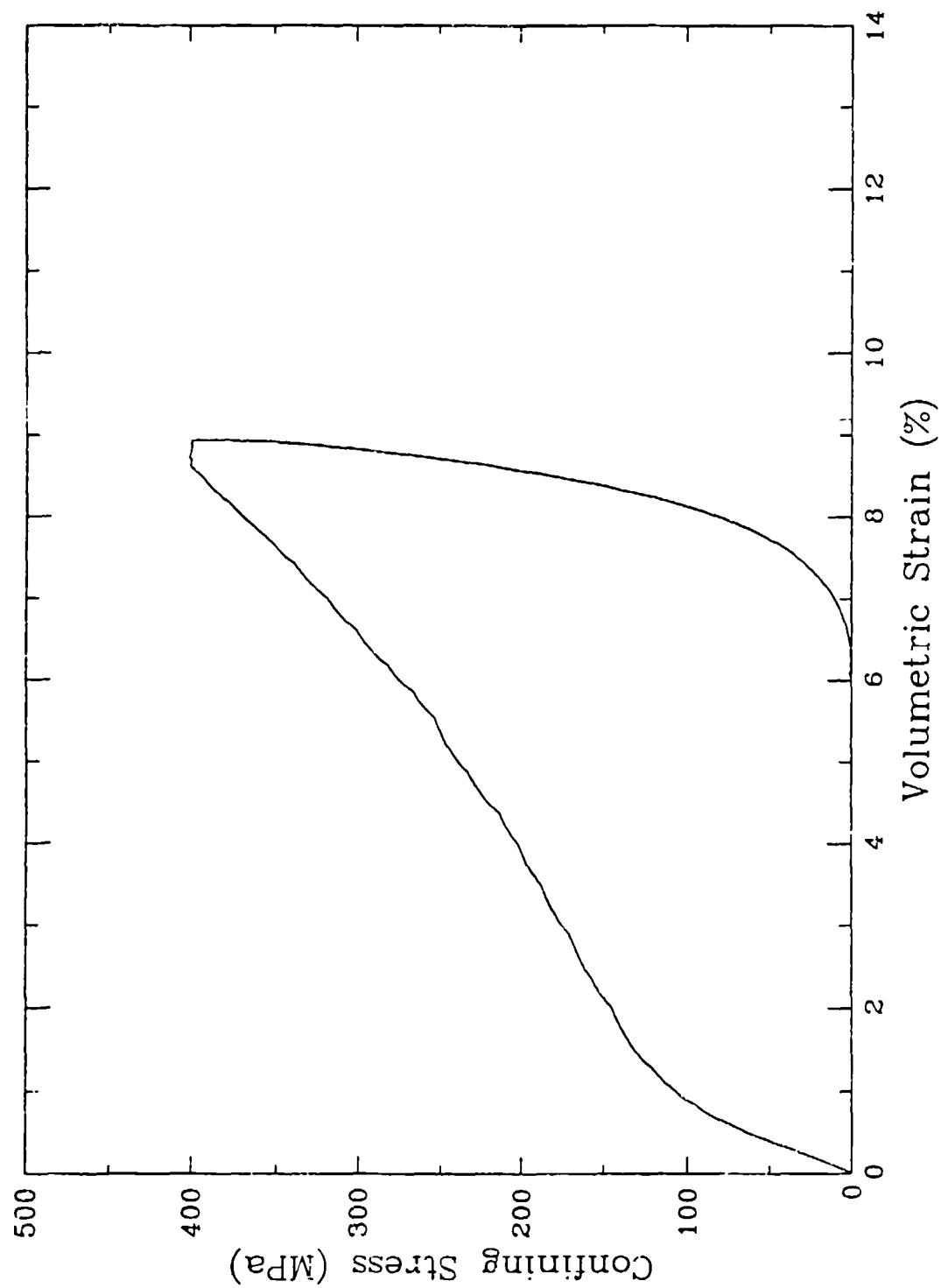


Figure 5-i2. Typical relationship between confining pressure and volumetric strain for intact Salem limestone loaded in hydrostatic compression.



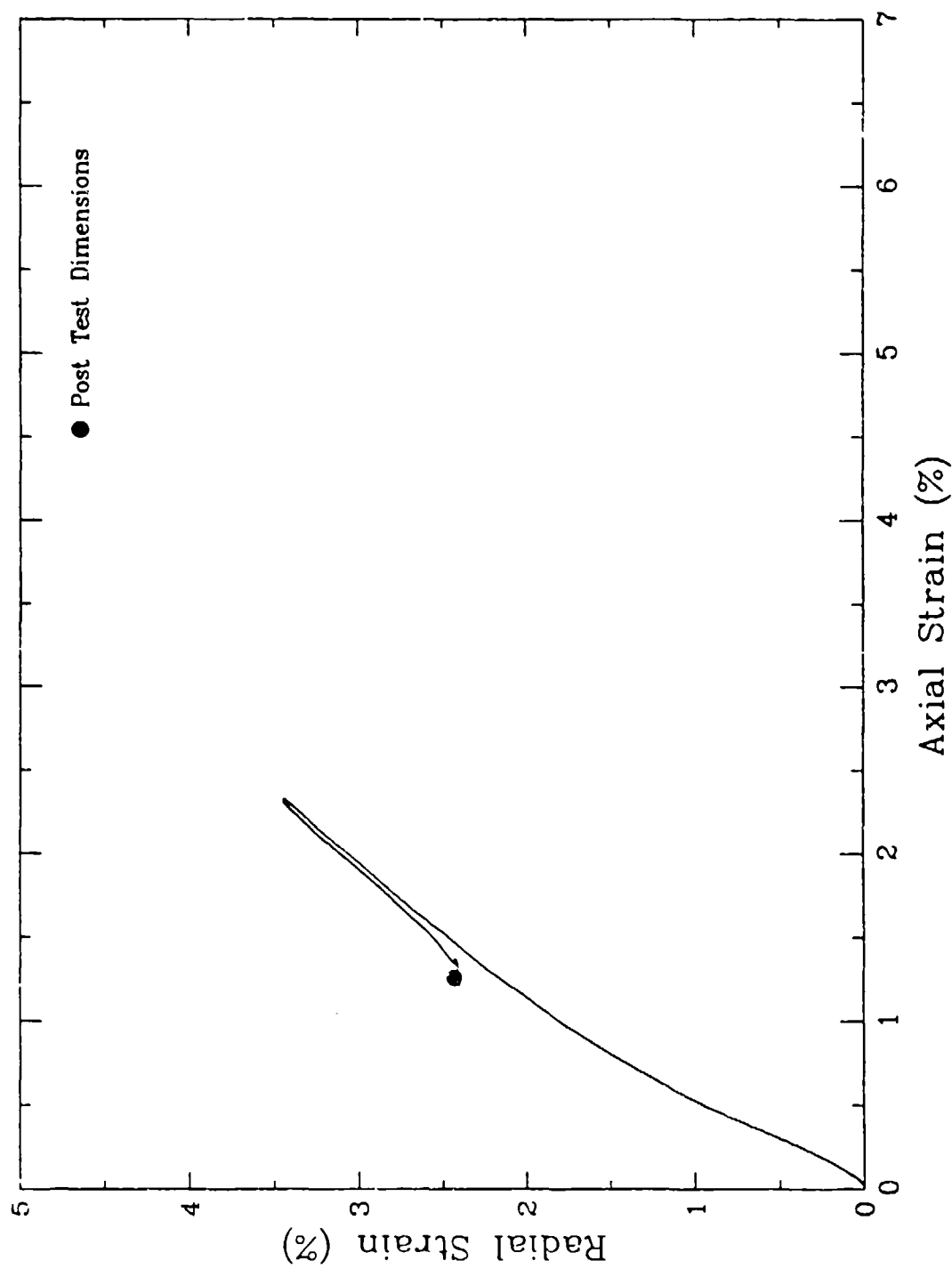


Figure 5-13. Typical relationship between axial and radial strain for intact Salem limestone loaded in hydrostatic compression.

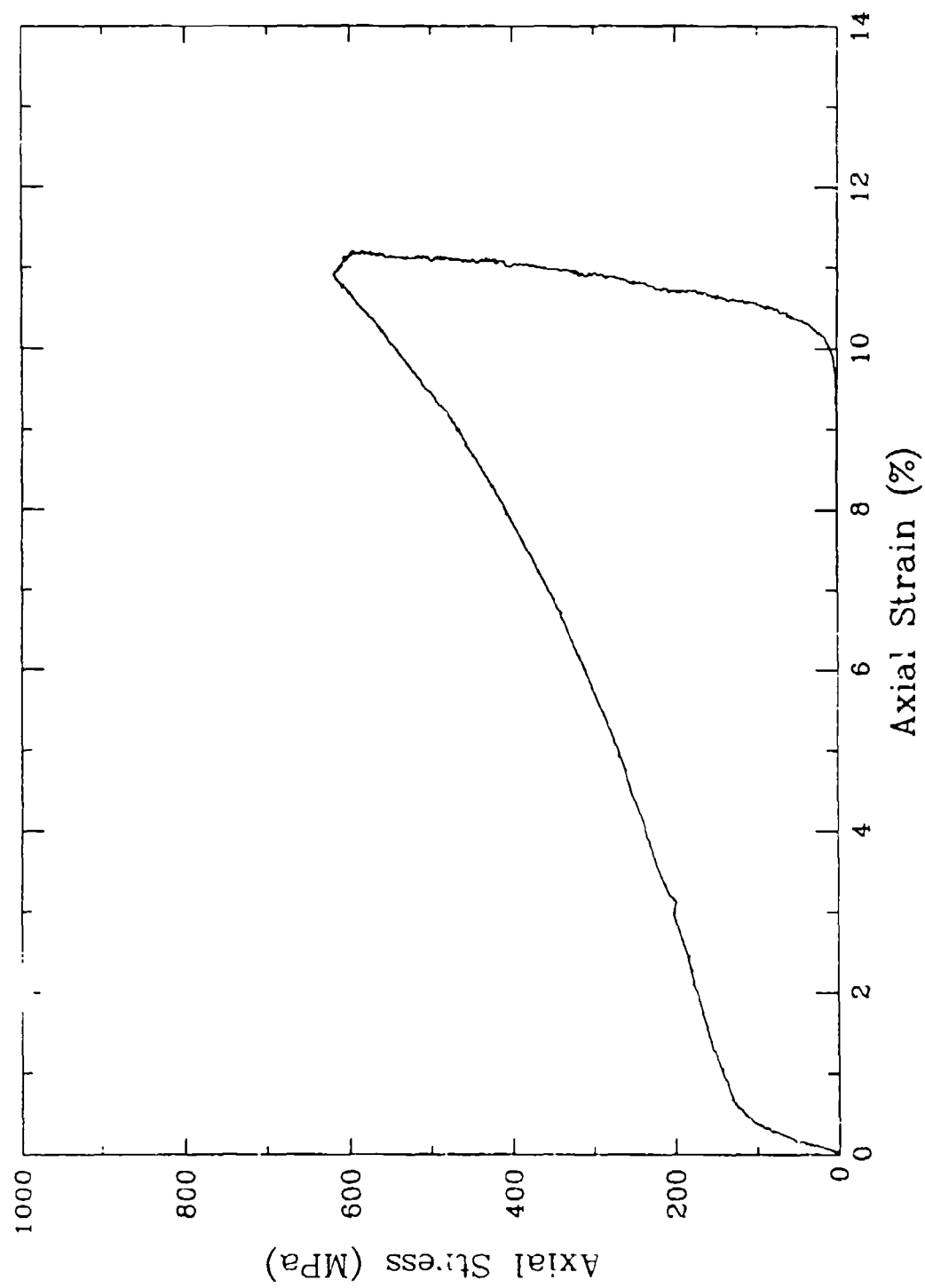


Figure 5-14. Typical relationship between axial stress and axial strain for intact Salem limestone loaded in uniaxial strain.

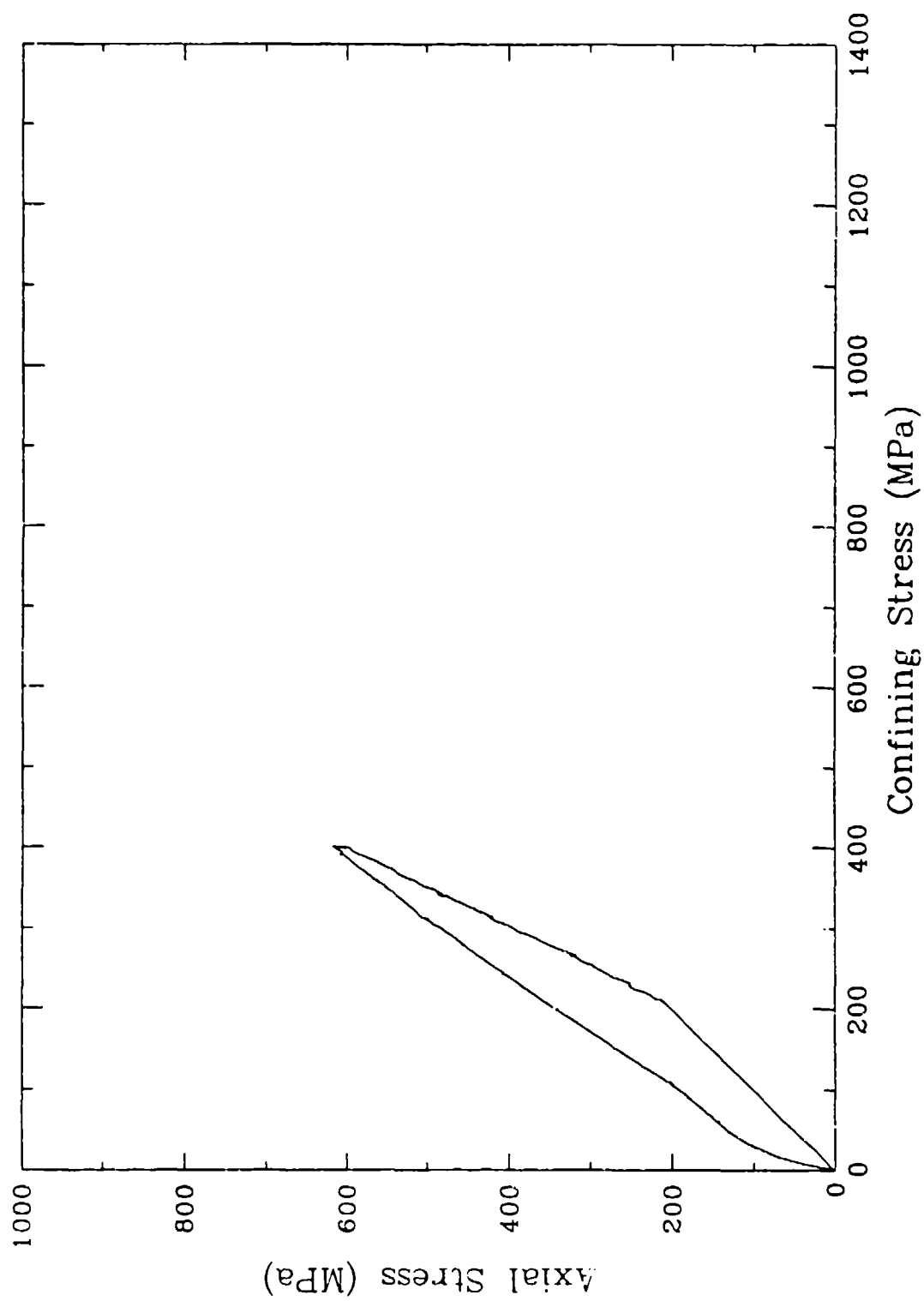


Figure 5-15. Typical relationship between axial stress and confining pressure for intact Salem limestone loaded in uniaxial strain.

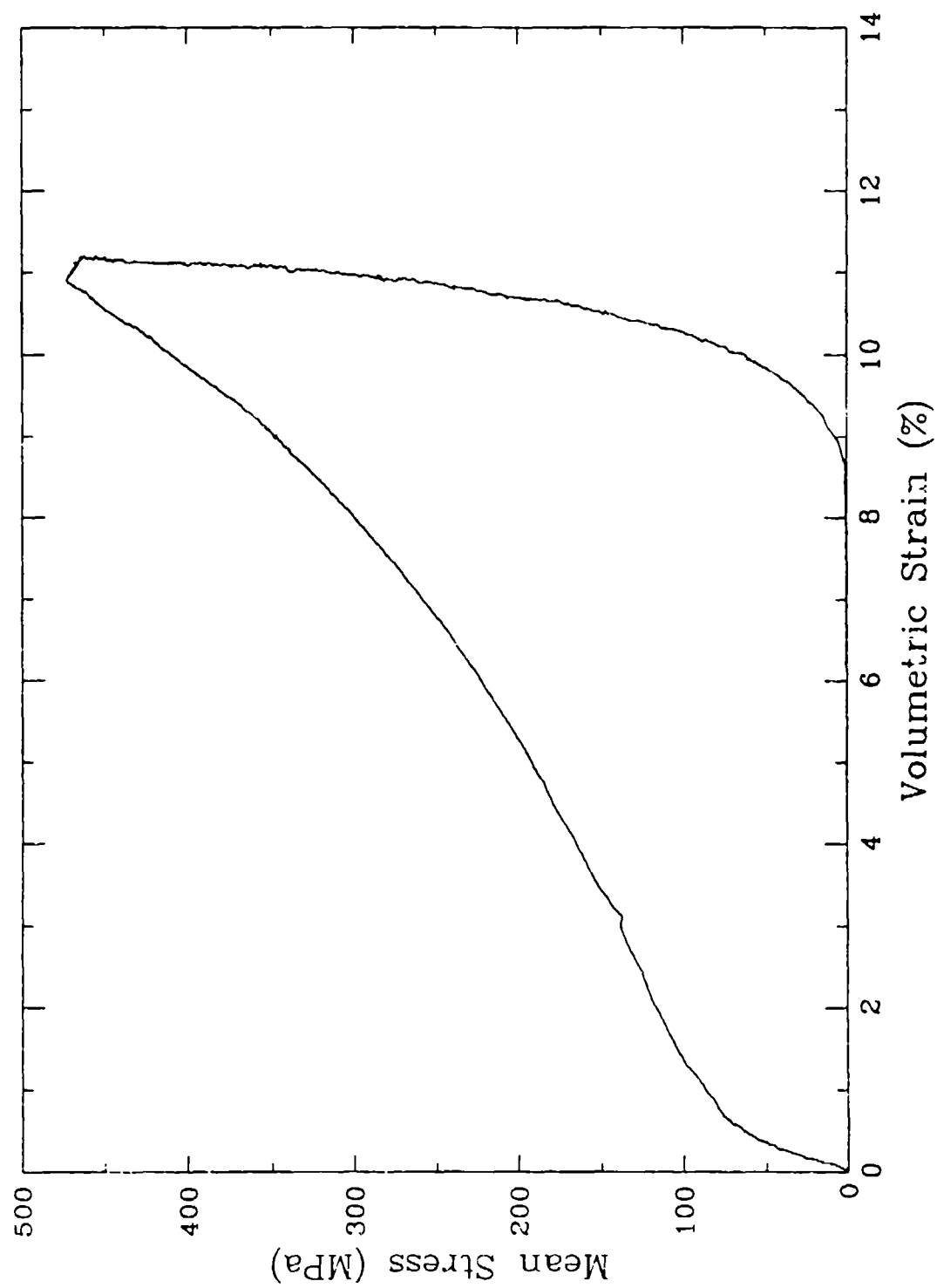


Figure 5-16. Typical relationship between mean stress and volumetric (axial) strain for intact Salem limestone loaded in uniaxial strain.

## SECTION 6

### MECHANICAL PROPERTY TESTS ON JOINTED LIMESTONE SPECIMENS

Strength and deformation properties of the three types of joint surfaces described in Section 3 were measured by conducting triaxial compression tests on cylindrical specimens with joints oriented approximately  $30^\circ$  to the axes of the cores. Identical tests were performed on intact specimens, and the differences in deformations were used to derive measures of the shear and normal deformations of the joints under load. Table 6-1 summarizes the joint tests performed, including tests on intact specimens to support determination of joint deformations.

#### 6.1 TEST PROCEDURES.

The test specimens, prepared as described in Section 3, were sealed inside a flexible membrane which was sealed on both ends to hardened steel endcaps. At confining pressures below 10 MPa, the confining fluid was nitrogen gas and a latex membrane was used. At higher pressures, a heat-shrinkable polyolefin membrane was used in a hydraulic fluid-kerosene mix. In all cases, lubricating membranes were placed between the ends of the specimen and the steel endcaps. These consist of a 0.13-mm layer of copper next to the rock and two 0.05-mm layers of PTFE. This system results in a coefficient of friction of 0.02 - 0.05 in the stress range of interest. Figure 4-1 is a schematic view of a prepared test specimen, including the lubricating materials.

The tests reported here were all conducted along a conventional triaxial compression load path. The confining pressure was raised to a specified level and then held constant while controlled axial deformation of the specimen was imposed with the piston.

Two diametrically opposite LVDTs (displacement transducers) attached to the endcaps were used to measure axial deformation of each test specimens. Corrections were applied to the data for deformation of the endcaps and lubricating materials. Radial deformation measurements were made with a third LVDT attached to a floating reference ring. In jointed specimens, it was installed horizontally at mid-height of the specimen in the vertical plane perpendicular to the

plane of the joint. Since all of the measurements were made at constant confining pressure, any change in membrane thickness in the course of the tests was considered negligible. In joint tests, a correction was made for tilt of the radial ring due to relative displacement of the specimen halves.

At low confining pressures, Salem limestone exhibits higher strengths when tested dry than when moist, but not saturated. Since the objective of this effort is to support modeling of saturated in situ materials, all tests were conducted on specimens with approximately 2.5% moisture expressed as fraction of the dry mass of the rock. This amount of water fills less than half of the available pore space, and thus there is little chance of saturation during specimen deformation except at higher (100's of MPa) confining pressures.

## 6.2 STRENGTH TEST RESULTS.

The average unconfined strength of the Salem limestone used in these tests is 58.3 MPa when tested dry and 48.5 MPa when tested at 2.5% moisture content. To provide a basis for comparison with the joint tests, the strength envelope of the intact material was determined by a series of triaxial compression tests on intact specimens. Figure 5-3 presents the stress difference-axial strain curves for 6 tests at pressures ranging from 1 to 35 MPa, which covers the range of interest to joint behavior. The behavior of all of the test specimens can be classified as brittle except for the 35-MPa test which is in the brittle-ductile transition. The specimens were also instrumented for radial deformation, but the location of the failure is unpredictable on specimens tested with lubricated endcaps. Thus, the single radial deformation measurement at mid-height often misses the post-failure radial expansion. For purposes of computing joint deformations, this is not a drawback because only the elastic portions of the deformation records from the intact specimens are used.

Since all of the stress-strain curves in Figure 5-3 exhibit well defined peaks, their strengths can be defined unambiguously as the states of stress at the peaks of the stress-strain curve. Figure 5-5 presents the strength points from 9 tests in terms of stress difference and mean stress. For the stress conditions of a triaxial compression test, these are the same, except

for a constant multiplier, as the first invariant of stress and the square root of the second invariant of the stress deviator, and are defined as follows:

$$\text{stress difference} = \sigma_a - \sigma_r \quad (6.1)$$

$$\text{mean stress} = (\sigma_a + 2\sigma_r)/3 \quad (6.2)$$

where:  $\sigma_a$  = total axial stress  
 $\sigma_r$  = confining pressure

Suites of stress difference-deformation curves for smooth ground, tensile fracture, and synthetic jointed specimens are presented in Figure 6-1 through 6-3, respectively. The deformation quantities plotted there are the overall axial and radial deformations of the jointed cylindrical test specimen and thus include deformations of both the joints and the intact material. Figure 6-4 through 6.9 present a comparisons of force-deformation curves for tests at 1, 2, 5, 10, 20, and 35 MPa confining pressures, respectively, on all three of the joint types described above and intact rock. In spite of having a slightly higher magnitude of roughness the synthetic joint exhibits a lower strength than the tensile fracture. There is also significantly more deformation associated with the synthetic joint prior to reaching the strength limit. These characteristics are probably due to the imperfect match in the smallest details between the halves of the synthetic joint.

As with the intact tests, the stress-deformation curves for tensile fracture and synthetic joints have well defined peak load points indicating the limiting state of stress for the confining pressure level of that test. In contrast, the smooth ground joints gradually approach a peak stress level, which then remains approximately constant under further shearing deformation. For smooth ground joints, that constant stress level was considered to be the strength. In order to understand joint behavior, the measured stress quantities, axial stress and confining pressure, were rotated to obtain the values of shear and normal stress acting on the joint planes. The equations for the stress rotation are found in any text on mechanics of materials. Table 6-1 lists

the strength of each test specimen in terms of the measured stress difference. In addition, the peak strengths of the joints are listed in terms of the shear and normal stress acting on the joint at the time of failure. Figure 6-10 presents strength data from joint tests on all three surface types in terms of the shear and normal stresses on the joint planes. For the joint tests, it is possible to plot the strengths as single points because the plane of interest is known. In contrast, for the tests on intact specimens, the stress states plot as circles, known as Mohr's circles, with different points on each circle corresponding to different orientations of the reference plane in the corresponding specimen. Since the plane of failure is not precisely known, the strength envelope line for intact material in Figure 6-10 was constructed by plotting Mohr's circles for all of the intact tests and making a judgement fit of a curve that approximates a tangent to all tests.

The data points indicated by the square symbols in Figure 6-10 are from specimens with tensile fractured joint surfaces. In all of those tests, failure occurred by sliding along the joint. The dot-dashed line, which is an approximate fit to those data points represents a strength envelope for the fractured surface. It runs roughly parallel to the intact strength and about 5 MPa lower. The highest point shown, at about 46 MPa normal stress, is from a test at 25 MPa confining pressure. In a similar test, performed at 35 MPa, failure did not occur by relative displacement along the joint. Instead, there was localized shear banding and radial deformation characteristic of the failure of an intact specimen at that confining pressure. This is an indication that as the test progressed, some point on the Mohr's circle reached the intact strength envelope before the stress on the joint reached the joint strength envelope. This is illustrated in Figure 6-10. The circular segment at the right side of the figure is the Mohr's circle representing the stress state in the specimen at failure. The line at  $30^\circ$  to the vertical originating at 35 MPa on the normal stress axis is the stress path experienced by the joint as the test progressed from hydrostatic to failure. The intersection of the joint stress path with the circle represents the state of stress on the joint when the specimen failed elsewhere. Thus, the strength envelope of the joint must be at least slightly higher than that point.

The strengths derived from tests on synthetic (machined) joints are shown as triangles on Figure 6-10. The fit to these points falls 3-4 MPa below the tensile fracture strength line and



has somewhat less curvature. As in the case of the tensile fracture joint, a synthetic joint tested in triaxial compression at 35 MPa confining pressure exhibited the same response (strength, deformation, and failure mode) as an intact specimen subjected to the same loading.

The joint strength points from smooth ground surfaces are plotted as circles in Figure 6-10. In contrast to the curved envelopes formed by the intact, fracture, and synthetic joint data, the strengths of the smooth ground joints can be well approximated by a straight line passing through the origin, i.e. Coulomb friction. As with the other joint surface types tested, a triaxial compression test performed on a smooth ground joint at 35 MPa confining pressure resulted in a failure in the intact mode rather than by slip of the joint, suggesting that the strength envelope for smooth ground joints must also pass above the stress experienced by the joint in the 35 MPa test.

From the stress-deformation curves presented in Figures 6-2 a - 6-5, it is apparent that the shear stress supported by the joints with interlocking asperities (tensile fracture and synthetic) peaks on initial loading and then diminishes to a residual value as the asperities are sheared off. In addition to the peak strength data, Table 6-1 presents values of residual strength for each joint test. For the tensile fracture and synthetic joints as well as intact specimens, the residual strength is the value reached after the peak, when stress difference becomes relatively constant. For the smooth ground joints, residual strength is the same as peak strength. Figure 6-11 presents the residual strength data for the three different types of joints and intact material. The strength points for the intact limestone were computed for the failure plane defined by the point on the peak strength envelope for the particular test. For comparison, the peak strength envelopes for the various joints and the intact limestone are shown along with the data points for residual strength. The residual strengths for intact limestone and tensile fracture and synthetic joints fall significantly lower than their respective peak strengths. All of the residual strength envelopes converge to the peak intact strength envelope at approximately 75 MPa normal stress.

### 6.3 JOINT DEFORMATION.

The normal and tangential deformations of the joints under shear loading were inferred from two tests that were as nearly identical as possible, except for the presence of a joint in one and not the other. In joint tests where failure occurred by sliding along the joint, the two halves remained essentially elastic. Thus, the net deformation of the intact portion of the jointed test specimen can be approximated by the initial elastic loading region of the corresponding intact specimen at the same stress difference level. In both the axial and radial directions, the joint deformation was computed as the difference between the total deformation of the jointed test specimen and the deformation of the intact specimen under like stress conditions. A vector rotation was then performed to arrive at components of deformation normal and tangential to the joint.

Figures 6-12 through 6-14 present joint deformation data for smooth ground, tensile fracture, and synthetic joint surfaces, respectively. The normal and shear stresses on the joints are plotted against joint normal and tangential displacements, respectively, for tests at three confining pressures, 5, 10, and 20 MPa. The tensile fracture joints exhibit essentially zero displacement until the strength limit of the joint is reached, at which time slip on the joint is accompanied by a reduction in strength. In contrast, displacement of the smooth ground joints begins well below the strength limit, and when the limit is reached, displacement continues with no significant change in stress. The synthetic joints exhibit response intermediate between those of the tensile fracture and smooth ground surfaces. Like the tensile fractures, the shear stress supported by the synthetic joints reaches a limit and then diminishes with additional deformation. However, the synthetic joints also exhibited significant tangential deformation prior to reaching the strength limit. This is apparently a result of the imperfect between the halves of the synthetic joints.

In Figures 6-15 through 6-17, joint normal deformation is plotted against joint tangential deformation for the same sets of joint tests. During shear of the smooth ground joints there is no tendency to dilate, and tests at all three confining pressures exhibit a slight joint compaction under shear loading. Initially, the tensile fracture joints exhibit a minute amount ( $\sim 0.02$  mm)

of compaction prior to failure of the joint. After failure occurs, the tensile fracture joints tested at confining pressures below 10 MPa show some normal dilation, presumably a result of asperities riding over each other, and those tested at higher confining pressures exhibit very slight compaction as the asperities are sheared off and ground up. Upon joint failure, the normal displacement curves shown in Figure 6-16 fall in order according to confining pressure, with the greatest dilation at the lowest pressure and the highest compaction at the highest pressure. After approximately 2 mm of tangential displacement, there is some crossing of the curves, probably due to variations in the surfaces between specimens. As with the tensile fractures, the synthetic joints compact slightly on initial loading, after which the curves separate in order of confining pressure.

Table 6-1. Summary of mechanical property tests on jointed Salem limestone specimens.

Test ID	Specimen ID	Joint Angle (deg)	Conf. Pressure (MPa)	Stress Diff (MPa)	Peak			Residual			
					Mean Stress (MPa)	Normal Stress (MPa)	Shear Stress (MPa)	Stress Diff (MPa)	Mean Stress (MPa)	Normal Stress (MPa)	Shear Stress (MPa)
INTACT											
M4B2	SL26-1D1	23.0	1	53.8	18.9	9.2	19.4	8.0	3.7	2.2	2.9
M4A2	SL26-1A1	24.4	2	58.0	21.3	11.9	21.8	5.0	3.7	2.9	1.9
N15A1	SL26-3A1	29.0	5	68.6	27.9	21.1	29.1	23.0	12.7	10.4	9.8
N11A1	SL26-3D1	37.5	10	75.4	35.1	37.9	36.4	48.0	26.0	27.8	23.2
M5A2	SL26-2A2	35.0	15	82.3	42.4	42.1	38.7	67.0	37.3	37.0	31.5
N18B1	SL26-3A2	36.0	20	84.0	48.0	49.0	39.9	78.0	46.0	46.9	37.1
M11B2	SL26-3D2	44.0	35	92.0	65.7	79.4	46.0	92.0	65.7	79.4	46.0
SMOOTH GROUND											
G18A2	SL24-5	29.7	1	4.9	2.6	2.2	2.1	4.9	2.6	2.2	2.1
G19A2	SL24-6	29.3	2	8.1	4.7	3.9	3.5	8.1	4.7	3.9	3.5
N15B1	SL26-42	29.6	5	13.0	9.3	8.2	5.6	11.9	9.0	7.9	5.1
N13A1	SL26-44	30.4	10	29.5	19.8	17.6	12.9	28.0	19.3	17.2	12.2
N15C1	SL26-46	29.6	20	52.0	37.3	32.7	22.3	50.0	36.7	32.2	21.5
M12B2	SL26-47	30.0	25	68.5	47.8	42.1	29.6	68.5	47.8	42.1	29.6
M17A2	SL26-48	29.8	35	89.0	64.7	Failed as Intact		89.0	64.7		
TENSILE FRACTURE											
M6A2	SL26-1CB2	28.2	1	25.6	9.5	6.7	10.7	6.5	3.2	2.5	2.7
N14B1	SL26-3BA1	31.9	2	21.4	9.1	8.0	9.6	10.0	5.3	4.8	4.5
M9A2	SL26-1BA2	30.9	2	36.3	14.1	11.6	16.0	12.5	6.2	5.3	5.5
M6B2	SL26-2BC	28.7	3	39.0	16.0	12.0	16.4	16.0	8.3	6.7	6.7
N14A1	SL26-3CB1	31.7	5	49.5	21.5	18.7	22.1	27.5	14.2	12.6	12.3
N12A1	SL26-3DC1	30.7	10	62.6	30.9	26.3	27.5	42.1	24.0	20.9	18.5
N12B1	SL26-3BA2	28.3	20	74.5	44.8	36.7	31.1	62.0	40.7	33.9	25.9
N18A1	SL26-3DC2	30.9	20	76.2	45.4	40.0	33.5	68.0	42.7	37.9	29.9
M9B2	SL26-2BA	31.0	25	80.0	51.7	46.3	35.3	75.0	50.0	44.9	33.1
M10A2	SL26-3CB2	27.9	35	90.5	65.2	Failed as Intact		90.5	65.2		
SYNTHETIC											
G18B2	SL22-1	32.9	1	15.5	6.2	5.6	7.1	8.2	3.7	3.4	3.7
G19C2	SL22-2	32.6	2	21.5	9.2	8.2	9.8	12.5	6.2	5.6	5.7
G19D2	SL22-4	33.1	5	31.4	15.5	14.4	14.4	24.0	13.0	12.2	11.0
M11A2	SL26-62	32.2	10	48.5	26.2	23.8	21.9	37.0	22.3	20.5	16.7
M10B2	SL26-61	31.7	20	72.0	44.0	39.8	32.2	69.0	43.0	39.0	30.8
S18A2	SL24-11	33.3	35	95.3	66.8	Failed as Intact		95.3	66.8		

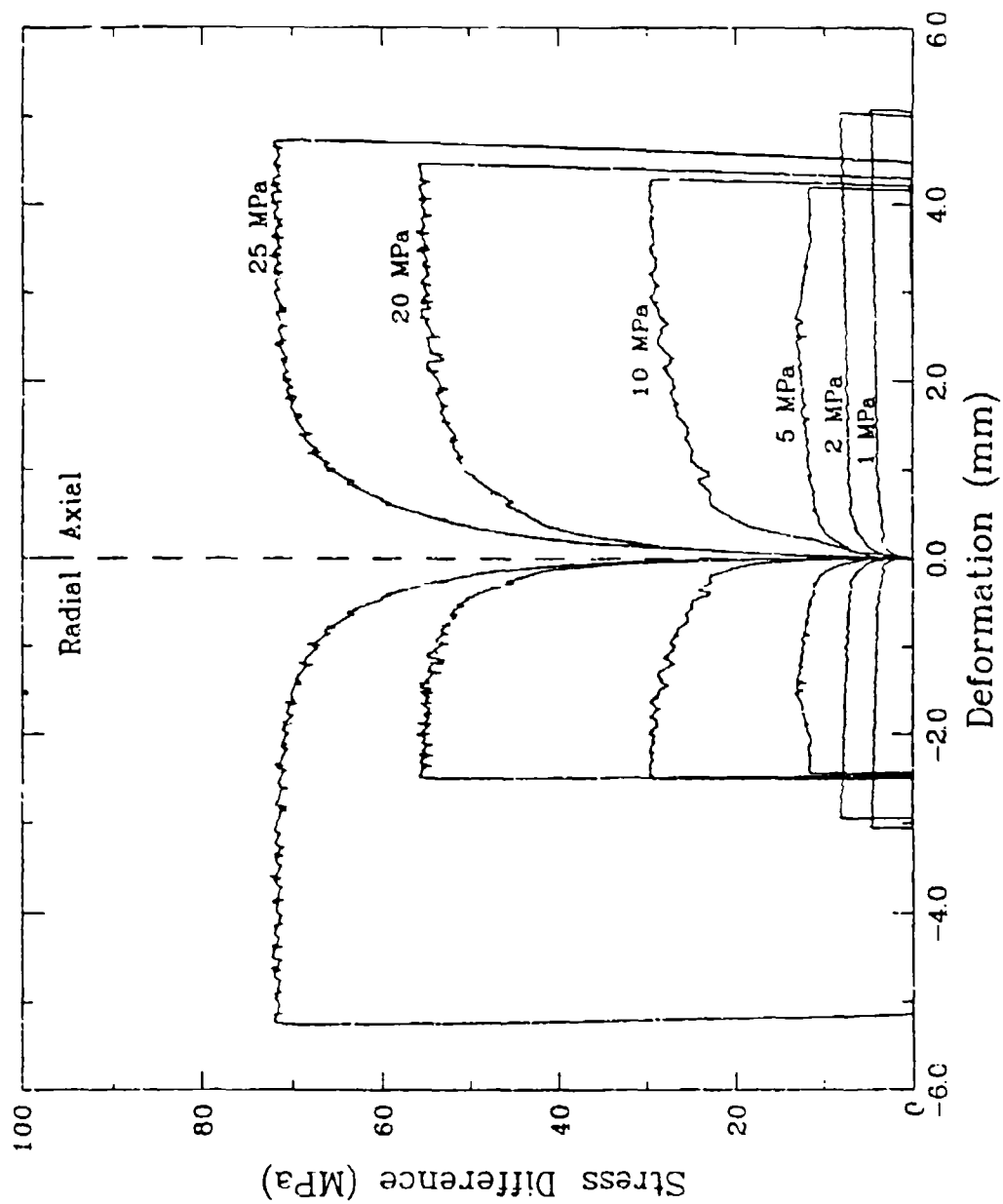


Figure 6-1. The relationships between stress difference and gross specimen deformations for specimens of Salem limestone with  $-30^\circ$  smooth ground joints tested in triaxial compression at various confining pressures.

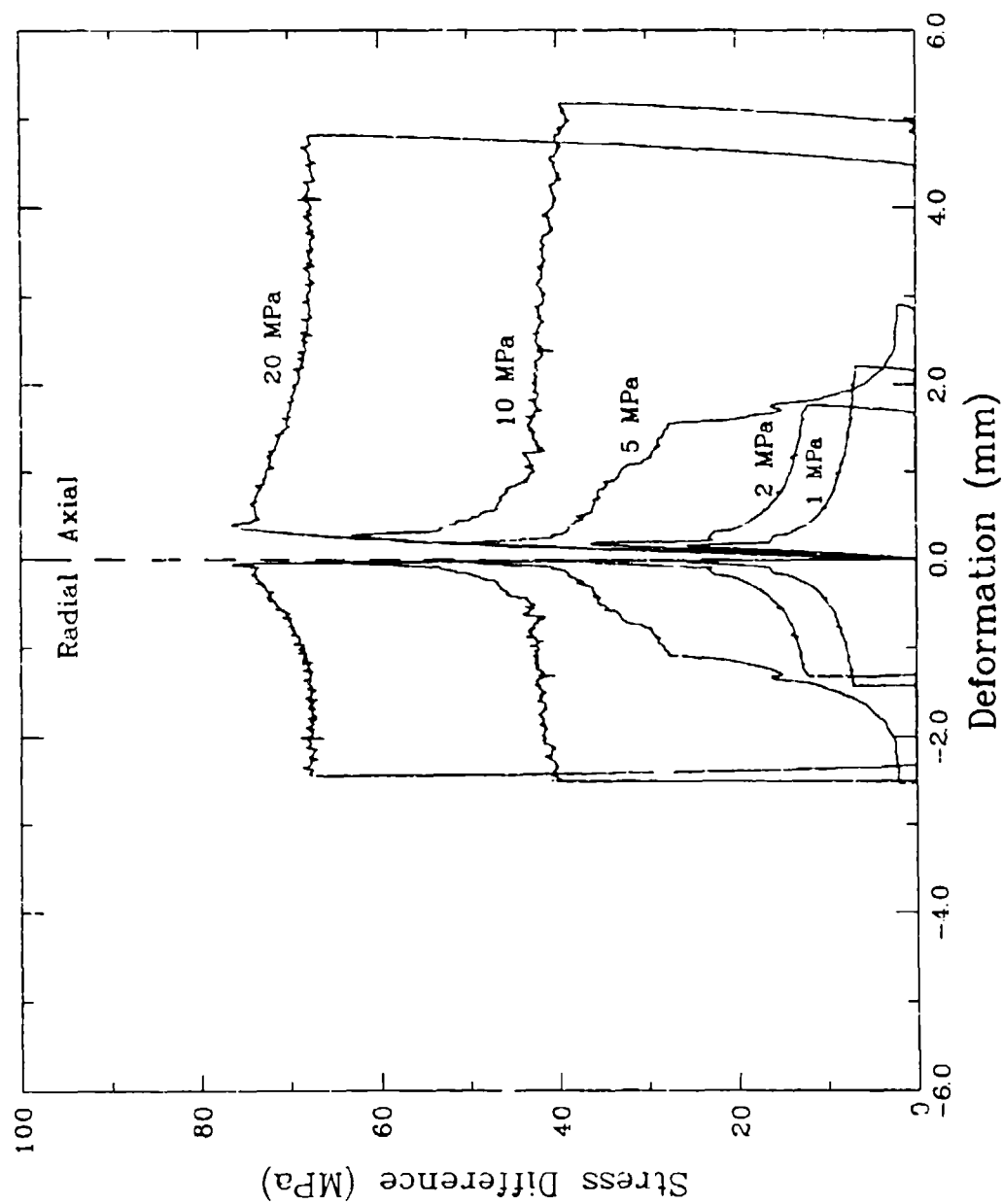


Figure 6-2. The relationships between stress difference and gross specimen deformations for specimens of Salem limestone with  $\sim 30^\circ$  tensile fracture joints tested in triaxial compression at various confining pressures.

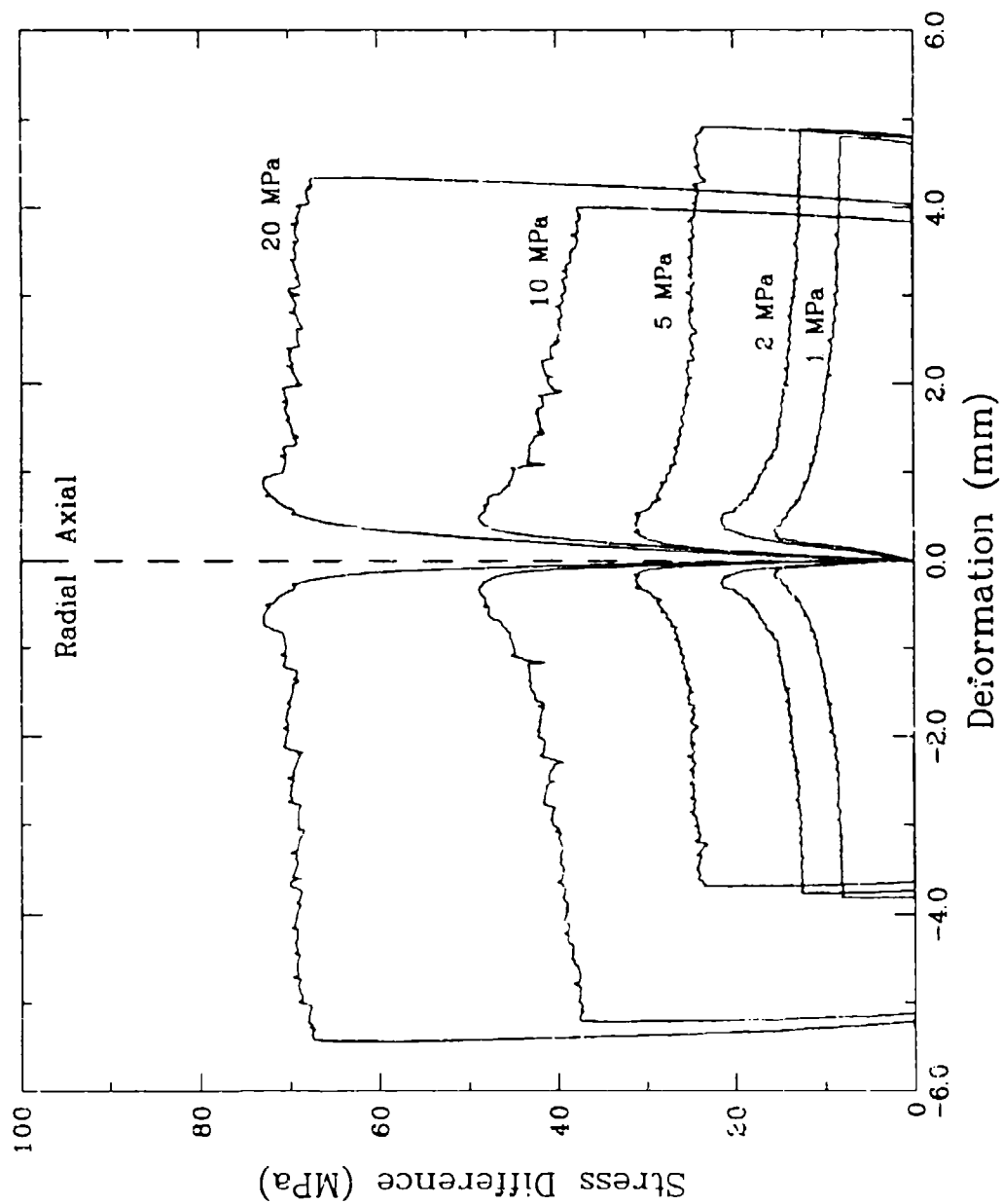


Figure 6-3. The relationships between stress difference and gross specimen deformations for specimens of Salem limestone with  $\sim 30^\circ$  synthetic joints tested in triaxial compression at various confining pressures.

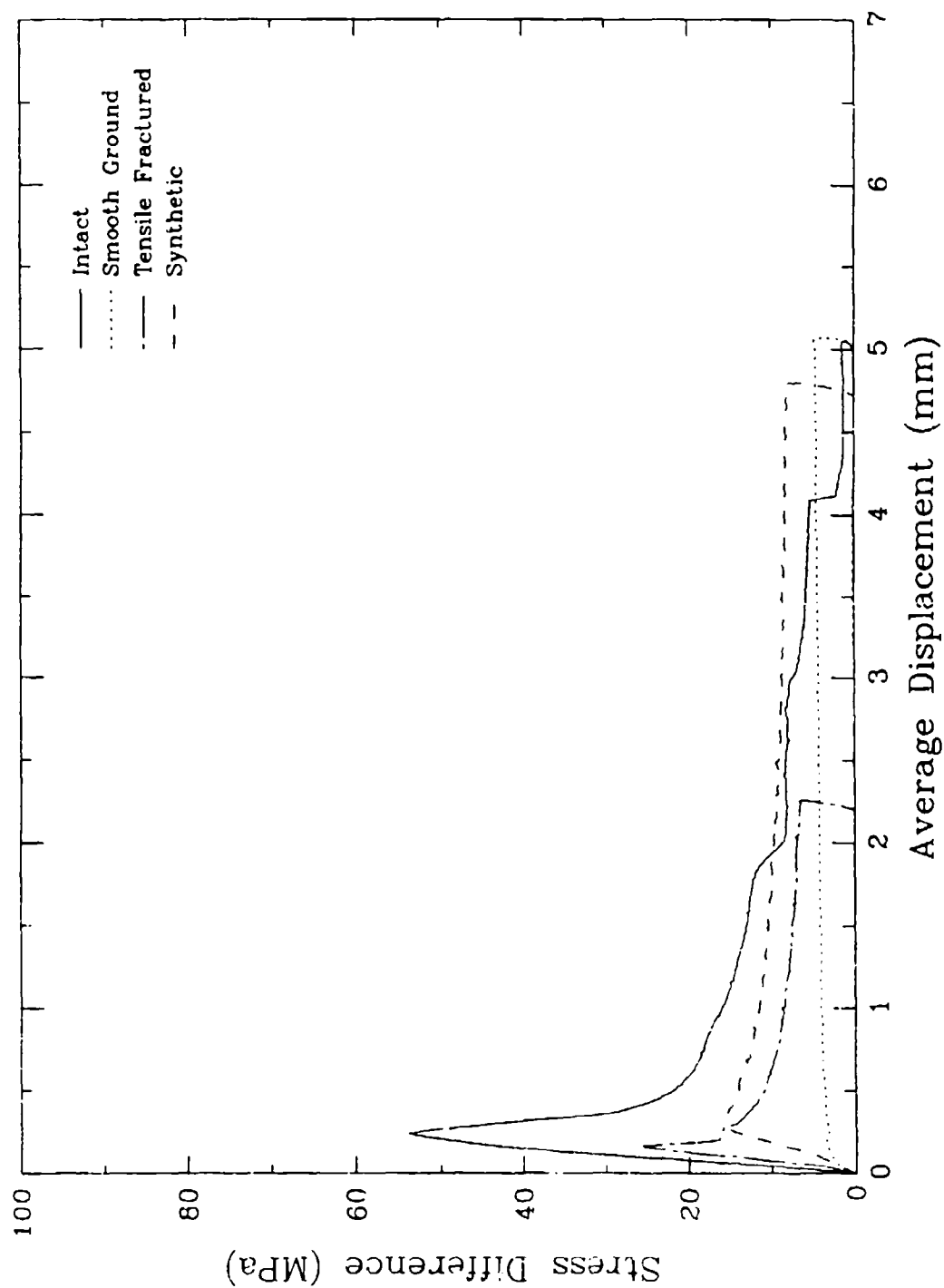


Figure 6-4. The relationships between stress difference and gross specimen deformations for specimens of Salem limestone, both intact and with three types of  $\sim 30^\circ$  smooth ground joints, tested in triaxial compression at 1 MPa confining pressure.



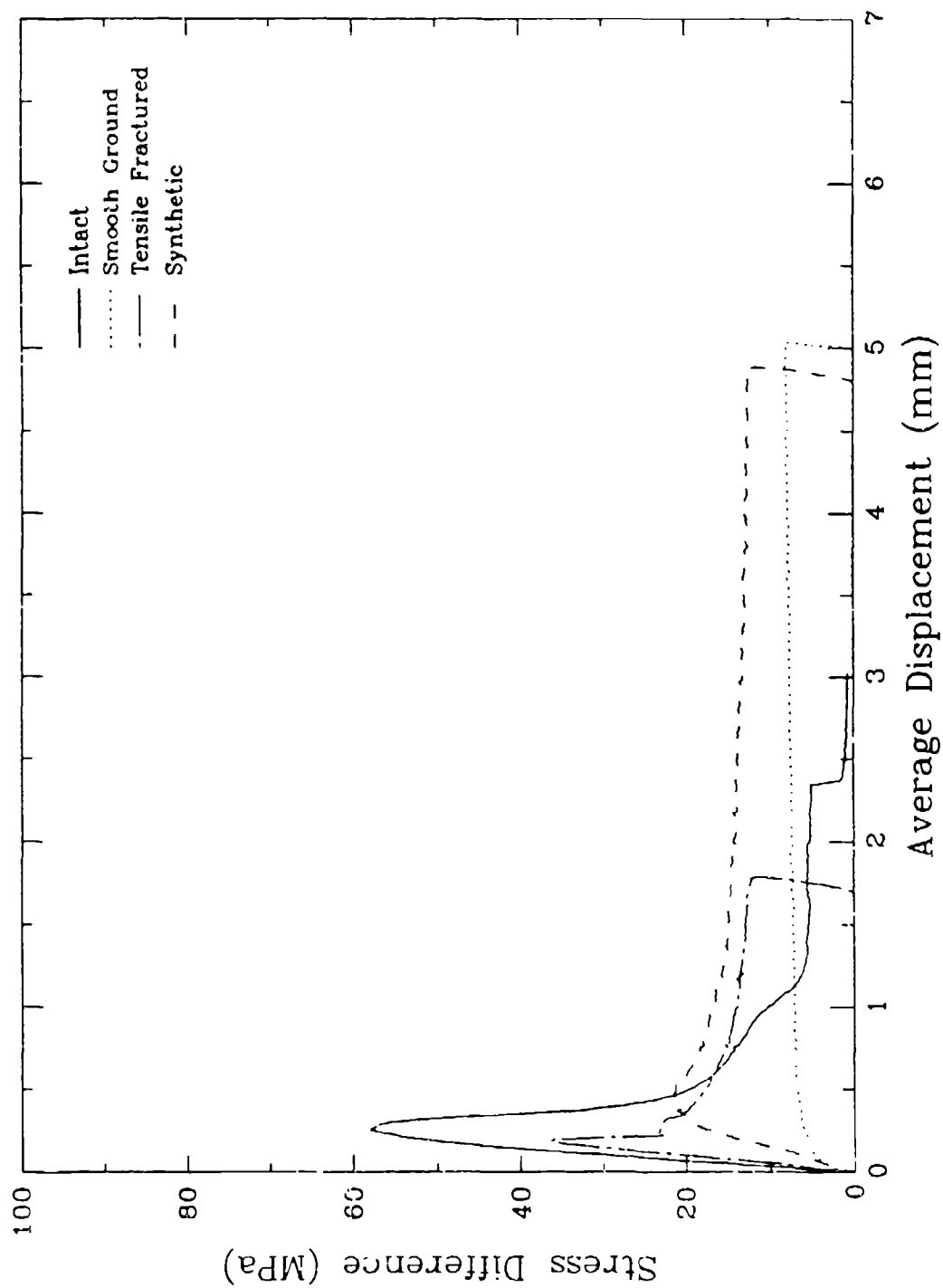


Figure 6-5. The relationships between stress difference and gross specimen deformations for specimens of Salem limestone, both intact and with three types of  $\sim 30^\circ$  smooth ground joints, tested in triaxial compression at 2 MPa confining pressure.

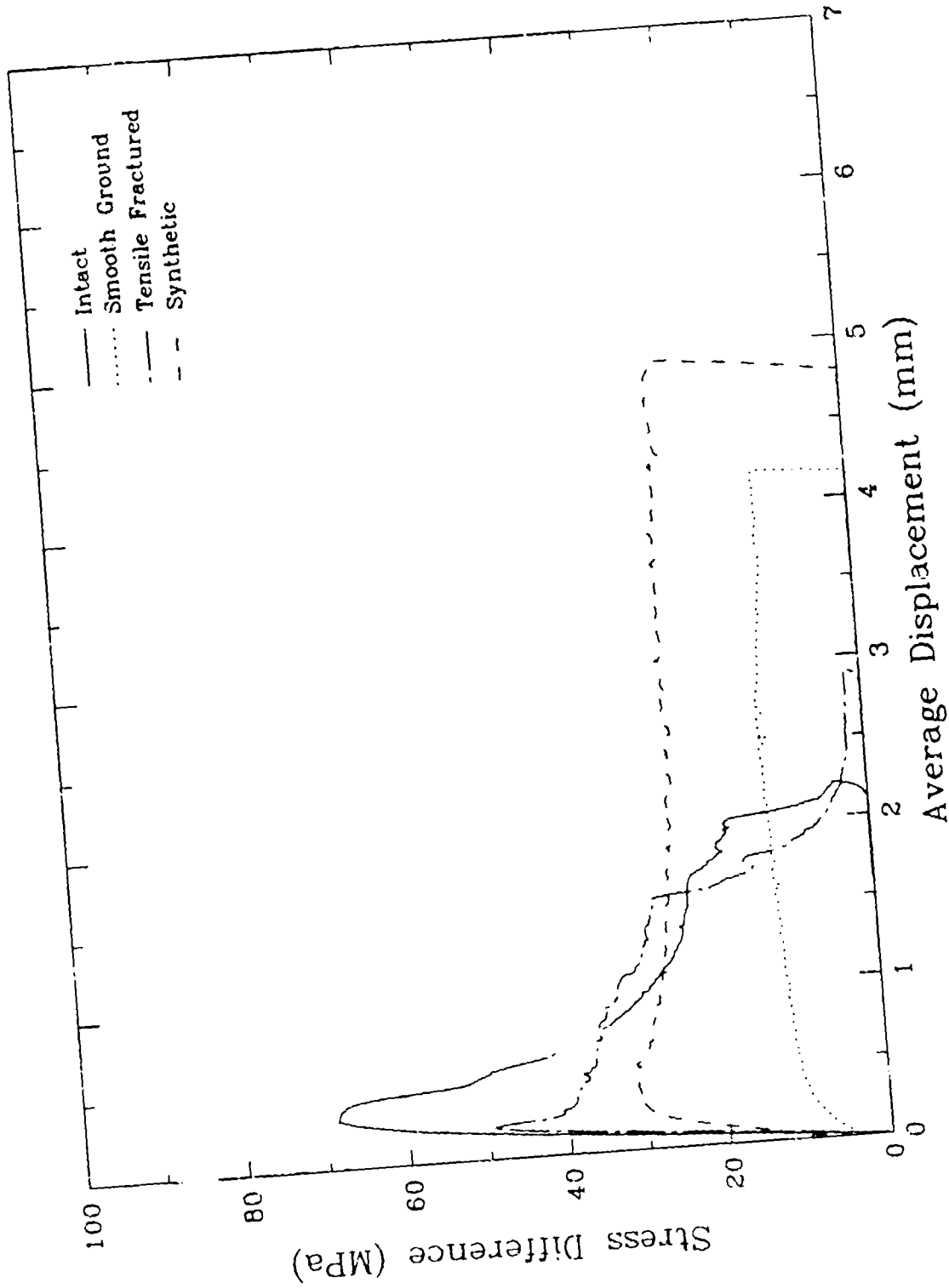


Figure 6-6. The relationships between stress difference and gross specimen deformations for specimens of Salem limestone, both intact and with three types of  $\sim 30^\circ$  smooth ground joints, tested in triaxial compression at 5 MPa confining pressure.

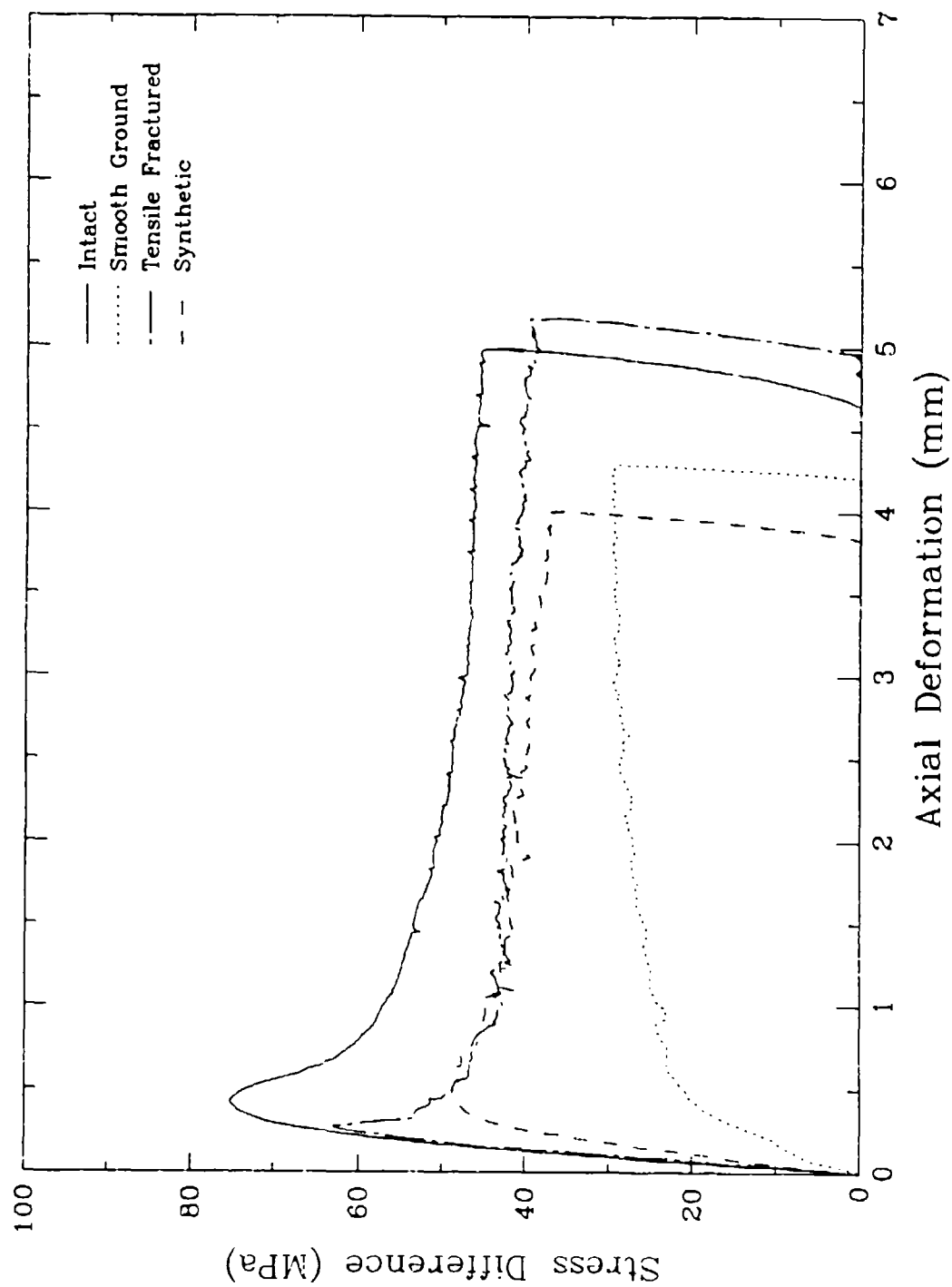


Figure 6-7. The relationships between stress difference and gross specimen deformations for specimens of Salem limestone, both intact and with three types of ~30° smooth ground joints, tested in triaxial compression at 10 MPa confining pressure.

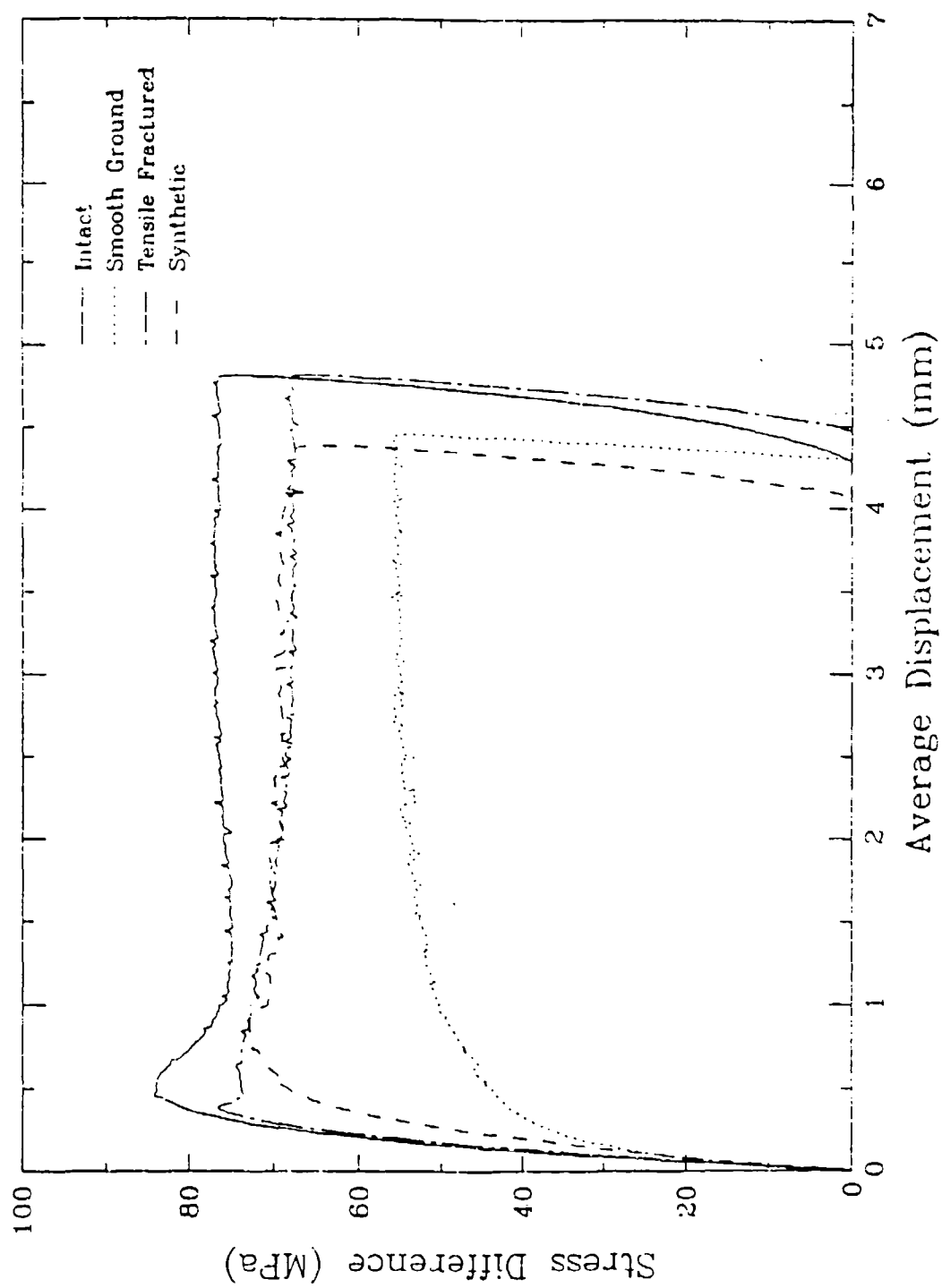


Figure 6-8. The relationships between stress difference and gross specimen deformations for specimens of Salem limestone, both intact and with three types of  $\sim 30^\circ$  smooth ground joints, tested in triaxial compression at 20 MPa confining pressure.

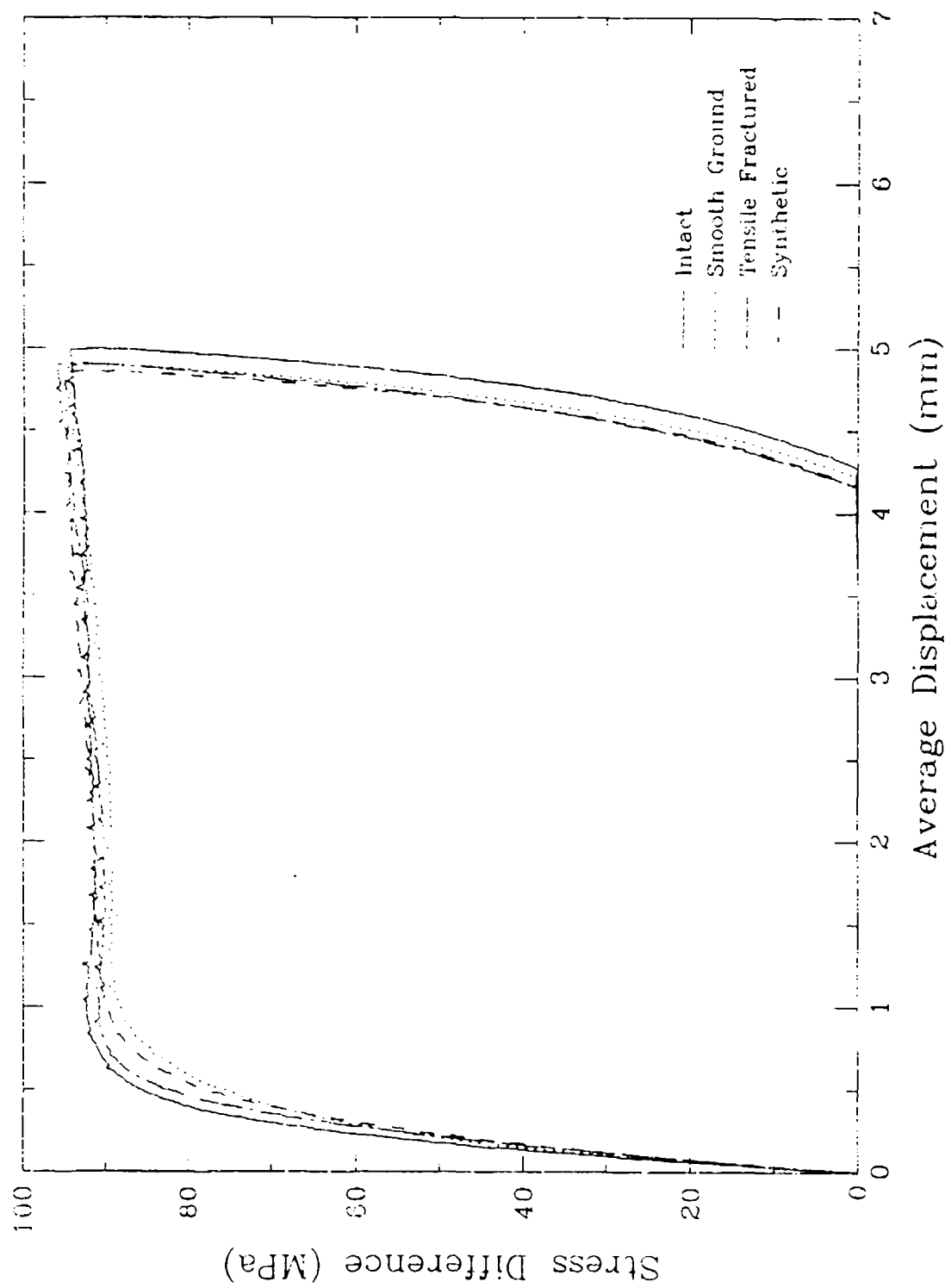


Figure 6-9. The relationships between stress difference and gross specimen deformations for specimens of Salem limestone, both intact and with three types of  $\sim 30^\circ$  smooth ground joints, tested in triaxial compression at 35 MPa confining pressure.

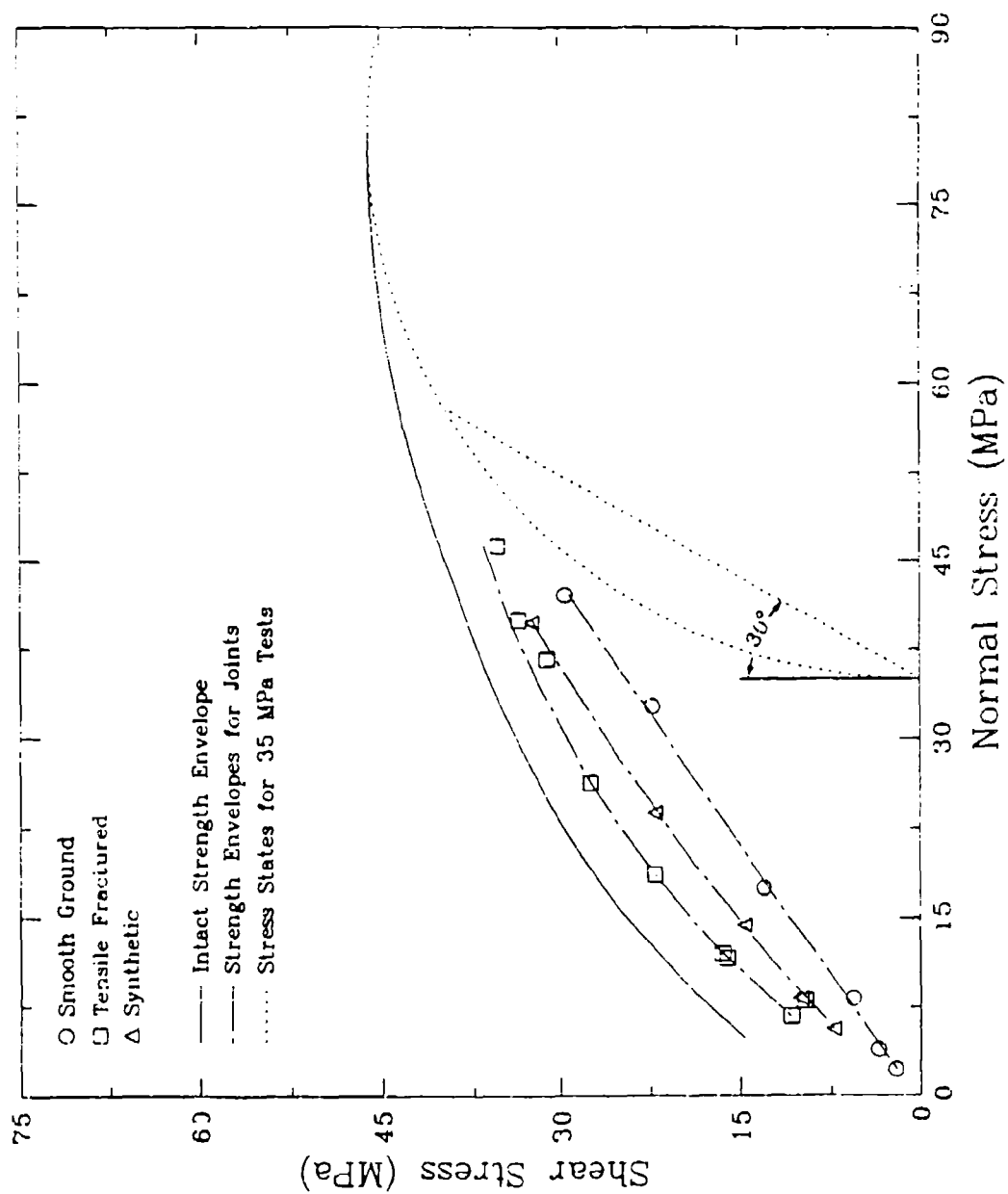


Figure 6-10. Peak strength data for three types of joints in Salem limestone with the strength envelope for intact rock shown for comparison.

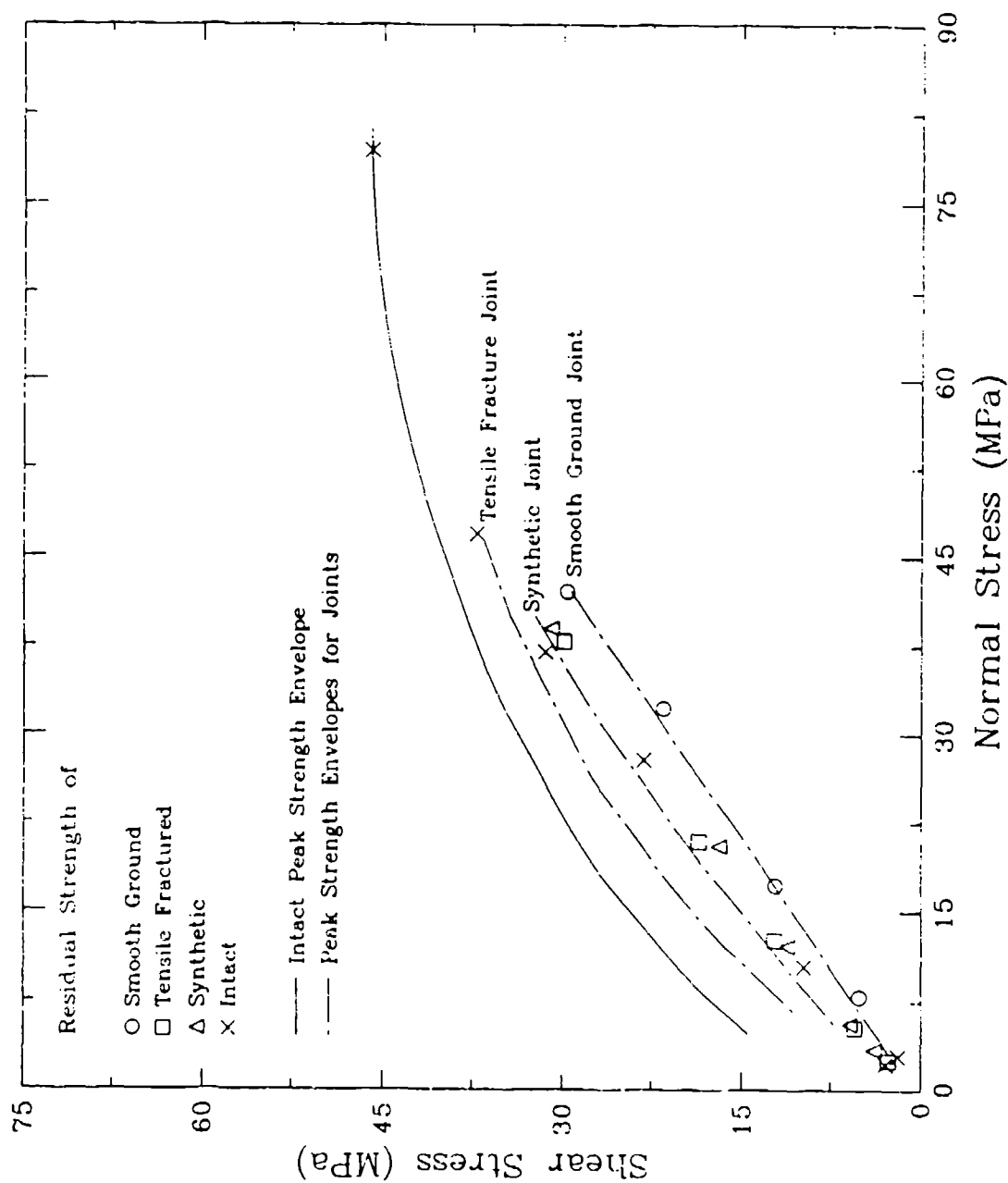


Figure 6-11. Residual strength data for three types of joints and intact Salem limestone with the peak strength envelopes shown for comparison.

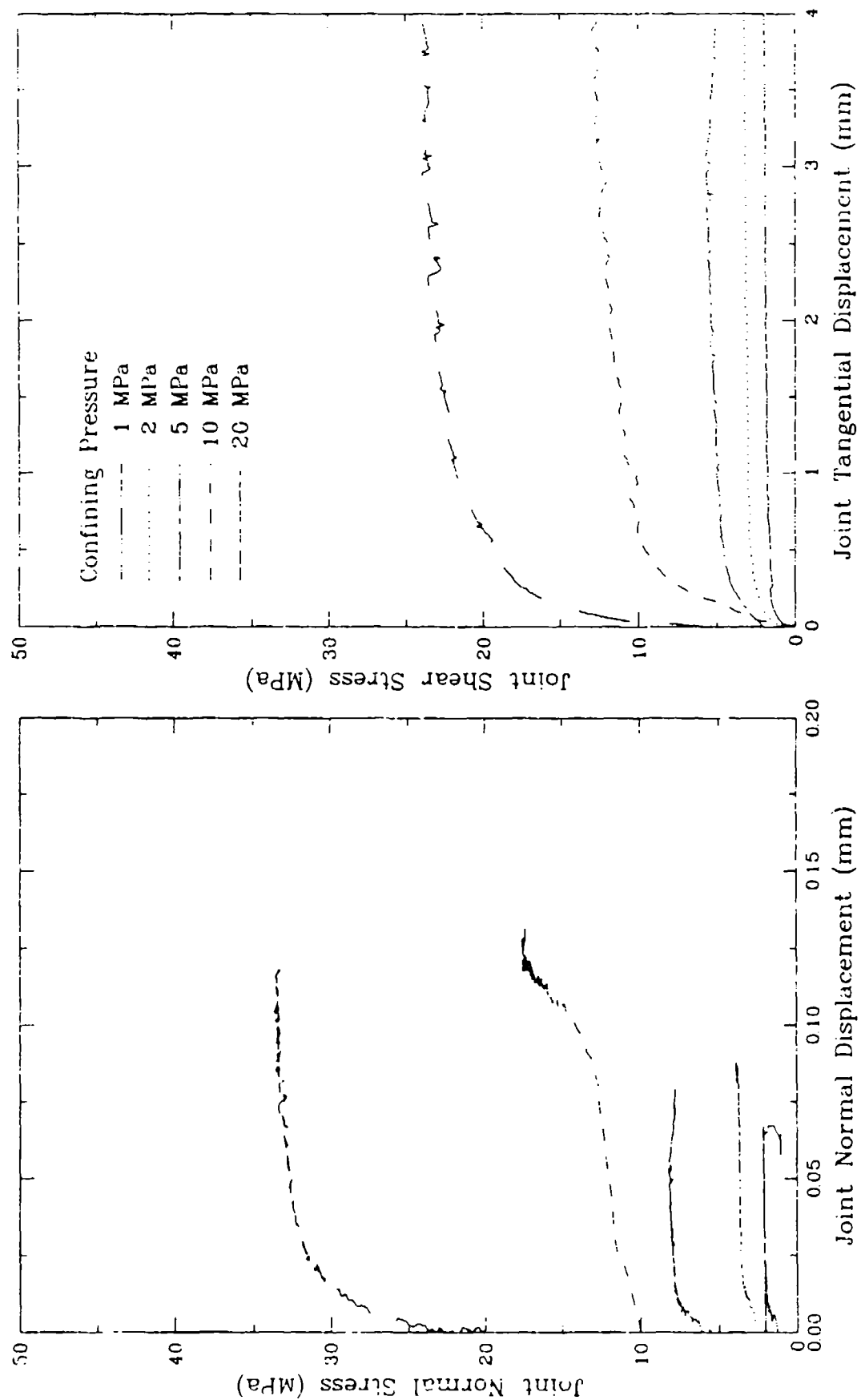


Figure 6-12. Normal and tangential deformations of smooth ground joints in Salem limestone plotted against normal and tangential deformations, respectively, for a range of confining pressure conditions.



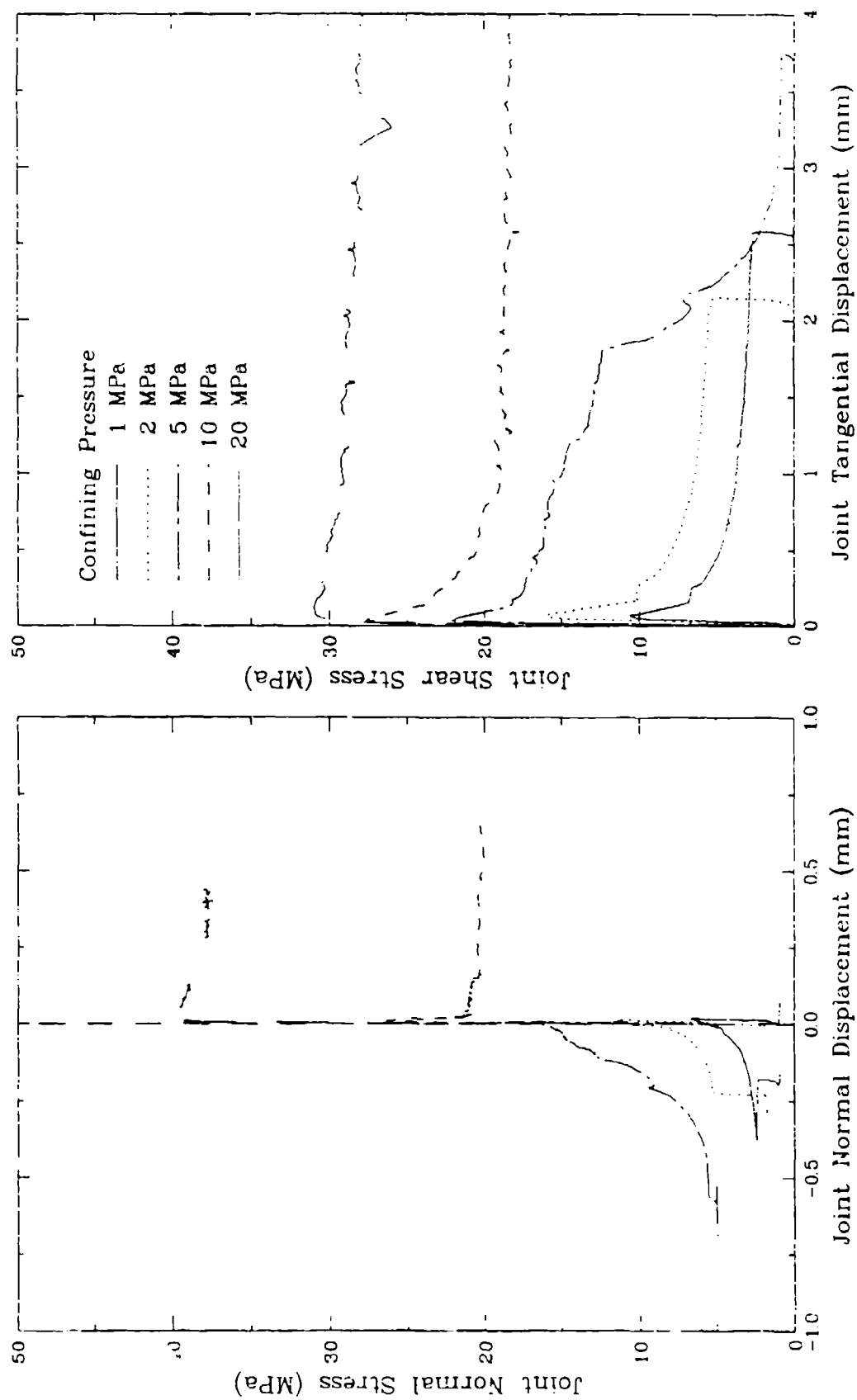


Figure 6-13. Normal and tangential deformations of tensile fracture joints in Salem limestone plotted against normal and tangential deformations, respectively, for a range of confining pressure conditions.

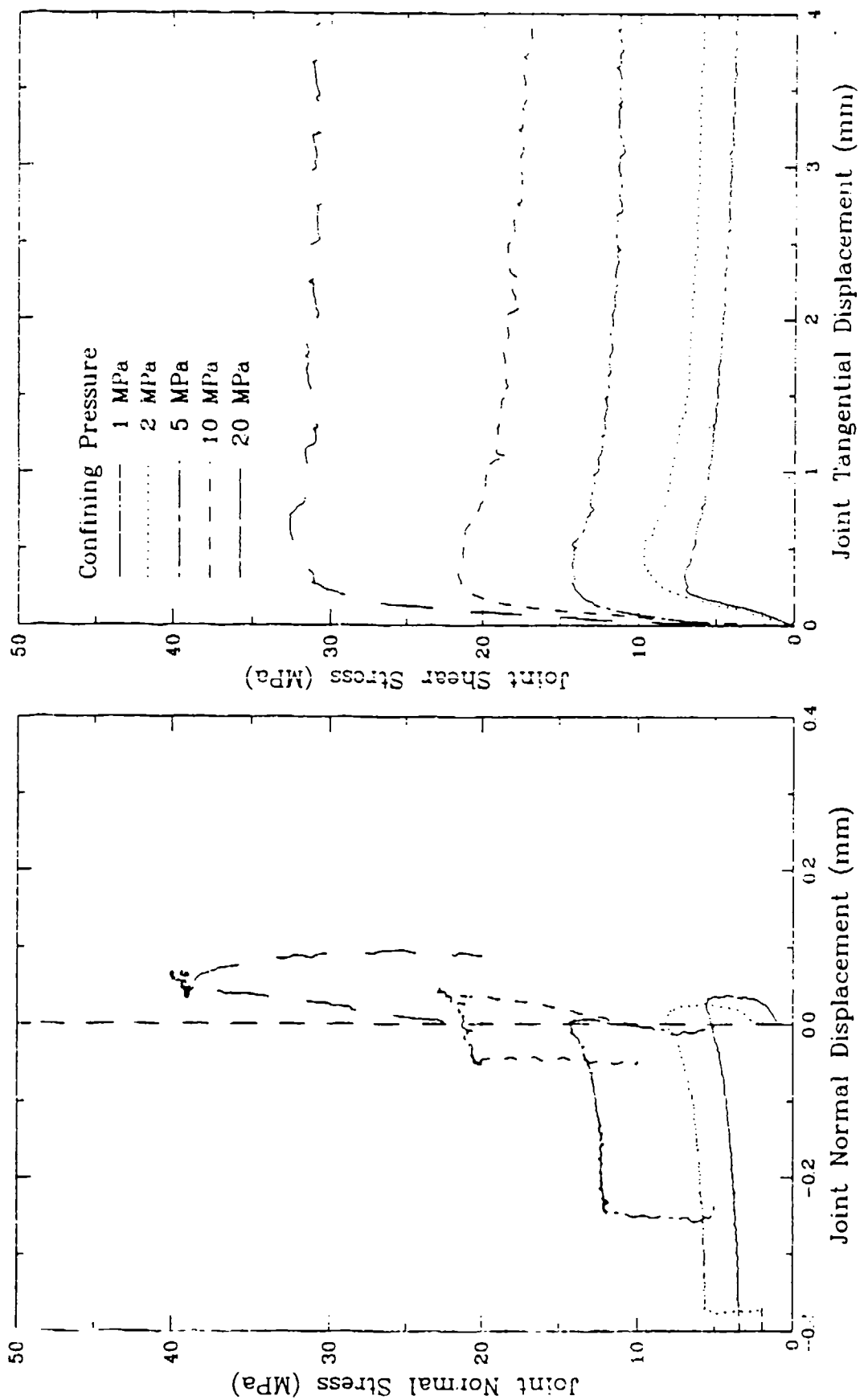


Figure 6-14. Normal and tangential deformations of synthetic joints in Salem limestone plotted against normal and tangential deformations, respectively, for a range of confining pressure conditions.

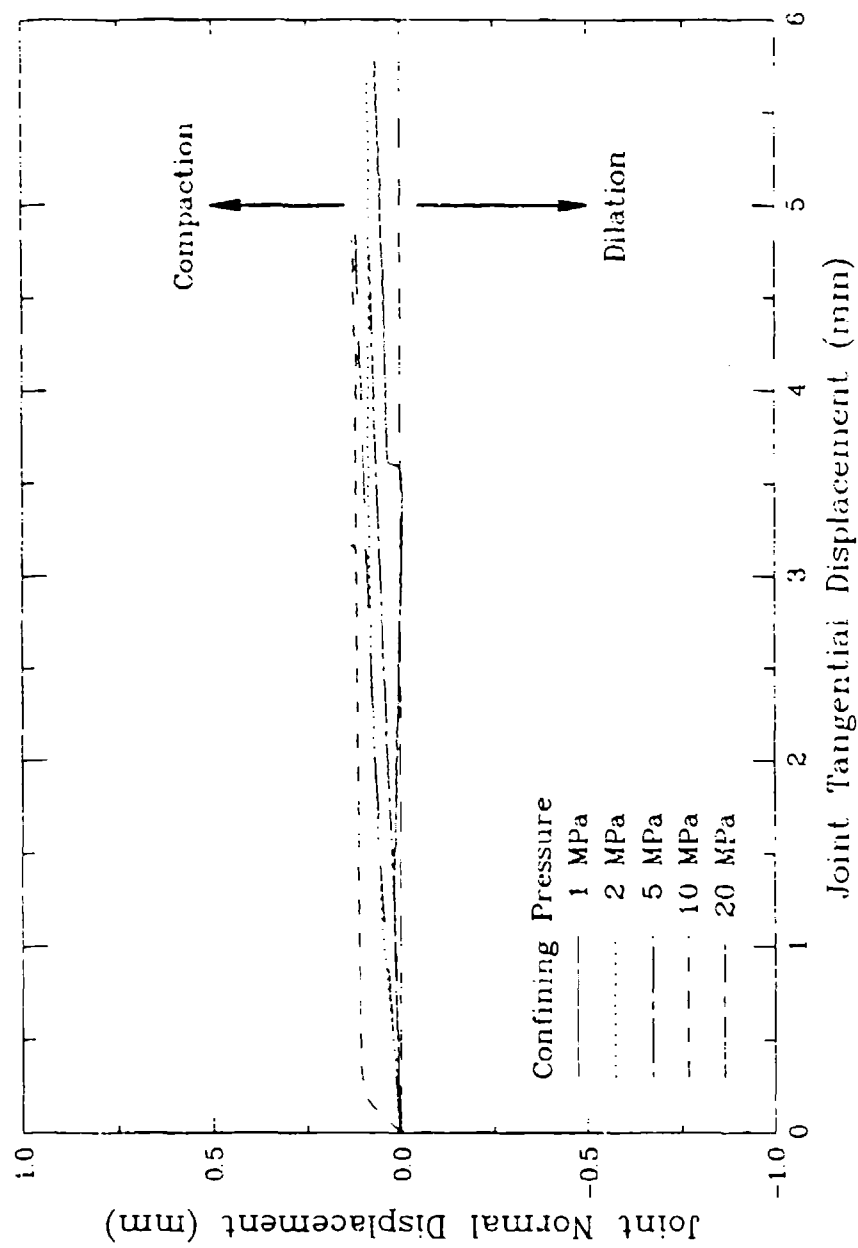


Figure 6-15. Relationship between normal and tangential deformation of smooth ground joints in Salem limestone under a range of confining pressure conditions.

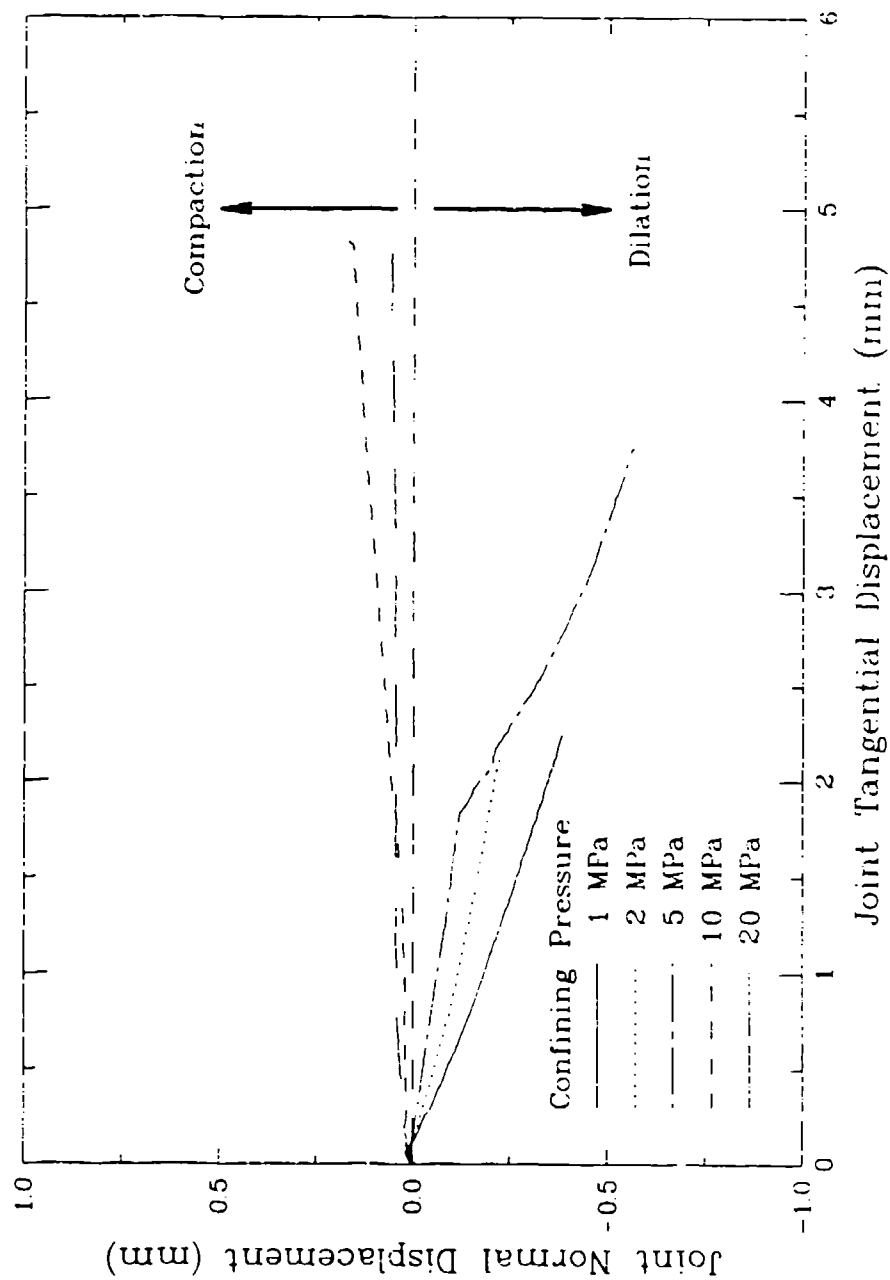


Figure 6-16. Relationship between normal and tangential deformation of tensile fracture joints in Salem limestone under a range of confining pressure conditions.

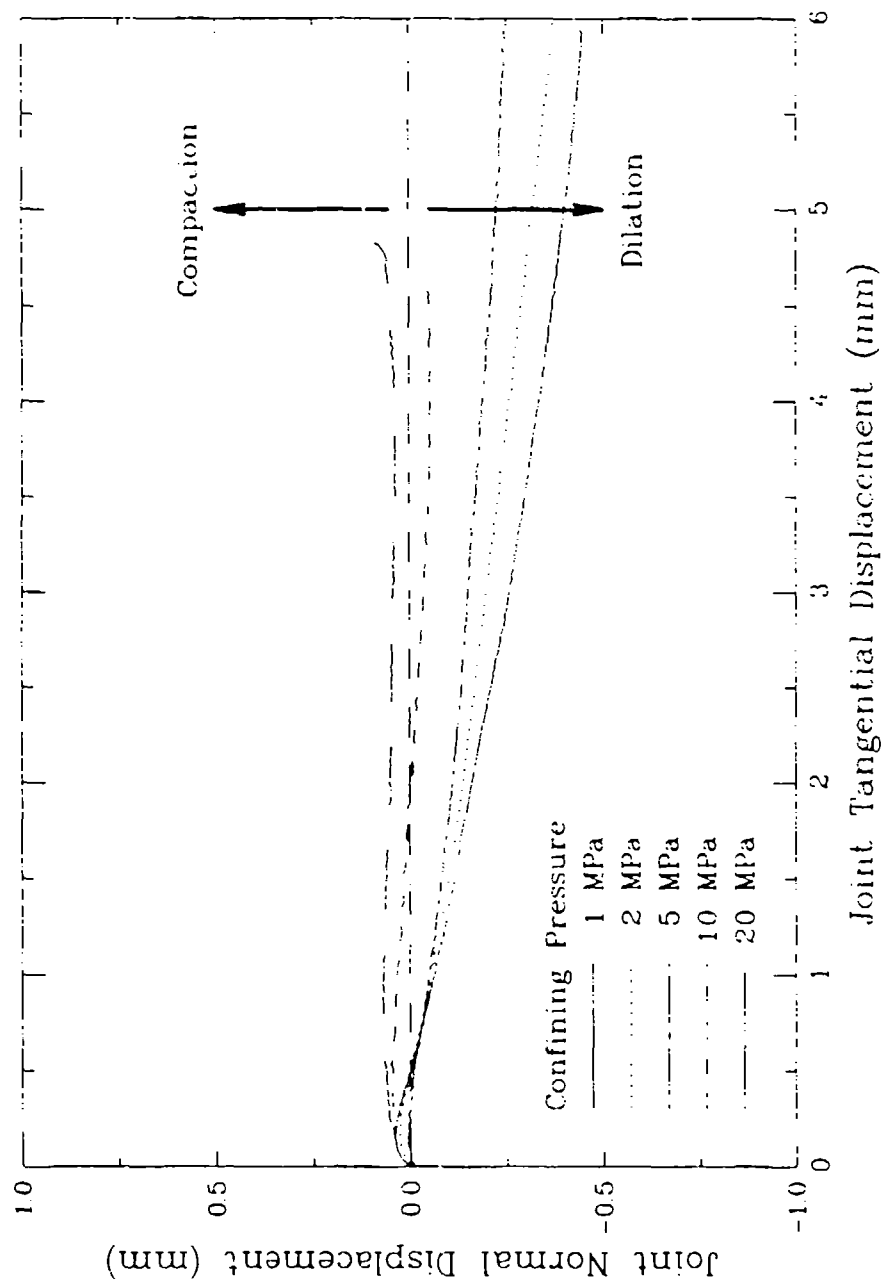


Figure 6-17. Relationship between normal and tangential deformation of synthetic joints in Salem limestone under a range of confining pressure.

## SECTION 7

### EFFECTS OF VARIATIONS IN DEFORMATION RATE

This section describes a series of tests that was performed to investigate the influence of deformation rate on the strength of Salem limestone as measured in triaxial compression tests. Tests were performed at strain rates ranging from  $10^{-5}$  to  $10^{-2} \text{ s}^{-1}$  on specimens of both intact and jointed limestone, and tests were performed on both damp (2.5% water content) specimens and specimens which were fully saturated and then allowed to drain during loading. This section documents the results of those tests as well as a series of numerical simulations of the tests on intact specimens.

#### 7.1 STRAIN RATE TESTS ON INTACT SALEM LIMESTONE.

For the purpose of investigating the dependence on strain rate of the strength and deformation properties of the limestone, triaxial compression tests were performed, as described in Section 4.3.1, at 20 MPa confining pressure on intact specimens of Salem limestone at strain rates of  $10^{-5}$  and  $10^{-3} \text{ s}^{-1}$ . One set of tests was performed on limestone that was damp, but not saturated (2.5% water content), and a companion set was performed on specimens that were fully saturated, but allowed to drain during testing. In addition to those two rates, a 20-MPa test was performed on an unsaturated specimen at  $10^{-4} \text{ s}^{-1}$  as part of the joint strength and deformation study described in Section 6. Lubricating materials were used between the specimen ends and the steel endcaps in all tests. In the saturated drained tests, drainage was allowed through a single 1.6-mm diameter hole in the lubricating membranes and the solid steel base cap. Figure 7-1 presents the measured stress difference as a function of axial strain for the unsaturated tests. The corresponding data for the saturated drained tests are shown in Figure 7-2.

In addition to the 20-MPa tests described in the preceding paragraph, a similar set of tests was performed on specimens of damp (unsaturated) Salem limestone at 25 MPa confining pressure with loading at rates of  $10^{-5}$ ,  $10^{-4}$ ,  $10^{-3}$ , and  $10^{-2} \text{ s}^{-1}$ . The stress-strain curves from those tests are presented in Figure 7-3. No saturated drained tests were performed at 25 MPa confining pressure.

The peak stresses recorded in all three test series are plotted against strain rate in Figure 7-4. The plot illustrates a clear dependence of strength on strain rate in all three cases. In unsaturated tests, the strength increases approximately 5% per decade increase in strain rate.

As shown in Figure 7-4, the limestone exhibited strengths approximately 5% lower in the saturated drained condition than when tested damp but not saturated. One possible explanation for this is that there was insufficient drainage to prevent the build-up of pore pressure in the specimen. If significant pore pressure did develop, the resulting decrease in effective stress could cause the observed decrease in strength. The only pore pressure measurement made during the test was at the base of the specimen adjacent to the drain port. No significant pressure was measured there. However, that does not preclude the possibility of elevated pore pressure at locations more distant from the drain port.

#### **7.1.1 Numerical Simulations of Intact Tests.**

In order to assess the possibility that the reduction in strength observed in the saturated drained tests was a result of pore pressure developed in the specimen at locations distant from the drain port, numerical simulations of the saturated drained tests were performed. The simulations were run using the Material Element Model (MEM) program (Chitty, et al. 1993). MEM is a special-purpose finite element code developed to support material modeling of fully or partially saturated porous materials, including fluid transport. It implements a fully coupled compressibility model, which is based on the effective stress concept. This model includes independent constitutive relationships for the porous skeleton, the solid grains, and the pore fluid, and enforces the compatibility relationships among all the materials. It can simulate arbitrary skeleton boundary conditions specified in terms of either stress or deformation, as well as various fluid flow conditions.

As shown by the triaxial compression test data presented in Figure 7-1, the Salem limestone at 20 MPa confinement exhibits brittle response. That is, the axial stress reaches a peak and then decreases with additional axial deformation, a phenomenon sometimes called strain softening. Since none of the available nonlinear skeleton constitutive models were

capable of modeling that behavior, a linear skeleton model was used to simulate the pre-failure portions of the tests. The test data presented in Figure 7-5 show that the limestone is stiffer when loaded at the rate of  $10^{-3} \text{ s}^{-1}$  than when loaded at the lower rate of  $10^{-5} \text{ s}^{-1}$ . This is due to the time-dependent behavior of the rock skeleton. A significant body of literature exists on the subject of time-dependent behavior of geologic materials. Sun (1986) and Hardy and Sun (1986) developed a nonlinear constitutive relation to describe this phenomenon. Although the overall compliance of the rock specimen is a complex combination of the elasticity, plasticity, and viscosity of the rock, it can be described by a constant modulus or apparent modulus at a particular load rate. Based on the results of the unsaturated tests presented in Figure 7-5, elastic bulk moduli of 13,000 MPa and 17,500 MPa were selected to model the response of the porous Salem limestone skeleton loaded at  $10^{-5} \text{ s}^{-1}$  and  $10^{-3} \text{ s}^{-1}$ , respectively. In both cases, a Poisson's ratio of 0.25 was used.

The simulations of the saturated drained tests were performed using the axisymmetric finite element mesh shown in Figure 7-6. On one end of the specimen, drainage was allowed through the on-axis node and the next closest node to simulate the drain port in the actual experiment. Based on the measurements reported in Section 9, the permeability of the limestone was set to  $2 \times 10^{-15} \text{ m}^2$ . This value is slightly lower than the permeability observed for the Salem limestone at the highest mean stress (approx. 50 MPa) reached in the 20 MPa triaxial compression test being simulated. It was chosen to accentuate any possible effect of poor drainage and saturation of the test specimens. Since lubricated endcaps were used in all of the tests, the radial degrees of freedom were not constrained at the specimen ends. In the axial direction, a displacement boundary condition was specified with the peak displacement corresponding to the actual peak displacement during the test being simulated. The 20-MPa confining pressure was applied radially.

Figures 7-7 and 7-8 show comparisons of the numerical predictions by MEM and the test data. As expected, the linear elastic skeleton properties derived from the unsaturated tests result in reasonable agreement between the saturated drained test data and the multi-phase numerical simulations, although the measured stress-strain curve for the saturated drained test at the slow ( $10^{-5} \text{ s}^{-1}$ ) strain rate is not as linear as those from the other tests. Figures 7-7 and 7-8 also show



the pore pressures computed by the simulations for the ends of the specimens away from the drain port. In the slow ( $10^{-5} \text{ s}^{-1}$ ) strain rate case, no significant pore pressure developed in the simulation, and the curve is barely visible at the bottom of the plot. In the simulation of the faster ( $10^{-3} \text{ s}^{-1}$ ) strain rate test, the pore pressure away from the drain increased to 4 MPa and remained there for the remainder of the simulation. Because of the value of permeability selected for the simulation, this represents an upper bound on the pore pressure that would be expected to develop in the actual test. If 4 MPa of pore pressure did develop, then the effective normal stress on the rock skeleton would be reduced by that amount and the strength exhibited by the material in the test would be lower. To estimate how much lower, consider the strength envelope in Figure 5.6. In that figure, the strength developed by the specimen tested at 15 MPa confining pressure was about 2 MPa lower than the corresponding value for the 20 MPa test. This does not account for the fact that the unsaturated specimen reached a strength 5 MPa higher than the saturated drained specimen. A similar conclusion can be drawn for the case of the lower strain rate. While the simulation results suggest that no significant pore pressure was developed in the saturated drained specimen at the  $10^{-5} \text{ s}^{-1}$  strain rate, its strength was 5 MPa less than that of the unsaturated specimen loaded at the same rate.

It appears that some factor that is not treated in the current test and analysis techniques is responsible for the difference in strength between the unsaturated and saturated drained tests. This could possibly be a chemical interaction, similar to the phenomenon that results in higher strengths in oven dried unconfined compression tests than in damp tests. Alternatively, it could possibly result from saturation and reduction of effective stress on a microscopic level in dead-end pores which are not adequately represented by the permeability tests.

## **7.2 STRAIN RATE TESTS ON JOINTED SALEM LIMESTONE.**

Triaxial compression tests were also performed on limestone specimens containing joints of the three types described in Section 3 oriented at  $30^\circ$  to the axes of the specimens. As with the tests on intact rock described in the previous subsection, tests were performed on specimens that were both damp and saturated drained. The stress-deformation curves for the tensile fracture, smooth ground, and synthetic joints are presented in Figures 7-9 through 7-11,

respectively. Due to slight differences in joint angle, it is not possible to make direct comparisons among the maximum values of stress difference reached by the various tests. A more meaningful comparison can be made on the strength plots presented in Figures 7-12 through 7-14 for the three joint types. Shown for comparison in each figure is the strength envelope reported in Section 6 for the corresponding joint type tested at a strain rate of  $10^{-4} \text{ s}^{-1}$ .

The strengths for tensile fracture joints are shown in Figure 7-12. The higher strain rate ( $10^{-3} \text{ s}^{-1}$ ) tests in both saturated drained and unsaturated tests exhibited strengths approximately 5% higher than the corresponding points in the strength envelope derived from tests conducted at  $10^{-4} \text{ s}^{-1}$ , and relative to the strength envelope, there is essentially no difference between the saturated drained and unsaturated tests. At the lower strain rate ( $10^{-5} \text{ s}^{-1}$ ), the unsaturated strength is virtually the same as the envelope for  $10^{-4} \text{ s}^{-1}$  envelope and the saturated drained strength falls approximately 5% below the envelope. Overall, there appears to be a strain rate effect of similar magnitude to the intact material, but the initial saturation does not appear to significantly influence the result of a test in this configuration. A jointed specimen tested under saturated drained conditions is probably less likely to develop pore pressure in a 20-MPa triaxial compression test than an intact specimen tested under the same conditions. Although the joints compact slightly while shearing at this confining pressure, the sliding of the two halves of the joint tends to create small gaps where the joint intersects the jacket that actually increase the volume available for the pore water to occupy, and thus minimize the chance of development of any significant pore pressure in the specimen.

The tests on smooth ground joints, for which strengths are shown in Figure 7-13, all fall very close to the original strength envelope from the tests conducted at  $10^{-4} \text{ s}^{-1}$ . Only the saturated drained test data point lies slightly above the envelope. However, based on the small number of data points, the difference is insignificant. The conclusion from this limited study is that neither strain rate within the range studied, nor initial saturation significantly affects the strength of smooth ground joints.

The results of tests on synthetic joints are presented in Figure 7-14. As with the smooth ground joints, only one of the four points deviates from the original fit line. In contrast to the

smooth ground tests, it is a higher strain rate test which falls slightly below the envelope. Since the deviation is very small and in the opposite direction from the trends exhibited by the intact and tensile fracture jointed specimens, it is considered to be natural scatter. As with the smooth ground joints, it is concluded that neither strain rate within the range tested nor initial saturation significantly affect the strength of the synthetic joints.

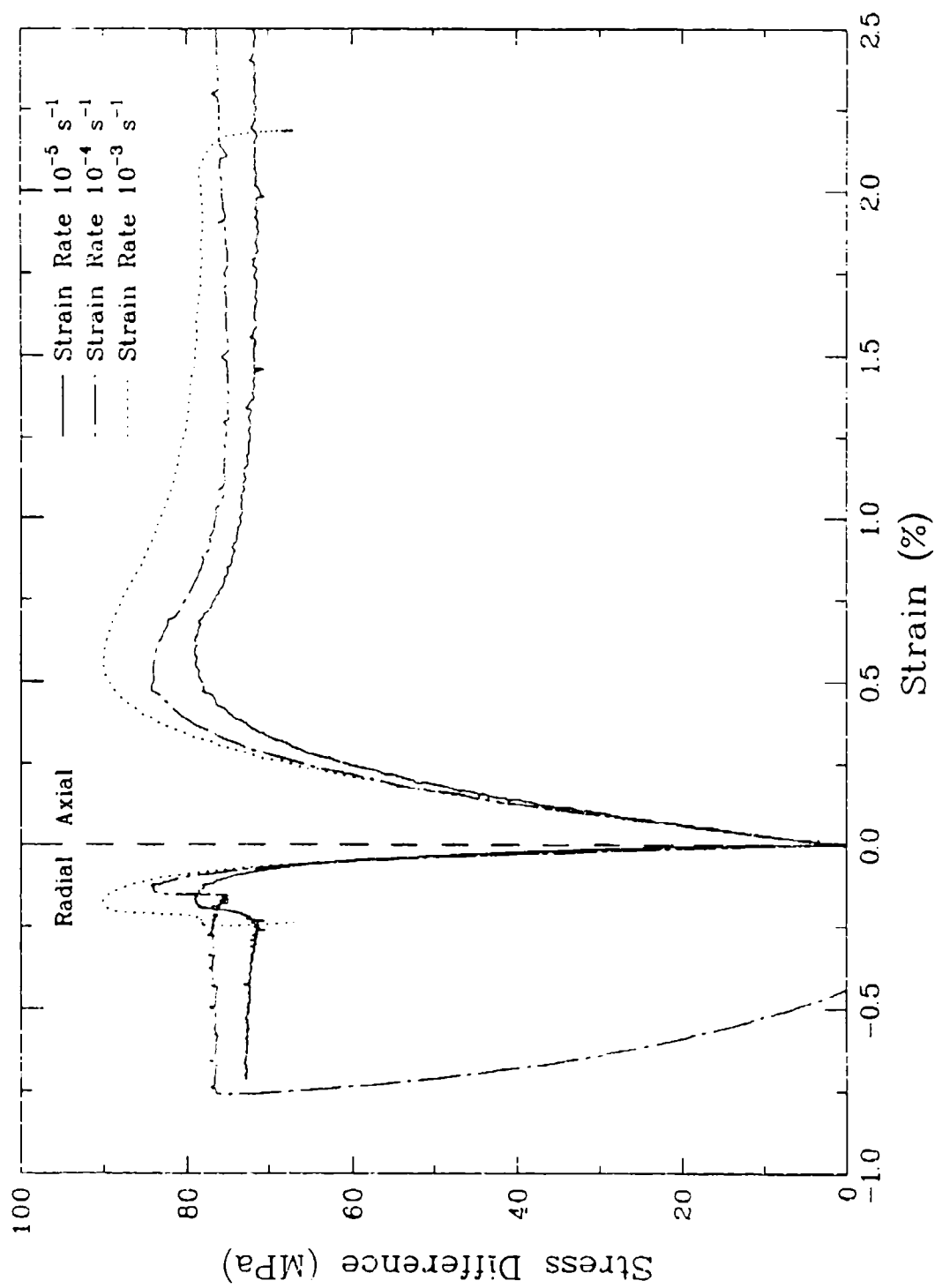


Figure 7-1. Comparison of stress-strain curves from intact unsaturated (2.5% water content) Salem limestone specimens tested in triaxial compression with 20 MPa confining pressure at strain rates of  $10^{-5}$ ,  $10^{-4}$ , and  $10^{-3} \text{ s}^{-1}$ .

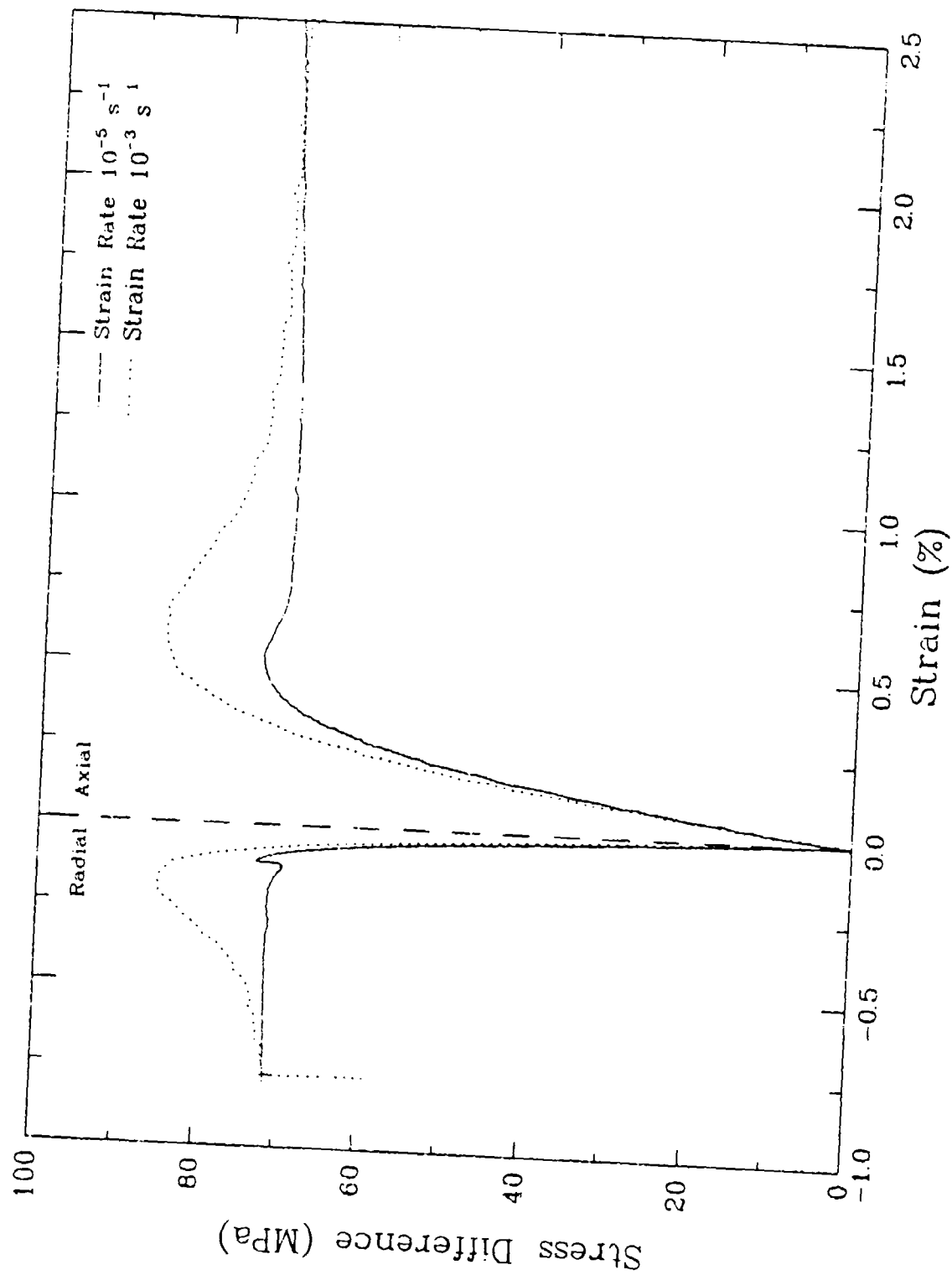


Figure 7-2. Comparison of stress-strain curves from intact saturated Salem limestone specimens tested in Drained triaxial compression with 20 MPa confining pressure at strain rates of  $10^{-5}$  and  $10^{-3} \text{ s}^{-1}$ .

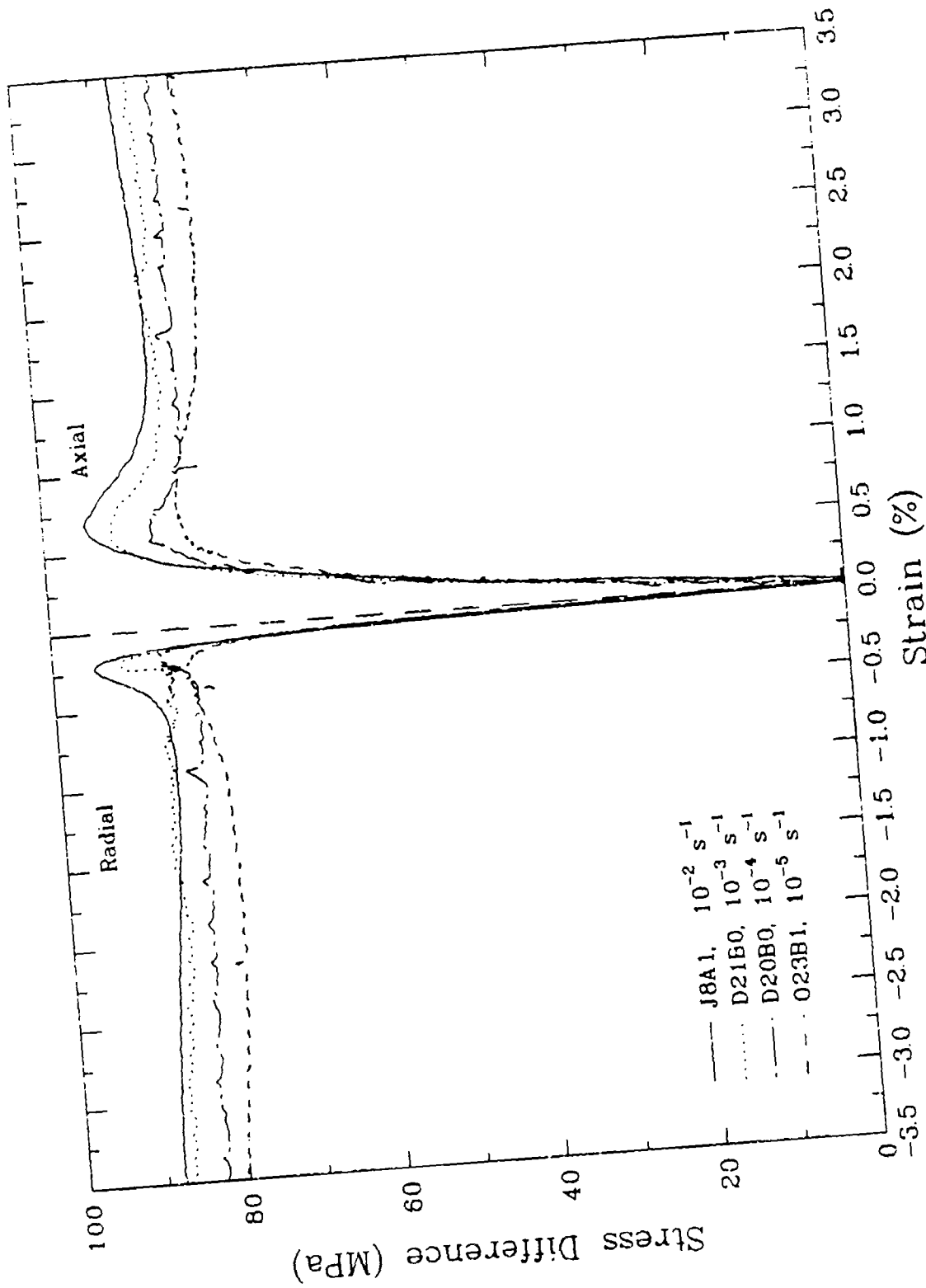


Figure 7-3. Comparison of stress-strain curves from intact unsaturated (2.5% water content) Salem limestone specimens tested in triaxial compression with 25 MPa confining pressure at strain rates of  $10^{-5}$ ,  $10^{-4}$ ,  $10^{-3}$ , and  $10^{-2} \text{ s}^{-1}$ .

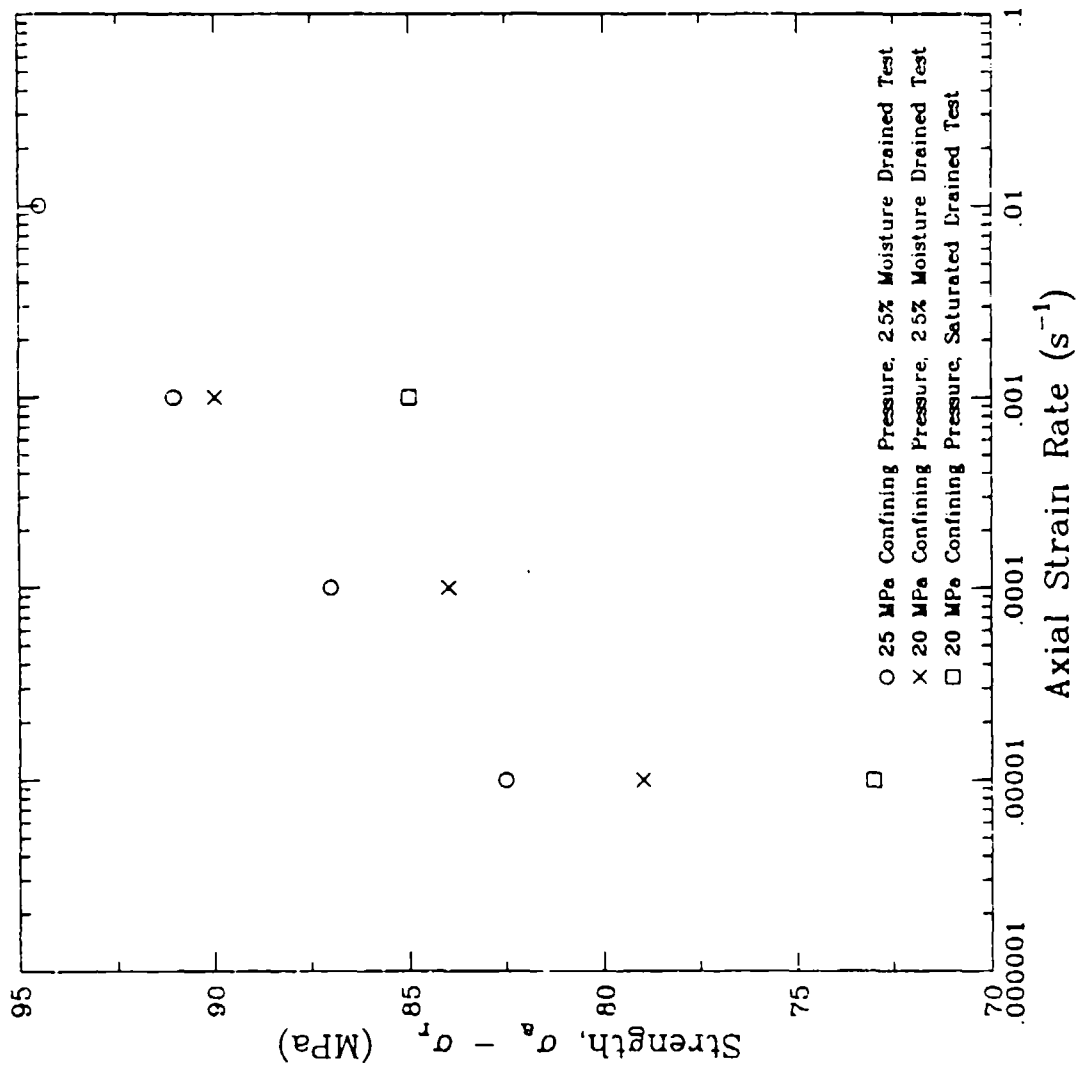


Figure 7-4. Summary of the relationship between strength and strain rate for the test data presented in Figure 7-1 through 7-3.

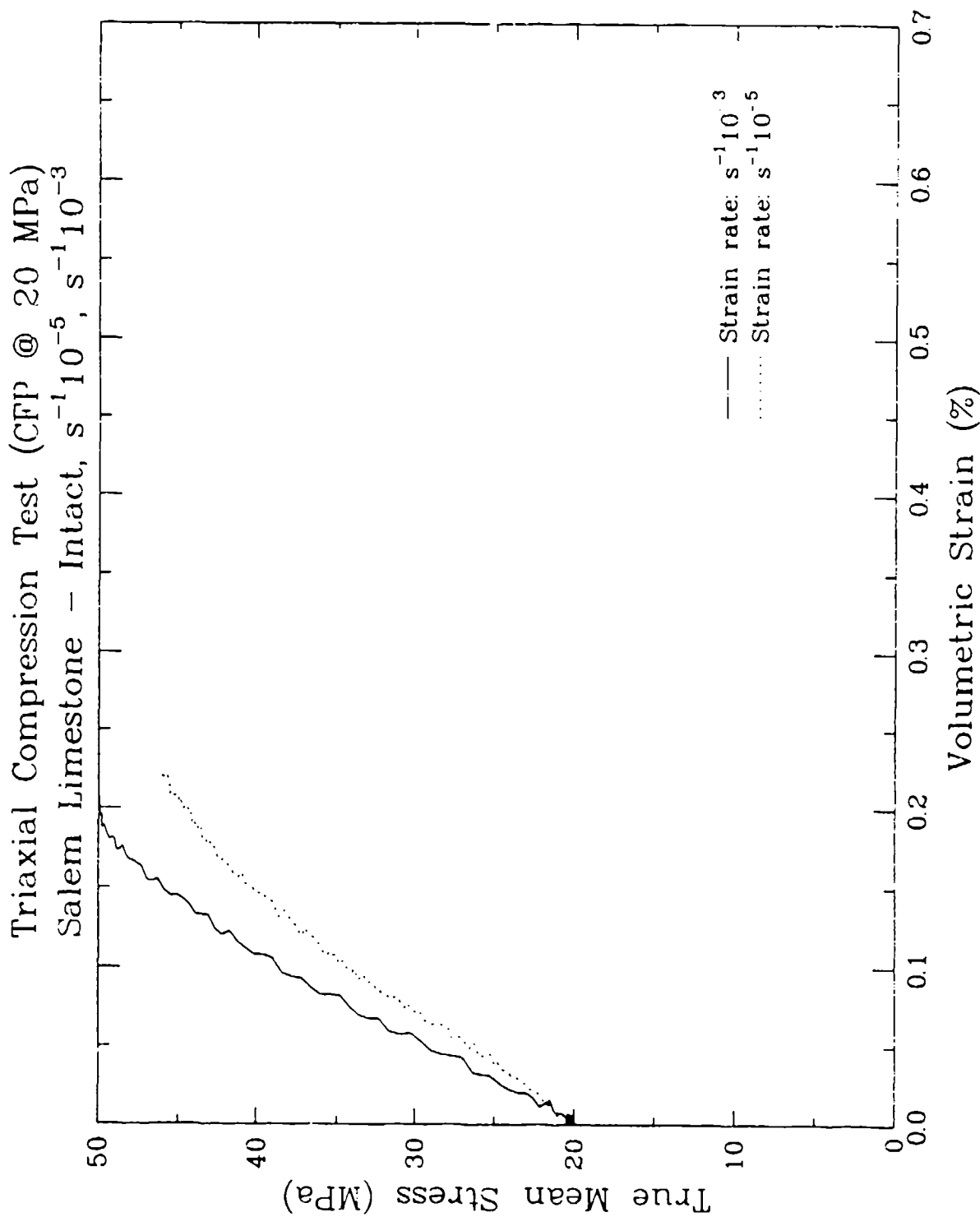


Figure 7-5. Comparison of mean stress-volume strain curves from intact unsaturated (2.5% water content) Salem limestone specimens tested in triaxial compression with 20 MPa confining pressure at strain rates of  $10^{-5}$ , and  $10^{-3} s^{-1}$ .



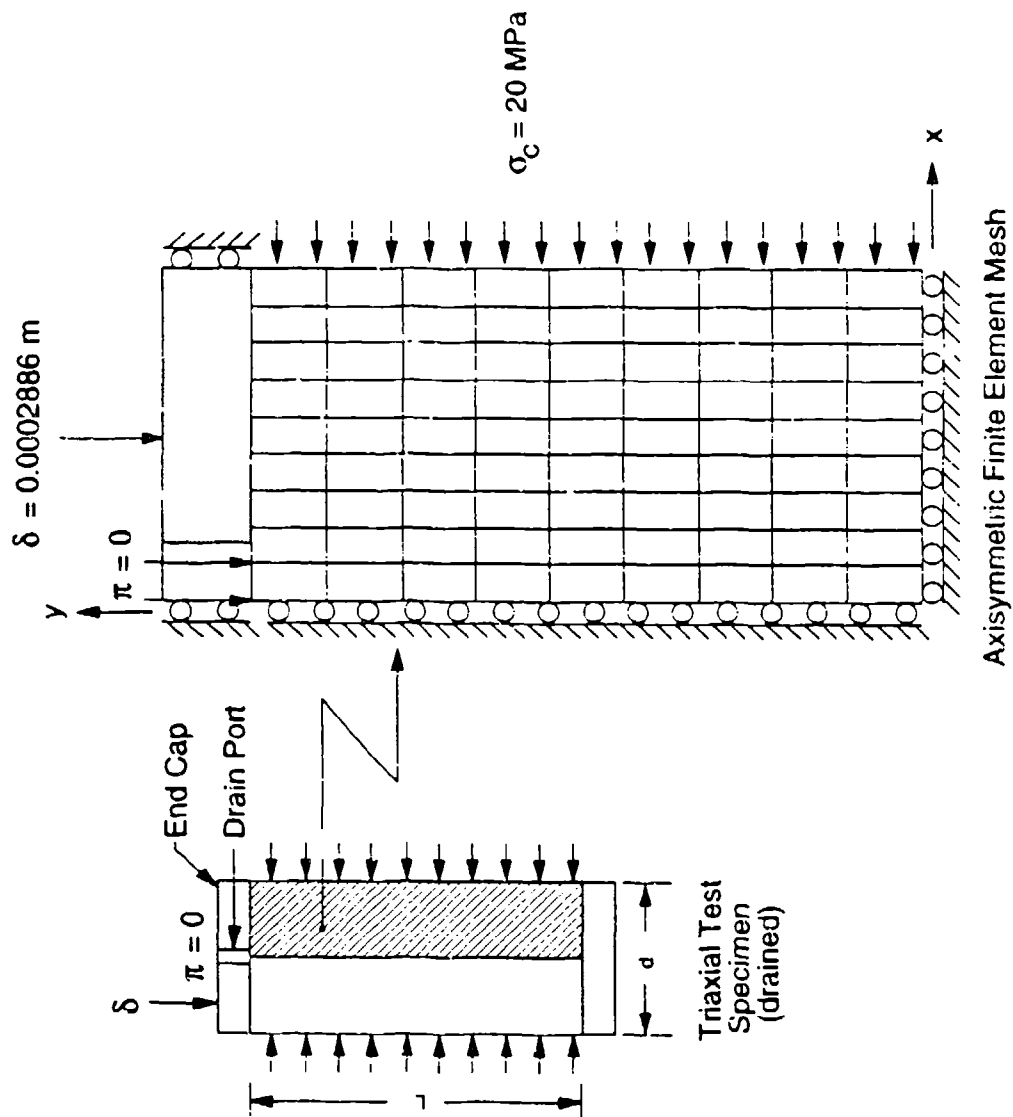


Figure 7-6. Illustration of the finite element mesh used to simulate the saturated drained tests on intact limestone specimens.

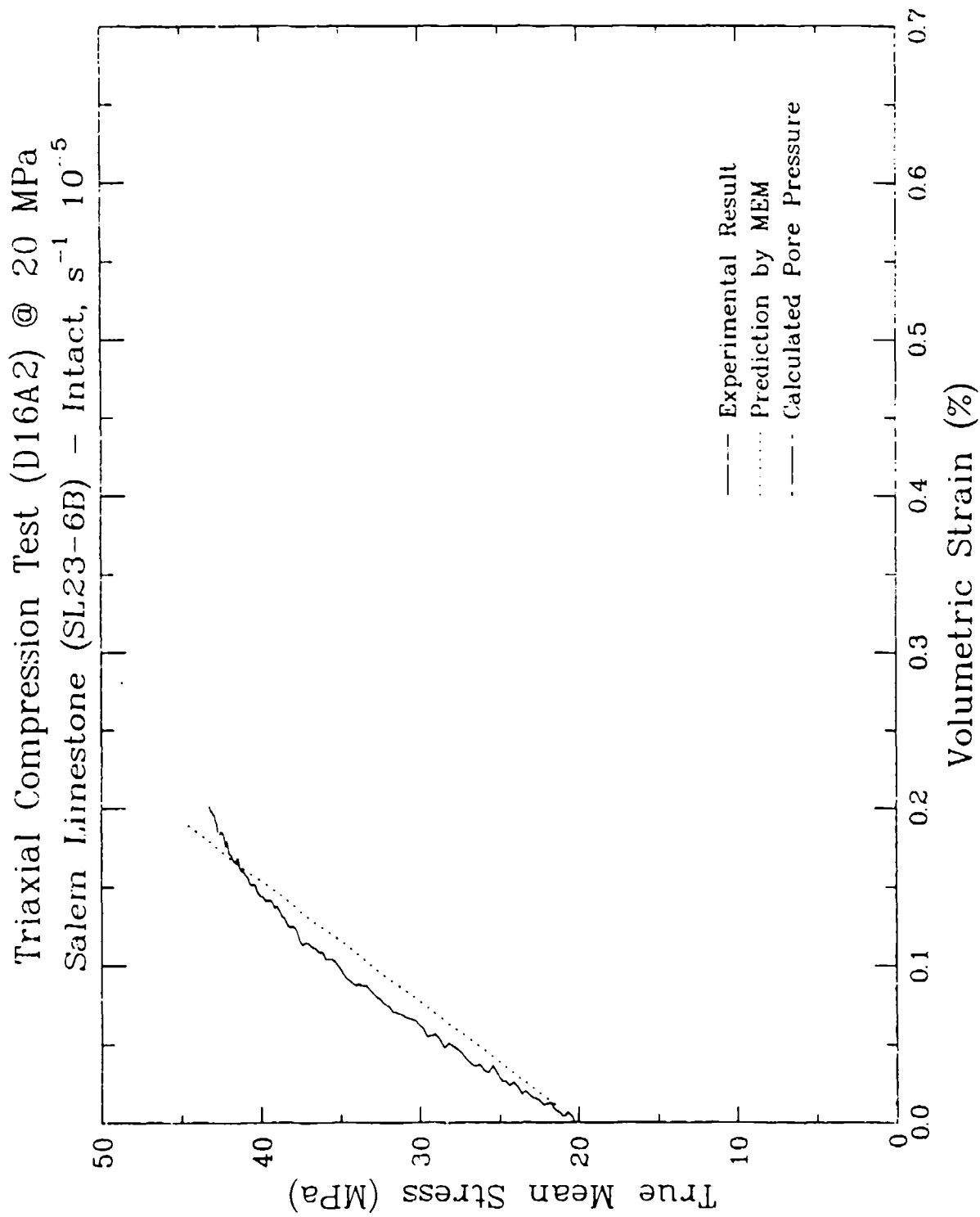


Figure 7-7. Mean stress and pore pressure as functions of volume strain from a numerical simulation of the saturated drained 20-MPa triaxial compression test at  $10^{-5}, s^{-1}$  strain rate, showing the measured mean stress for comparison.

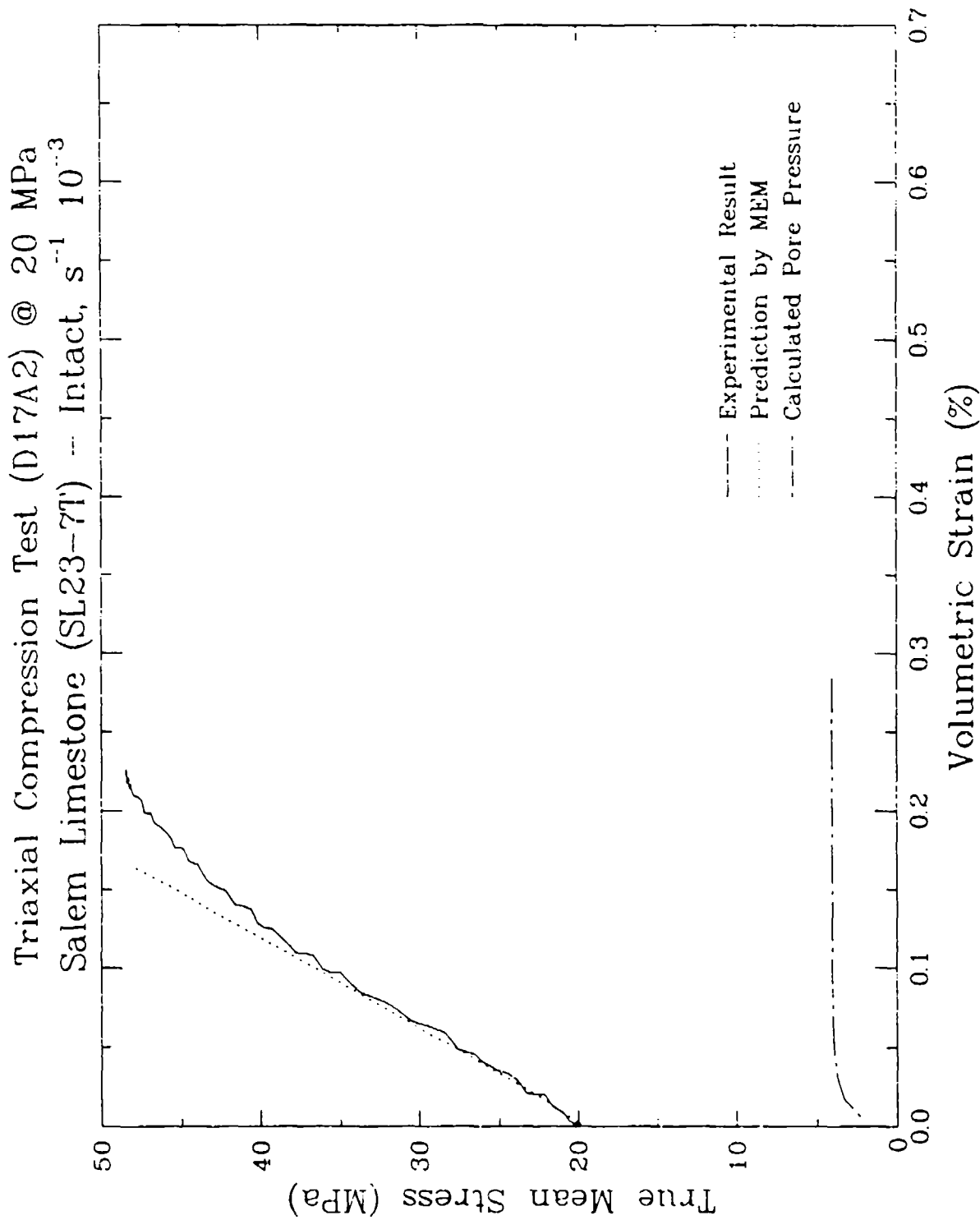


Figure 7-8. Mean stress and pore pressure as functions of volume strain from a numerical simulation of the saturated drained 20-MPa triaxial compression test at  $10^{-3} s^{-1}$  strain rate, showing the measured mean stress for comparison.

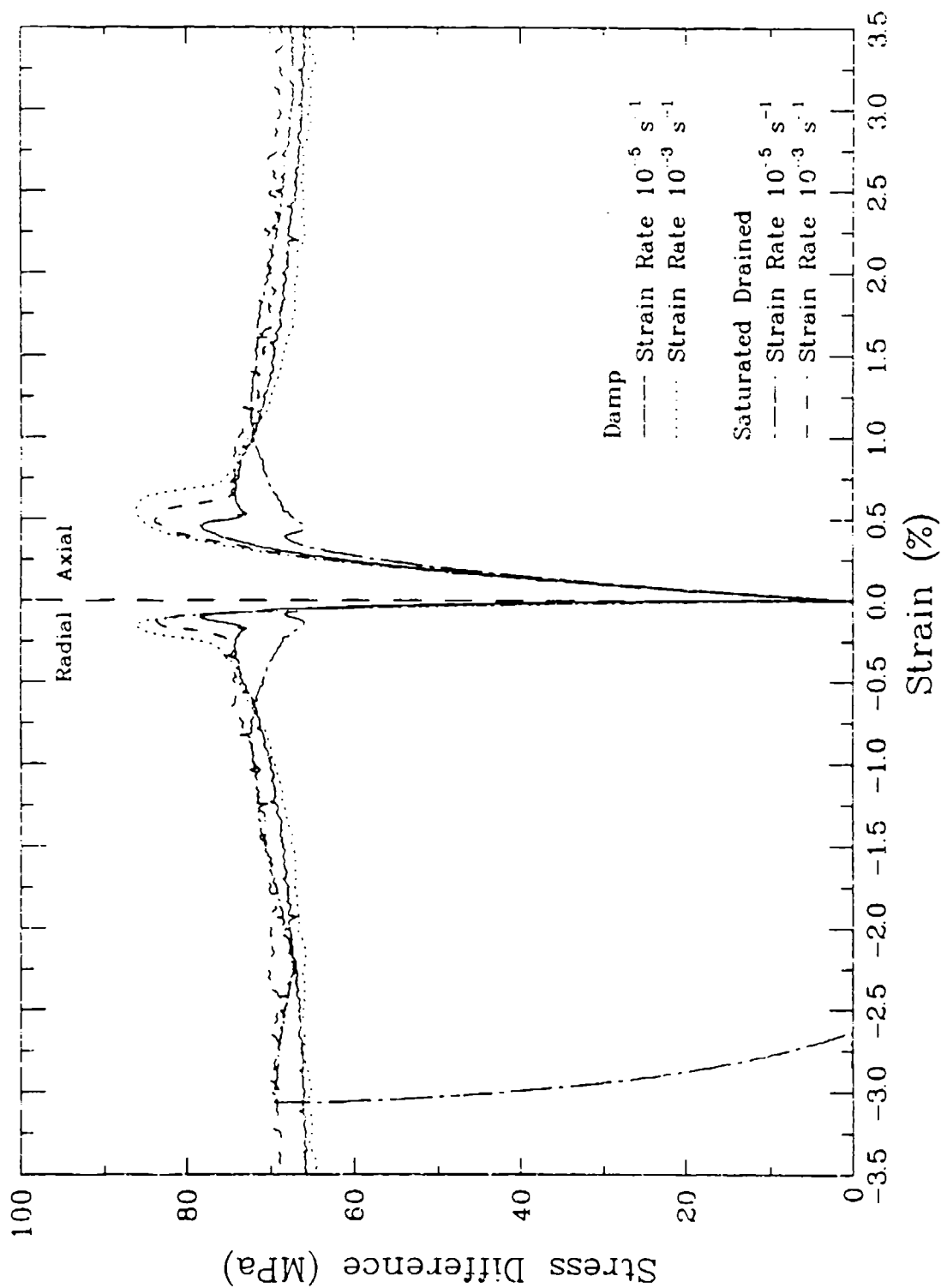


Figure 7-9. Comparison of stress-strain curves from 30° tensile fracture jointed Salem limestone specimens tested in triaxial compression with 20 MPa confining pressure at strain rates of  $10^{-5}$ , and  $10^{-3}$ ,  $s^{-1}$  and different initial saturation conditions.

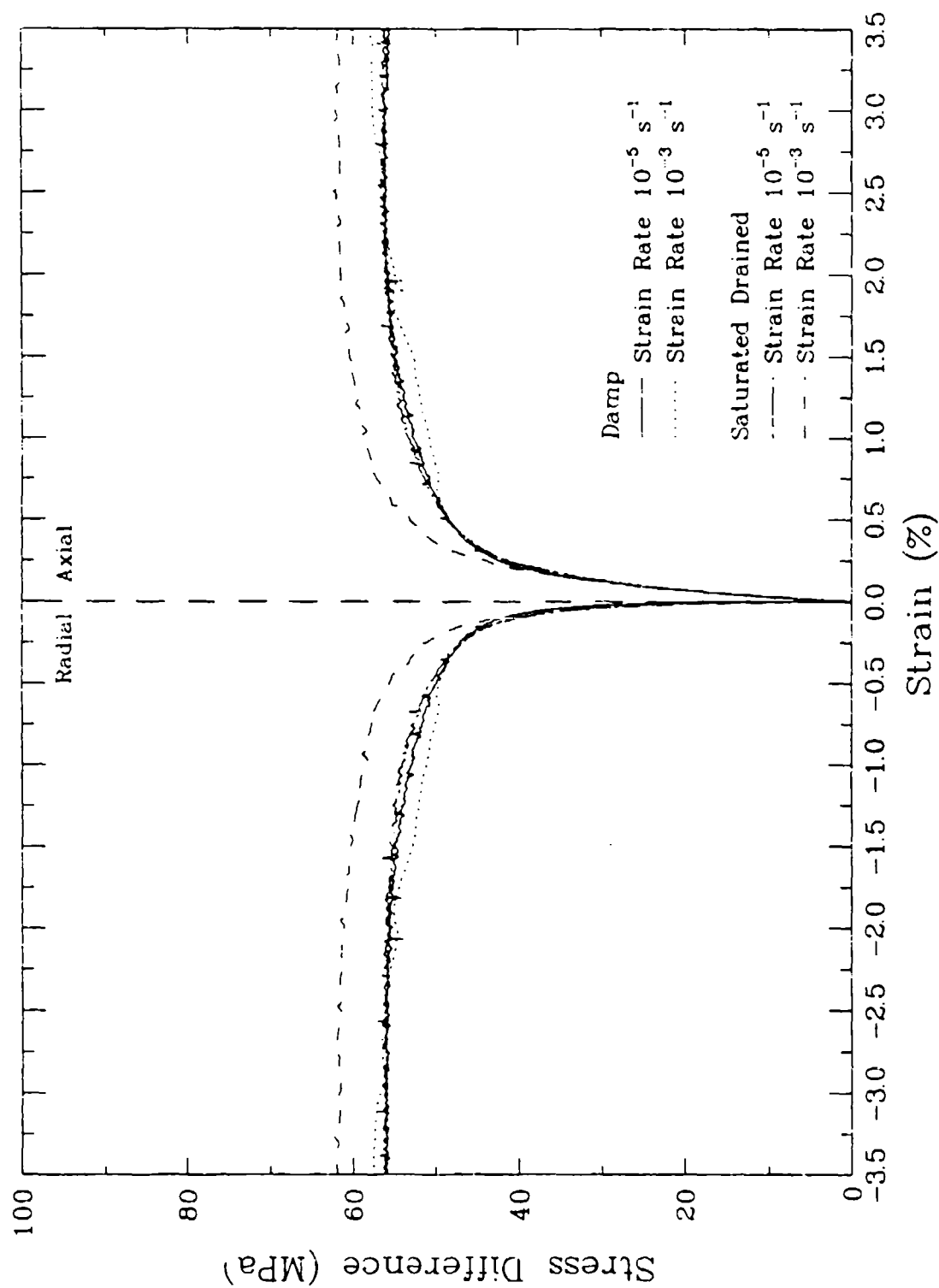


Figure 7-10. Comparison of stress-strain curves from 30° smooth ground jointed Salem limestone specimens tested in triaxial compression with 20 MPa confining pressure at strain rates of  $10^5$  and  $10^3$  s<sup>-1</sup> and different initial saturation conditions.

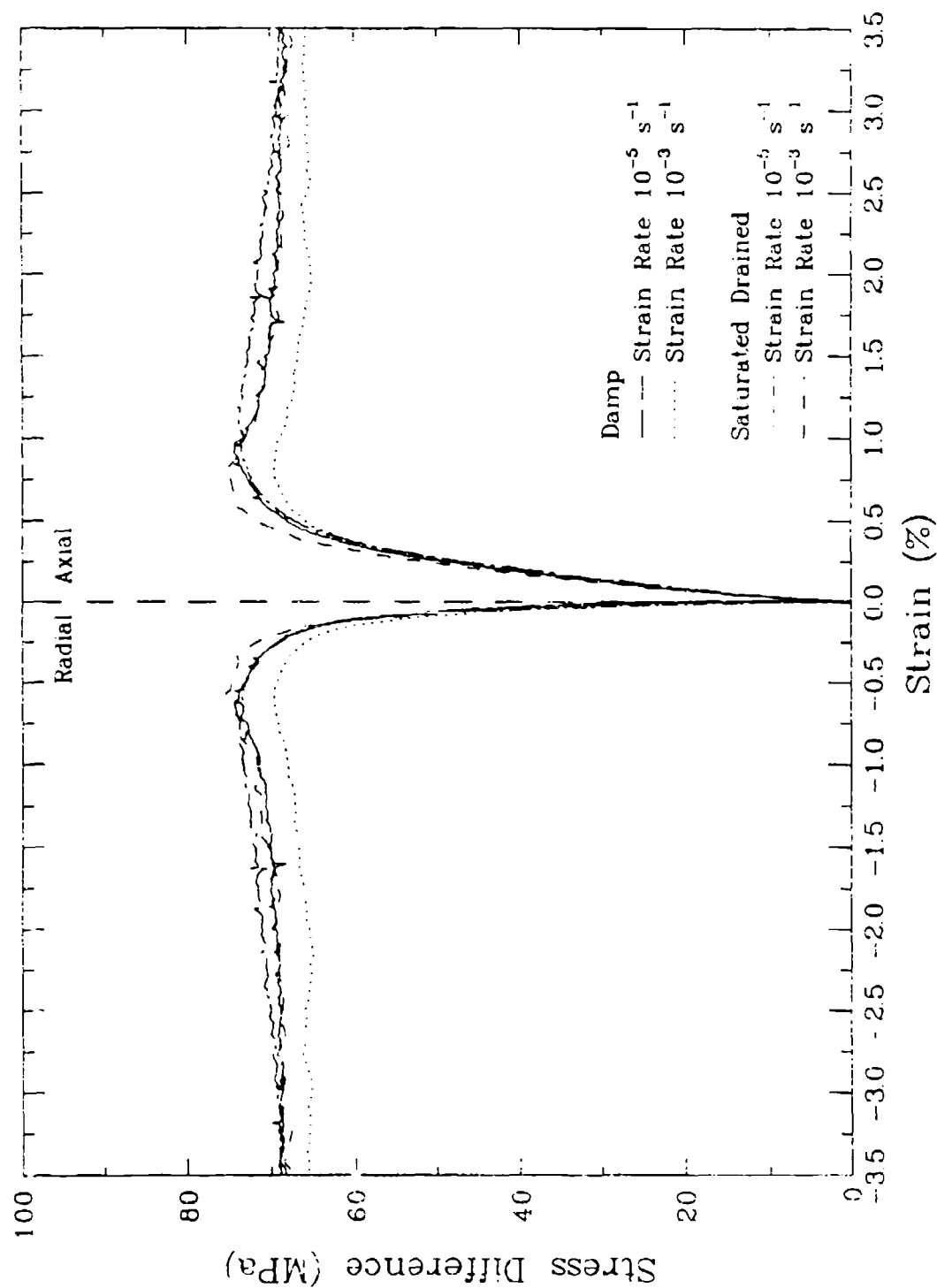


Figure 7-11. Comparison of stress-strain curves from 30° synthetic jointed Salem limestone specimens tested in triaxial compression with 20 MPa confining pressure at strain rates of  $10^5$  and  $10^3$  s<sup>-1</sup> and different initial saturation conditions.

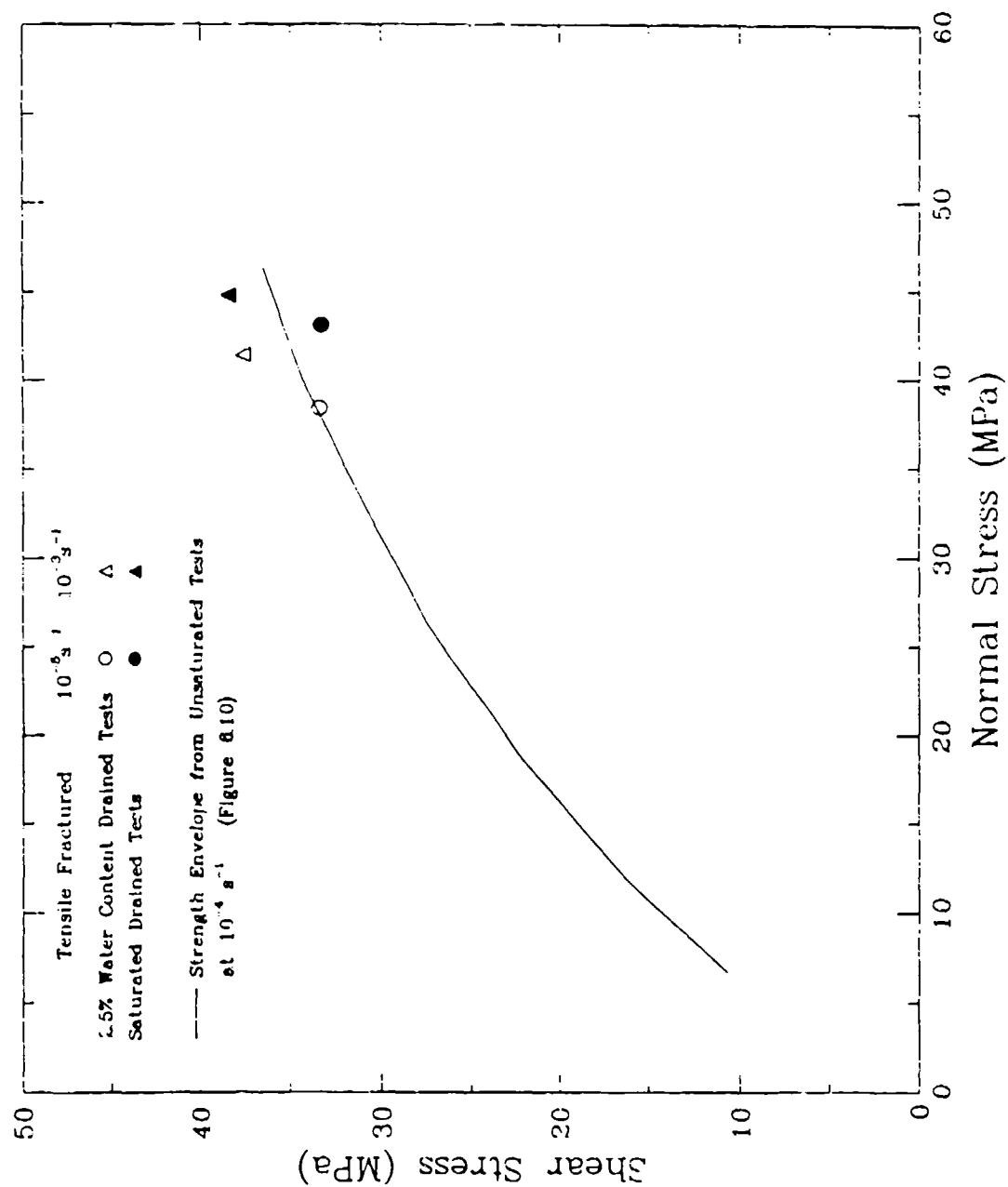


Figure 7-12. Comparison of the strengths of tensile fracture joints tested at various strain rates and initial saturation conditions with the strength envelope for the same type joints tested unsaturated at  $10^{-4} \text{ s}^{-1}$  strain rate.

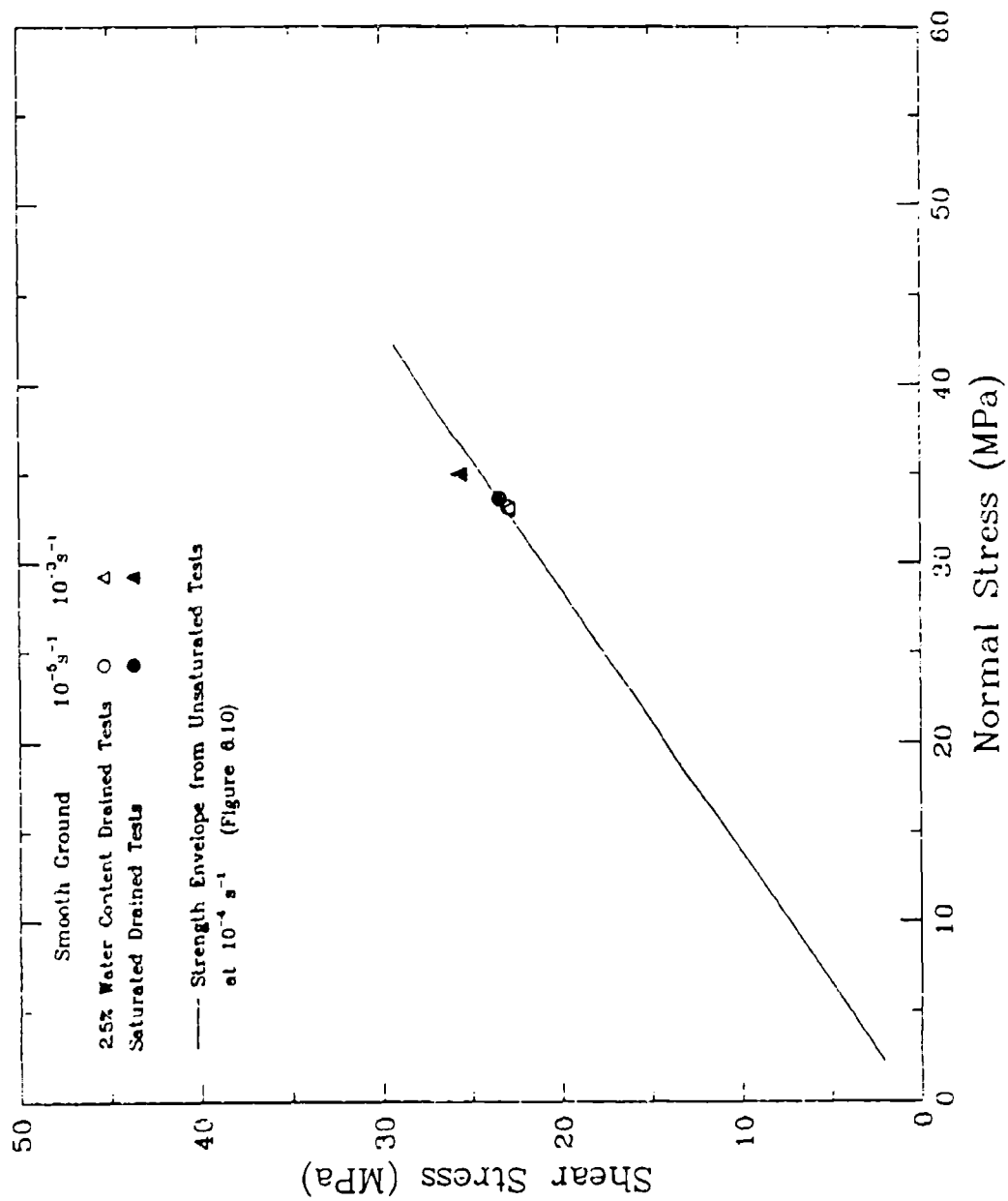


Figure 7-13. Comparison of the strengths of smooth ground joints tested at various strain rates and initial saturation conditions with the strength envelope for the same type joints tested unsaturated at  $10^{-4} \text{ s}^{-1}$  strain rate.



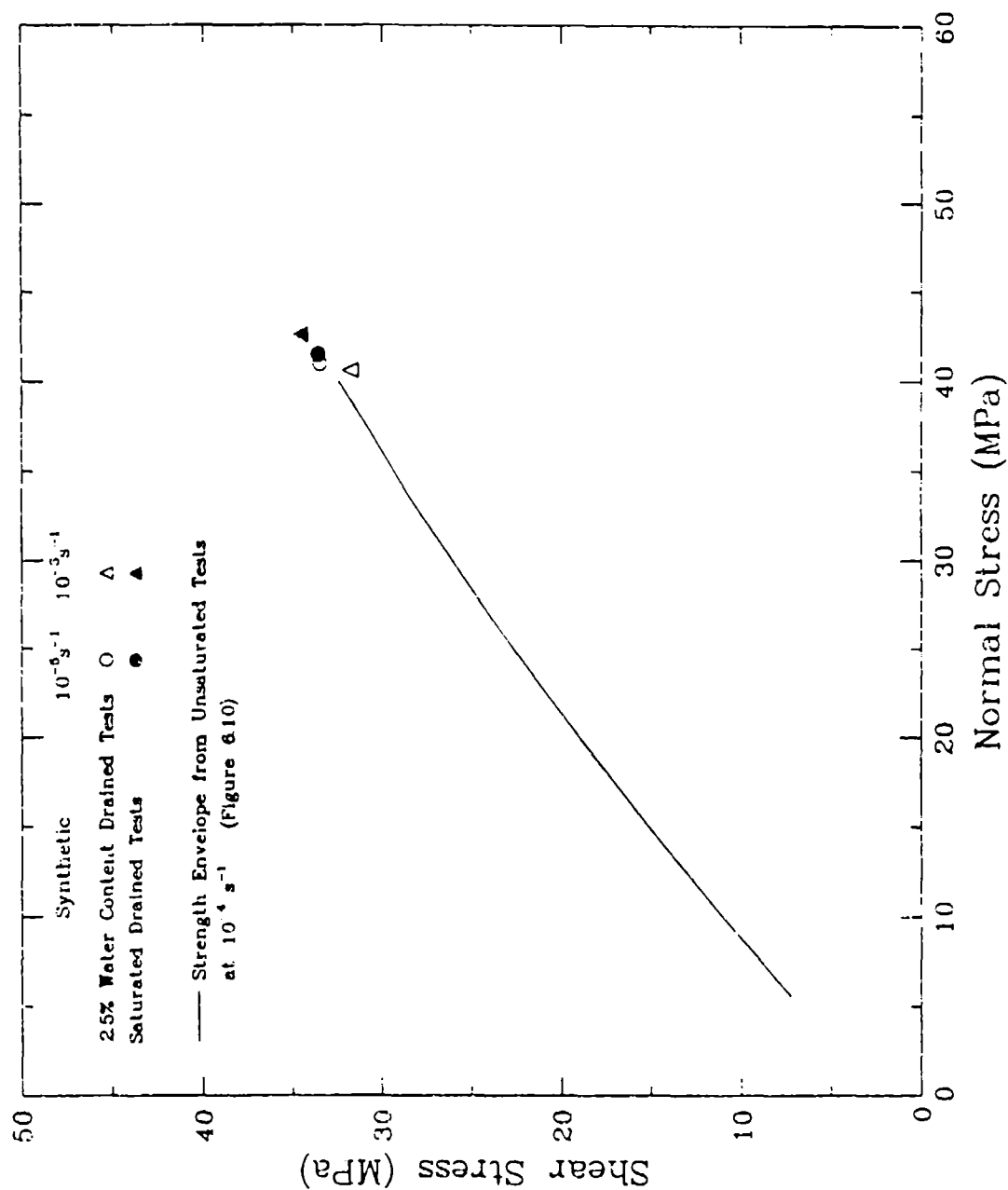


Figure 7-14. Comparison of the strengths of synthetic joints tested at various strain rates and initial saturation conditions with the strength envelope for the same type joints tested unsaturated at  $10^{-4} \text{ s}^{-1}$  strain rate.

## SECTION 8

### SATURATED UNDRAINED HYDROSTATIC COMPRESSION TEST AND SPECIFIC STORAGE MEASUREMENT

A series of saturated undrained hydrostatic compression tests were performed to determine the ratio between induced pore pressure and imposed hydrostatic stress, and to evaluate the specific storage of saturated Salem Limestone. This section describes those tests and presents an analysis of the results.

#### 8.1 TEST PROCEDURES.

These tests were performed on intact specimens prepared with a polyolefin jacket as described in Section 4.1. They were instrumented with axial and radial LVDTs and strain gages as described in Section 4.4, and saturated with water as described in Section 4.2.2. In addition to the usual complement of instrumentation, a gage was installed to measure the volume of pore fluid drained from the specimen. It consisted of a small (approx. 20-mm diameter) hydraulic cylinder with an LVDT installed that measured displacement of the piston relative to the cylinder. It was plumbed into the pore pressure drain line in such a way that it could be evacuated and saturated with water in a manner similar to the rock specimen. Approximately 0.7 MPa of air pressure was applied to the cylinder on the pore fluid side to prevent any cavitation.

With the pore pressure drain valve closed, the hydrostatic pressure increased to 137 MPa (20,000 psi). The pore pressure drain valve in the basecap directly beneath the test specimen was then opened slightly allowing the pore pressure in the specimen to slowly diminish, while monitoring the pore pressure with the pore pressure transducer, also located in the specimen's basecap. During each test, volume of pore water draining from the specimen during this consolidation process was measured using the volumetric device described above.

## 8.2 TEST RESULTS.

There were five specimens tested in this manner. Typical results are shown in Figures 8-1 through 8-3. Figure 8-1 presents the hydrostatic confining pressure (total stress), pore pressure, and effective stress changing with volumetric strain. Through the entire initial loading phase of the test, the rock skeleton remains elastic, and the total stress is approximately equally divided between the pore fluid and the rock skeleton (effective stress). When the confining pressure reached the predetermined value of 138 MPa, the volumetric strain in the specimen was approximately 0.7%. At that point, the confining pressure was held constant while the excess pore fluid was slowly drained. As the pore pressure dropped, the effective stress increased, until it equalled the confining pressure. In Figure 8-2, radial strain is plotted against axial strain. The anisotropy in the rock skeleton illustrated in Figure 8-2 is consistent with the drained hydrostatic compression test data presented in Figure 5-8. Figure 8-3 shows the total amount of water expelled from the specimen as a function of the instantaneous pore pressure inside the specimen. The drainage of pore pressure depicted in Figure 8-3 occurred over a period of approximately 20 minutes.

## 8.3 RATIO BETWEEN PORE PRESSURE AND HYDROSTATIC STRESS.

The ratio between the induced pore pressure and the imposed hydrostatic stress depends on the compressibility properties of the materials involved. Based on the fully coupled compressibility model presented by Blouin and Kim (1984), the total strain in a fully saturated rock in hydrostatic compression can be viewed as either the sum of the strain in the grain/water mixture under pore pressure,  $\pi$ , plus that of the solid grains caused by effective stress,  $\bar{P}$ , or as the sum of the strain in the skeleton due to effective stress plus the strain in the grains under pore pressure. Setting both of these expressions equal, since they are descriptions of the same total strain in different ways, gives:

$$\frac{\pi}{K_m} + \frac{\bar{P}}{K_g} = \frac{\bar{P}}{K_s} + \frac{\pi}{K_g} \quad (8.1)$$

in which  $K_g$  is the grain bulk modulus of the rock,  $K_s$  is the bulk modulus of the skeleton, and  $K_m$  is the bulk modulus of the water/grain mixture, which is expressed as:

$$K_m = \frac{K_s K_w}{K_w + n(K_s - K_w)} \quad (8.2)$$

where  $K_w$  is the bulk modulus of water and  $n$  is porosity of the rock. From Equation (8.1), the relation between pore pressure and effective stress can be obtained:

$$\beta = \frac{\bar{P}}{\pi} = \frac{K_s(K_s - K_m)}{K_m(K_s - K_s)} \quad (8.3)$$

Since the total hydrostatic stress or confining pressure,  $P = \bar{P} + \pi$ , the ratio between pore pressure and hydrostatic stress can be found by:

$$\frac{\pi}{P} = \frac{\pi}{\bar{P} + \pi} = \frac{1}{\frac{\bar{P}}{\pi} + 1} = \frac{1}{\beta + 1} \quad (8.4)$$

Equations 8.3 and 8.4 define, theoretically, the ratio of pore pressure to total (hydrostatic) stress. Published values for the bulk moduli of water and solid calcium carbonate are, respectively,  $K_w = 2260$  MPa,  $K_s = 82000$  MPa. For the Salem limestone used as a test specimen,  $n = 0.169$ , and  $K_m = 14085$  MPa (from the data presented in Section 5). Substituting these values into Equations 8.3 and 8.4, it can be found that  $\beta = 1.237$  and the ratio of pore pressure to total stress,  $\pi/P$ , is 0.447.

The computation of the pressure ratio in the preceding paragraph was based on the assumption of constant linear bulk moduli for all constituent materials. A more detailed simulation, based on nonlinear pressure-volume strain relationships, was also performed using a version of the program NKOCF (Kim, Blouin, and Timian, 1986) that was modified to include a grain compressibility model for calcium carbonate based on test data specific to that mineral. It also includes a nonlinear compressibility formulation for water. In addition to the pore fluid and grain compressibility models, this program requires input of the rock skeleton compressibility in the form of a pressure-volume strain curve from a drained hydrostatic compression test on the material of interest. For this calculation, the test data shown in Figure 5-7 were used to define the skeleton compressibility. NKOCF numerically integrates along the

skeleton compressibility curve using the fully coupled formulation, which maintains full strain compatibility, to calculate the response of the material in the saturated undrained condition. Figure 8-4 presents comparisons between the stresses measured in a saturated undrained hydrostatic compression test and those calculated using NKOCP with input from a drained hydrostatic compression test on the same material. Total stress, effective stress, and pore pressure are compared independently in the figure. There is very good agreement between the test data and the numerical simulations which are based on the effective stress approach. Figure 8-5 shows the ratio of pore pressure to total confining pressure computed by the NKOCP simulation and compared with the results of two saturated undrained tests. Again, the agreement is very good, especially considering that this presentation tends to exaggerate small differences.

Laboratory experience showed that the ratio of pore to confining pressure will eventually converge to the same level with increasing hydrostatic stress, regardless of the initial pressure ratio imposed at the beginning of the test. In order to provide a theoretical rationale for this phenomenon, additional numerical simulations were conducted with NKOCP using different initial conditions of pore to confining pressure ratio. The results are plotted in Figure 8-6, with initial pressure ratios of 0.2, 0.4, and 0.6. This plot confirms the convergence of the pore to hydrostatic pressure ratio with increasing hydrostatic pressure, as observed in laboratory. Furthermore, the simulations show the dependance on the initial pressure ratio at the beginning of the experiment.

#### 8.4 SPECIFIC STORAGE.

Most standard methods for specific storage measurement, such as those from ASTM, NGWA, apply to field tests on underground aquifers. The specific storage of a saturated aquifer is defined as the volume of water that a unit volume of aquifer releases from storage under a unit decline in hydraulic head (Freeze and Cherry, 1979). In a laboratory test, the aquifer referred to in this definition is the rock specimen under study. Based on this definition, the following formula was developed for derivation of specific storage from the laboratory data described in Section 8.2:

$$S_s = \frac{V_w - V_{w0}}{V_t(\pi_0 - \pi)} \quad (8.5)$$

where  $S_s$  is the specific storage of the rock specimen,  $V_t$  is the total volume of the specimen,  $V_w$  is the measurement of the volume of pore fluid drained from the rock specimen,  $\pi$  is the pore pressure.  $V_{w0}$  and  $\pi_0$  are the drained water volume and pore pressure measurements, respectively, at point a, where the specific storage measurement is started. For the calculation presented here, the point a was selected as the point of maximum pore pressure at which the drainage port was opened in the experiment. This is illustrated in Figure 8-3, where the specific storage is the negative of the slope of the curve, normalized by the volume of the specimen. In order to eliminate the noise that would result from performing an instantaneous numerical differentiation on the data in Figure 8-3, the specific storage curves were derived from the test data by taking successive secant slopes, all beginning with the starting point a. Those specific storage results for the Salem limestone specimens, which have values ranging from  $1.4$  to  $2.8 \times 10^{-4} \text{ MPa}^{-1}$ , are plotted in Figure 8-7 against the effective stress on the rock specimen.

From an analytical point of view, the total volume of water expelled from the rock specimen,  $\Delta V_w$ , can be considered as two parts. The first part,  $\Delta V_{w1}$ , is the pore water expansion caused by decline of pore pressure, which can be expressed as:

$$\Delta V_{w1} = \frac{1}{K_w} n \Delta \pi V_t \quad (8.6)$$

where  $n$  is porosity,  $K_w$  is the bulk modulus of pore water. Because of the decline of pore pressure,  $\Delta \pi$ , the effective stress  $\sigma_e$  increases. The increment,  $\Delta \sigma_e$ , will further squeeze the rock skeleton and reduce its pore volume. This volume reduction will expel an equal amount of water from the specimen, which constitutes the second part,  $\Delta V_{w2}$ . According to the fully coupled compressibility model (Blouin and Kim, 1984):

$$\Delta V_{w2} = -\Delta e_t V_t = -\left(\frac{\Delta \sigma_e}{K_s} + \frac{\Delta \pi}{K_s}\right) V_t \quad (8.7)$$

where  $K_s$  and  $K_g$  are bulk moduli of the rock skeleton and solid grains, respectively. Then the total volume of water expelled from the specimen is:

$$\Delta V_w = \Delta V_{w1} + \Delta V_{w2} = \left( n \frac{\Delta \pi}{K_w} - \frac{\Delta \sigma_e}{K_s} - \frac{\Delta \pi}{K_g} \right) V_i \quad (8.8)$$

Since the total hydrostatic load is unchanged as the water drains,  $\Delta \sigma_e = -\Delta \pi$ . According to the definition given by Equation 8.5, the specific storage is given by:

$$S_s = n \frac{1}{K_w} + \frac{1}{K_s} - \frac{1}{K_g} \quad (8.9)$$

Equation 8.9 is an expression for specific storage in terms material properties. Taking the bulk moduli of the grains and water as constants (82000 MPa and 2260 MPa, respectively), and using the hydrostatic test data from Figure 5-7 to define the skeleton bulk modulus,  $K_s$ , as a function of effective stress, a simple prediction of specific storage of the limestone is obtained. This prediction is plotted in Figure 8-7 along with the experimental results.

Comparison of specific storage values from pore fluid drainage volume measurements with those derived from material properties showed good agreement at the beginning part of the experiment, where the pore pressure was highest. The measured responses diverge from the computed curve at effective stresses above about 75 MPa.

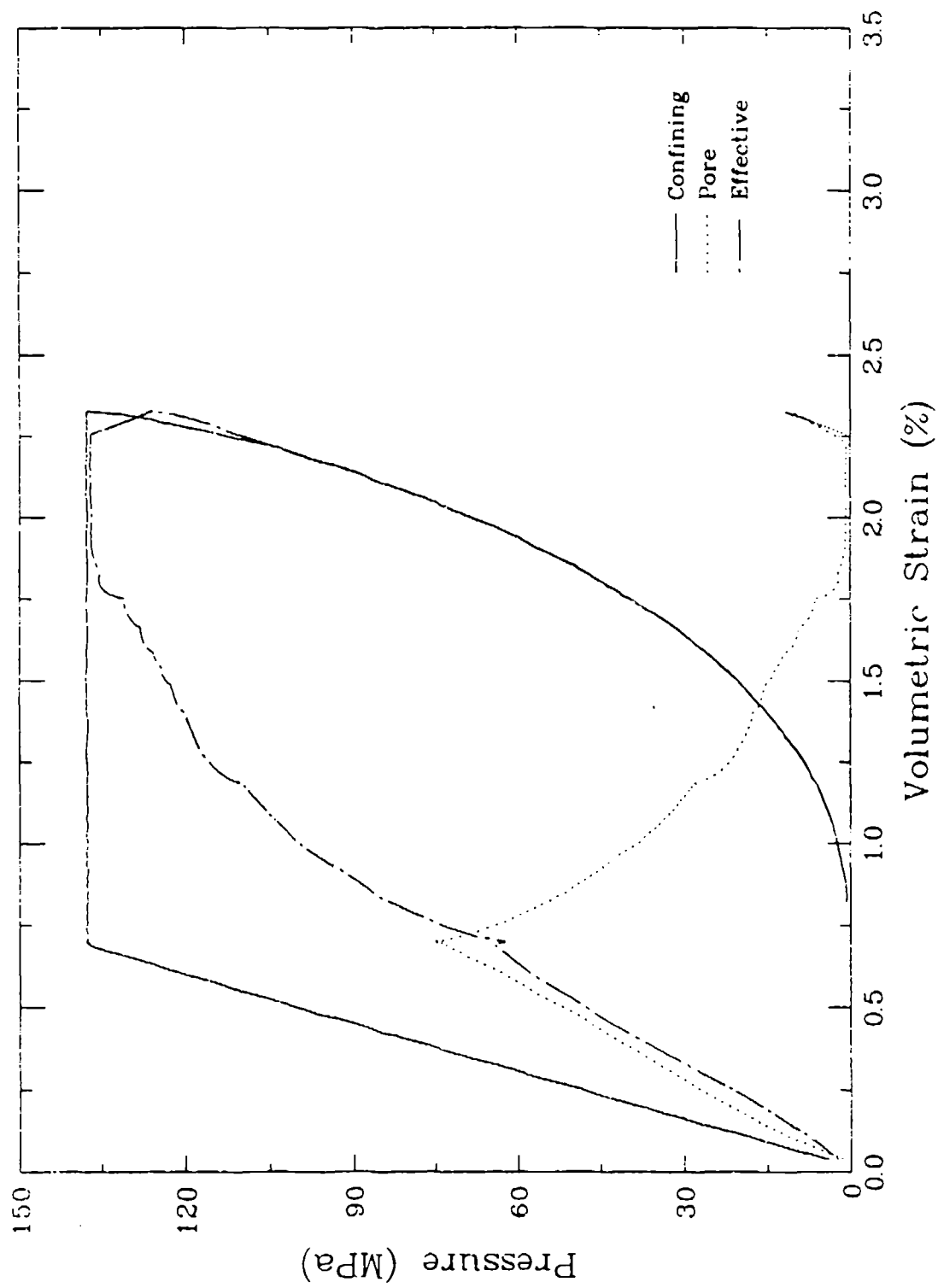


Figure 8-1. Results of test in which a saturated specimen of Salem limestone was loaded hydrostatically to 138 MPa without drainage and then allowed to drain, showing total stress, effective stress, and pore pressure.



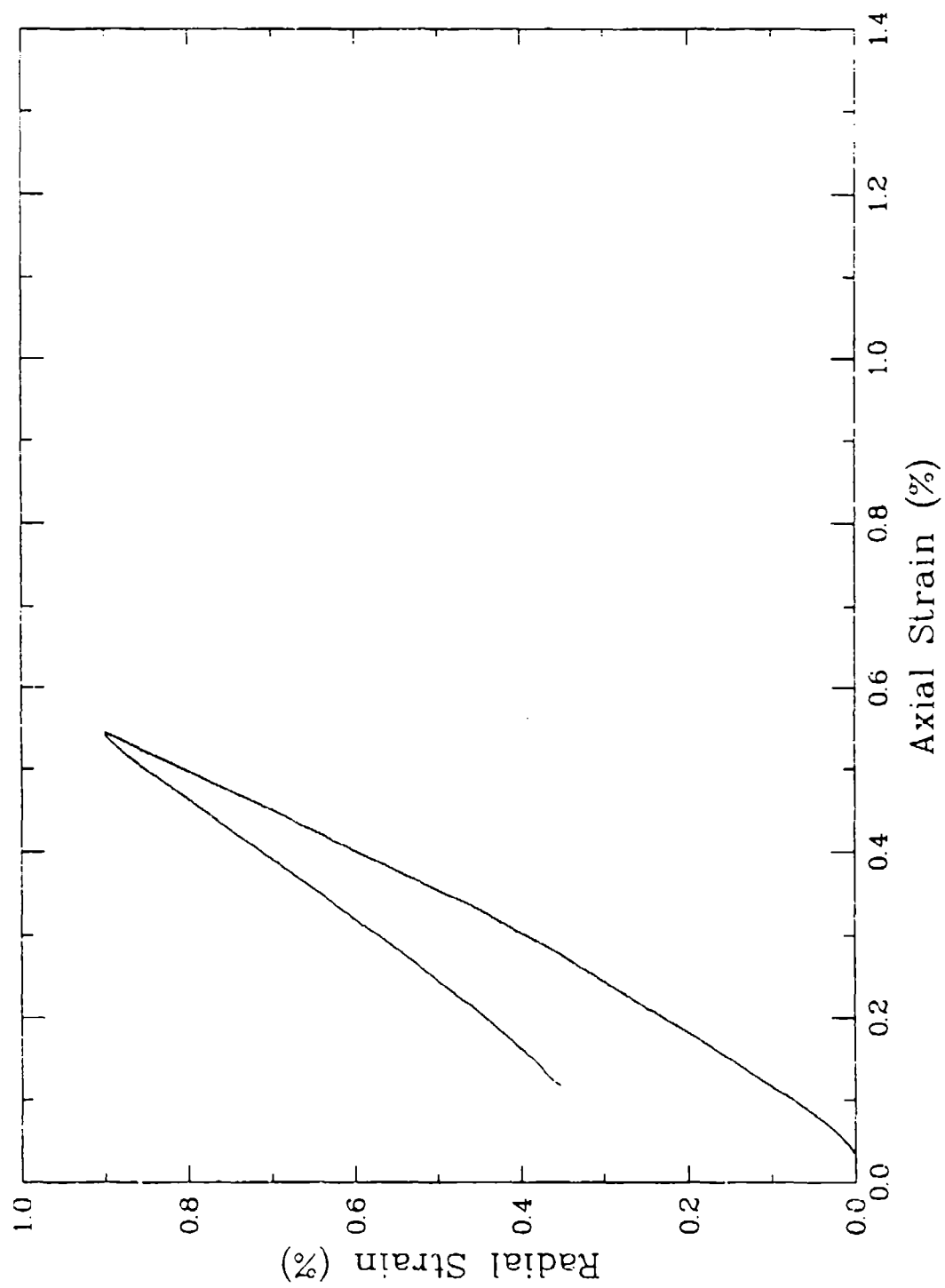


Figure 8-2. Relationship between axial and radial skeleton strain from the test shown in Figure 8-1.

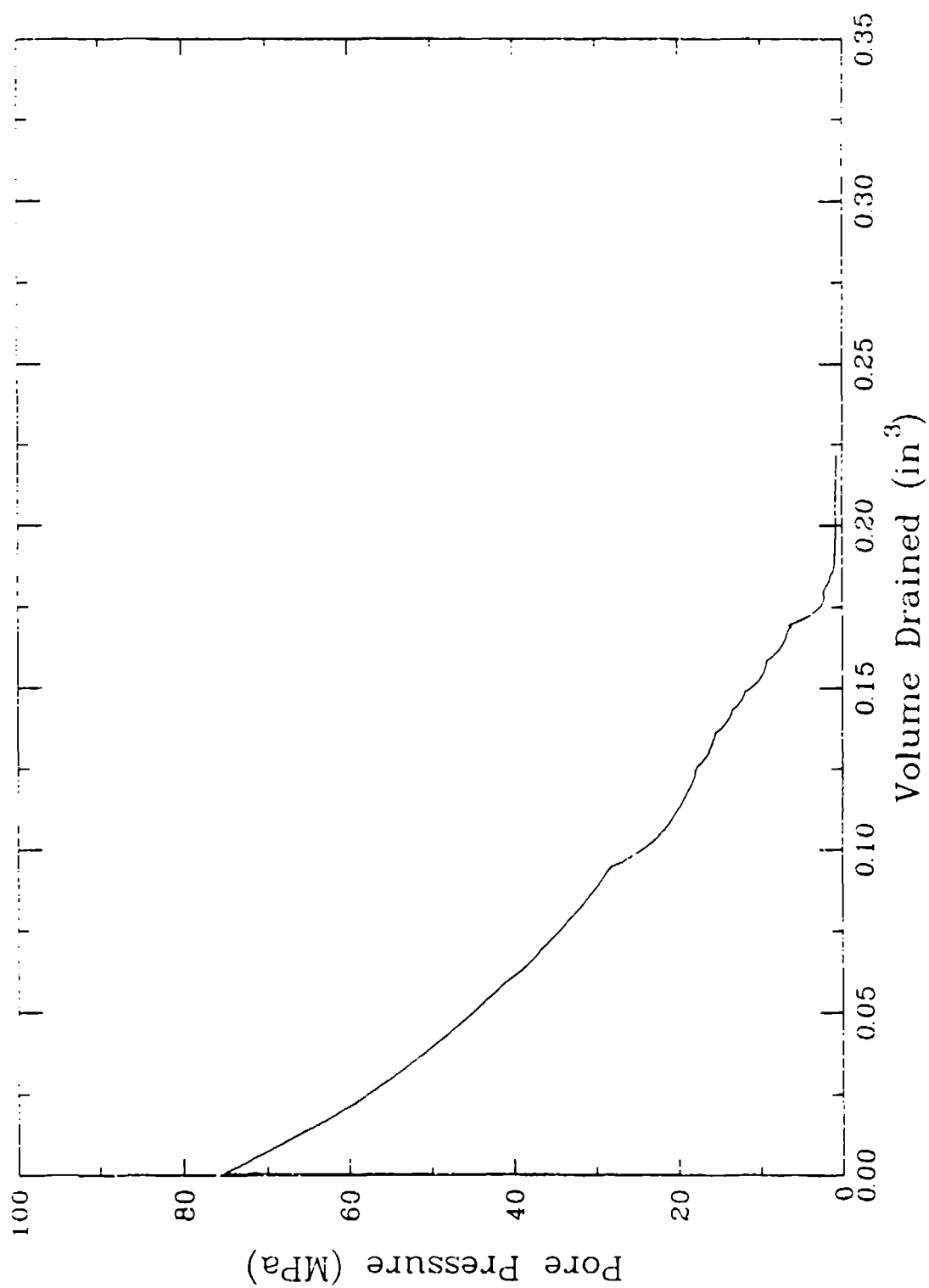


Figure 8-3. The relationship between pore pressure and the volume of drained water for a Salem limestone specimen that were first saturated and loaded hydrostatically to 138 MPa without drainage.

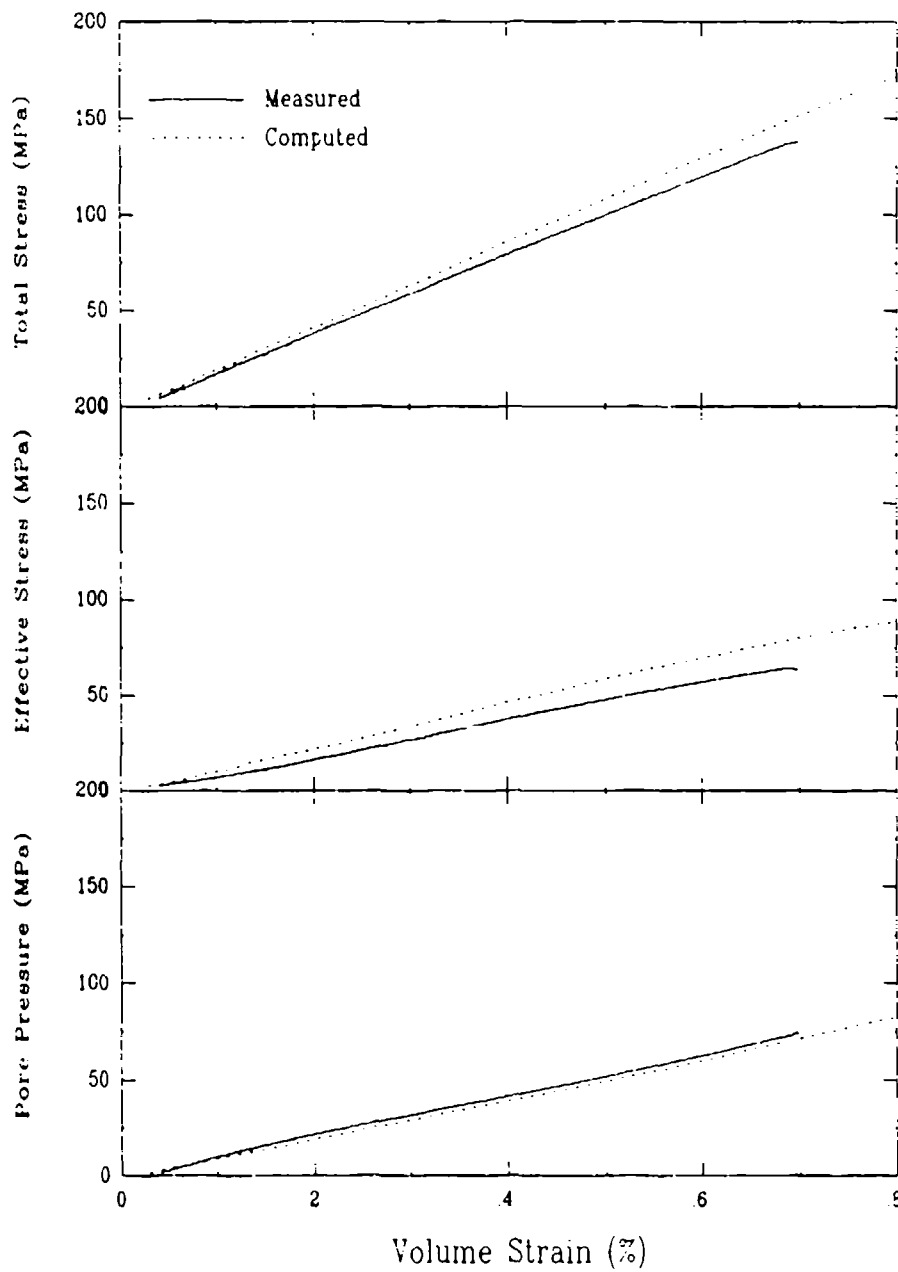


Figure 8-4. Comparison between the results of a saturated undrained hydrostatic compression test on Salem limestone with a numerical simulation based on drained rock skeleton properties.

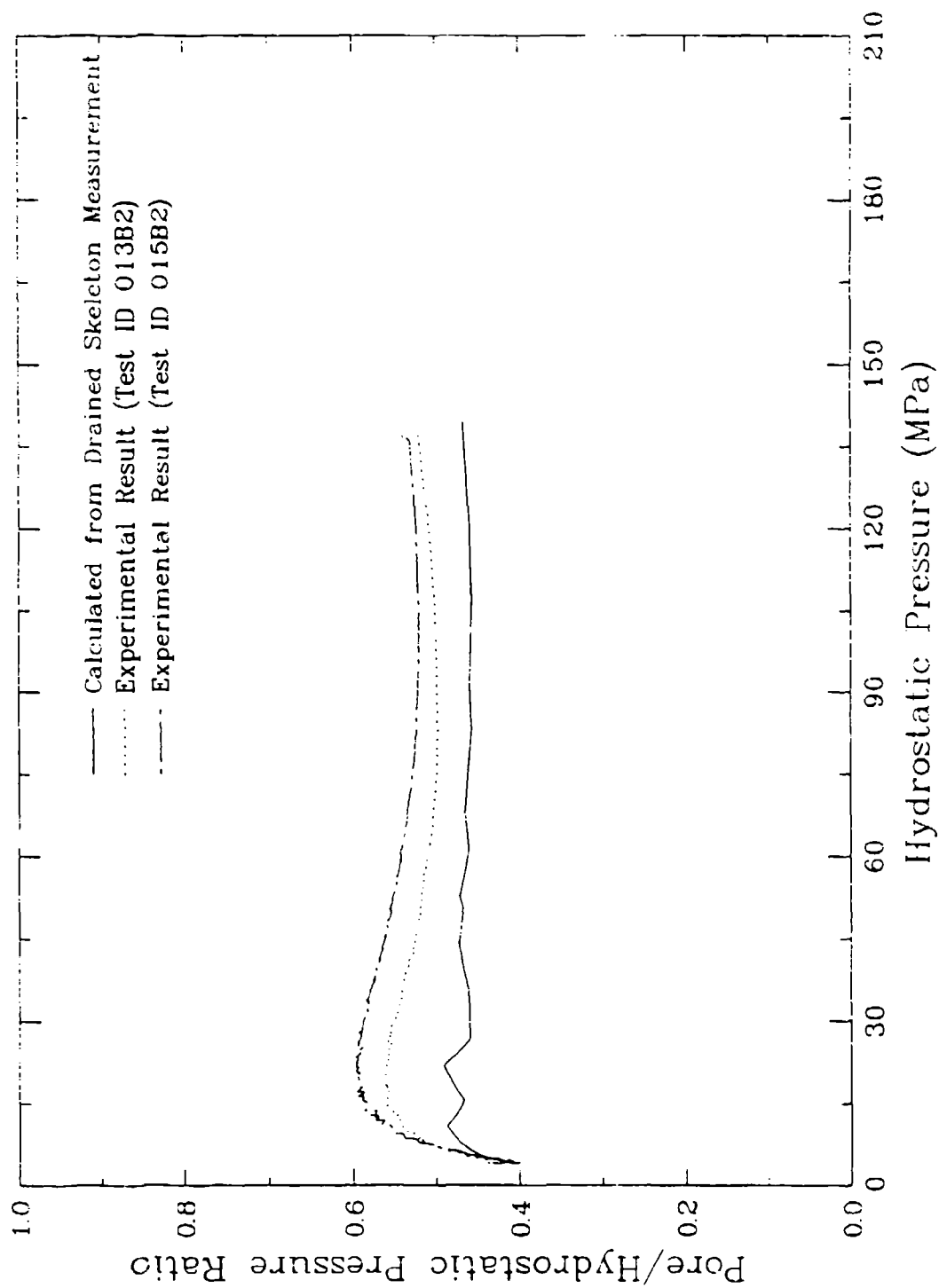


Figure 8-5. Comparison of the pore to confining pressure ratios from two tests with the results of a numerical simulation based on drained rock skeleton properties.

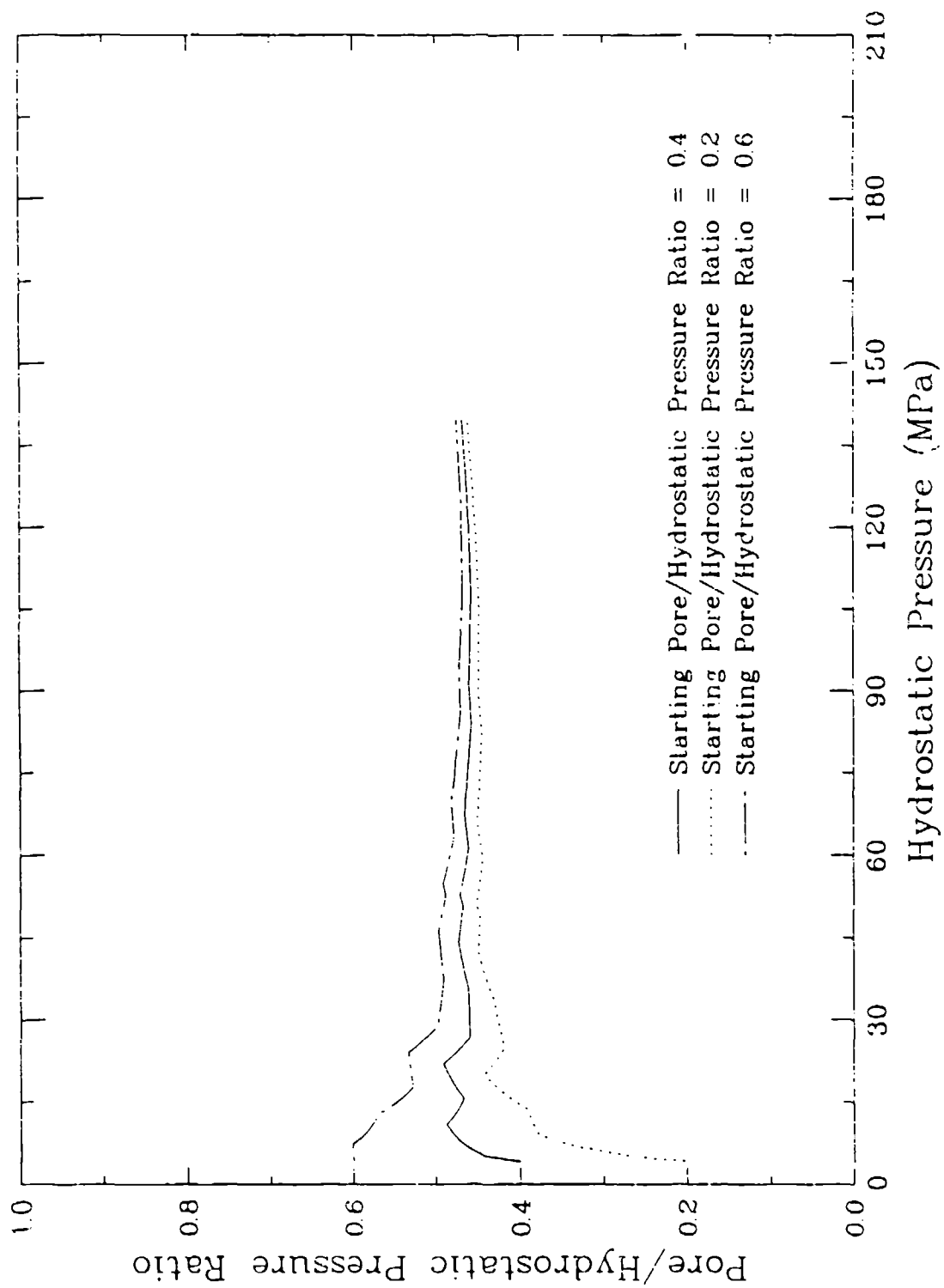


Figure 8-6. Comparison of the pore to confining pressure ratios resulting from numerical simulations with different initial pressure ratios.

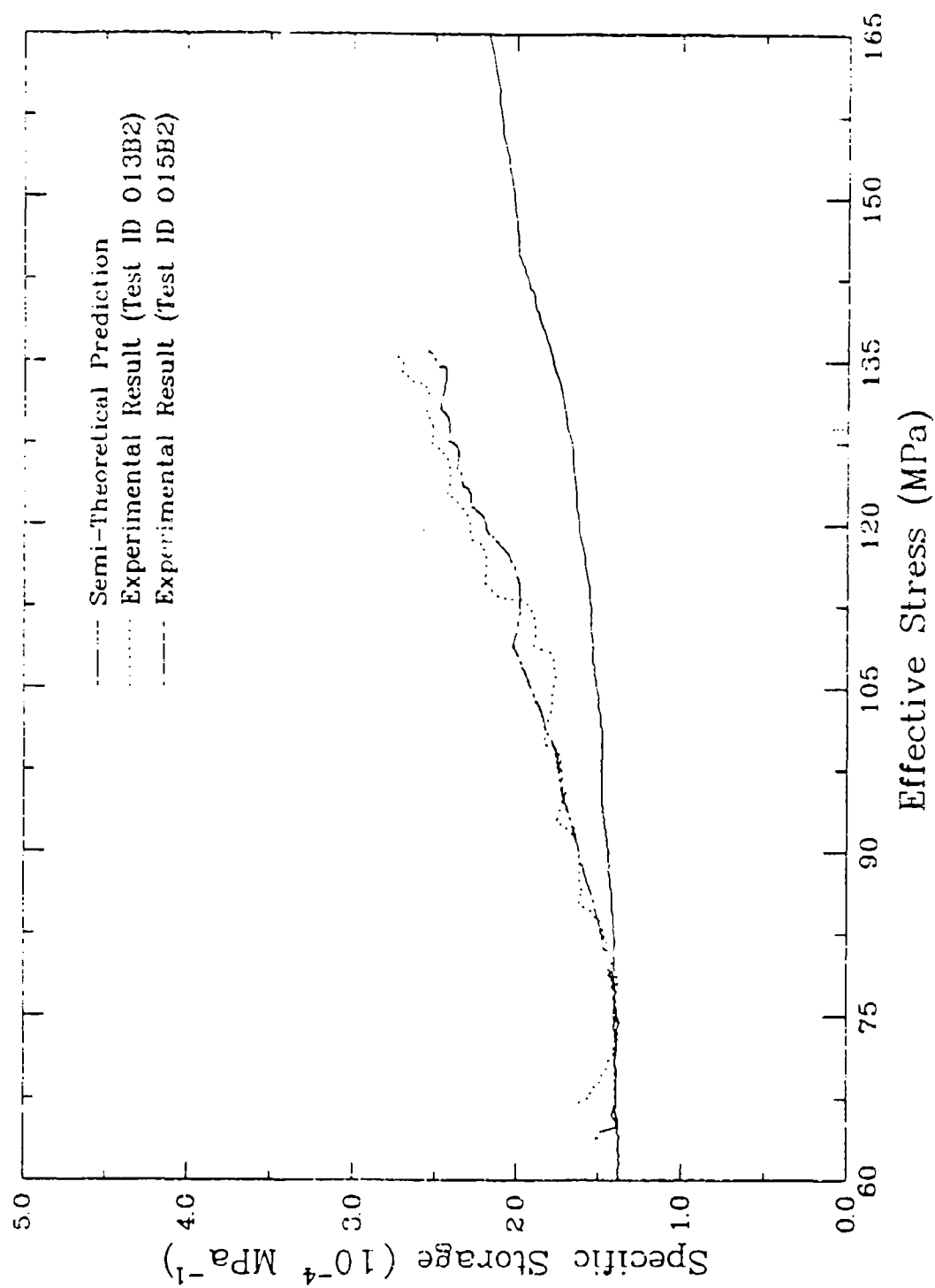


Figure 8-7. The relationship between specific storage and effective stress resulting from two tests and a numerical simulation based on drained rock skeleton properties.

## SECTION 9

### PERMEABILITY OF INTACT AND JOINTED LIMESTONE

A series of laboratory tests was performed to measure fluid flow through intact and jointed Salem limestone specimens under a wide range of stress conditions. The objectives of this effort were to measure the permeability properties of the intact rock and rock joints and to correlate these properties with the mechanical response of the rock.

For intact specimens, permeability tests were first conducted under hydrostatic loadings over a range of pressures, and an empirical relationship between permeability and hydrostatic stress was developed. Then permeability was measured for the limestone specimens under different triaxial stress conditions with confining pressures ranging from 5 to 90 MPa. Based on the empirical relationship for hydrostatic loading, a component of permeability related to the deviatoric deformation was identified. An empirical model relating permeability and mechanical response was developed for Salem limestone.

Fluid flow tests under a range of hydrostatic stress conditions were performed on the three different types of joint surfaces described in Section 3: tensile fractures, smooth ground surfaces, and synthetic joints consisting of mating surfaces produced on a numerically controlled milling machine. Comparisons were made between the measured flows through intact and jointed specimens, and the results used to develop empirical models relating permeability of the different joint types to joint normal stress.

#### 9.1 DESCRIPTION OF EXPERIMENT.

This section describes the equipment and procedures used to perform the hydraulic permeability tests and presents background on the formulation of flow laws for permeable materials.

### 9.1.1 Test Specimens, Equipment, and Instrumentation.

The experiments were carried out in a computer controlled triaxial compression apparatus that had been specially modified to perform fluid flow tests. Figure 9-1 presents a schematic of the equipment used in these tests. The permeability tests were performed on cylindrical specimens of Salem limestone approximately 48 mm in diameter and 96 mm long, the same as those used in the mechanical property tests. For measurements of joint permeability, specimens were prepared with the three types of joint surfaces described in Section 3. However, the permeability specimens had the joint oriented parallel to their axis and, ideally, in a plane containing the axis. Preparation and instrumentation of the permeability test specimens closely followed the procedures described in Section 4. As in the mechanical property tests, the rock specimen was installed in the triaxial chamber between upper and lower endcaps and sealed with a polyolefin jacket. The endcaps had flow conduits, and pore fluid diffusers were placed at each end between the specimen and the endcap to evenly distribute flow over the ends of the specimen through a series of equally spaced holes. In order to limit variations in the rock skeleton stress field, the total cross sectional area of the holes was no more than 10% of the end area of the specimen. At the bottom of the specimen, fluid was pumped in through the same port in the pressure vessel that is used for saturation of porous specimens. At the top, fluid was allowed to flow out through holes in a specially modified piston in the triaxial apparatus which was sealed to the specimen endcap by means of an O-ring. The upper endcap was also strain gaged to serve as a load cell for axial stress measurement. Where deformation instrumentation was used, it was of the same type as in the mechanical property tests as described in Section 4.4.

The flow of fluid to the limestone specimen was supplied by an intensifier, i.e. a small diameter hydraulic cylinder driven by a larger diameter cylinder. By supplying approximately 20 MPa hydraulic fluid pressure to the large diameter side of the intensifier, it was possible to generate up to 138 MPa of water pressure on the small diameter side. This is illustrated schematically in Figure 9-1. The rate of pore fluid flow was controlled by regulating the flow of hydraulic fluid to the low-pressure side of the intensifier. By installing a displacement transducer (LVDT) to measure piston displacement, the intensifier also provided a means of measuring the water flow through the specimen. To determine the flow rate, a least squares fit



was made to the constant-velocity portion of the piston displacement time history. The resulting slope is the piston velocity,  $V_p$ . The apparent fluid velocity,  $V_a$ , was then computed as:

$$V_a = V_p \frac{A_i}{A_s} \quad (9.1)$$

where:  $A_i$  = area of the high-pressure end of the intensifier

$A_s$  = cross section area of the test specimen

A transducer installed in the bottom end cap of the test specimen was used to measure the pore fluid pressure on the upstream end of the rock specimen. On the downstream end (the top) of the specimen, the fluid drain was open to the atmosphere. The pressure drop between the end of the rock specimen and the atmosphere was negligible, and a downstream pressure measurement was not made. The pressure transducer was calibrated with zero output indicating atmospheric pressure. Thus, assuming a constant pressure gradient along the length of the specimen, the pressure gradient,  $G_p$ , was computed as:

$$G_p = \frac{P_u}{l_s} \quad (9.2)$$

where:  $P_u$  = fluid pressure at the upstream end of the test specimen

$l_s$  = length of the test specimen = length of flow path

As with the mechanical property tests, measurements made by the active instrumentation were recorded by a microcomputer-based multi-channel digital data acquisition system.

### 9.1.2 Test Procedures.

All of the permeability tests were performed using distilled de-aired water as the pore fluid. In preparation for fluid flow testing, the test specimen and water supply system were fully saturated with water. The triaxial chamber was first pressurized to 1-2 MPa to hold the jacket tight against the specimen. The specimen and water supply system were sealed from the atmosphere and evacuated, and water was forced into the specimen with the intensifier.

Once the specimen and associated piping were fully saturated, the total stress state for the particular test was imposed on the specimen using the normal triaxial compression loading functions. It was always necessary to keep the confining pressure in the triaxial chamber higher than the upstream pore pressure in the specimen. Failure to do so would result in gaps opening between the specimen and the jacket, allowing erroneous fluid flow. At each total stress state, multiple fluid flow tests were conducted, each at a constant pressure gradient. In all cases the downstream pressure was zero. In a typical test series the upstream pressure ranged from approximately 1 MPa to 90% of the confining pressure. In each permeability run, the upstream pressure gradient was held constant for a period of 20 to 100 s while data were recorded. The durations of the tests were selected to allow time for sufficient intensifier displacement to provide adequate resolution for pore fluid velocity determination.

### 9.1.3 Fluid Flow Equations.

In traditional civil engineering, where pressure gradients and the resulting flow velocities are typically small, problems are almost exclusively formulated using the Darcy flow equation which assumes a linear relationship between pressure gradient and flow velocity. However, in weapons effects problems of interest, pore pressure gradients and flow rates can be of sufficient magnitude that the Darcy equation does not adequately describe the pore fluid response. To analytically treat the dynamic problems, Kim, et.al. (1988) adopted a more general expression for pressure gradient which includes a term that is proportional to the square of the fluid velocity in addition to the linear (Darcy) term, along with inertial terms related to fluid acceleration. The use of the velocity-squared term was apparently first proposed by Forchheimer (1901), and has been used in various forms by investigators over the years. Forchheimer's equation, which does not consider fluid acceleration, has the general form:

$$G_p = \frac{d\pi}{dx} = aV_x + bV_x^2 \quad (9.3)$$

where:  $G_p$  = pore pressure gradient in the x direction  
 $V_x$  = apparent fluid velocity in the x direction  
 $a, b$  = constants which are functions of both skeleton and fluid properties

While Forchheimer's equation appears to be virtually unknown in the civil engineering literature, its use is widespread in chemical engineering, particularly with reference to porous metal filters. The constants,  $a$  and  $b$ , in Equation 9.1 are functions of the properties of both the pore fluid and the porous medium. If Equation 9.1 is divided through by  $V_a$ , the result is:

$$\frac{G_p}{V_a} = a + bV_a \quad (9.4)$$

This represents a linear relationship between  $V_a$  and  $G_p/V_a$ . When the test data are plotted with  $G_p/V_a$  on the vertical axis and  $V_a$  on the horizontal, the slope of the resulting line is the quadratic coefficient,  $b$ , and the intercept with the vertical axis is the linear coefficient,  $a$ . This form is convenient for derivation of the coefficients from test data, but for fundamental understanding of the physical phenomena, a more useful form of the equation will result if it can be expressed in terms of constants that are dependent on either fluid or porous medium properties, but not both. Green and Duwez (1951) argue, based on dimensional analysis, that if the factors controlling the pressure gradient are assumed to be fluid viscosity, fluid density, a length characterizing the pore openings, and the apparent fluid velocity, then Forchheimer's equation must have the form:

$$G_p = \text{const}_1 \frac{\mu V_a}{\delta^2} + \text{const}_2 \frac{\rho_f V_a^2}{\delta} \quad (9.5)$$

where:

- $\mu =$  dynamic viscosity of the fluid
- $\rho_f =$  mass density of the fluid
- $\delta =$  unknown length related to pore geometry

If the constants are combined with the unknown pore dimension term,  $\delta$ , and called  $\alpha$  and  $\beta$ , the resulting expression has the desired separation between quantities dependent on skeleton properties and those dependent on fluid properties:

$$G_p = \frac{\mu}{\alpha} V_a + \frac{\rho_f}{\beta} V_a^2 \quad (9.6)$$

The relationship between the two sets of coefficients is:

$$\begin{aligned}\alpha &= \frac{\mu}{a} \\ \beta &= \frac{\rho_f}{b}\end{aligned}\tag{9.7}$$

Here,  $\alpha$  has units of length squared and  $\beta$  has units of length. A linear approximation to the Forchheimer equation is the familiar Darcy equation:

$$G_p = \frac{\mu}{K} V_s = \frac{\rho_f g}{k} V_s\tag{9.8}$$

where:       $K$  =      absolute permeability (length<sup>2</sup>)  
                   $k$  =      Darcy permeability coefficient (length/time)  
                   $g$  =      acceleration of gravity

The absolute permeability,  $K$ , in Equation 9.5 has the same form as  $\alpha$  in Equation 9.3. However, it can be numerically different because a quadratic fit to a given data set will yield a different linear coefficient than a linear fit to the same data. The relationship between the two permeability measures is:

$$\begin{aligned}K &= \frac{k \mu}{\rho_f g} \\ k &= \frac{K \rho_f g}{\mu}\end{aligned}\tag{9.9}$$

## 9.2 PERMEABILITY OF INTACT SALEM LIMESTONE.

Permeability measurements were made on intact specimens of Salem limestone over a wide range of pressure gradient and skeleton stress and strain conditions, including hydrostatic confining pressures up to 150 MPa and pressure gradients up to 1500 MPa/m. Included were tests in which the rock skeleton was loaded in triaxial compression past failure with axial strains up to 10%. Tables 9-1 through 9-8 show the test conditions applied to each specimen. Under each loading condition there was a series of eight to twelve flow tests conducted at different pore pressure gradients. Figures 9-2 and 9-3 show typical recordings of upstream pore fluid pressure and pore fluid intensifier displacement, respectively. As shown in Figure 9-3, piston displacement was held as a linear function of time. In all cases, the correlation coefficients of the linear fits to piston displacement were greater than 0.99, showing an almost perfect linear relation between the variables.

### 9.2.1 Flow Tests with Hydrostatic Skeleton Loading.

Fluid flow tests were performed on intact specimens of Salem limestone which were subjected to hydrostatic skeleton loading ranging from 1 MPa to 150 MPa. The results of those tests are summarized in Tables 9-1 and 9-2. Figure 9-4 presents data from the test described in Table 9-1 in a format for determination of both the linear and quadratic flow coefficients described by Equation 9.2, where the slope is  $b$ , and the intercept is  $a$ . At the lower pressures, the curves have small, but non-zero slopes. At pressures above about 70 MPa, the lines curve downward with increasing fluid velocity. We believe this nonlinear response is a result of non-uniform effective stress in the rock specimen which becomes increasingly significant as the upstream pore pressure approaches the confining pressure. Under this condition, the effective stress in the rock skeleton approaches zero. As that happens, the flow resistance of the rock skeleton becomes more like that in the same rock loaded to a lower confining pressure. In order to minimize the effect of effective stress variations on flow coefficient determination, fits were performed on only the lower pressure half of the test records. In fits to the 130- and 150-MPa confining pressure test data, the data points from the lowest pressure gradient tests were also omitted because they appear to represent some initial flow resistance that is not characteristic

of the overall tests. The resulting flow coefficients are tabulated in Table 9-1 and shown graphically in Figures 9-5 and 9-6 for a and b, respectively. As expected, the increasing values of both a and b with increasing confining pressure correspond to decreased flow. Recommended empirical fits to the data are also shown on the figures. The break in slope of the fits is related to the onset of pore collapse in the rock skeleton.

While we believe the Forchheimer equation, including the quadratic term, is more fundamentally correct than the linear Darcy equation for representing flow through porous media, practicality suggests that a linear approximation be evaluated. Rather than simply setting the quadratic coefficient to zero, the data were re-fit assuming the linear form. The data shown in Figure 9-4 are presented in different form in Figure 9-7. Here, the axes are pressure gradient and apparent fluid velocity, and the absolute permeability coefficient, K, is:

$$K = \frac{\mu}{a'} \quad (9.10)$$

where:  $a'$  = the slope of a linear fit to the data as presented in Figure 9-7

$\mu$  = dynamic viscosity =  $1.002 \times 10^{-9}$  MPa\*s for water at 20°C

Figure 9-8 presents the values of absolute permeability determined by combining the data in Table 9-1 (Figure 9-7) along with another data set from a different specimen, listed in Table 9-2, which includes tests conducted at lower confining pressures ranging from 1 to 12 MPa. There is clearly some difference in measured permeability between the two specimens at about 10 MPa where they overlap. However, the fit shown in Figure 9-8 is in reasonable agreement with all of the data. As shown in Figure 9-8, the variation in absolute permeability with skeleton stress,  $\sigma$ , is given by:

$$K = 9.68 e^{-0.024 \sigma} \quad (9.11)$$

For those limestone specimens tested in hydrostatic compression, the confining pressure (mean stress) is a very convenient independent variable to use in modeling the permeability

change with loading. However, variations in permeability are fundamentally related to changes in geometry of the pore space in the rock. Thus, to support extension of the model to other more complex stress and strain states, the data were also analyzed in terms of volumetric strain. Deformation instrumentation was not used in the hydrostatic permeability tests. However, the deformation properties of the intact limestone skeleton were very well characterized, as reported in Section 5. Based on the hydrostatic compression test data presented in Figure 5.12, the flow test data shown in Figure 9-8 were replotted in terms of volumetric strain, as shown in Figure 9-9. A fit, in two segments, to those data is also presented in Figure 9-9.

### **9.2.2 Flow Tests with Triaxial Skeleton Loading.**

To investigate the influence of shear loading on permeability of the limestone, a series of flow tests was performed on intact limestone specimens while they were subjected to triaxial compression loading. Tables 9-3 through 9-8 present summary data for the six tests conducted at confining pressures ranging from 5 to 90 MPa. A virgin rock specimen was used for the set of tests at each confining pressure level. Initially, the specimen was loaded hydrostatically to the specified level. First, a set of flow tests at a range of pressure gradients was performed on the rock under hydrostatic load only. The axial strain was then incremented and held constant while the next set of flow tests was run. The strain increment and flow testing were repeated until the axial strain reached 10%, if possible. In some cases, jacket failures cut the test short. Prior to failure of the rock skeleton, where the stress-strain curve is steep, the strain increments were specified in terms of stress difference. After failure, they were specified in terms of axial stress. Both stress difference and strain at each step are shown in Tables 9-3 through 9-8.

Figure 9-10 summarizes the flow data from the triaxial loading tests. For each confining pressure level, the measured permeability is plotted as a function of volumetric strain in the rock skeleton. For the tests performed above the brittle-ductile transition, (50 and 90 MPa), data from the entire test are shown in the figure. For the lower pressure tests where failures are localized and volume strain is not well defined, only the pre-failure portions of the tests are shown. Also shown on the figure for comparison is the fit to the data from specimens that were loaded only in hydrostatic compression from Figure 9-9. Up to the volume strain level of

approximately 0.01, the permeability of the material under triaxial loading is well characterized by the fit to the hydrostatic loading. At larger volume strains, corresponding to ductile deformation of the specimens, the permeability remains higher at a given volumetric strain level than would be predicted by the hydrostatic measurements. This difference is apparently related to the shearing deformation. Additional measurements would be required to accurately quantify this difference.

In triaxial tests in the brittle regime, failures are localized, resulting in nonuniform strain fields and volumetric strains that are not well defined. For this reason, the post-failure data from the brittle triaxial tests were not shown in Figure 9-10. Those data are presented in Figures 9-11 through 9-13, corresponding to confining pressures of 5, 10, and 20 MPa, respectively. Each of those figures shows both stress difference and permeability as functions of axial strain. These figures show that the permeability was reduced, relative to the initial hydrostatic loading state, as the specimens were sheared under triaxial loading. After failure of the rock skeleton, the permeability stabilized and exhibited no significant changes over the range of axial loads imposed. It is hypothesized that this is related to the fact that failures tend to be localized in the brittle regime, leaving the bulk of the rock in the specimen undamaged.

### **9.3 PERMEABILITY OF JOINTED SALEM LIMESTONE SPECIMENS.**

Permeability tests were conducted on specimens of Salem limestone with single joints of each of the three surface types described in Section 3.1, smooth ground, tensile fracture, and synthetic. As in the case of the intact limestone, these permeability tests were performed on cylindrical specimens that were nominally 48 mm in diameter and 96 mm long. The joint in each specimen was oriented parallel to the specimen axis and across a diameter. The tests were performed using the equipment and procedures described in Section 9.1. All of the joint permeability tests were performed with hydrostatic loading only (no additional axial load), and the primary emphasis was on confining pressures in the range of 1 - 12 MPa. Each specimen was tested sequentially at a range of confining pressures, and at each confining pressure, flow tests were performed at range of pressure gradients. The pore fluid pressures at the upstream end of the specimen was typically varied between approximately 10% and 90% of the confining pressure. The approach to determining the flow rate through the various joints was similar to



that used to determine the deformation of joints under shear loading. Similar specimens with and without joints were subjected to the same loading, and the difference in response was assumed to result from the presence of the joint. In each individual flow test, the pressure gradient was held constant while pressure and flow measurements were made. From each test, the values of steady state pressure gradient and apparent fluid velocity were determined as described in Section 9.1.1.

### 9.3.1 Joint Permeability Formulations.

To determine the quantity of fluid flowing through the joint under a given set of confining pressure and pore pressure gradient conditions, it is assumed that the flow rate,  $Q_s$  (volume/time), of the entire jointed specimen is equal to the flow rate,  $Q_i$ , through the intact portion of the specimen plus the flow rate  $Q_j$ , through the joint, i.e.

$$Q_s = Q_i + Q_j \text{ or } Q_j = Q_s - Q_i \quad (9.12)$$

For convenience, the equivalent absolute permeability of the jointed specimen,  $K_s^*$  is defined as the permeability that would result if the total flow through the intact material and joint were uniformly distributed over the cross sectional area,  $A_s$ , of the specimen. The quantity,  $K_s^*$ , is not a property of either the intact material or the joint, but merely a convenient intermediate step in the computation of the joint flow. Then, from Equation 9.8,

$$K_s^* = \frac{\mu V_s}{G_p} = \frac{\mu Q_s}{A_s G_p} \quad (9.13)$$

Equation 9.8 can be re-written:

$$K_i = \frac{\mu V_i}{G_p} = \frac{\mu Q_i}{A_s G_p} \quad (9.14)$$

By substituting the difference between Equations 9.13 and 9.14 into Equation 9.12, an expression for the flow rate through the joint is obtained:

$$Q_j = (K_s^* - K) \frac{A_s G_p}{\mu} \quad (9.15)$$

The fluid flow properties of intact limestone have been characterized by a single parameter, the absolute permeability, which is a function of the deformation of the material. In order to derive a similar characterization of rock joints, a linear relationship is assumed between flow rate and pressure gradient. The joint is idealized as a two-dimensional structure with the flow occurring in the joint plane, and no variation in flow along the dimension perpendicular to the flow. This is the two-dimensional equivalent to Darcy flow, and is represented with the expression:

$$Q_j = \frac{G_p d \kappa_j}{\mu} \quad (9.16)$$

where       $d$  = joint length perpendicular to the flow direction  
               = specimen diameter for the test geometry

$\kappa_j$  = joint permeability (length<sup>3</sup>)

Equating Equations 9.15 and 9.16 and rearranging yields the following expression for  $\kappa_j$  in terms of quantities which were all measured in the experiments:

$$\kappa_j = (K_s^* - K) \frac{A_s}{d} \quad (9.17)$$

### 9.3.2 Tensile Fracture Joint Permeability Test Results.

Five different series of flow tests were performed on specimens of Salem limestone with tensile fracture joints. The results of a typical test series (G5A2) are shown in Figure 9-14.

The data points plotted as small dots in the Figure 9-14 represent the steady state values of pressure gradient and apparent fluid velocity measured in an individual flow test, and all data points for flow tests at one value of confining pressure are connected with a line. Equation 9.13 was used to define the equivalent permeability,  $K_e^*$  of the jointed specimen at each confining pressure based on linear fits to the data. This is the value of permeability that an intact specimen of the same dimensions would have if all of the flow in the jointed test specimen were distributed over its full cross section. The results of the five flow test series are summarized in Tables 9-10 through 9-14.

The test results for intact specimens that were used to define the flow through the intact portions of the jointed specimens are presented in Tables 9-2 and 9-3. Figure 9-15 presents the measured permeability (from Tables 9-2 and 9-3) of intact Salem limestone specimens from two different blocks that were tested with hydrostatic confinement at pressures up to 12 MPa. Both specimens exhibit a slight decrease in permeability with increasing pressure over the range shown, but there is a significant difference in the absolute magnitude of the permeability of the two specimens. Both data sets can be well represented by linear fits over this pressure range, and these fits are also shown in Figure 9-14. The values of equivalent permeability,  $K_e^*$  of the tensile fracture specimens are presented to the same scale in Figure 9-16. For clarity, only the fits to the intact data are shown. Clearly, there is sufficient variation in intact limestone permeability that a single curve can not be used as a reference for removing the influence of flow through intact material for all of the joint tests. To facilitate the determination of the quantity of flow associated with the joints, small adjustments were made to the intact reference permeabilities to make them consistent with the individual joint flow tests. This was done based on the assumption that the joints were fully closed when the variation with pressure of the equivalent permeability of the jointed specimen became the same as that of an intact specimen. In other words, it was assumed that there is no fluid flow through the joint when a pressure is reached at which the slope of the curve for the jointed specimen in Figure 9-16 reaches the slope of the line representing the intact material. Since there was a slight difference between the slopes of the two intact tests, they were averaged to obtain a generic intact permeability line that was then adjusted to match the high pressure end of the joint flow test data in Figure 9-16. In practice this involved the application of some judgement on the part of the analyst. However, the potential range for locating the line for any given test was small in comparison with the

permeability of the intact material so the potential for errors in judgement was not large. Physically, it seems reasonable to believe that some quantity of flow occurred in the joints at pressures above the point at which they were assumed to be closed. However, as the flow through the joint in the test specimen becomes small in comparison with flow through the intact material, it becomes impossible to resolve the difference. Due to variations in the test data, it is possible to resolve differences in equivalent permeability of the order of  $0.5 \cdot 10^{-15} \text{ m}^2$ . For the 48-mm diameter specimens used in these tests, this corresponds to a resolution in effective permeability,  $\kappa$ , of about  $10^{-17} \text{ m}^3$ .

The data used to compute the joint flow for the five different tensile fracture joints are presented in Figures 9-17 through 9-21. Three curves are shown on each figure. In each figure, the total flow measurements for the jointed specimen are shown as around symbols. The solid line represents the flow behavior of the intact reference material as it was adjusted to the particular joint flow test. The difference between those two curves is indicated by square symbols. The difference data shown in Figures 9-17 through 9-21 corresponds to the  $(K_j^* - K_i)$  term in Equation 9.17. Only scaling to account for specimen geometry is necessary to arrive at the joint permeability,  $\kappa_j$ . Figure 9-22 is a semi-log plot of all of the joint permeability data as a function of confining pressure, which corresponds approximately to normal stress on the joint. Actually, the effective stress on the joint varies due to the variation in pore pressure. At pressures up to about 4 MPa, the data fall in a band that can be represented by the expression:

$$\kappa_j = 622 e^{-0.92 \sigma} \quad (9.18)$$

However, due to the variation in joint geometry, the permeability data fall on either side of that expression by approximately a factor of two. At higher pressures, the lack of ability to distinguish between joint flow and flow through intact material makes the data questionable.

In planning this test series it was originally envisioned that the permeability of the intact limestone would be consistent enough from specimen to specimen that a nominal value could be chosen at each pressure level to serve as a reference for the joint permeability tests. As

discussed in the preceding paragraphs, this did not turn out to be the case. The history of one set of tests provides an interesting illustration of the variability that was incurred. In order to have the best possible comparison between a jointed specimen and its intact reference, a tensile fracture jointed permeability specimen (Specimen ID SL23-1T) and an intact permeability specimen (Specimen ID SL23-1TI) were prepared from the same horizon at immediately adjacent locations in the same block. Tables 9-2 and 9-11 present the results of the intact and jointed tests, respectively. At 1 and 2 MPa confining pressure, there was significantly more flow through the jointed specimen as evidenced by comparison of the apparent permeabilities listed in Tables 9-2 and 9-11. The flow data for the higher confining pressures are essentially the same for the intact and jointed tests, although there is some scatter. At some pressure levels, the test data indicate more flow through the intact specimen than through the one with the joint. The ability to resolve joint flow is clearly limited by the variation in flow properties between the intact portion of the jointed specimen and the intact reference specimen. In an attempt to eliminate that as a variable, the intact specimen (SL23-1TI) was split between knife edges to form a tensile fracture joint. The surfaces where the knife edges contacted rock were ground smooth to eliminate any possible short-cut path for fluid flow. The results of the first flow test on that jointed specimen are presented in Table 9-12. While the permeability of the intact specimen was originally measured as  $7.95 \times 10^{-15} \text{ m}^2$  at 12 MPa confining pressure, the jointed specimen exhibited only  $5.8 \times 10^{-15} \text{ m}^2$ . Since this result appeared to be erroneous, the test was repeated. The results of the repeat test, presented in Table 9-13 indicate even less flow than the previous test on the same jointed specimen. It was then hypothesized that the specimen was being somehow altered by the testing. Apparently the pores of the intact material were being clogged by something. The source of the particles clogging the pores could possibly have been either internal or external to the specimen. Available resources did not permit a thorough investigation of the unexpected behavior, but one additional test was performed. It was hypothesized that, whatever the source, of the clogging particles, they were likely to be concentrated at the upstream end of the specimen. Approximately 2.5 mm of material was ground off of the upstream end of the specimen and it was re-tested. The results of that test are presented in Table 9-14. In this test, the equivalent permeability was back up to the level of the first test after creation of the joint, but not back to where it was as an intact specimen. While the mechanism of reduction of the rock permeability was not specifically identified, the phenomenon was clearly identified as a problem that needs consideration in any further rock

permeability test program. This effect is also the source of some uncertainty in the measurements reported here. Although the error was not well quantified, it appears to be no more than a factor of two. Since permeability is often expressed only as the closest power of ten, this uncertainty is not overwhelming.

In the preceding discussion, joint permeability data are presented in terms of the normal stress acting on the joint. Normal stress is an attractive independent variable because of the ease with which it can be measured and because it was used to control the actual tests. However, fluid flow through a joint is actually related to the geometry of the joint opening, and a more fundamentally correct independent variable would be a measure of the joint geometry. In two of the joint permeability tests, displacement gages were installed to monitor the closure of the joint as confining pressure was increased. Gages were located at the top and bottom quarter points of the specimen and measured deformation normal to the joint plane. The mounts for the gages penetrated the jacket and attached directly to the rock. A correction for the deformation of the intact rock was made based on the bulk modulus of the material measured in the hydrostatic compression tests that are reported in Section 5.3. The resulting data represent only the deformations of the joints. The joint opening, or aperture, is very difficult to quantify precisely. For the purpose of this analysis, it was approximated based on the normal deformation measurements. Figure 9-23 presents the corrected joint deformation measurements from two of the tensile fracture joint permeability tests. The measured joint deformation data points in Figure 9-23 were derived by averaging the outputs of both normal deformation gages in the steady state portion of each run, correcting for deformation of the intact rock, and then averaging all runs at a given confining pressure. As shown in Figure 9-23, at approximately 4-6 MPa confining pressure, the joint deformation becomes constant, and there is no further closure with increasing stress. For computation of the joint aperture, it was assumed that the joint was fully closed at that point, and the aperture was computed as the difference between the measured joint deformation at the fully closed point and the same quantity at a lower confining pressure of interest. The apertures computed in that way are also shown in Figure 9-23 for both specimens.

A plot of joint permeability as a function of joint aperture is presented in Figure 9-24. Unfortunately, reliable deformation measurements are only available for two of the tensile

fracture tests. The two sets of measurements are from two different jointed specimens. They are well fit by the expression:

$$\kappa_j = 11.7 e^{431 \delta} \quad (9.19)$$

where:  $\delta$  = joint aperture

There is much less scatter in the relationship between joint permeability and joint aperture than the relationship with confining pressure shown in Figure 9-22. For a well-mated tensile fracture joint, there is a good correlation between joint opening and fluid flow. As shown in Figure 9-23, there is significantly more scatter in the relationship between normal stress and joint opening.

### 9.3.3 Smooth Ground Joint Permeability Test Results.

Figure 9-25 is a plot of the steady-state values of pressure gradient and apparent fluid velocity measured in the test series on a limestone specimen containing a smooth ground joint. The values of equivalent permeability,  $K_e$ , derived from the data in Figure 9-25 are summarized in Table 9-15. The equivalent permeability measurements on the smooth ground specimen from Table 9-15 are plotted against confining pressure in Figure 9-26. Also included in Figure 9-26 are the linearized permeability of intact limestone adjusted to the fully closed permeability of the jointed specimen and the difference between the two representing the flow in the joint. The derivation of these curves is discussed in more detail in Section 9.3.2. At the time the smooth ground joint test was performed it was believed that the joint was fully closed at a pressure within the test range. However, upon further analysis of the data, it appears that the slope of the curve for the jointed specimen in Figure 9-26 did not quite reach the intact slope, and hence the joint was probably not fully closed. To facilitate analysis of the data, a judgement was made as to where the two curves would come tangent to each other and the linearized intact rock permeability curve was adjusted to that point for further processing. The joint flow data in Figure 9-26 were converted to joint permeability,  $\kappa_j$ , using Equation 9.17, and the log of joint permeability is shown as a function of confining pressure in Figure 9-27. As in the case of the tensile fracture data, an expression was fit to only those data with permeabilities of at least 10

$\times 10^{-18} \text{ m}^3$ , where the flow through the joint is distinguishable from the flow through the intact rock. The flow data from the smooth ground joint test are well fit by the expression:

$$k_j = 557 e^{-0.38\sigma} \quad (9.20)$$

The fit to the tensile fracture joint data is also shown for comparison. There is significantly more flow through the smooth joint than through the fracture joint at the same normal stress level. Due to the very small joint normal deformations, usable aperture data were not obtained for the smooth ground joint test.

#### 9.3.4 Synthetic Joint Permeability Test Results.

One flow test series was performed on a specimen of Salem limestone containing a synthetic joint as described in Section 3.1.3. The steady state values of pressure gradient and apparent fluid velocity which were measured in that test are presented in Figure 9-28. Table 9-16 summarizes the permeabilities at each confining pressure which were computed with Equation 9.13. It is apparent from Figure 9-28 that there is significant nonlinearity in the flow test results, an indication that the pressure gradient has some dependence on the square of the apparent velocity. However, the equivalent permeabilities listed in Table 9-16 are based on simple linear fits. Figure 9-29 presents a plot of the equivalent permeability of the cylindrical specimen containing the synthetic joint as a function of confining pressure. Also shown in Figure 9-29 is the average permeability of an intact specimen. At 1 MPa confining pressure, the equivalent permeability of the jointed specimen is approximately two orders of magnitude greater than that of the intact specimens. The equivalent permeability of the specimen with the synthetic joint decreased significantly as the pressure was raised to 12 MPa, but was still about on order of magnitude greater than the equivalent intact specimen. Due to the relative magnitudes of flow through the intact rock and the joint, the precise choice of reference permeability to subtract from the total is does not significantly affect the result, and the average of the two curves in Figure 9-15 was used for that purpose. The resulting values of joint permeability are plotted against confining pressure in Figure 9-30. Also shown in Figure 9-30 are fits to the tensile fracture and smooth ground joint data.



It is clear from Figure 9-30 that there was significant fluid flow through the joint at the highest confining pressure tested. The irregular surfaces of the synthetic joint were machined to the specified shape with a numerically controlled milling machine. Due to the finite dimension of the smallest practical cutter, the fit between the two halves of the joint was imperfect, apparently to a much greater degree than a man-made fracture. A joint of this type could probably not be completely closed without significant crushing of the asperities. Hence, the methodology used to define the joint aperture for tensile fracture and smooth ground joints is not well defined for the synthetic joint, and no attempt was made to characterize the joint permeability in terms of joint aperture.

**Table 9-1. Summary of high-pressure permeability tests on intact Salem limestone under hydrostatic loading.**

Test Type	Confining Pressure (MPa)	Upstream Pore Pressure (MPa)	Pore Pressure Gradient (MPa/.n)	Absolute Permeability ( $10^{-15} \text{ m}^2$ )
Hydrostatic	10	2—8	24—92	6.11
Hydrostatic	15	2—14	23—150	5.69
Hydrostatic	20	2—18	22—200	5.20
Hydrostatic	25	2—23	23—250	4.84
Hydrostatic	30	2—28	22—310	4.40
Hydrostatic	40	2—37	24—410	3.69
Hydrostatic	50	2—47	22—520	3.05
Hydrostatic	70	2—66	23—740	2.02
Hydrostatic	90	2—87	25—970	1.22
Hydrostatic	110	2—106	26—1200	0.74
Hydrostatic	130	2—126	24—1400	0.40
Hydrostatic	150	2—135	28—1500	0.23

Test ID: S26A1  
Core: SL26-53

**Table 9-2. Summary of low-pressure permeability tests on intact Salem limestone under hydrostatic loadings.**

Test Type	Confining Pressure (MPa)	Upstream Pore Pressure (MPa)	Pore Pressure Gradient (MPa/m)	Absolute Permeability ( $10^{-15} \text{ m}^2$ )
Hydrostatic	1	0.06—0.83	0.66—8.6	9.62
Hydrostatic	2	0.14—1.8	1.4—19	9.11
Hydrostatic	3	0.23—2.7	2.4—28	8.68
Hydrostatic	4	0.29—3.6	3.0—37	8.76
Hydrostatic	6	0.39—5.4	4.0—56	8.28
Hydrostatic	8	0.53—7.7	5.5—80	8.18
Hydrostatic	10	0.71—9.7	7.4—100	7.87
Hydrostatic	12	0.840—11.366	8.71—117.88	7.95

Test ID: L2A2

Core: SL23-1TI

**Table 9-3. Summary of low-pressure permeability tests on intact Salem limestone under hydrostatic loading (second specimen).**

Test Type	Confining Pressure (MPa)	Upstream Pore Pressure (MPa)	Pore Pressure Gradient (MPa/in)	Absolute Permeability ( $10^{-15} \text{ m}^2$ )	Volume Strain
Hydrostatic	2	0.276-0.999	3.1-11	6.15	0.000225
Hydrostatic	4	0.413-2.05	4.7-23	6.27	0.0004
Hydrostatic	6	0.622-3.08	7.1-35	6.04	0.00059
Hydrostatic	8	0.668-4.12	7.6-47	5.87	0.00078
Hydrostatic	10	1.03-5.19	12.0-59	5.73	0.00092

Test ID: AAA162

Core: SL26-55

**Table 9-4. Summary of permeability tests on intact Salem limestone loaded in triaxial compression at 5 MPa confining pressure.**

Test Type	Confining Pressure (MPa)	Axial Stress (MPa)	Axial Deformation (%)	Upstream Pore Pressure (MPa)	Pore Pressure Gradient	Absolute Permeability ( $10^{-15} \text{ m}^2$ )
Hydrostatic	5	0	0.140	0.26–2.5	2.7–26	7.15
Triaxial	5	25	0.163	0.27–2.5	2.8–26	6.14
Triaxial	5	50	0.196	0.275–2.5	2.85–26	5.12
Triaxial	5	31.02	1	0.258–2.5	2.67–26	4.43
Triaxial	5	20.16	2.42	0.256–2.5	2.65–26	3.64
Triaxial	5	22.79	4	0.278–2.5	2.89–26	3.76
Triaxial	5	19.71	6	0.269–2.5	2.78–26	4.09
Triaxial	5	22.00	8	0.279–2.5	2.89–26	3.81
Triaxial	5	20.35	10	0.261–2.5	2.70–26	3.47
Hydrostatic after unloading	5	0		0.233–2.5	2.41–26	4.15

Test ID: G6A2  
Core: SL23-2BI

Table 9-5. Summary of permeability tests on intact Salem limestone loaded in triaxial compression at 10 MPa confining pressure.

Test Type	Confining Pressure (MPa)	Axial Stress (MPa)	Axial Deformation (%)	Upstream Pore Pressure (MPa)	Pore Pressure Gradient	Absolute Permeability ( $10^{-15} \text{ m}^2$ )
Hydrostatic	10	0	0.00102	1.9—9.5	14—99	6.36
Triaxial	10	20	0.0860	0.7—9.6	7—100	5.38
Triaxial	10	40	0.196	0.7—9.5	7—98	5.04
Triaxial	10	60	0.397	0.7—8.8	8-85	3.73
Triaxial	10	26	1.2	0.8—9.7	7.8—100	3.34
Triaxial	10	33	3	0.5—9.8	5—100	2.28

Test ID: L7B2

Core: SL23-1B1

Table 9-6. Summary of permeability tests on intact Salem limestone loaded in triaxial compression at 10 MPa confining pressure (repeat test).

Test Type	Confining Pressure (MPa)	Axial Stress (MPa)	Axial Deformation (%)	Upstream Pore Pressure (MPa)	Pore Pressure Gradient	Absolute Permeability ( $10^{-15} \text{m}^2$ )
Hydrostatic	10	0	0.042	0.7–7.0	7.5–72	7.42
Triaxial	10	25	0.162	0.7–6.7	7.4–70	6.65
Triaxial	10	50	0.311	0.7–7.0	7.7–73	5.70
Triaxial	10	43	1	0.8–6.3	8.0–65	4.06
Triaxial	10	37	2	0.6–6.7	6.9–70	3.64
Triaxial	10	33	4	0.8–6.9	7.8–71	3.45
Triaxial	10	33	6	0.7–7.0	7.7–73	3.12
Triaxial	10	33	8	0.8–6.8	8.2–70	3.01
Triaxial	10	33	10	0.7–6.8	7.0–71	2.90
Hydrostatic after unloading	10	0	9.6	0.6–6.8	6.5–71	2.63

Test ID: JAA43

Core: SL23-7B

**Table 9-7. Summary of permeability tests on intact Salem limestone loaded in triaxial compression at 20 MPa confining pressure.**

Test Type	Confining Pressure (MPa)	Axial Stress (MPa)	Axial Deformation (%)	Upstream Pore Pressure (MPa)	Pore Pressure Gradient (MPa/m)	Absolute Permeability ( $10^{-15} \text{ m}^2$ )
Hydrostatic	20	0	0.051	1.4—14	15—140	6.49
Triaxial	20	25	0.158	1.5—14	15—140	6.20
Triaxial	20	50	0.30	1.4—14	15—140	5.34
Triaxial	20	56	1	1.5—14	15—140	2.86
Triaxial	20	51	2	1.5—14	15—140	2.41
Triaxial	20	48	4	1.3—14	14—140	2.02
Triaxial	20	45	6	1.5—14	15—140	1.77
Triaxial	20	40	8	1.3—14	13—140	1.62
Triaxial	20	48	10	1.5—14	15—150	1.52
Hydrostatic after unloading	20	0	9.5	1.3—14	13—140	1.18

Test ID: J-53  
Core: SL23-8T



**Table 9-8. Summary of permeability tests on intact Salem limestone loaded in triaxial compression at 50 MPa confining pressure.**

Test Type	Confining Pressure (MPa)	Axial Stress (MPa)	Axial Deformation (%)	Upstream Pore Pressure (MPa)	Pore Pressure Gradient (MPa/m)	Absolute Permeability ( $10^{-15} \text{ m}^2$ )
Hydrostatic	50	0	0.244	2.7-26	28-260	4.09
Triaxial	50	25	0.287	2.5-25	26-260	3.48
Triaxial	50	50	0.396	2.6-25	27-260	2.52
Triaxial	50	70	1	2.6-25	27-260	1.38
Triaxial	50	74	2	2.6-25	27-260	0.89
Triaxial	50	76	4	2.8-25	29-260	0.58
Triaxial	50	89	6	2.4-25	25-260	0.41
Triaxial	50	97	8	2.5-25	26-260	0.30
Triaxial	50	108	10	2.8-25	29-260	0.25
Hydrostatic after unloading	50	0	4.53	2.5-25	26-260	0.22

Test ID: L22A2  
Core: SL23-2TI

Table 9-9. Summary of permeability tests on intact Salem limestone loaded in triaxial compression at 90 MPa confining pressure.

Test Type	Confining Pressure (MPa)	Axial Stress (MPa)	Axial Deformation (%)	Upstream Pore Pressure (MPa)	Pore Pressure Gradient	Absolute Permeability ( $10^{-15} \text{ m}^2$ )
Hydrostatic	90	0	0.026	3.6—34	30—360	1.96
Triaxial	90	25	0.044	3.6—35	37—360	1.81
Triaxial	90	50	0.9	3.6—34	37—360	1.24
Triaxial	90	56	2	3.4—34	35.5—360	0.64
Triaxial	90	75	4	3.4—34	35.1—360	0.30
Triaxial	90	91	6	3.5—35	35.8—360	0.17
Triaxial	90	115	8	3.5—34	35.9—360	0.11
Triaxial	90	130	10	3.6—34	36.9—360	0.088
Triaxial	90	0	9.3	3.7—35	38.2—360	0.079

Test ID: JA263  
Core: 23-8B

**Table 9-10. Summary of permeability tests on tensile fracture jointed Salem limestone specimen (A15A2).**

Test Type	Confining Pressure (MPa)	Upstream Pore Pressure (MPa)	Pore Pressure Gradient (MPa/m)	K <sub>i</sub>
Hydrostatic	1	0.04 ~ 0.7	0.5 ~ 8	15.16
Hydrostatic	2	0.144 ~ 1.835	1.6 ~ 21	9.85
Hydrostatic	3	0.282 ~ 2.783	3.2 ~ 32	8.31
Hydrostatic	4	0.344 ~ 3.811	3.9 ~ 43	7.54
Hydrostatic	6	0.572 ~ 2.774	6.5 ~ 32	6.40
Hydrostatic	8	0.687 ~ 4.110	7.8 ~ 47	6.24
Hydrostatic	10	1.019 ~ 5.144	12 ~ 58	5.84

Test ID: A15A2  
Core: SL26-51

Table 9-11. Summary of permeability tests on tensile fracture jointed Salem limestone specimen (U30A2).

Test Type	Confining Pressure (MPa)	Upstream Pore Pressure (MPa)	Pore Pressure Gradient (MPa/m)	K <sub>y</sub>
Hydrostatic	1	0.06 ~ 0.8	0.6 ~ 9	12.0
Hydrostatic	2	0.12 ~ 1.8	1.3 ~ 19	9.88
Hydrostatic	3	0.23 ~ 2.7	2.3 ~ 28	8.85
Hydrostatic	4	0.23 ~ 3.6	2.3 ~ 37	8.50
Hydrostatic	6	0.37 ~ 5.0	3.9 ~ 51	8.09
Hydrostatic	8	0.57 ~ 7.6	5.9 ~ 79	7.97
Hydrostatic	10	0.71 ~ 9.7	7.4 ~ 100	8.01
Hydrostatic	12	0.78 ~ 11.6	8.1 ~ 120	8.00

Test ID: U30A2  
Core: SL23-1T

**Table 9-12. Summary of permeability tests on tensile fracture jointed Salem limestone specimen (G5A2).**

Test Type	Confining Pressure (MPa)	Upstream Pore Pressure (MPa)	Pore Pressure Gradient (MPa/m)	K <sub>v</sub>
Hydrostatic	1	0.07 ~ 0.84	0.7 ~ 9	13.08
Hydrostatic	2	0.15 ~ 1.8	1.5 ~ 18	9.06
Hydrostatic	3	0.23 ~ 2.7	2.3 ~ 28	7.65
Hydrostatic	4	0.32 ~ 3.6	3.4 ~ 37	7.16
Hydrostatic	6	0.47 ~ 5.4	4.9 ~ 56	6.90
Hydrostatic	8	0.61 ~ 7.7	6.4 ~ 80	6.63
Hydrostatic	10	0.67 ~ 9.6	7.0-100	6.13
Hydrostatic	12	0.89 ~ 11.5	9.2-119	5.80

Note: This specimen was tested first in the intact condition in Test L2A2 (Table 9-2).

Test ID: G5A2

Core: SL23-1TI

**Table 9-13. Summary of permeability tests on tensile fracture jointed Salem limestone specimen (OAA282).**

Test Type	Confining Pressure (MPa)	Upstream Pore Pressure (MPa)	Pore Pressure Gradient (MPa/m)	K <sub>v</sub>
Hydrostatic	1	0.07 ~ 0.8	0.8 ~ 8	15.43
Hydrostatic	2	0.15 ~ 1.8	1.5 ~ 17	8.62
Hydrostatic	3	0.21 ~ 2.7	2.1 ~ 28	6.32
Hydrostatic	4	0.29 ~ 3.6	3.0 ~ 37	5.44
Hydrostatic	6	0.44 ~ 5.4	4.6 ~ 56	5.03
Hydrostatic	8	0.60 ~ 7.2	6.2 ~ 74	4.82
Hydrostatic	10	0.73 ~ 9.6	7.6 ~ 100	4.46
Hydrostatic	12	0.88 ~ 11.5	9.2 ~ 120	4.66

Note: This is a repeat of Test G5A2 (Table 9.12).

Test ID: OAA282

Core: SL23-1TI

**Table 9-14. Summary of permeability tests on tensile fracture jointed Salem limestone specimen (OAA302).**

Test Type	Confining Pressure (MPa)	Upstream Pore Pressure (MPa)	Pore Pressure Gradient (MPa/m)	K <sub>v</sub>
Hydrostatic	1	0.14 ~ 0.8	1.4 ~ 9	15.18
Hydrostatic	2	0.28 ~ 1.6	2.9 ~ 17	10.54
Hydrostatic	3	0.45 ~ 2.5	4.7 ~ 26	8.06
Hydrostatic	4	0.55 ~ 3.3	5.7 ~ 35	7.11
Hydrostatic	6	0.82 ~ 5.0	8.5 ~ 51	6.39
Hydrostatic	8	1.11 ~ 7.7	11.5 ~ 80	6.15
Hydrostatic	10	1.41 ~ 9.6	14.6 ~ 100	5.85
Hydrostatic	12	1.68 ~ 11.6	17.4 ~ 120	5.84

Note: This is a repeat of Test OAA282 after grinding approximately 2.5 mm off the upstream end of the specimen.

Test ID: OAA302  
Core: SL23-1TI

**Table 9-15. Summary of permeability tests on a smooth ground jointed Salem limestone specimen.**

Test Type	Confining Pressure (MPa)	Upstream Pore Pressure (MPa)	Pore Pressure Gradient (MPa/m)	K <sub>v</sub>
Hydrostatic	1	0.07 ~ 0.8	0.7 ~ 9	19.85
Hydrostatic	2	0.14 ~ 1.8	1.5 ~ 19	15.18
Hydrostatic	3	0.19 ~ 2.7	2.0 ~ 28	12.37
Hydrostatic	4	0.30 ~ 3.6	3.1 ~ 37	10.47
Hydrostatic	6	0.41 ~ 5.4	4.3 ~ 56	9.18
Hydrostatic	8	0.58 ~ 7.6	6.0 ~ 79	8.18
Hydrostatic	10	0.69 ~ 9.7	7.2 ~ 101	7.38

Test ID: L15A2  
Core: SL22-9



**Table 9-16. Summary of permeability tests on a synthetic jointed Salem limestone specimen with synthetic fracture.**

Test Type	Confining Pressure (MPa)	Upstream Pore Pressure (MPa)	Pore Pressure Gradient (MPa/m)	K <sub>v</sub>
Hydrostatic	1	0.07-0.7	0.7 ~ 7	883
Hydrostatic	2	0.15 ~ 1.1	1.6 ~ 12	546
Hydrostatic	3	0.21 ~ 1.5	2.2 ~ 16	427
Hydrostatic	4	0.29 ~ 1.8	3.0 ~ 19	343
Hydrostatic	6	0.35 ~ 2.6	3.6 ~ 27	228
Hydrostatic	8	0.35 ~ 3.6	3.6-37	179
Hydrostatic	10	0.34 ~ 4.5	3.5-46	140
Hydrostatic	12	0.41 ~ 5.2	4.3 ~ 54	112

Test ID: L20A2  
Core: SL22-7

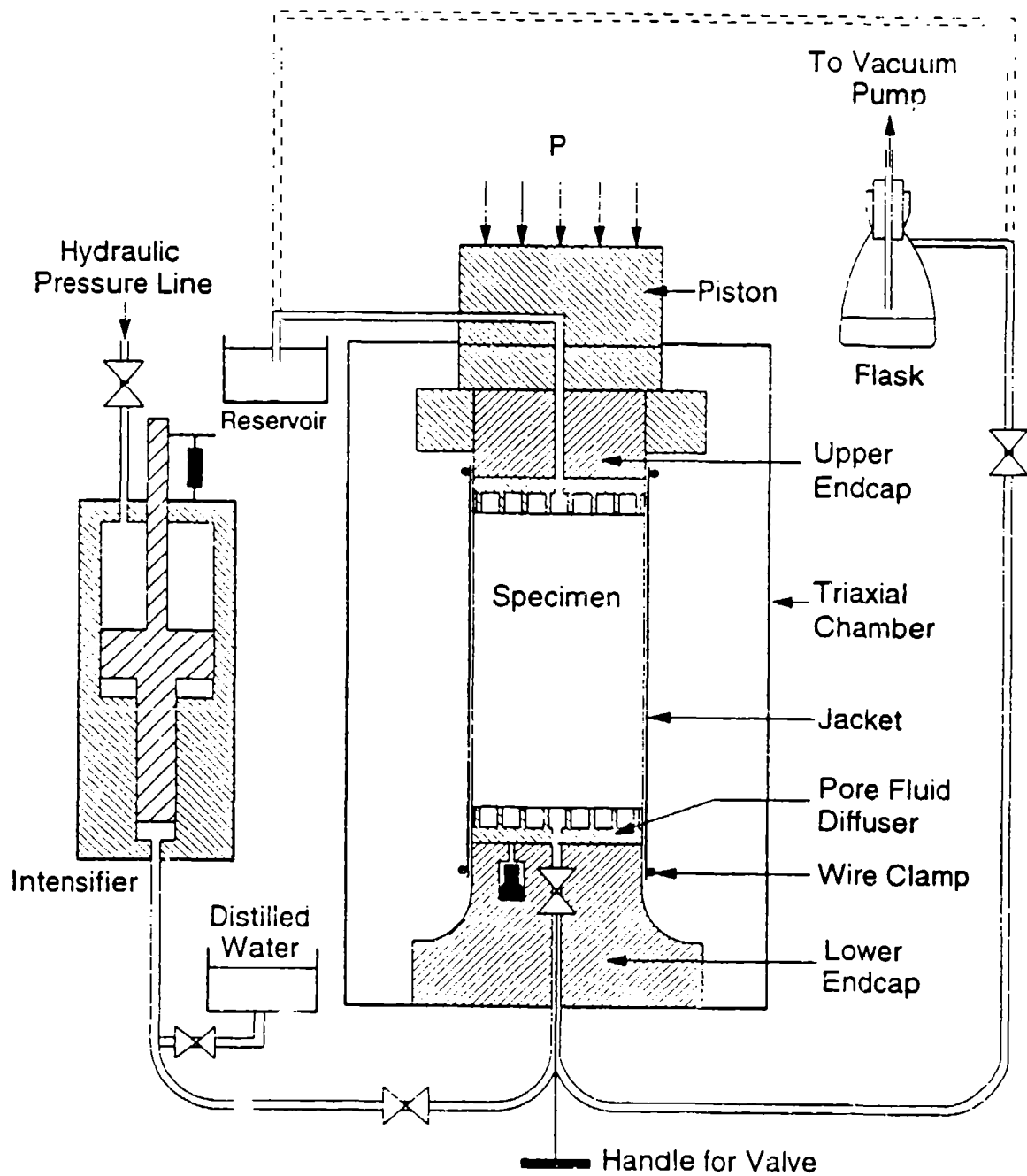


Figure 9-1. Schematic section of permeability test apparatus.

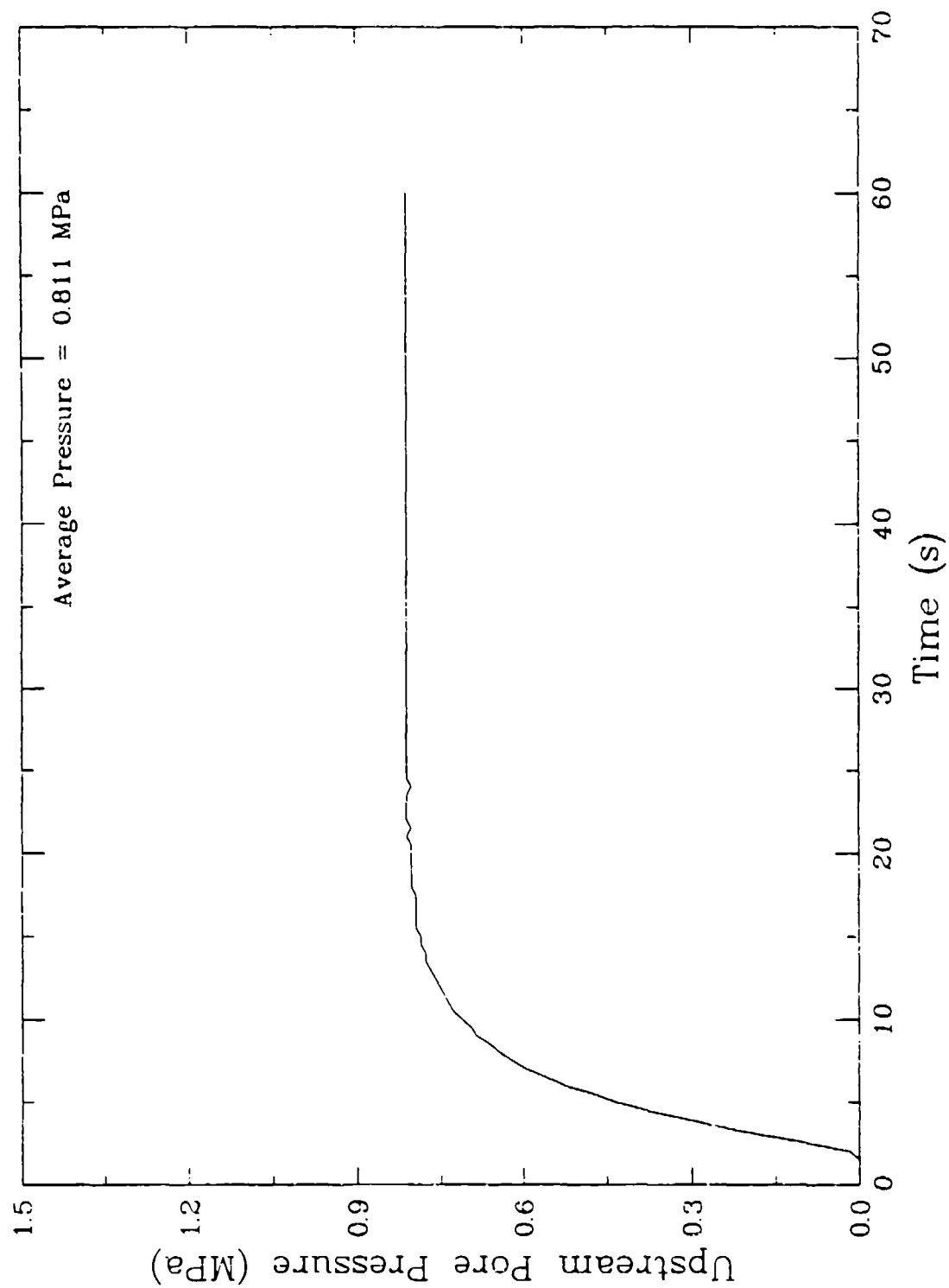


Figure 9-2. Typical upstream pore pressure time history.

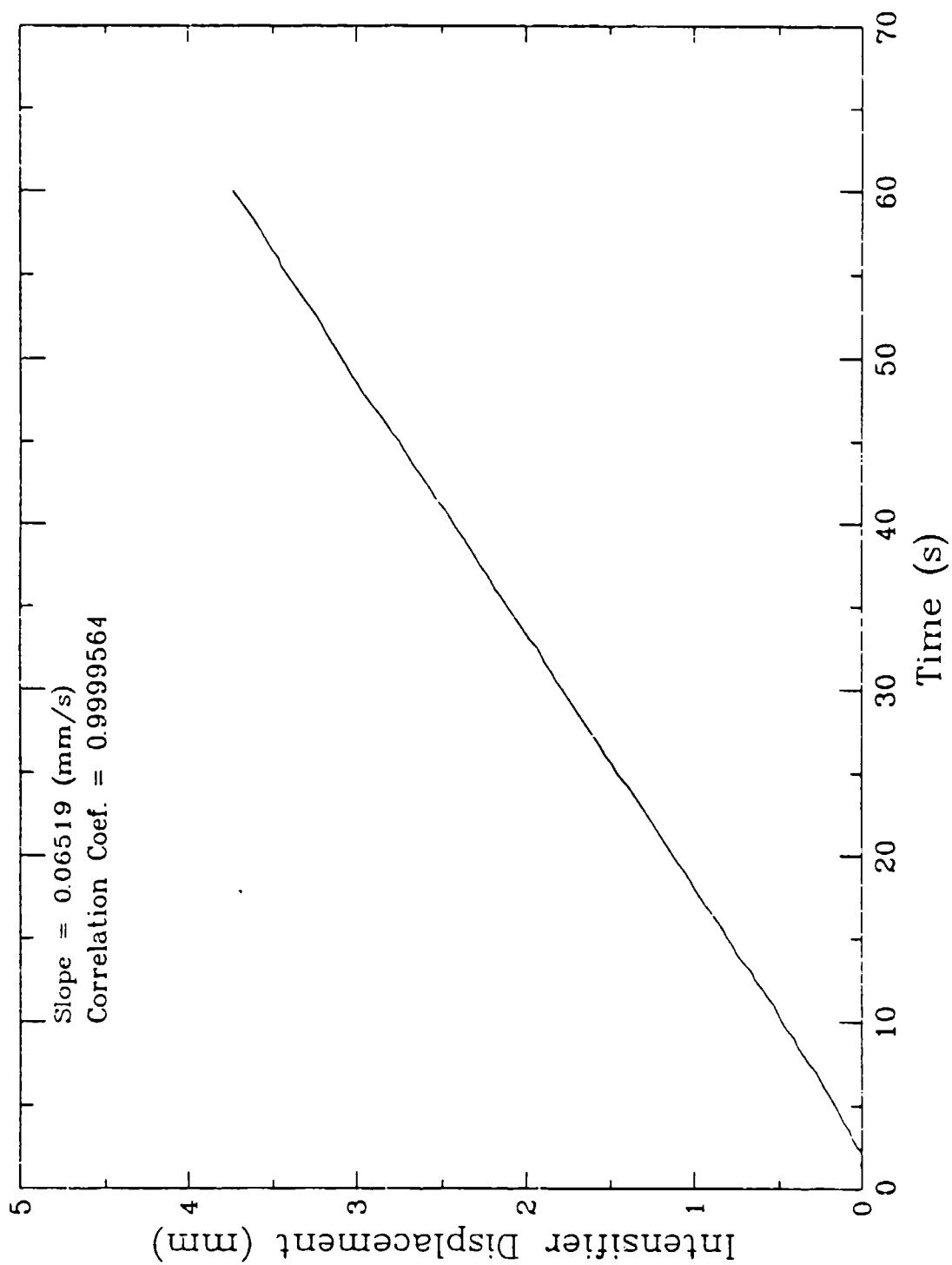


Figure 9-3. Typical intensifier displacement time history, which is proportional to pore fluid displacement.

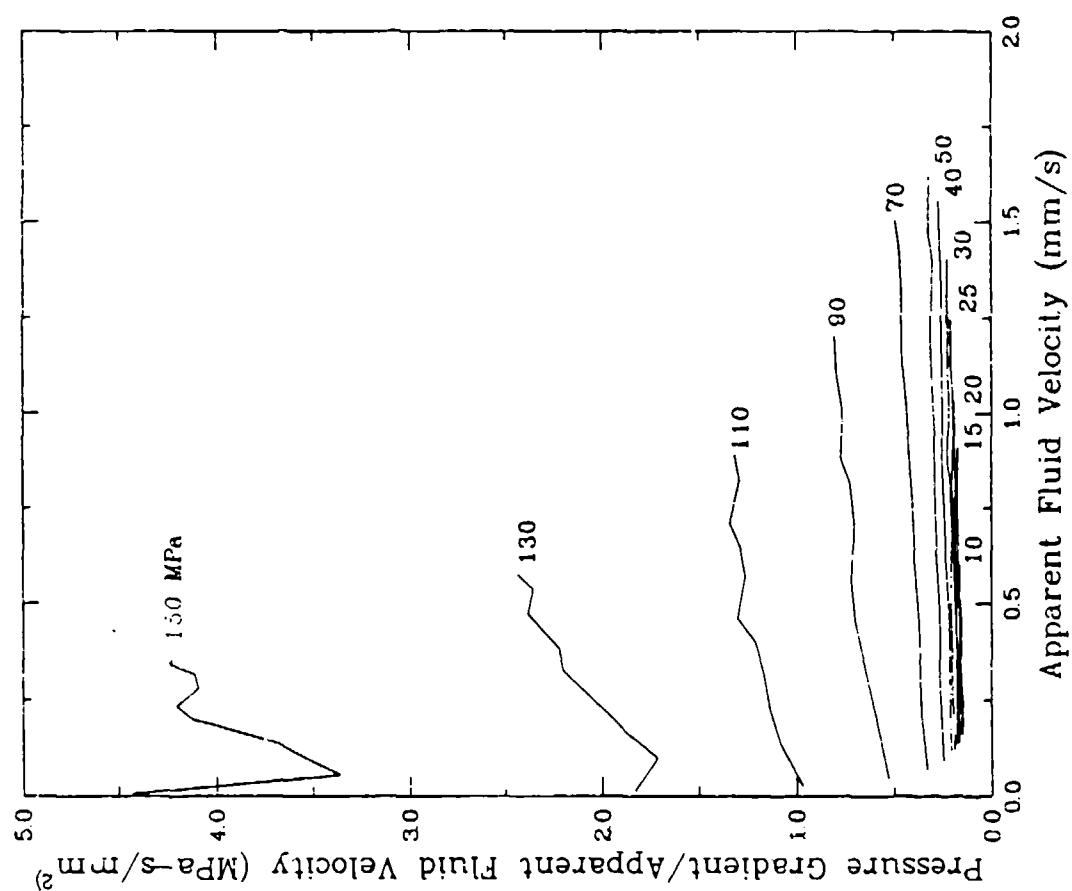


Figure 9-4. High-pressure permeability measurements on intact limestone under hydrostatic loading illustrating the linear and quadratic dependence of pressure gradient on apparent fluid velocity.

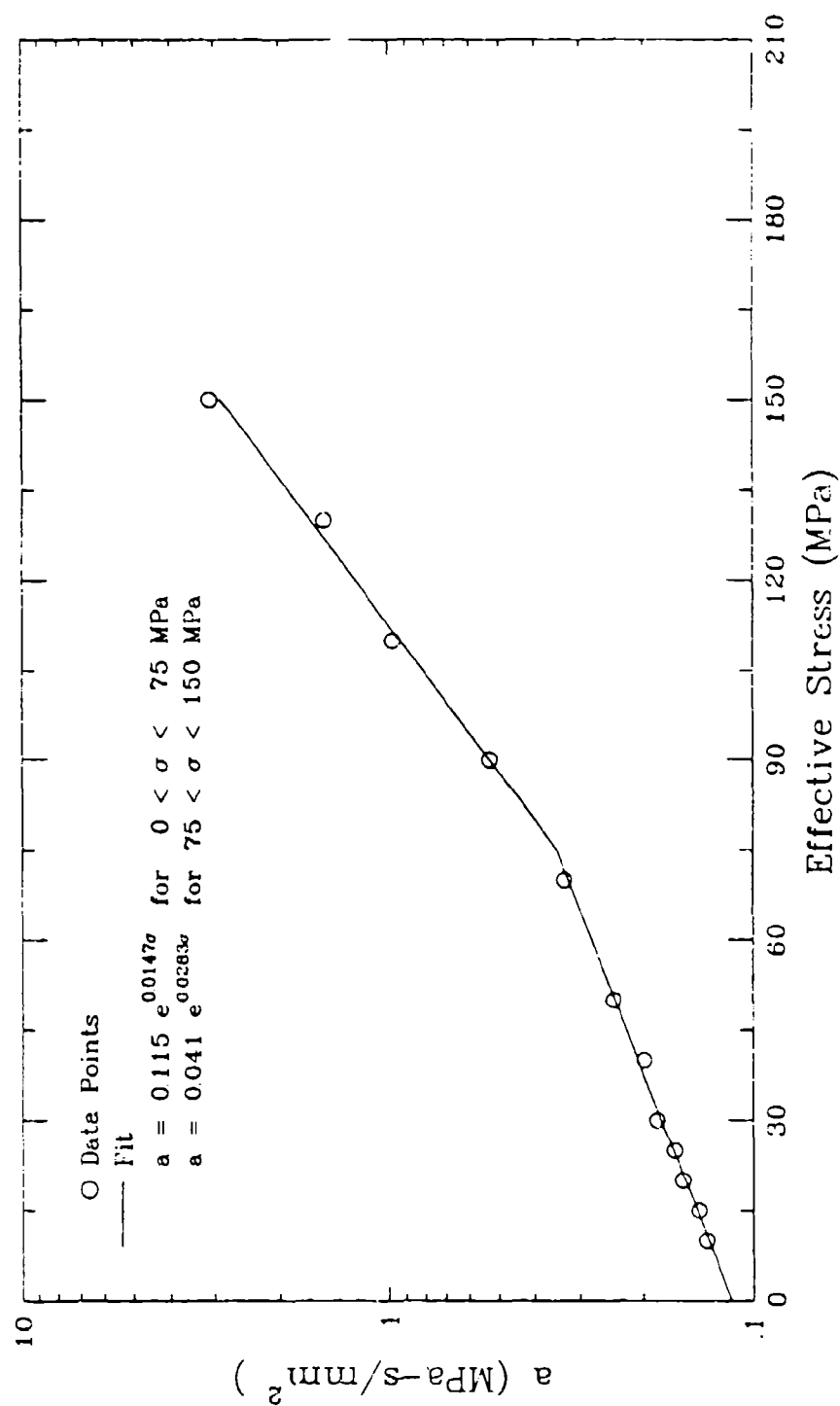


Figure 9-5. The linear flow coefficient,  $a$ , for Forchheimer's equation as function of effective stress in the rock skeleton

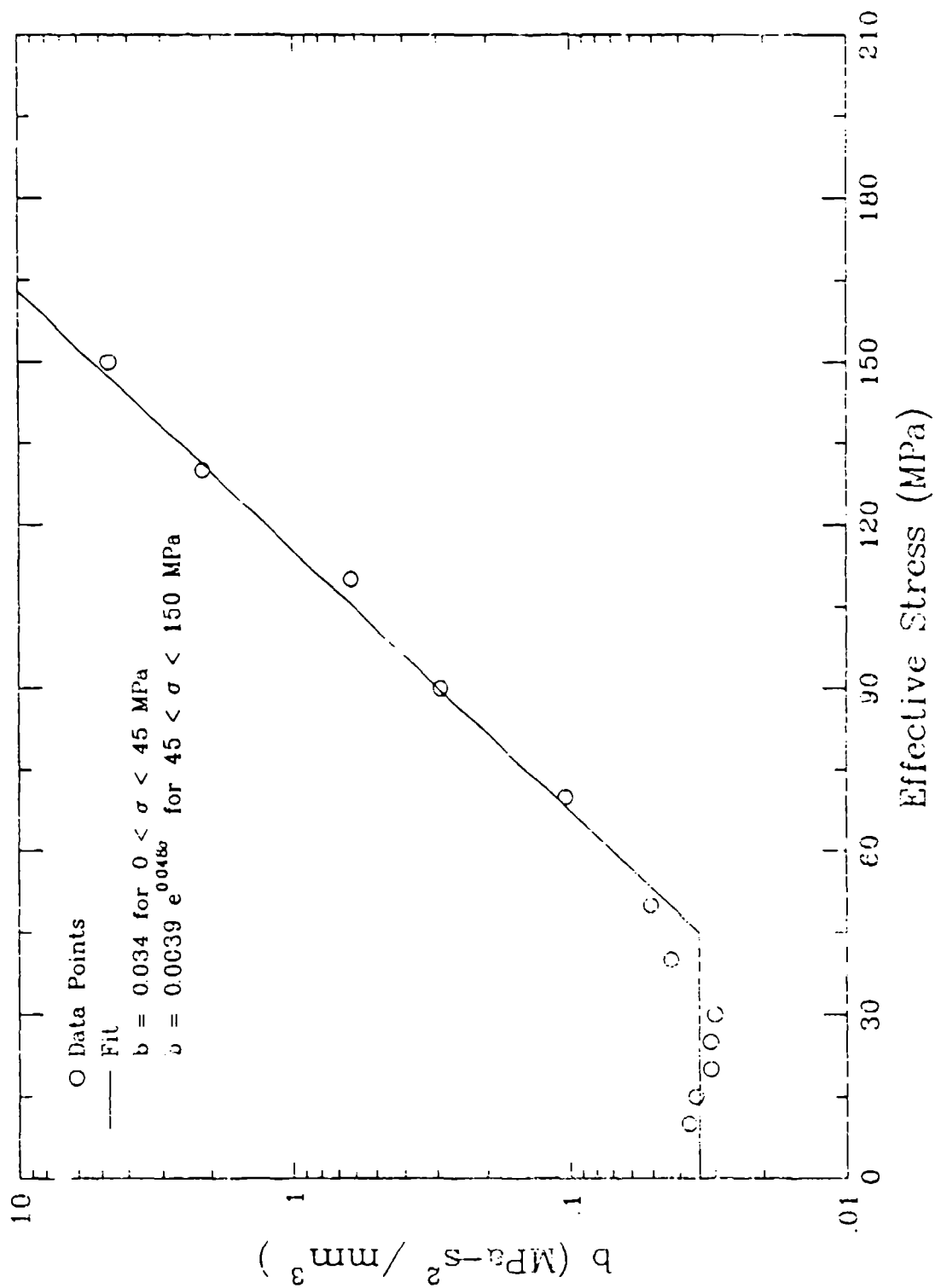


Figure 9-6. The quadratic flow coefficient,  $b$ , for Forchheimer's equation as function of effective stress in the rock skeleton.

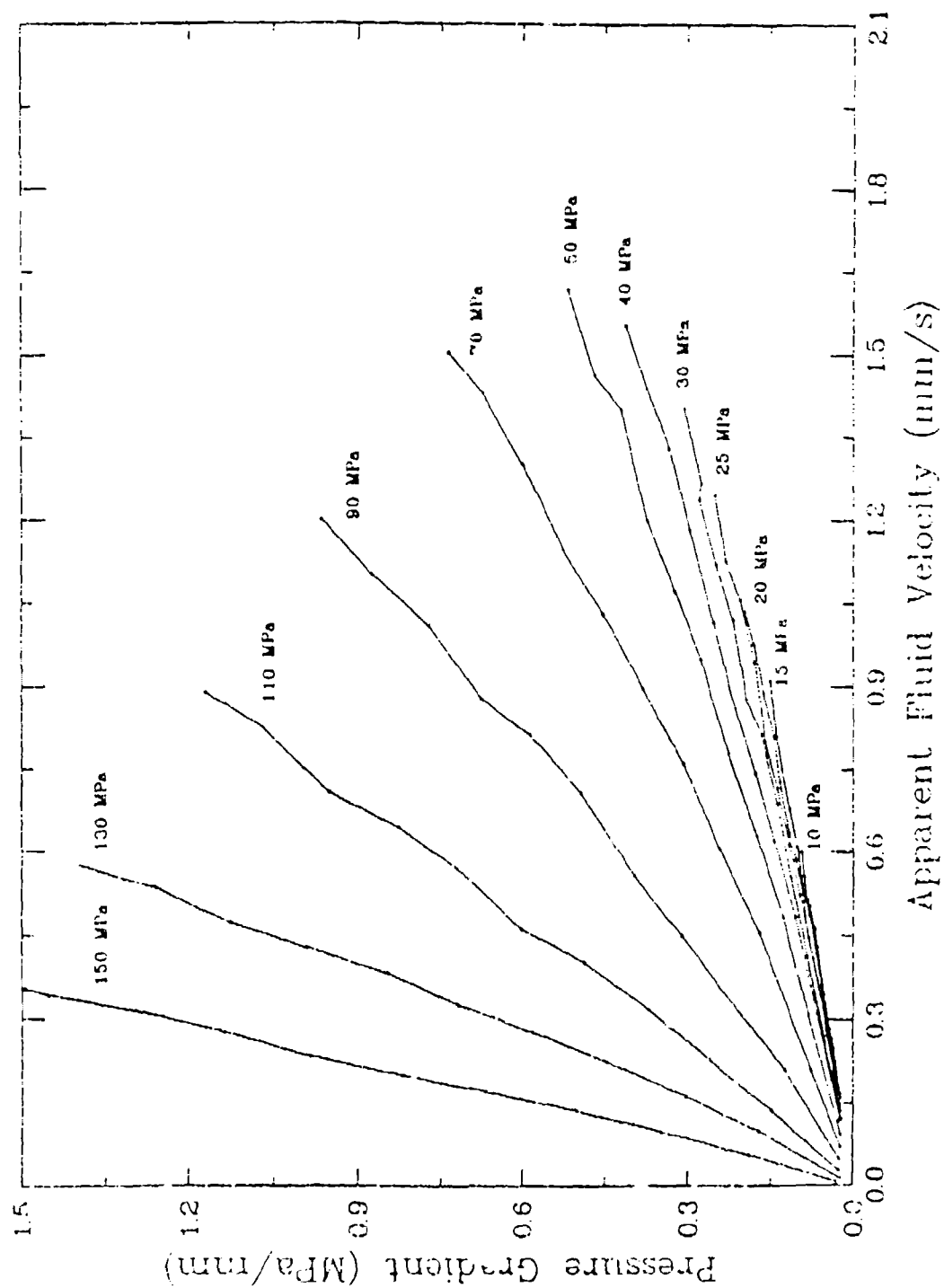


Figure 9-7. High-pressure permeability measurements on intact limestone under hydrostatic loading illustrating the linear approximation of the dependence of pressure gradient on apparent fluid velocity.



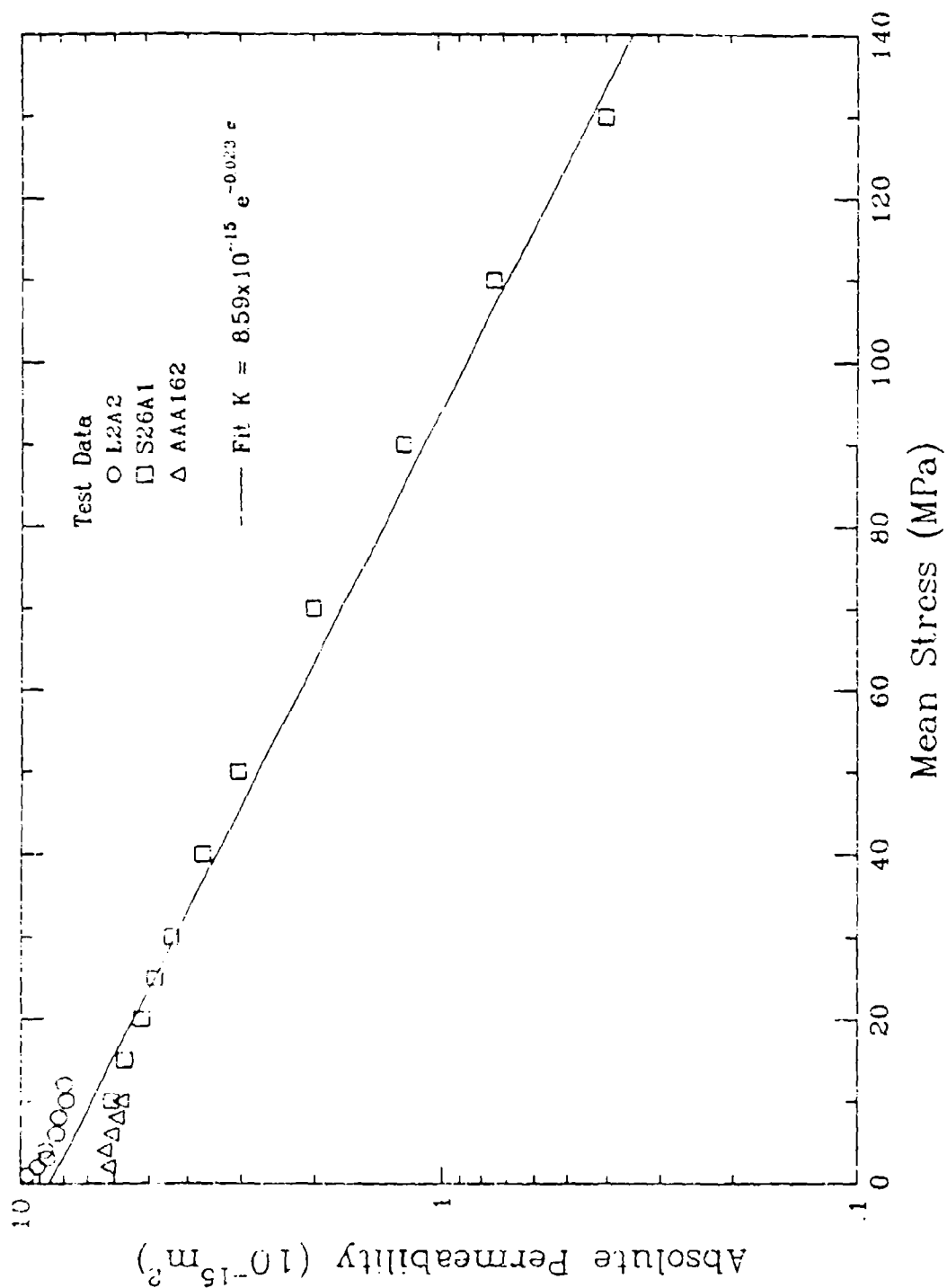


Figure 9-8. Absolute permeability of intact limestone under hydrostatic loading as a function of effective stress in the rock skeleton.

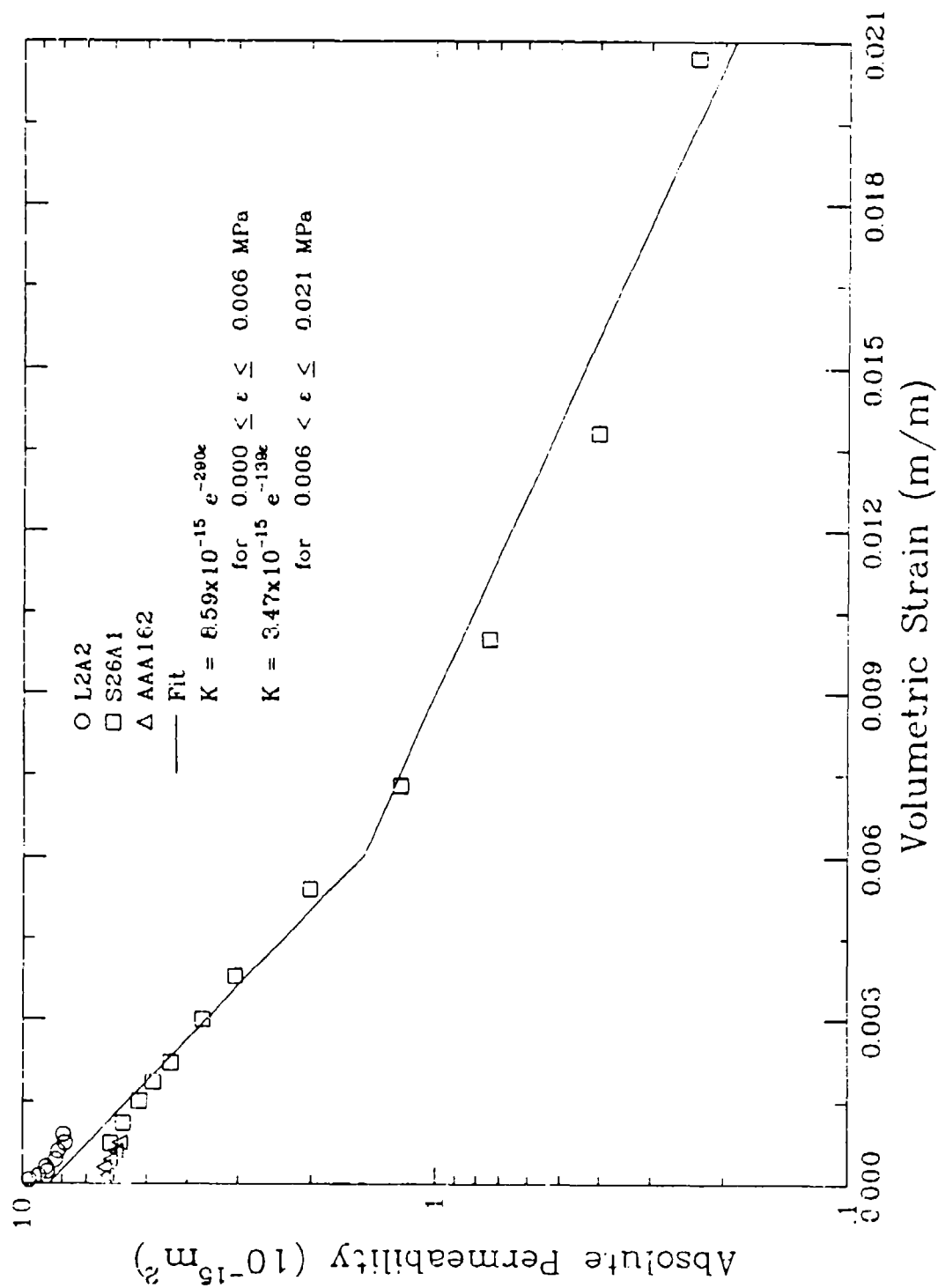


Figure 9-9. 2 Absolute permeability of intact limestone under hydrostatic loading as a function of volumetric strain in the rock skeleton.

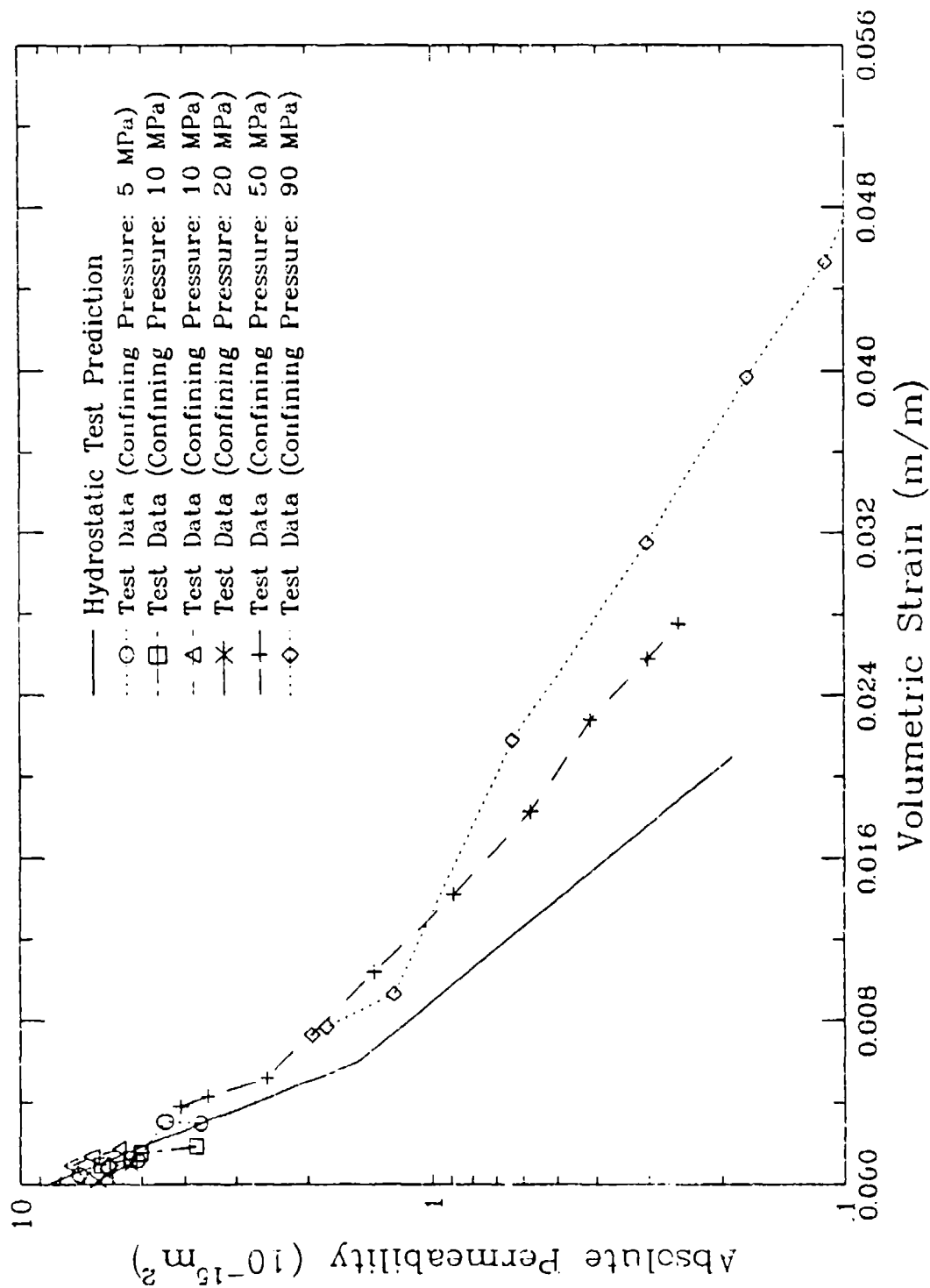


Figure 9-10. Absolute permeability of intact limestone under triaxial compression loading as a function of volumetric strain in the rock skeleton.

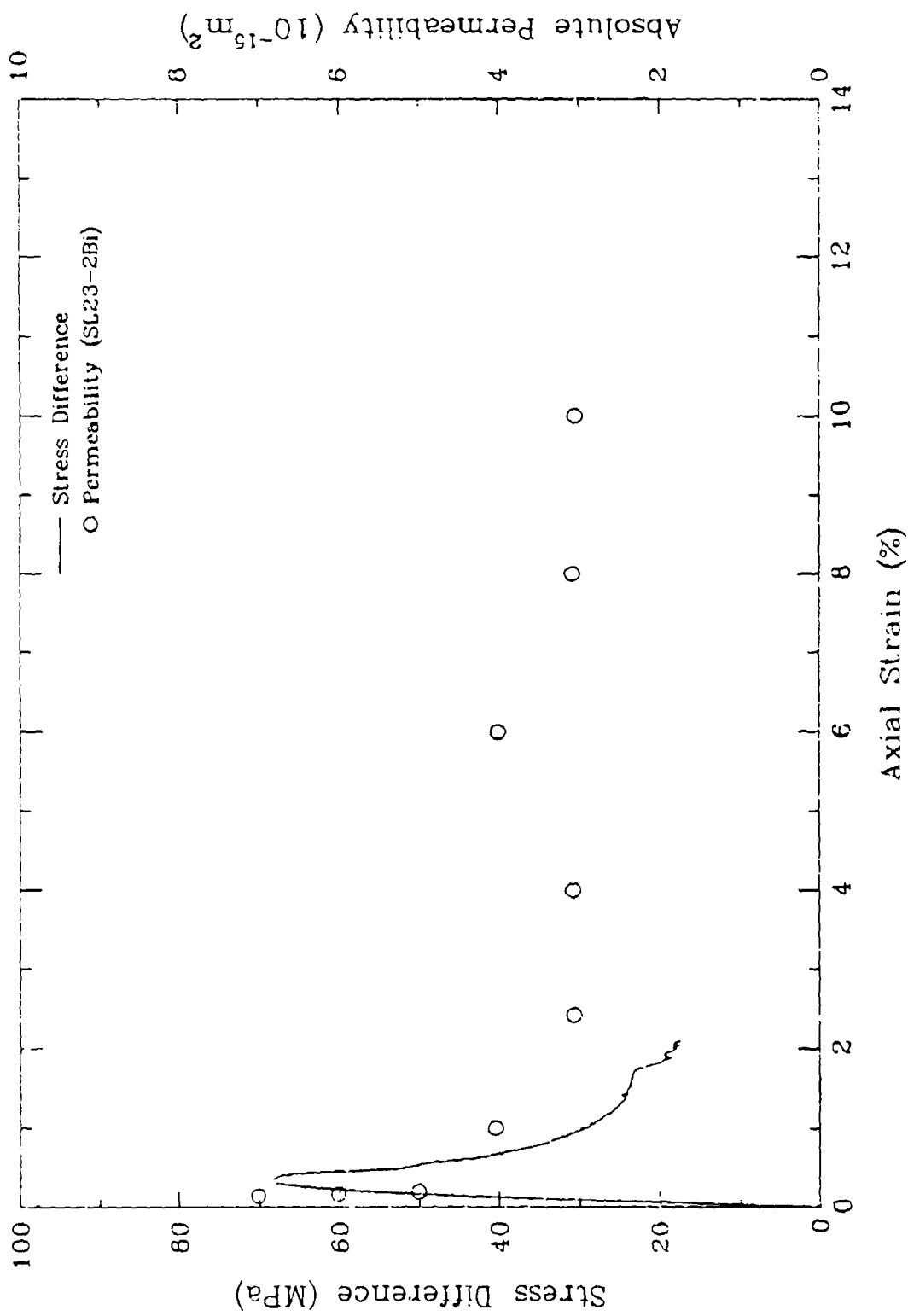


Figure 9-11. Illustration of the relationship between the mechanical response and permeability of limestone subjected to triaxial compression at 5 MPa.

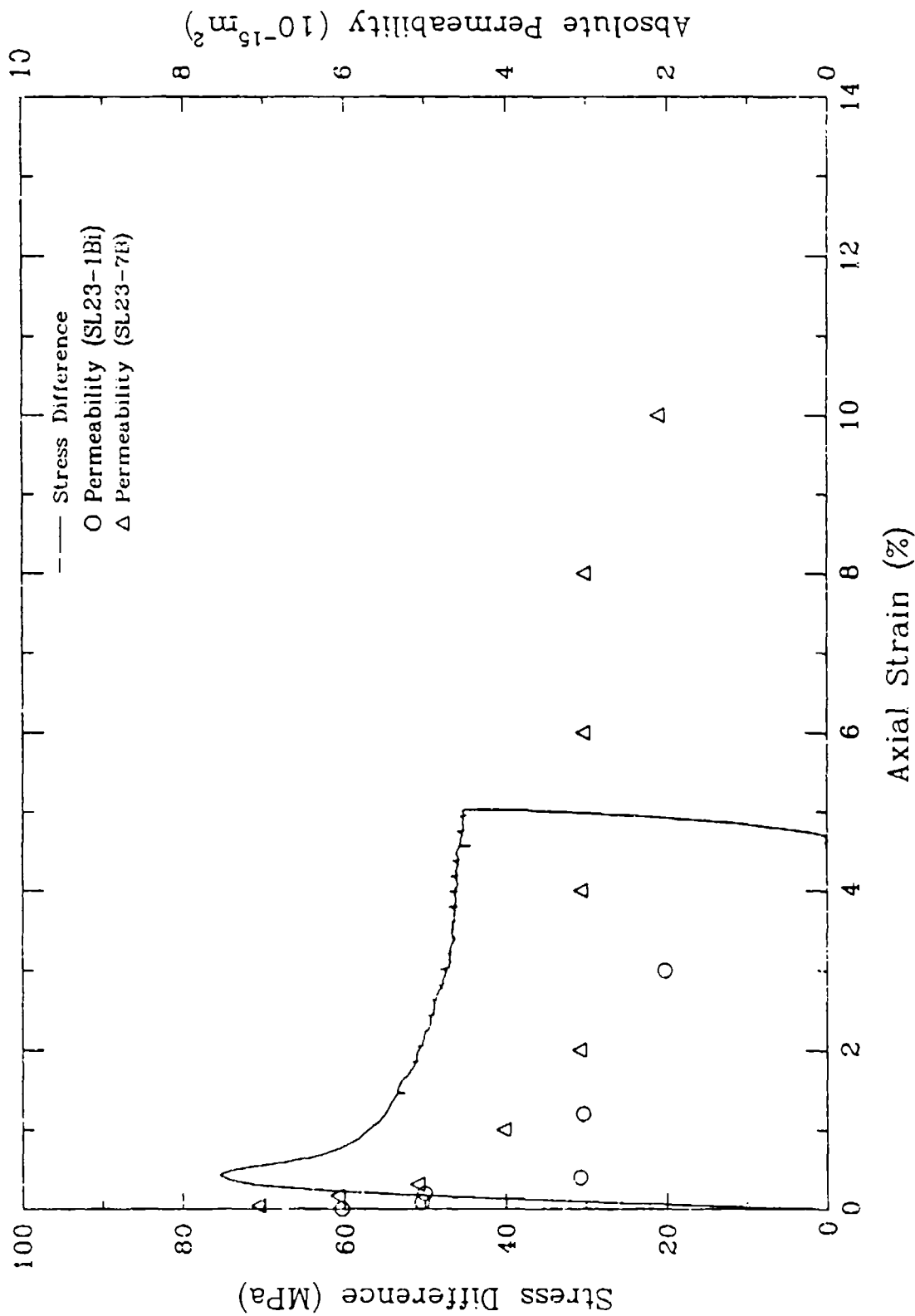


Figure 9-12. Illustration of the relationship between the mechanical response and permeability of limestone subjected to triaxial compression at 10 MPa.

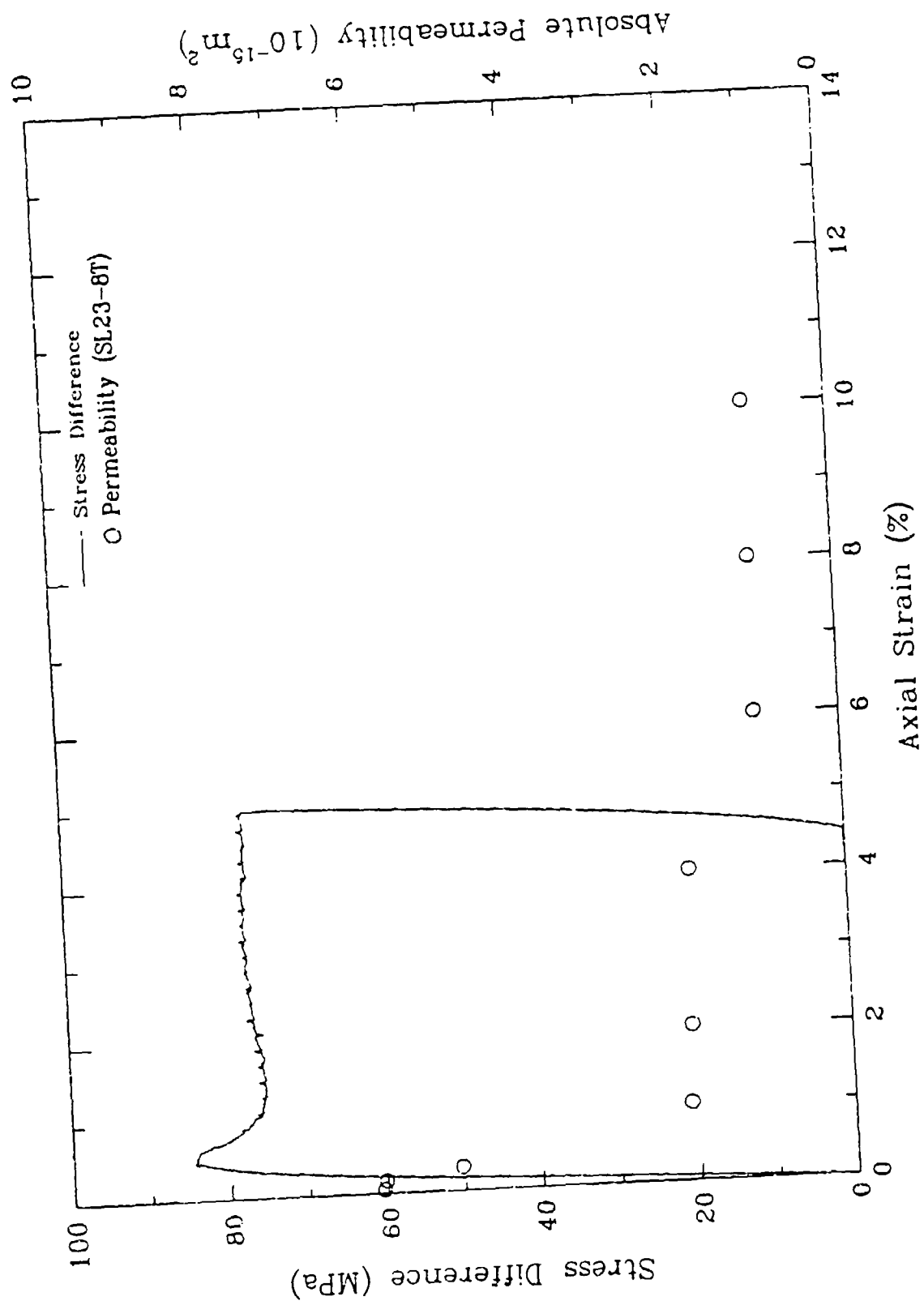


Figure 9-13. Illustration of the relationship between the mechanical response and permeability of limestone subjected to triaxial compression at 20 MPa.

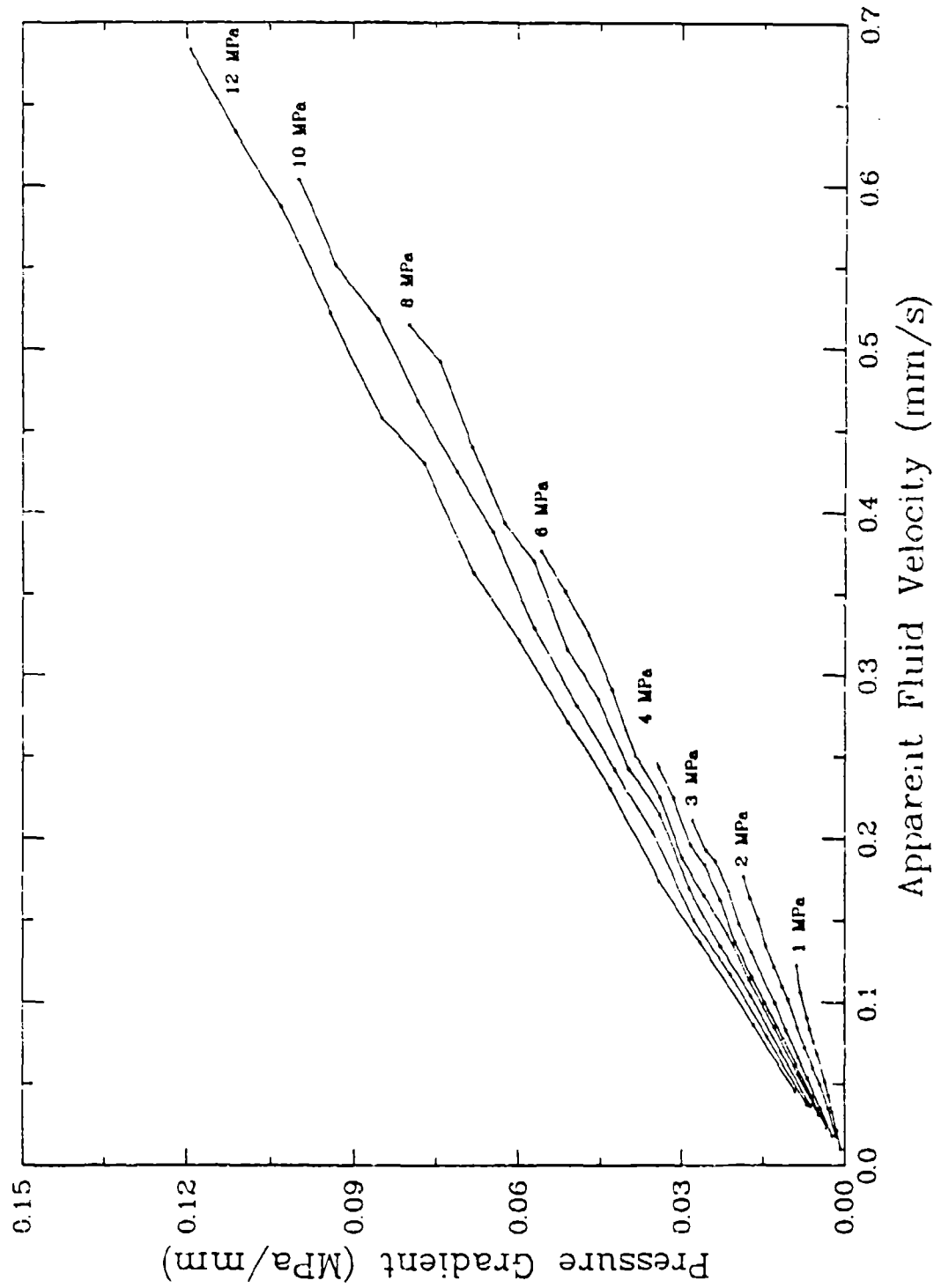


Figure 9-14. Typical set of permeability measurements on a limestone specimen with a tensile fracture joint under hydrostatic loading illustrating the linear approximation of the dependence of pressure gradient on apparent fluid velocity.

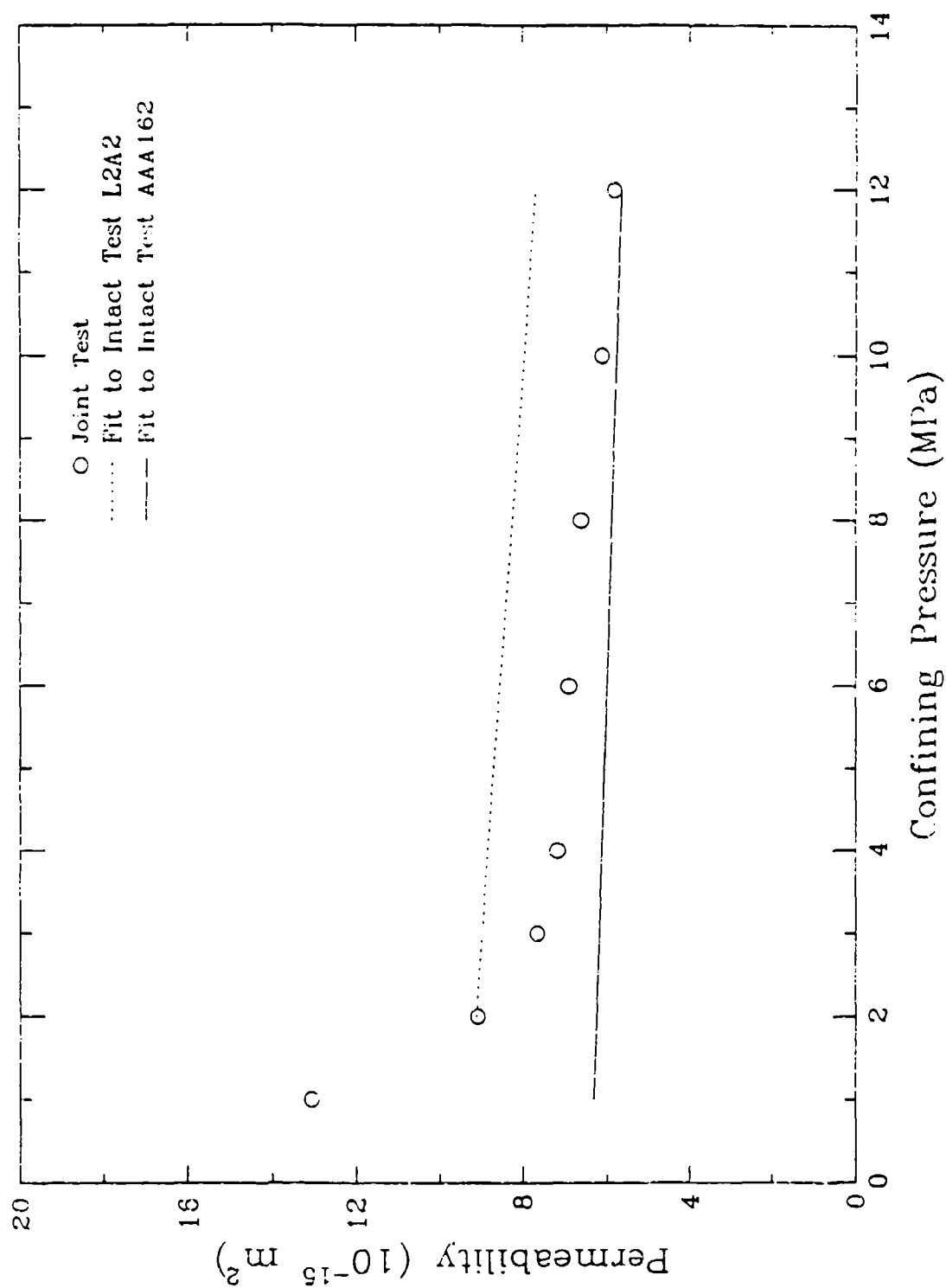


Figure 9-15. Measured variation in permeability with confining pressure for two different intact limestone specimens showing fits each test and the average of the two fits.



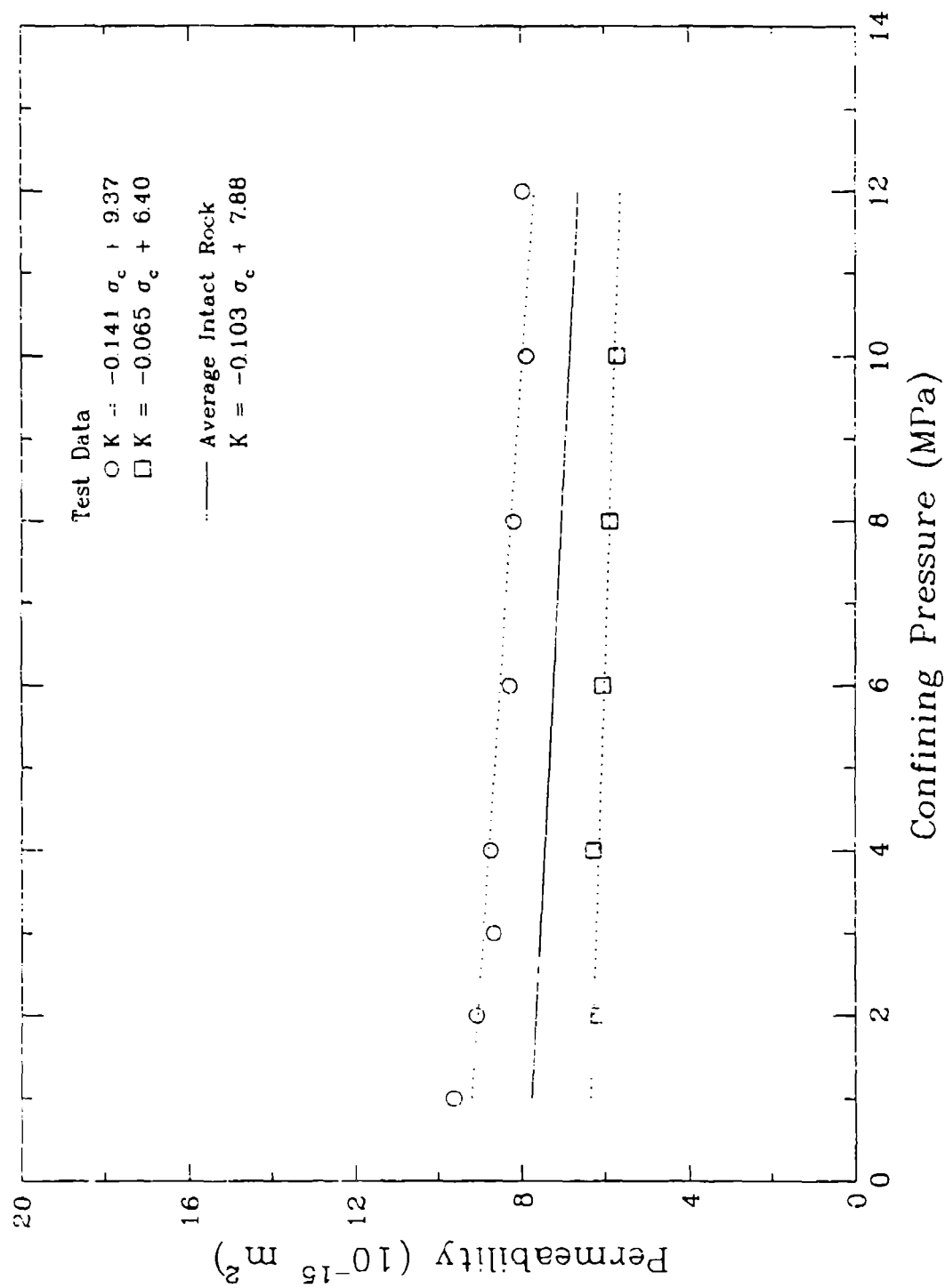


Figure 9-16. Equivalent permeability measurements from a limestone specimen with a tensile fracture joint (G5A2) compared with the fits to the two intact permeability tests shown in Figure 9-15.

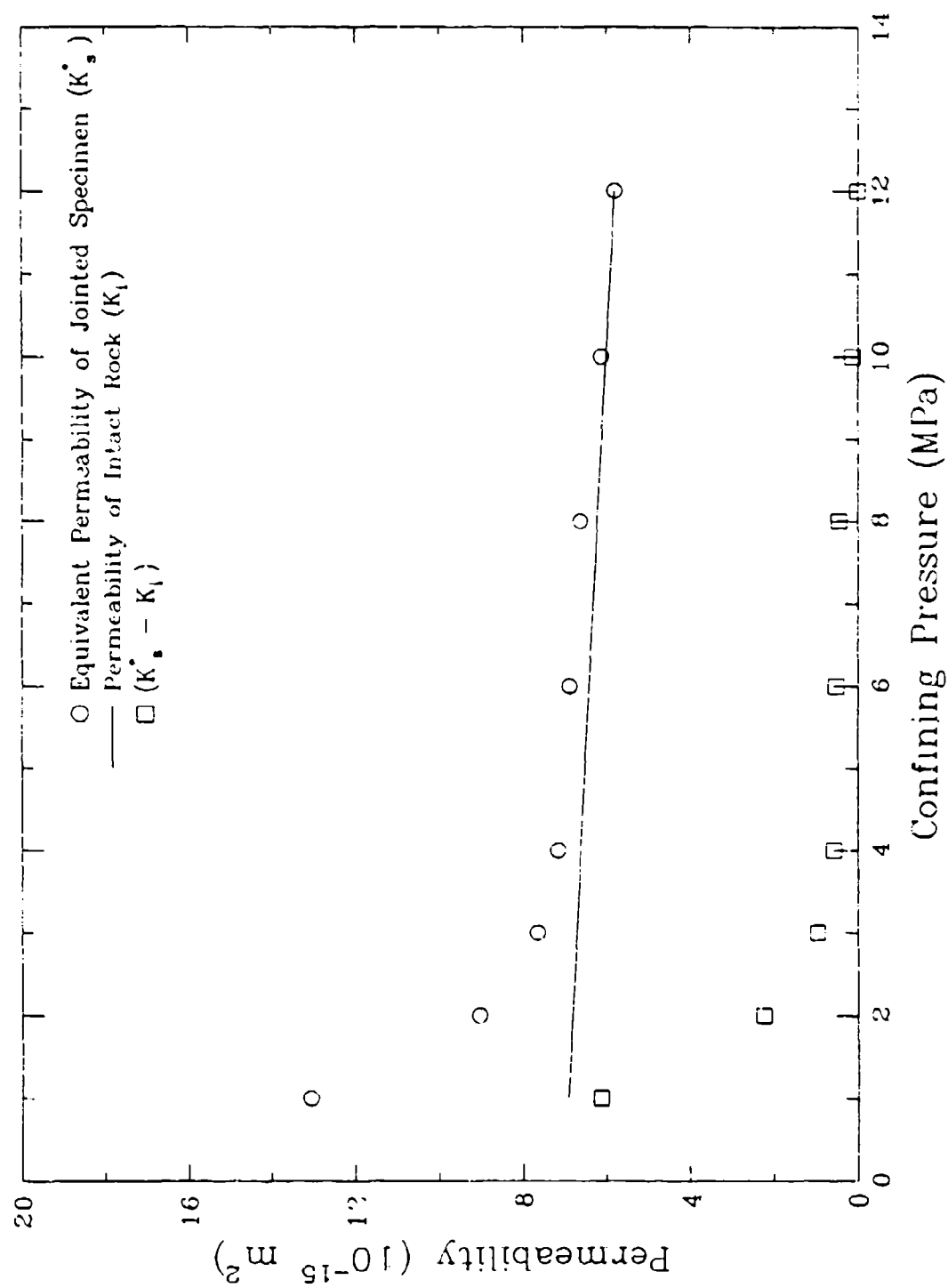


Figure 9-17. Data used in the derivation of joint permeabilities for a tensile fracture joint, Test G5A2.

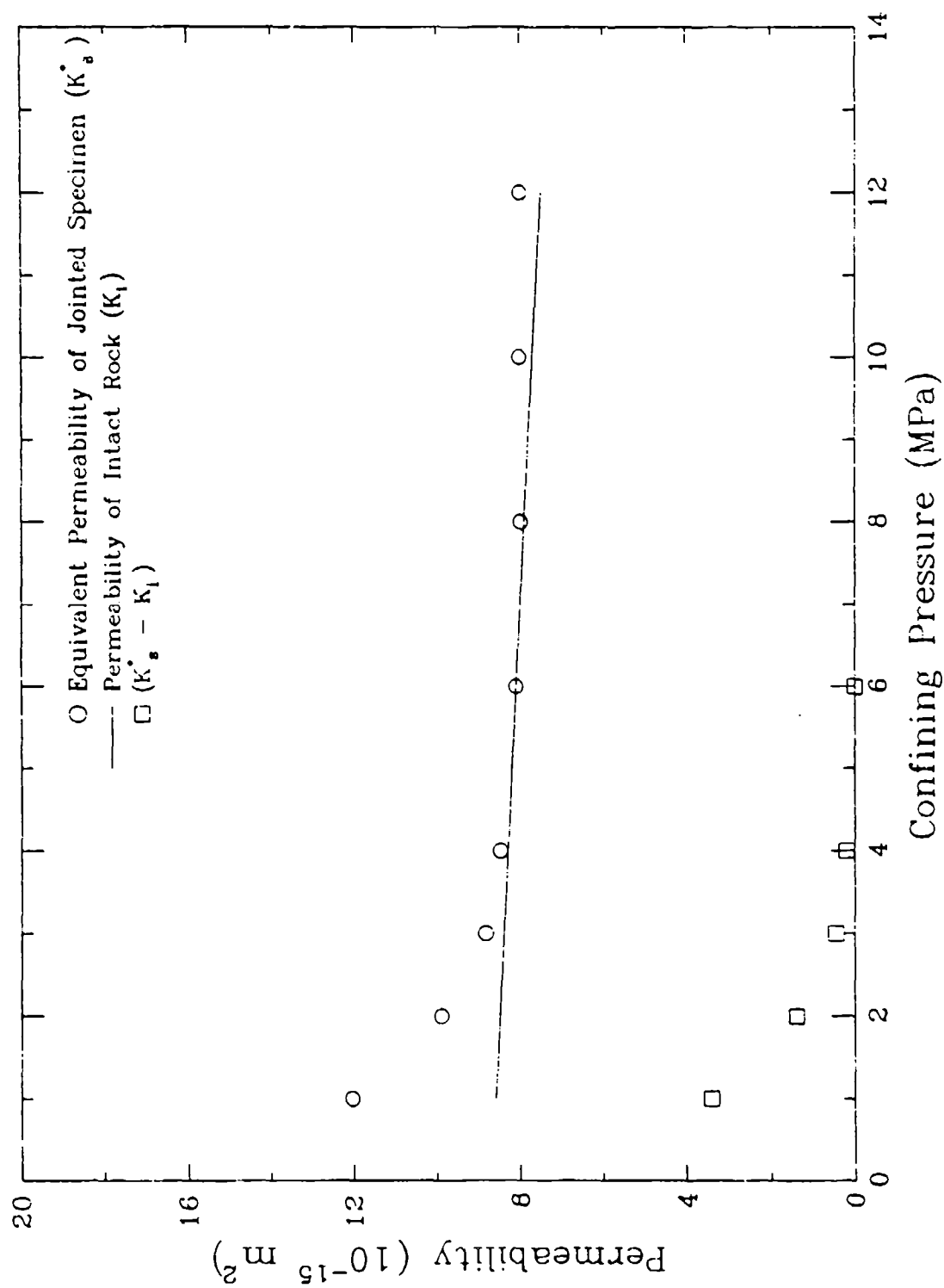


Figure 9-18. Data used in the derivation of joint permeabilities for a tensile fracture joint, Test U30A2.

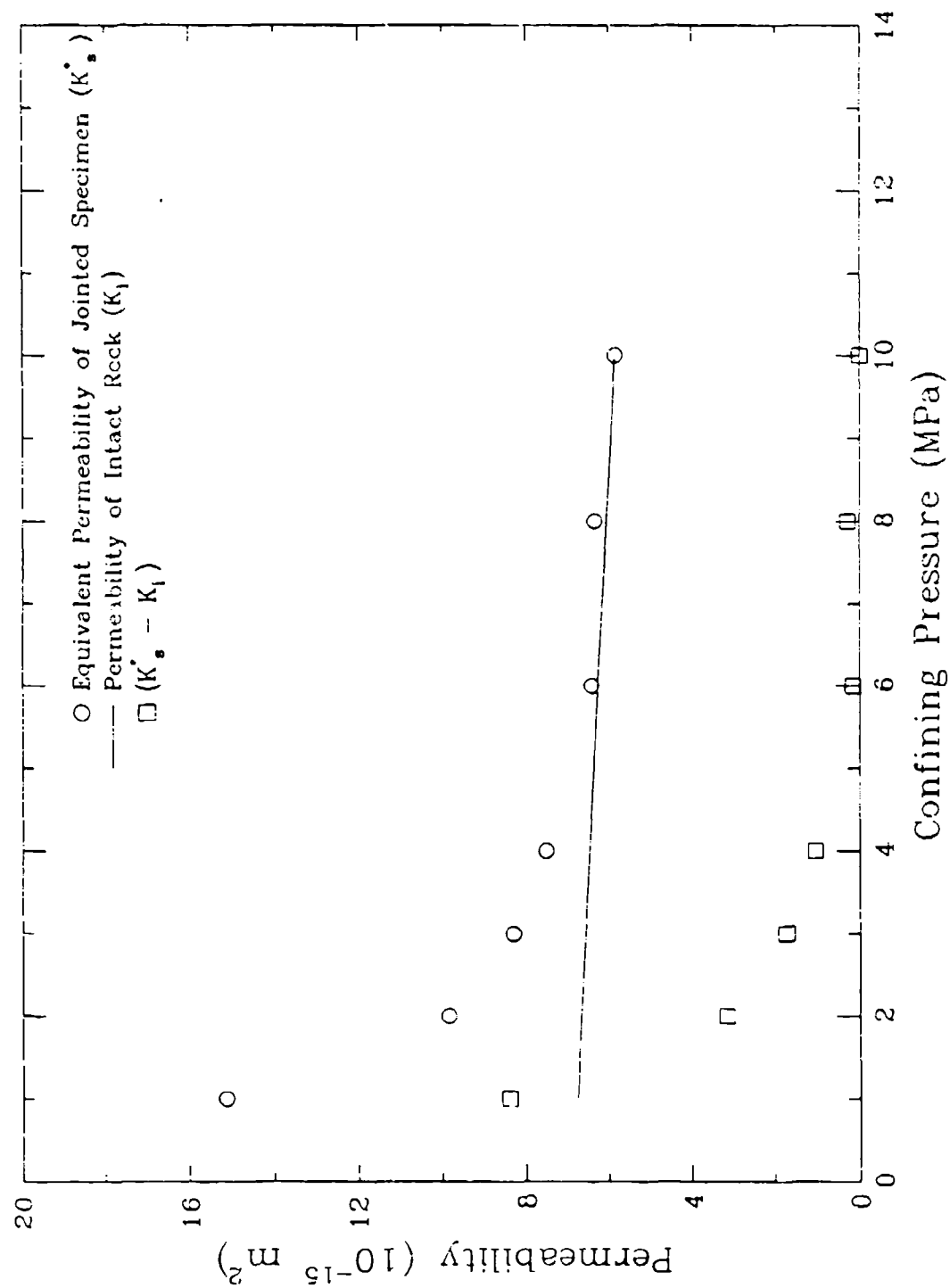


Figure 9-19. Data used in the derivation of joint permeabilities for a tensile fracture joint, Test A15A2.

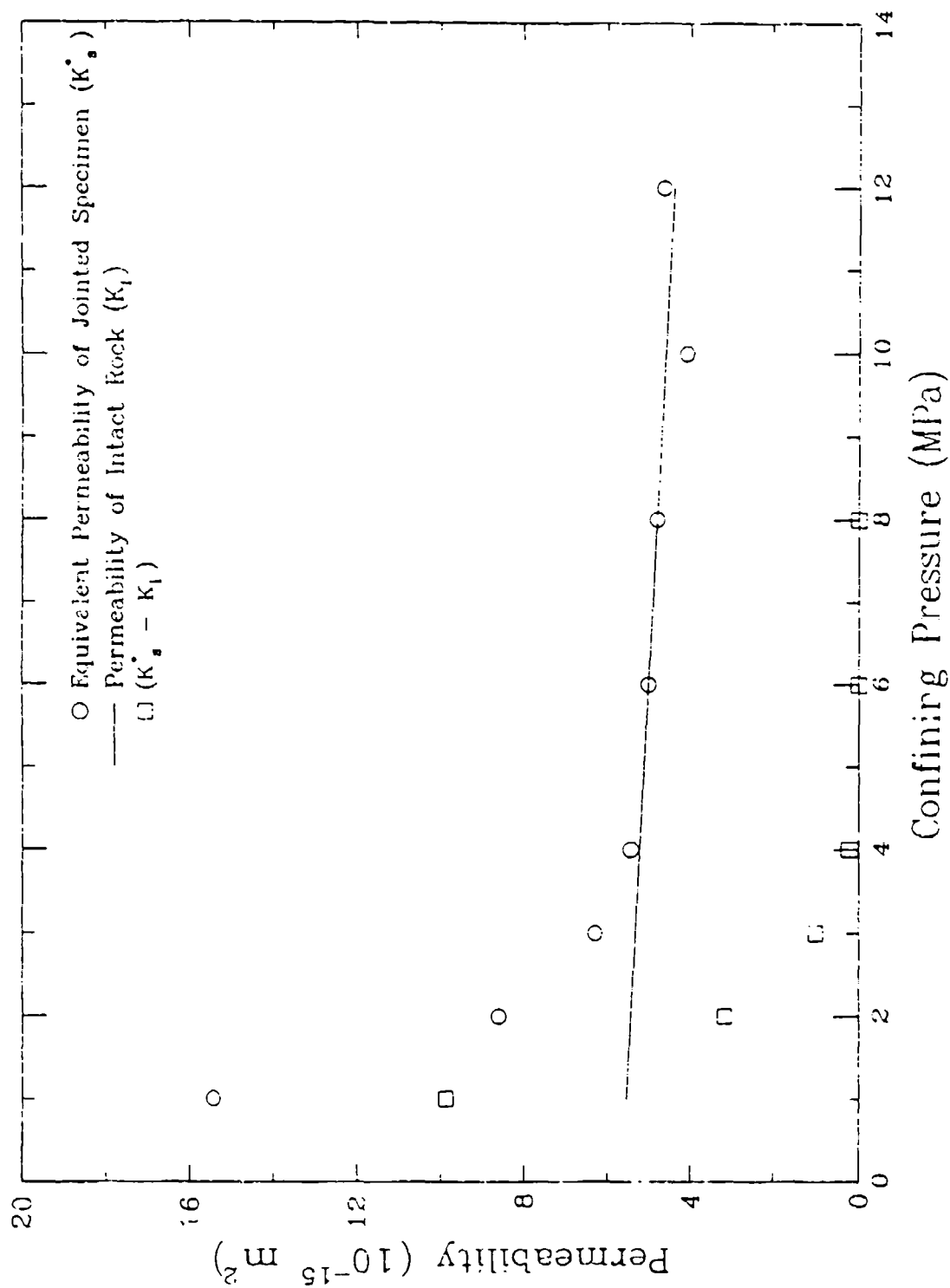


Figure 9-20. Data used in the derivation of joint permeabilities for a tensile fracture joint, Test OAA282.

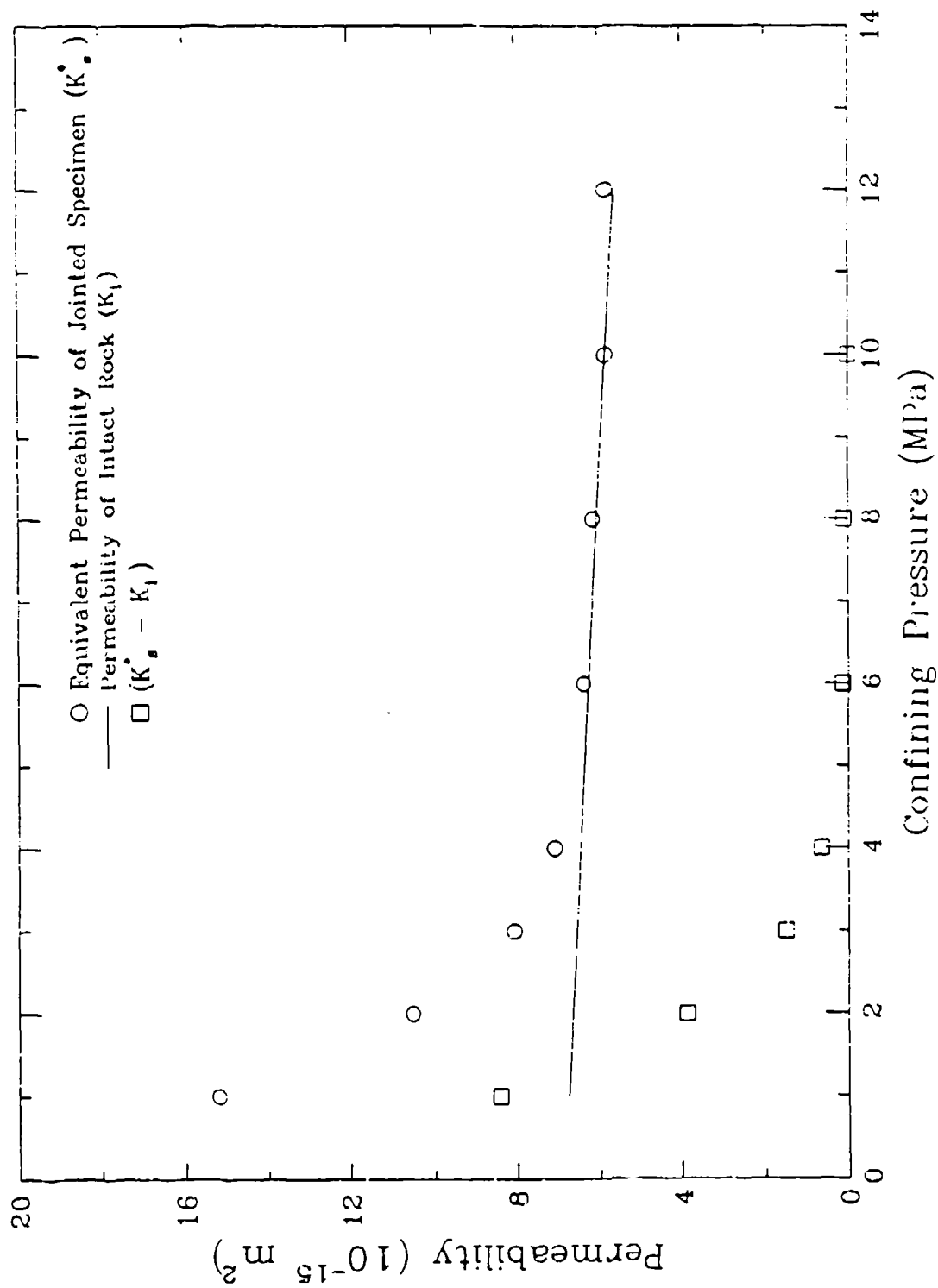


Figure 9-21. Data used in the derivation of joint permeabilities for a tensile fracture joint, Test OAA302.

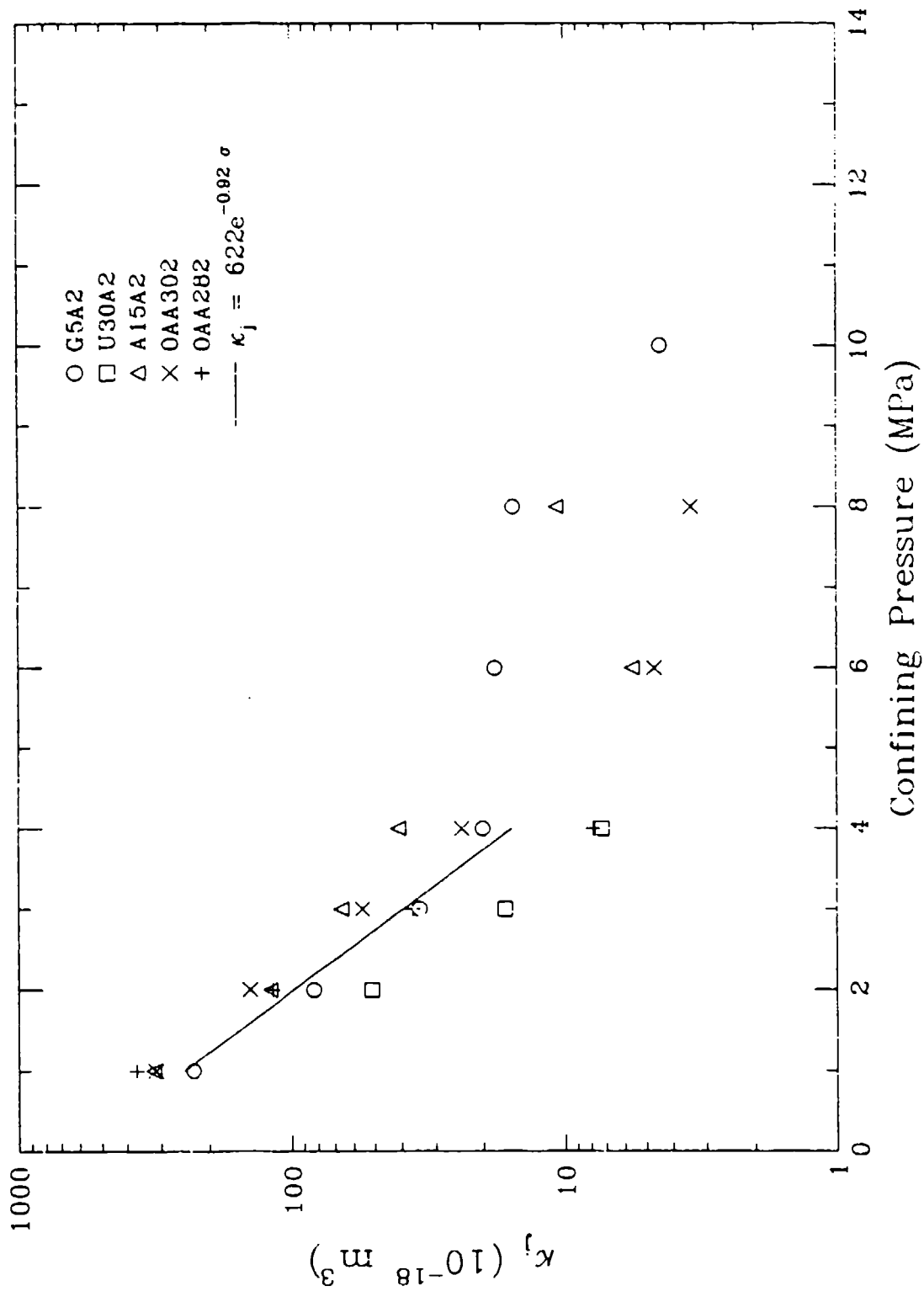


Figure 9-22. Summary of the relationships between joint permeability,  $\kappa_j$ , and confining pressure for five tensile fracture joint tests.

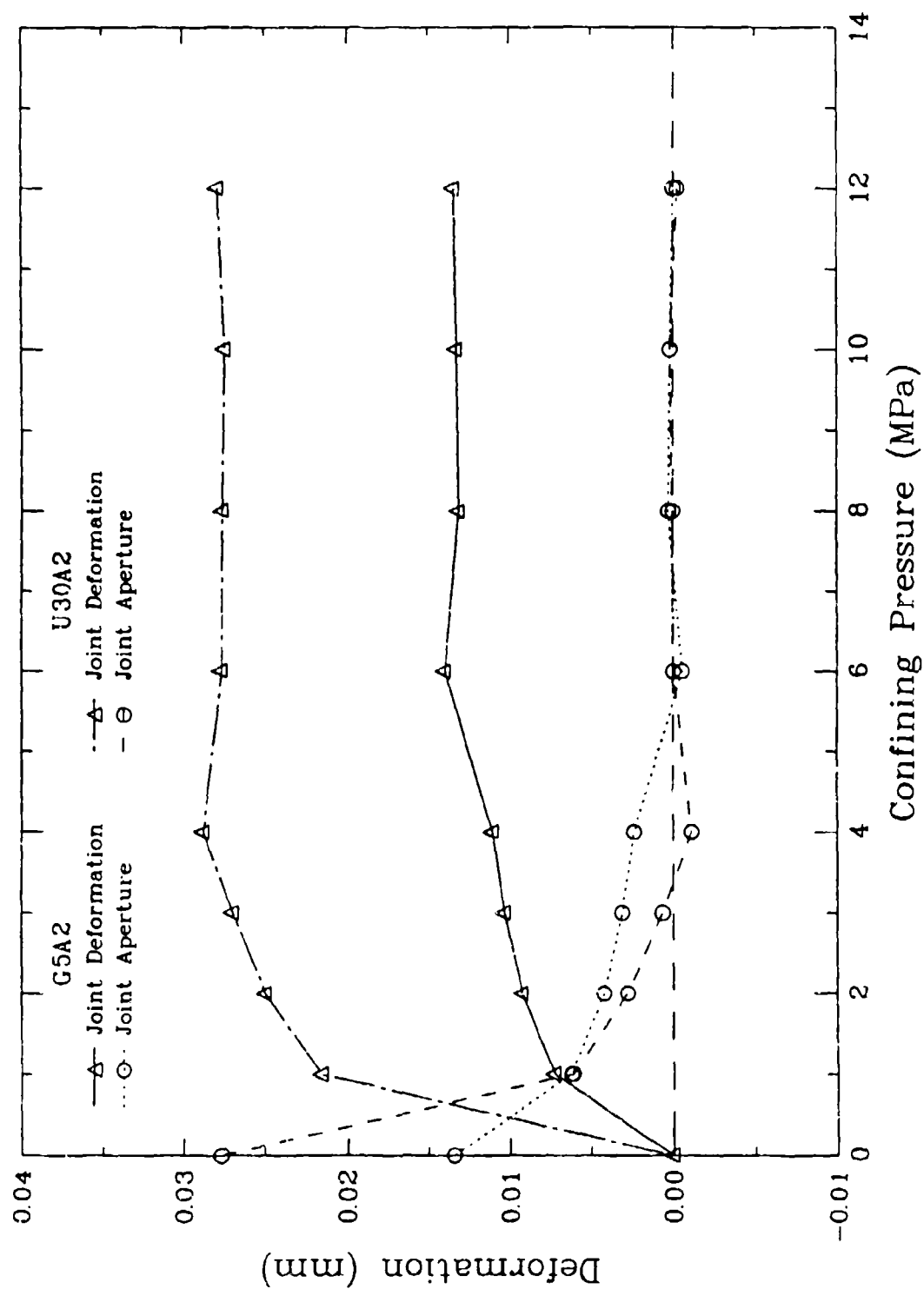


Figure 9-23. Measured normal deformations of two tensile fracture joints and the derived joint aperture values.



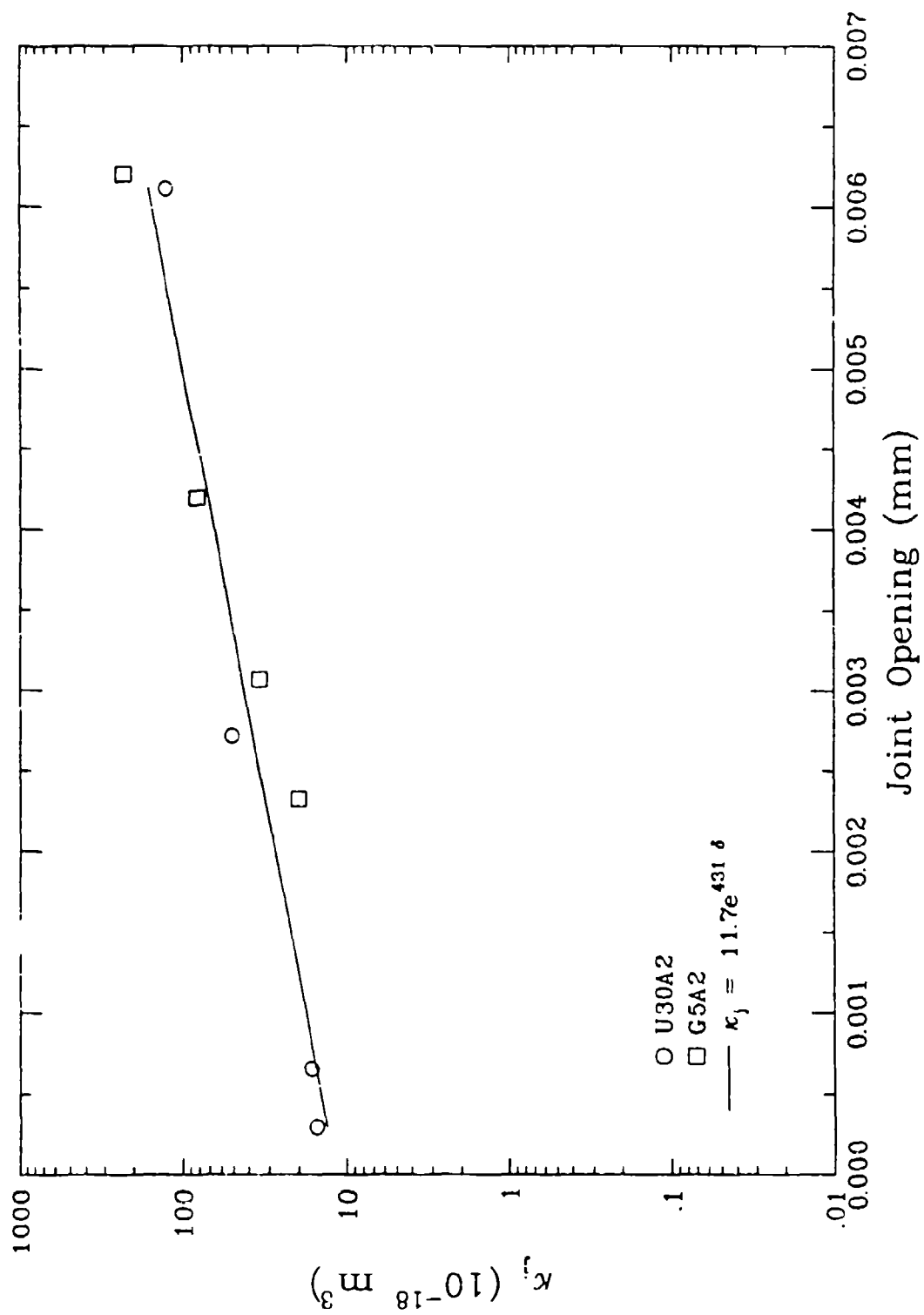


Figure 9-24. Relationships between joint permeability and joint aperture for two unsile fracture joints.

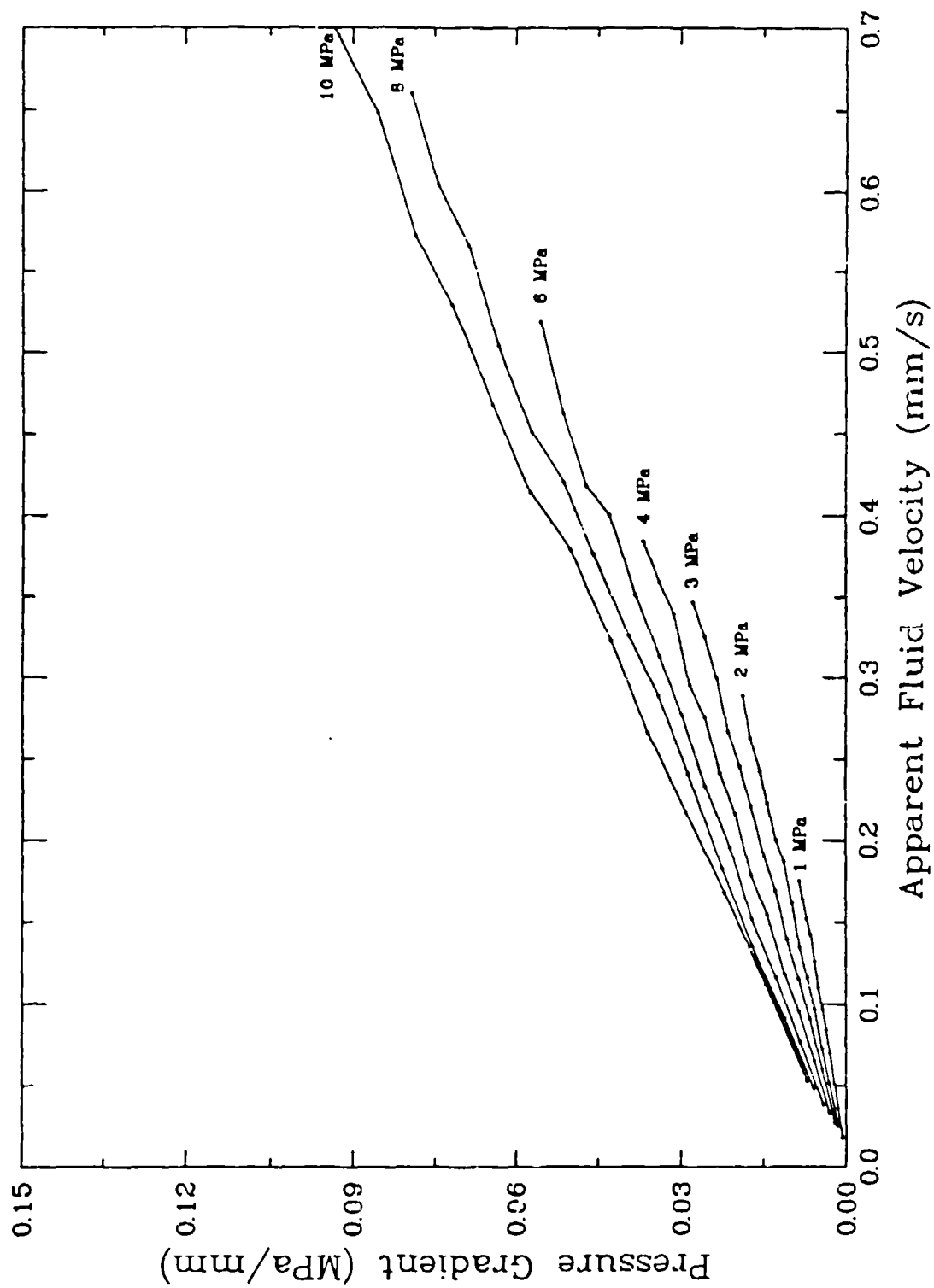


Figure 9-25. Set of permeability measurements on a limestone specimen with a smooth ground joint under hydrostatic loading illustrating the linear approximation of the dependence of pressure gradient on apparent fluid velocity.

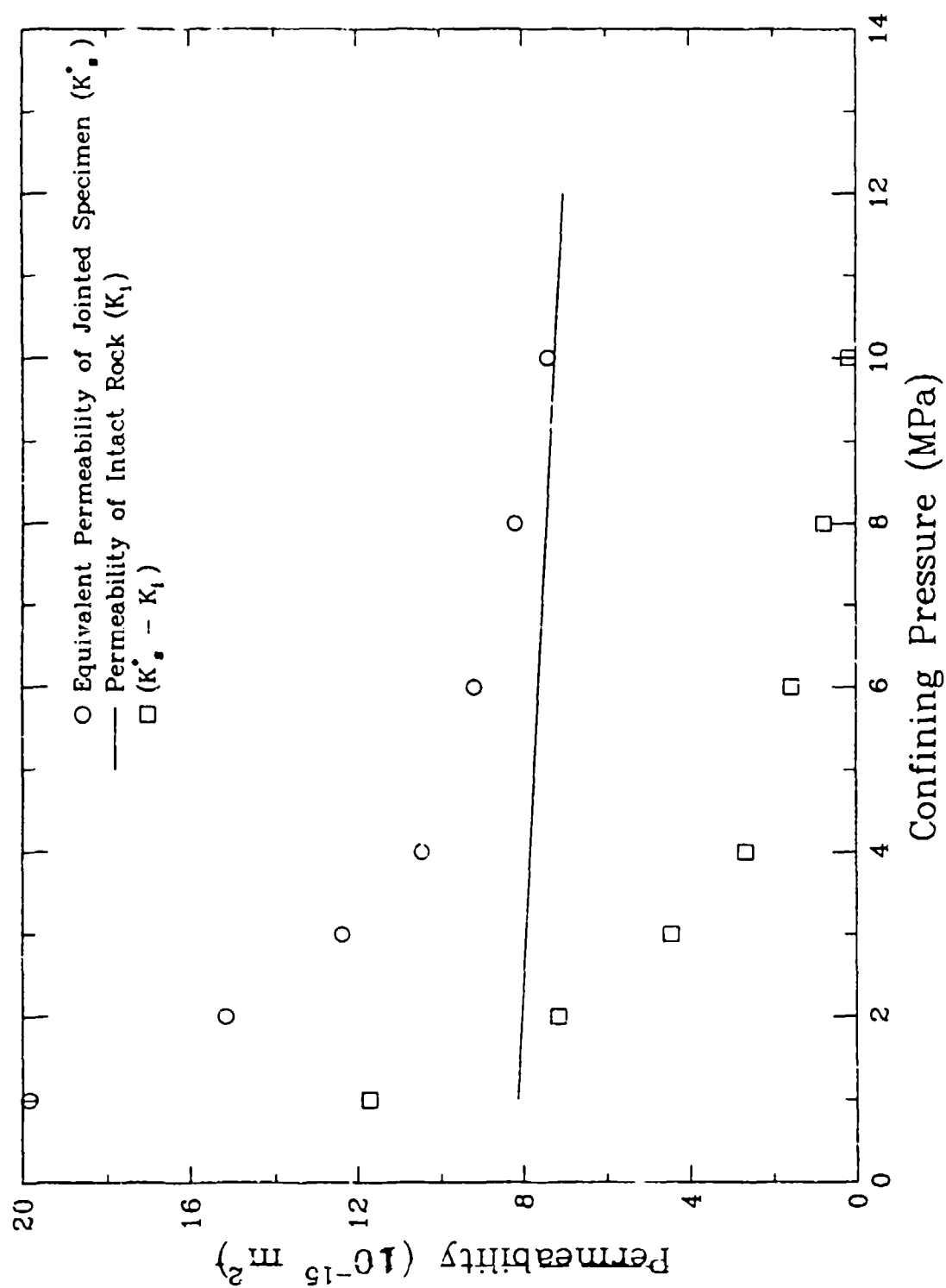


Figure 9-26. Data used in the derivation of joint permeabilities for a smooth joint, Test L15A2.

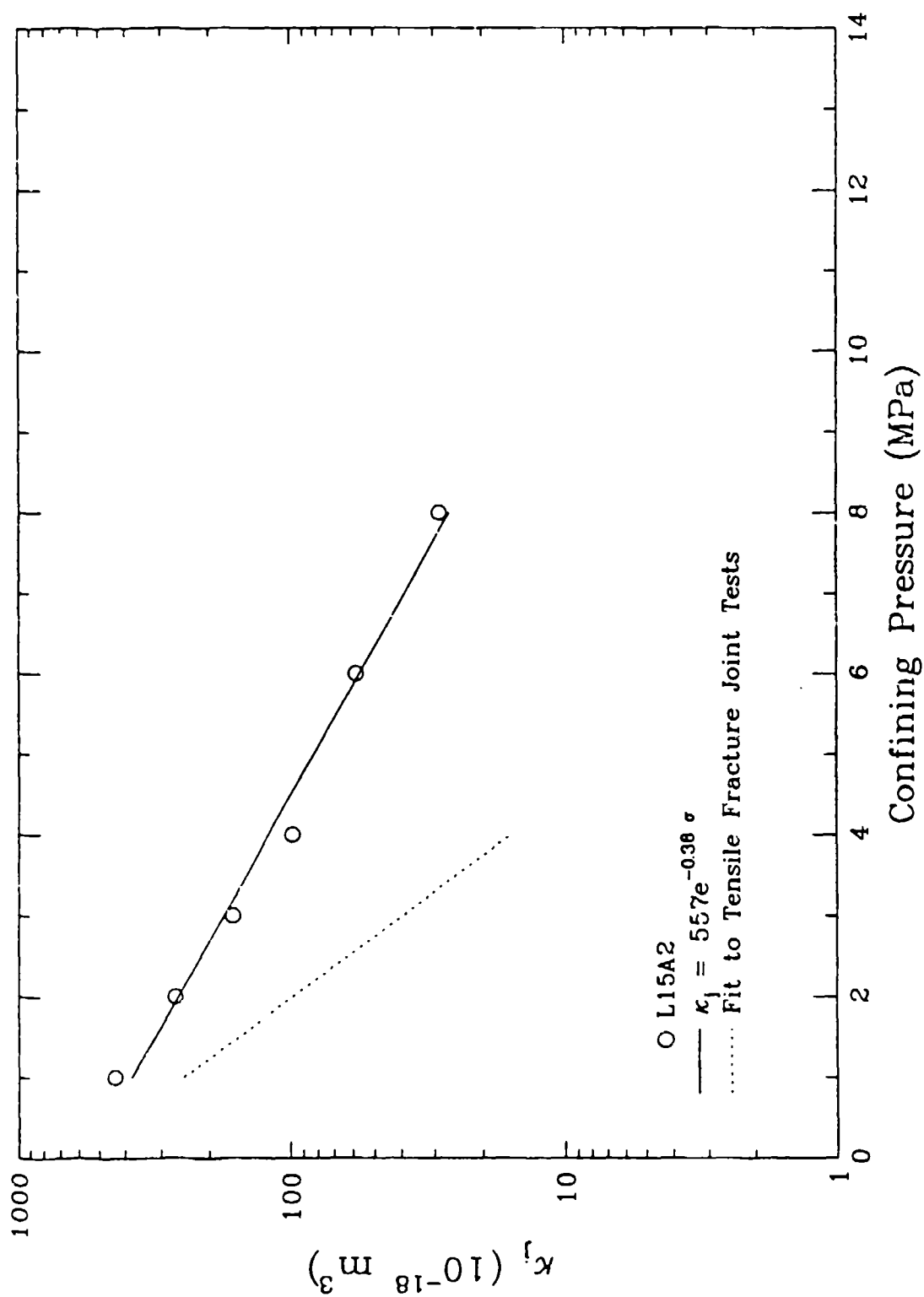


Figure 9-27. Relationship between joint permeability,  $\kappa_j$ , and confining pressure for a smooth ground joint test.

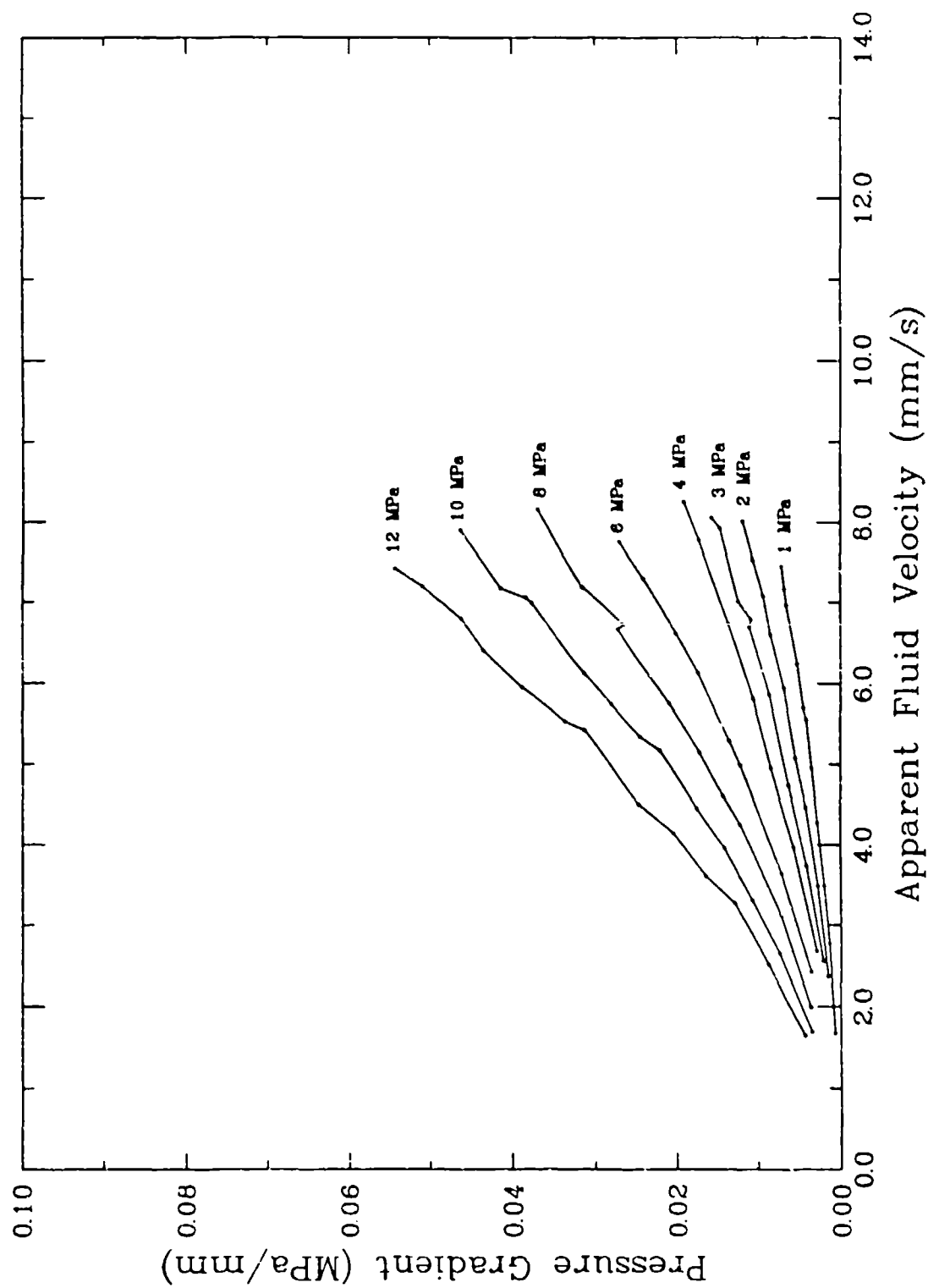


Figure 9-28. Set of permeability measurements on a limestone specimen with a synthetic joint under hydrostatic loading illustrating the dependence of pressure gradient on apparent fluid velocity.

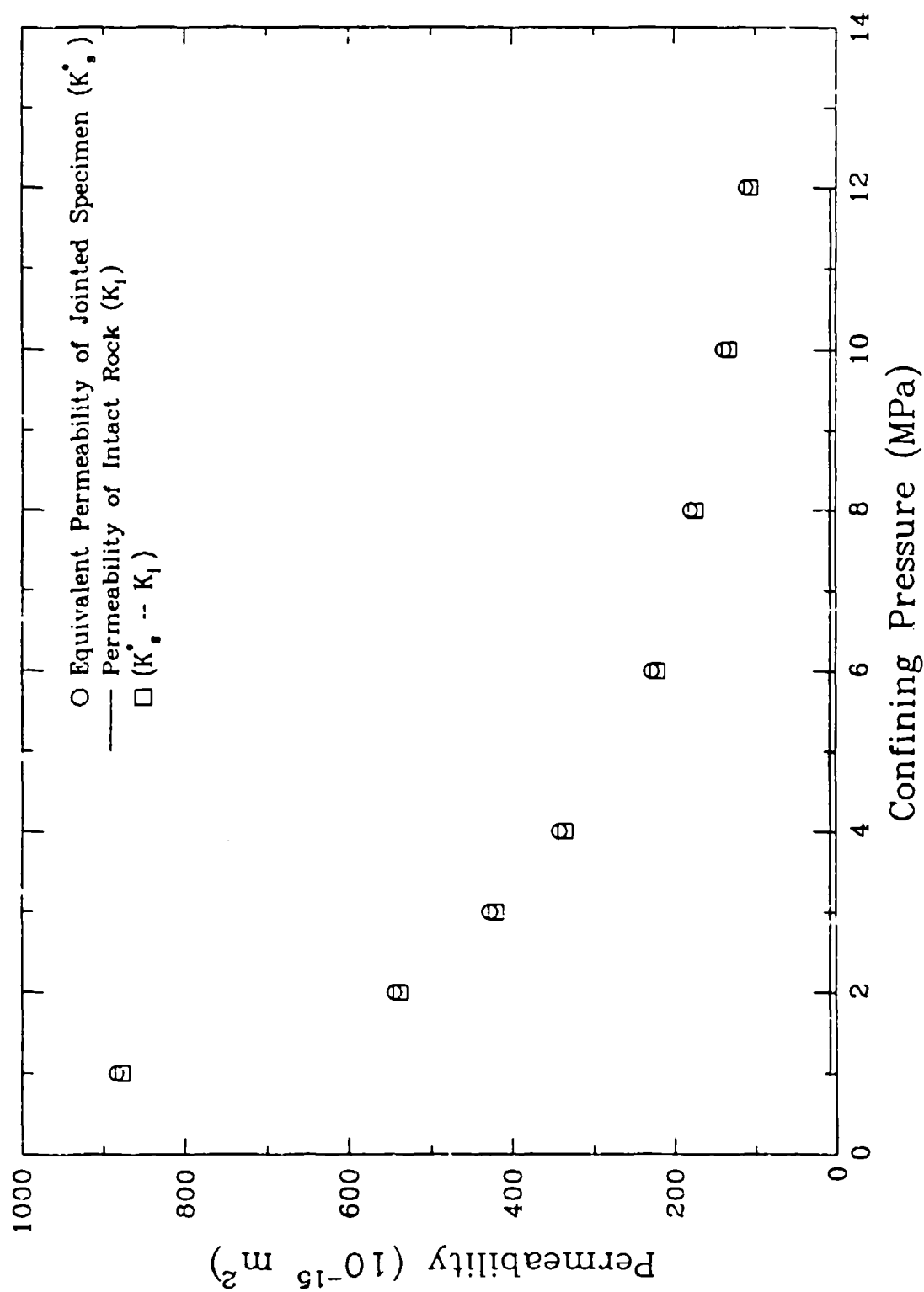


Figure 9-29. Data used in the derivation of joint permeabilities for a synthetic joint, Test L20A2.

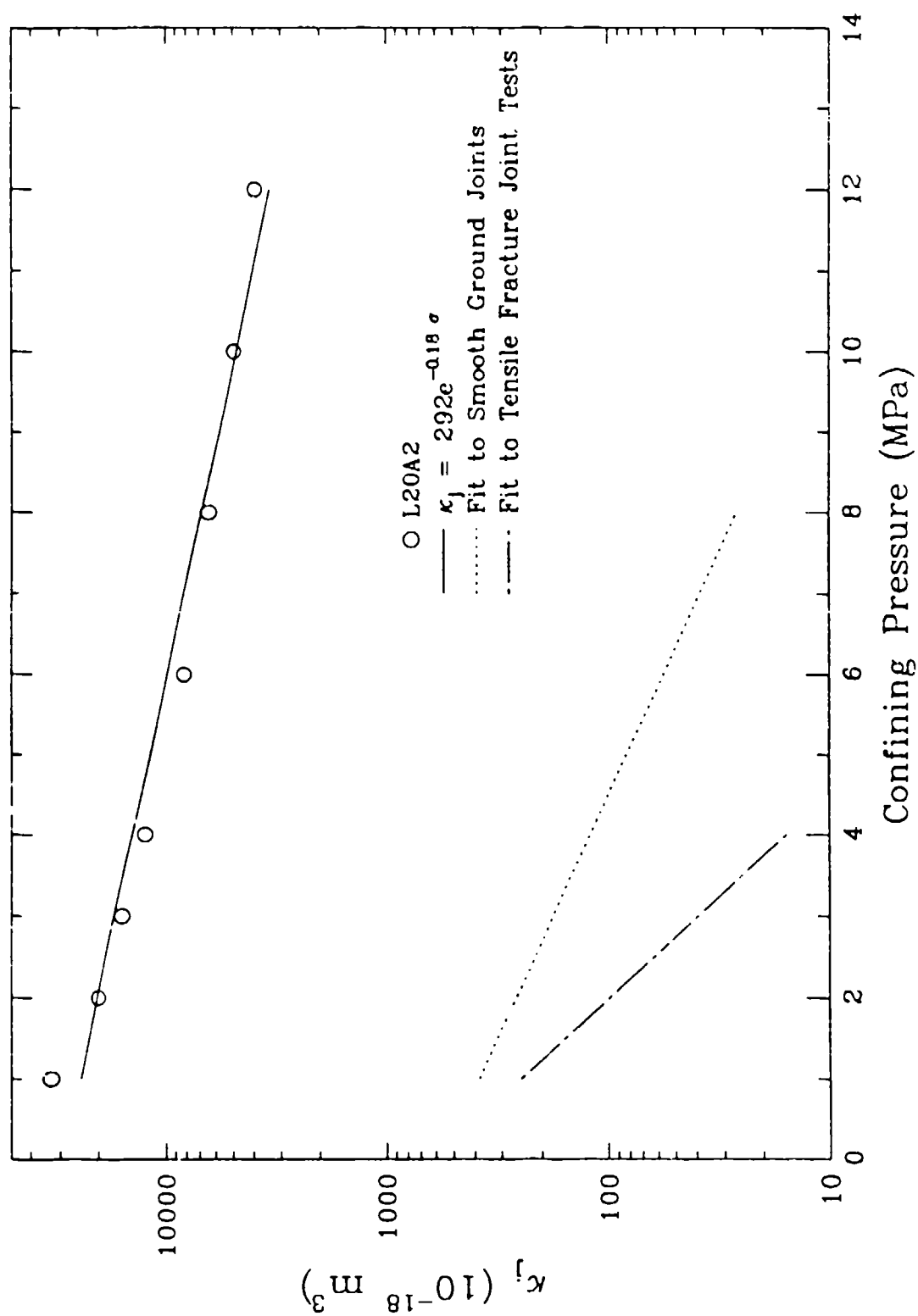


Figure 9-30. Relationship between joint permeability,  $\kappa_j$ , and confining pressure for a synthetic joint test.

## SECTION 10

### NUMERICAL SIMULATION OF ROCK JOINT RESPONSE

This section describes the development of a constitutive model for rock joints that can be implemented in a finite element program for explicit simulation of joints in a rock mass. The model treats the joint as a thin porous continuum with finite thickness so that in forming material constitutive relationships, stresses and strains are used instead of forces and displacements. The stress-strain relationships were derived based on elastoplastic theory, and strain softening in the brittle and brittle-ductile transition regions are expressed in terms of plastic work. The following subsections present the theoretical derivation of the model, procedures for parameter evaluation, and a verification problem.

#### 10.1 THEORETICAL DERIVATION OF ELASTOPLASTIC RESPONSE OF JOINTS.

This derivation is based on the assumption that the joint has finite thickness. Thus the constitutive relationship is formulated in terms of stress and strain. The stress space is assumed to be composed of two regions as shown schematically in Figure 10-1. Region I represents the brittle and brittle-ductile transition zones where continued shearing causes the material to reach a shear strength limit and then decrease to the residual strength. Region II represents ductile zone where the stress-strain response of the joint is the same as that of the intact material. In Region II, the joint shear responses are assumed to be elastic below the strength envelope and elastoplastic along the strength envelope. In Region I, the joint shear responses are assumed to be elastic up to the peak strength and elastoplastic with strain softening when the shear strain is increased beyond the point at which the peak strength is reached. Strain softening in this region is related to the accumulated plastic work. In the following, incremental stress-strain relations for softening are derived based on the theory of plasticity.

##### 10.1.1 Notations.

This subsection lists the notation used in the derivation. In keeping with the usual geotechnical convention, positive signs indicate compression.



$\{d\epsilon\}$  : total strain increment vector  
 $\{d\epsilon_e\}$  : elastic strain increment vector  
 $\{d\epsilon_p\}$  : plastic strain increment vector  
 $d\epsilon_n$  : normal (axial) strain increment  
 $d\epsilon_{ne}$  : elastic normal (axial) strain increment  
 $d\epsilon_{np}$  : plastic normal (axial) strain increment  
 $d\gamma$  : shear (tangential) strain increment  
 $d\gamma_e$  : elastic shear (tangential) strain increment  
 $d\gamma_p$  : plastic shear (tangential) strain increment  
 $\{d\sigma'\}$  : (effective) stress increment vector  
 $d\sigma'_n$  : (effective) normal stress increment  
 $d\tau$  : shear (tangential) stress increment  
 $P_a$  : atmospheric pressure  
 $[D^e]$  : elastic stress-strain matrix  
 $[D^p]$  : elastoplastic stress-strain matrix  
 $E$  : Young's modulus  
 $G$  : shear modulus  
 $W_p$  : plastic work  
 $W_{p,s=0.5}$  : plastic work at  $s=0.5$   
 $\xi_p$  : normalized plastic work  
 $s$  : softening variable  
 $T$  : apparent tensile strength  
 $\eta_1$  : yield constant  
 $m$  : yield constant  
 $\phi_r$  : residual friction angle  
 $F$  : yield function  
 $G$  : potential function  
 $a$  : softening constant  
 $b$  : softening constant  
 $c$  : plastic potential constant  
 $d$  : plastic potential constant

### 10.1.2 Total Strain Increment.

The total strain is comprised of the elastic and plastic components of strain as given by:

$$\{d\epsilon\} = \{d\epsilon_e\} + \{d\epsilon_p\} \quad (10.1)$$

or

$$\begin{Bmatrix} d\epsilon_n \\ d\gamma \end{Bmatrix} = \begin{Bmatrix} d\epsilon_{ne} \\ d\gamma_e \end{Bmatrix} + \begin{Bmatrix} d\epsilon_{np} \\ d\gamma_p \end{Bmatrix}$$

### 10.1.3 Elastic Stress-Strain Relationship.

The incremental elastic constitutive law can be expressed in the following matrix form:

$$\{d\sigma\} = [D^e] \{d\epsilon_e\} \quad (10.2)$$

or

$$\begin{Bmatrix} d\sigma_n \\ d\tau \end{Bmatrix} = \begin{bmatrix} E & 0 \\ 0 & G' \end{bmatrix} \begin{Bmatrix} d\epsilon_{ne} \\ d\gamma_e \end{Bmatrix}$$

The elastic modulus,  $E$ , is assumed to be expressed as a function of effective normal stress:

$$E = E(\sigma_n') \quad (10.3)$$

and the shear modulus is assumed to be constant:

$$G' = \text{constant} \quad (10.4)$$

### 10.1.4 Yield Equation.

The proposed joint model does not allow hardening. Thus the yield surface coincides with the failure surface. The joint model, however, allows strain softening which is related to the plastic work.

$$F(\sigma'_{ij}, \epsilon^p_{ij}) = F(\sigma'_{ij}, W_p(\epsilon^p_{ij})) = 0 \quad (10.5)$$

The explicit form of yield equation is given by:

$$F(\sigma'_n, \tau, \xi_p) = (1-s) X_r + s X_p - \frac{\sigma'_n}{P_a} = 0 \quad (10.6)$$

where:

$$X_r = \frac{1}{\tan \phi_r} \cdot \frac{\tau}{P_a} \quad (10.7)$$

$$X_p = -\frac{\tau}{P_a} + \frac{\left(\frac{\tau}{P_a}\right)}{\eta_1 - m\left(\frac{\tau}{P_a}\right)} \quad (10.8)$$

$$s = e^{-0.693\xi_p} \quad (10.9)$$

$$\xi_p = \frac{W_p}{W_{p, s=0.5}} \quad (10.10)$$

$$dW_p = \{\sigma\}^T \{d\epsilon_p\} = \left\{ \frac{\partial W_p}{\partial \epsilon_p} \right\}^T \{d\epsilon_p\} \quad (10.11)$$

or

$$dW_p = \sigma'_n \cdot d\epsilon_{np} + \tau \cdot d\gamma_p$$

Note that  $W_{p,s=0.5}$  in Equation 10.10 is the plastic work at  $s=0.5$  and is expressed as a function of effective normal stress.

$$W_{p,s=0.5} = a \cdot \sigma_n' + b \quad (10.12)$$

### 10.1.5 Flow Rule.

A nonassociated flow rule is assumed. Thus, the plastic strain increment,  $\{d\epsilon_p\}$ , is in the direction normal to the potential surface:

$$\{d\epsilon_p\} = d\lambda \left\{ \frac{\partial G}{\partial \sigma'} \right\} \quad (10.13)$$

or

$$\begin{Bmatrix} d\epsilon_p \\ d\gamma_p \end{Bmatrix} = d\lambda \begin{Bmatrix} \frac{\partial G}{\partial \sigma_n'} \\ \frac{\partial G}{\partial \tau} \end{Bmatrix}$$

where  $d\lambda$  is a non-negative proportionality constant and the derivatives of the potential function with respect to the stress components are given by:

$$\frac{\partial G}{\partial \sigma_n'} = c \cdot \sigma_n' + d \quad (10.14)$$

and

$$\frac{\partial G}{\partial \tau} = 1 \quad (10.15)$$

### 10.1.6 Normal to the Yield Function.

The derivatives of the yield function with respect to the stress components are given by:

$$\left\{ \frac{\partial F}{\partial \sigma'} \right\} = \left\{ \begin{array}{c} \frac{\partial F}{\partial \sigma'_n} \\ \frac{\partial F}{\partial \tau} \end{array} \right\} \quad (10.16)$$

where:

$$\frac{\partial F}{\partial \sigma'_n} = S (X_r - X_p) \frac{0.693 a \xi_p}{(a \sigma'_n + b)} - \frac{1}{P_a} \quad (10.17)$$

and

$$\frac{\partial F}{\partial \tau} = \frac{(1-s)}{P_a \tan \phi_r} + \frac{s \eta_1}{P_a \left( \eta_1 + m \frac{\tau}{P_a} \right)^2} \quad (10.18)$$

### 10.1.7 Consistency Equation.

During yielding, the consistency equation forces the stresses to move along the yield surface.

$$dF = \left\{ \frac{\partial F}{\partial \sigma'} \right\}^T \{d\sigma'\} + \frac{\partial F}{\partial W_p} \cdot dW_p = 0 \quad (10.19)$$

where:

$$dW_p = \left\{ \frac{\partial W_p}{\partial \epsilon_p} \right\}^T \{d\epsilon_p\} = \{\sigma\}^T \{d\epsilon_p\} \quad (10.20)$$

Substitution of Equation 10.13 into Equation 10.20 yields:

$$dW_p = d\lambda \{\sigma\}^T \left\{ \frac{\partial G}{\partial \sigma'} \right\} \quad (10.21)$$

And the partial derivative of yield function with respect to the plastic work is given by:

$$\frac{\partial F}{\partial W_p} = (X_r - X_p) s \frac{0.693}{a\sigma_n' + b} \quad (10.22)$$

### 10.1.8 Formulation of Elastoplastic Stress-Strain Matrix.

Equation 10.21 is substituted into Equation 10.19, to obtain:

$$\left\{ \frac{\partial F}{\partial \sigma'} \right\}^T \{d\sigma\} + \frac{\partial F}{\partial W_p} d\lambda \{\sigma\}^T \left\{ \frac{\partial G}{\partial \sigma'} \right\} = 0 \quad (10.23)$$

The elastic strain vector in Equation 10.2 is rewritten in terms of the plastic strain vector using Equation 10.1, to obtain:

$$\{d\sigma\} = [D] \{d\epsilon\} - \{d\epsilon_p\} \quad (10.24)$$

The plastic strain vector in Equation 10.24 can be expressed in terms of the derivatives of potential function with the aid of Equation 10.13.

$$\{d\sigma\} = [D] \{d\epsilon\} - [D] d\lambda \left\{ \frac{\partial G}{\partial \sigma'} \right\} \quad (10.25)$$

Now substituting Equation 10.25 into Equation 10.23 and solving for  $d\lambda$ , to obtain:

$$d\lambda = \frac{\left\{ \frac{\partial F}{\partial \sigma'} \right\}^T [D] \{d\epsilon\}}{\left\{ \frac{\partial F}{\partial \sigma'} \right\}^T [D] \left\{ \frac{\partial G}{\partial \sigma'} \right\} - \frac{\partial F}{\partial W_p} \{\sigma'\}^T \left\{ \frac{\partial G}{\partial \sigma'} \right\}} \quad (10.26)$$

By backsubstituting this  $d\lambda$  into Equation 10.25, the effective stress increment is directly related to the total strain increment as follows:

$$\{d\sigma'\} = [D^{ep}] \{d\epsilon\} \quad (10.27)$$

where the incremental elastoplastic constitutive matrix is expressed as:

$$[D^{ep}] = [D] - \frac{[D] \left\{ \frac{\partial G}{\partial \sigma'} \right\} \left\{ \frac{\partial F}{\partial \sigma'} \right\}^T [D]}{\left\{ \frac{\partial F}{\partial \sigma'} \right\}^T [D] \left\{ \frac{\partial G}{\partial \sigma'} \right\} - \frac{\partial F}{\partial W_p} \{\sigma'\}^T \left\{ \frac{\partial G}{\partial \sigma'} \right\}} \quad (10.28)$$

## 10.2 EVALUATION OF MODEL PARAMETERS FOR TENSILE FRACTURE JOINTS OF SALEM LIMESTONE.

Section 10.3 presents an example of the joint model used to predict the stresses and strain softening for specified input strains. The determination of material parameters used in that verification problem are described in this section. Since the development of the model was done in parallel with the laboratory testing, the example is based on test data from a previous joint testing effort (Chitty and Blouin, 1992).

### 10.2.1 Elastic Constants.

Based on the unload and reload slopes of unconfined compression tests of tensile fracture joints, the following elastic modulus ( $E_w$ ) and shear modulus ( $G'$ ) for a fully closed joint were obtained.

$$E_w = 31,000 \text{ MPa}$$

$$G' = 12,500 \text{ MPa}$$

### 10.2.2 Joint Compressibility.

The model treats the joint as a thin continuum with finite thickness so that determination of the joint thickness is necessary to relate the measured joint displacements to joint strains. Joint thickness,  $t$  consists of the average thickness of roughness,  $t_r$  and the gap between top and bottom surfaces,  $t_g$ . That is,

$$t = t_r + t_g \quad (10.29)$$

The roughness,  $t_r$ , was estimated as 0.66 mm from the joint profile shown in Figure 10-2. The gap,  $t_g$ , was estimated from the normal compressibility test (A3C0). The value for  $t_g$  of 0.074 mm was obtained at the lock-up point of the joint normal displacement. Thus, from the Equation 10.29, the estimated joint thickness is

$$t = 0.66 + 0.074 = 0.73 \text{ mm}$$

Figure 10-3 presents the results of a normal compressibility test on a tensile fracture joint in Salem limestone. In this test, a V-shaped groove approximately 3 mm deep was cut around the circumference of the limestone specimen at mid-height. Two sets of mounting fixtures were attached to the sides of the specimen with epoxy adhesive and LVDTs were attached to measure axial deformation of a portion of the specimen including the groove at two diametrically opposed locations. The specimen was loaded axially in unconfined compression and the output of the axial deformation gages was recorded and averaged. The solid line labeled "Pre-Fracture" in Figure 10-3a represents that record. Without disturbing the LVDT mounting fixtures, the specimen was placed in special grips and loaded in tension until it broke along the groove.



creating a tensile fracture joint. It was then re-loaded in unconfined compression. The data recorded in that test are shown as the dashed line in Figure 10-3a labeled "Post-Fracture". The difference between those two displacements, which is shown in Figure 10-3b, represents the normal displacement of the joint, assuming that the joint has no thickness when it is completely closed. However the model formulation, presented here is based on the assumption that the joint has a finite thickness. The following analysis was performed to convert the data to a form that will support this analysis.

It is necessary to estimate gage length ( $h$ ) to interpret the joint normal compressibility data shown in Figure 10-3 in terms of axial stress and strain. Figure 10-3a shows the axial stress vs. axial displacement plot for intact sample (A3A0). The axial displacement  $U_i$  at  $\sigma_n' = 30$  MPa is 0.016 mm. Since the Young's modulus of intact Salem limestone is  $E_i = 31,000$  MPa, the axial strain of the intact sample at  $\sigma_n' = 30$  MPa can be computed as:

$$\epsilon_i = \frac{\sigma_n'}{E_i} = \frac{30}{31,000} = 0.00097$$

Thus the gage length can be estimated from the measured displacement and the computed strain as:

$$h = \frac{U_i}{\epsilon_i} = \frac{0.016}{0.00097} = 16.5 \text{ mm}$$

To support the analysis assuming finite joint thickness, the joint stress-strain curve was computed from specimen normal displacement,  $U_n$ , represented by the Post-Fracture curve in Figure 10-3a, by subtracting the elastic deformation of the material in the gage length less the joint thickness,  $t$ , as follows:

$$\epsilon_n = \frac{1}{t} \left( U_n - (h - t) \frac{\sigma_n'}{E_i} \right) \quad (10.30)$$

Using Equation 10.30, the joint normal stress-strain curve, shown in Figure 1-.4 was constructed in idealized form.

### 10.2.3 Peak and Residual Shear Strength Parameter.

The peak strength envelope was obtained by substituting  $s=1$  into the expression for the failure envelope, Equation 10.6.

$$\frac{\tau}{P_a} = \frac{\eta_1}{\frac{P_a}{\sigma'_n + T} + m} \quad (10.31)$$

Equation 10.31 can be expressed in the following form for a linear regression fit to the laboratory strength data transformed to variables  $(\sigma'_n + T)/\tau$  and  $(\sigma'_n + T)/P_a$ :

$$\frac{\sigma'_n + T}{\tau} = \frac{1}{\eta_1} + \frac{m}{\eta_1} \left( \frac{\sigma'_n + T}{P_a} \right) \quad (10.32)$$

This requires that the apparent tensile strength,  $\tau$ , first be selected by eye. From the linear regression fit to the joint peak strength data, the intercept  $\left(\frac{1}{\eta_1}\right)$  and the slope  $\left(\frac{m}{\eta_1}\right)$  are obtained.

The computed values for the data set shown in Figure 10-5 (from Chitty and Blouin, 1992) are:

$$\eta_1 = 1.11$$

and

$$m = 0.000717$$

$T$  was selected to be 6 MPa before fitting to the data. The resulting fit is also shown in Figure 10-5.

The residual strength envelope was obtained by substituting  $s=0$  into Equation 10.6. The resulting expression for residual strength is:

$$\frac{\tau}{P_a} = \tan \phi_r \cdot \frac{\sigma_n'}{P_a} \quad (10.33)$$

The residual friction angle,  $\phi_r = 40^\circ$ , was obtained by a straight line fit to the sawcut joint strength as shown in Figure 10-5.

#### 10.2.4 Strain Softening Parameter.

The joint model assumes that the strain softening is related to the normalized plastic work,  $\xi_p$ , which is related to the softening variable,  $s$ , by Equation 10.9. Thus, when  $\xi_p = 0$ ,  $s=1$  and yield equation coincides with peak strength envelope. When  $\xi_p = 1$ ,  $s = 0.5$  and yield equation is half way between the peak and residual strength envelopes. When  $\xi_p$  approaches infinity,  $s=1$  and the yield equation coincides with the residual strength envelope.

It should be noted that  $\xi_p$  in Equation 10.10 is the current plastic work,  $W_p$ , normalized by the plastic work at  $s=0.5$  ( $W_{p, s=0.5}$ ). As shown in Figure 10-1, the triaxial compression stress path for a given confining pressure,  $\sigma_{nc}'$ , crosses the yield equation ( $s=0.5$ ) at the stress point  $(\sigma_m', \tau_m)$ . From a plot of joint shear stress,  $\tau$  as a function of plastic work  $W_p$ , for each confining pressure,  $W_{p, s=0.5}$  at  $\tau=\tau_m$  is found, as shown in Figure 10-6. For each confining pressure,  $\sigma_m'$  and  $W_{p, s=0.5}$  are listed in Table 10-1. The softening parameters,  $a$  and  $b$ , in Equation 10.12 can be found by a least squares fit to the data as shown in Figure 10-7. The resulting values are:

$$a = 0.474$$

$$b = 1.7$$

#### 10.2.5 Plastic Potential Parameters.

The flow rule specifies the direction of the plastic strain increment. This model uses a nonassociative flow rule so that the plastic strain increment vector is normal to a potential surface which is different from the yield surface.

The plastic potential parameters,  $c$  and  $d$  in Equation 10.14, can be related to the slope of the normal to the shear strain by combining Equations 10.13, 10.14, and 10.15.

$$\frac{\frac{\partial G}{\partial \sigma'_n}}{\frac{\partial G}{\partial \tau}} = \frac{d\epsilon_{np}}{d\gamma_p} = c \cdot \sigma'_n + d \quad (10.34)$$

Figure 10-8 shows the measured joint normal displacement plotted as a function of joint tangential displacement at confining pressures of 1, 5, 10, 15, and 20 MPa. The slope of these curves represents very closely the ratio of the normal to shear plastic strain increment in Equation 10.34 since the elastic strains in this softening region are very small compared to the plastic strains. Figure 10-9 shows the values of these slopes plotted as a function of the effective normal stresses. These effective normal stresses are not the confining pressures but the stresses at the average of peak and residual strength envelopes. A least squares fit to the data gives the following plastic potential parameters:

$$c = 0.00783$$

$$d = -0.236.$$

### 10.3 VERIFICATION PROBLEM.

This section presents two verification problems for the material model using the parameter values for tensile fracture joints in Salem limestone that were determined in Section 10.2. The incremental constitutive relations were formulated in the form of stiffness matrix. Thus, for a known strain increment, the constitutive matrix computes the corresponding stress increment. For verification, the model will be used to simulate laboratory triaxial compression tests. Two triaxial tests at confining pressures of 5 and 15 MPa were selected. The ratio of input normal strain to shear strain is estimated as -0.133 for 5 MPa confining test and 0.029 for 15 MPa confining test based on the measured displacement slopes shown in Figure 10-8. Both predictions begin at stress points on the peak strength envelope and continue until they approach to the residual strength envelope.

Figure 10-10 shows predicted and measured stress paths during the strain softening portion of triaxial compression test. Though the predicted stresses do not decrease as a single straight line as in the triaxial compression test, the trend of predicted stress paths generally follows those measured in the laboratory. Figure 10-11 shows predicted and measured strain softening plotted as a function of plastic work. There is good agreement between the predicted and measured strain softening.

#### **10.4 CONCLUSIONS RELATED TO JOINT SIMULATION.**

A joint material model was developed based on the results of laboratory tests conducted on tensile fracture joints of Salem limestone. The proposed joint model is a first step in the development of more complicated models for in situ rock joints. In addition to multi-linear segments for the normal compressibility, the joint model has nine parameters describing elastic and elastoplastic responses with strain softening. These material parameters can be systematically extracted from laboratory test results as described in Section 10.2. The joint model can easily be adapted to a continuum based numerical simulation program to represent the discontinuities between intact rock blocks.

**Table 10-1. Plastic work at  $s=0.5$  tabulated as a function of normal stress.**

<b>Confining Pressure <math>\sigma'_{nc}</math> (MPa)</b>	<b>Average Normal Stress <math>\sigma'_n</math> (MPa)</b>	<b><math>W_{p,s=0.5}</math> in Displacement (MPa-mm)</b>	<b><math>W_{p,s=0.5}</math> in Strain (MPa)</b>
1	7.95	3.5	4.8
5	16.95	6.5	8.9
10	25.14	11.5	15.8
15	34.00	13.5	18.5
20	42.60	15.0	20.5

Note that joint thickness  $t=0.73$  mm is used to compute strains from displacements.

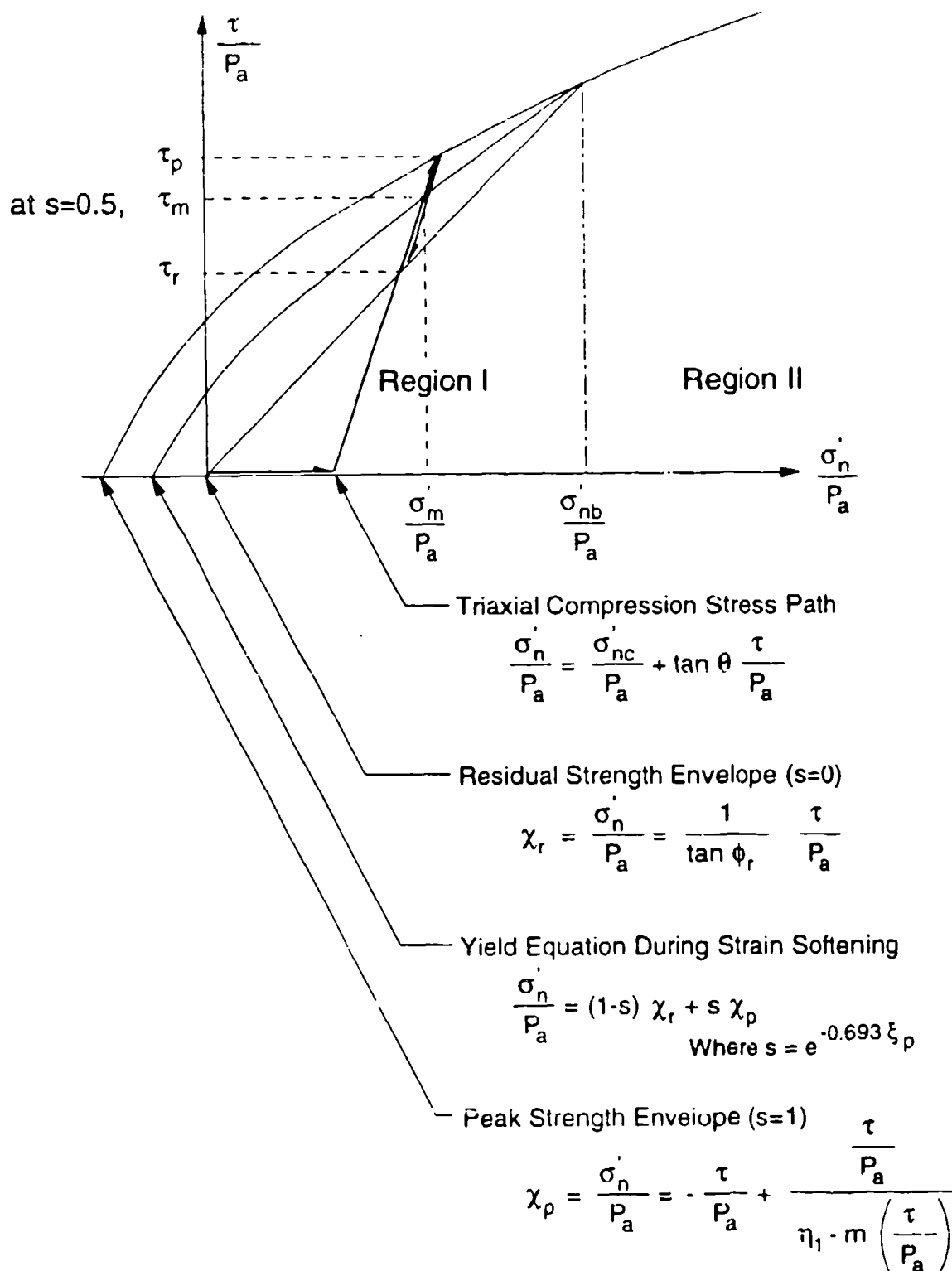


Figure 10-1. Illustration of the yield and strength envelopes for the joint model.

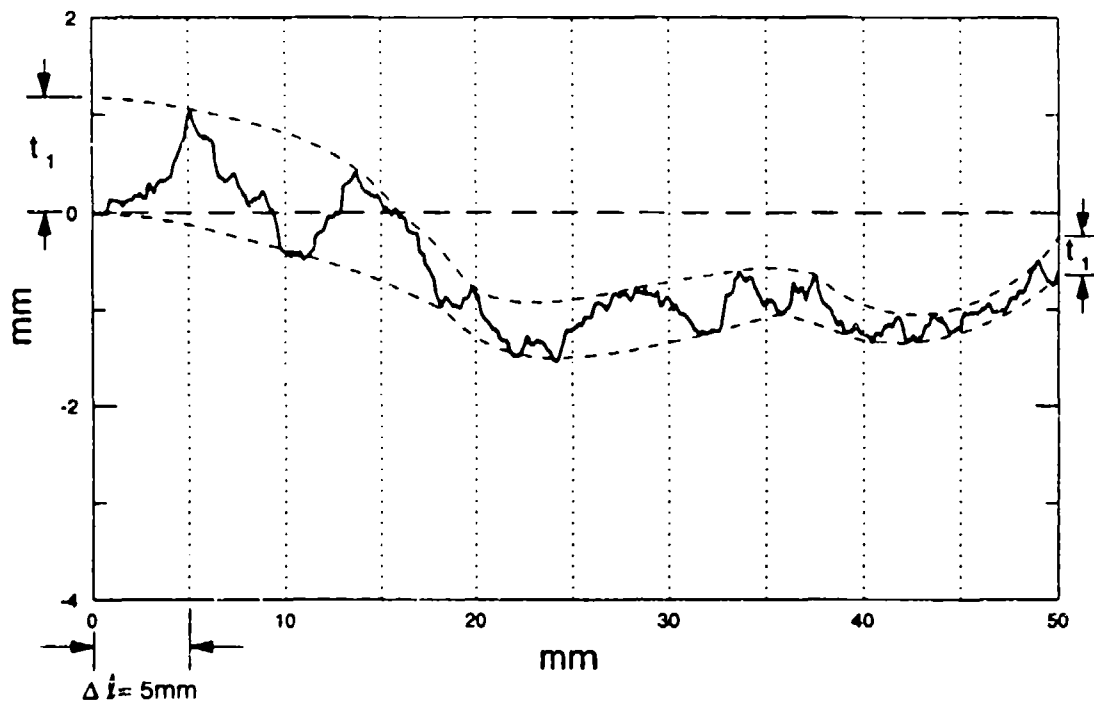


Figure 10-2. Measured joint roughness profile that was used to derive the joint thickness.



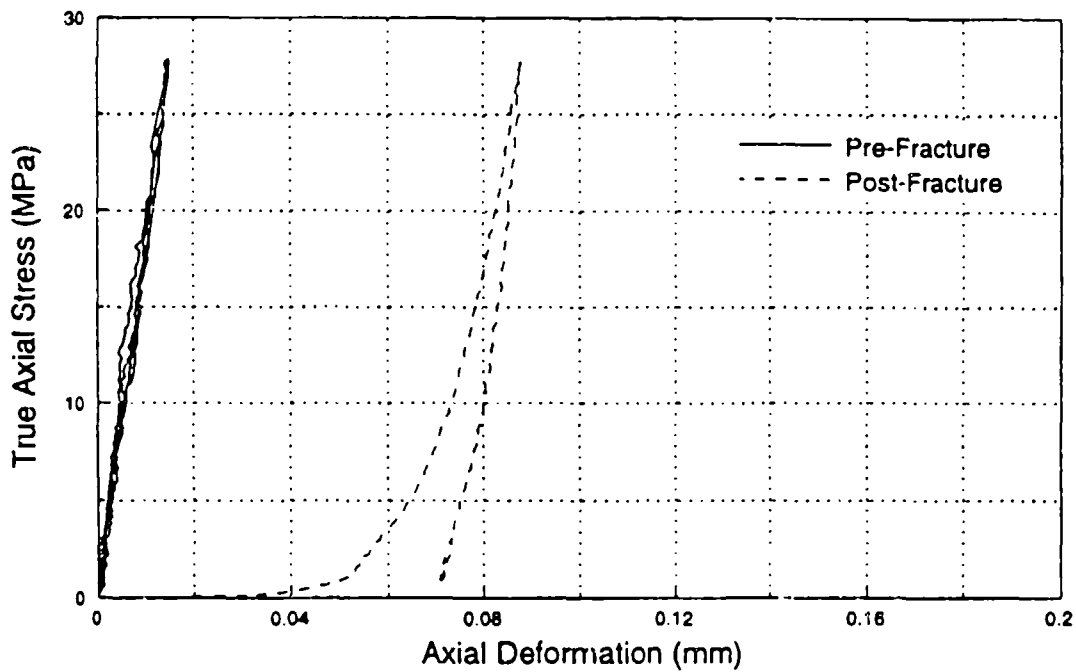


Figure 10-3a. Axial deformation measurements from an unconfined normal compressibility test on a tensile fracture joint.

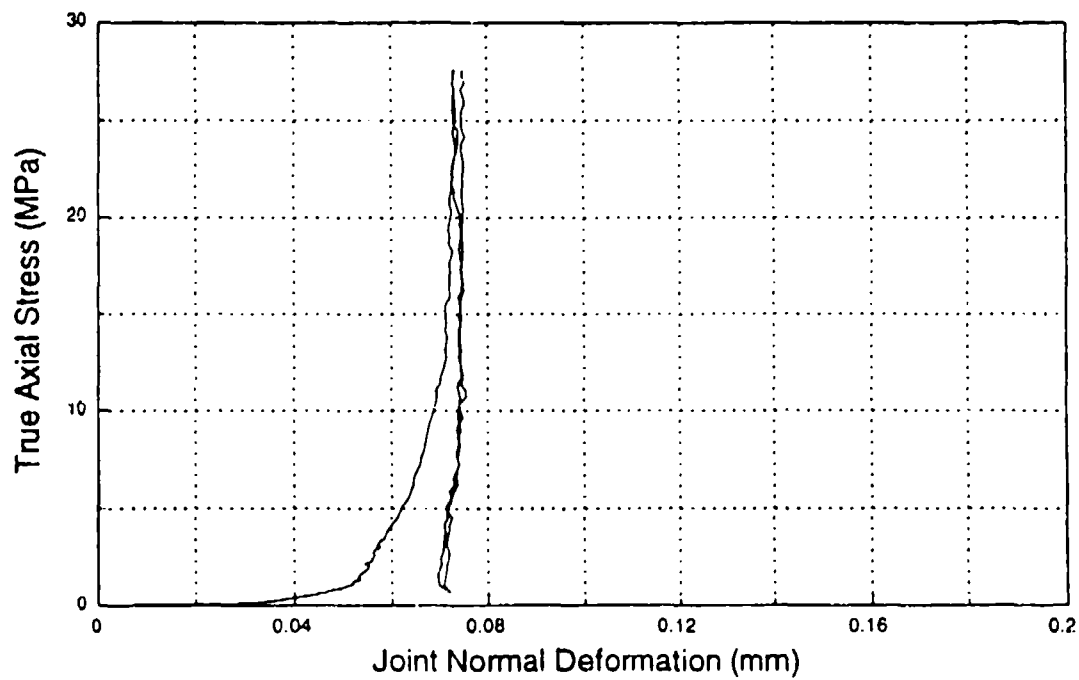


Figure 10-3b. Joint compressibility curve derived from the data shown in Figure 10-3a.

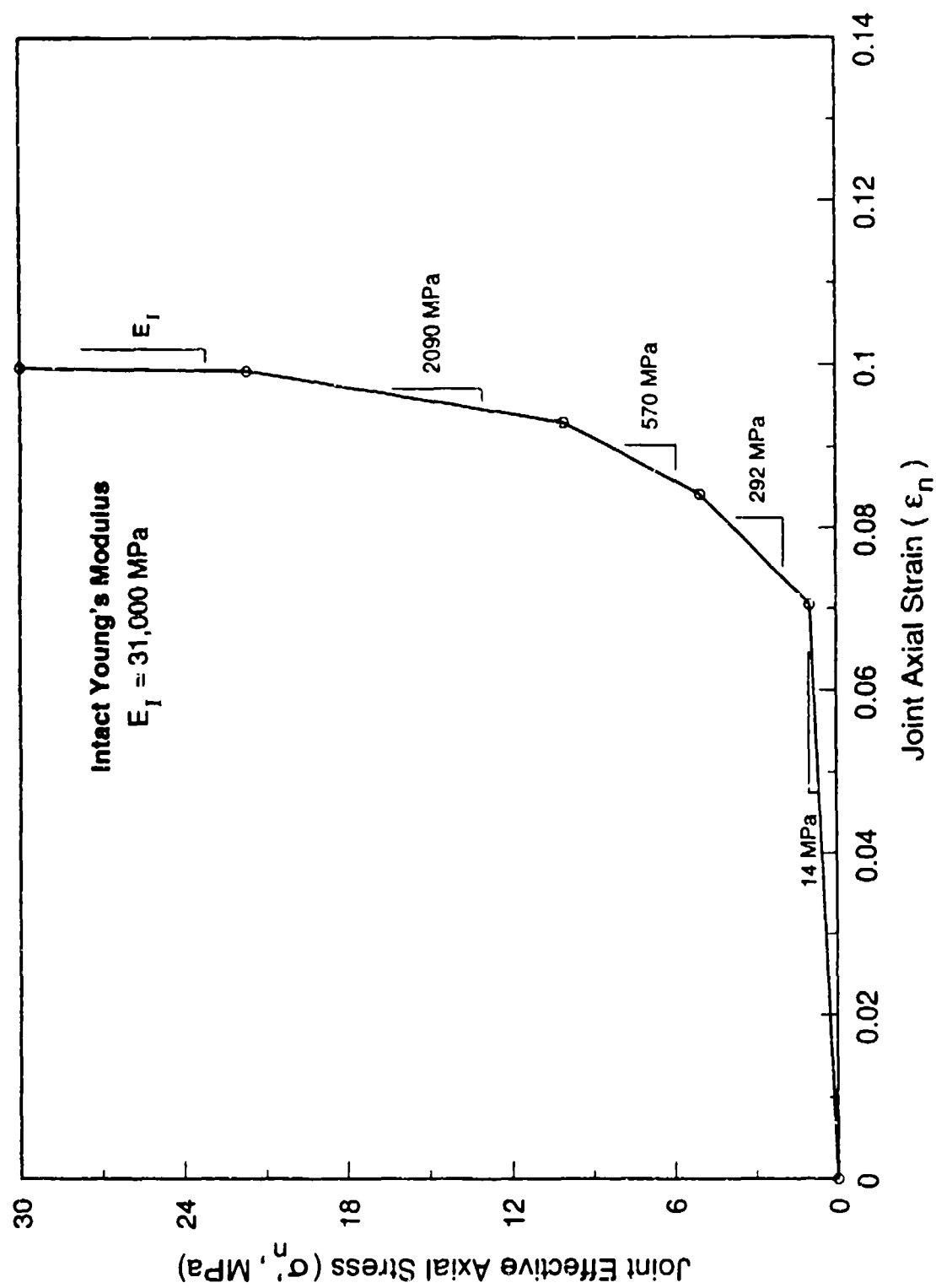


Figure 10-4. Nonlinear elastic modulus curve derived from the data shown in Figure 10-3a, assuming a joint thickness of 0.75 mm.

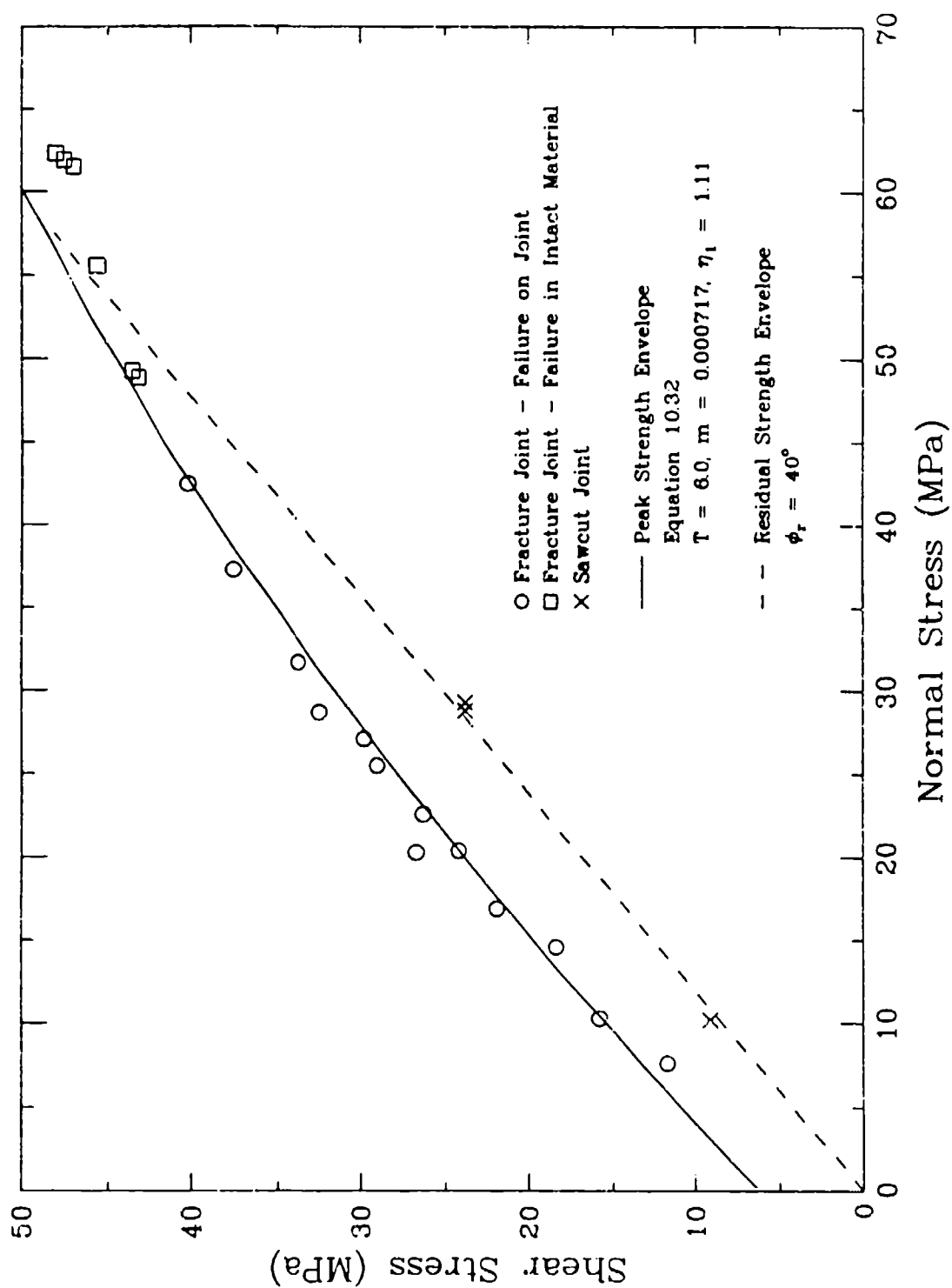


Figure 10-5. Strength data from triaxial compression tests on 30° jointed Salem limestone specimens (Ref. Chitty and Blouin, 1992) with fits used to derive the strength parameters for the joint model.

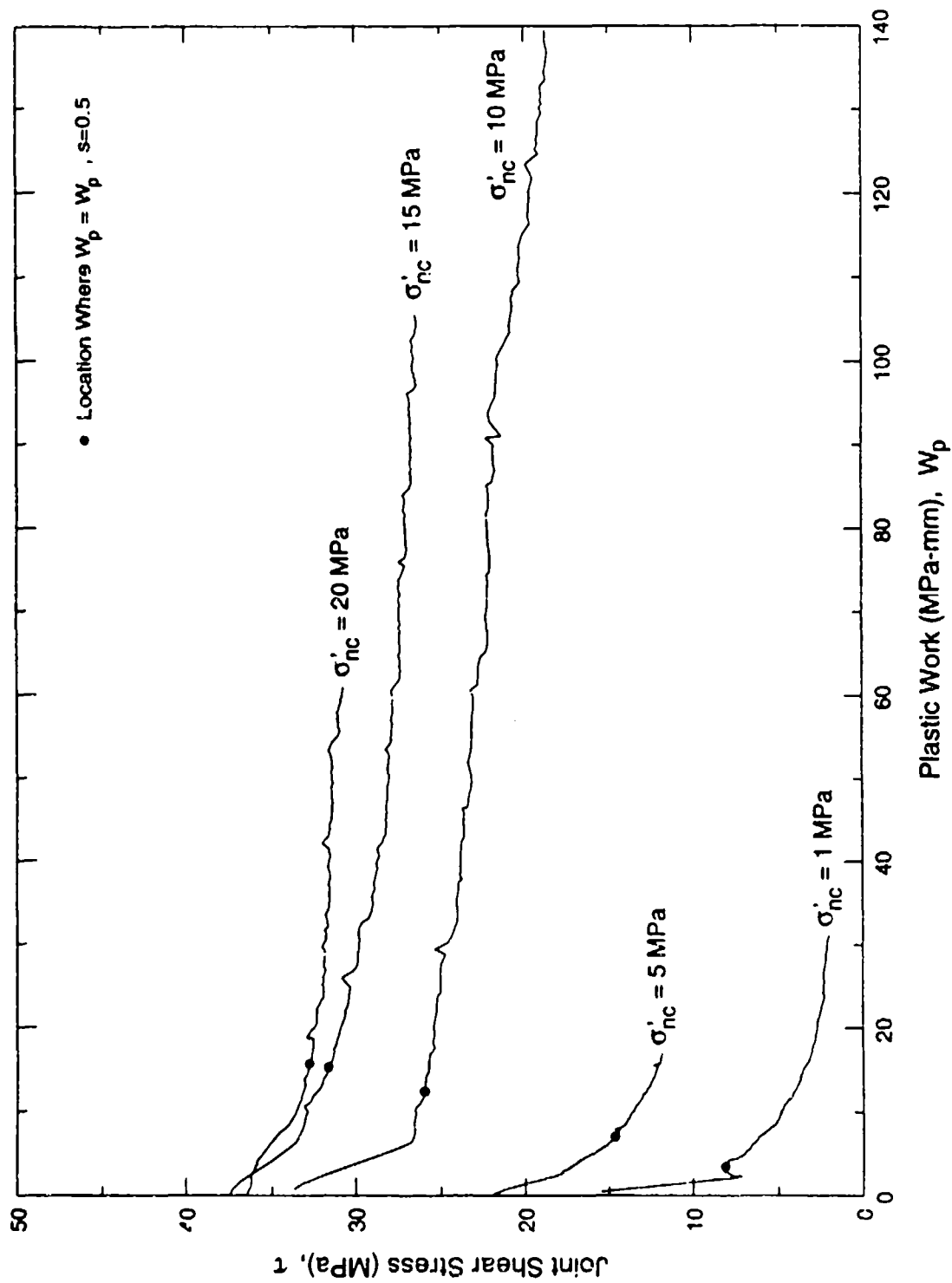


Figure 10-6. Relationships between joint shear stress and plastic work derived from triaxial compression tests at various confining pressures on 30° tensile fracture jointed specimens of Salem limestone.

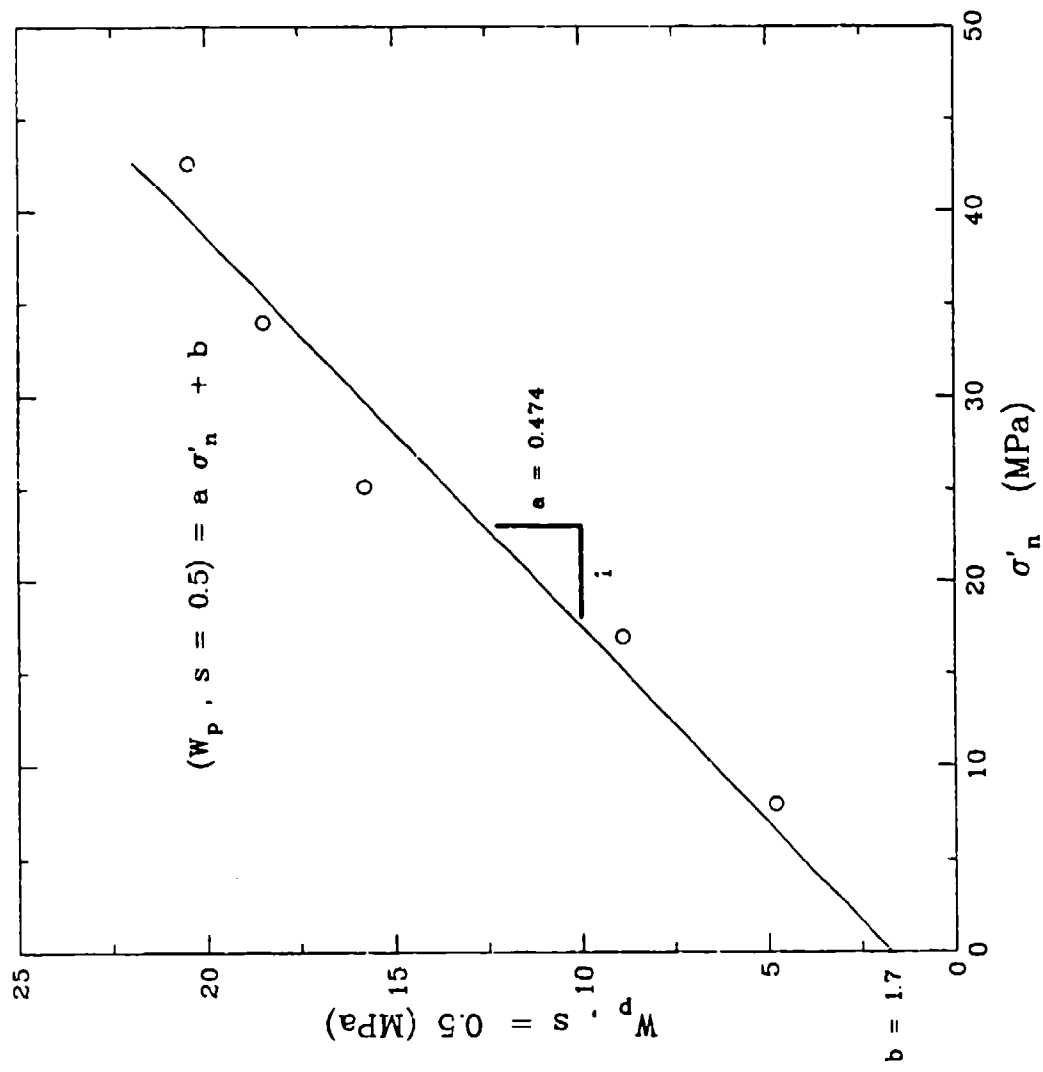


Figure 10-7. Definition of strain softening parameters during joint shear.

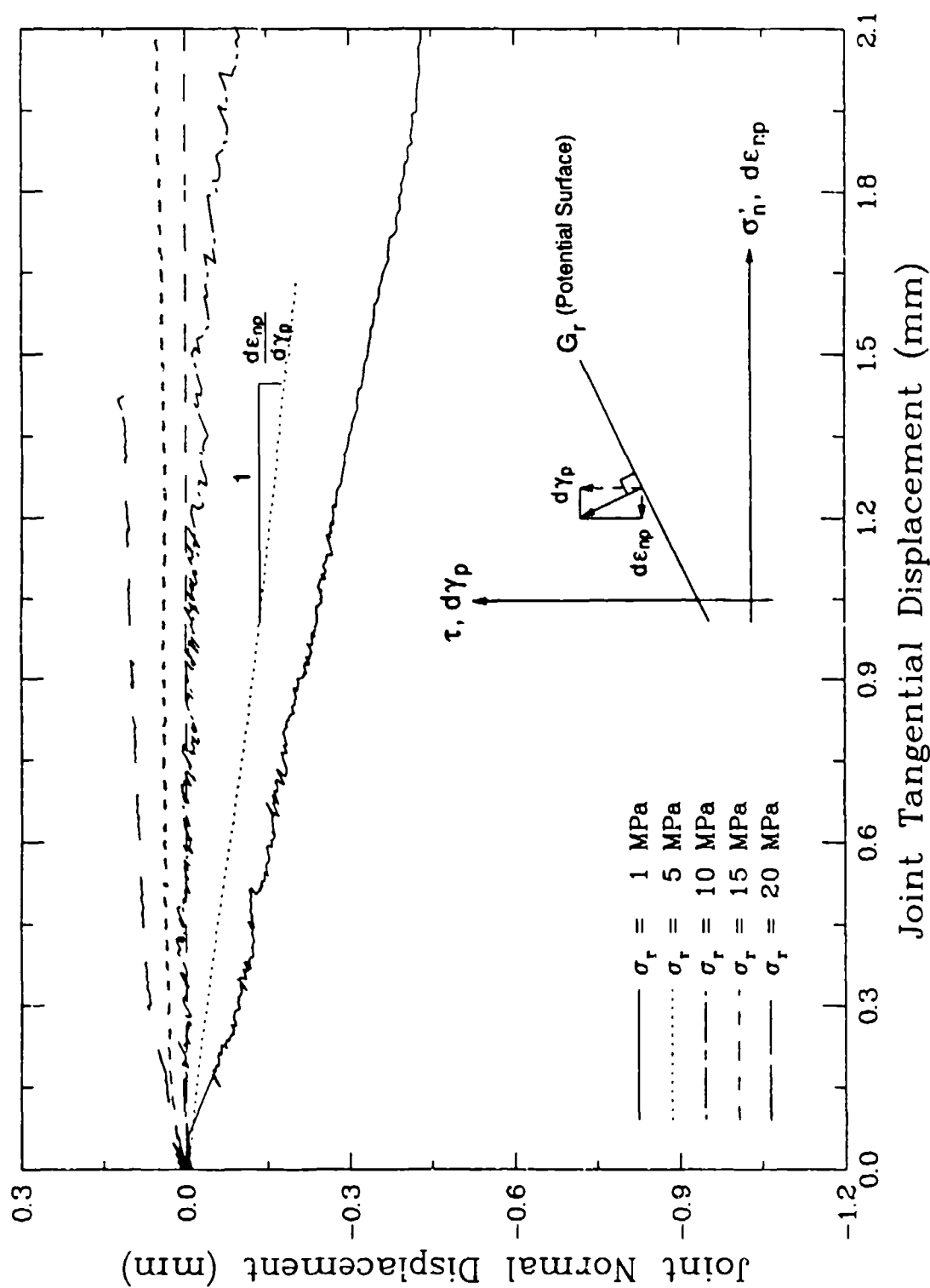


Figure 10-8. The relationship between normal and tangential joint displacement for tensile fracture joints in Salem limestone loaded in triaxial compression at a range of confining pressures.

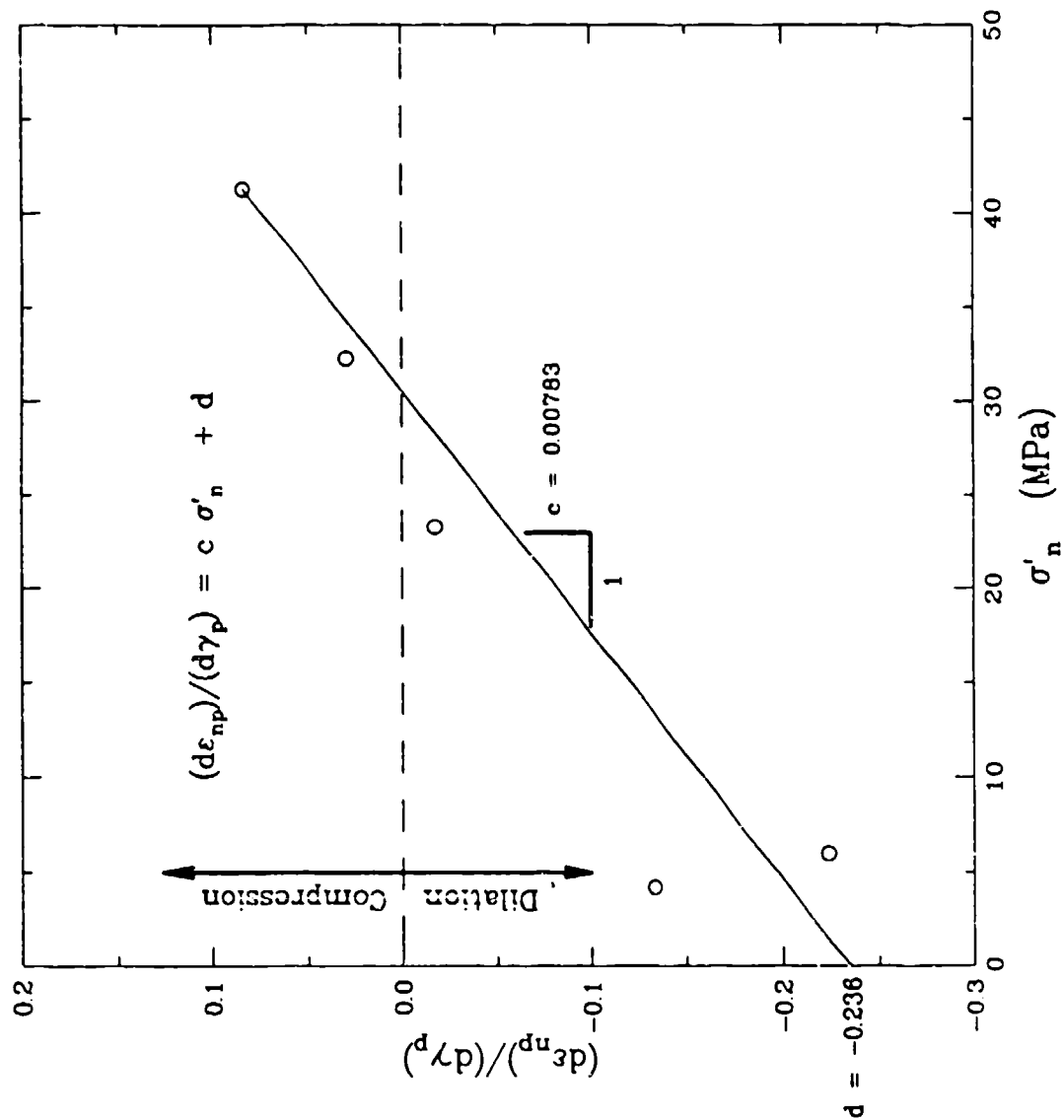


Figure 10-9. Direction of the plastic strain vector as a function of confining pressure.

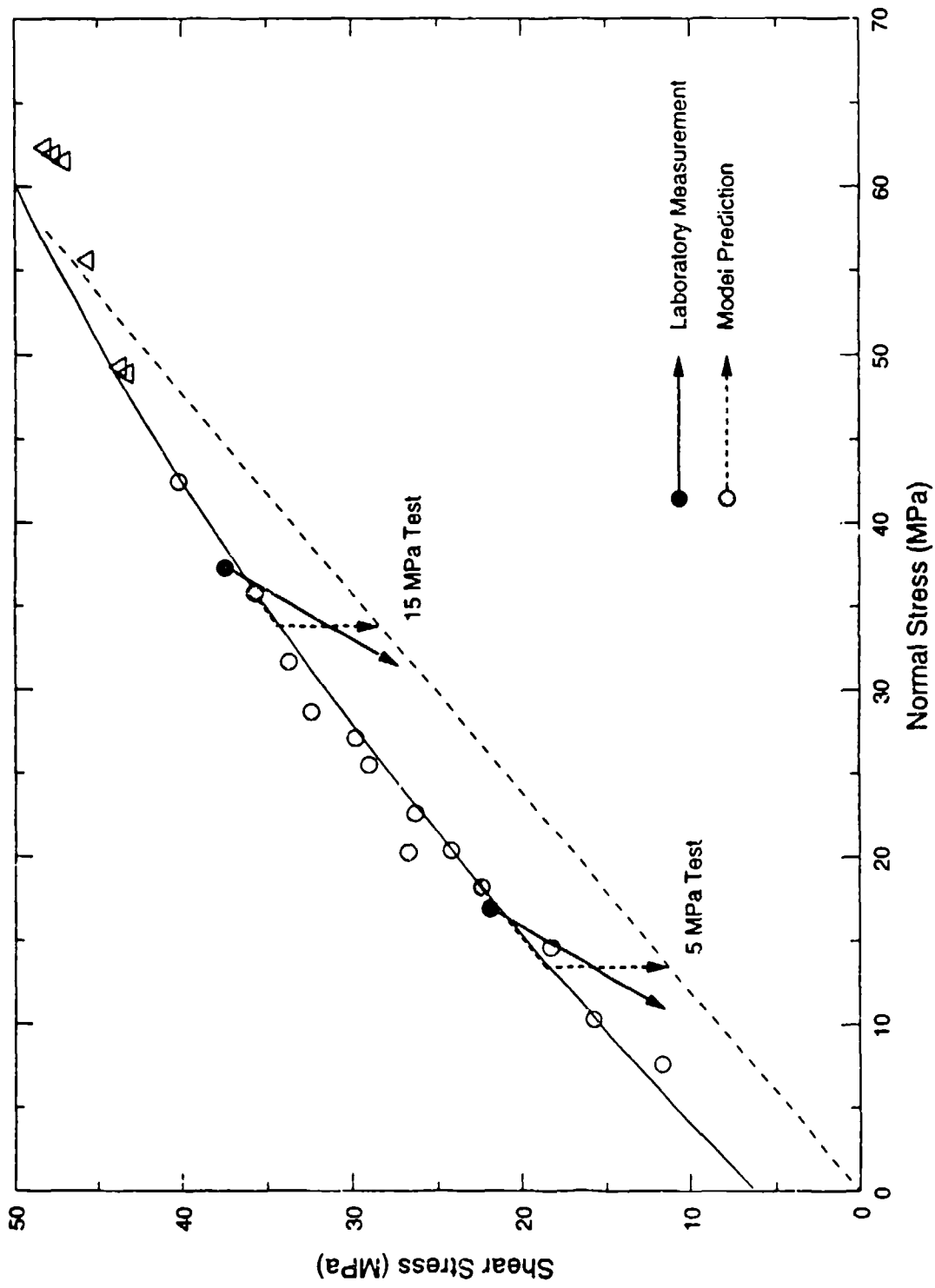


Figure 10-10. Stress paths computed from a specified strain loading for tensile fracture joints by the model.



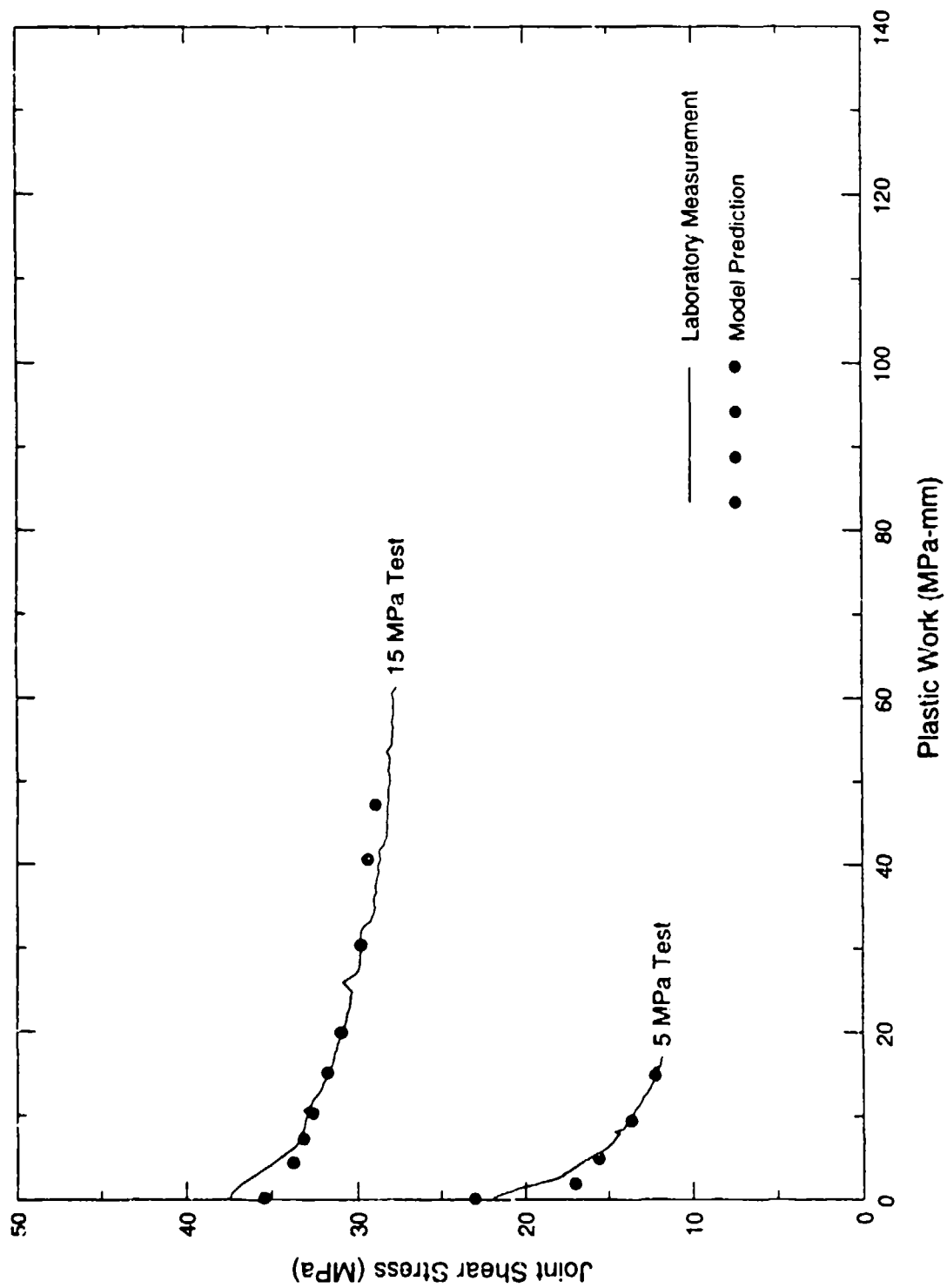


Figure 10-11. Relationships between joint shear stress and plastic work computed for tensile fracture joints by the model.

## SECTION 11

### ASTM/ISR INTERLABORATORY TEST PROGRAM

This section presents the results of laboratory rock property tests performed by ARA as part of the Interlaboratory Testing Program for Rock Properties, which is being conducted by the Institute for Standards Research, a subsidiary of the American Society for Testing and Materials. The laboratory work was performed by ARA's Materials Testing Laboratory located in South Royalton, Vermont during August and September 1991, and during May and June 1993.

The test program was conducted in two parts. Under Phase 1, ARA prepared and tested specimens of four different types of rock:

Barre granite	2.645 Mg/m <sup>3</sup>
Berea sandstone	2.150 Mg/m <sup>3</sup>
Salem limestone	2.265 Mg/m <sup>3</sup>
Tennessee marble	2.690 Mg/m <sup>3</sup>

After an extensive series dimensional and tolerance measurements, all four rock types were tested to determine ultrasonic wavespeeds in compression and shear; elastic constants and strength in unconfined compression; and splitting tensile strength. Under Phase 2 of the program, the same types of rock, except Salem limestone, were tested in triaxial compression to determine elastic constants and strength. The Phase 2 tests were performed on specimens that were supplied in finished form by the study's organizers.

#### 11.1 SPECIMEN PREPARATION AND MEASUREMENT.

For the Phase 1 tests, the rock materials were supplied to ARA in the form of cores with rough ends. The specimens for the Phase 2 tests were supplied in finished form with ground

ends. In both phases of the program, dimensional tolerance checks were made by the ARA laboratory prior to testing.

#### **11.1.1 Phase 1 Specimen Preparation.**

The sample material of all four rock types arrived at the ARA laboratory in the form of cores approximately 55 mm in diameter and 225 mm in length. Of each rock type four specimens were prepared with length to diameter ratio (L/D) in the range of 2.0 to 2.5 for unconfined compression testing, and four were prepared with L/D between 0.5 and 1.0 for splitting tensile tests.

The cores were cut to the required lengths and the ends were ground using a 170 grit diamond wheel on a precision surface grinder. The specimens for the unconfined compression tests were prepared with their ends parallel within 0.0005 in. over the specimen diameter. For each specimen that was to be tested in unconfined compression a complete dimensional tolerance check was performed in accordance with ASTM D 4543, and all specimens were in conformance with the specification prior to testing. In addition since the tests were not conducted with a spherical bearing head in the load path, the protocols for the interlaboratory test program required that the ends be parallel to each other within 0.0005 inch (0.013 mm) over the (nominal 54-mm) specimen diameter. Since no method was specified, determination of parallelism of the ends was based on the measurements were used to evaluate end flatness and perpendicularity, as specified by ASTM D 4543, Paragraph 5.2. Special care was taken with these measurements to ensure that the specimen was not moved in the V-block while both ends were measured.

#### **11.1.2 Phase 2 Specimen Preparation.**

For Phase 2 of the interlaboratory test program, the program organizers supplied the specimens to ARA in finished form with ground ends. These specimens were measured in the ARA laboratory to insure that they met the dimension tolerances specified by ASTM D 4543.

## 11.2 ULTRASONIC WAVESPEED MEASUREMENTS.

Ultrasonic compression and shear wavespeeds were measured in accordance with ASTM D 2845 on the Phase I test specimens prior to destructive testing. These measurements were made using two piezoelectric transducers, one to send and one to receive, and a 20 MHz digital storage oscilloscope to measure the transit time. The P-wavespeed measurements were made on the same specimens that were later used for the unconfined compression tests, having length to diameter ratio approximately equal to two ( $L/D \approx 2$ ). Since the shear waves were highly attenuated over the 100-mm length of the unconfined compression test specimens, the shear wavespeeds were measured on the splitting tensile test specimens which had  $L/D < 1$ .

The results of the wavespeed determinations are summarized for each rock type in Tables 11-1 through 11-4. Each table presents the mean of the five wavespeed measurements for each specimen of a given rock type, and the mean and standard deviation of the individual specimen means.

## 11.3 UNCONFINED COMPRESSION TESTS.

Elastic constants and unconfined strengths were determined from unconfined compression tests conducted in accordance with ASTM D 3148 and D 2938. The tests were performed in a press designed by ARA that is typically used for triaxial compression testing of rocks at confining pressures up to 400 MPa and axial loads up to 3.5 MN. It is a four-column frame with movable crosshead. In the unstressed condition, the upper and lower loading surfaces are parallel within 0.005 mm (0.0002 inches) over their entire 3-inch diameter. The machine is not equipped with a spherical head. This is the same machine used to conduct the Pilot Tests.

Aluminum rings of slightly larger diameter than the test specimen were attached near the top and bottom of the specimen by means of three set screws with conical pointed tips spaced  $120^\circ$  apart. The two axial LVDTs were attached to the rings at diametrically opposite locations. The LVDT body was attached to the top ring and a rod connected to the LVDT core was affixed

to the bottom ring. This resulted in a gage length of approximately 0.40 inches less than the specimen length. A third floating ring was used to hold a single radial LVDT. The radial LVDT was clamped to the ring with the core rod spring loaded to maintain contact with the specimen. A screw on the opposite side of the ring served as a reference point for the radial deformation measurement. A strain gage bridge load cell in the load path provided a measurement of the applied load. The load and deformation measurements were digitized at 1-second intervals and recorded by a microcomputer based digital data acquisition system.

Tables 11-5 through 11-8 present the unconfined compressive strength and values of elastic modulus and Poisson's ratio determined at 25%, 50%, and 75% of the unconfined strength. The modulus and Poisson's ratio values were determined by a least squares fit to the appropriate data set over a range of  $\pm 5\%$  of the unconfined strength around the nominal value. Plots of the measured axial and radial strain against axial stress and of axial strain against radial strain are presented in Appendix F for each test specimen.

#### **11.4 SPLITTING TENSILE STRENGTH TESTS.**

Splitting tensile strengths of the four rock types were determined in accordance with ASTM D3967, as modified by the protocols. The tests were performed in the same load frame as the unconfined compression tests. As instructed by the test protocol, bearing strips were from the cardboard approximately 0.7 mm thick. The specimens loaded on the orientation line that was marked on the specimen material provided by the committee. The times for loading the various specimens ranged between 3 and 6 minutes. In all cases, failures occurred along the plane of loading. Tables 11-9 through 11-12 present the test results including specimen dimensions and summary statistics.

#### **11.5 TRIAXIAL COMPRESSION TESTS.**

Triaxial compression tests were performed under Phase 2 of the interlaboratory test program on specimens of three rock types, Barre granite, Berea sandstone, and Tennessee

marble. Four specimens each of three different rock types were tested at confining pressures of 10, 25, and 40 MPa, for a total of 36 tests. The tests were performed in a triaxial apparatus which was designed by ARA, and has closed-loop servo control of both the confining pressure and axial loading piston. It is a four-column frame with movable crosshead. In the unstressed condition, the upper and lower loading surfaces are parallel within 0.005 mm (0.0002 inches) over their entire 3-inch diameter. The machine is not equipped with a spherical head.

All specimens were oven dried prior to testing. The tests were performed with the test specimens at room temperature (approx. 20°C). In preparation for testing, each specimen was placed between hardened steel endcaps without lubricating materials. To separate the specimen from the confining fluid, a jacket of heat-shrinkable polyolefin tubing was placed over the specimen and shrunk to a tight fit. The ends of the jacket were sealed to the steel endcaps with epoxy adhesive and held in place with wire clamps.

Measurements of specimen deformations were made with two axial LVDTs and two radial LVDTs placed as indicate in Figure 4-1. Two radial deformation measurements were made at locations oriented 90° to each other. The two radial gages were as close as practical to mid-height of the specimen, one approximately 10 mm below and the other approximately 10 mm above. In both the axial and radial directions, the two deformation gage outputs were averaged and scaled to obtain the reported radial deformation strains. The axial load was measured with a load cell placed directly on top of the top cap, inside the pressure vessel. This location avoids any errors due to seal friction. The load cell consists of a solid steel cylinder with eight strain gages wired into a full bridge. The load cell was designed and built by ARA. The load and deformation measurements were digitized at 1-second intervals and recorded by a microcomputer based digital data acquisition system. The calibrations of all of the instruments used to measure the pressure, load, and deformation are traceable to NIST.

Tables 11-13 through 11-15 present the values of elastic modulus and Poisson's ratio determined by least squares fits to the appropriate data sets over the ranges, 25-50% of peak axial load and 40-60% of peak axial load for Barre granite, Berea sandstone and Tennessee

Marble, respectively. Each fit included approximately 50 data points. Appendix F contains a complete set of response data from the triaxial compression tests, including plots of axial and radial strain against stress difference and of axial strain against radial strain.

Table 11-1. Summary of ultrasonic wavespeed measurements on Barre granite.

Specimen ID	Rock Type	Compression (km/s)	Shear (km/s)
BG/91/1-7	Barre Granite	3.54	2.30
BG/91/2-15	Barre Granite	3.52	2.48
BG/91/3-4	Barre Granite	3.53	2.55
BG/91/5-4	Barre Granite	3.53	2.50
BG/91/6-8	Barre Granite	3.57	2.48
	Mean	3.54	2.46
	Std.Dev.	0.017	0.085
	Coef. of Var.	0.49%	3.45%



Table 11-2. Summary of ultrasonic wavespeed measurements on Berea sandstone.

Specimen ID	Rock Type	Compression (km/s)	Shear (km/s)
BS/91/1-7/1	Berea Sandstone	2.13	1.51
BS/91/2-15	Berea Sandstone	2.20	1.43
BS/91/3-4	Berea Sandstone	2.18	1.51
BS/91/4-1	Berea Sandstone	2.07	1.48
BS/91/4-16	Berea Sandstone	1.99	1.46
	Mean	2.11	1.48
	Std.Dev.	0.077	0.031
	Coef. of Var.	3.62%	2.07%

Table 11-3. Summary of ultrasonic wavespeed measurement on Salem limestone.

Specimen ID	Rock Type	Compression (km/s)	Shear (km/s)
SL/91/1-7	Salem Limestone	4.30	2.48
SL/91/2-4	Salem Limestone	4.35	2.36
SL/91/3-3	Salem Limestone	4.32	2.35
SL/91/3-20	Salem Limestone	4.34	2.40
SL/91/4-15	Salem Limestone	4.37	2.37
	Mean	4.34	2.39
	Std.Dev.	0.024	0.047
	Coef. of Var.	0.56%	1.97%

Table 11-4. Summary of ultrasonic wavespeed measurements on Tennessee marble.

Specimen ID	Rock Type	Compression (km/s)	Shear (km/s)
TM/91/1/2-19	Tennessee Marble	5.98	3.48
TM/91/3/2-19B	Tennessee Marble	6.40	3.28
TM/91/4/1-2 T&B	Tennessee Marble	6.26	3.41
TM/91/4/2-5 T&B	Tennessee Marble	6.27	3.29
TM/91/4/2-20	Tennessee Marble	6.36	3.35
	Mean	6.25	3.36
	Std.Dev.	0.147	0.075
	Coef. of Var.	2.35%	2.24%

Table 11-5. Summary of unconfined compression test data for Barre granite.

Specimen ID	Unconfined Compressive Strength (MPa)	Elastic Modulus (GPa) at fraction of Unconfined Strength			Poisson's Ratio at fraction of Unconfined Strength		
		25%	50%	75%	25%	50%	75%
BG/91/1-7	222.0	47.17	54.19	52.30	0.180	0.302	0.504
BG/91/2-15	219.0	45.99	54.15	52.72	0.160	0.261	0.423
BG/91/3-4	221.7	47.32	55.30	53.44	0.171	0.264	0.447
BG/91/5-4	220.0	47.78	56.25	55.67	0.166	0.264	0.427
BG/91/6-8	216.9	50.06	57.96	53.37	0.151	0.265	0.406
Mean	219.4	47.79	55.92	53.80	0.162	0.264	0.426
Std. Dev.	1.736	1.467	1.395	1.116	0.007	0.002	0.015
Coef. of Var.	0.79%	3.07%	2.50%	2.07%	4.60%	0.57%	3.43%

Table 11-6. Summary of unconfined compression test data for Berea sandstone.

Specimen ID	Unconfined Compressive Strength (MPa)	Elastic Modulus (GPa) at fraction of Unconfined Strength			Poisson's Ratio at fraction of Unconfined Strength		
		25%	50%	75%	25%	50%	75%
BS/91/1-7/1	65.9	12.79	17.58	17.73	0.251	0.457	0.835
BS/91/2-15	66.4	12.68	17.08	17.11	0.279	0.467	0.846
BS/91/3-4	66.0	13.06	17.25	17.28	0.254	0.461	0.878
BS/91/4-1	66.7	13.29	17.61	17.46	0.338	0.516	0.915
BS/91/4-16	64.7	12.95	17.66	17.26	0.325	0.540	0.907
Mean	65.94	12.95	17.44	17.37	0.29	0.49	0.88
Std. Dev.	0.683	0.213	0.231	0.211	0.036	0.034	0.032
Coef. of Var.	1.04%	1.64%	1.32%	1.21%	12.45%	6.86%	3.61%

Table 11-7. Summary of unconfined compression test data for Salem limestone.

Specimen ID	Unconfined Compressive Strength (MPa)	Elastic Modulus (GPa) at fraction of Unconfined Strength			Poisson's Ratio at fraction of Unconfined Strength		
		25%	50%	75%	25%	50%	75%
SL/91/1-7	58.2	30.81	29.53	24.73	0.236	0.307	0.474
SL/91/2-14	59.2	32.78	31.58	26.22	0.234	0.311	0.458
SL/91/3-3	59.3	32.62	31.53	26.52	0.241	0.311	0.461
SL/91/3-20	59.5	32.93	31.56	25.90	0.262	0.318	0.426
SL/91/4-15	61.5	32.89	31.26	26.66	0.247	0.313	0.475
Mean	59.54	32.41	31.09	26.01	0.24	0.31	0.46
Std. Dev.	1.078	0.808	0.791	0.689	0.010	0.004	0.018
Coef. of Var.	1.81%	2.49%	2.55%	2.65%	4.11%	1.13%	3.85%

Table 11-8. Summary of unconfined compression test data for Tennessee marble.

Specimen ID	Unconfined Compressive Strength (MPa)	Elastic Modulus (GPa) at fraction of Unconfined Strength			Poisson's Ratio at fraction of Unconfined Strength		
		25%	50%	75%	25%	50%	75%
TM/91/1/2-19	126.6	70.56	68.49	58.11	0.267	0.301	0.397
TM/91/3/2-19B	143.9	81.74	85.74	72.62	0.318	0.359	0.430
TM/91/4/1-2B	140.8	75.90	77.75	73.18	0.286	0.328	0.351
TM/91/4/2-5B	145.0	79.96	78.96	69.92	0.315	0.328	0.429
TM/91/4/2-20	154.5	76.38	73.26	65.15	0.322	0.351	0.422
Mean	142.16	76.91	76.84	67.80	0.30	0.33	0.41
Std. Dev.	9.026	3.855	5.781	5.616	0.021	0.020	0.030
Coef. of Var.	6.35%	5.01%	7.52%	8.28%	7.12%	6.10%	7.34%

Table 11-9. Splitting tensile strength data for Barre granite.

Specimen ID	Rock Type	Specimen Length (in.)	Specimen Diameter (in.)	Dry Mass (g)	Tensile Strength (MPa)
BG/91/1-7	Barre Granite	1.655	2.169	264.4	16.17
BG/91/2-15	Barre Granite	1.595	2.169	255.1	13.77
BG/91/3-4	Barre Granite	1.591	2.169	254.2	14.12
BG/91/5-4	Barre Granite	1.629	2.168	260.1	14.46
BG/91/6-8	Barre Granite	1.594	2.172	255.5	14.33
				Mean	14.57
				Std. Dev.	0.833
				Coef. of Var.	5.72%



Table 11-10. Splitting tensile strength data for Berea sandstone.

Specimen ID	Rock Type	Specimen Length (in.)	Specimen Diameter (in.)	Dry Mass (g)	Tensile Strength (MPa)
BS/91/1-7/1	Berea Sandstone	1.648	2.148	207.2	3.94
BS/91/2-15	Berea Sandstone	1.689	2.152	213.7	3.86
BS/91/3-4	Berea Sandstone	1.667	2.157	212.7	4.04
BS/91/4-1	Berea Sandstone	1.649	2.169	211.0	3.61
BS/91/4-16	Berea Sandstone	1.619	2.169	207.9	3.77
				Mean	3.84
				Std. Dev.	0.147
				Coef. of Var.	3.83%

Table 11-11. Splitting tensile strength data for Salem limestone.

Specimen ID	Rock Type	Specimen Length (in.)	Specimen Diameter (in.)	Dry Mass (g)	Tensile Strength (MPa)
SL/91/1-7	Salem Limestone	1.639	2.161	221.1	5.09
SL/91/2-14	Salem Limestone	1.658	2.160	225.7	5.74
SL/91/3-3	Salem Limestone	1.608	2.160	217.3	5.35
SL/91/3-20	Salem Limestone	1.645	2.160	222.6	5.41
SL/91/4-15	Salem Limestone	1.666	2.163	227.1	5.35
				Mean	5.39
				Std. Dev.	0.208
				Coef. of Var.	3.86%

Table 11-12. Splitting tensile strength data for Tennessee marble.

Specimen ID	Rock Type	Specimen Length (in.)	Specimen Diameter (in.)	Dry Mass (g)	Tensile Strength (MPa)
TM/91/1/2-19	Tennessee Marble	1.690	2.168	274.4	10.60
TM/91/3/2-19B	Tennessee Marble	1.669	2.161	269.8	8.20
TM/91/4/1-2T	Tennessee Marble	1.666	2.173	272.1	11.94
TM/91/4/2-5T	Tennessee Marble	1.613	2.171	263.2	11.27
TM/91/4/2-20	Tennessee Marble	1.645	2.171	268.6	11.01
				Mean	10.60
				Std. Dev.	1.278
				Coef. of Var.	12.06%

Table 11-13. Summary of triaxial compression test results on Barre granite.

Specimen ID	Test ID	Confining Pressure (MPa)	Elastic Modulus (GPa)		Poisson's Ratio		Ultimate Strength (MPa)	Strain at Ultimate Strength (%)
			25-50% of Ultimate Strength	40-60% of Ultimate Strength	25-50% of Ultimate Strength	40-60% of Ultimate Strength		
BG/91/1-1B	U2E3	10	55.38	56.35	0.254	0.296	289.4	0.655
BG/91/1-8T	U3B3	10	55.15	56.04	0.253	0.299	291.1	0.661
BG/91/3-1B	U2F3	10	54.97	55.90	0.251	0.295	287.0	0.659
BG/92/1/1-3	U3A3	10	55.31	56.45	0.248	0.293	292.1	0.665
Mean		10	55.20	56.17	0.252	0.296	289.9	0.660
Standard Deviation		10	00.16	00.22	0.002	0.002	1.9	0.004
BG/91/1-4B	U3E3	25	59.29	58.71	0.277	0.314	366.8	0.807
BG/92/1/1-24	U3C3	25	59.27	59.07	0.278	0.319	370.3	0.813
BG/92/1/1-27	U3D3	25	59.19	58.75	0.269	0.316	364.9	0.803
BG/92/1/2-13	U4A3	25	58.64	58.07	0.267	0.313	368.9	0.810
Mean		25	59.10	58.65	0.273	0.316	367.7	0.808
Standard Deviation		25	0.27	0.36	0.005	0.002	2.1	0.004
BG/91/1-12B	U4B3	40	60.92	59.84	0.289	0.327	434.5	0.934
BG/91/2-17T	U4E3	40	60.53	59.25	0.277	0.312	429.3	0.937
BG/91/6-4T	U4C3	40	60.61	59.15	0.292	0.328	428.8	0.930
BG/92/1/1-30	U4D3	40	61.27	59.92	0.289	0.326	432.3	0.936
Mean		40	60.83	59.54	0.287	0.323	431.2	0.934
Standard Deviation		40	0.29	0.34	0.006	0.007	2.3	0.003

Table 11-14. Summary of triaxial compression test results on Berea sandstone.

Specimen ID	Test ID	Confining Pressure (MPa)	Elastic Modulus (GPa)			Poisson's Ratio		Ultimate Strength (MPa)	Strain at Ultimate Strength (%)
			25-50% of Ultimate Strength	40-60% of Ultimate Strength	25-50% of Ultimate Strength	40-60% of Ultimate Strength			
BS/91/1-1	Y26C3	10	20.54	20.52	0.270	0.328	125.2	0.834	
BS/92/7/3-3	Y26D3	10	20.59	20.51	0.261	0.316	124.1	0.785	
BS/92/7/3-8	Y26A3	10	20.58	20.53	0.259	0.316	127.0	0.846	
BS/92/8/1-3	Y26B3	10	20.44	20.39	0.267	0.327	124.5	0.832	
Mean		10	20.54	20.49	0.264	0.322	125.2	0.824	
Standard Deviation		10	0.06	0.06	0.004	0.006	1.1	0.023	
BS/91/3-19T	Y27A3	25	22.10	21.23	0.223	0.263	175.9	1.117	
BS/92/7/1-10	Y26E3	25	22.47	21.52	0.230	0.271	174.6	1.085	
BS/92/7/2-18	Y27B3	25	22.01	21.12	0.228	0.271	166.6	1.048	
BS/92/7/3-6	Y27C3	25	22.23	20.63	0.228	0.260	173.2	1.045	
Mean		25	22.20	21.13	0.227	0.266	172.6	1.074	
Standard Deviation		25	0.17	0.32	0.003	0.005	3.6	0.030	
BS/91/1-8T	Y27E3	40	23.04	21.73	0.206	0.236	208.4	1.220	
BS/91/4-2T	Y27D3	40	22.95	21.70	0.203	0.234	207.2	1.187	
BS/91/4-4T	Y28A3	40	23.21	21.87	0.209	0.240	211.0	1.234	
BS/92/7/1-14	Y27F3	40	23.14	21.80	0.209	0.240	208.3	1.229	
Mean		40	23.09	21.78	0.207	0.238	208.7	1.218	
Standard Deviation		40	0.10	0.07	0.002	0.003	1.4	0.18	

Table 11-15. Summary of triaxial compression test results on Tennessee marble.

Specimen ID	Test ID	Confining Pressure (MPa)	Elastic Modulus (GPa)			Poisson's Ratio		Ultimate Strength (MPa)	Strain at Ultimate Strength (%)
			25-50% of Ultimate Strength	40-60% of Ultimate Strength	25-50% of Ultimate Strength	40-60% of Ultimate Strength			
TM/91/1/1-4	Y28D3	10	67.95	63.28	0.283	0.315	154.6	0.332	
TM/91/2/2-22	Y28B3	10	73.08	69.95	0.303	0.317	184.6	0.351	
TM/92/5/2-2	Y28C3	10	67.50	63.23	0.288	0.316	160.9	0.349	
TM/92/5/4-3	U1A3	10	65.92	61.97	0.294	0.320	159.4	0.353	
Mean		10	68.61	64.61	0.292	0.317	164.9	0.346	
Standard Deviation		10	2.69	3.13	0.007	0.002	11.6	0.008	
TM/91/1/2-23	U1B3	25	67.60	60.82	0.317	0.341	189.6	0.522	
TM/91/2/1-2	U1E3	25	72.02	66.23	0.318	0.334	224.2	0.520	
TM/92/5/1-2	U1C3	25	65.52	58.83	0.313	0.341	183.4	0.499	
TM/92/5/2-18	U1D3	25	69.72	64.87	0.316	0.339	204.5	0.521	
Mean		25	68.72	62.69	0.316	0.339	200.4	0.516	
Standard Deviation		25	2.42	2.99	0.002	0.003	15.7	0.010	
TM/91/1/2-15	U2C3	40	68.96	63.04	0.320	0.339	224.6	0.749	
TM/91/4/8-6/B	U2A3	40	70.30	63.01	0.332	0.350	234.5	0.700	
TM/92/5/2-10	U2D3	40	68.72	63.31	0.330	0.344	227.5	0.757	
TM/92/5/2-15	U2B3	40	67.34	62.05	0.331	0.353	228.7	0.781	
Mean		40	68.83	62.85	0.328	0.347	228.8	0.747	
Standard Deviation		40	1.05	0.48	0.005	0.005	3.6	0.029	

## SECTION 12

### SUMMARY AND CONCLUSIONS

This document reports the results of a program of laboratory test and supporting analysis that was conducted to investigate the mechanical response of porous jointed rock. The research addressed a variety of related topics, all designed to support development of first principles methodologies for simulation and prediction of the response of in situ rock masses to explosive loading. The tests were performed on a very uniform porous limestone from the Salem formation near Bedford, Indiana, USA. While a standard mechanical characterization of the intact rock was included in the program, it emphasized the mechanical behavior of joints and fluid flow through intact rock and rock joints. The following summarizes the major findings of the research effort.

- The test program included a complete physical and mechanical characterization of the Salem limestone, including bulk and grain densities, compressional and shear wavespeeds, hydrostatic compression and uniaxial strain tests at confining pressures up to 400 MPa, and triaxial compression tests to define the strength envelope at confining pressures up to 400 MPa, but emphasizing pressures less than 50 MPa. A series of unconfined compression tests on specimens with varying water contents showed that the strength of an oven dried specimen is approximately 20% greater than a nominally identical specimen with 2% or greater water content.
- Three different types of man-made joint surfaces were developed for strength/deformation and permeability testing. Tensile fracture joints were made by splitting intact pieces of limestone between knife edges. A lower bound on joint strength was developed from tests on smooth ground surfaces. A technique was developed to reproducibly synthesize mating surfaces using a fractal representation of the surface topography and numerically controlled machine tools to create the surface.

- The tensile fracture and synthetic joints were characterized using a laser profilometer and the fractal dimensions were determined.
- Strengths of the three types of joints were measured in triaxial compression tests on cylindrical specimens with joints oriented at  $30^\circ$  to the cylinder axes. Strength envelopes were defined in Mohr's circle space for the three joint types as well as the intact rock. At 35 MPa confining pressure (75 MPa normal stress), all three joint types behave like intact rock. At lower confining pressures, the tensile fracture joints reach a peak strength at which point the asperities begin to shear off and the stress that the joint will support drops to a residual strength level. The synthesized joints behave in a similar manner except that, due to imperfect mating, the peak strength is lower than a tensile fracture with the same roughness amplitude tested under the same conditions. Under shear loading, smooth ground surfaces reach a strength limit slightly less than the residual strength of the other joint types, which remains essentially constant under additional shearing.
- At confining pressures less than about 10 MPa, the tensile fracture and synthetic joints tend to dilate under shear loading, while at higher pressures, they undergo a slight compaction. The smooth ground joint exhibited slight compaction at all pressures tested.
- Specimens of Salem limestone were fully saturated with water and then loaded hydrostatically while measurements were made of rock skeleton deformation and pore pressure. In some tests, pore water was drained from the specimen and the relationship between the volume of drained water and the pore pressure change was used to compute the specific storage of the porous rock. Numerical simulations of the undrained tests were performed with a program which makes a closed form calculation using the compressibilities of the pore fluid, solid grains, and drained porous skeleton as inputs while enforcing all compatibility conditions. The results of the simulations were in good agreement with the test measurements, demonstrating the efficacy of the effective stress approach for



analysis of saturated porous materials.

- Triaxial compression tests were performed on intact limestone and specimens with three types of joints at strain rates ranging from  $10^{-2}$  to  $10^{-5} \text{ s}^{-1}$ . The strength of the intact limestone exhibited approximately 5% increase for each decade increase in strain rate. A similar trend was evident in the tensile fracture joints, but the data did not show the synthetic and smooth ground joints to have a significant strain rate dependence.
- A comparison test series of 20-MPa triaxial compression tests at a range of strain rates was run on intact and jointed specimens that were damp but not saturated (2.5% water content) and fully saturated but allowed to drain during testing. The saturated drained intact specimens developed strengths approximately 5% lower than the corresponding specimens that were not saturated. Numerical simulations based on measured permeabilities of the limestone indicate that no more than 5 MPa pore pressure developed in the saturated drained test at  $10^{-3} \text{ s}^{-1}$ , and no significant pore pressure developed in the slower ( $10^{-5} \text{ s}^{-1}$ ) strain rate test. Since the reduction in mean effective stress resulting from pore pressure build-up is not enough to cause the observed reduction in strength, it appears that saturation may have a small effect on strength through some other mechanism.
- The permeability of the intact limestone was measured under hydrostatic loads ranging from 1 to 150 MPa and under triaxial compression loading at confining pressures up to 90 MPa. The variation in permeability under all loading conditions investigated can be reasonably represented by an exponential function of mean stress. No significant increase in permeability was observed due to shearing of the limestone at low confining pressures.
- The permeability of three types of joints in Salem limestone was measured over a range of joint normal stress conditions. The variation in joint permeability was quantified in terms of both normal stress and joint aperture. In the tensile

fracture and smooth ground joints, which were well mated, the joint would fully close and joint flow became negligible in comparison with flow through the intact portions of the rock at normal stresses of approximately 5 MPa. Due to slight mismatches between the two sides of the synthetic joints, fluid flow through them was approximately an order of magnitude higher than the other types of joints at the same stress level.

- A joint constitutive model was developed based on data from triaxial compression tests on tensile fracture joints. It is an elastoplastic model based on a finite thickness of joint. It includes strain softening and employs a non-associative formulation to model the volume change resulting from joint shear deformation.

In addition to the main body of research that was performed on Salem limestone, this contract sponsored ARA's participation in an interlaboratory test program conducted by the Institute for Standards Research of the American Society for Testing and Materials to quantify the precision and bias of standard test methods for rock. Tests conducted under this program included ultrasonic wavespeed determinations, unconfined compression tests, splitting tensile tests, and triaxial compression tests at pressures up to 40 MPa. The results of tests on Barre granite, Berea sandstone, Salem limestone, and Tennessee marble are summarized in this report.

## SECTION 13

### REFERENCES

- ASTM, *1993 Annual Book of ASTM Standards* (U), Sec. 4, Vol. 4.08, ASTM, Philadelphia, PA, 1993. (UNCLASSIFIED)
- Blouin, S.E. and K.J. Kim, "Undrained Compressibility of Saturated Soil (U)," DNA-TR-87-42, Defense Nuclear Agency, Washington, DC, February 1984. (UNCLASSIFIED)
- Brown, S.R., "A Note on the Description of Surface Roughness Using Fractal Dimension (U)," *Geophys. Res. Lett.*, 14, 1095-1098, 1987. (UNCLASSIFIED)
- Brown, S.R., computer program, "FM2D," personal communications, 1991. (UNCLASSIFIED)
- Brown, S.R. and C.H. Scholz, "Broad Bandwidth Study of the Topography of Natural Rock Surfaces (U)," *Journal of Geophysical Research*, vol. 90, No. B14, pp. 12,575-12,582, December 1985. (UNCLASSIFIED)
- Chitty, D.E., and S.E. Blouin, "Special Purpose Mechanical Property Tests on Salem Limestone (U)," Final Report to U.S. Army Engineer Waterways Experiment Station, Vicksburg, MS, February 1990. (UNCLASSIFIED)
- Chitty, D.E., and S.E. Blouin, "Joint Shear and Compressibility Tests on Salem Limestone (U)," Final Report to U.S. Army Engineer Waterways Experiment Station, Vicksburg, MS, October 1992. (UNCLASSIFIED)
- Chitty, D.E. and S.E. Blouin, "Laboratory Investigation of the Strength and Deformation Properties of Carbonate Rocks and Soils (U)," DNA-TR-92-45, Report to the Defense Nuclear Agency, Alexandria, VA, March 1993. (UNCLASSIFIED)
- Chitty, D.E., S.E. Blouin, K.J. Kim, and A.F. Rauch, "Dynamic Response of Multiphase Porous Media (U)," Final Report to Air Force Office of Scientific Research, June 1993. (UNCLASSIFIED)
- Cummins, T.K., "Effective Stress Behavior of Intact Salem Limestone (U)," Technical Report SL-91-22, U.S. Army Engineer Waterways Experiment Station, Vicksburg, MS, November 1991. (UNCLASSIFIED)
- Forchheimer, P., "Wasserbewegung durch Boden," *Z. Ver. Deutsch Ing.*, 45, pp 1,782-1,788, 1901. (UNCLASSIFIED)
- Freeze, R.A. and J.A. Cherry, *Groundwater*, Prentice-Hall, Inc., Englewood Cliffs, NJ, 1979. (UNCLASSIFIED)

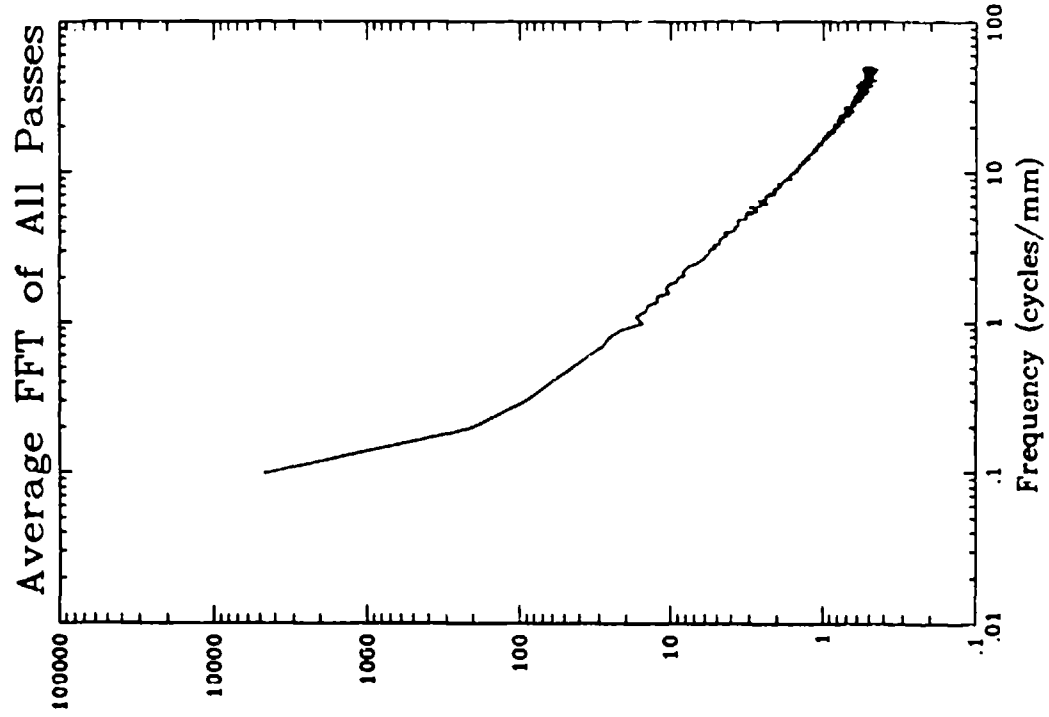
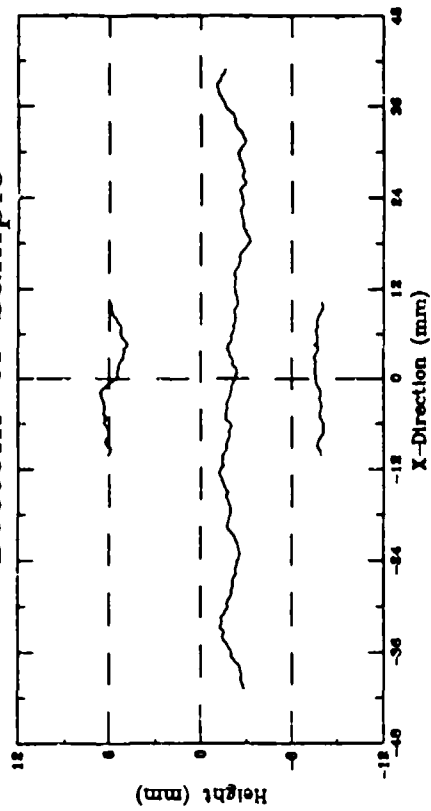
- Goddard, E.N., et al., Rock Color Chart (U), Geological Society of America, Boulder, CO. (UNCLASSIFIED)
- Green, L., Jr., and P. Duwez, "Fluid Flow Through Porous Metals (U)," *Journal of Applied Mechanics*, Vol. 18, pp 39-45, March 1951. (UNCLASSIFIED)
- Hardy, H.R., and X. Sun, "A Nonlinear Rheological Model for Time-Dependent Behavior of Geological Materials (U)," *27th Rock Mechanics Symposium, "Rock Mechanics: Key to Energy Product,"* pp 205-212, Society of Mining Engineers, Inc., Littleton, CO, 1986. (UNCLASSIFIED)
- Kennedy, T.E., "Dynamic Tests of a Model Flexible-Arch-Type Protective Shelter (U)," U.S. Army Engineer Waterways Experiment Station, Vicksburg, MS, April 1971. (UNCLASSIFIED)
- Kim, K.J., S.E. Blouin, and D.A. Timian, "Experimental and Theoretical Response of Multiphase Porous Media to Dynamic Loads (U)," Annual Technical Report 1, Report to U.S. Air Force Office of Scientific Research, Washington, DC, August 1986. (UNCLASSIFIED)
- Kim, K.J., S.E. Blouin, D.E. Chitty, and D.H. Merkle, "Experimental and Theoretical Response of Multiphase Porous Media to Dynamic Loads (U)," Final Report to U.S. Air Force Office of Scientific Research, Washington, DC, September 1988. (UNCLASSIFIED)
- Power, W.L., and T.E. Tullis, "Euclidean and Fractal Models for the Description of Rock Surface Roughness (U)," *J. Geophys. Res.*, 96, 415-424, 1991. (UNCLASSIFIED)
- Press, W.H., et al., *Numerical Recipes: The Art of Scientific Computing* (U), Cambridge University Press, pub., Cambridge, England, 1986. (UNCLASSIFIED)
- Saupe, D., "Algorithms for Random Fractals (U)," in H.O. Peitgen and D. Saupe, ed., *The Science of Fractal Images*, pp 71-136, New York: Springer-Verlag, 1988. (UNCLASSIFIED)
- Sun, X., "A Non-Constant Parameter Rheological Model for Time-Dependent Behavior of Geologic Materials (U)," Master's Thesis submitted to The Pennsylvania State University Department of Mineral Engineering, August 1986. (UNCLASSIFIED)

**APPENDIX A**  
**PROFILES OF JOINT SURFACES**

<b>Test ID</b>	<b>Joint Type</b>	<b>Page</b>
M6A2	Tensile Fracture	A-2
M6B2	Tensile Fracture	A-4
M9A2	Tensile Fracture	A-6
M9B2	Tensile Fracture	A-8
G20B2	Tensile Fracture	A-10
G21B2	Tensile Fracture	A-12
M10B2	Synthetic	A-14

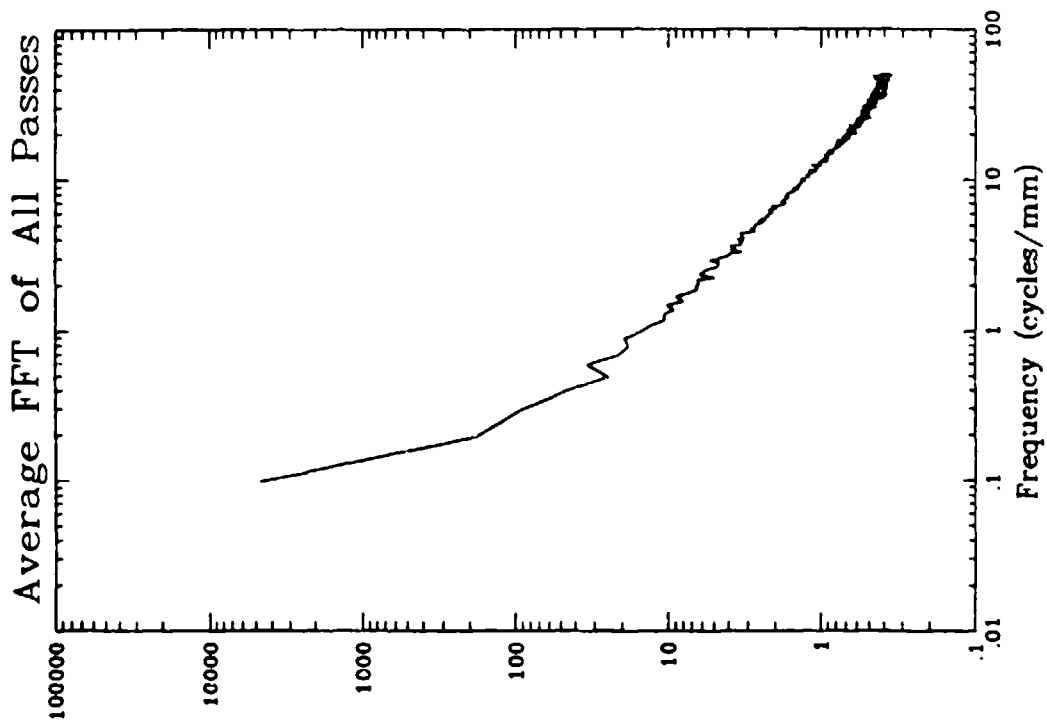
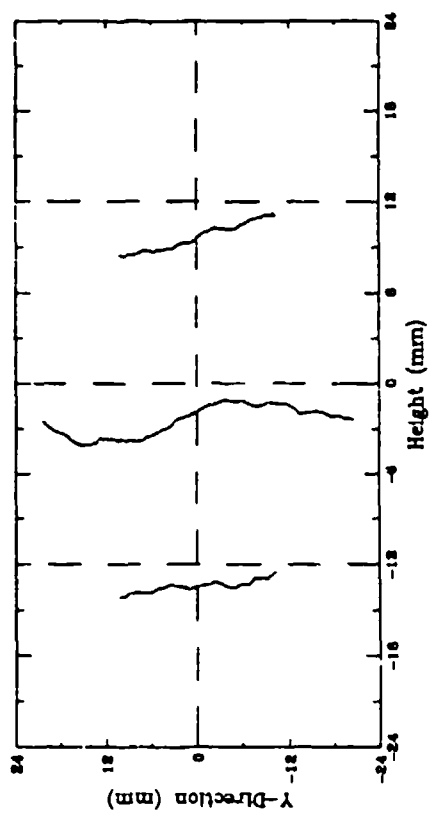
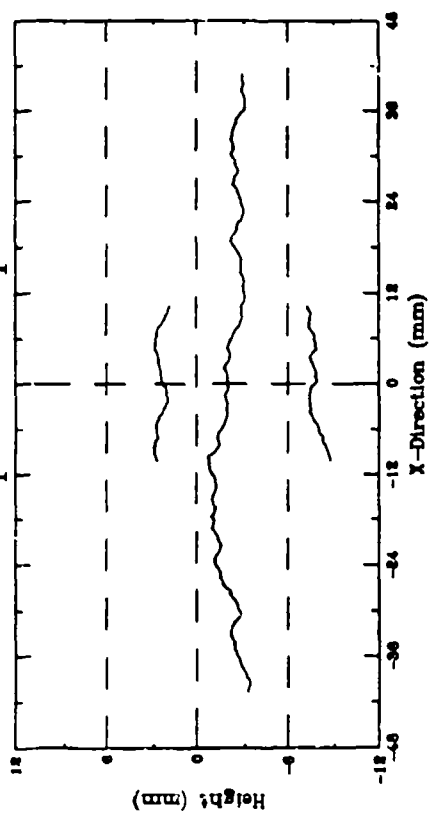
# Salem Limestone -- M6A2

Bottom of Sample



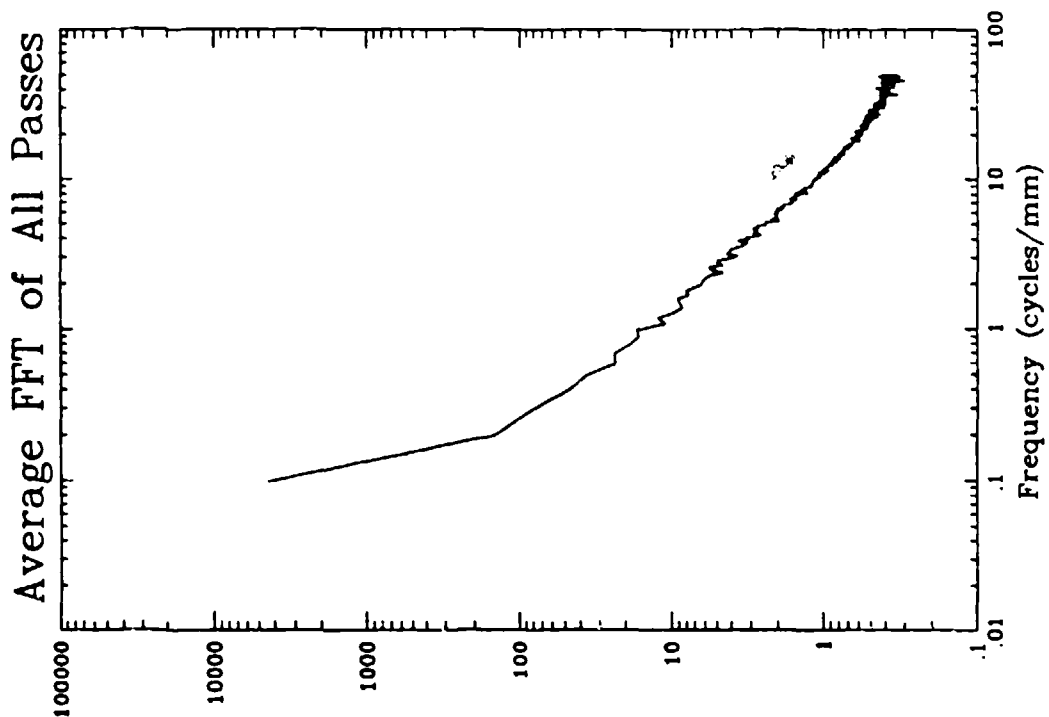
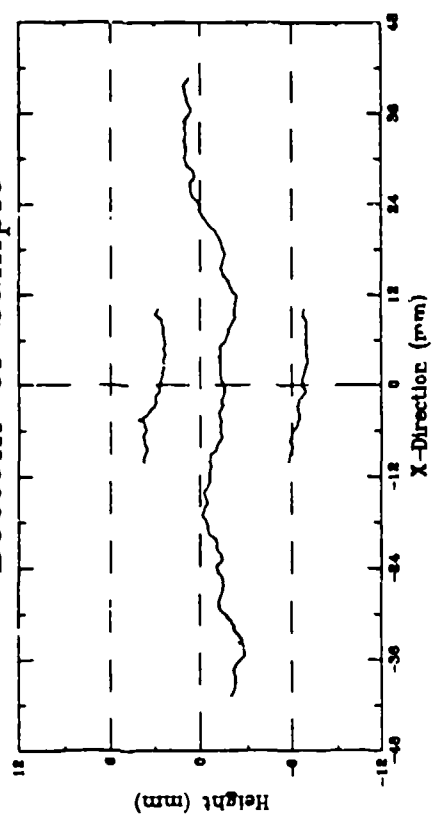
# Salem Limestone - M6A2

Top of Sample



# Salem Limestone - M6B2

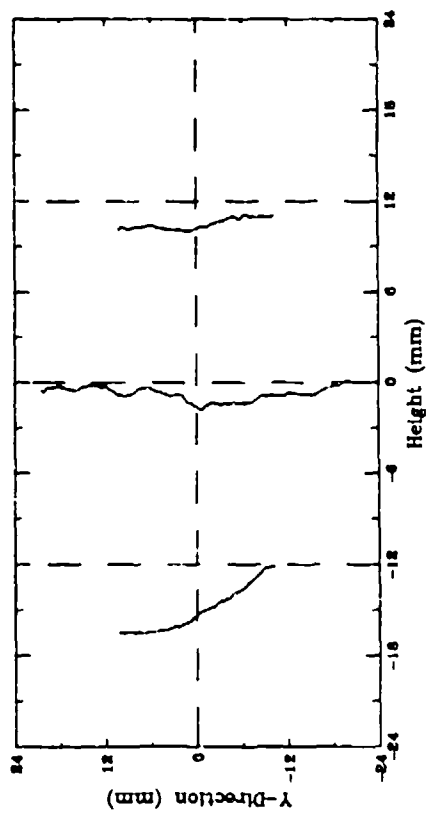
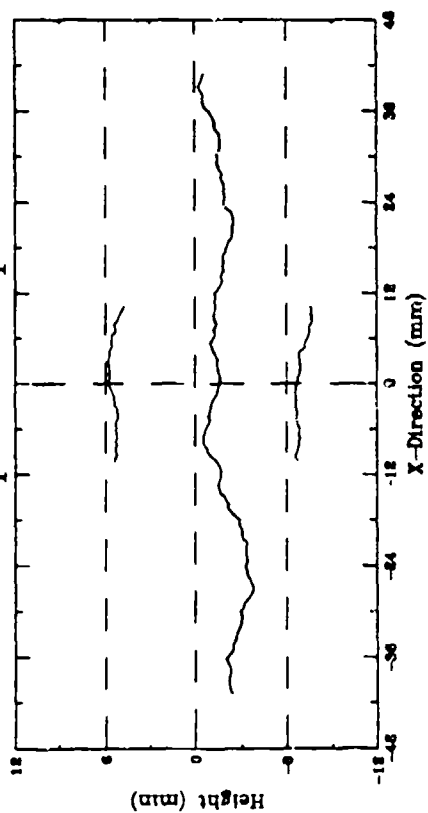
Bottom of Sample



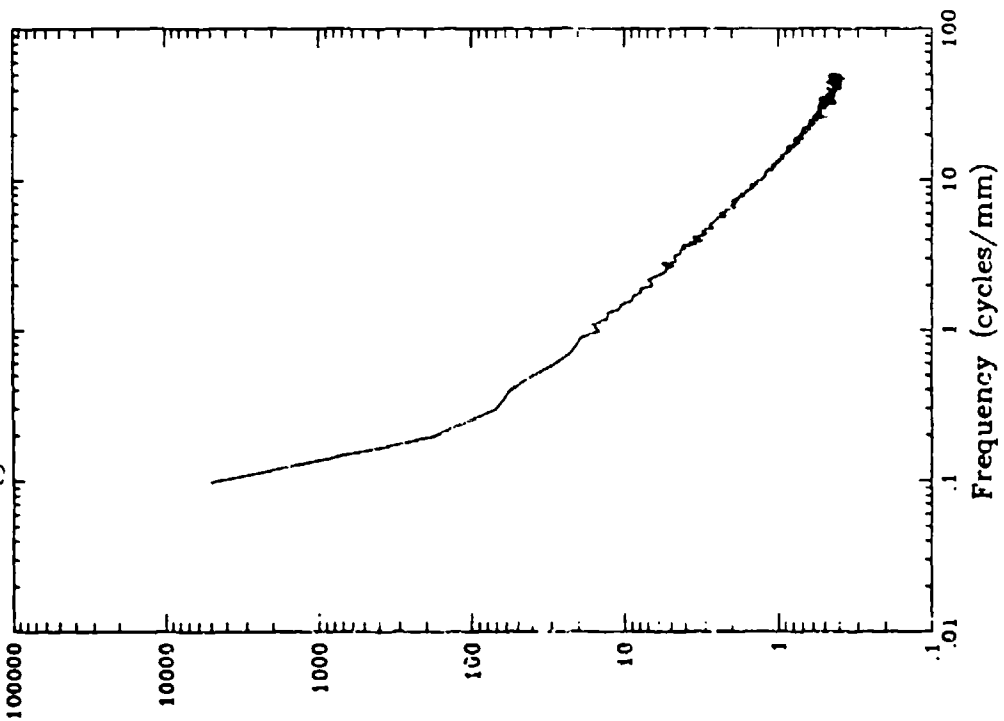


# Salem Limestone - M6B2

Top of Sample

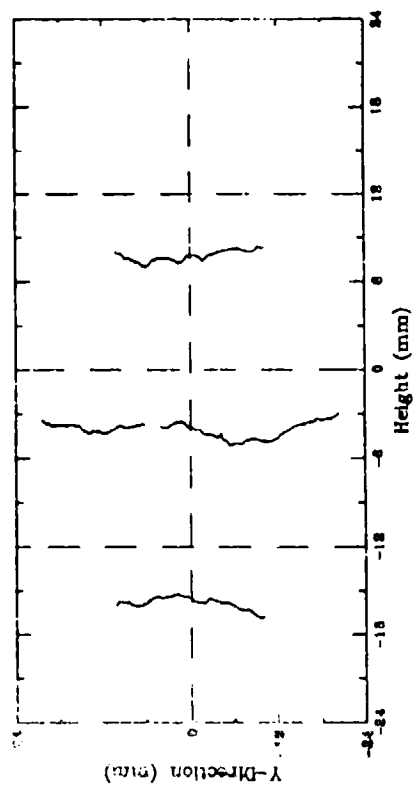
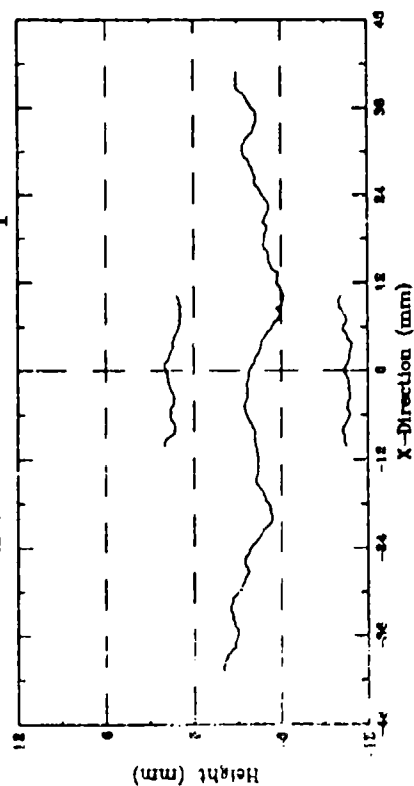


Average FFT of All Passes

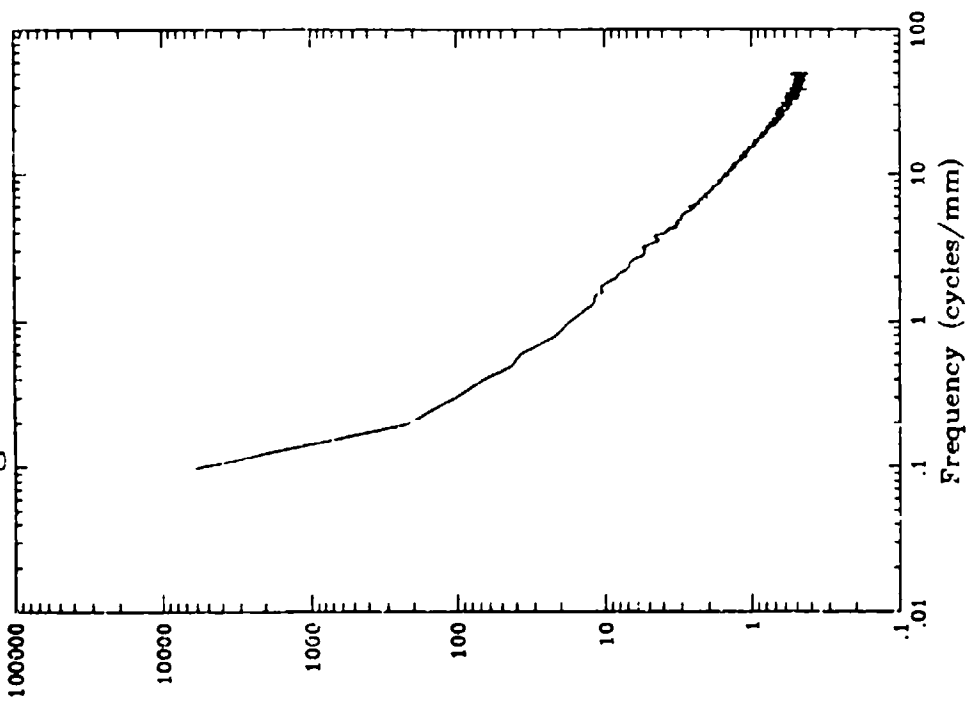


# Salem Limestone - M9A2

## Bottom of Sample

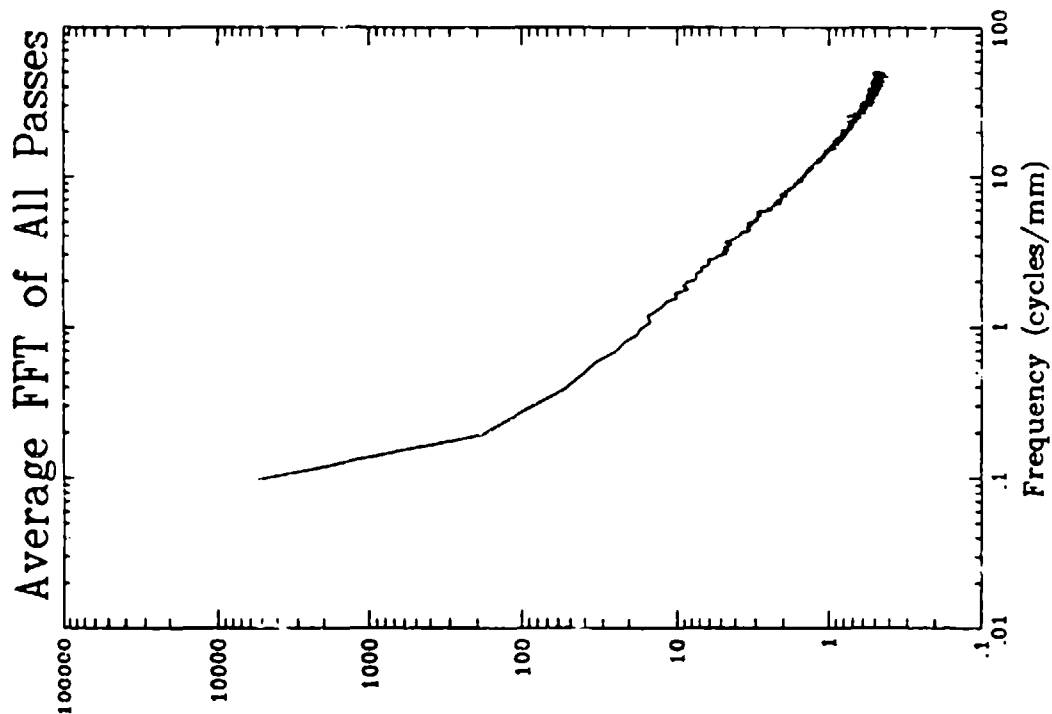
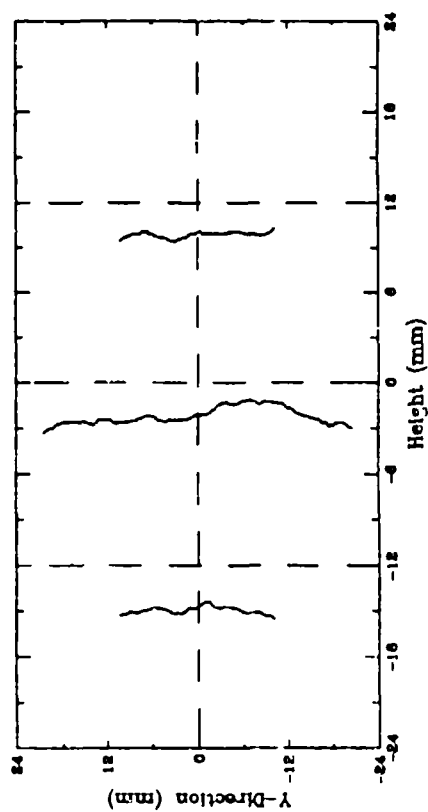
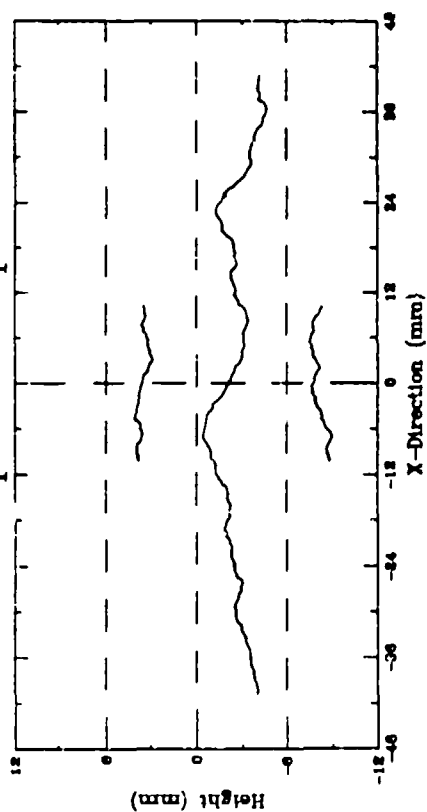


## Average FFT of All Passes



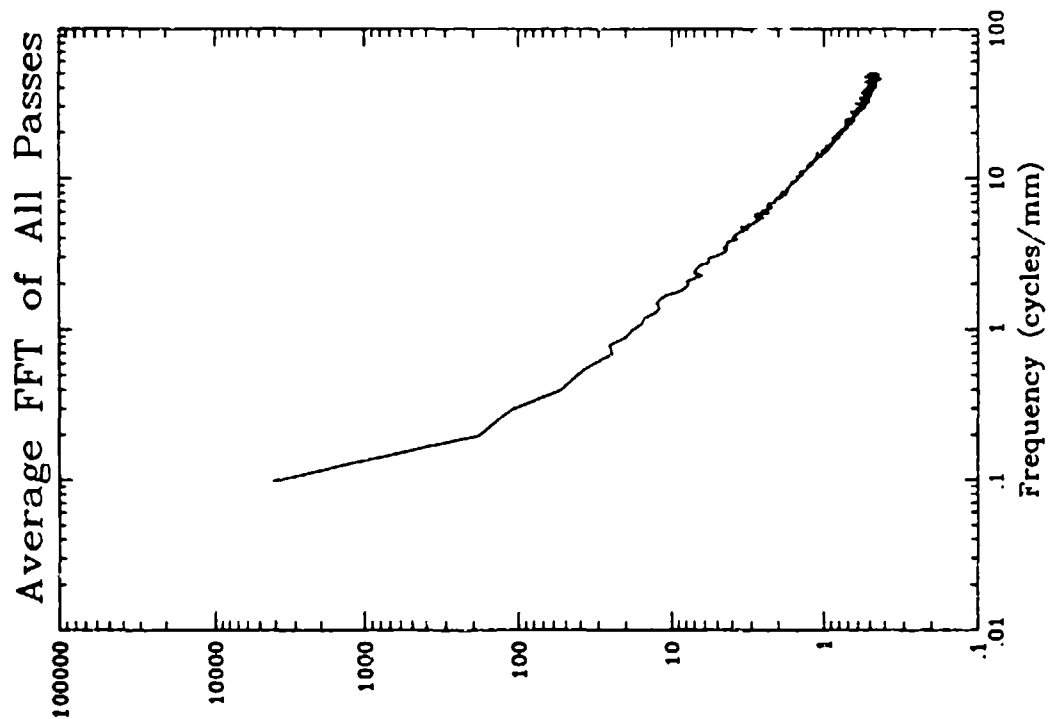
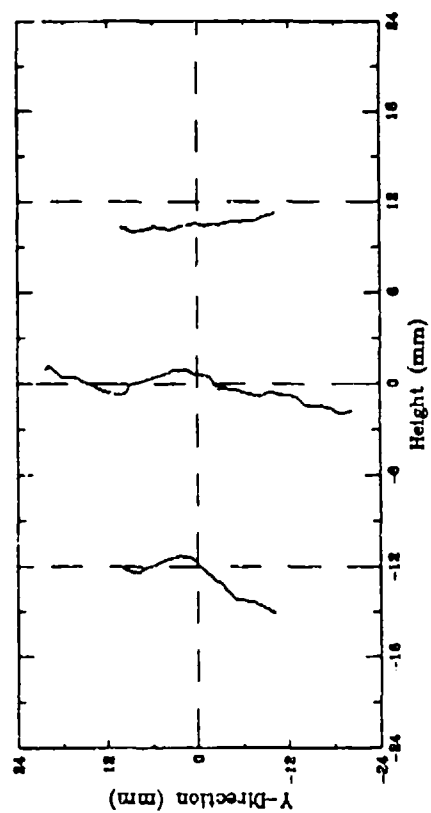
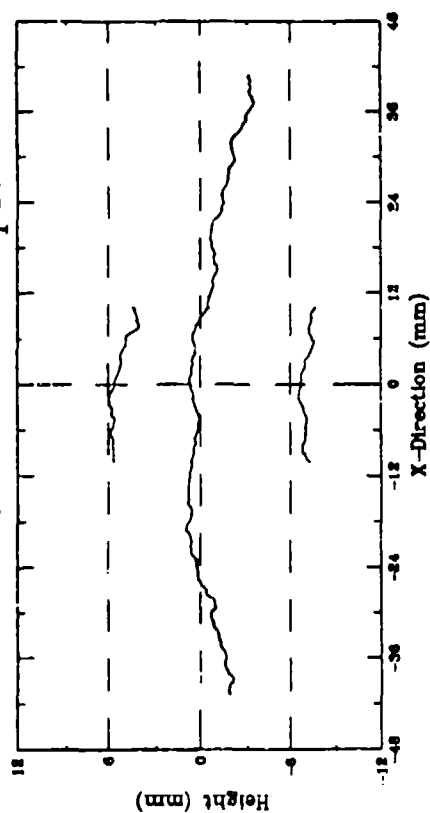
# Salem Limestone - M9A2

Top of Sample



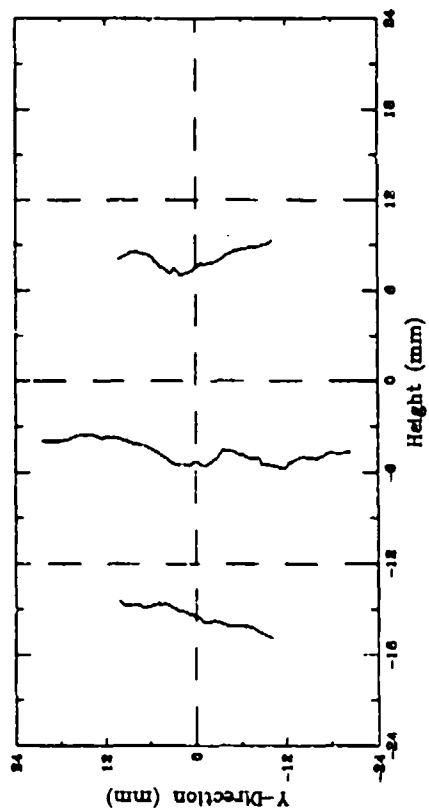
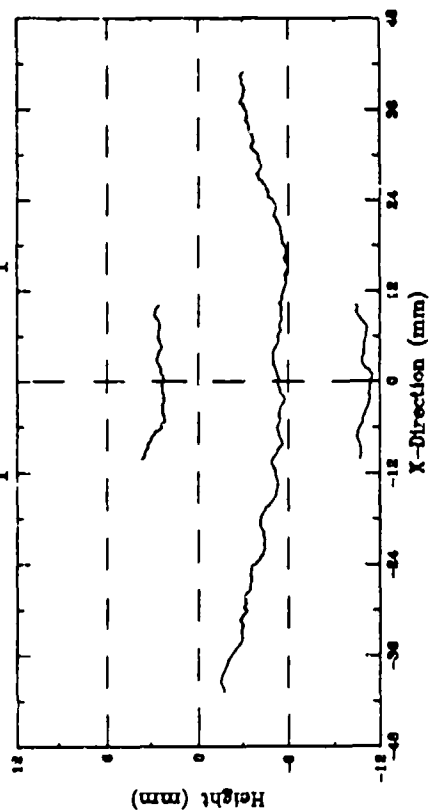
# Salem Limestone - M9B2

Bottom of Sample

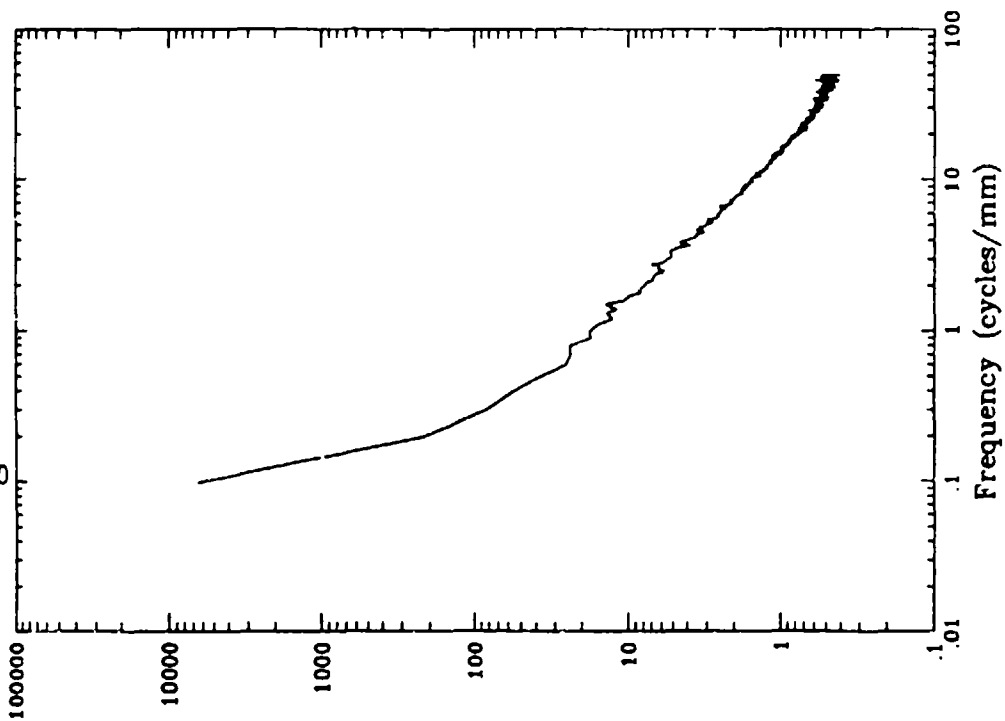


# Salem Limestone - M9B2

Top of Sample

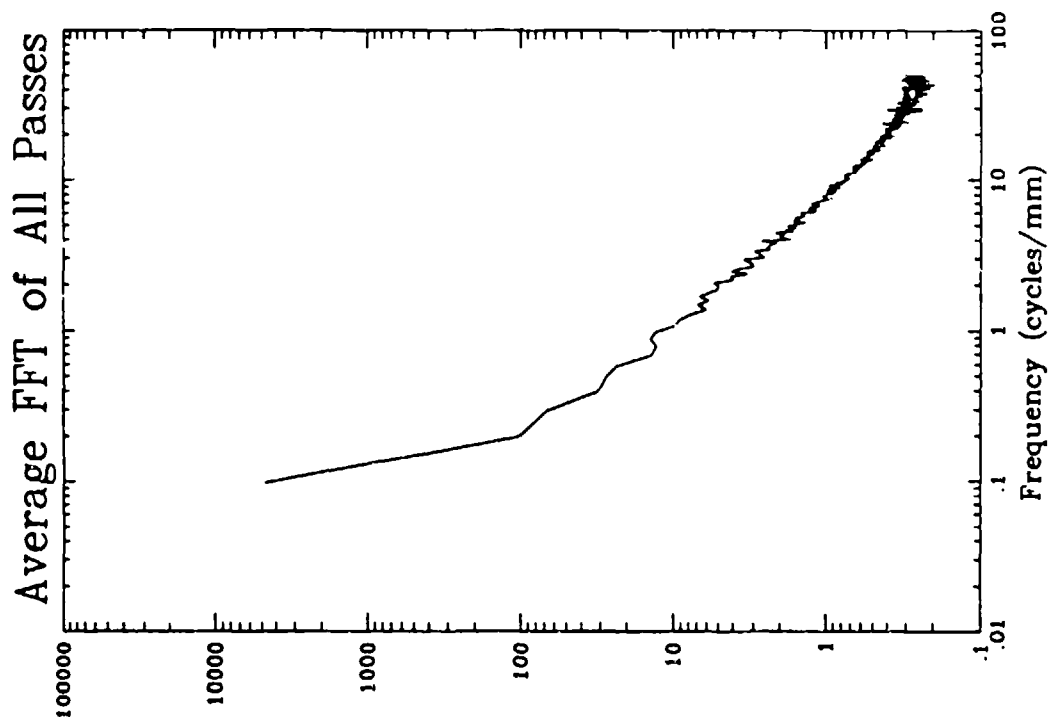
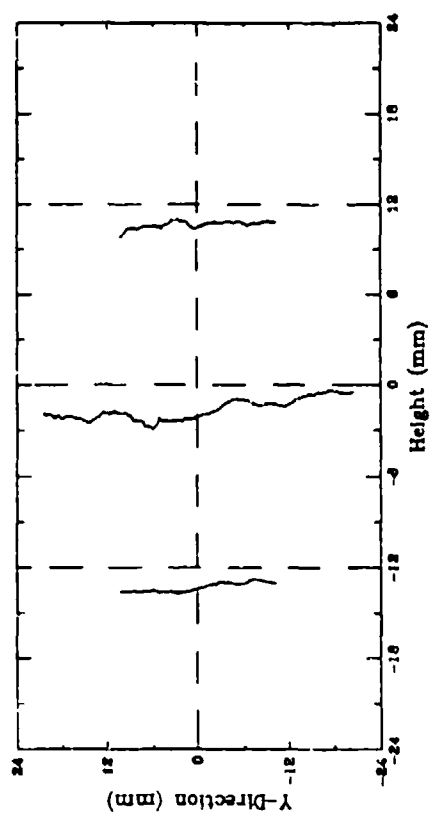
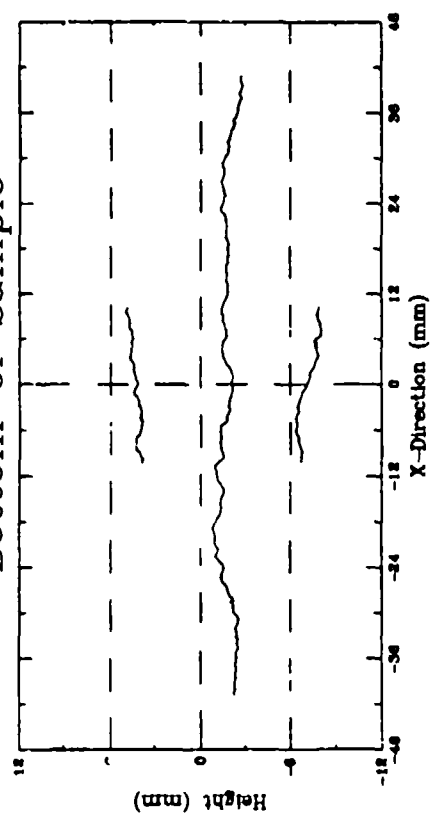


Average FFT of All Passes



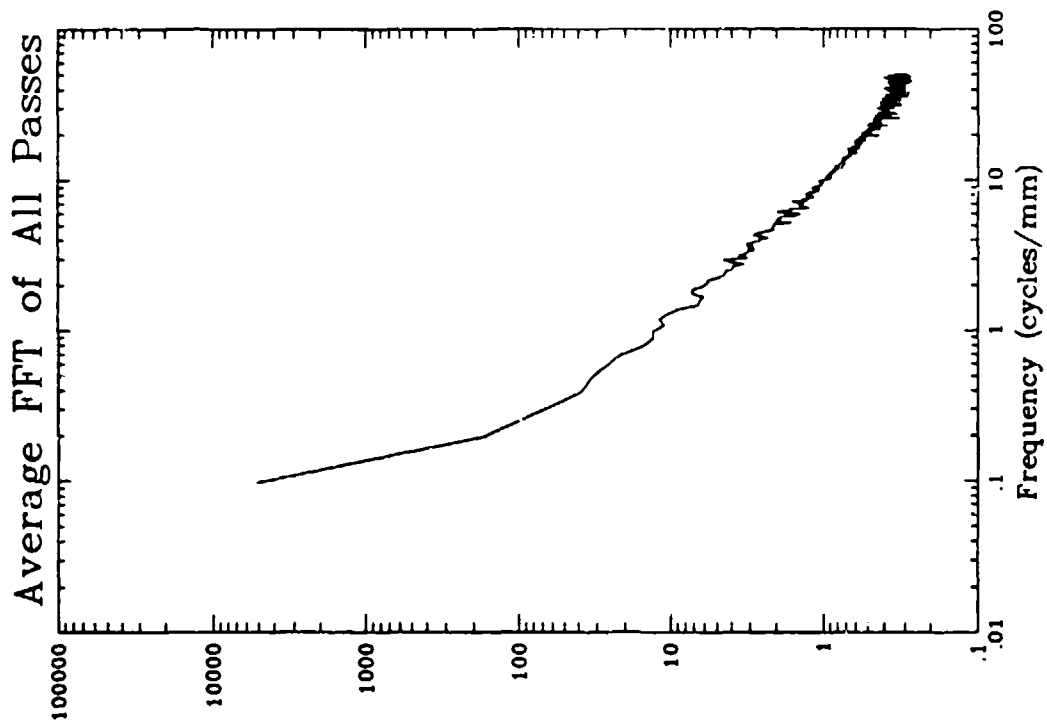
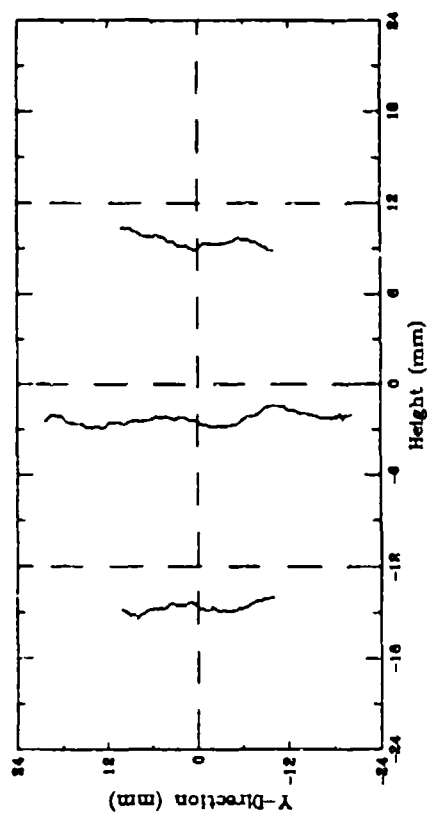
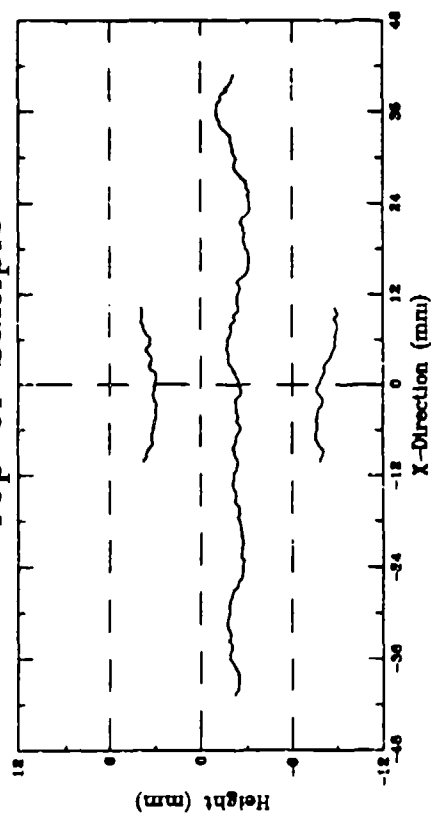
# Salem Limestone - G20B2

Bottom of Sample



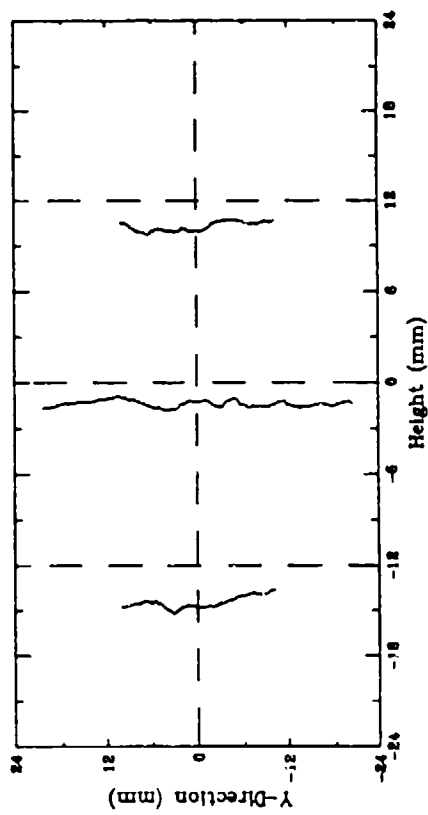
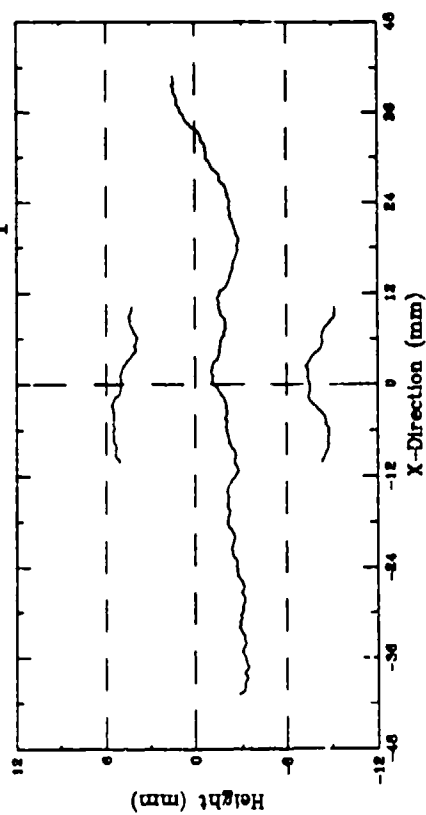
# Salem Limestone - G20B2

Top of Sample

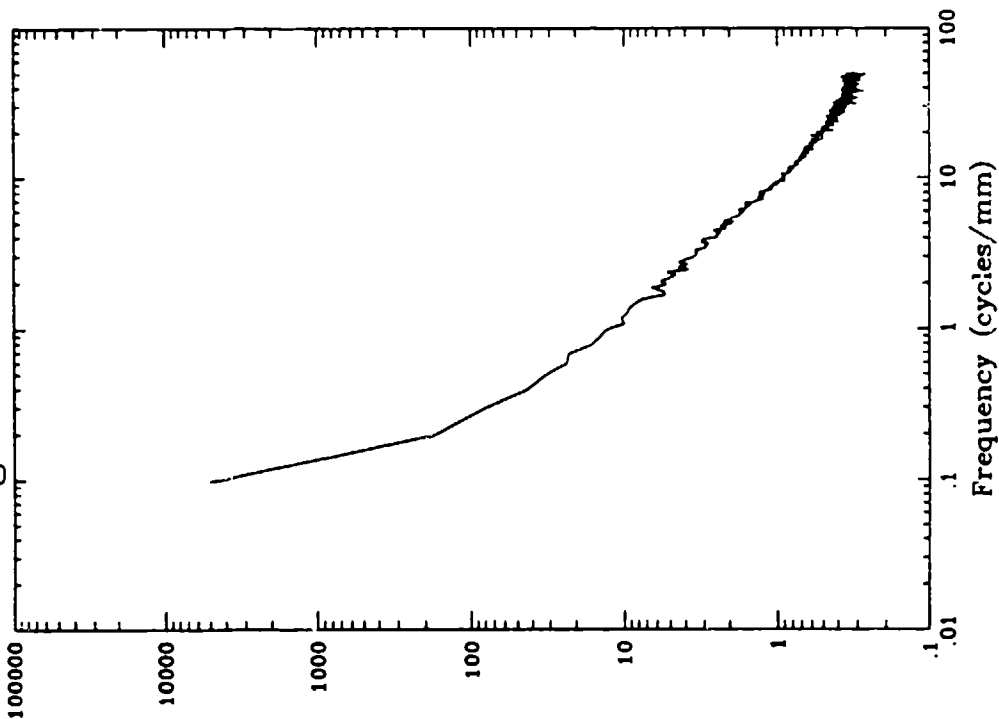


# Salem Limestone - G21B2

## Bottom of Sample



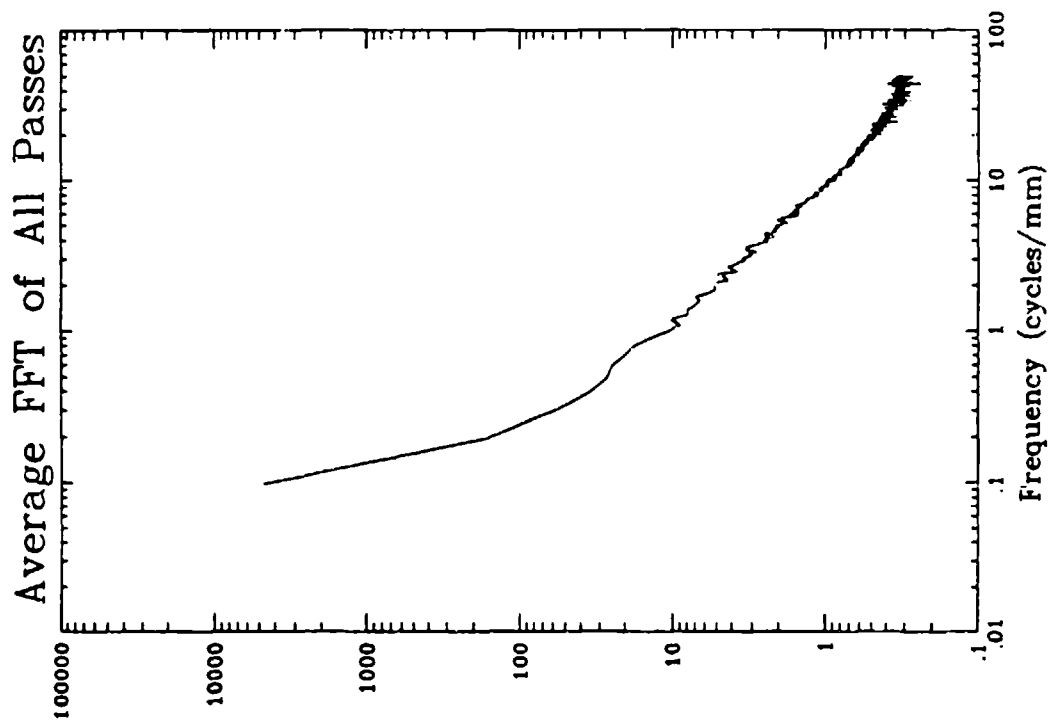
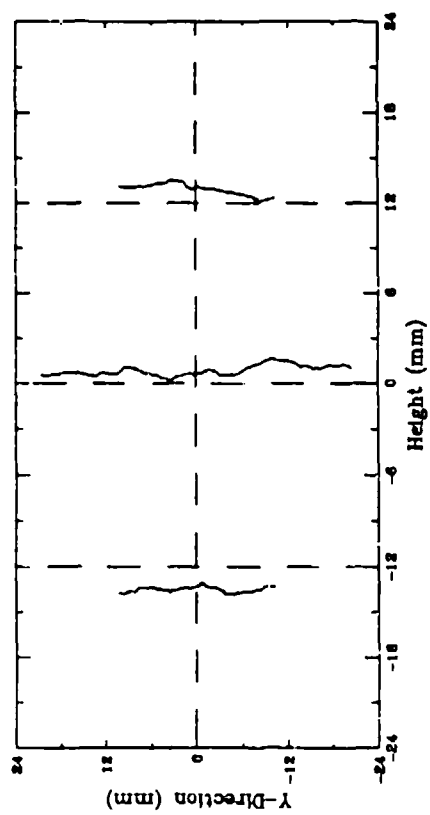
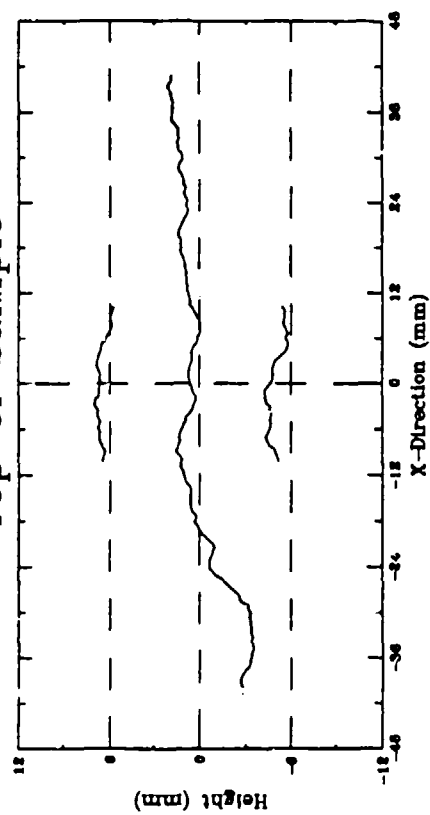
## Average FFT of All Passes



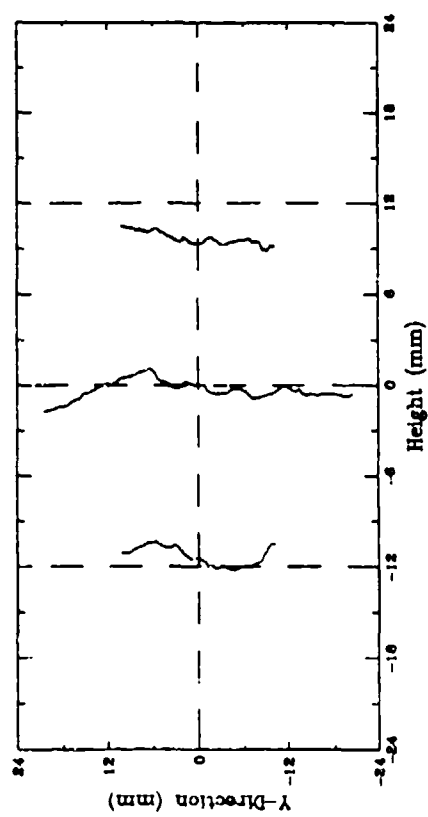
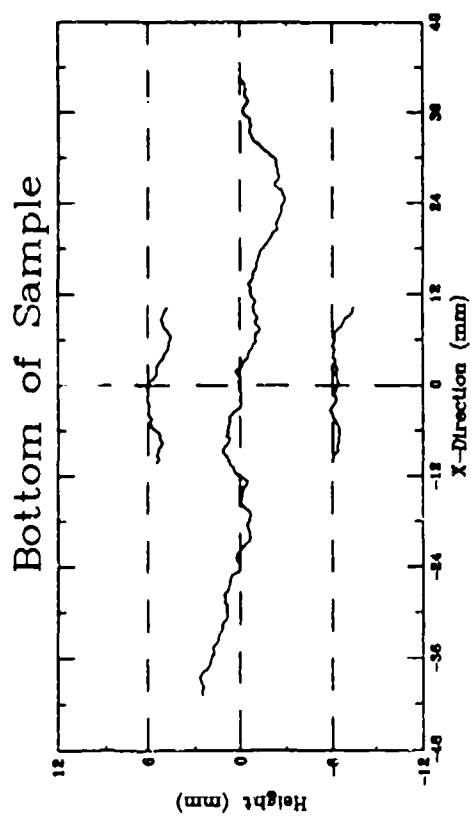
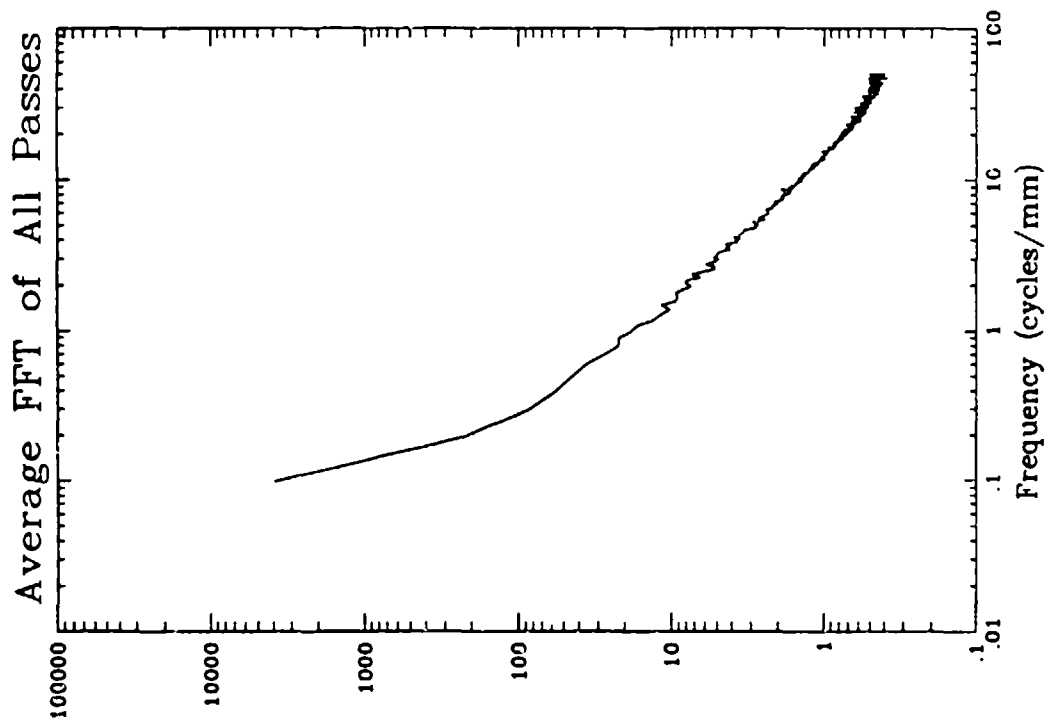


# Salem Limestone - G21B2

Top of Sample

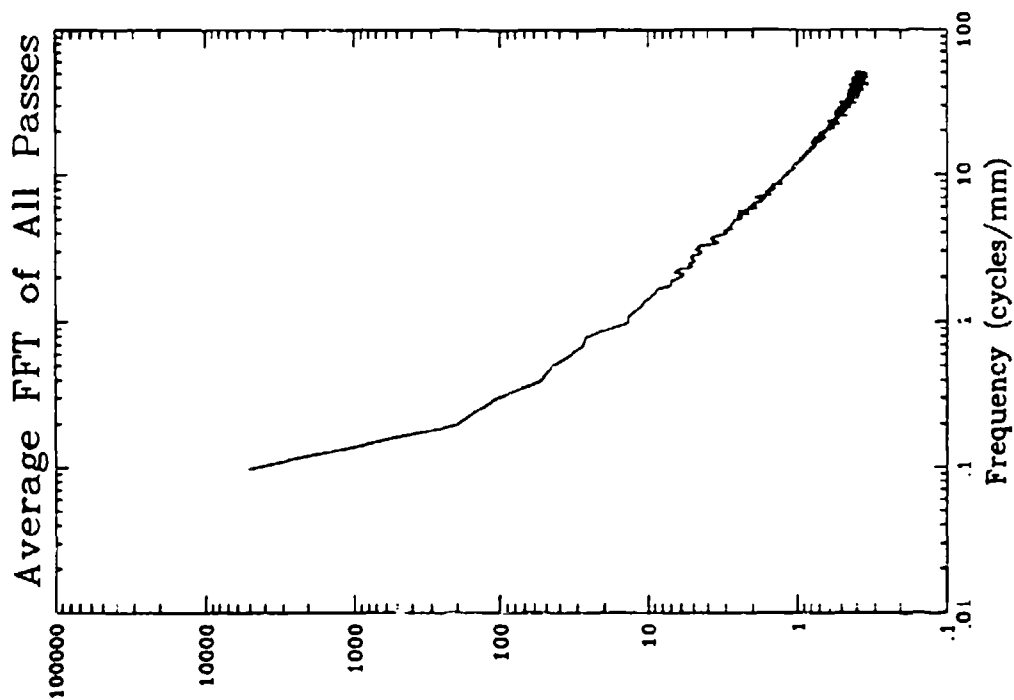
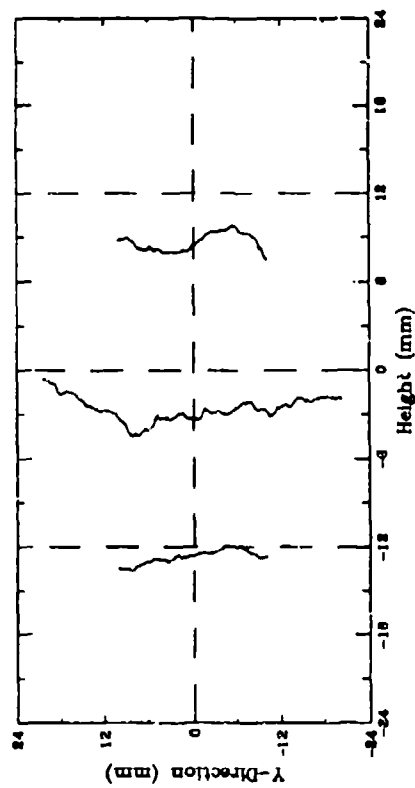
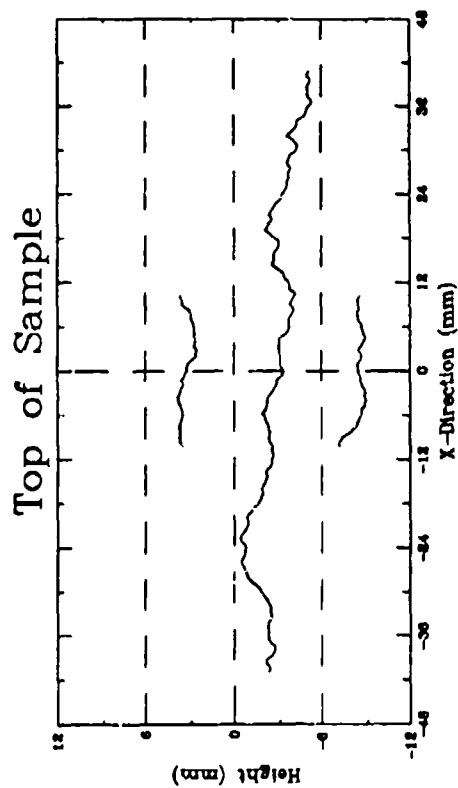


# Salem Limestone - M10B2



# Salem Limestone - M10B2

Top of Sample

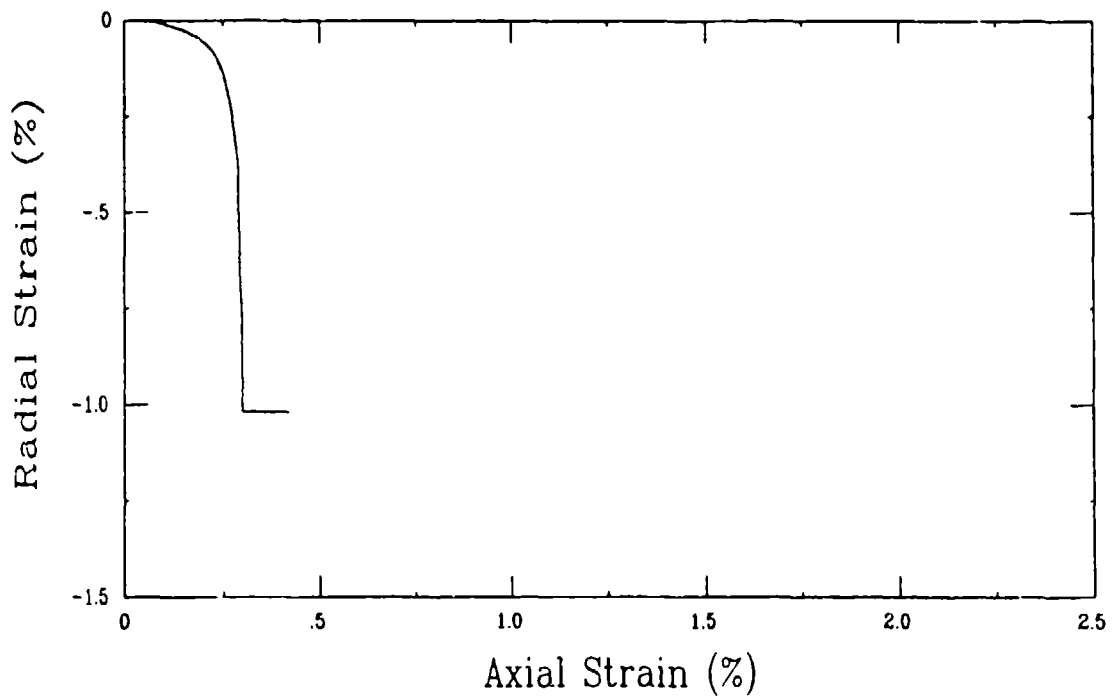
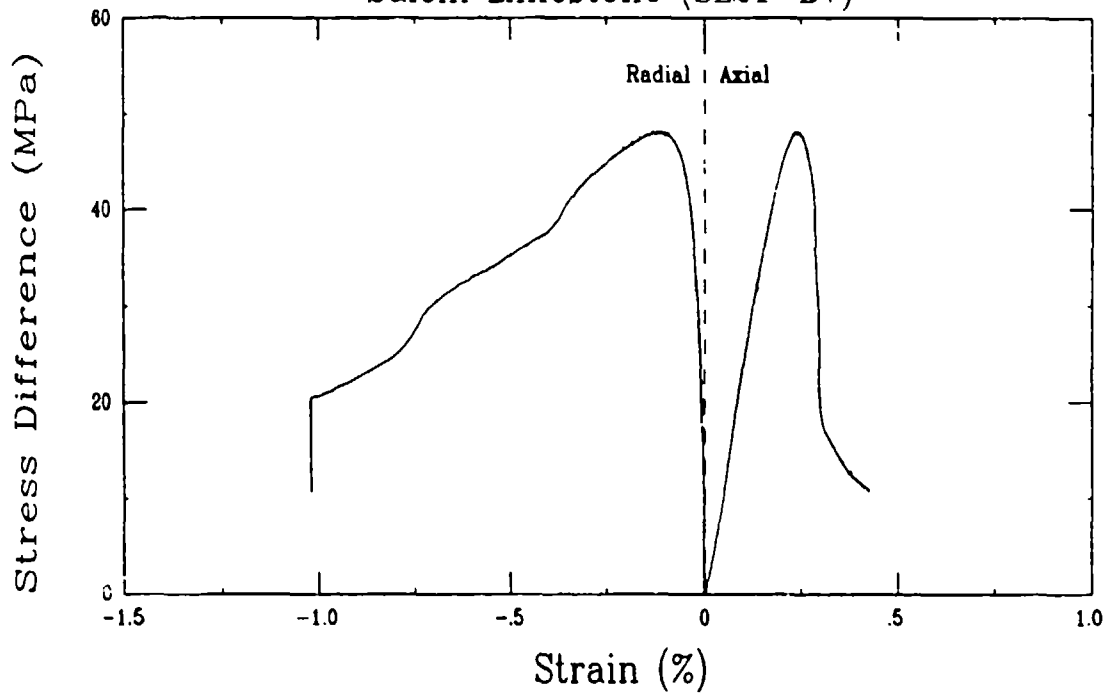


## APPENDIX B

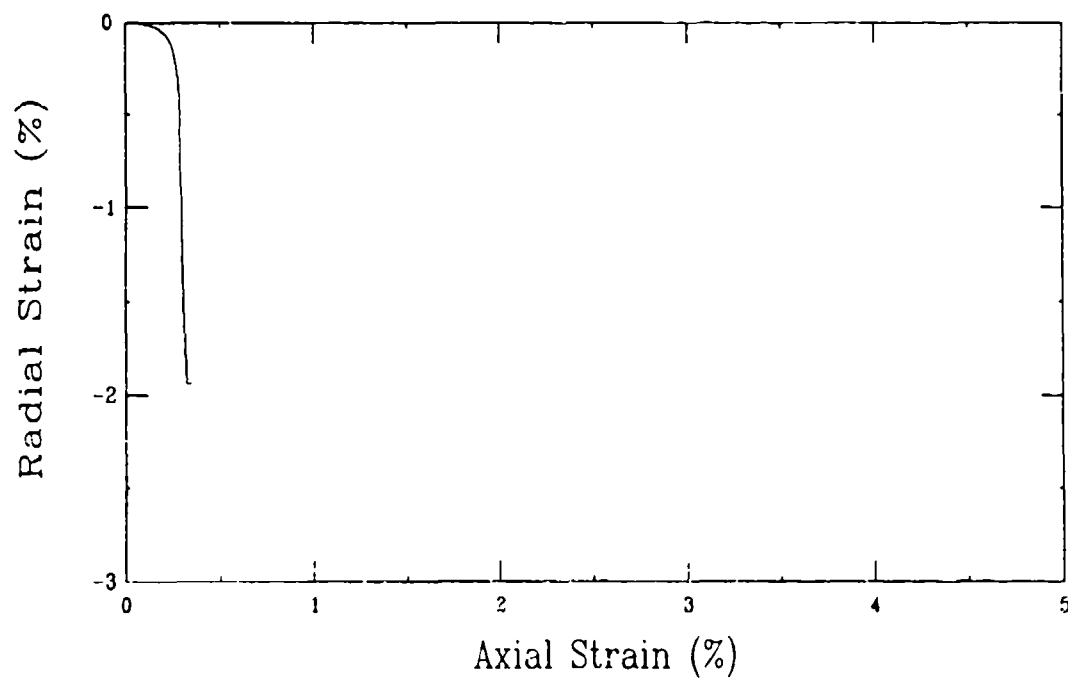
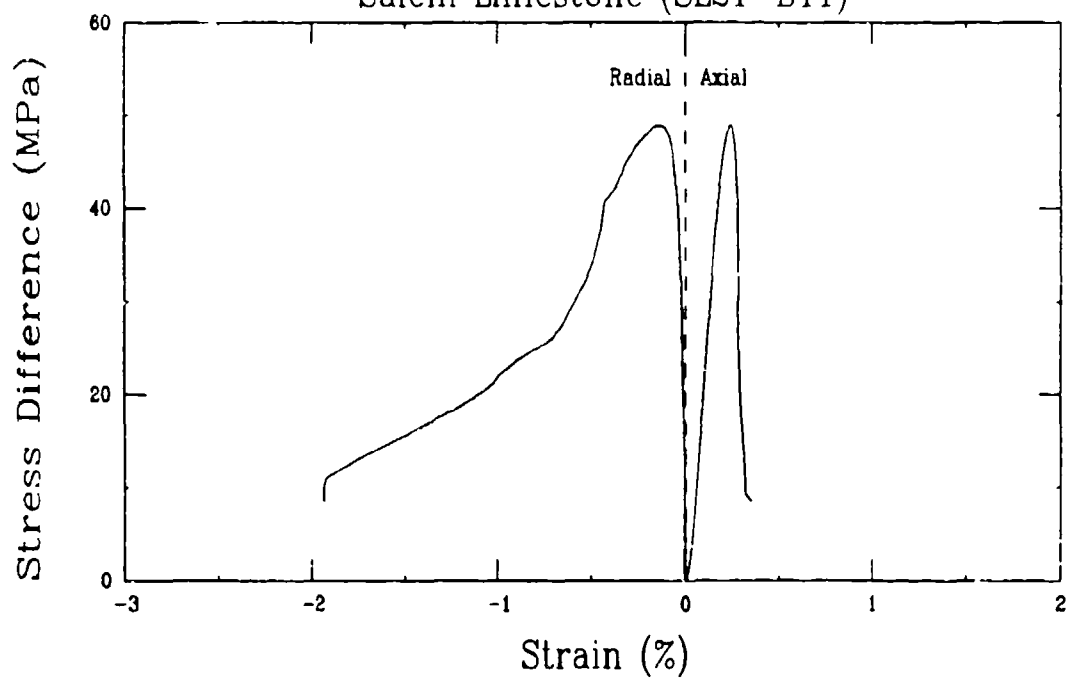
### UNCONFINED COMPRESSIVE TESTS WITH POST FAILURE RESPONSE

Test ID	Page
M12A1	B-2
M13B1	B-3
M13C1	B-4
M13E1	B-5
M13G1	B-6
M13F1	B-7

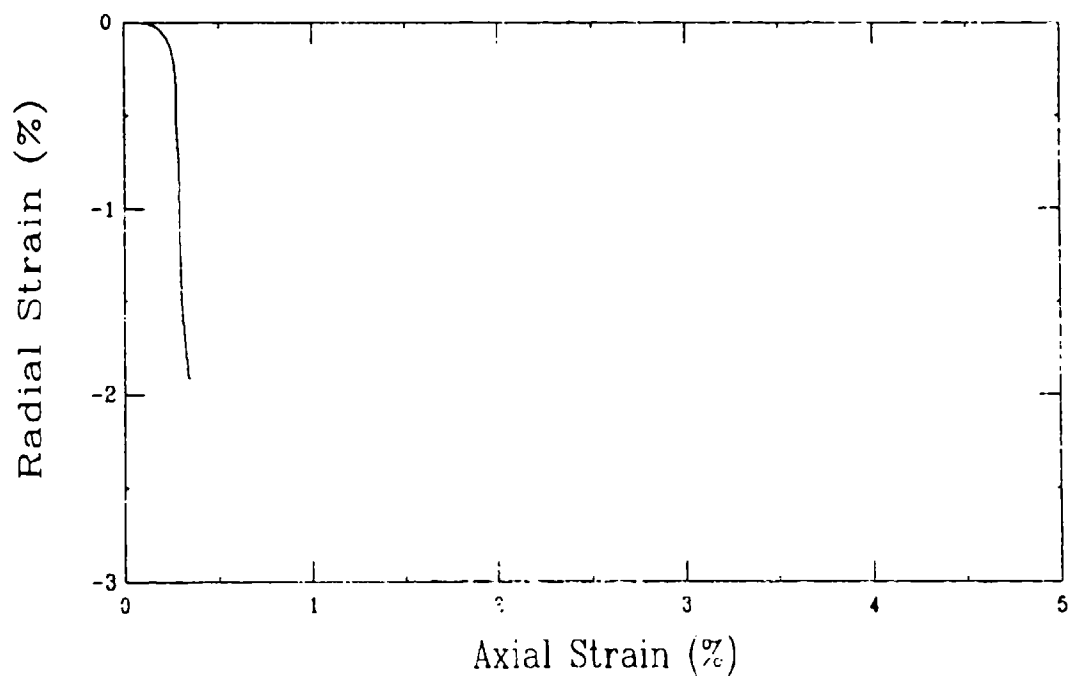
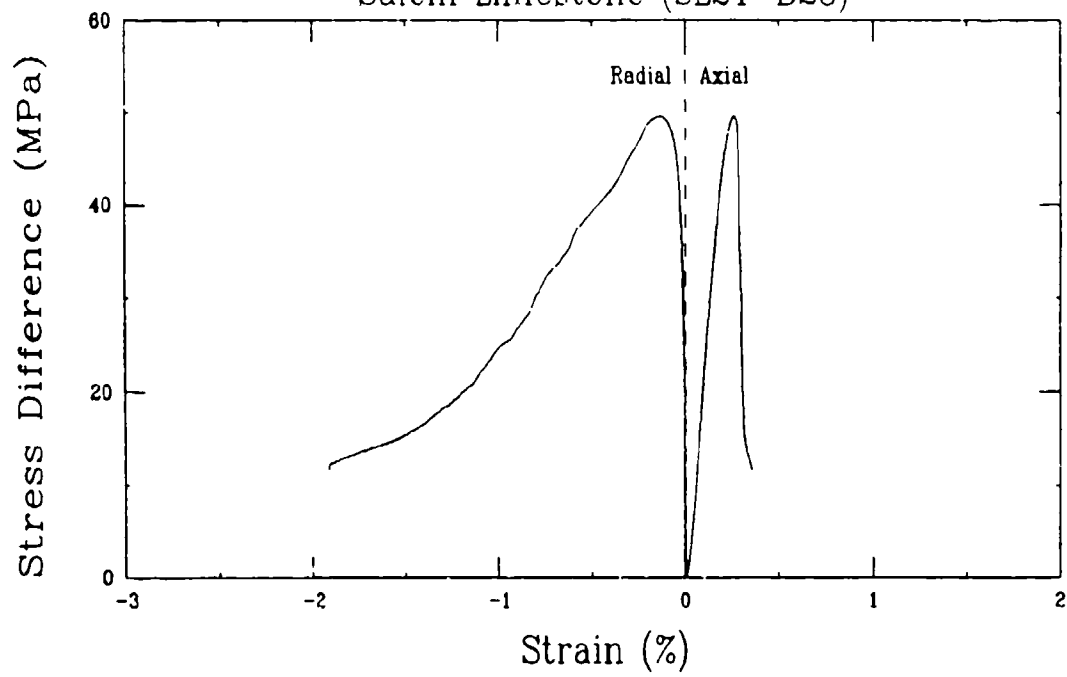
Unconfined Compression Test (M12A1)  
Salem Limestone (SL21-B7)



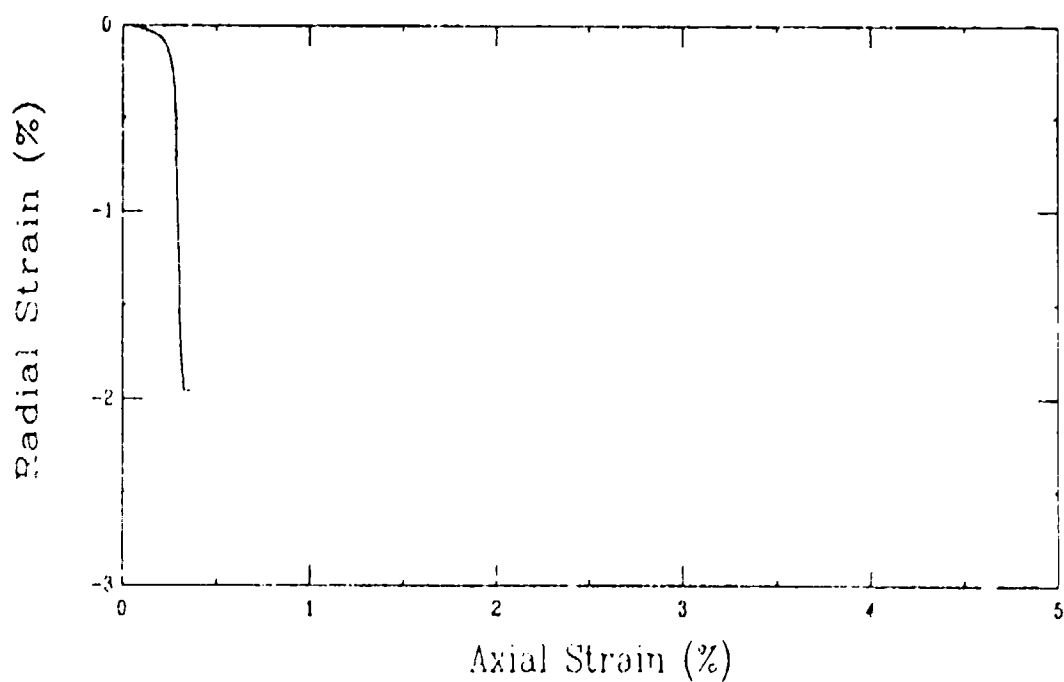
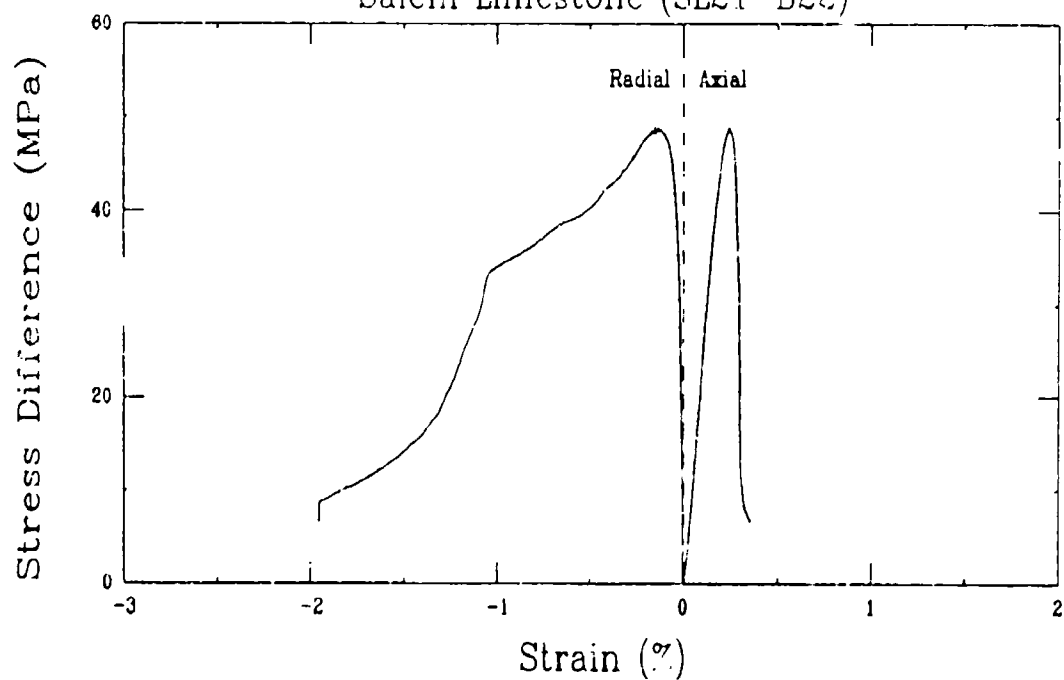
Unconfined Compression Test (M13B1)  
Salem Limestone (SL21-B11)



Unconfined Compression Test (M13C1)  
Salem Limestone (SL21-B23)

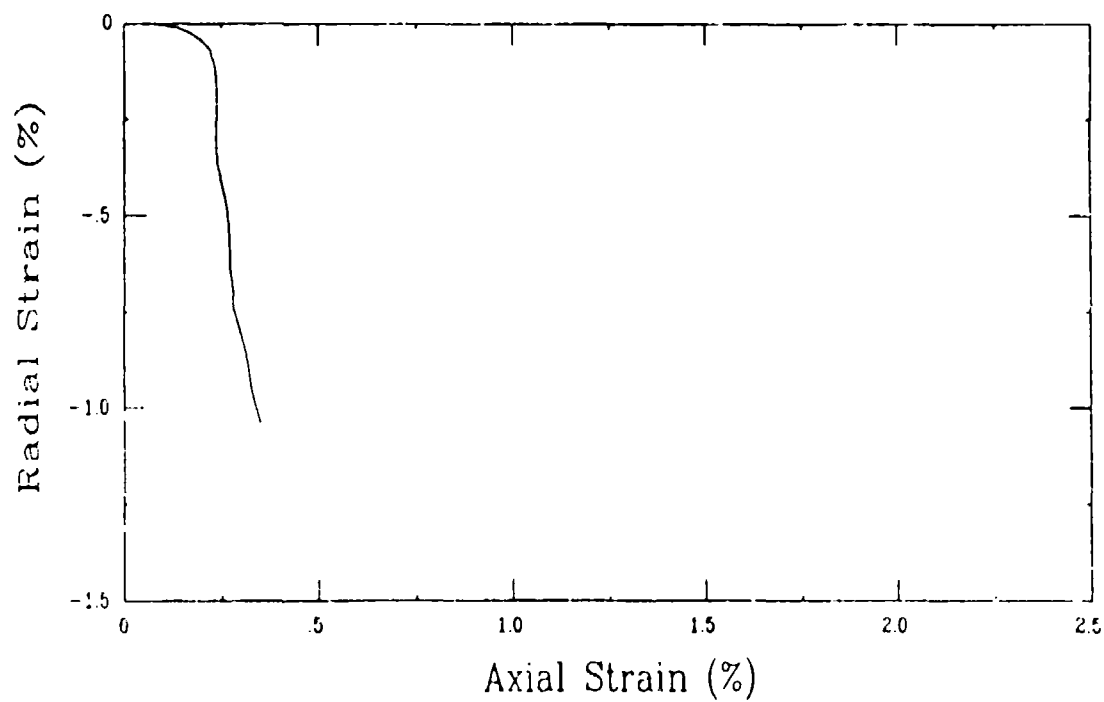
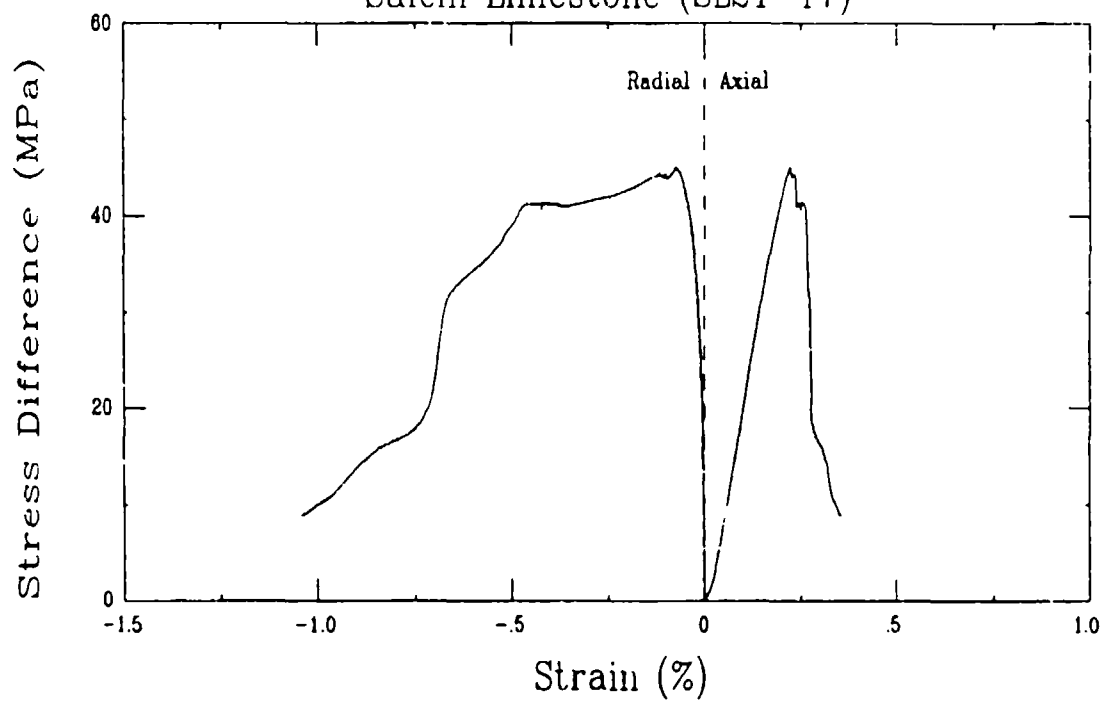


Unconfined Compression Test (M13E1)  
Salem Limestone (SL21-B22)

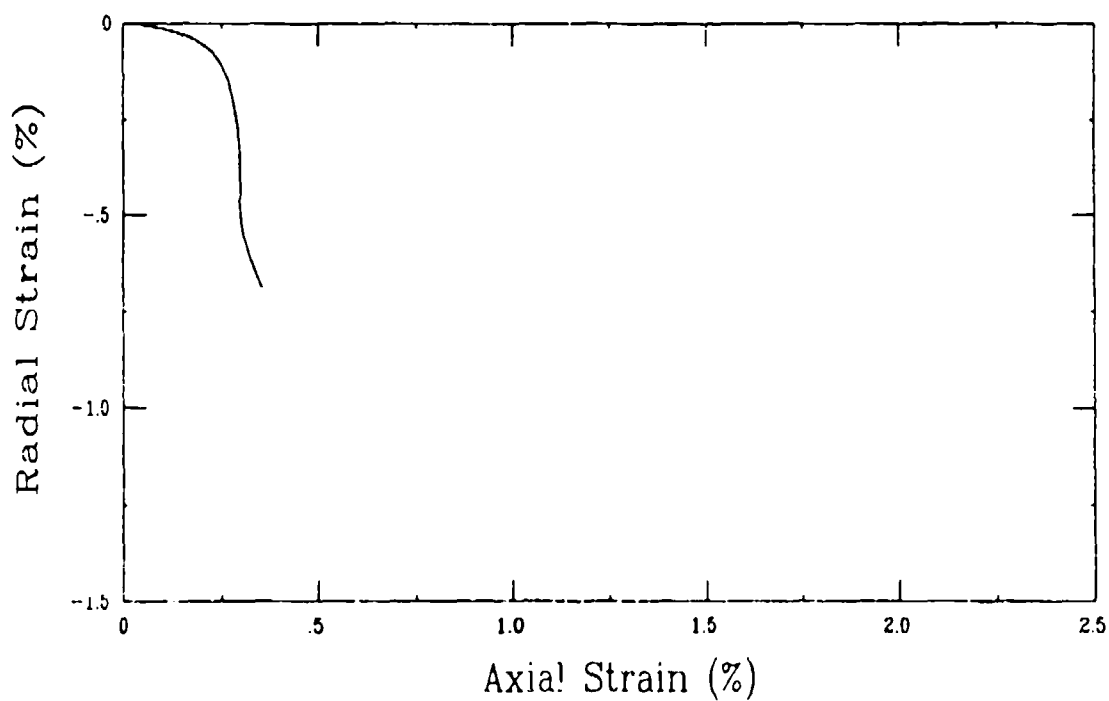
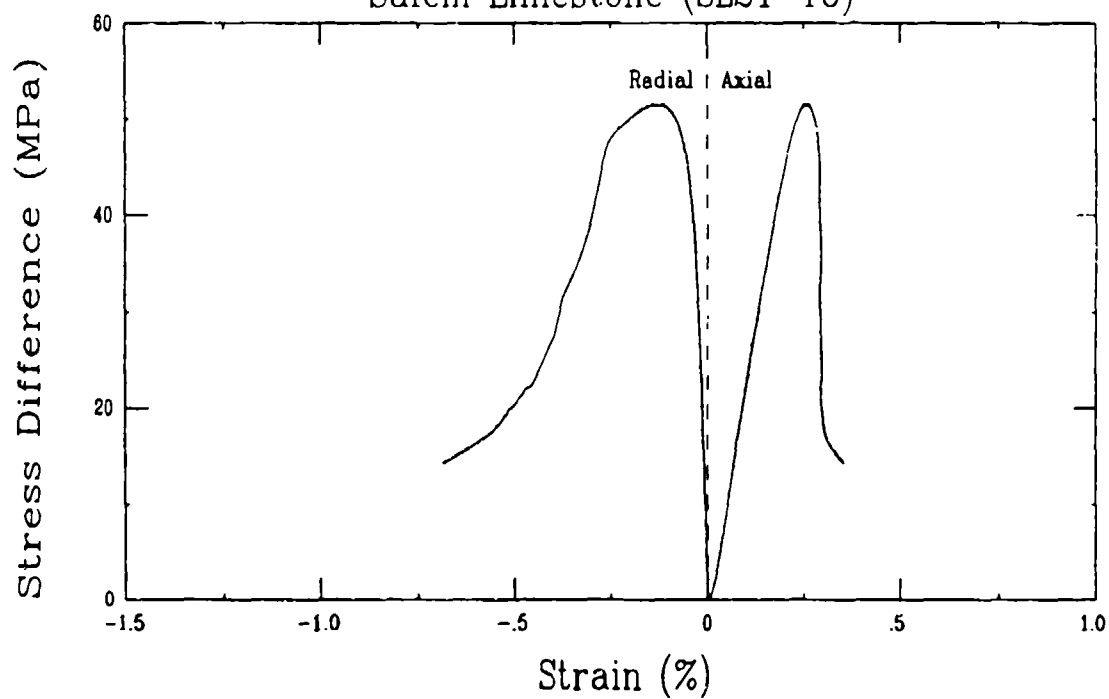




Unconfined Compression Test (M13F1)  
Salem Limestone (SL21-T7)



Unconfined Compression Test (M13G1)  
Salem Limestone (SL21-T6)



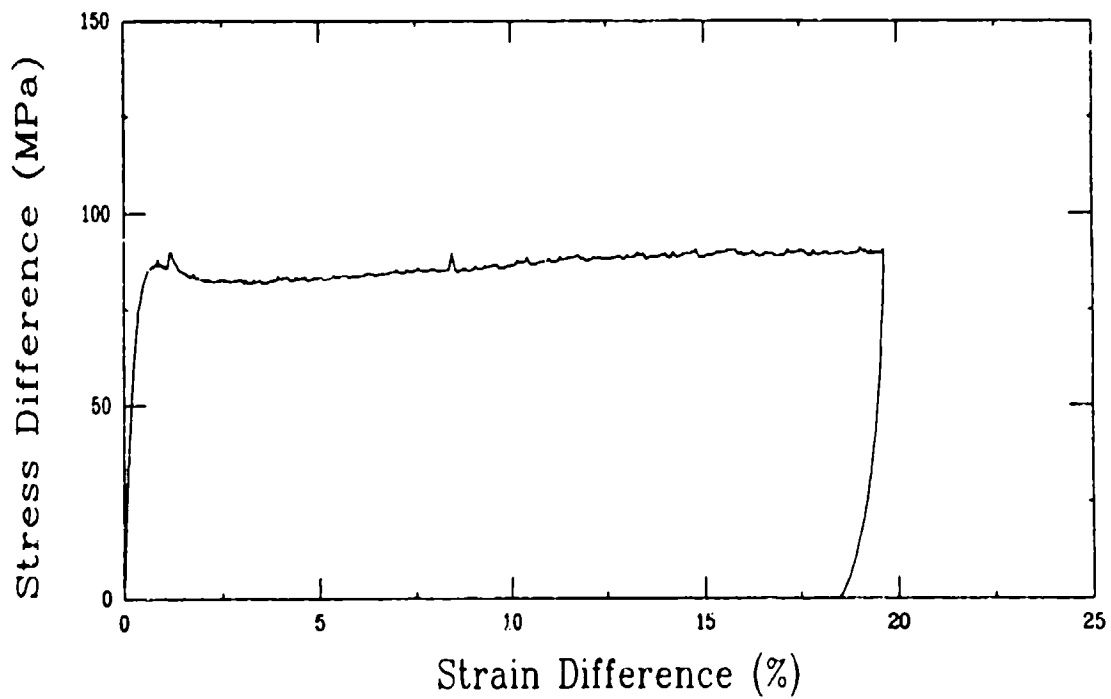
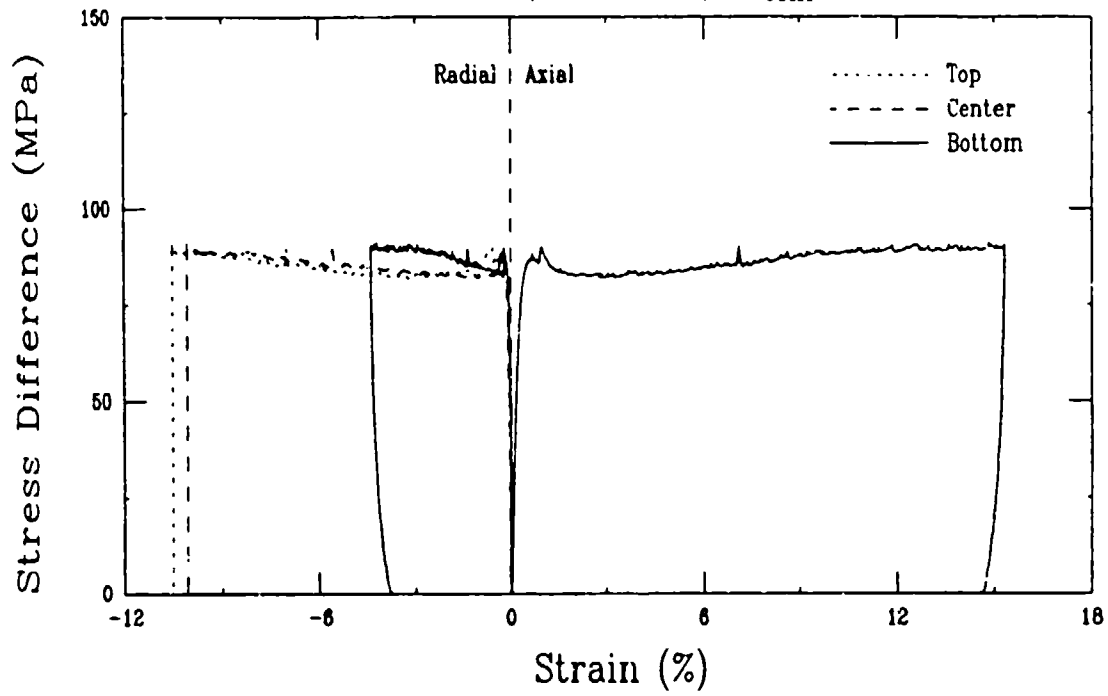
**APPENDIX C**

**TRIAXIAL COMPRESSION TESTS ON**

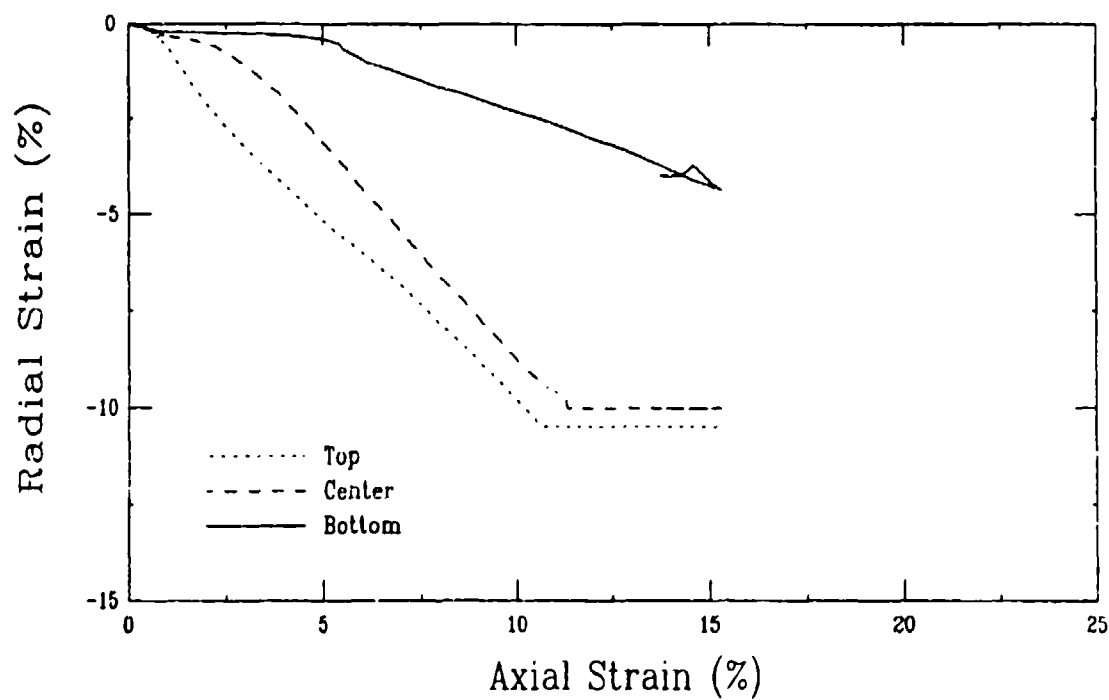
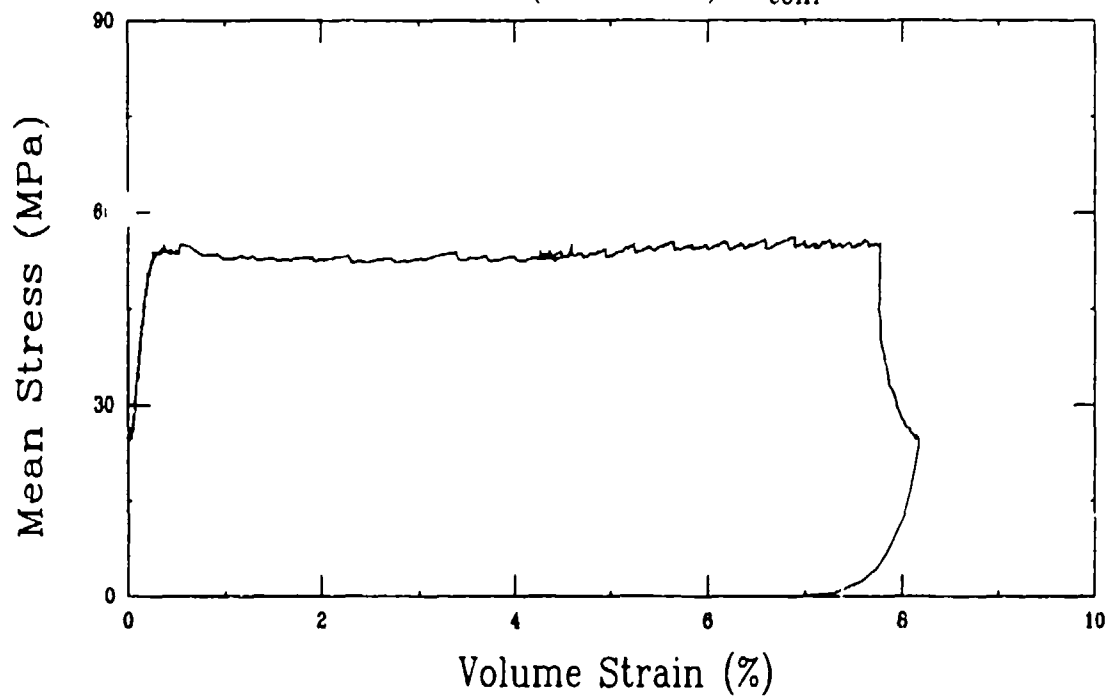
**INTACT SPECIMENS**

<b>Test ID</b>	<b>Confining Pressure (MPa)</b>	<b>Page</b>
D6D0	25	C-2
D20B0	25	C-4
D4B0	25	C-6
D3B0	50	C-8
D5B0	50	C-10
D6B0	50	C-12
O24E0	100	C-14
D7B0	100	C-16
O25B0	200	C-18
D7D0	200	C-20
O26B0	400	C-22

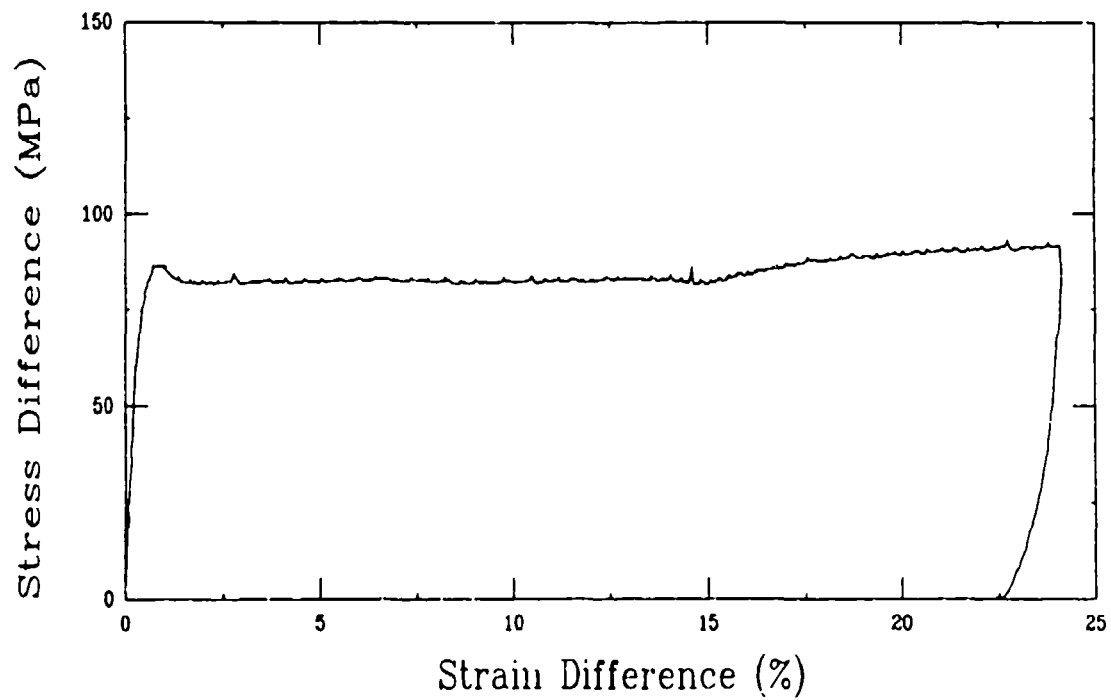
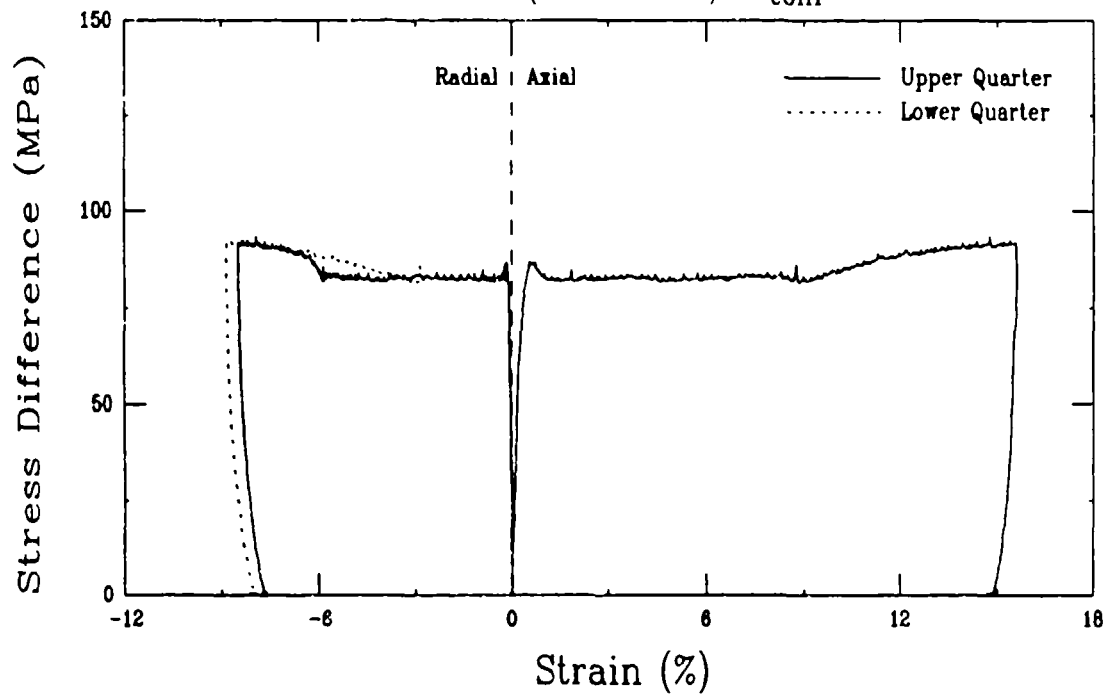
Triaxial Compression Test (D6D0)  
Salem Limestone (SL20-T18),  $\sigma_{\text{conf}} = 25 \text{ MPa}$



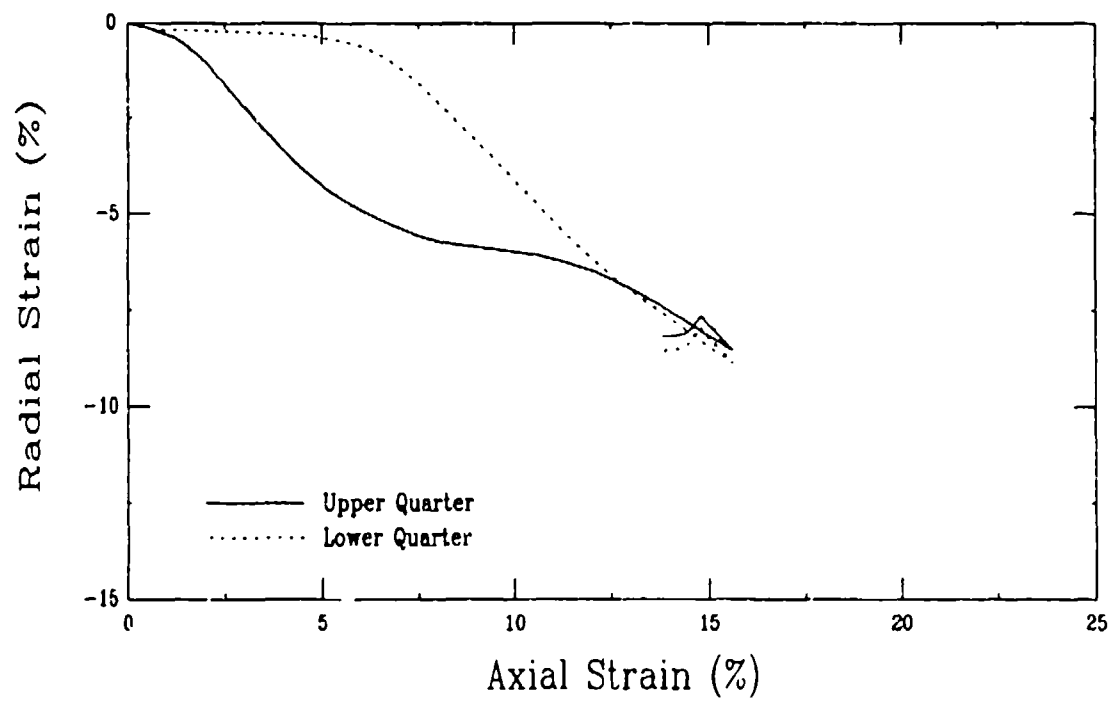
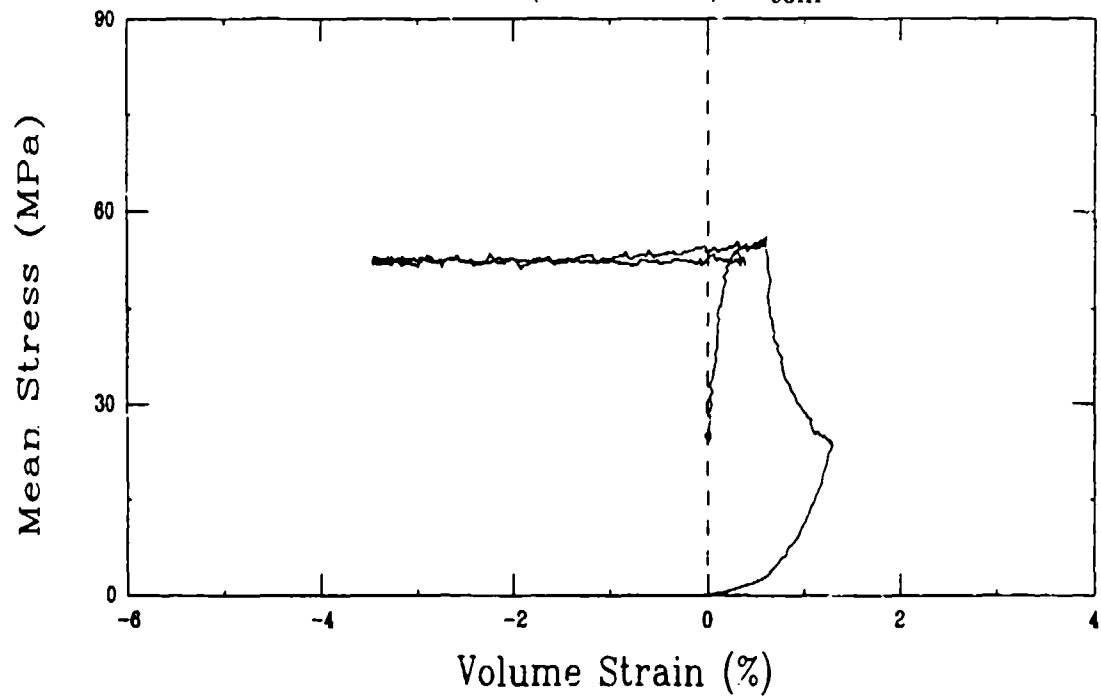
Triaxial Compression Test (D6D0)  
Salem Limestone (SL20-T18),  $\sigma_{\text{conf}} = 25 \text{ MPa}$



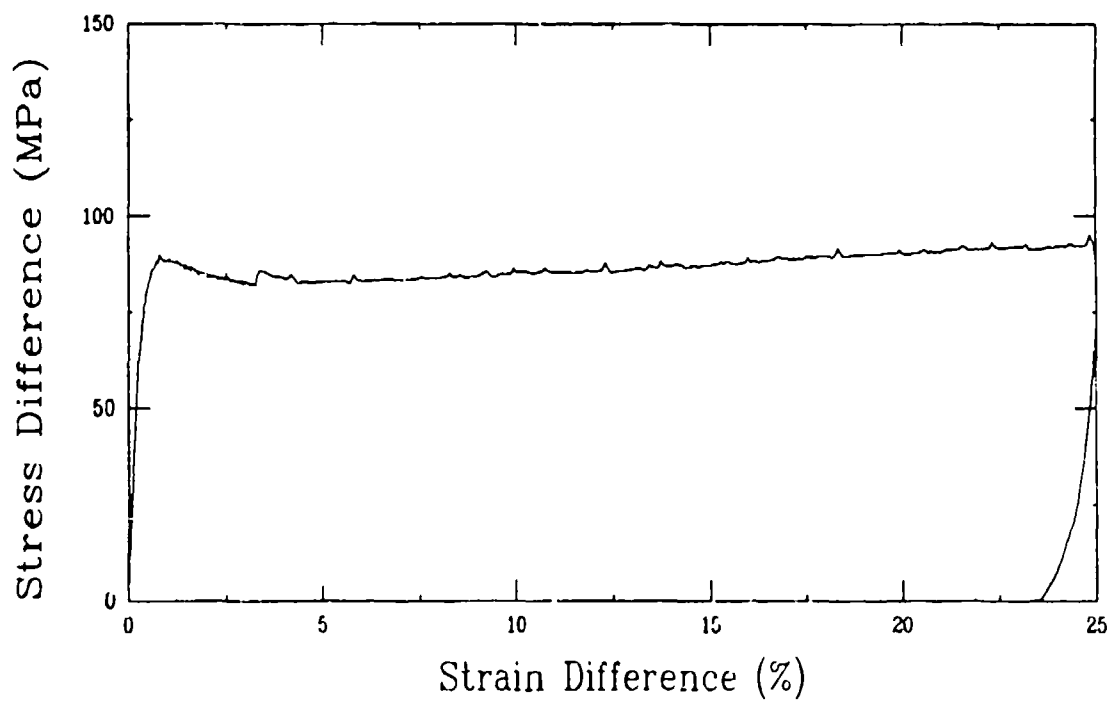
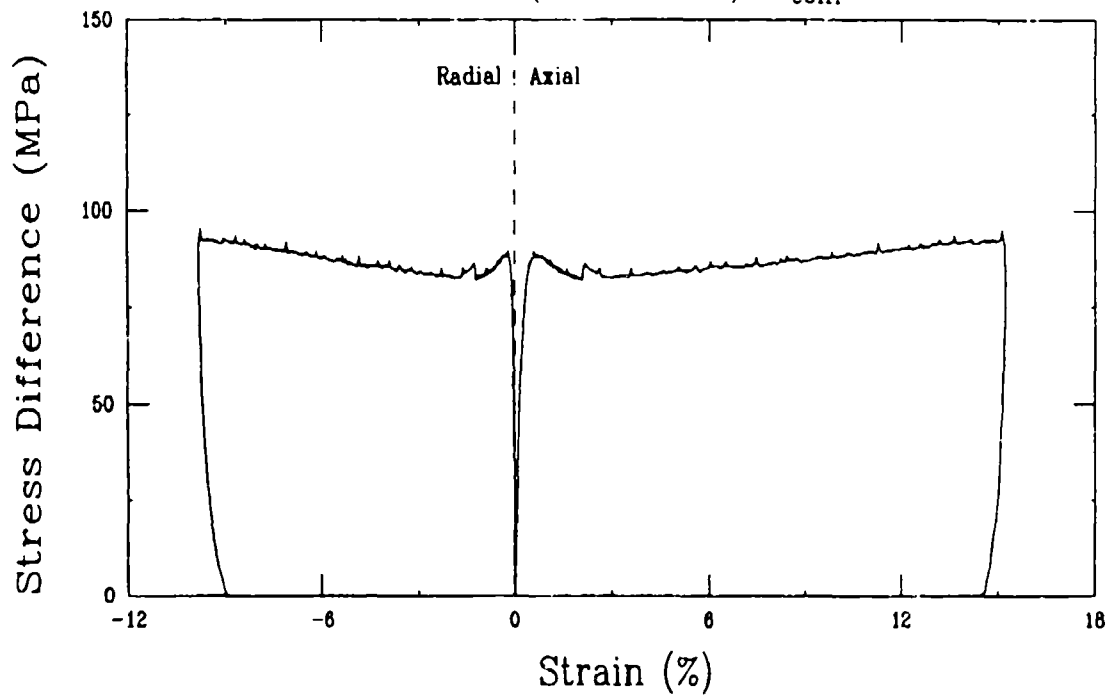
Triaxial Compression Test (D20B0)  
Salem Limestone (SL20-B14),  $\sigma_{\text{conf}} = 25 \text{ MPa}$



Triaxial Compression Test (D20B0)  
Salem Limestone (SL20-B14),  $\sigma_{\text{conf}} = 25 \text{ MPa}$

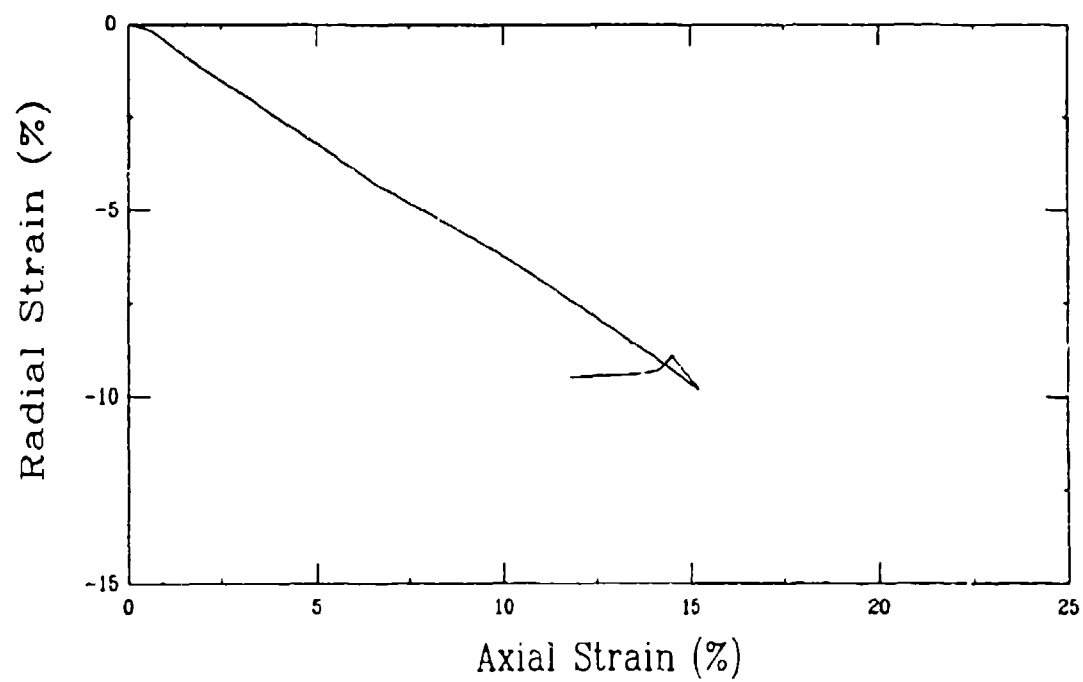
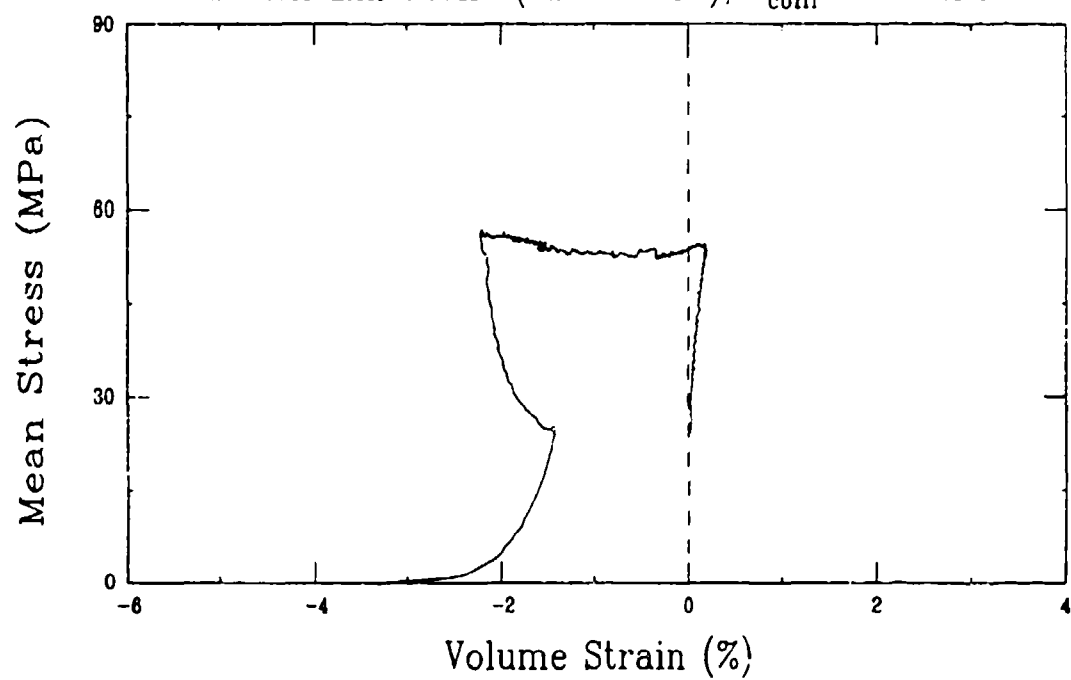


Triaxial Compression Test (D4B0)  
Salem Limestone (SL20-T21B),  $\sigma_{\text{conf}} = 25 \text{ MPa}$

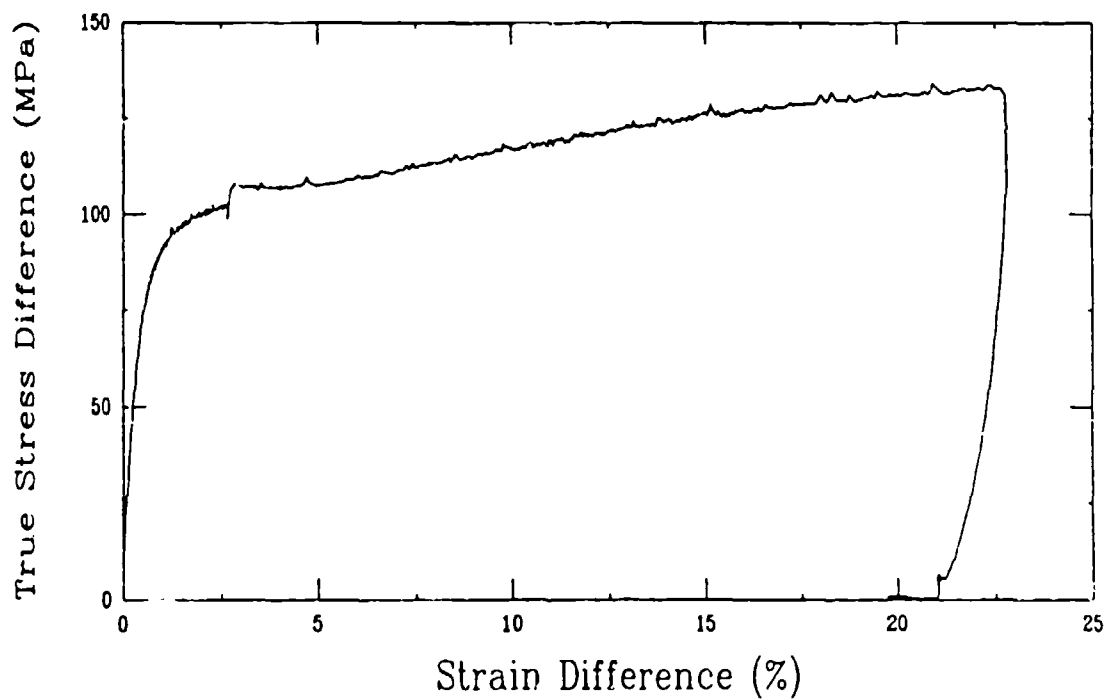
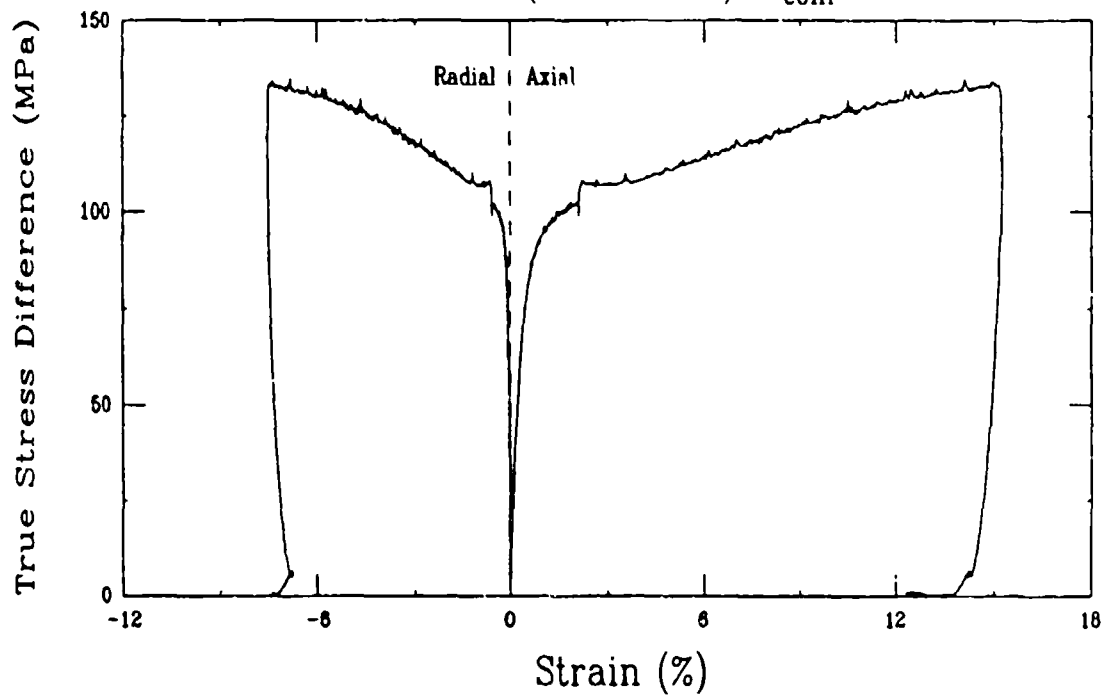




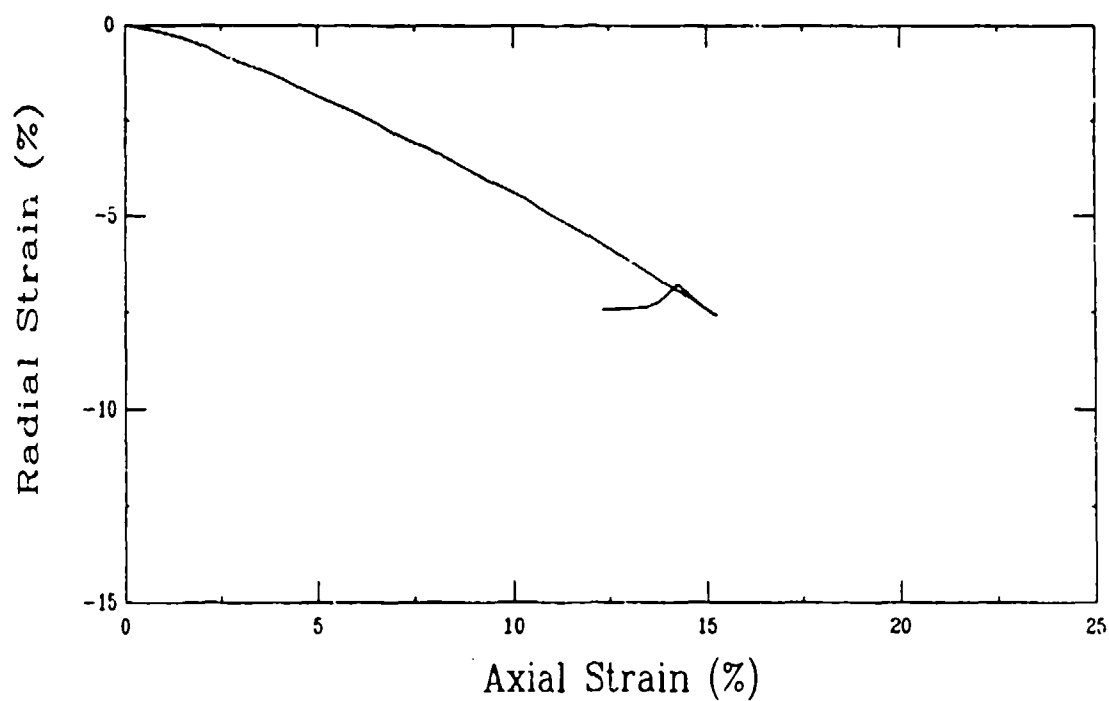
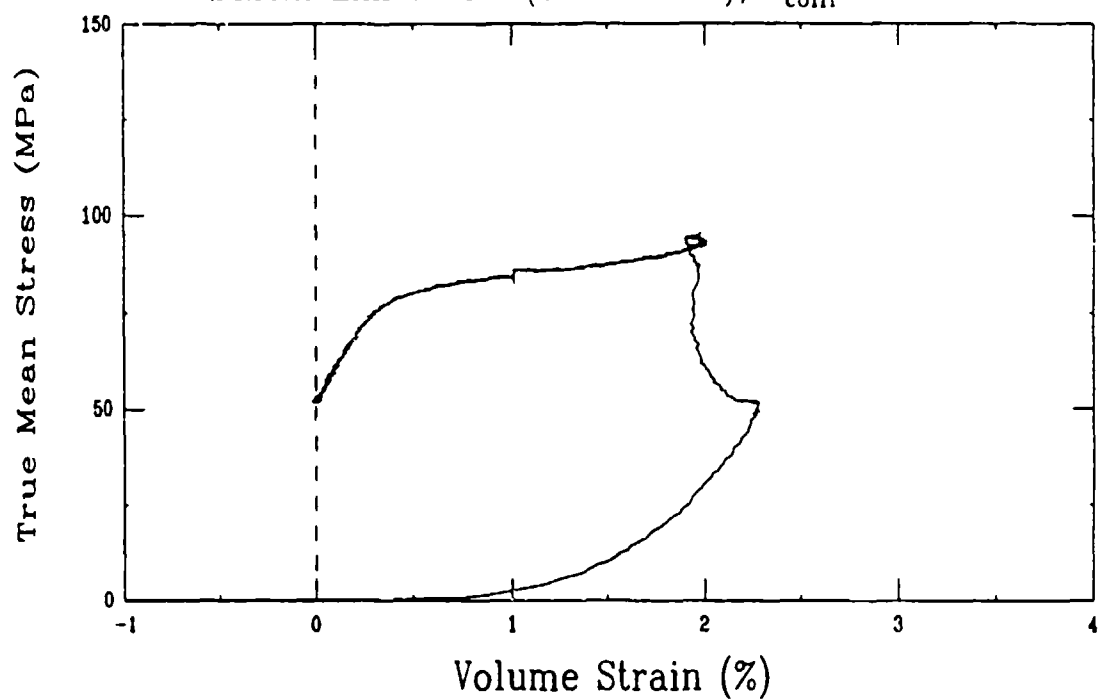
Triaxial Compression Test (D4B0)  
Salem Limestone (SL20-T21B),  $\sigma_{\text{conf}} = 25$  MPa



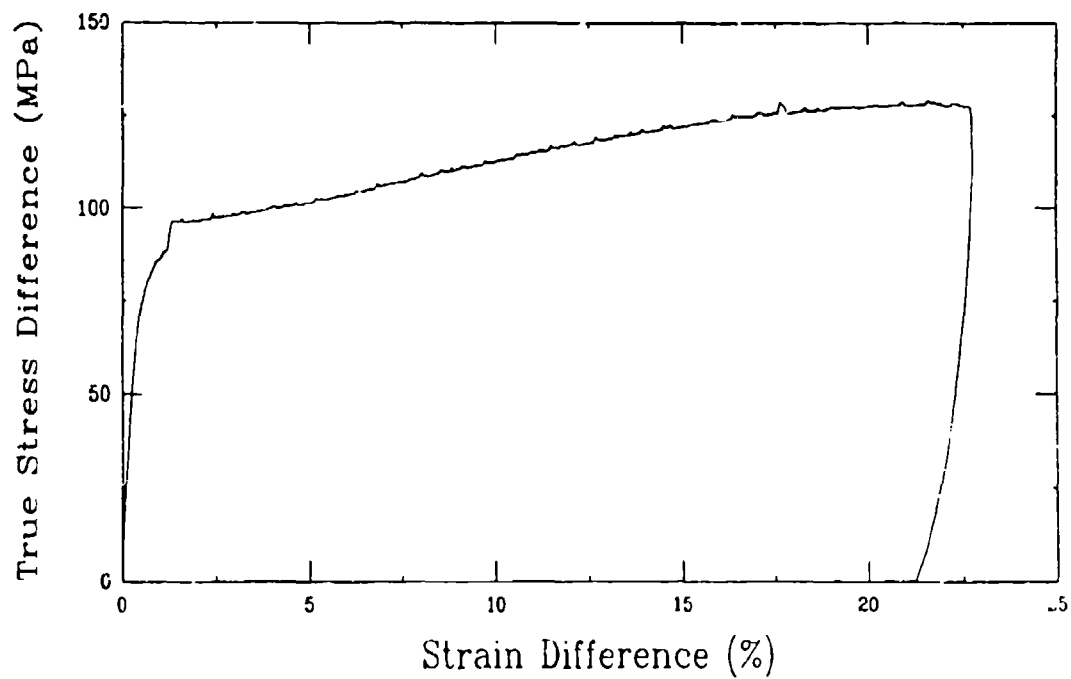
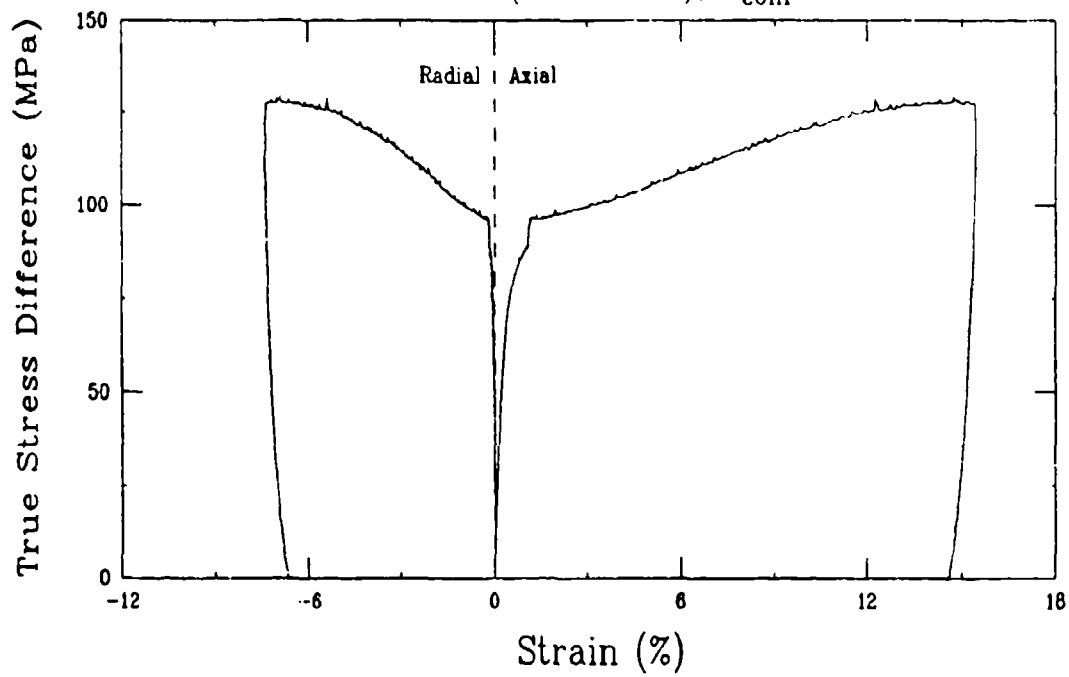
Triaxial Compression Test (D3B0)  
Salem Limestone (SL20-T16A),  $\sigma_{\text{conf}} = 50$  MPa



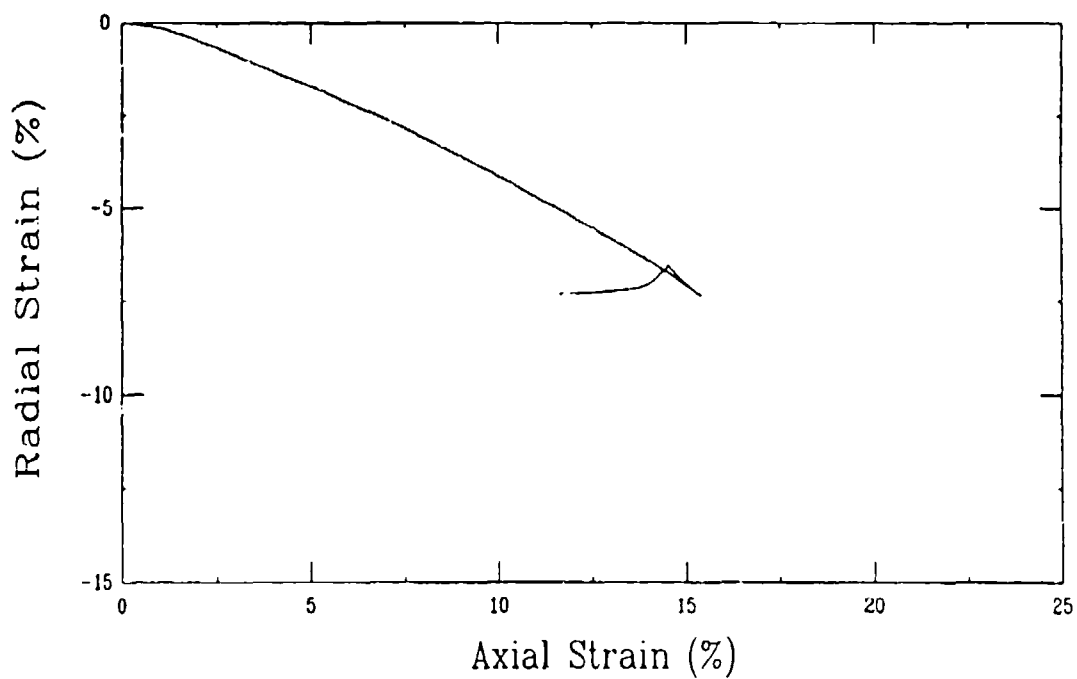
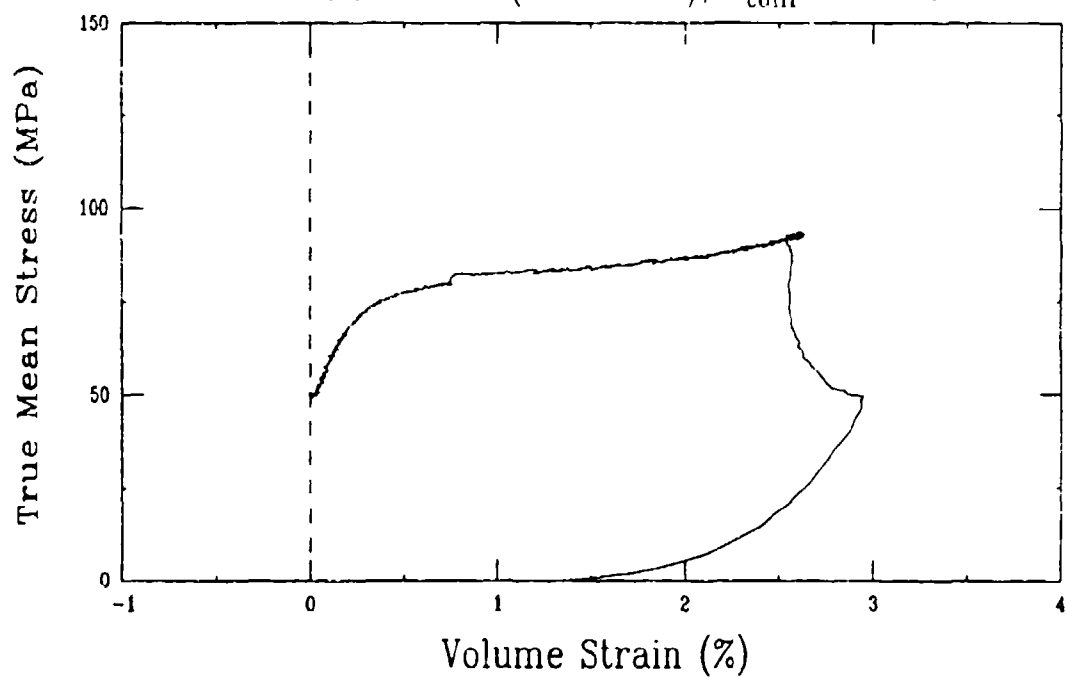
Triaxial Compression Test (D3B0)  
Salem Limestone (SL20-T16A),  $\sigma_{conf} = 50$  MPa



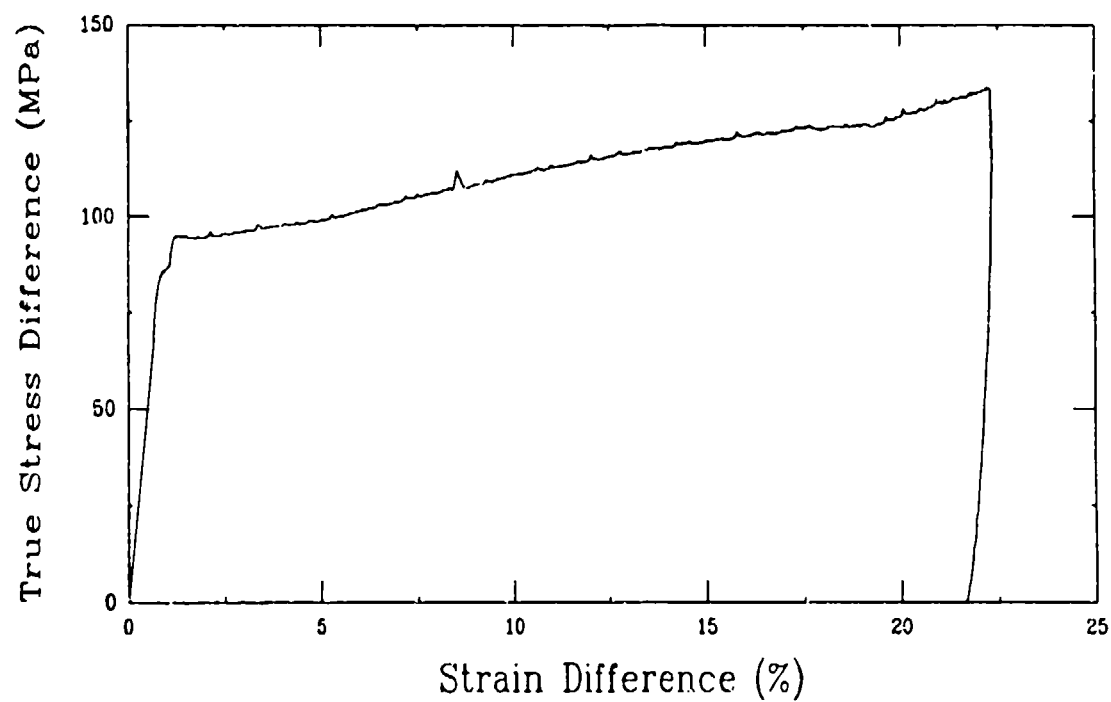
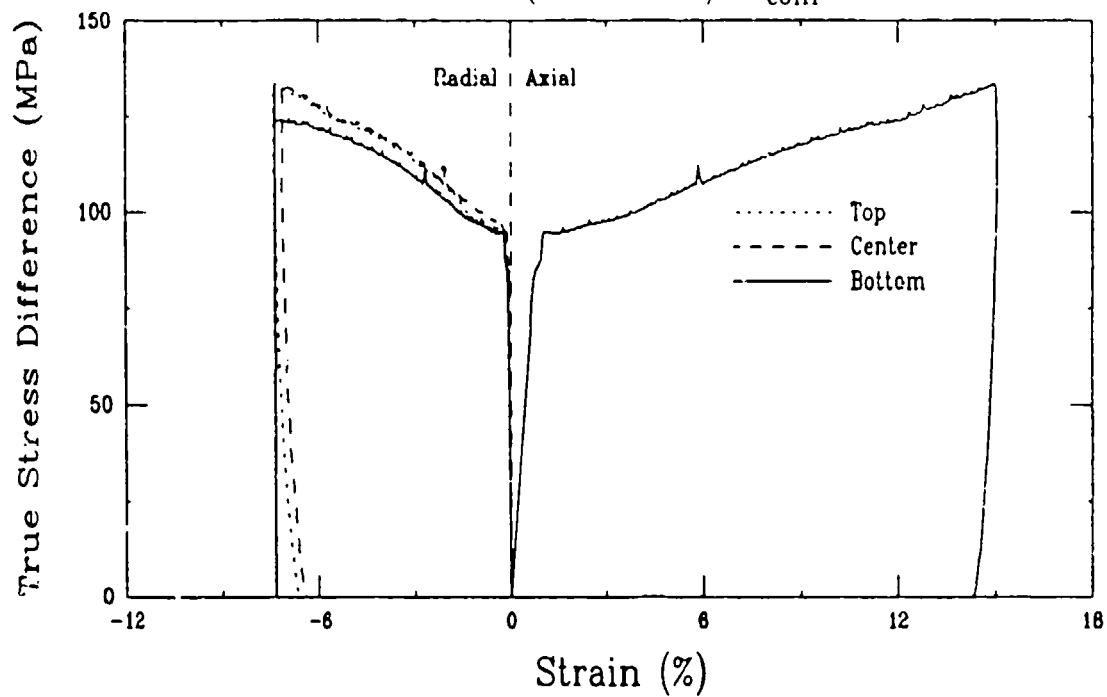
Triaxial Compression Test (D5B0)  
Salem Limestone (SL20-B21),  $\sigma_{\text{conf}} = 50$  MPa



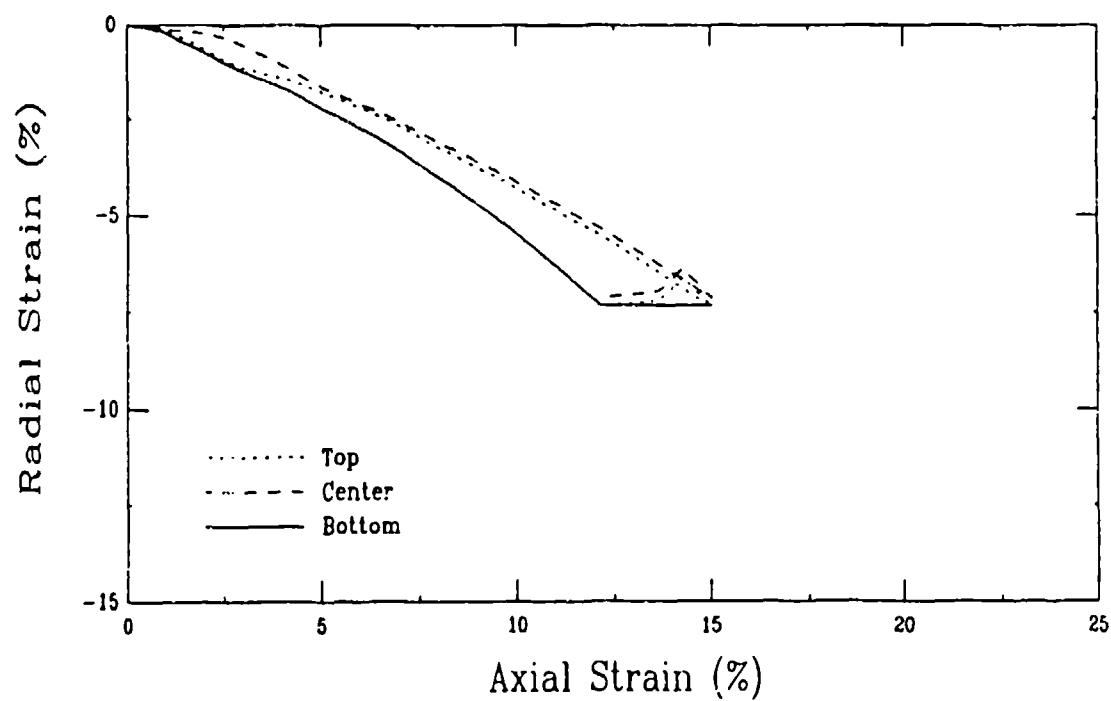
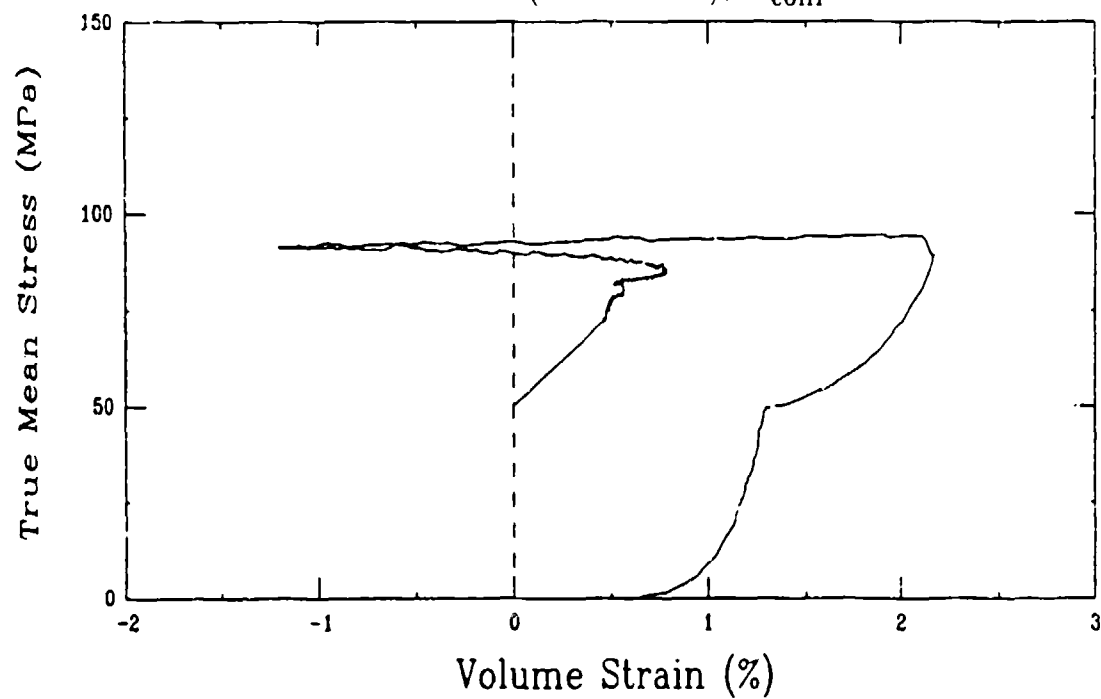
Triaxial Compression Test (D5B0)  
Salem Limestone (SL20-B21),  $\sigma_{conf} = 50$  MPa



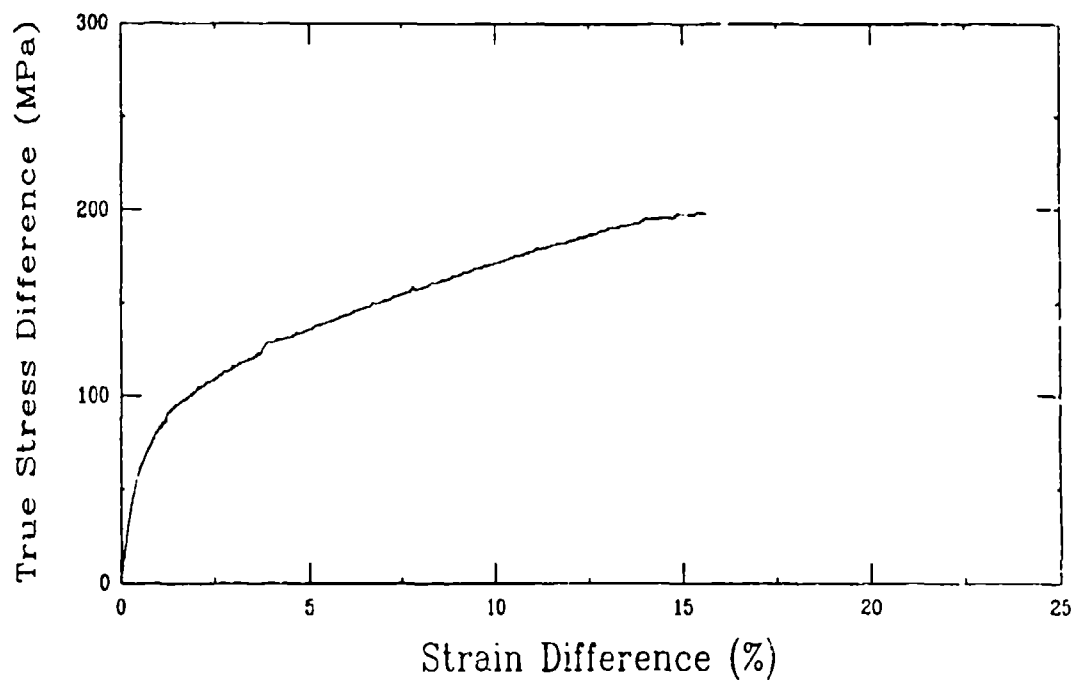
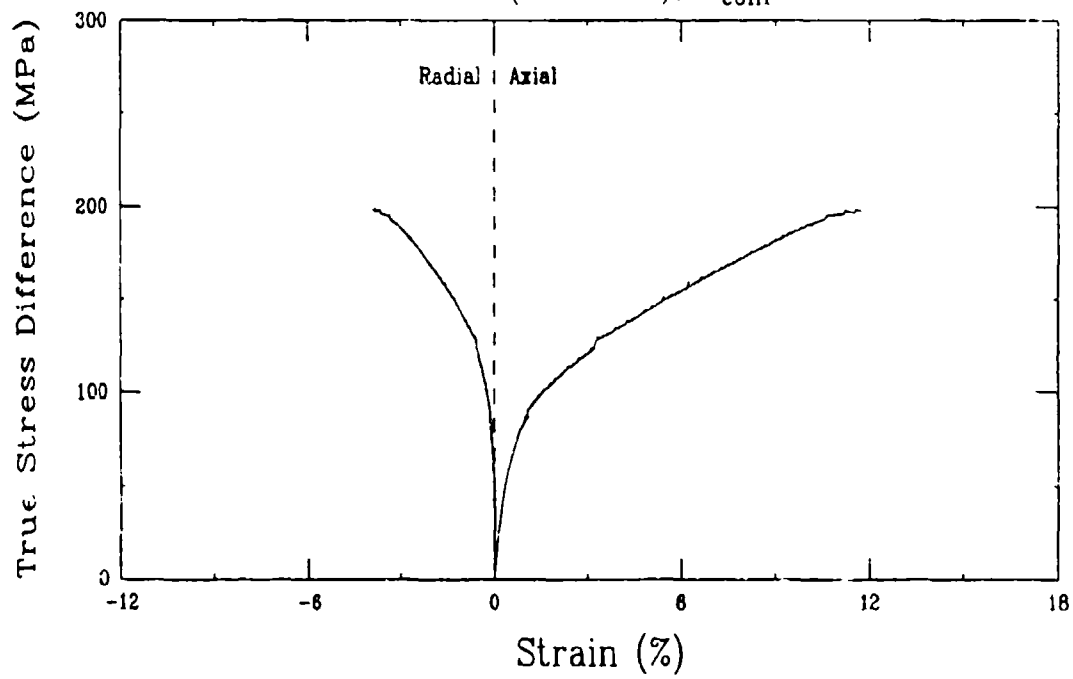
Triaxial Compression Test (D6B0)  
Salem Limestone (SL20-B13),  $\sigma_{\text{conf}} = 50$  MPa



Triaxial Compression Test (D6B0)  
Salem Limestone (SL20-B13),  $\sigma_{\text{conf}} = 50 \text{ MPa}$

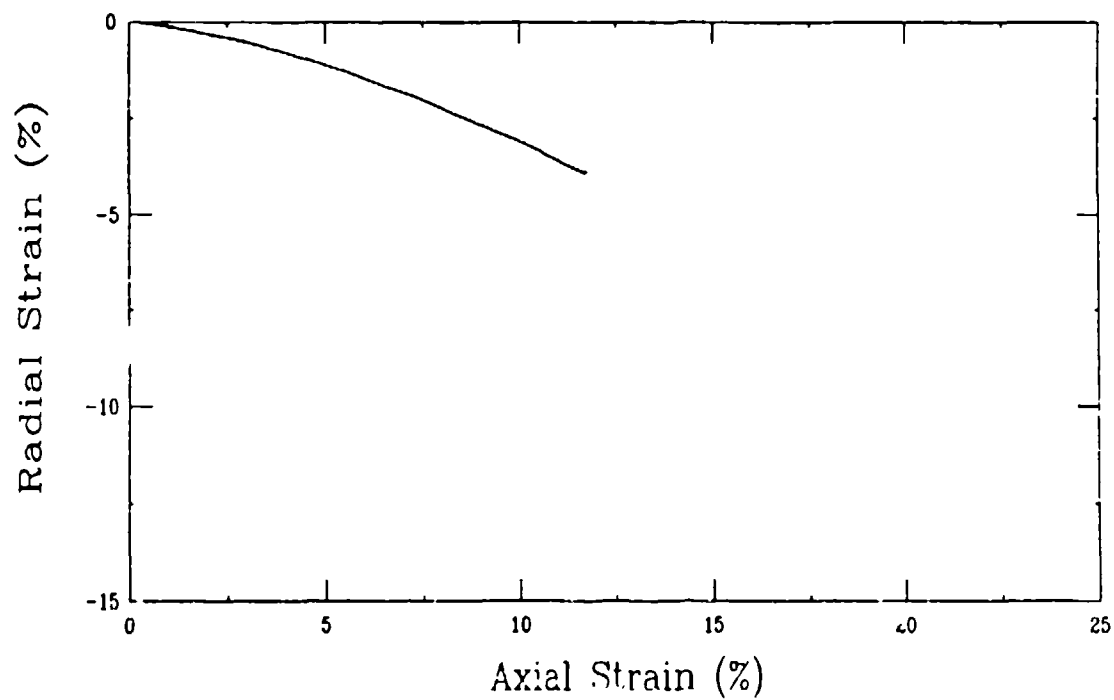
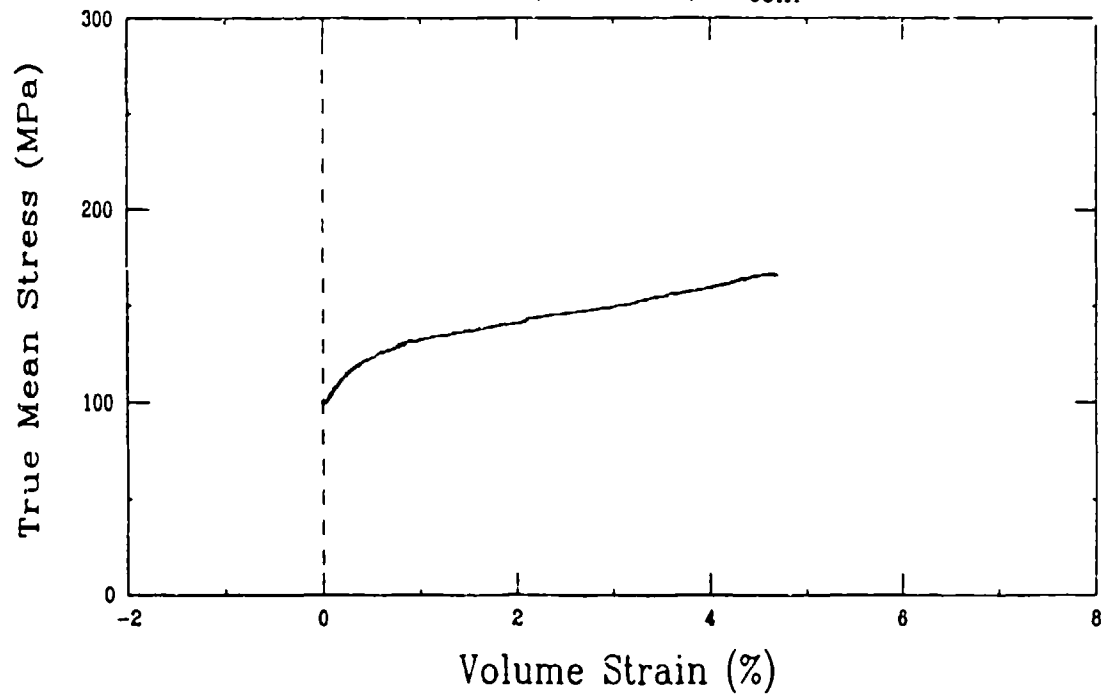


Triaxial Compression Test (024E0)  
Salem Limestone (SL20-T9),  $\sigma_{\text{conf}} = 100 \text{ MPa}$

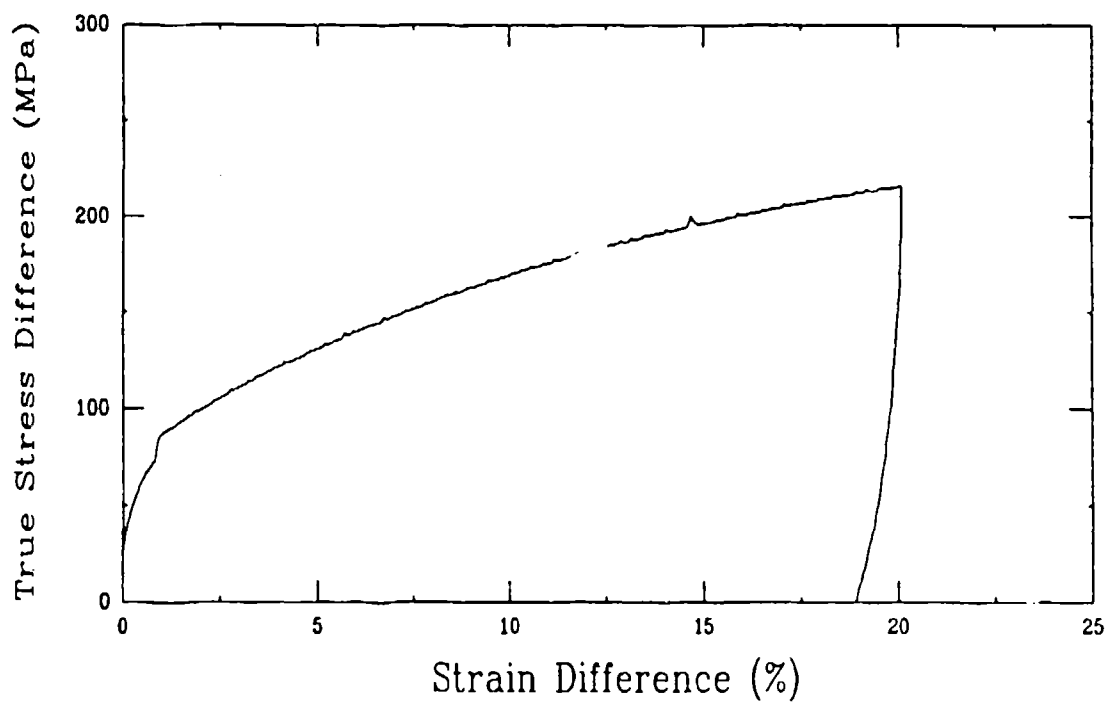
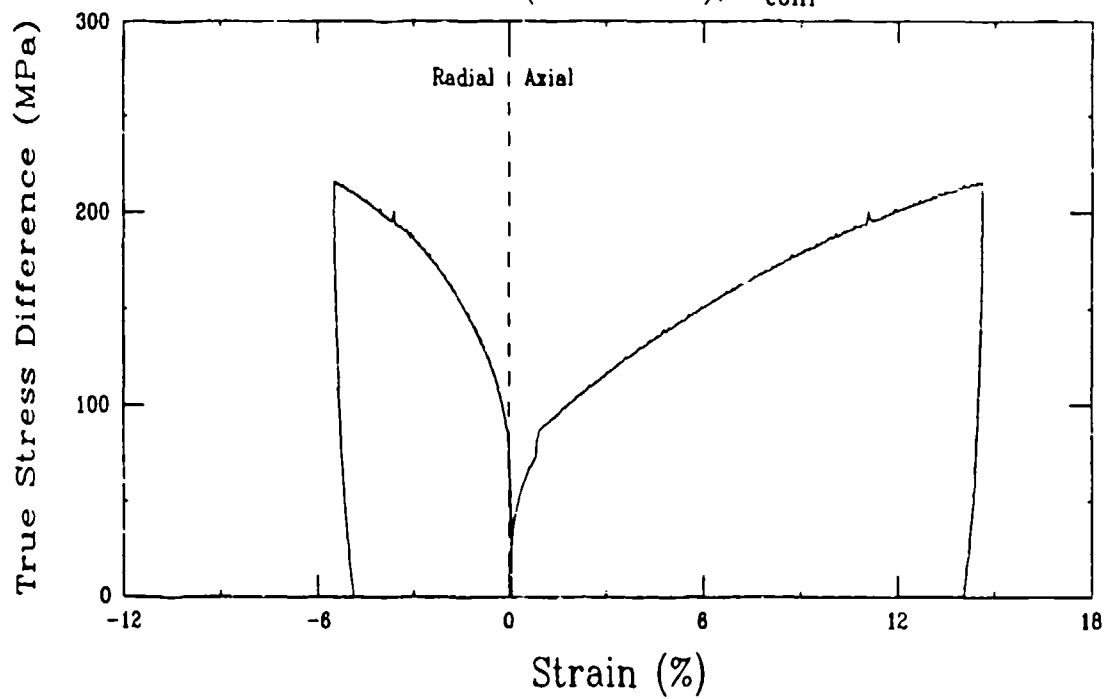




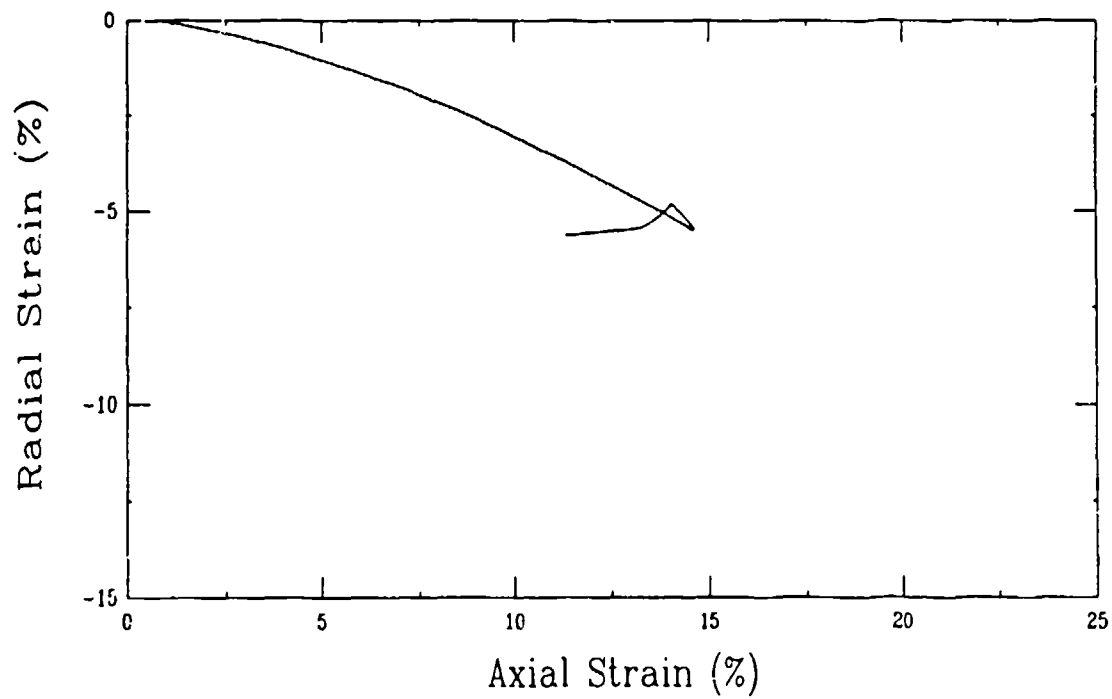
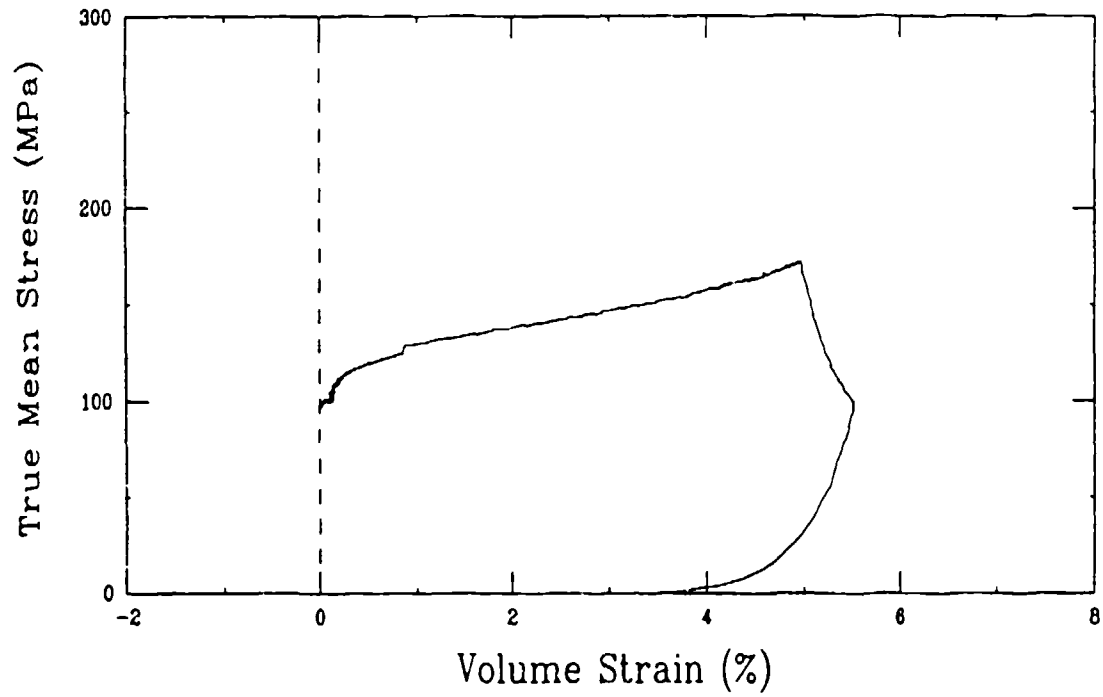
Triaxial Compression Test (024E0)  
Salem Limestone (SL20-T9),  $\sigma_{\text{conf}} = 100 \text{ MPa}$



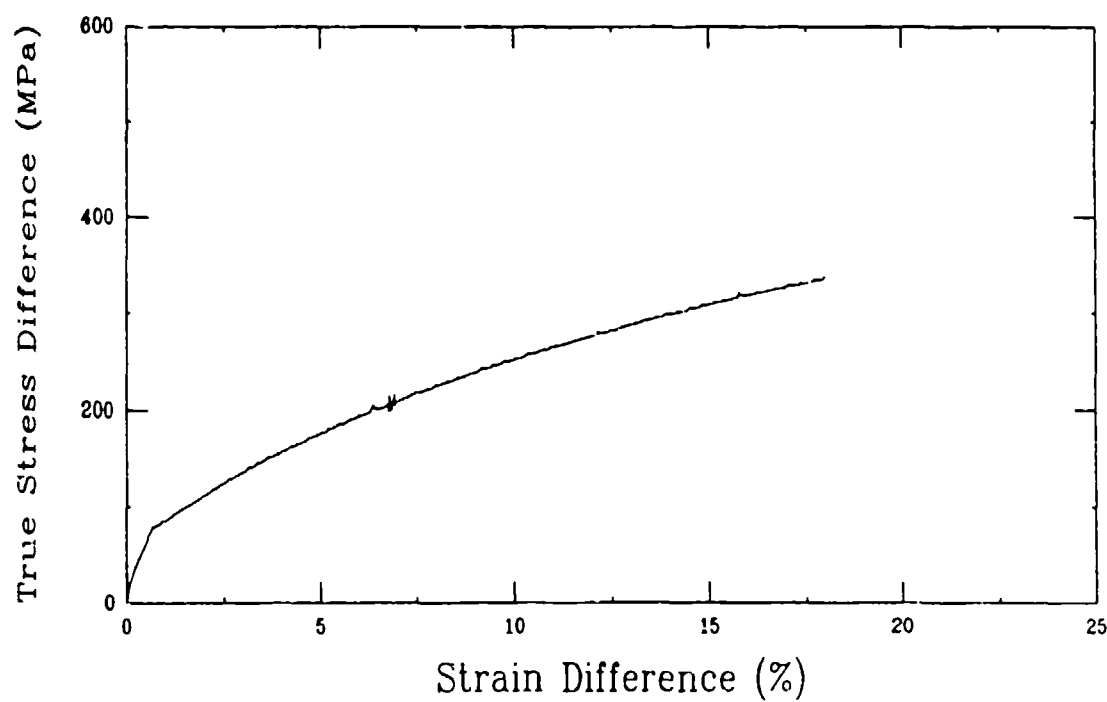
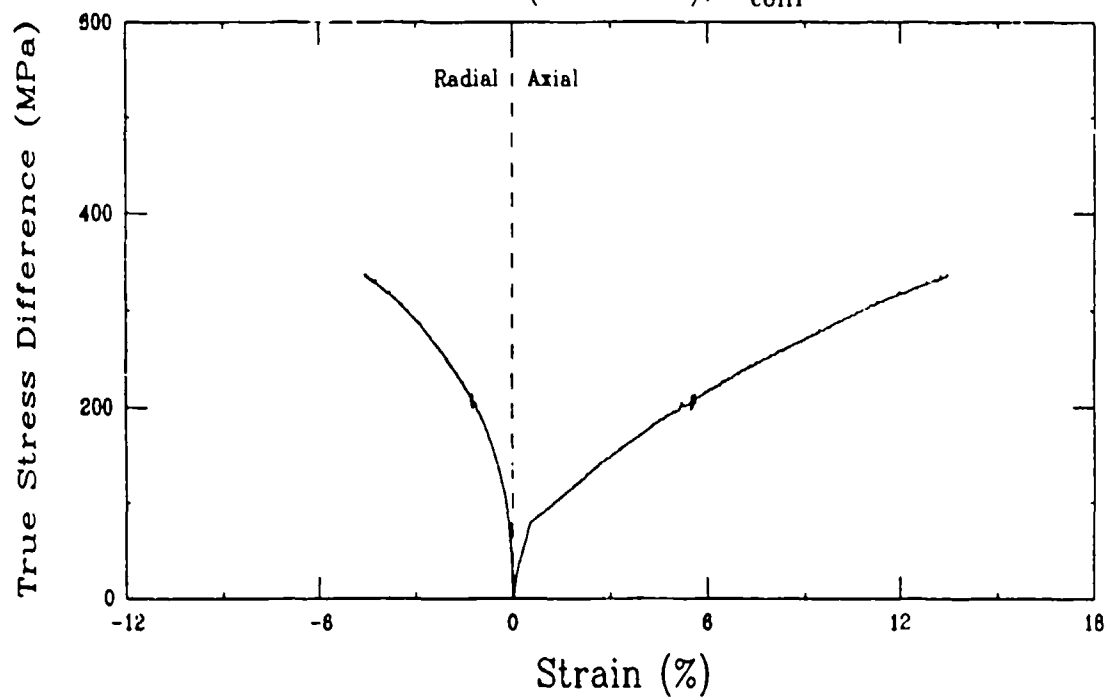
Triaxial Compression Test (D7B0)  
Salem Limestone (SL20-T19),  $\sigma_{\text{conf}} = 100 \text{ MPa}$



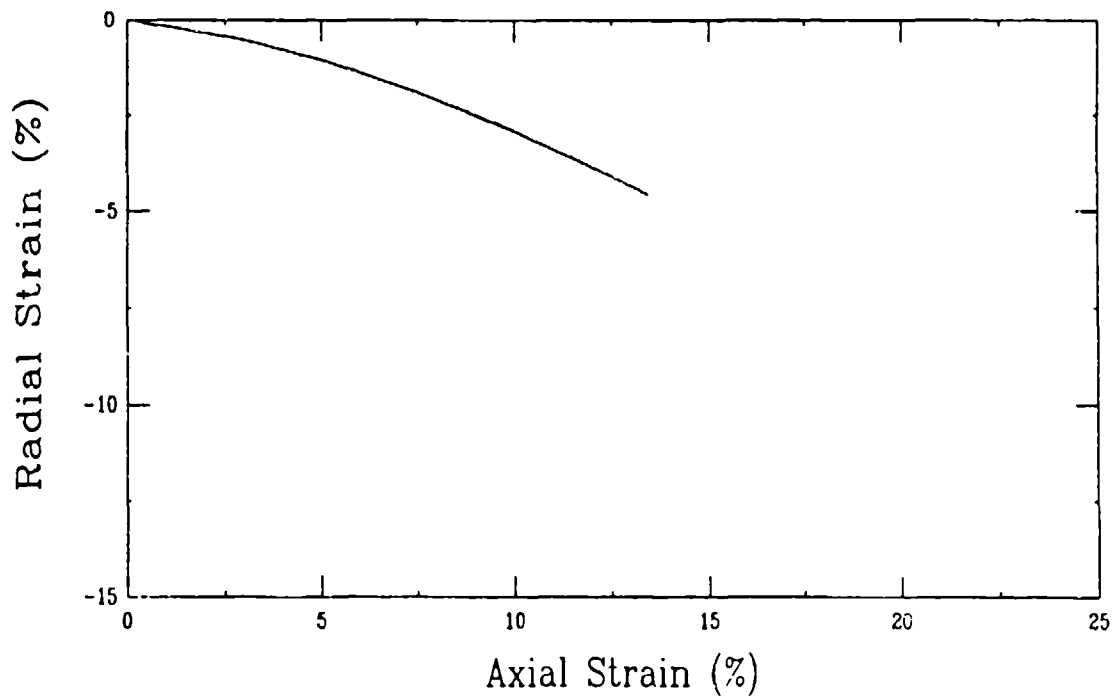
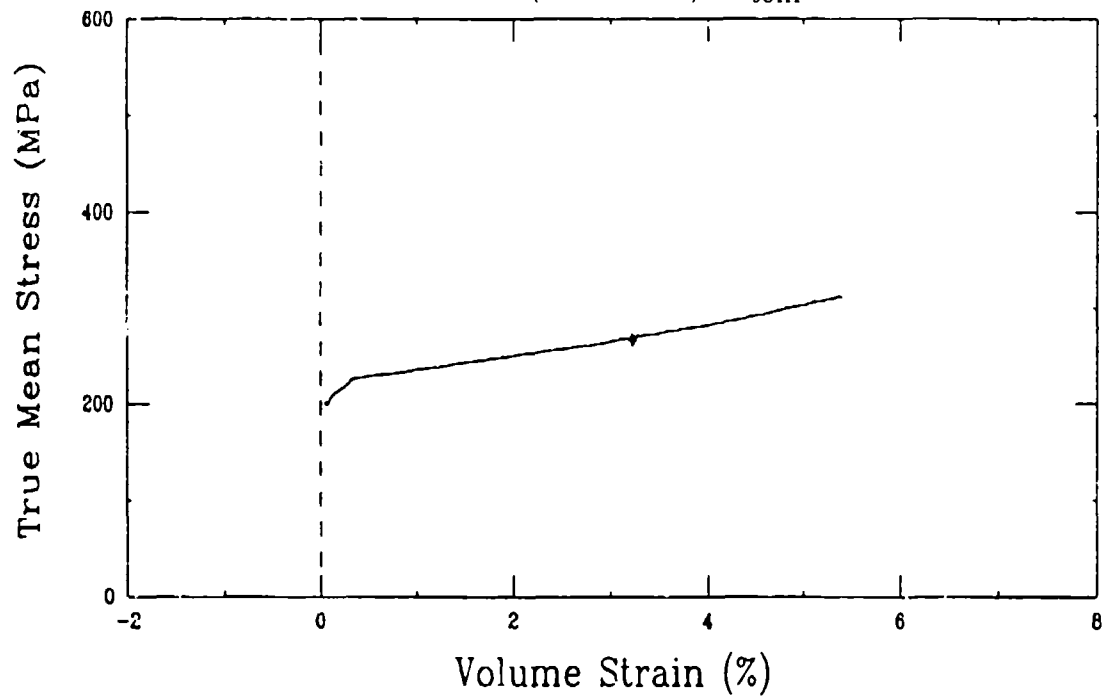
Triaxial Compression Test (D7B0)  
Salem Limestone (SL20-T19),  $\sigma_{\text{conf}} = 100 \text{ MPa}$



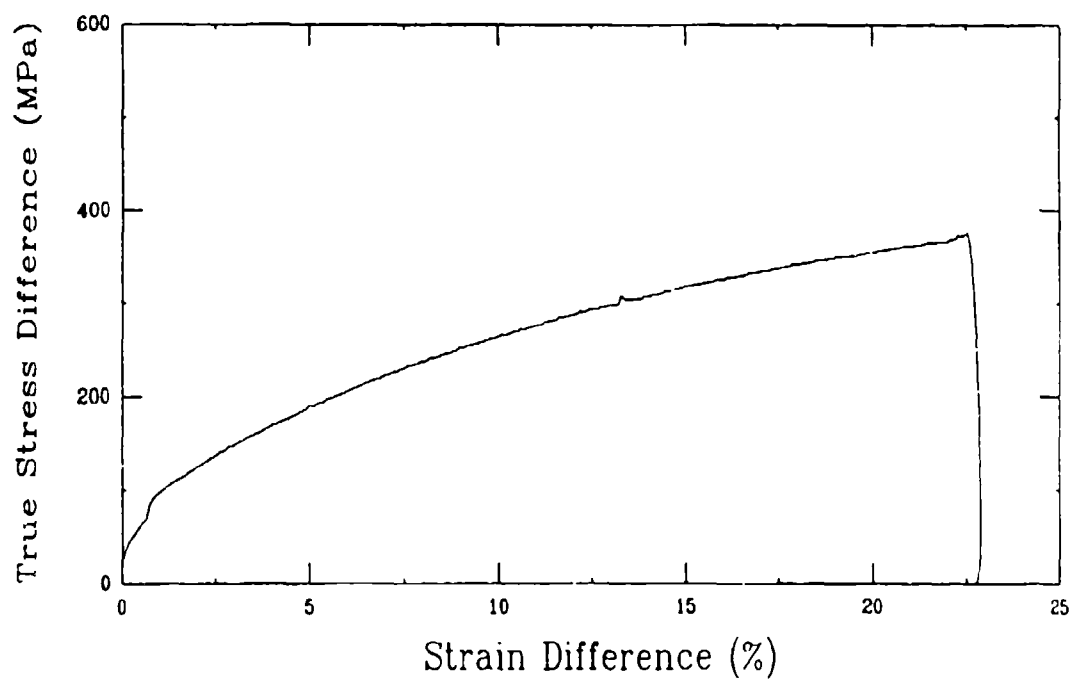
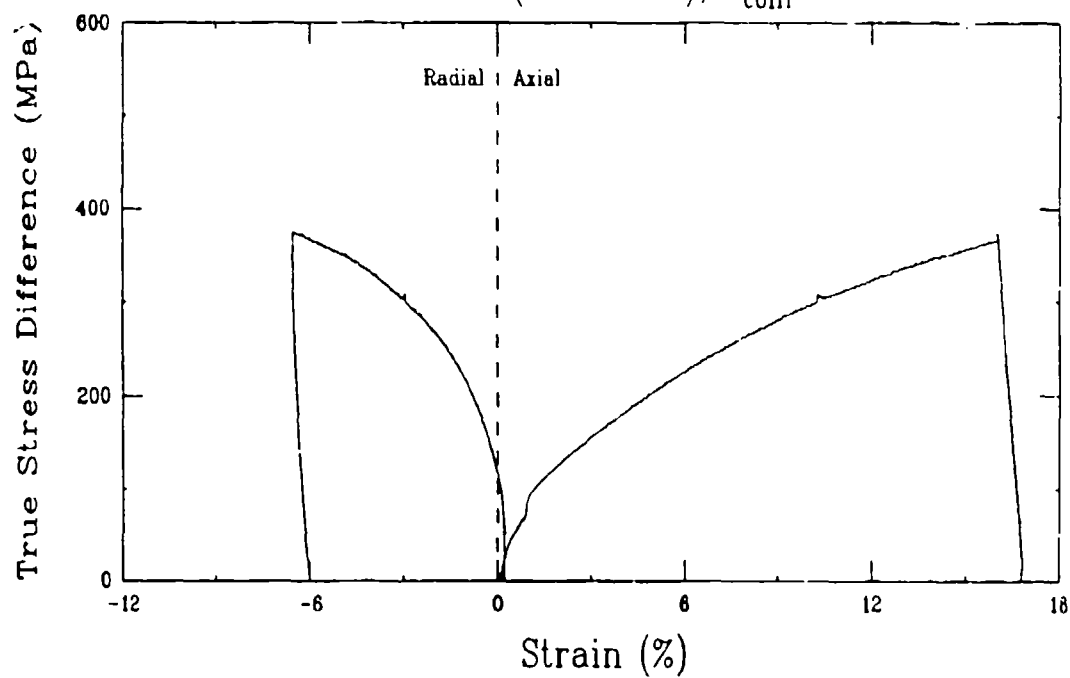
Triaxial Compression Test (025B0)  
Salem Limestone (SL20-B9),  $\sigma_{\text{conf}} = 200$  MPa



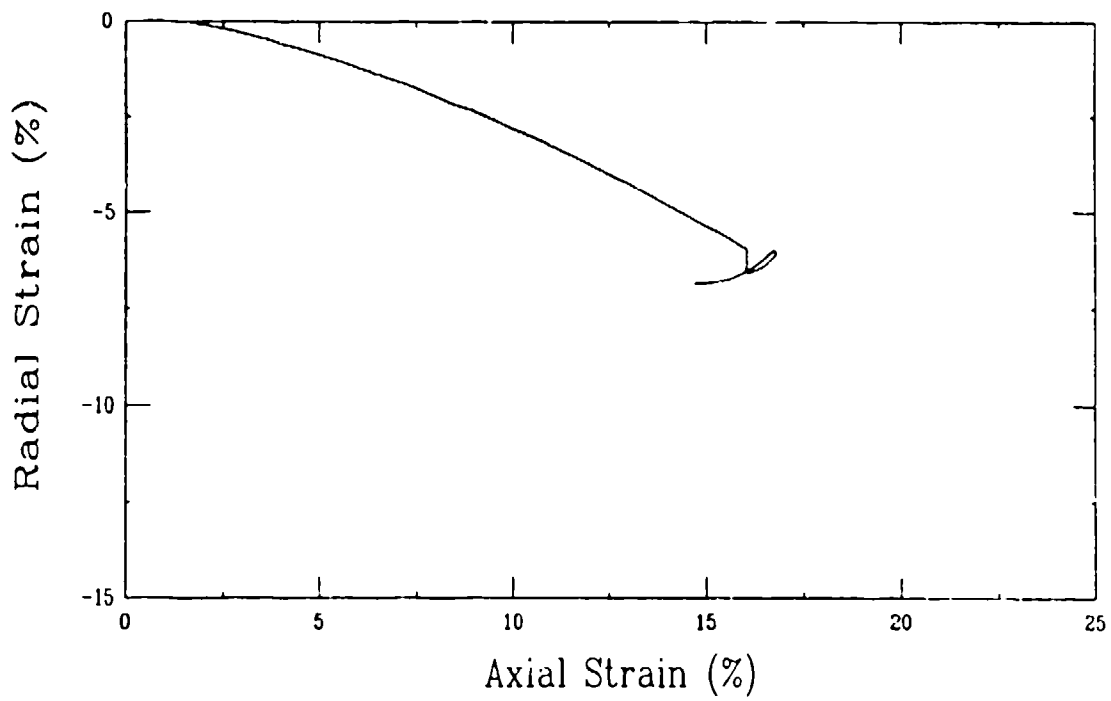
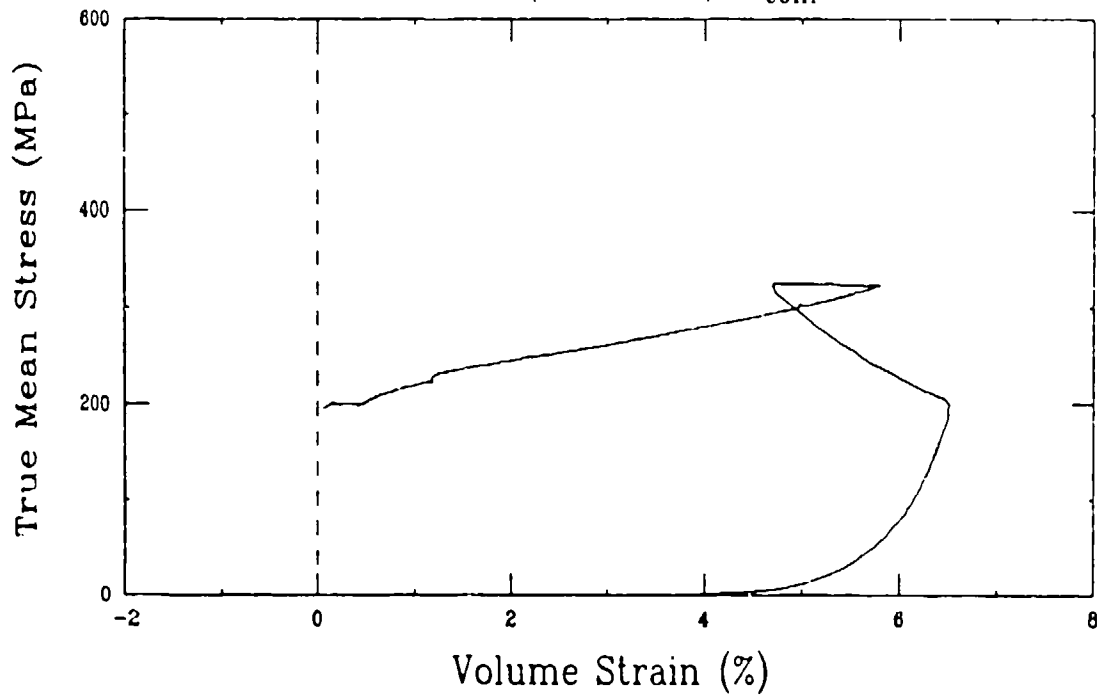
Triaxial Compression Test (025B0)  
Salem Limestone (SL20-B9),  $\sigma_{\text{conf}} = 200 \text{ MPa}$



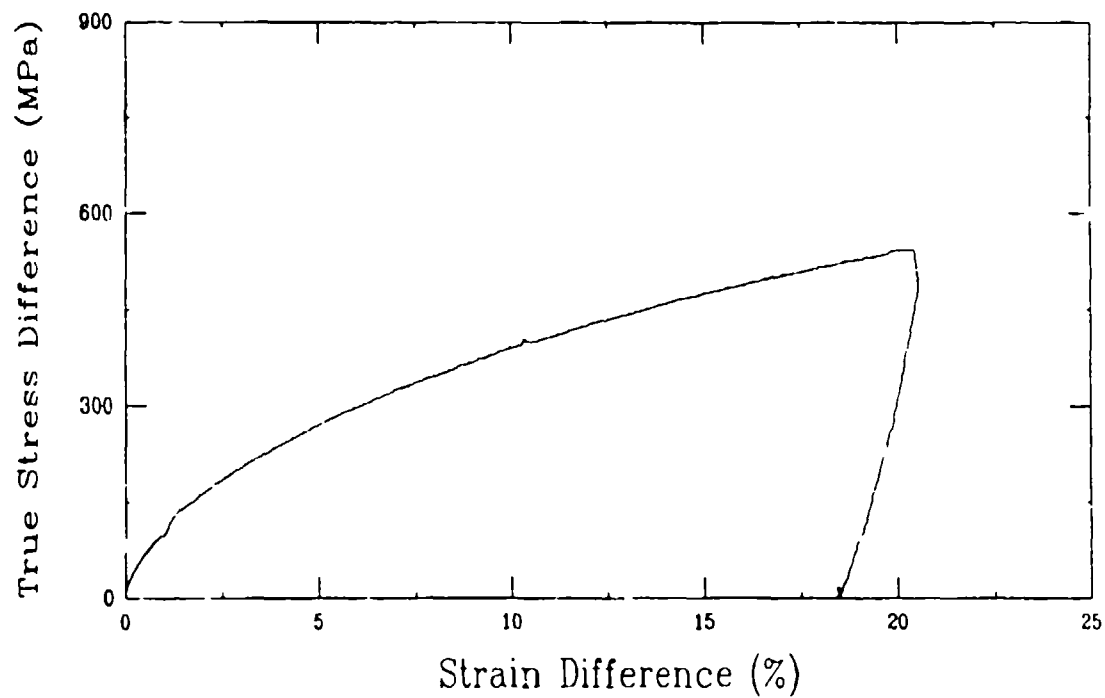
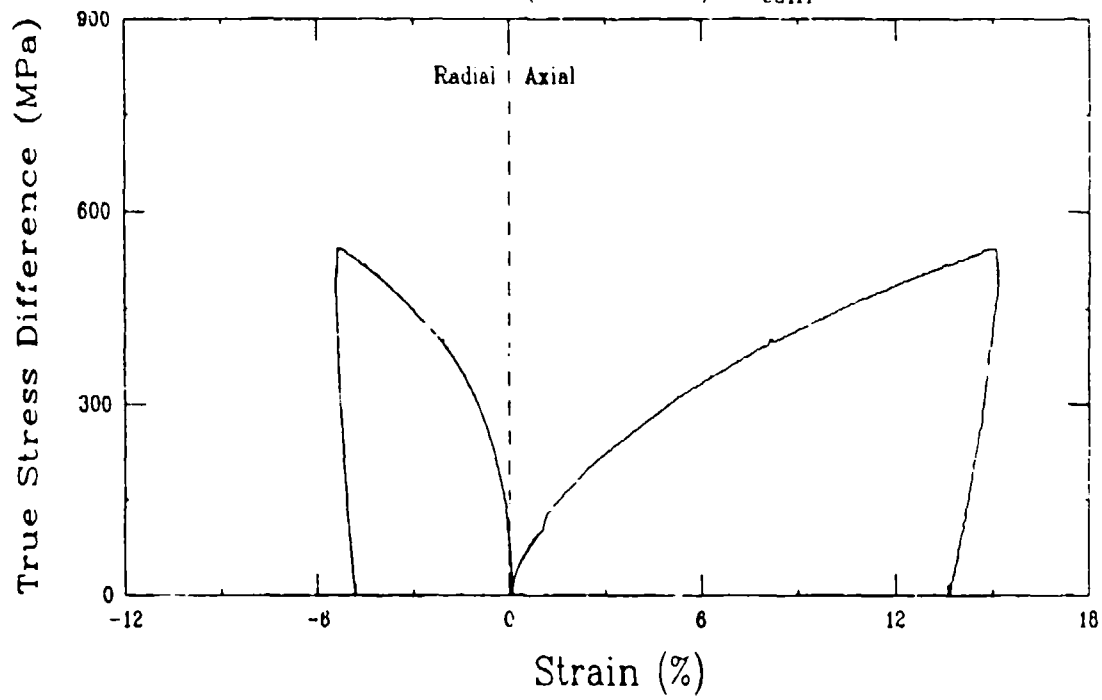
Triaxial Compression Test (D7D0)  
Salem Limestone (SL20-T13),  $\sigma_{\text{conf}} = 200 \text{ MPa}$



Triaxial Compression Test (D7D0)  
Salem Limestone (SL20-T13),  $\sigma_{\text{conf}} = 200 \text{ MPa}$

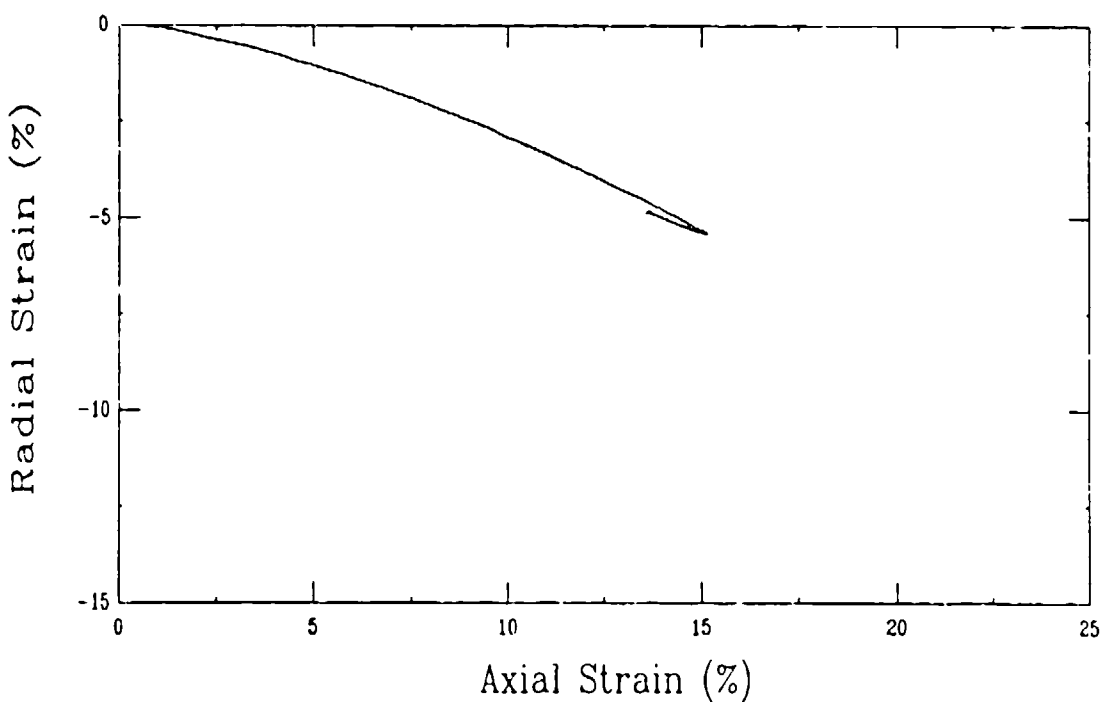
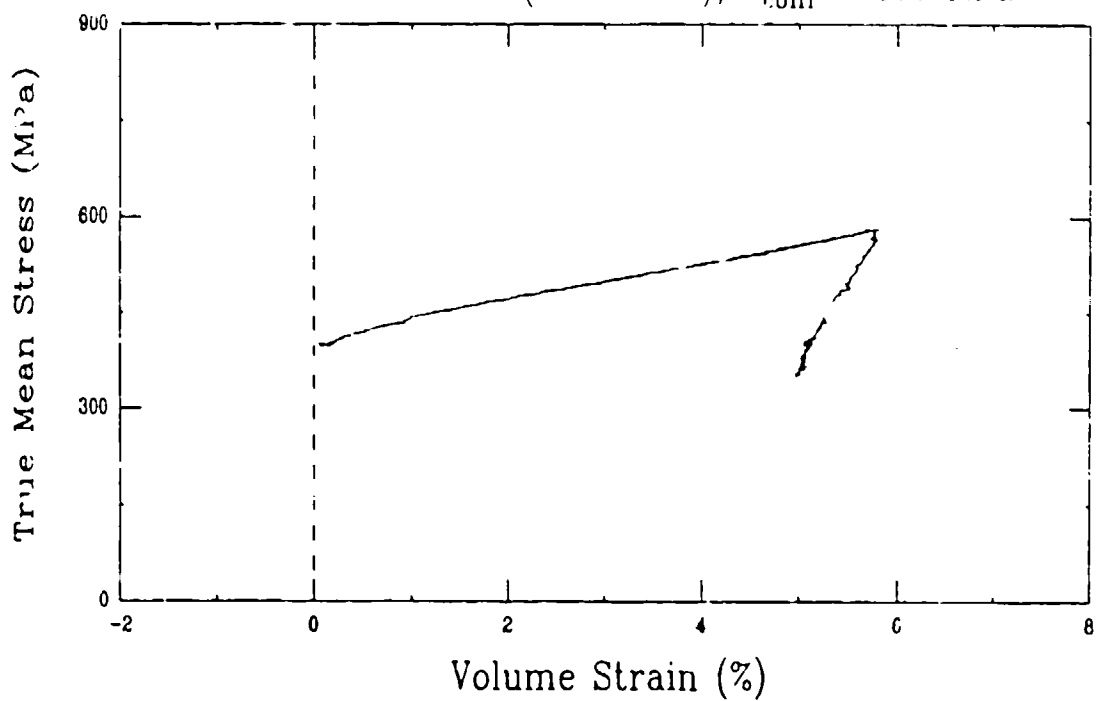


Triaxial Compression Test (026B0)  
Salem Limestone (SL20-T10),  $\sigma_{\text{conf}} = 400 \text{ MPa}$





Triaxial Compression Test (026B0)  
Salem Limestone (SL20-T10),  $\sigma_{conf} = 400$  MPa

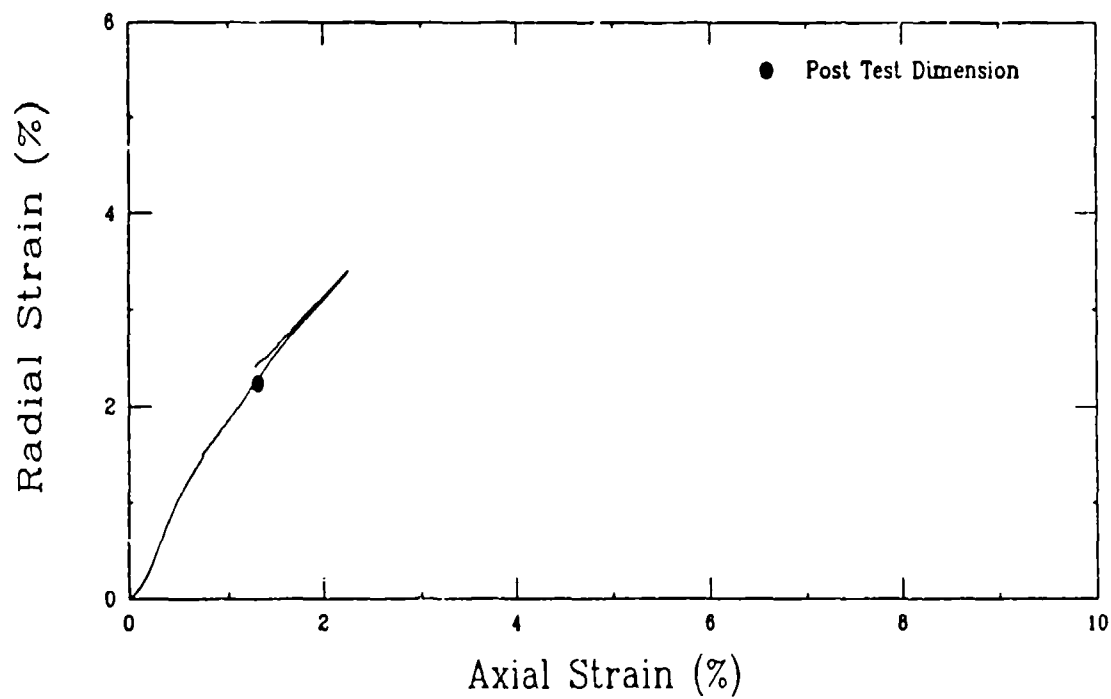
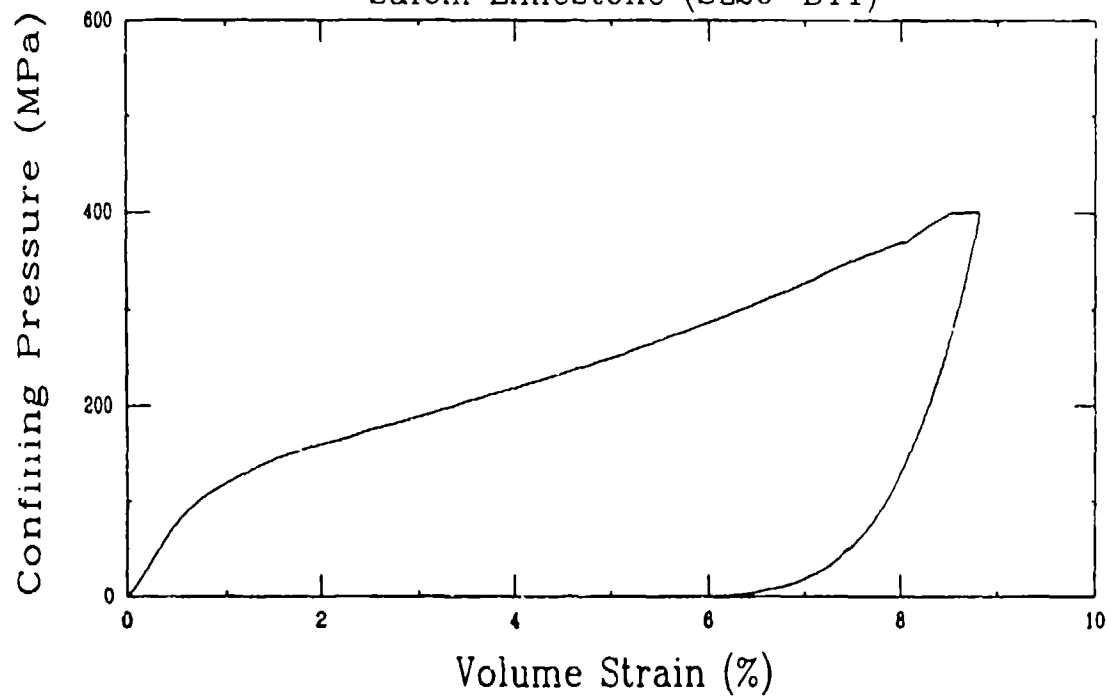


## APPENDIX D

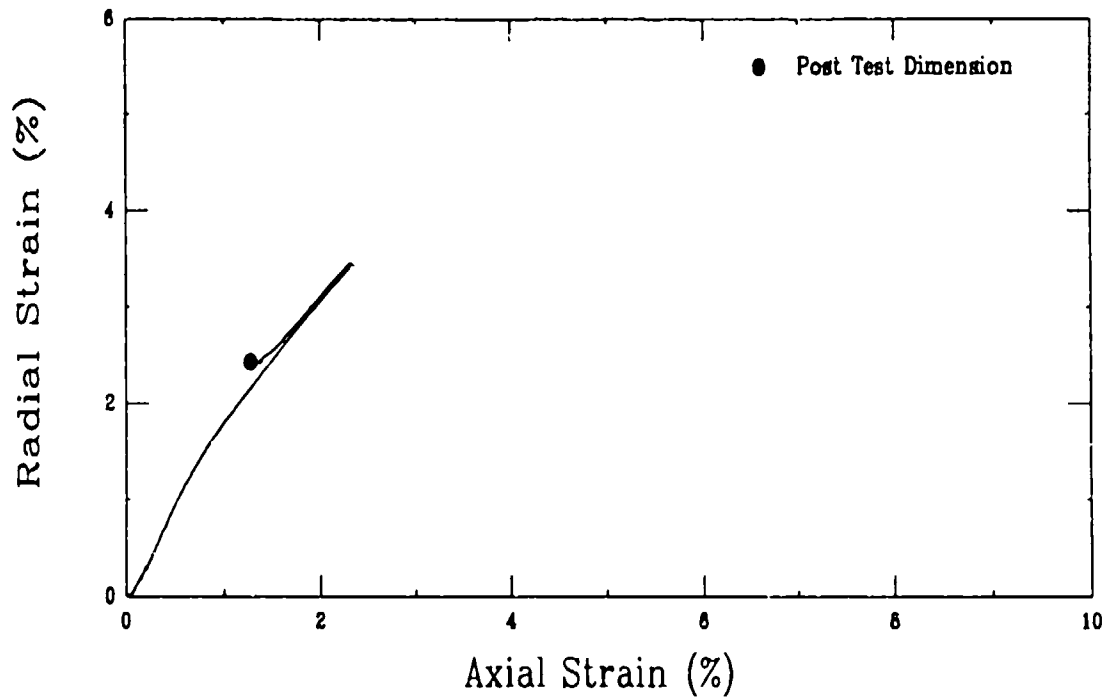
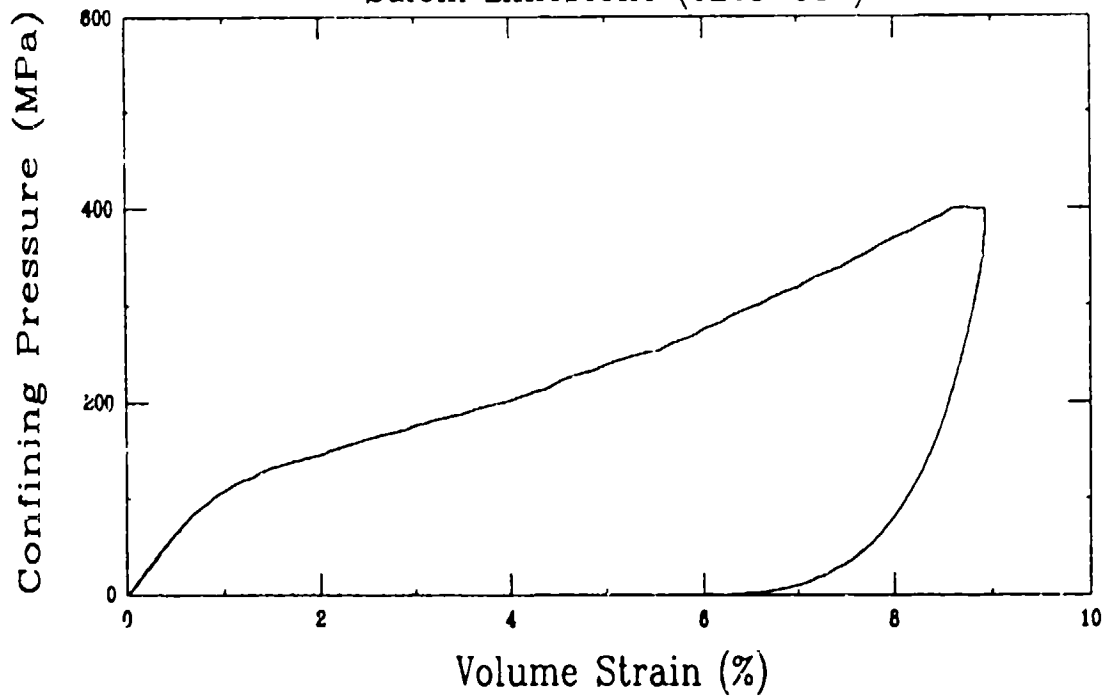
### HYDROSTATIC COMPRESSION TESTS

Test ID	Page
N1A0	D-2
Y15A1	D-3
Y15B1	D-4
Y16A1	D-5
Y17A1	D-6
Y20A1	D-7

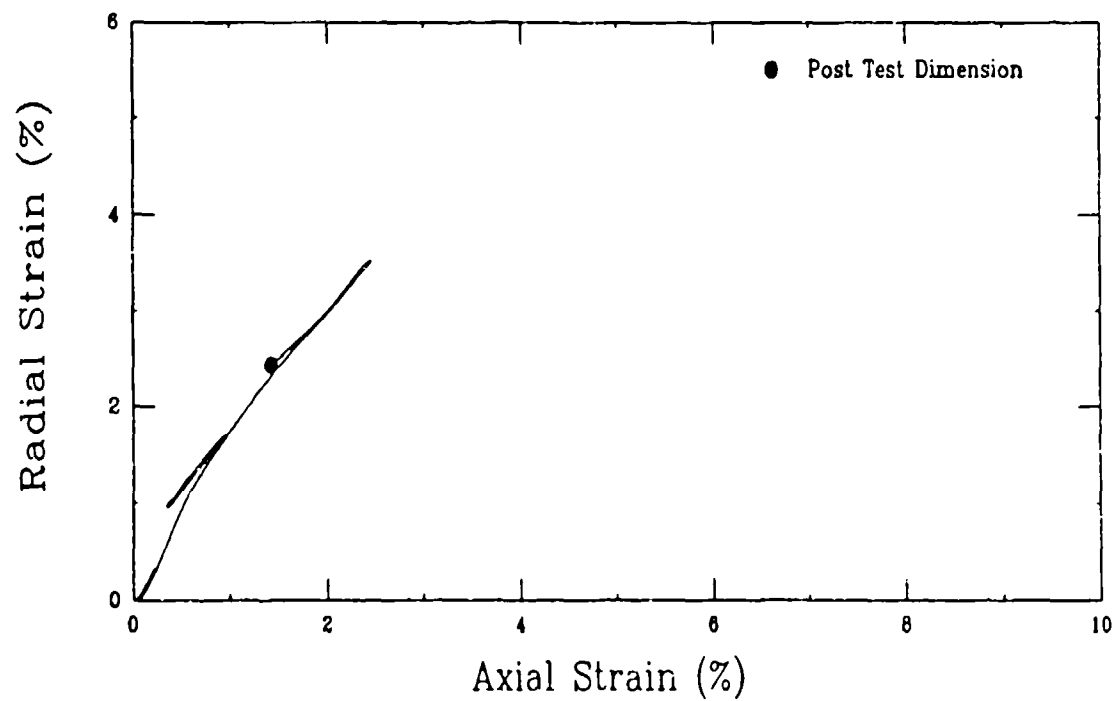
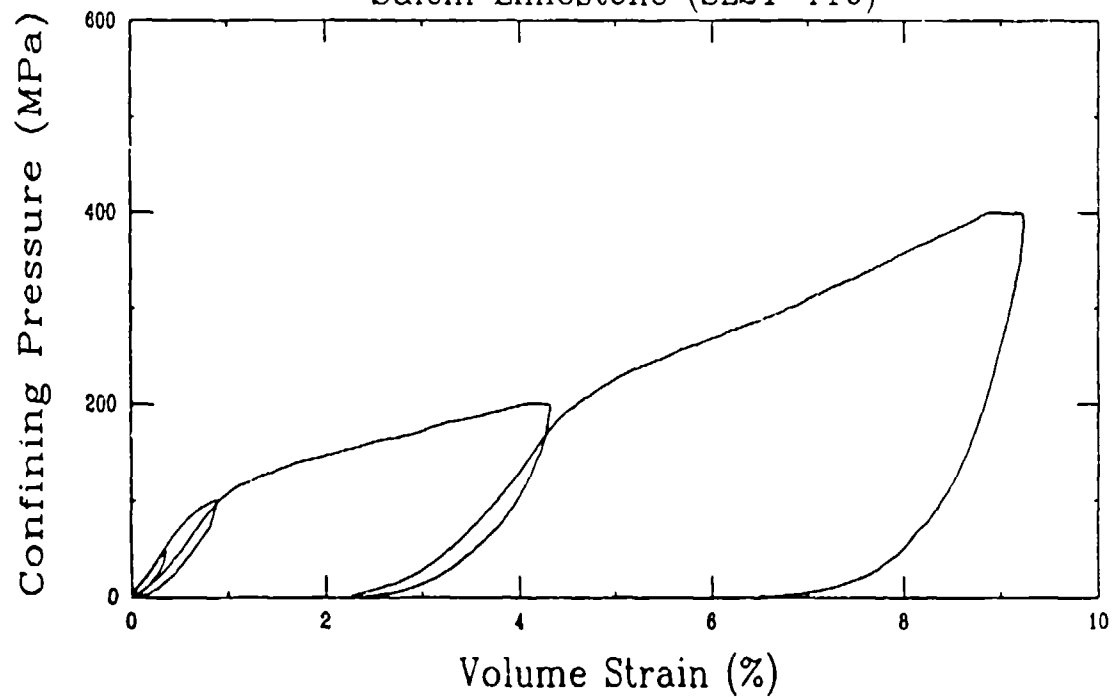
Hydrostatic Compression Test (N1A0)  
Salem Limestone (SL20-B11)



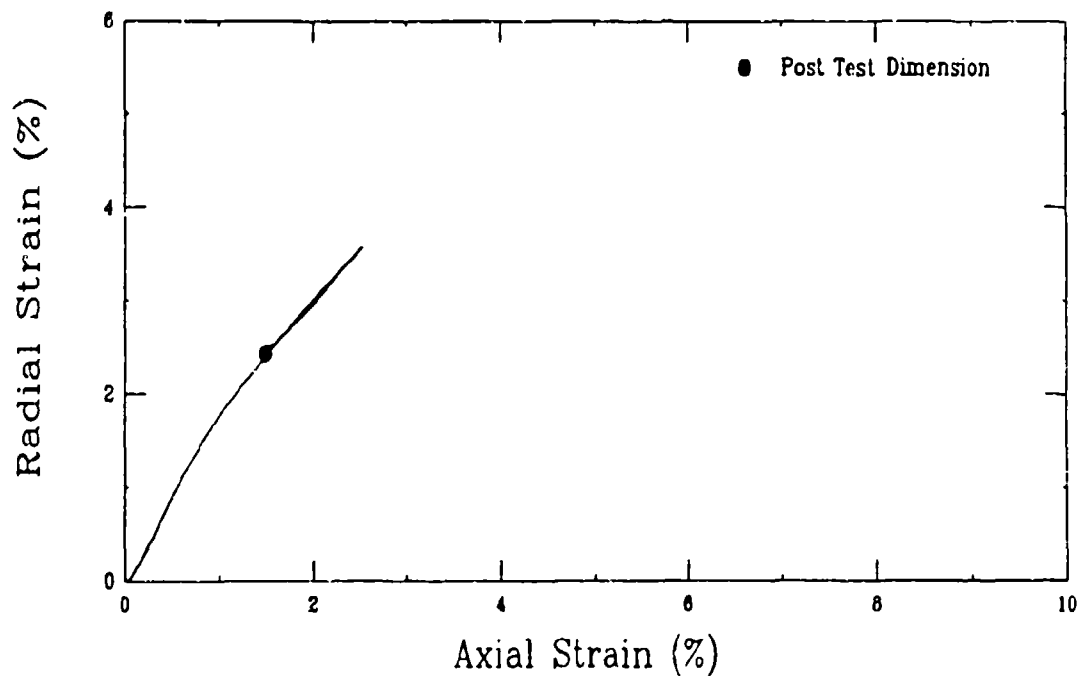
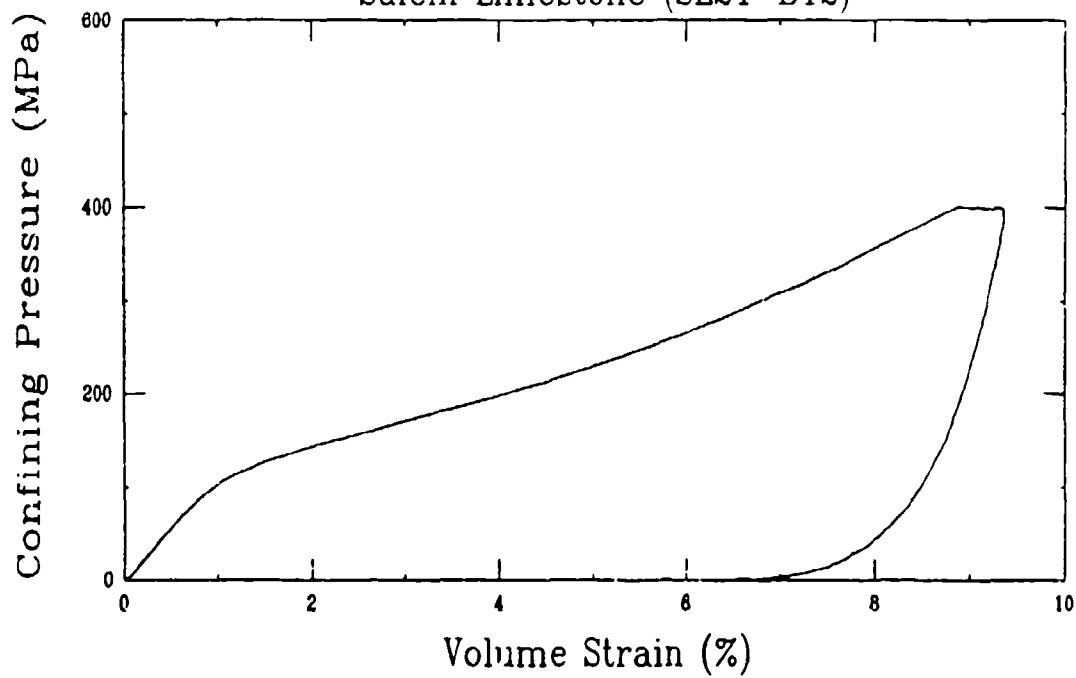
# Hydrostatic Compression Test (Y15A1) Salem Limestone (SL21-T17)



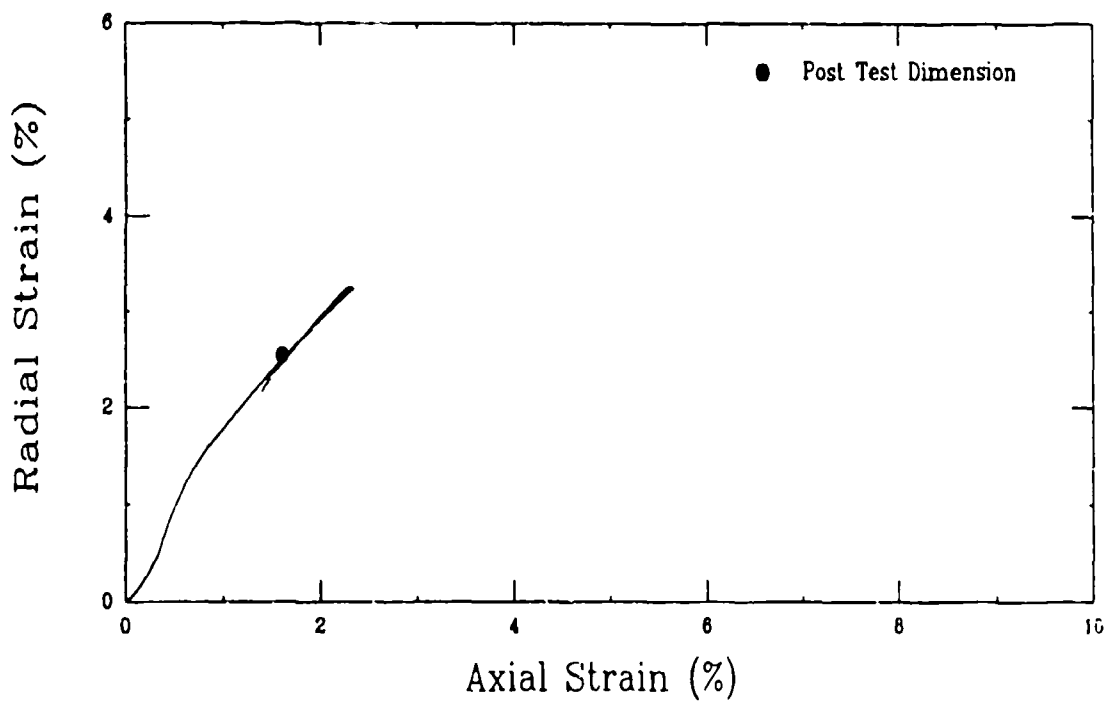
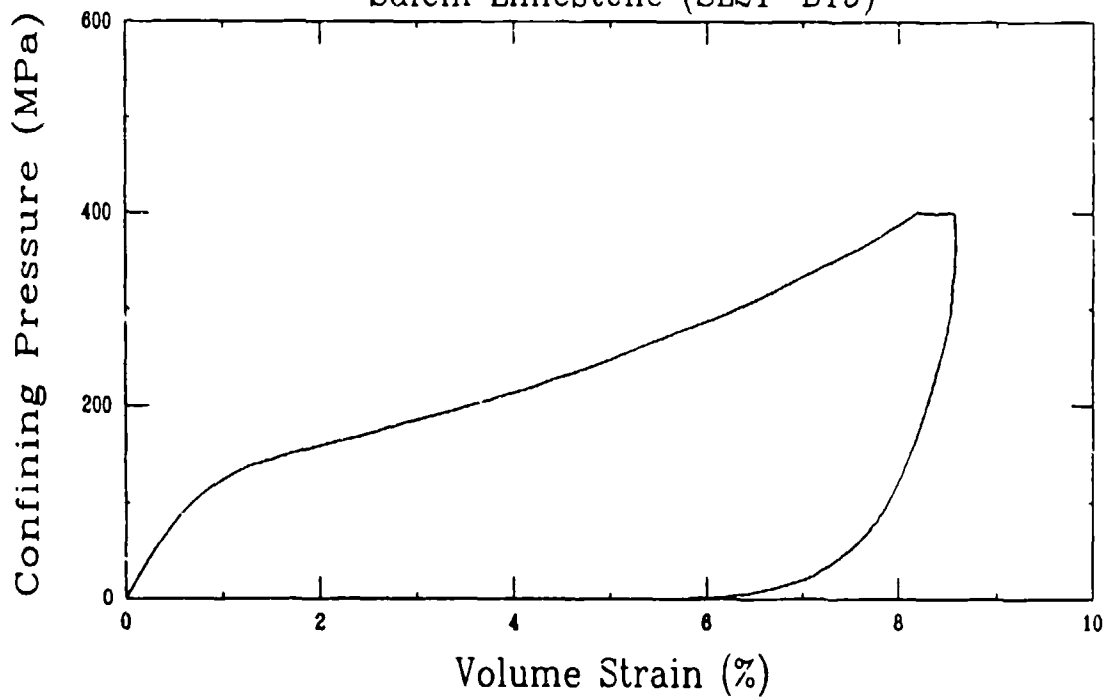
Hydrostatic Compression Test (Y15B1)  
Salem Limestone (SL21-T10)



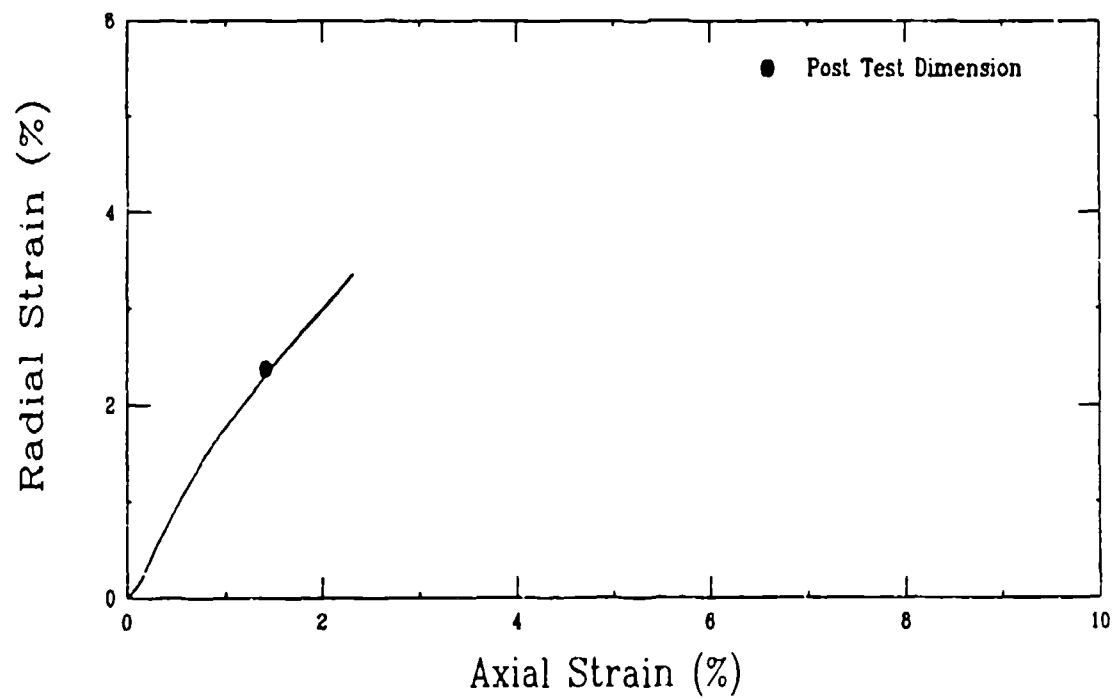
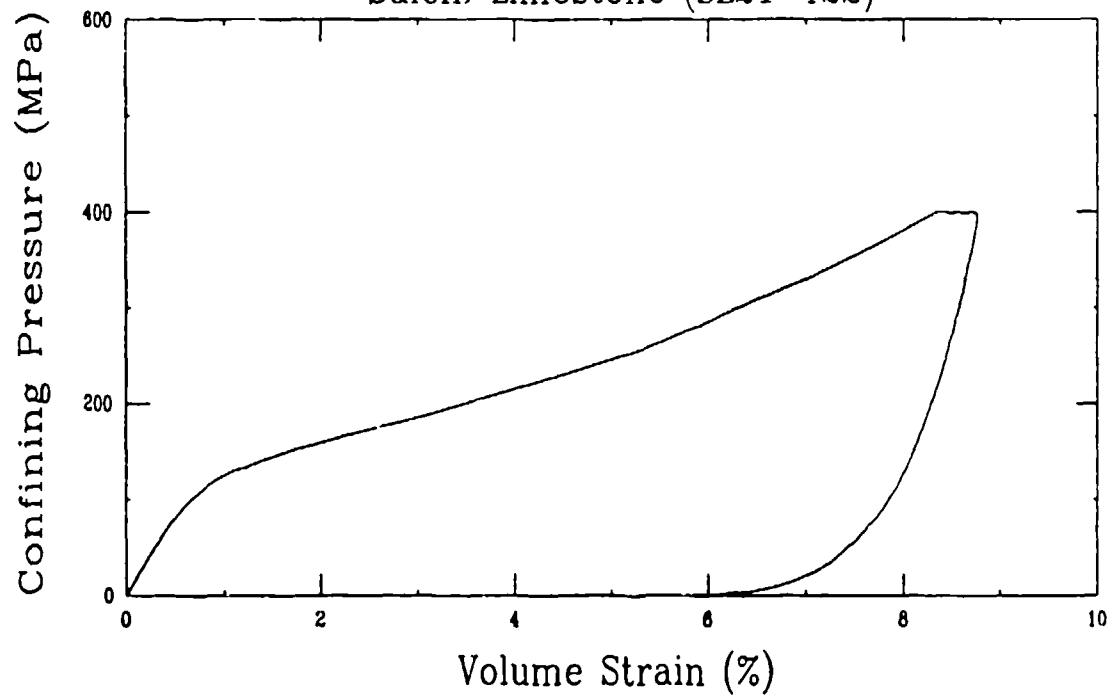
Hydrostatic Compression Test (Y16A1)  
Salem Limestone (SL21-B12)



Hydrostatic Compression Test (Y17A1)  
Salem Limestone (SL21-B19)



Hydrostatic Compression Test (Y20A1)  
Salem Limestone (SL21-T22)



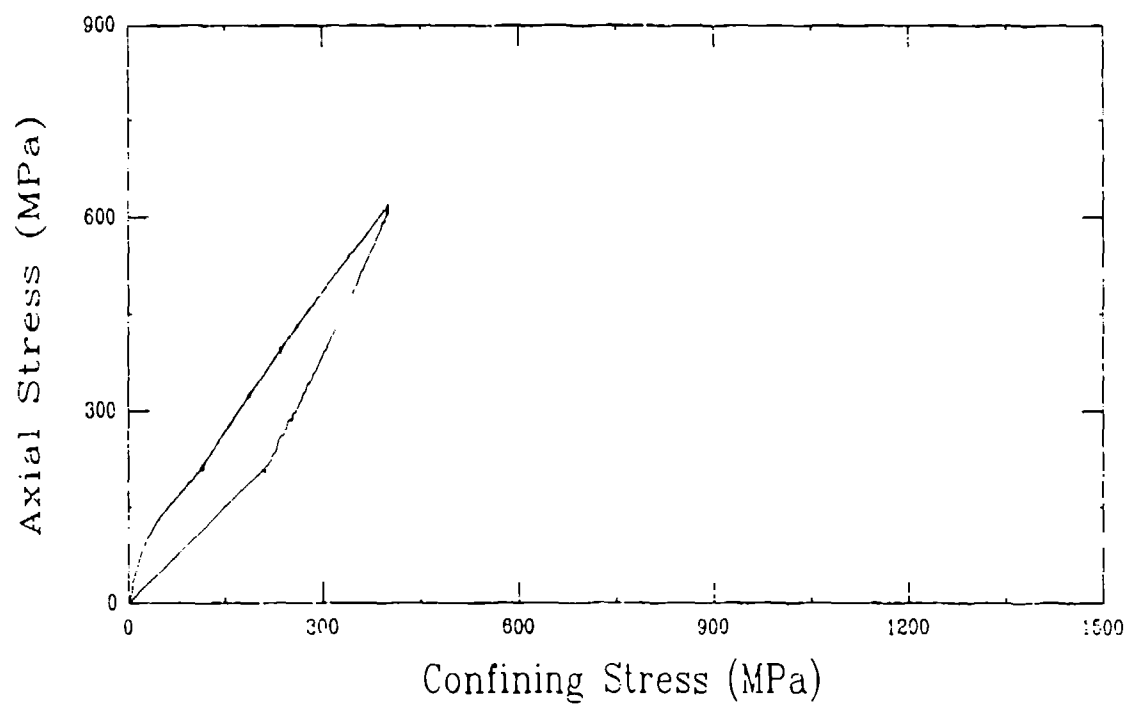
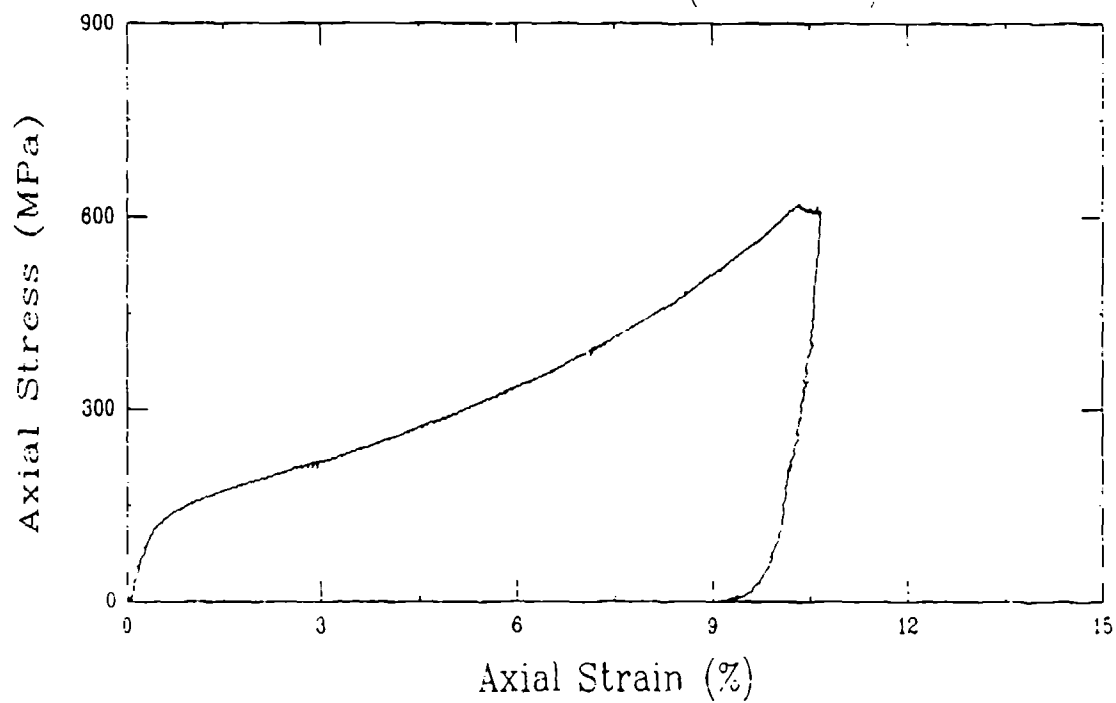


## APPENDIX E

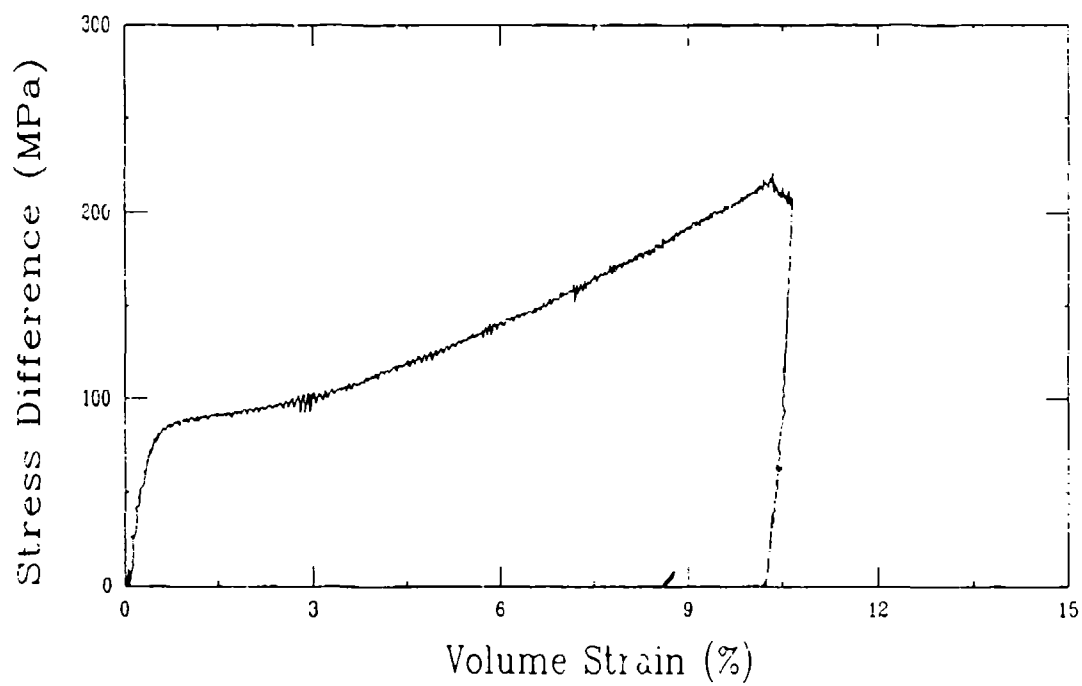
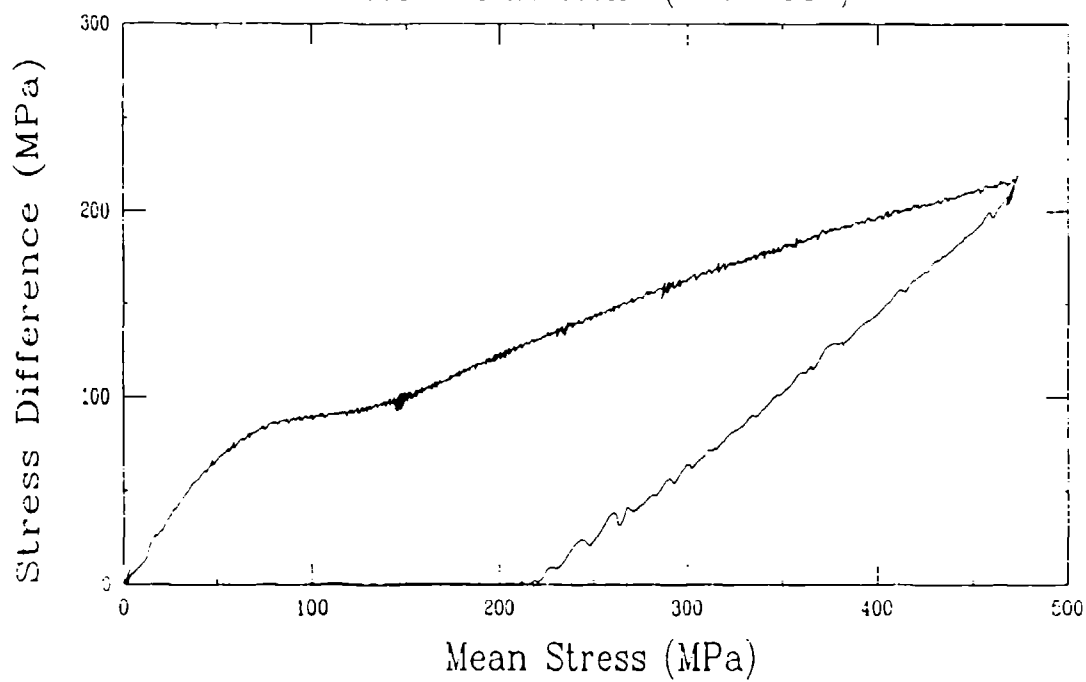
### UNIAXIAL STRAIN TESTS

Test ID	Page
Y23A1	E-2
U18A1	E-5
U19A1	E-8

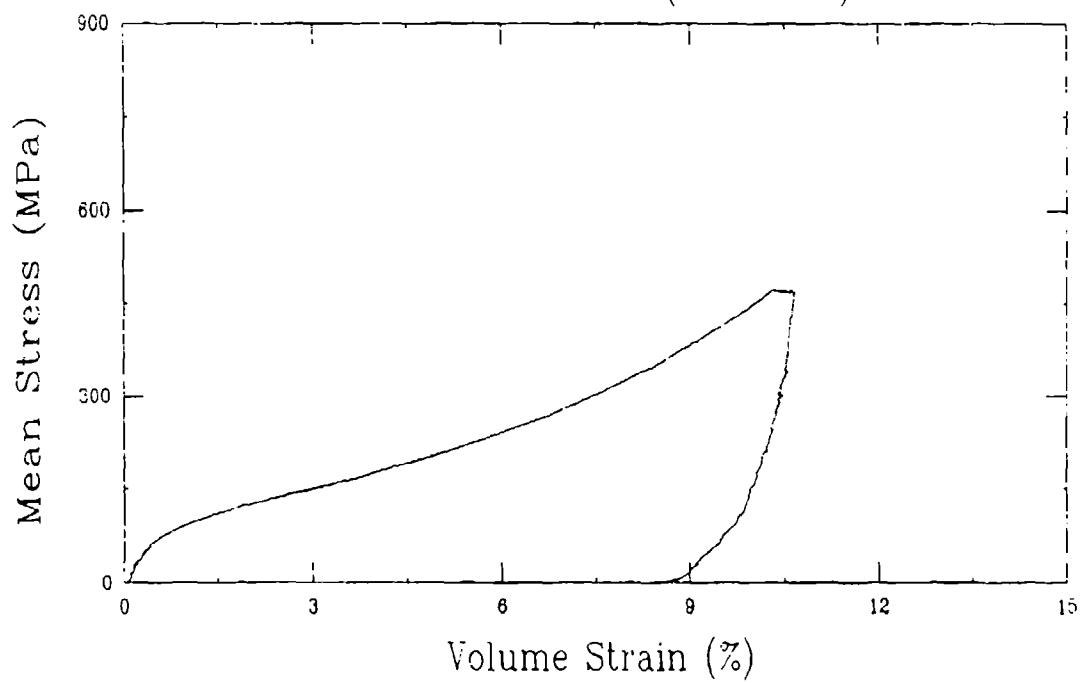
Uniaxial Strain Test (Y23A1)  
Salem Limestone (SL21--T19)



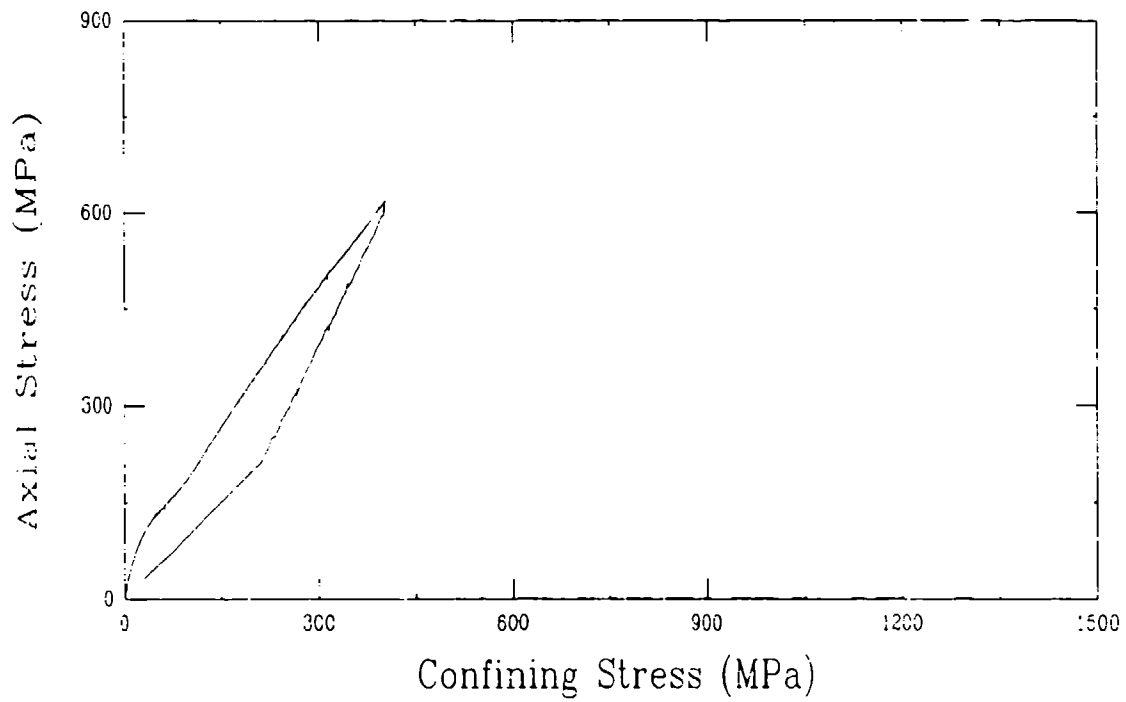
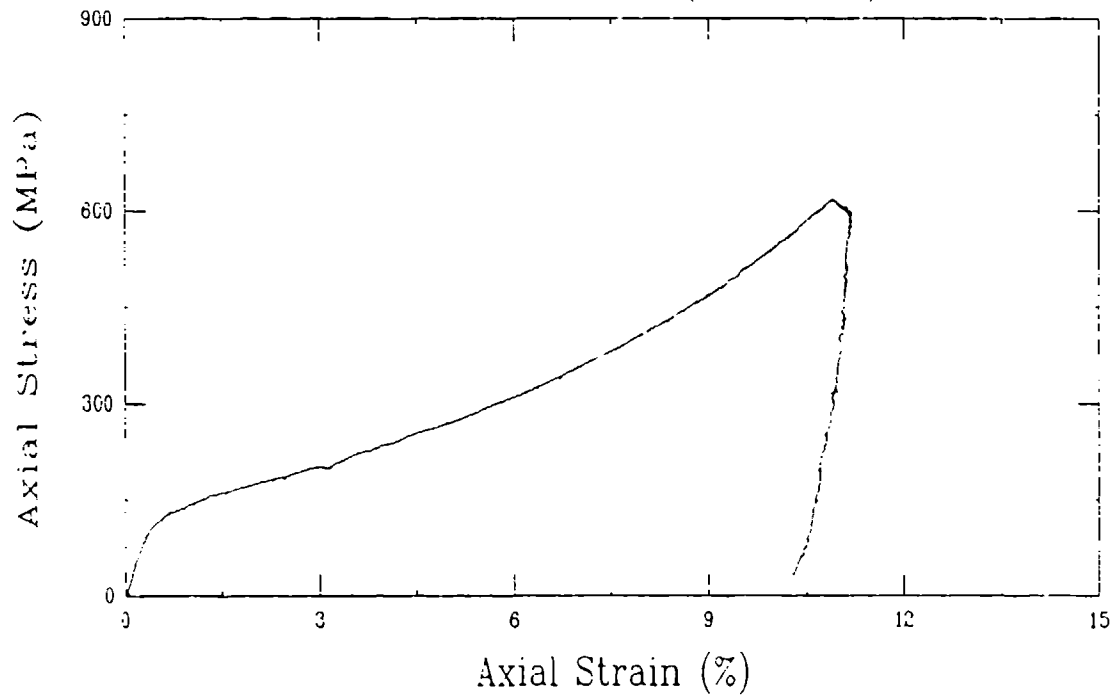
Uniaxial Strain Test (Y23A1)  
Salem Limestone (SL20-T19)



Uniaxial Strain Test (Y23A1)  
Salem Limestone (SL20-T19)

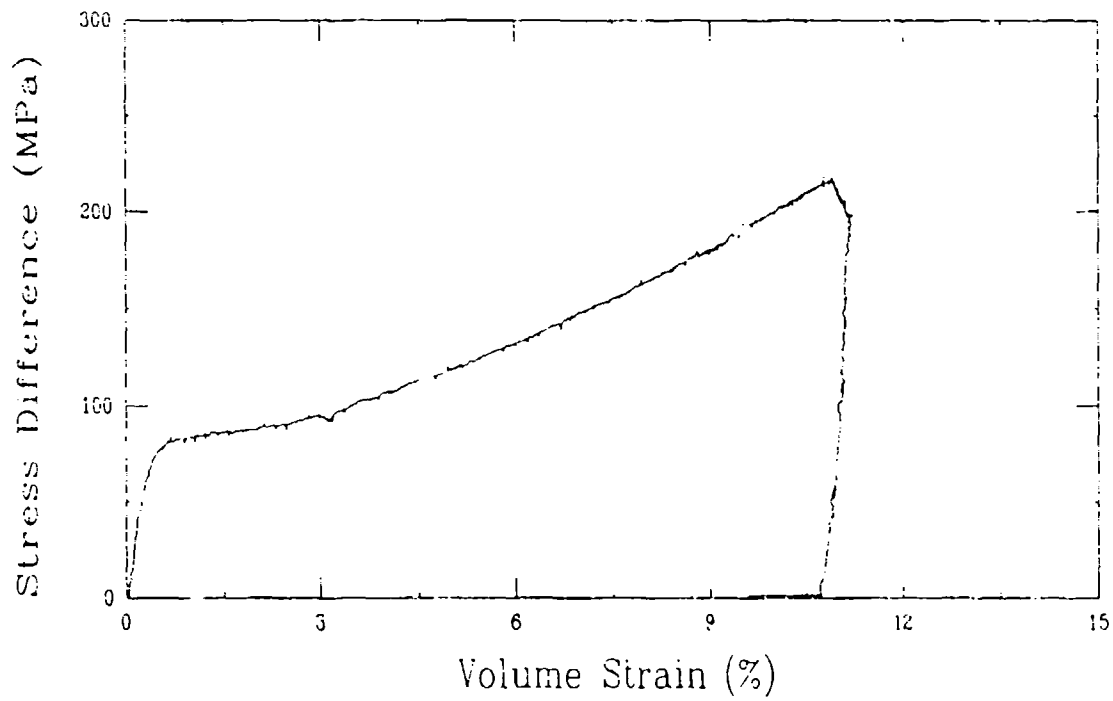
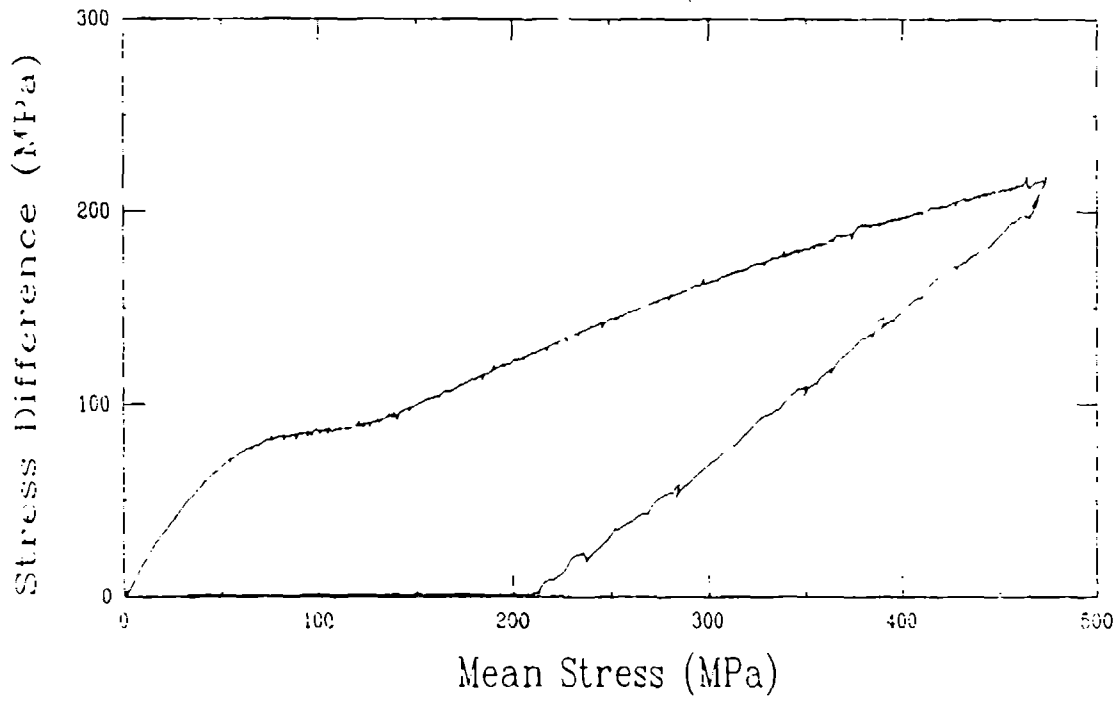


Uniaxial Strain Test (U18A1).  
Salem Limestone (SL21-B14)

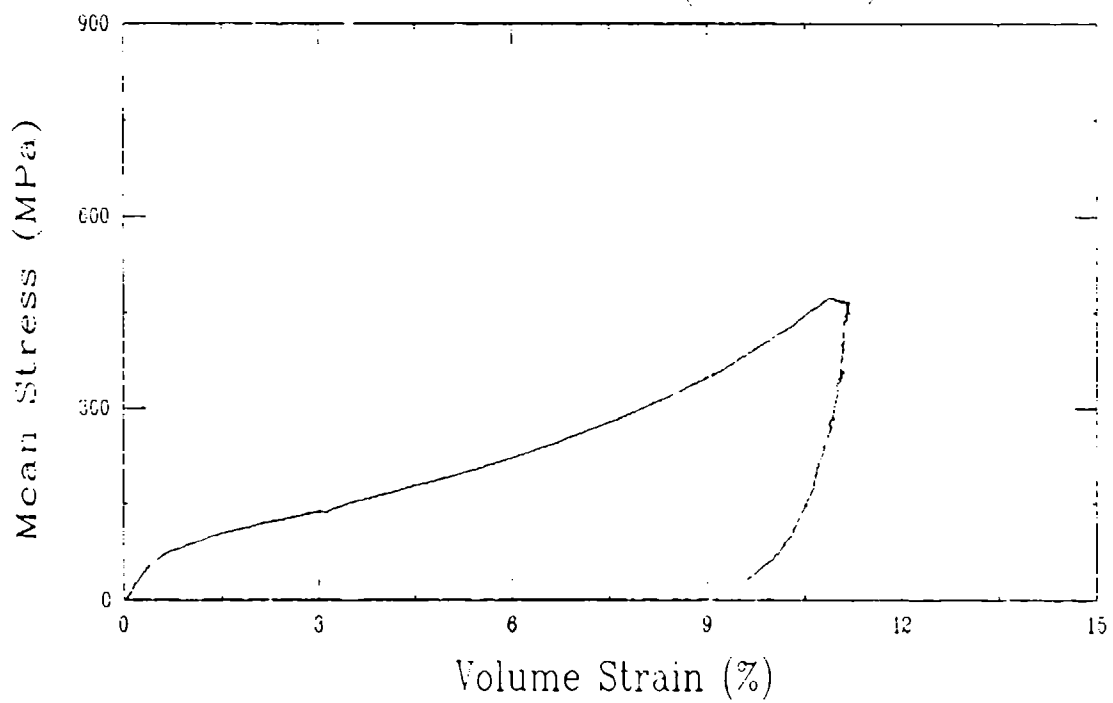


# Uniaxial Strain Test (U18A1)

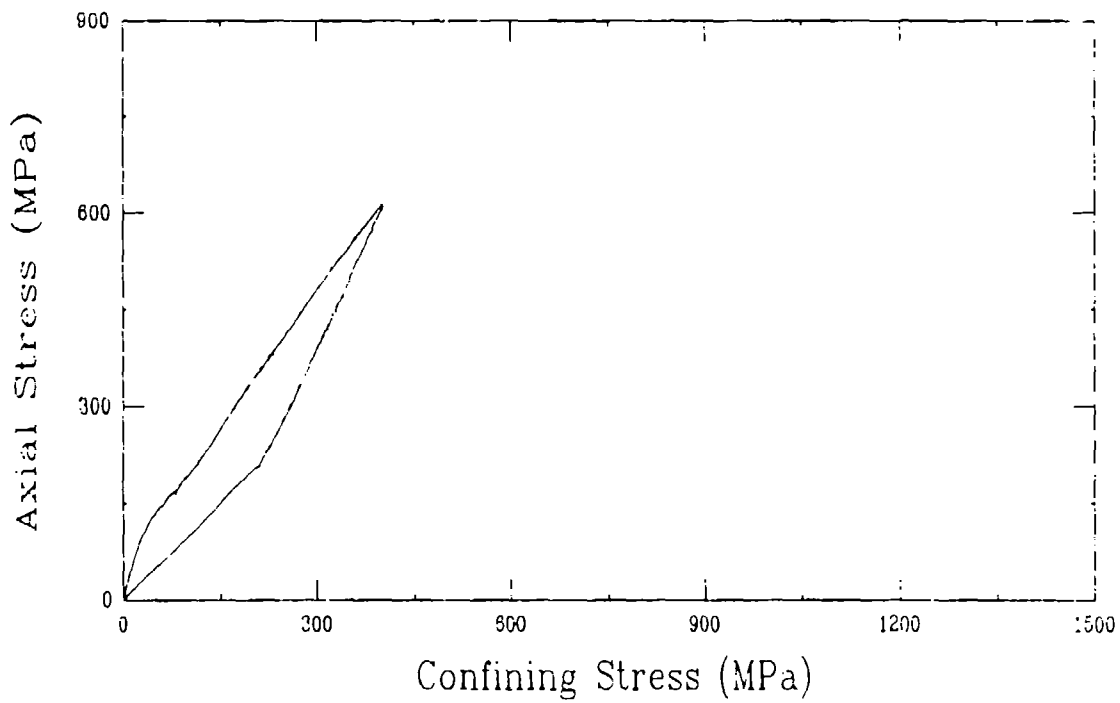
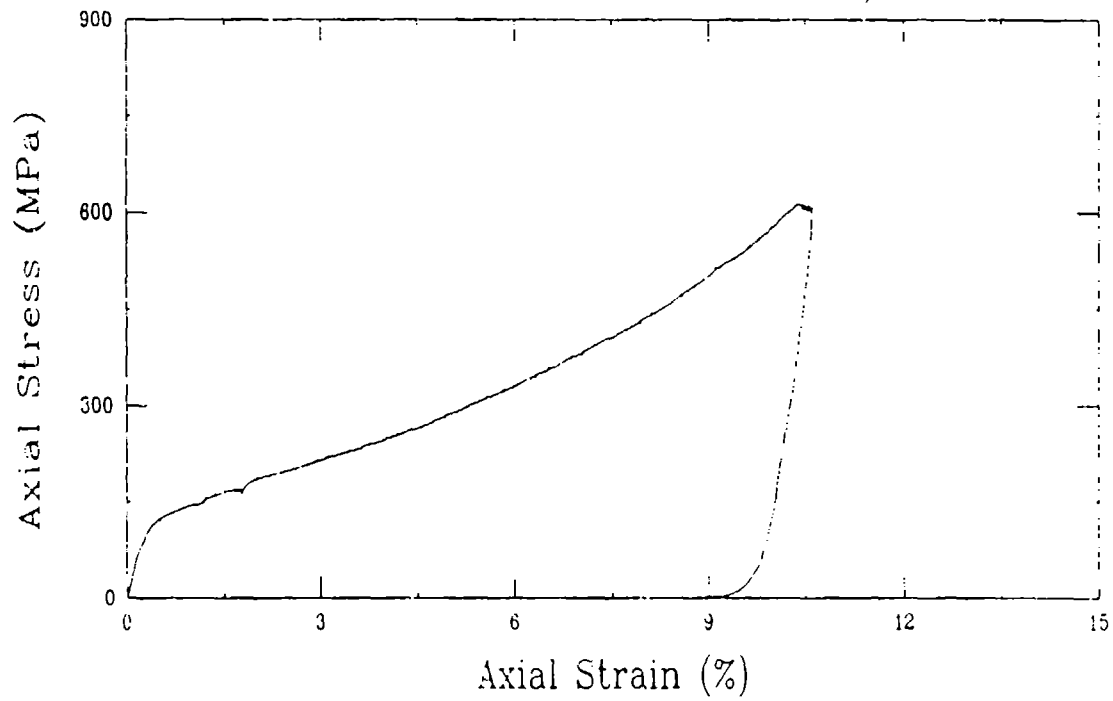
Salem Limestone (SL20-B14)



Uniaxial Strain Test (U18A1)  
Salem Limestone (SL20-B14)

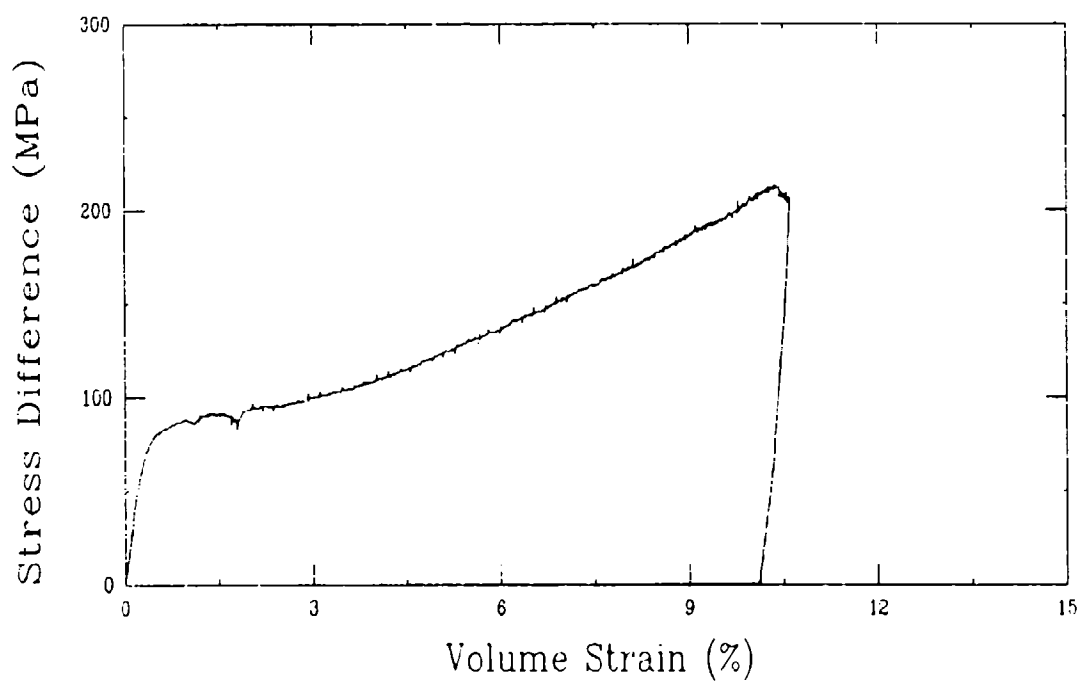
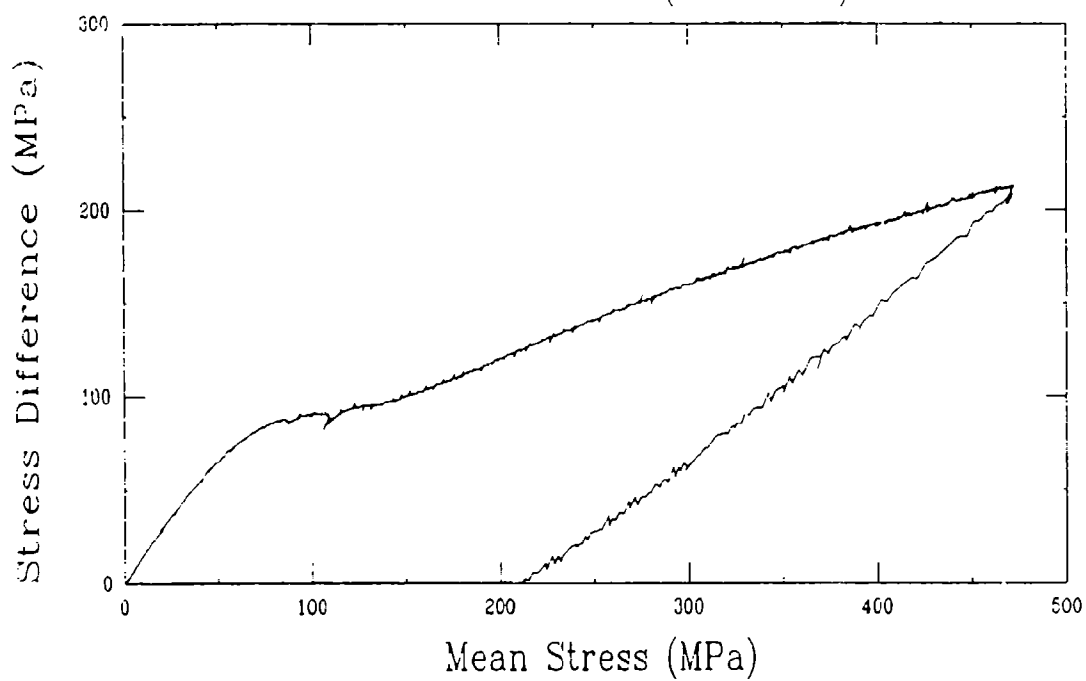


Uniaxial Strain Test (U19A1)  
Salem Limestone (SL21-T20)

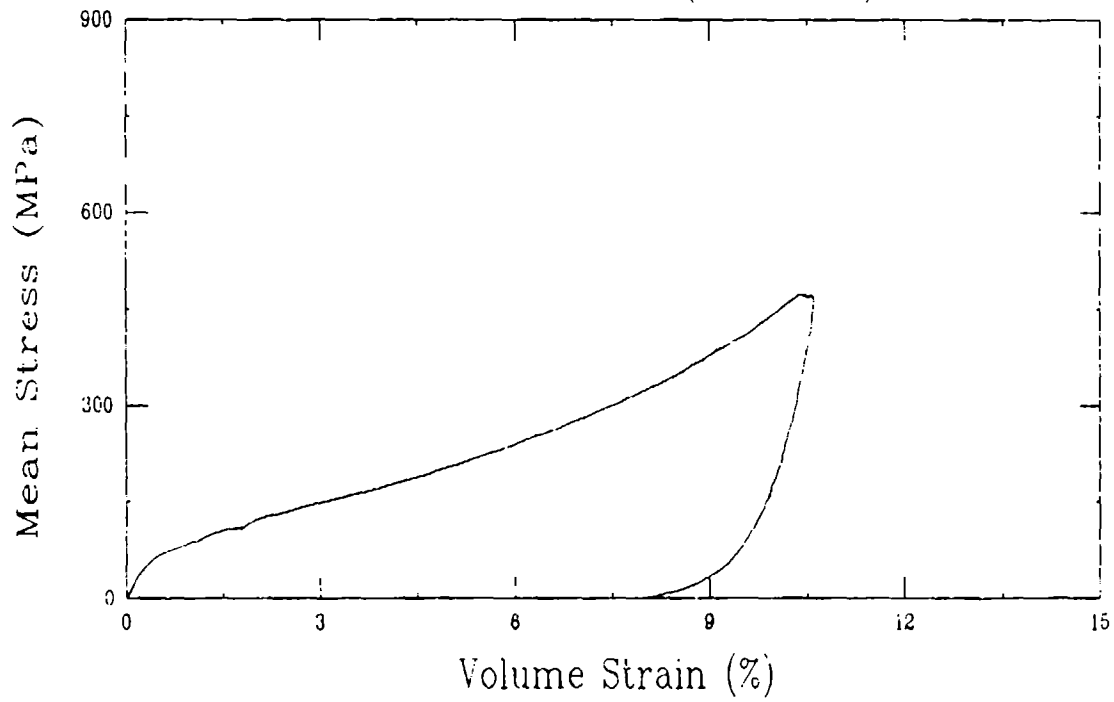




Uniaxial Strain Test (U19A1)  
Salem Limestone (SL20-T20)



Uniaxial Strain Test (U19A1)  
Salem Limestone (SL20-T20)

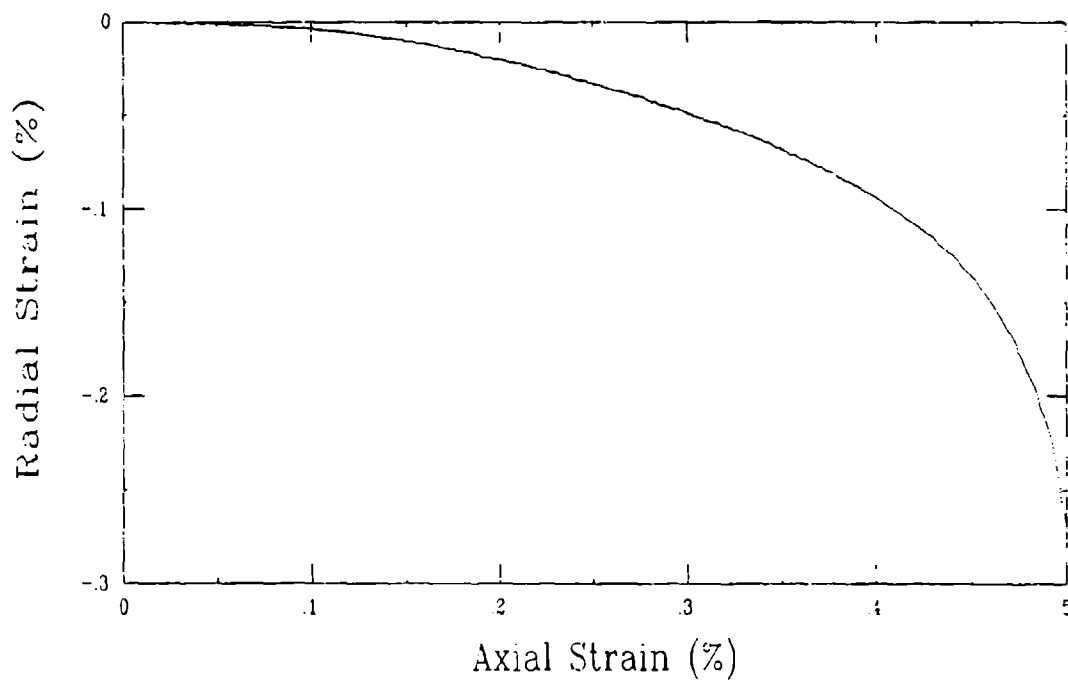
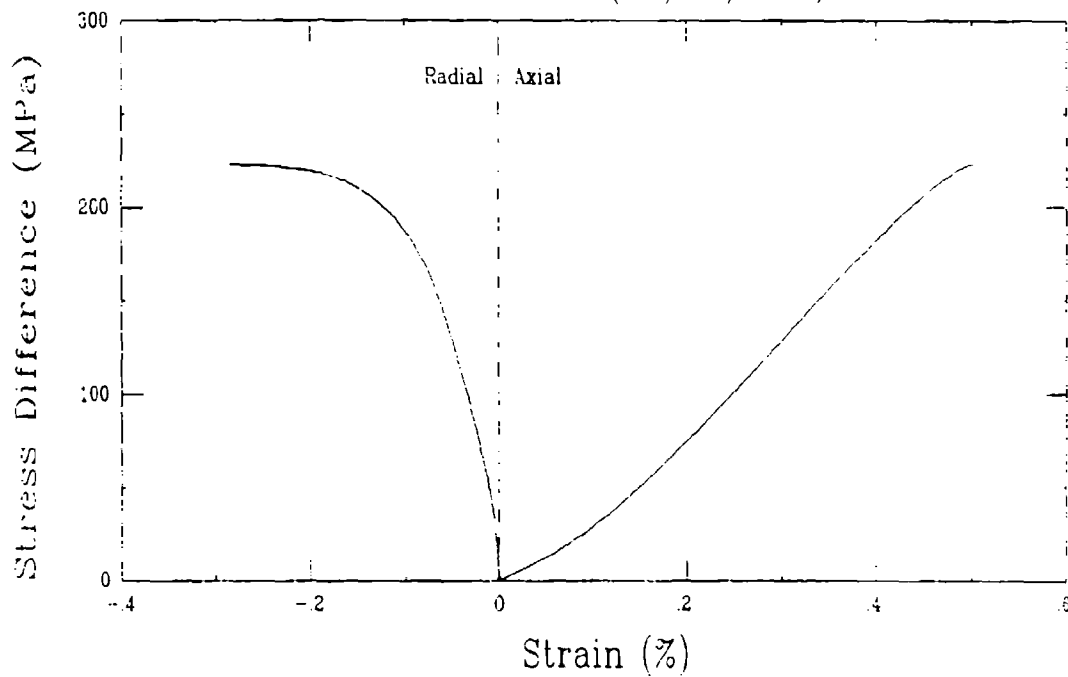


# APPENDIX F

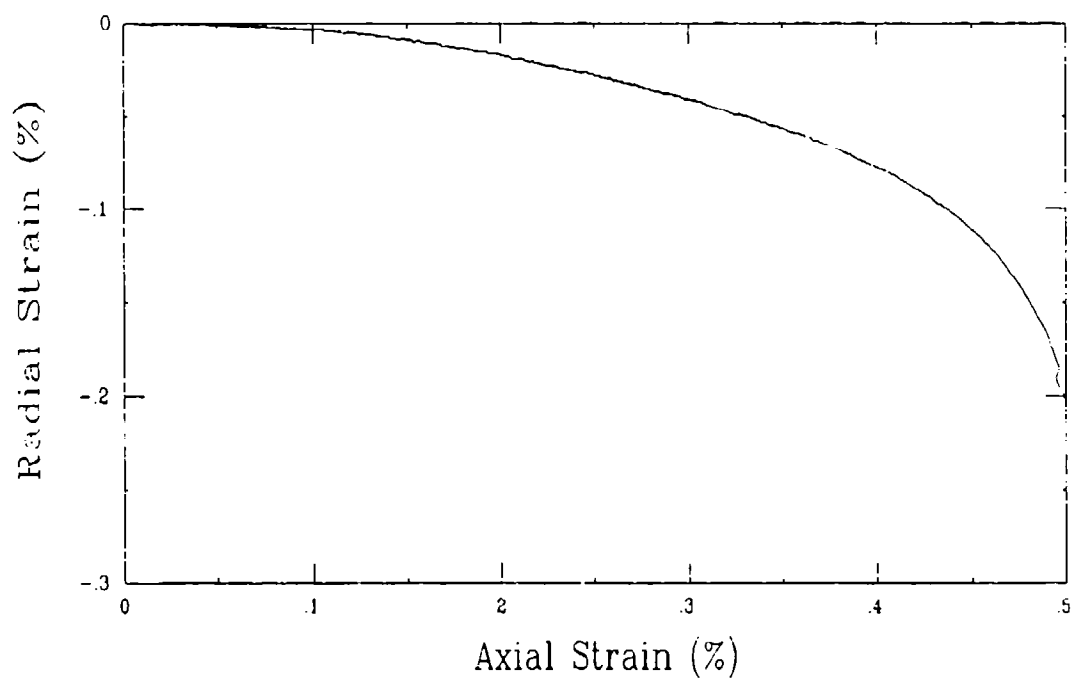
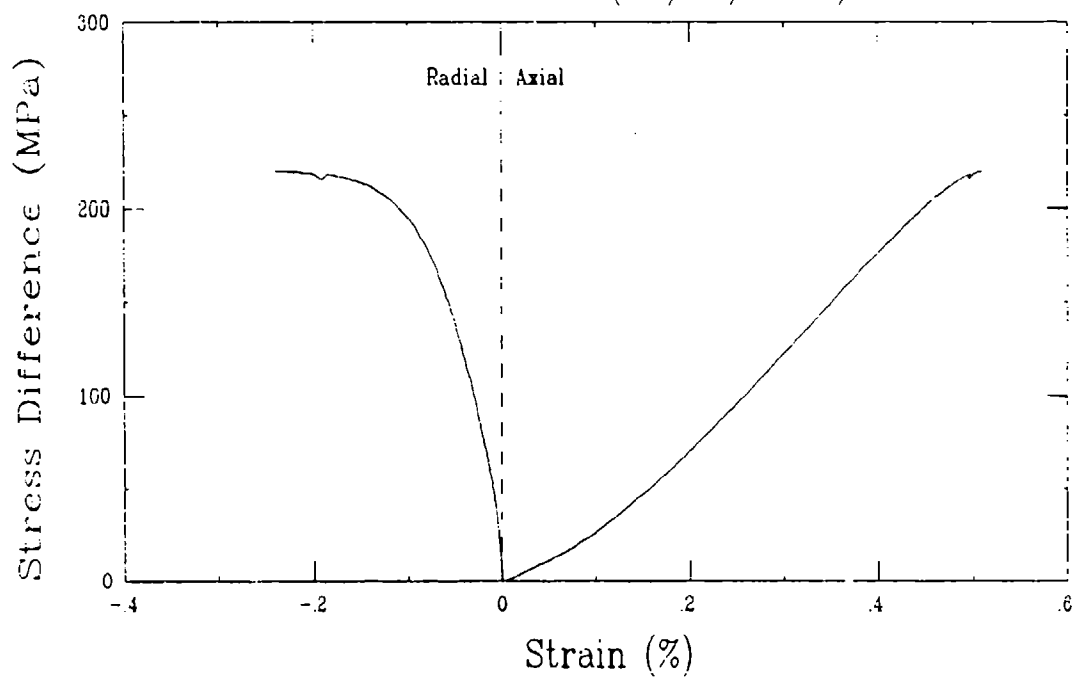
## ASTM/ISR INTERLABORATORY COMPARISON TESTS

Test ID	Material	Test Type	Page
G28F1	Barre Granite	Unconfined	F-2
G28H1	Barre Granite	Unconfined	F-3
G28G1	Barre Granite	Unconfined	F-4
G28E1	Barre Granite	Unconfined	F-5
G28D1	Barre Granite	Unconfined	F-6
G28B1	Berea Sandstone	Unconfined	F-7
G28A1	Berea Sandstone	Unconfined	F-9
G28G1	Berea Sandstone	Unconfined	F-10
G27F1	Berea Sandstone	Unconfined	F-11
G27A1	Salem Limestone	Unconfined	F-12
G27B1	Salem Limestone	Unconfined	F-13
G27E1	Salem Limestone	Unconfined	F-14
G27C1	Salem Limestone	Unconfined	F-15
G27D1	Salem Limestone	Unconfined	F-16
G29A1	Tennessee Marble	Unconfined	F-17
G29C1	Tennessee Marble	Unconfined	F-18
G29E1	Tennessee Marble	Unconfined	F-19
G29D1	Tennessee Marble	Unconfined	F-20
G29B1	Tennessee Marble	Unconfined	F-21
U2E3	Barre Granite	10 MPa Triaxial	F-22
U3B3	Barre Granite	10 MPa Triaxial	F-23
U2F3	Barre Granite	10 MPa Triaxial	F-24
U3A3	Barre Granite	10 MPa Triaxial	F-25
U3B3	Barre Granite	25 MPa Triaxial	F-26
U3C3	Barre Granite	25 MPa Triaxial	F-27
U3D3	Barre Granite	25 MPa Triaxial	F-28
U4A3	Barre Granite	25 MPa Triaxial	F-29
U4B3	Barre Granite	40 MPa Triaxial	F-30
U4E3	Barre Granite	40 MPa Triaxial	F-31
U4C3	Barre Granite	40 MPa Triaxial	F-32
U4D3	Barre Granite	40 MPa Triaxial	F-33
Y26C3	Berea Sandstone	10 MPa Triaxial	F-34
Y26D3	Berea Sandstone	10 MPa Triaxial	F-35
Y26A3	Berea Sandstone	10 MPa Triaxial	F-36
Y26B3	Berea Sandstone	10 MPa Triaxial	F-37
Y27A3	Berea Sandstone	25 MPa Triaxial	F-38
Y26E3	Berea Sandstone	25 MPa Triaxial	F-39
Y27B3	Berea Sandstone	25 MPa Triaxial	F-40
Y27C3	Berea Sandstone	25 MPa Triaxial	F-41
Y27E3	Berea Sandstone	40 MPa Triaxial	F-42
Y27D3	Berea Sandstone	40 MPa Triaxial	F-43
Y28A3	Berea Sandstone	40 MPa Triaxial	F-44
Y27F3	Berea Sandstone	40 MPa Triaxial	F-45
Y28D3	Tennessee Marble	10 MPa Triaxial	F-46
Y28B3	Tennessee Marble	10 MPa Triaxial	F-47
Y28C3	Tennessee Marble	10 MPa Triaxial	F-48
U1A3	Tennessee Marble	10 MPa Triaxial	F-49
U1B3	Tennessee Marble	25 MPa Triaxial	F-50
U1E3	Tennessee Marble	25 MPa Triaxial	F-51
U1C3	Tennessee Marble	25 MPa Triaxial	F-52
U1D3	Tennessee Marble	25 MPa Triaxial	F-53
U2C3	Tennessee Marble	40 MPa Triaxial	F-54
U2A3	Tennessee Marble	40 MPa Triaxial	F-55
U2D3	Tennessee Marble	40 MPa Triaxial	F-56
U2B3	Tennessee Marble	40 MPa Triaxial	F-57

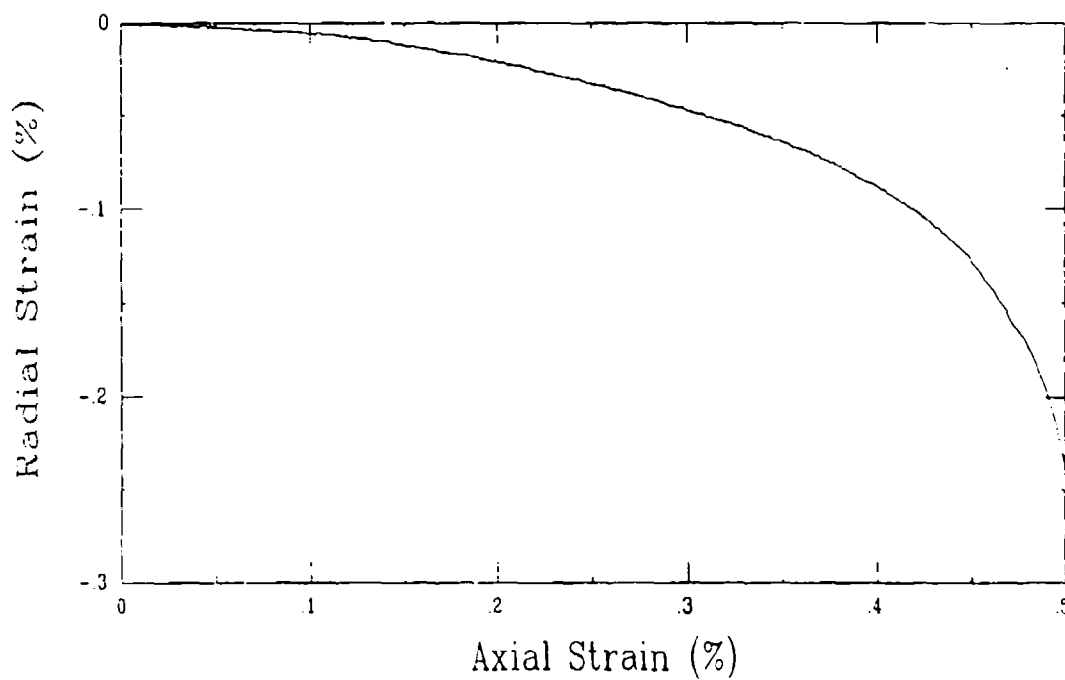
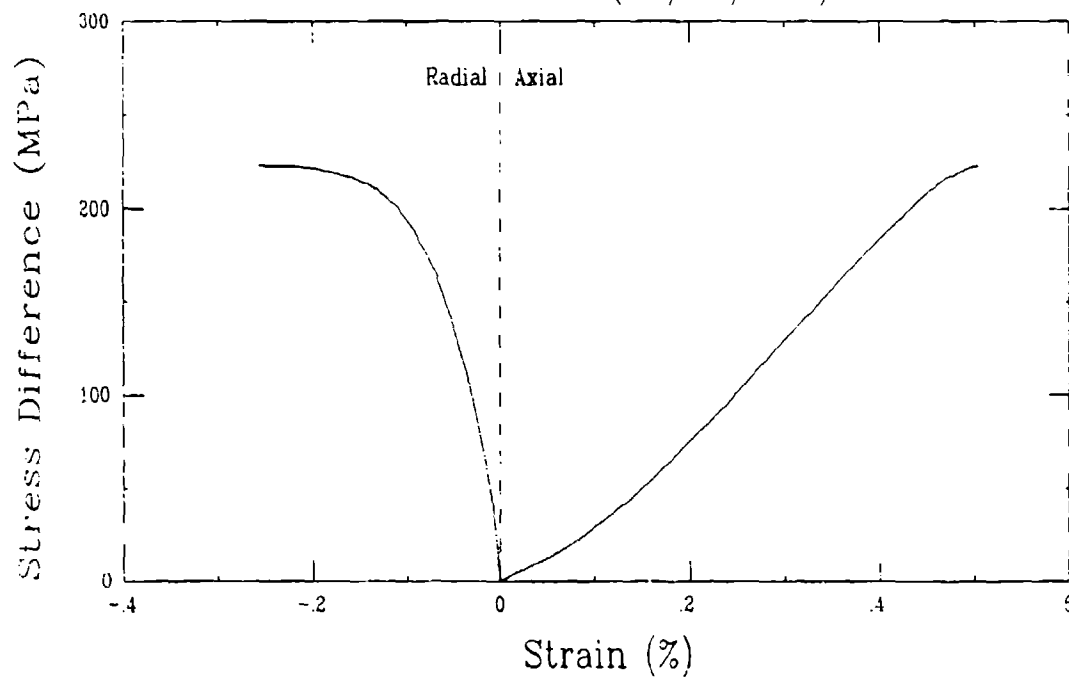
Unconfined Compression Test (G28F1)  
Barre Granite (BG/91/1-7)



Unconfined Compression Test (G28H1)  
Barre Granite (BG/91/2-15)

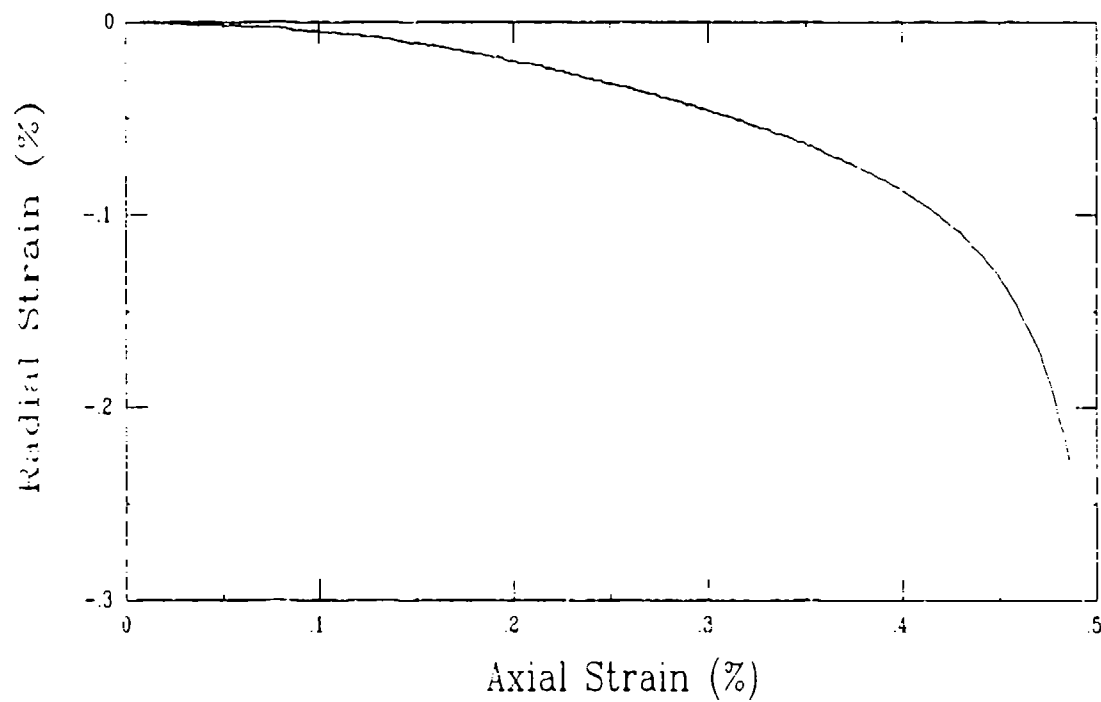
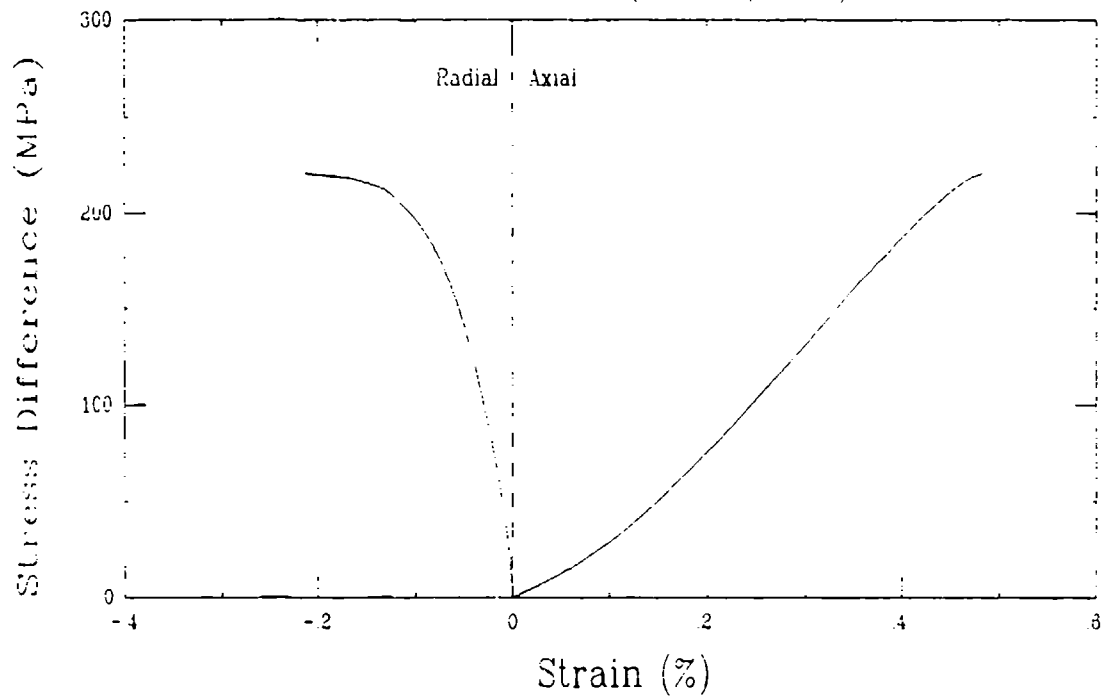


Unconfined Compression Test (G28G1)  
Barre Granite (BG/91/3-4)

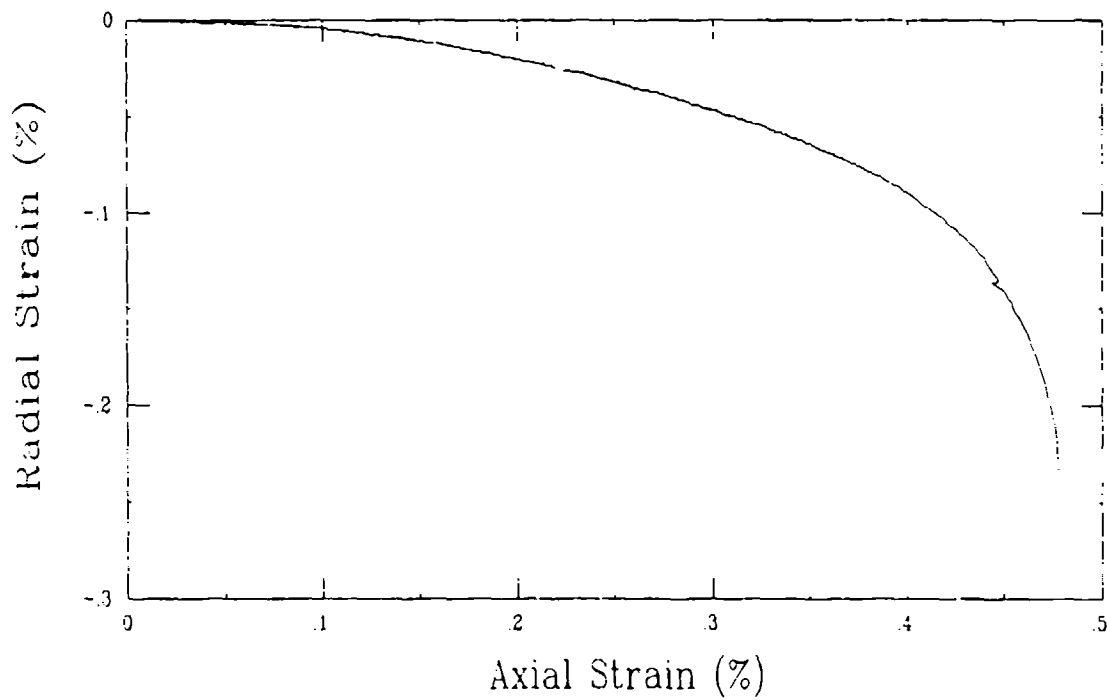
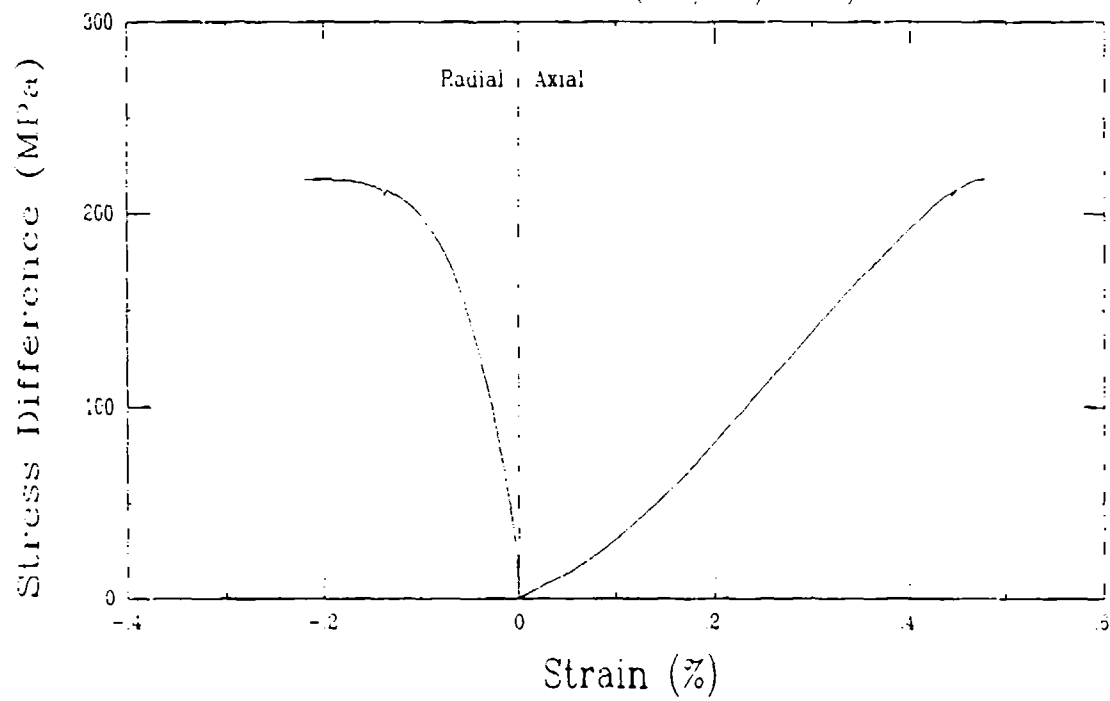


# Unconfined Compression Test (G28E1)

## Barre Granite (BG/91/5-4)



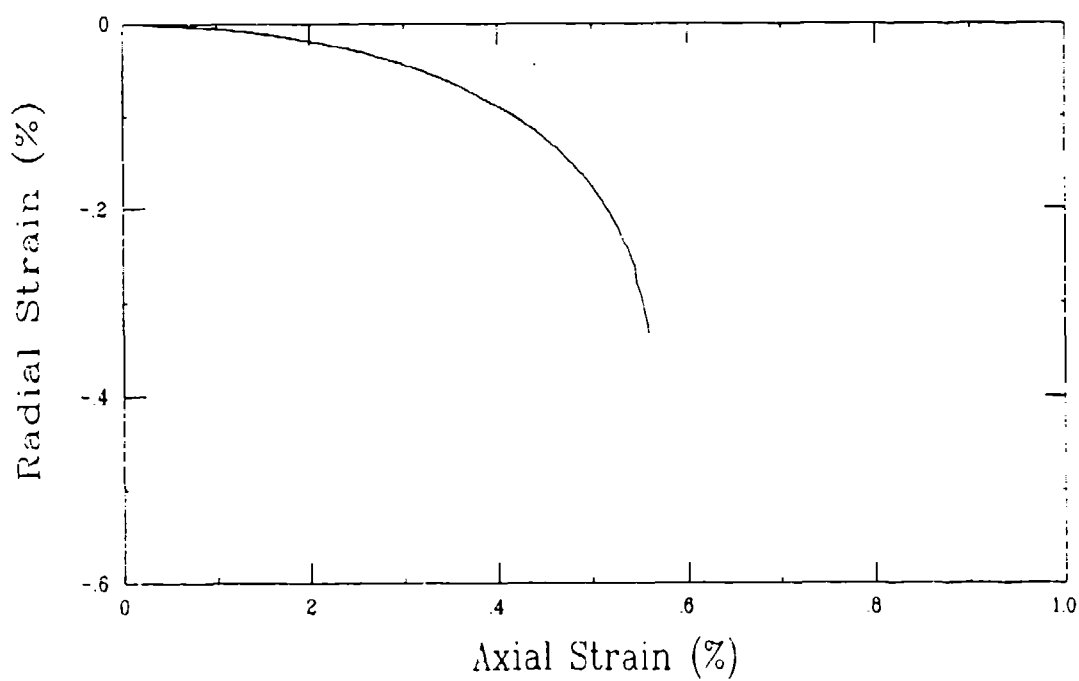
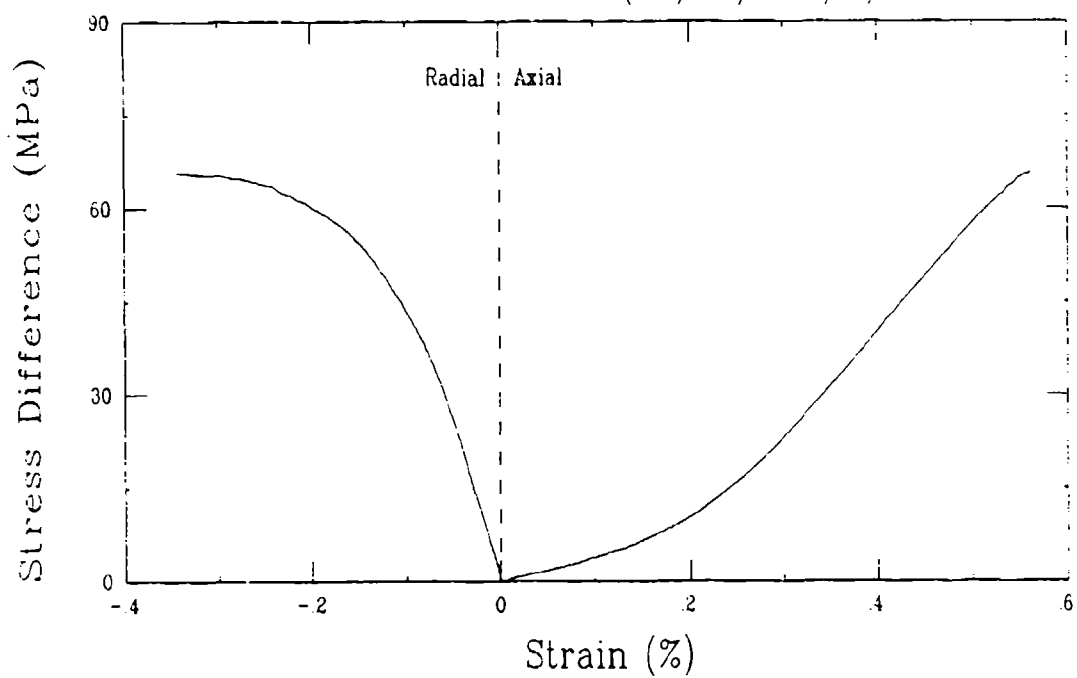
Unconfined Compression Test (G28D1)  
Barre Granite (BG/91/6-8)



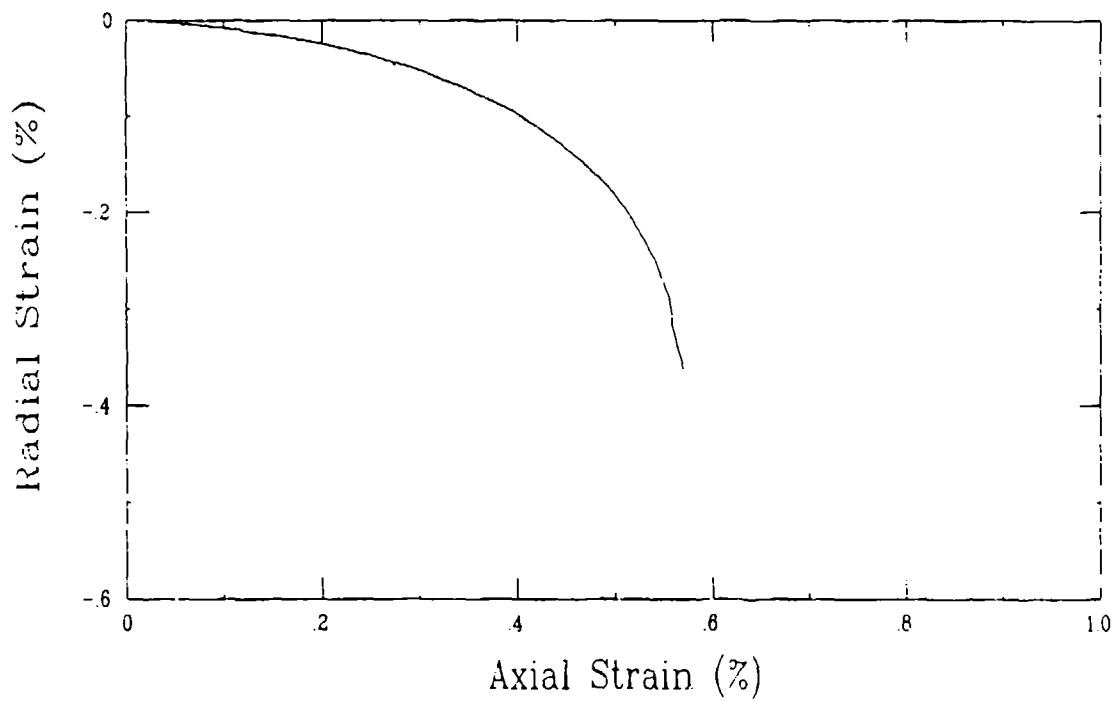
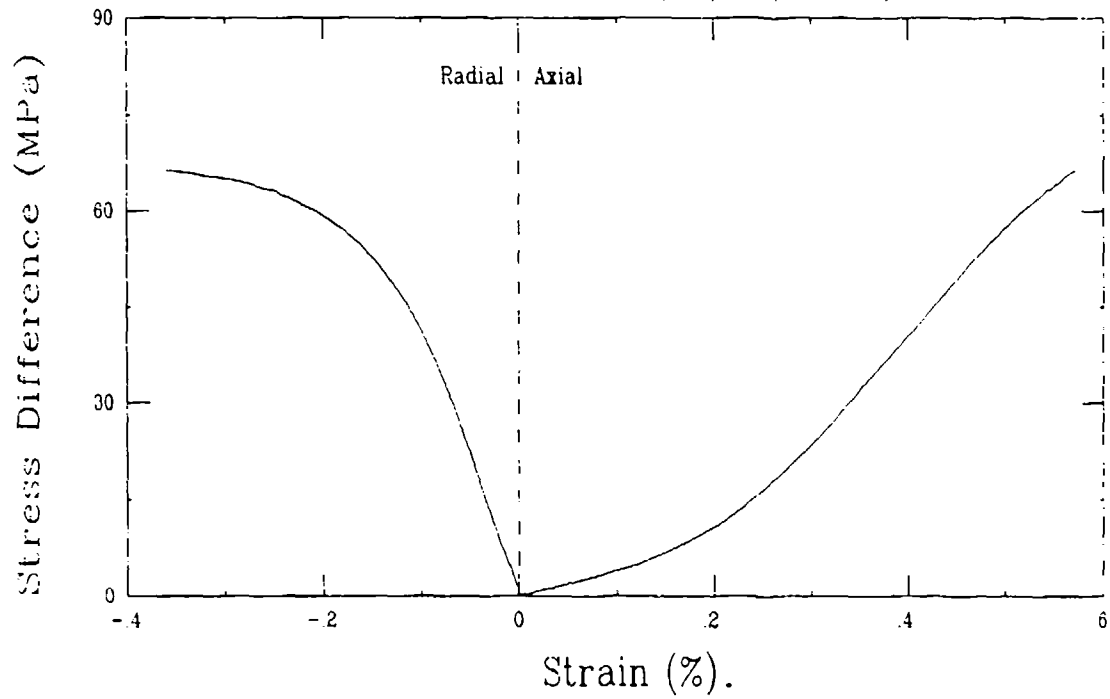


# Unconfined Compression Test (G28B1)

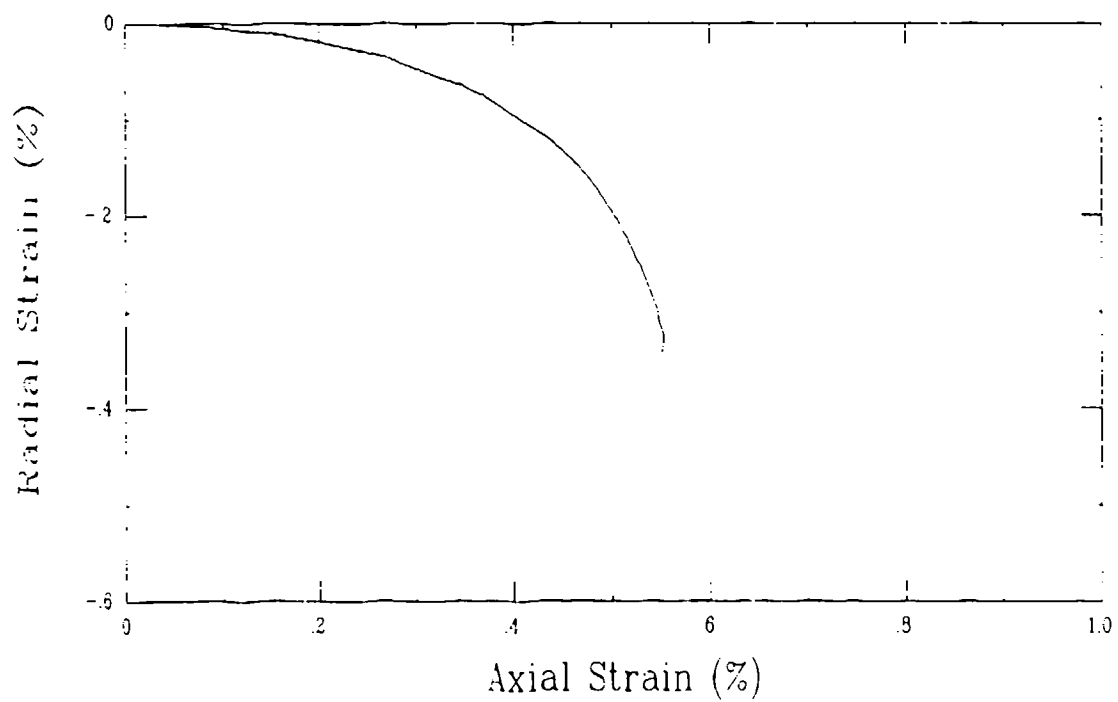
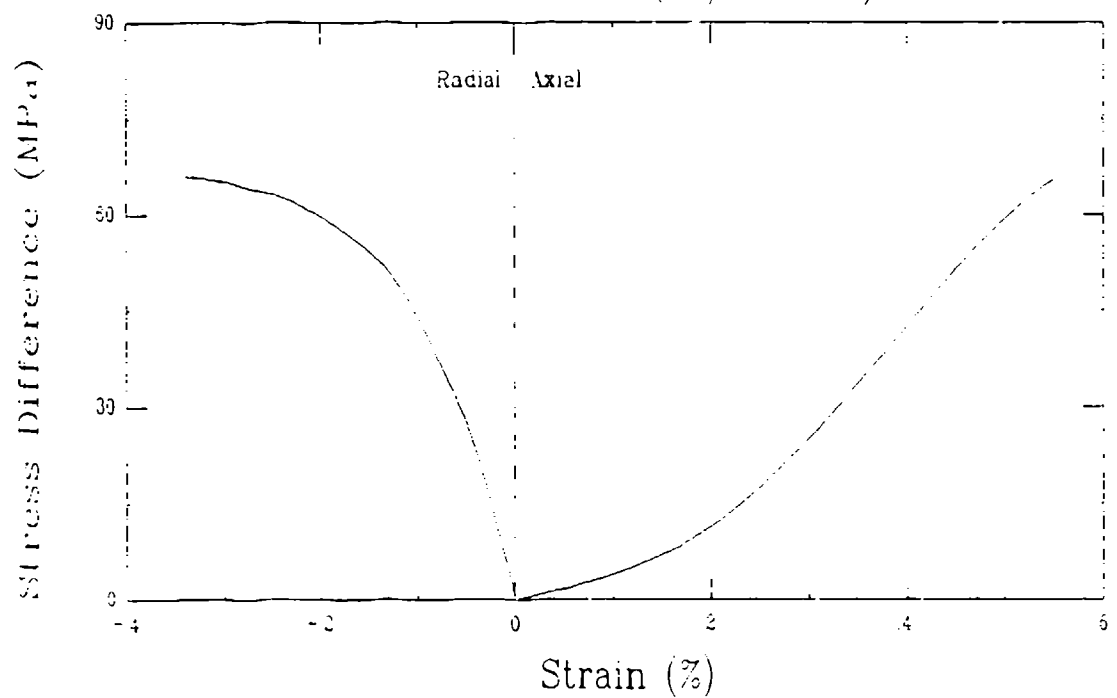
## Berea Sandstone (BS/91/1-7/1)



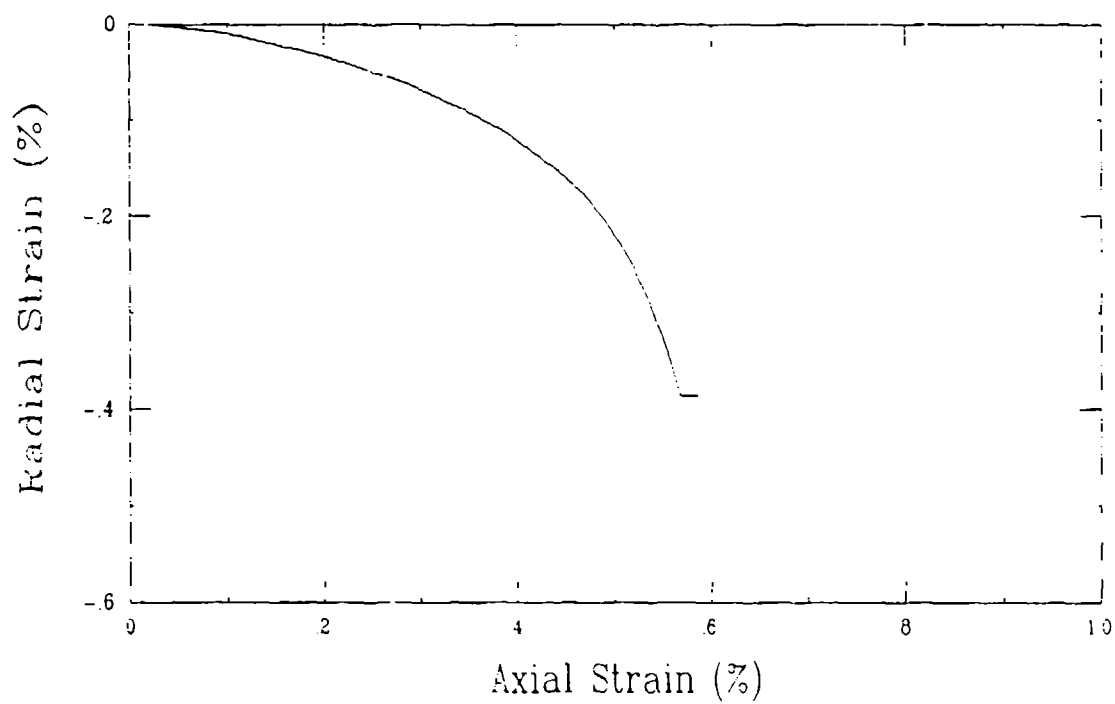
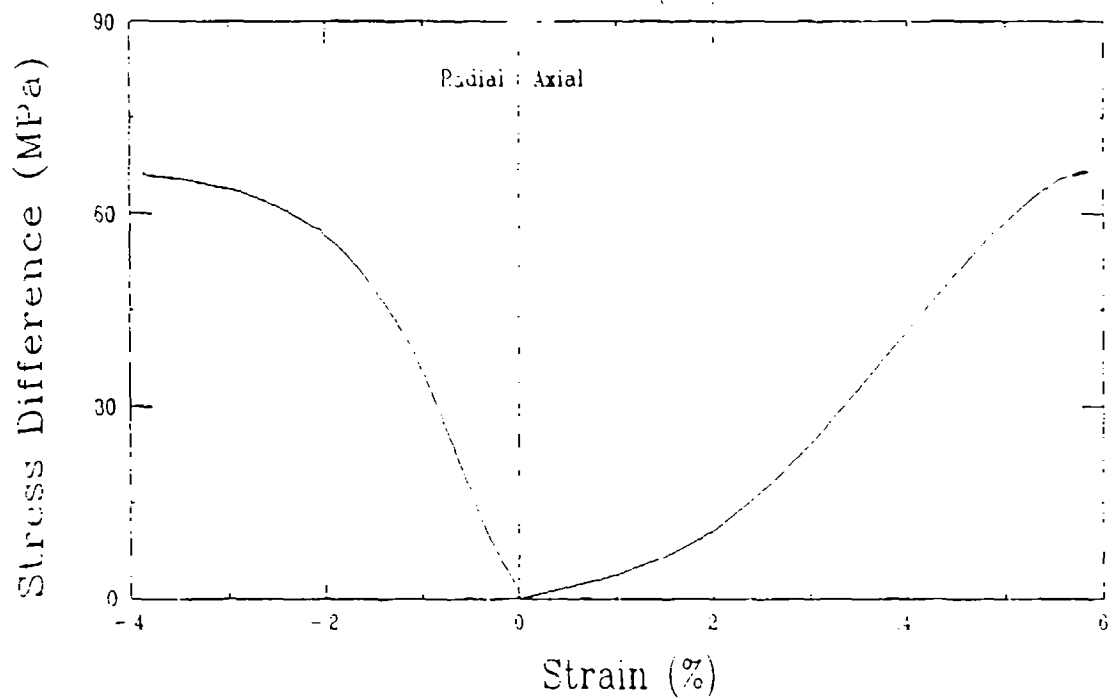
Unconfined Compression Test (G28A1)  
Berea Sandstone (BS/91/2-15)



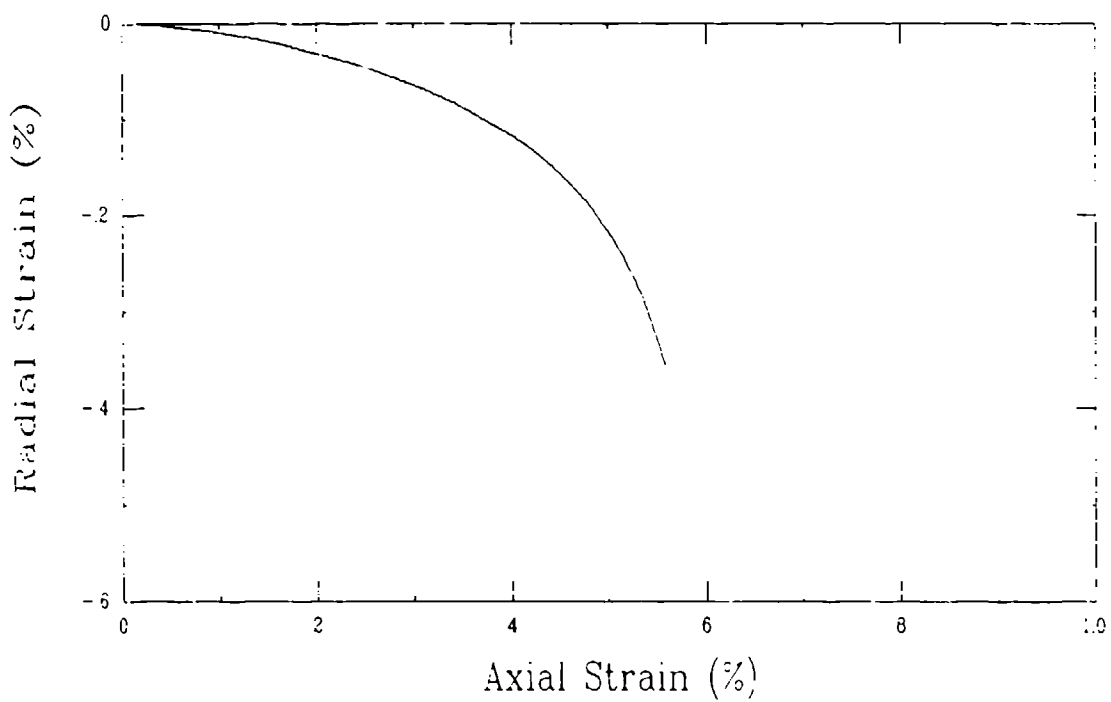
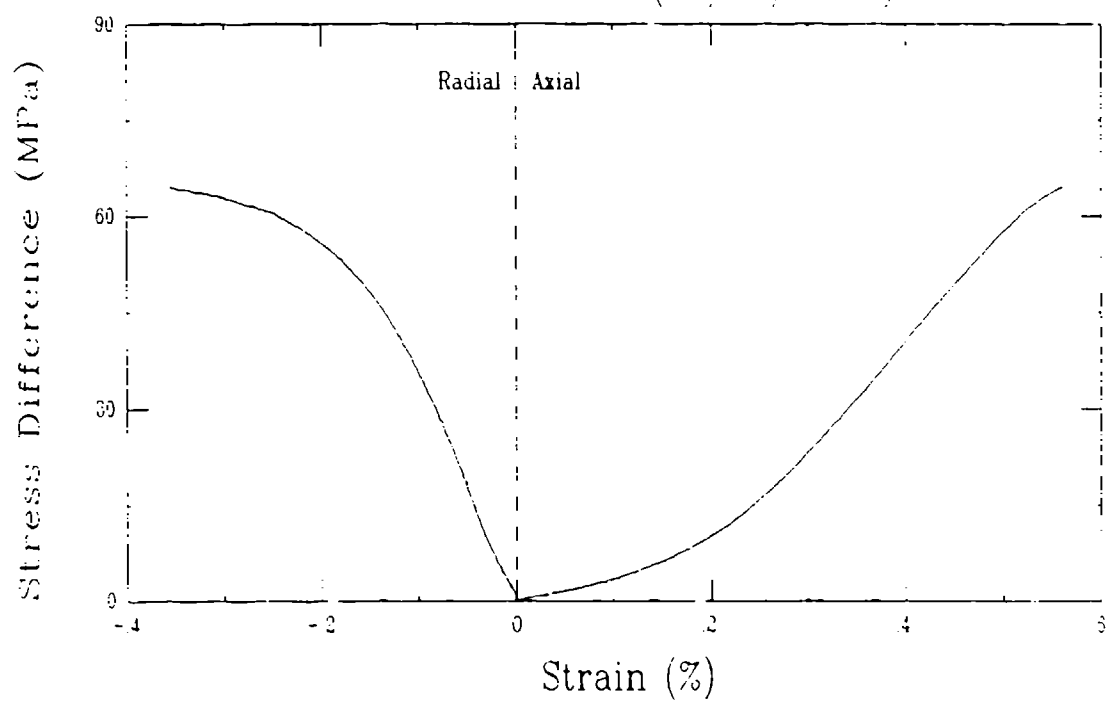
Unconfined Compression Test (G27G1)  
Berea Sandstone (BS, 91, 3-4)



Unconfined Compression Test (G28C1)  
Berea Sandstone (BS/91/4-1)

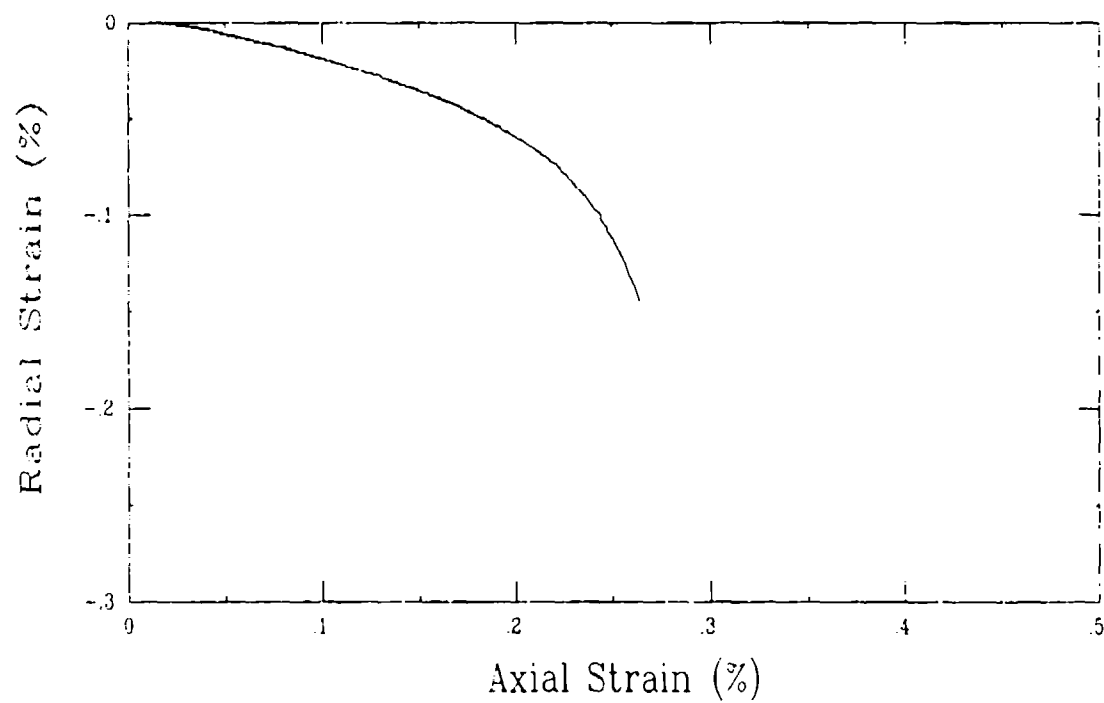
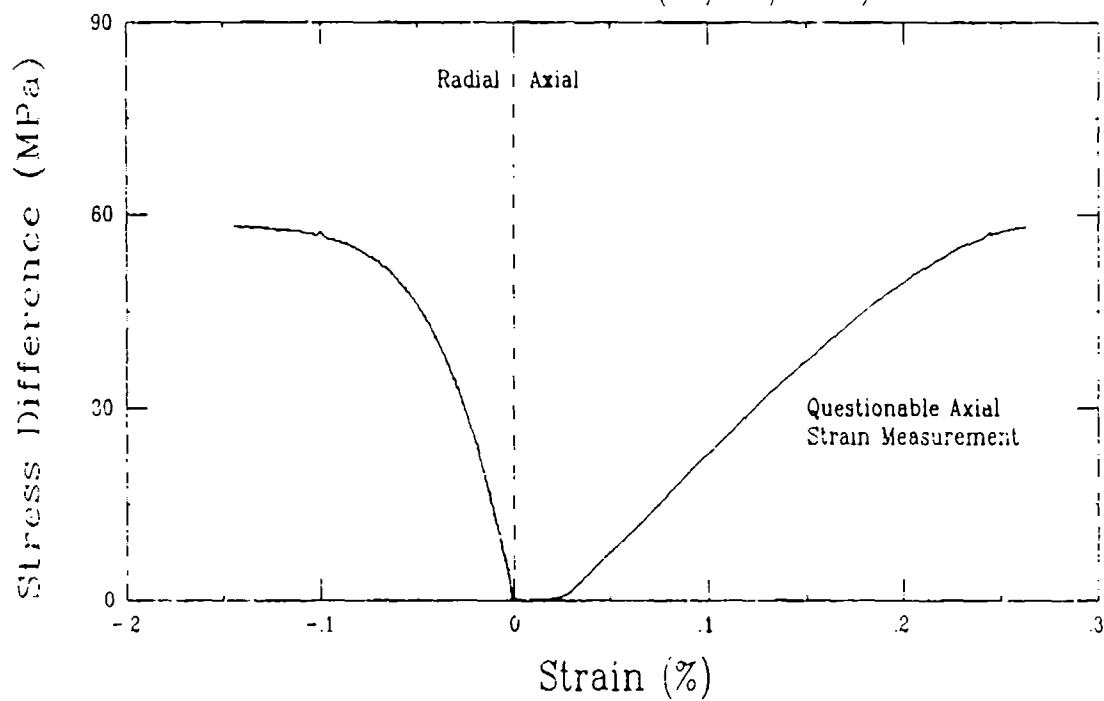


Unconfined Compression Test (G27F1)  
Berea Sandstone (BS/91/4-16)

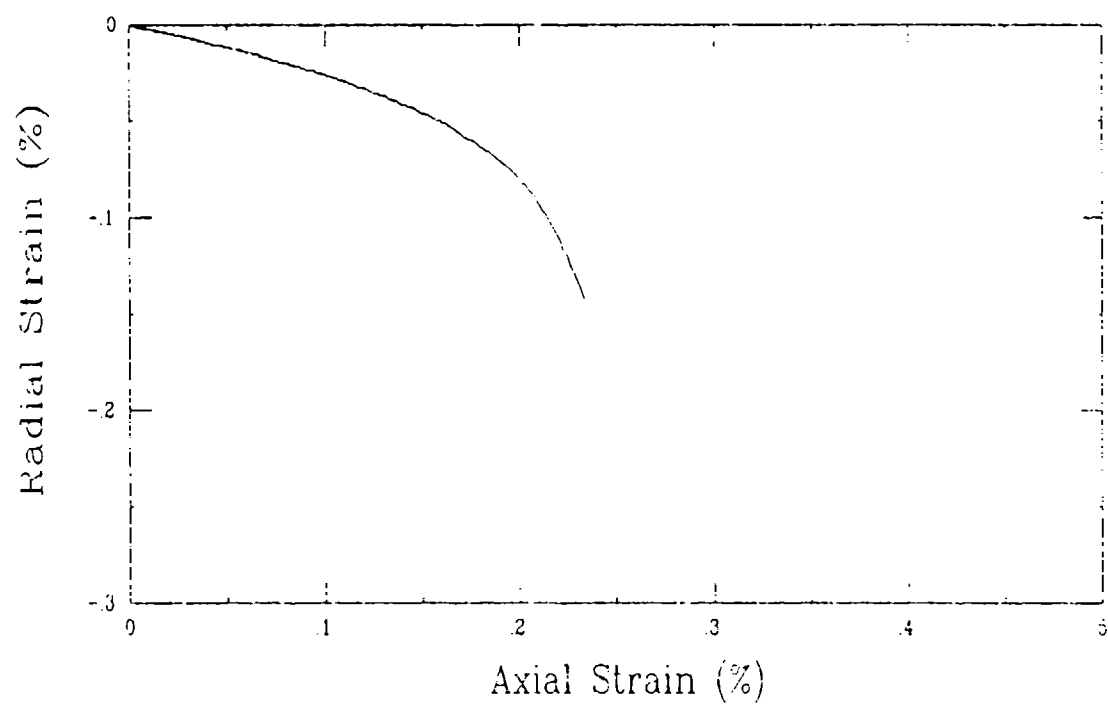
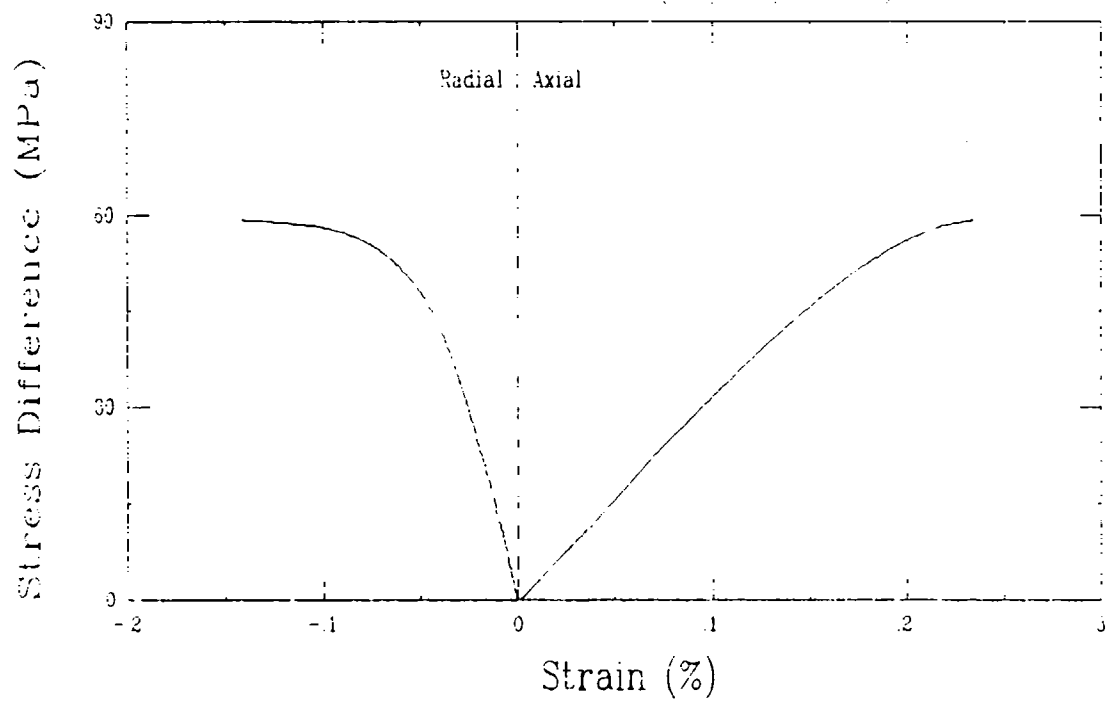


# Unconfined Compression Test (G27A1)

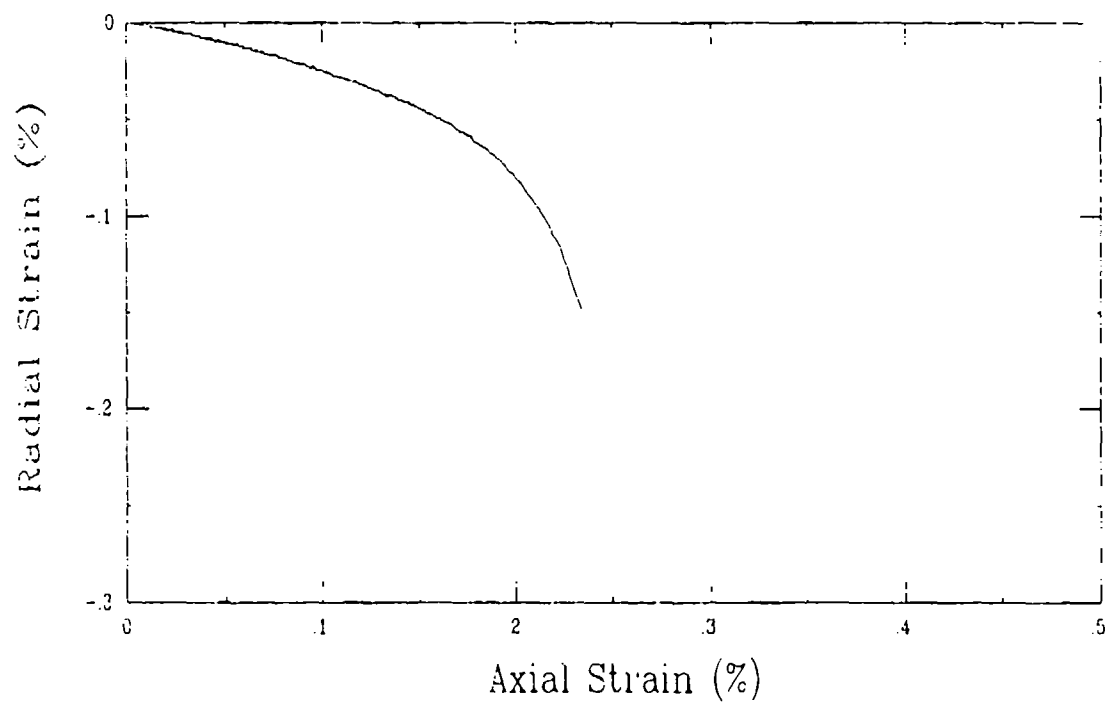
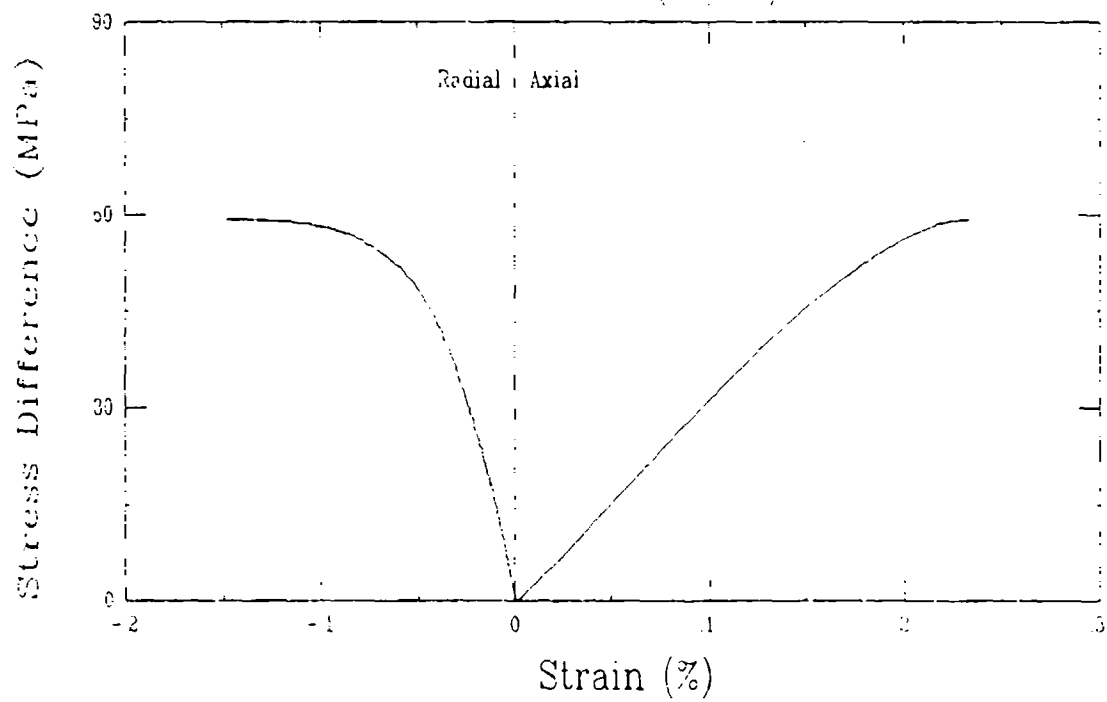
## Salem Limestone (SL/91/1-7)



Unconfined Compression Test (G27B1)  
Salem Limestone (SL/91/2-14)

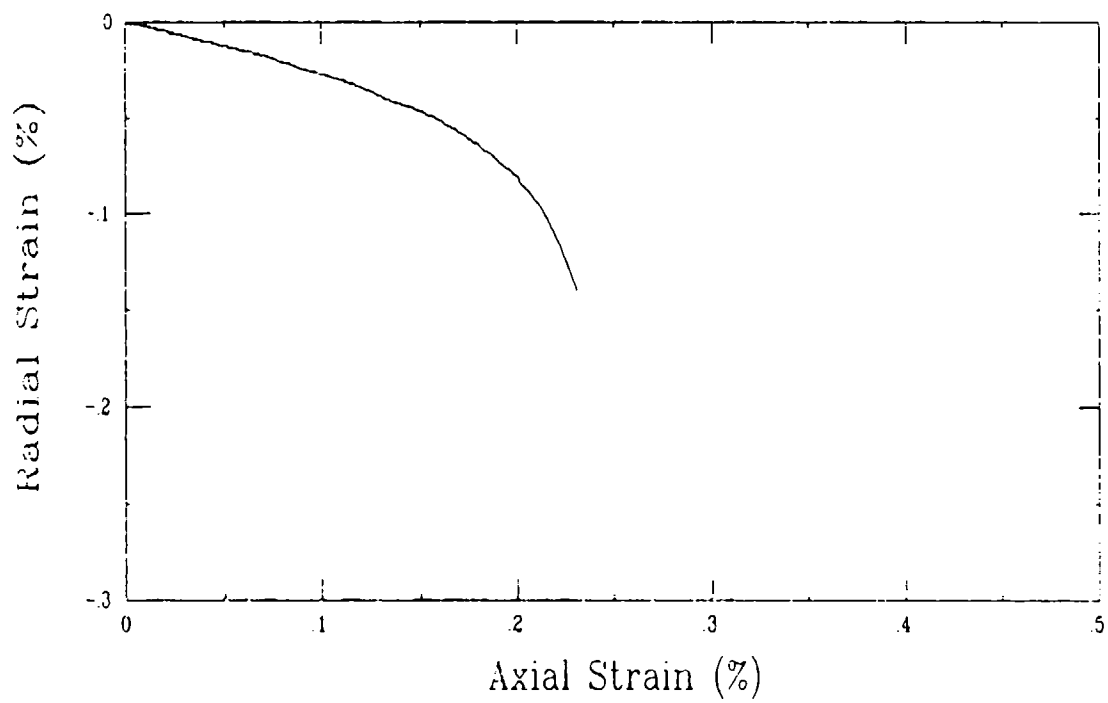
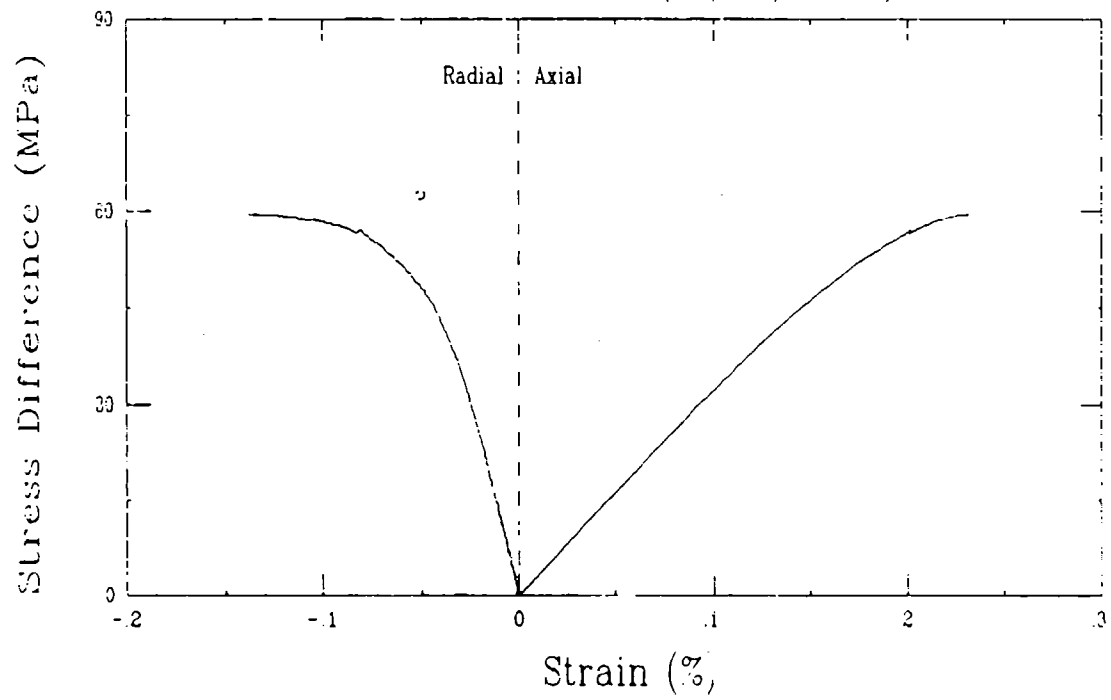


Unconfined Compression Test (G27E1)  
Salem Limestone (SL/91/3-3)

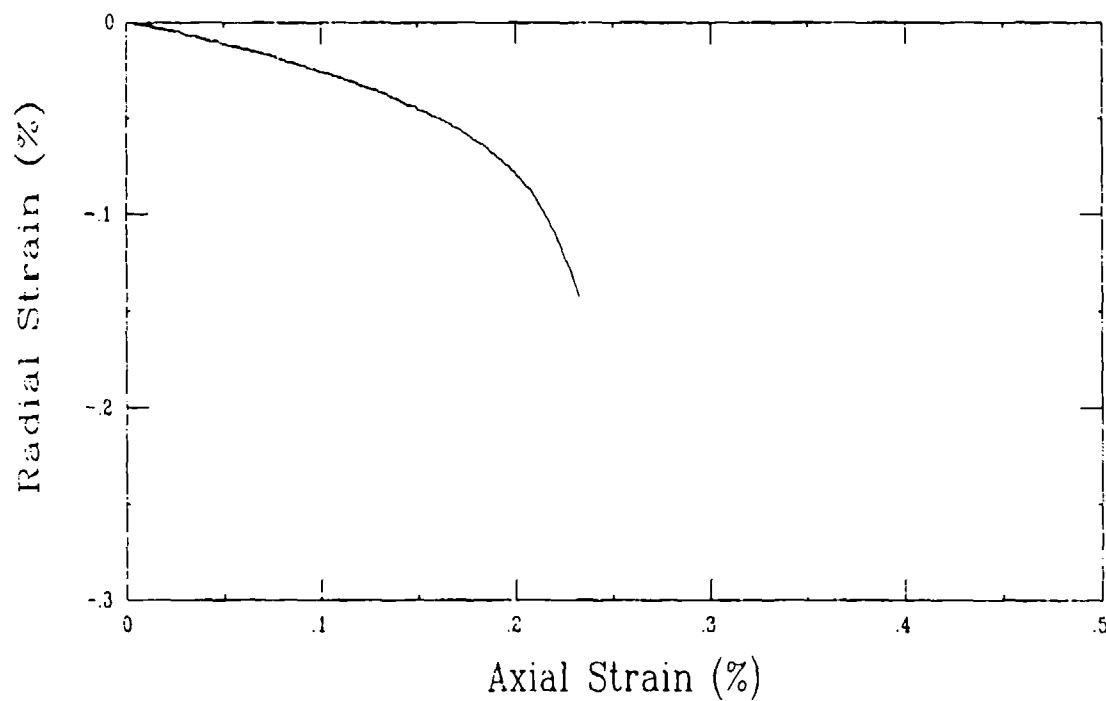
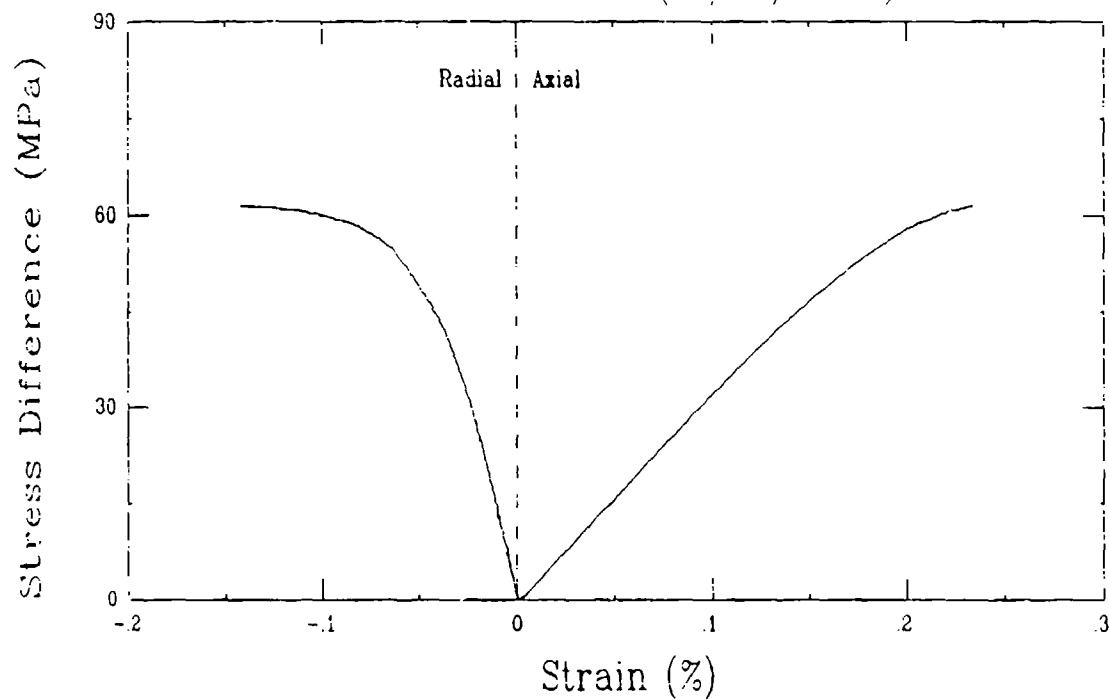




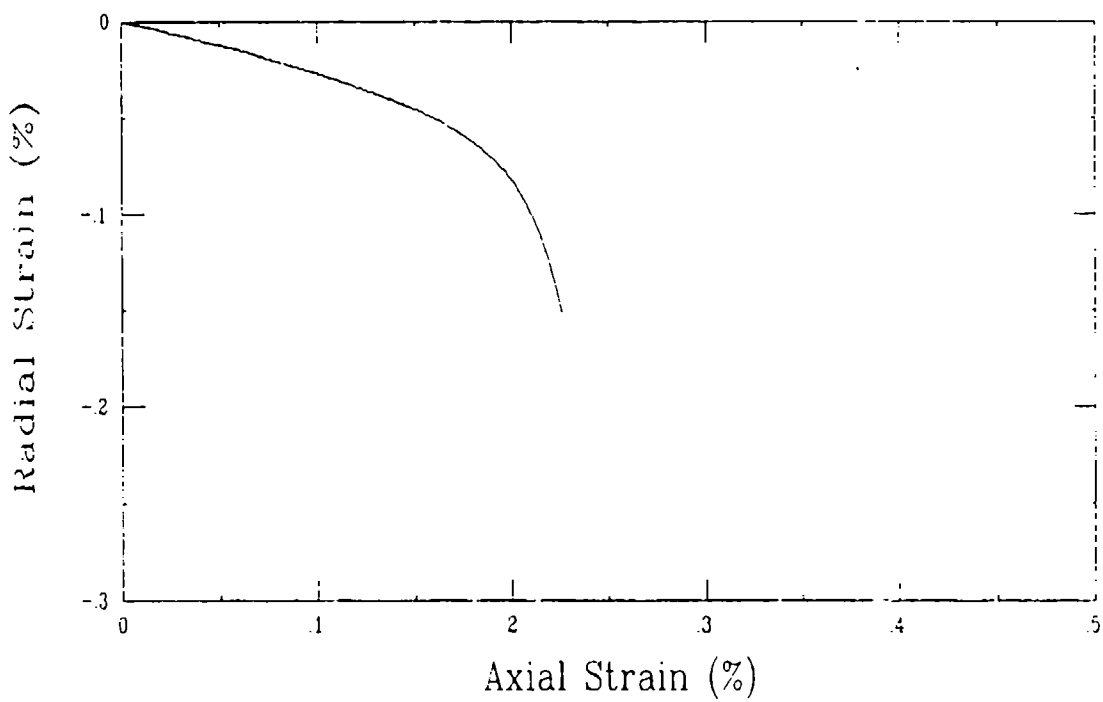
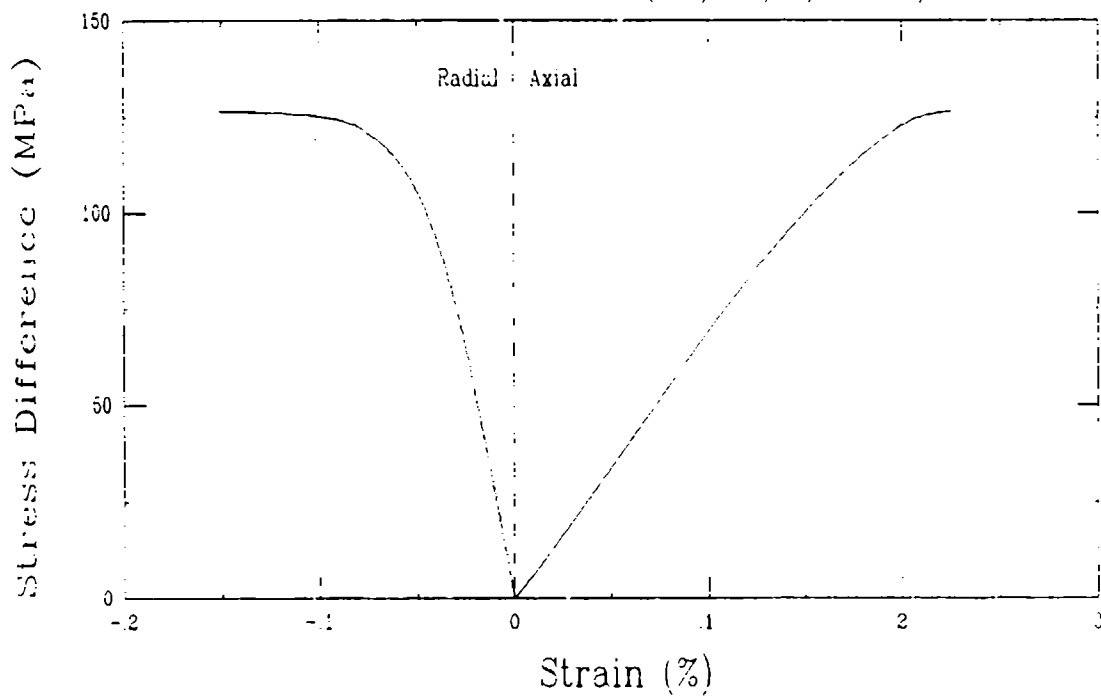
Unconfined Compression Test (G27C1)  
Salem Limestone (SL/91/3-20)



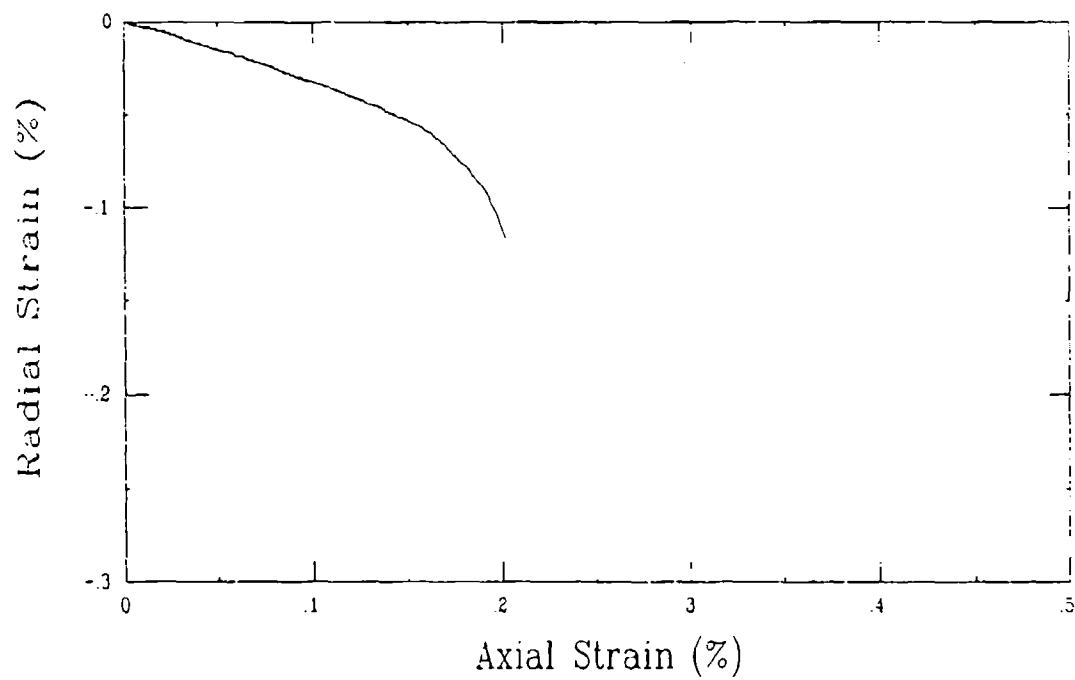
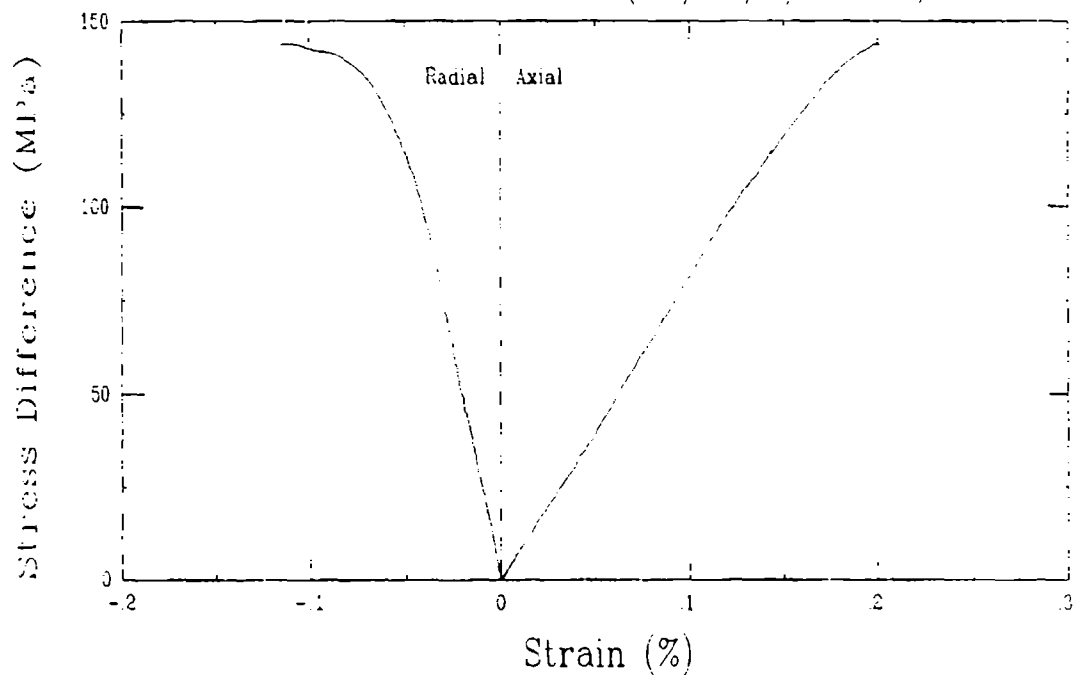
Unconfined Compression Test (G27D1)  
Salem Limestone (SL/91/4-15)



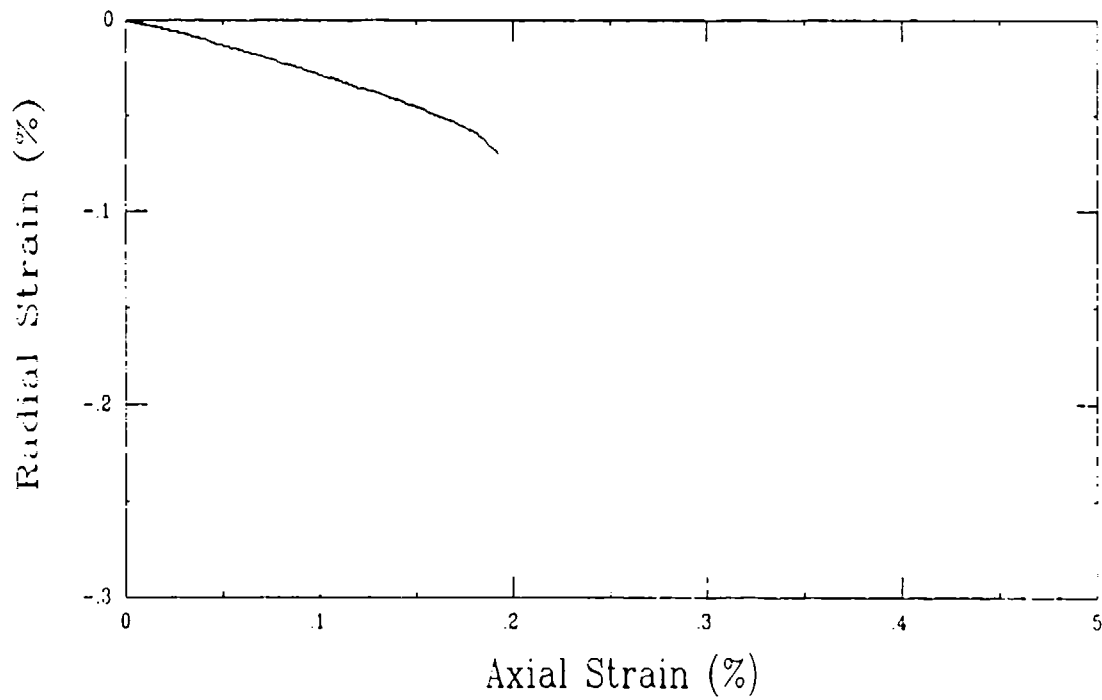
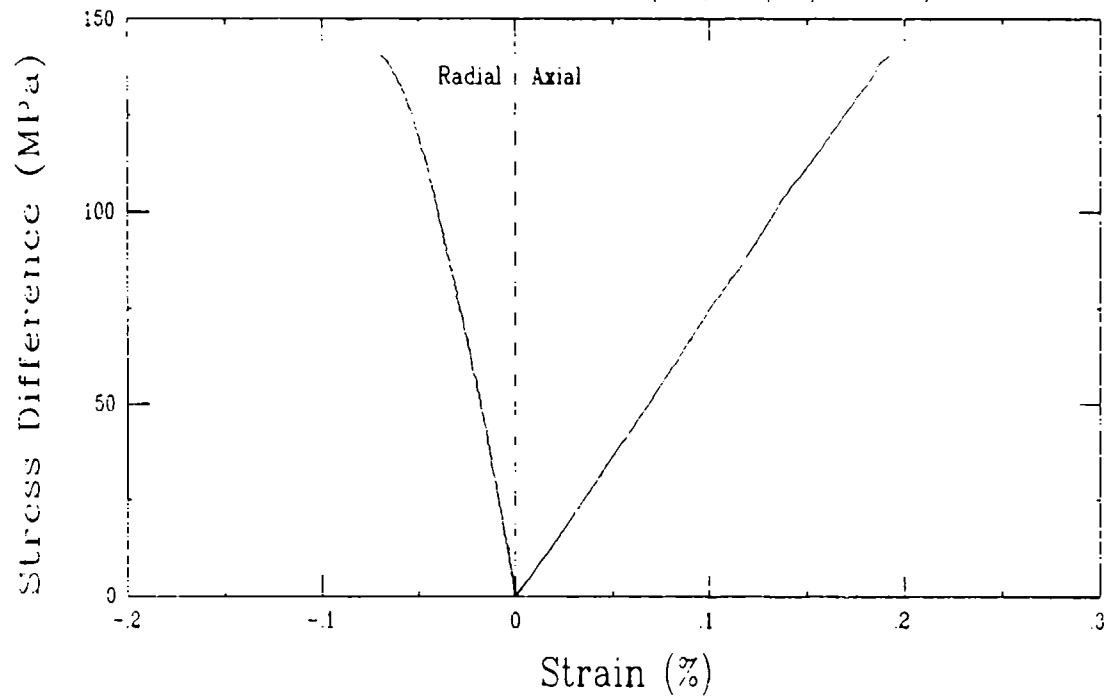
Unconfined Compression Test (G29A1)  
Tennessee Marble (TM/91/1/2-19)



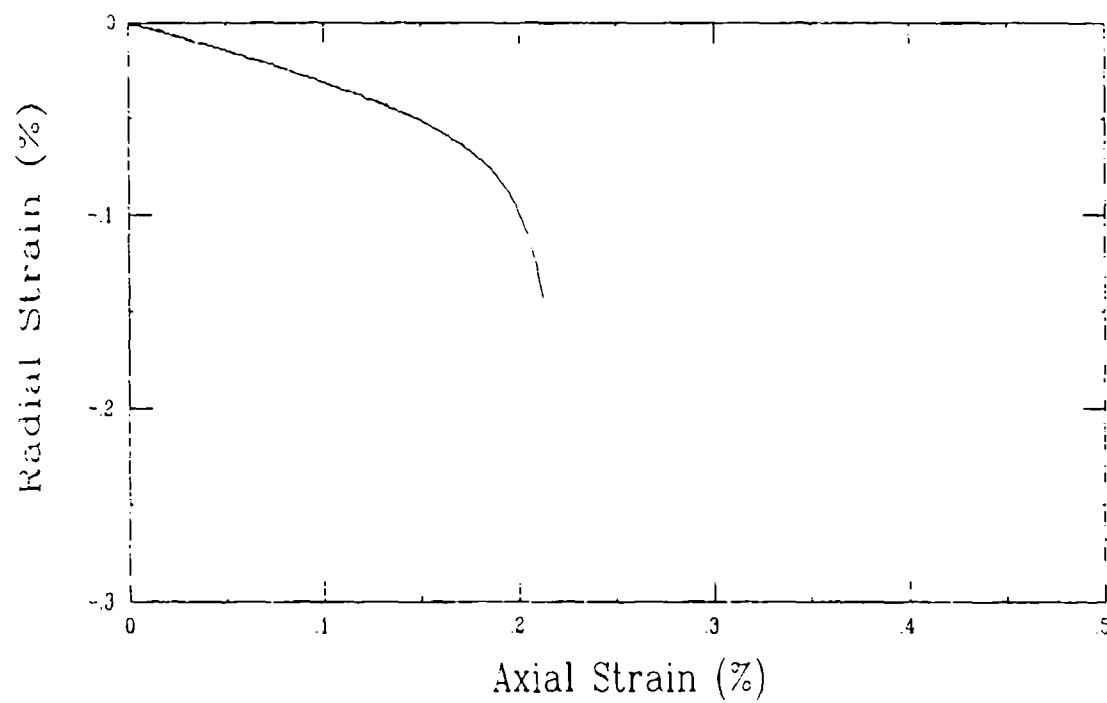
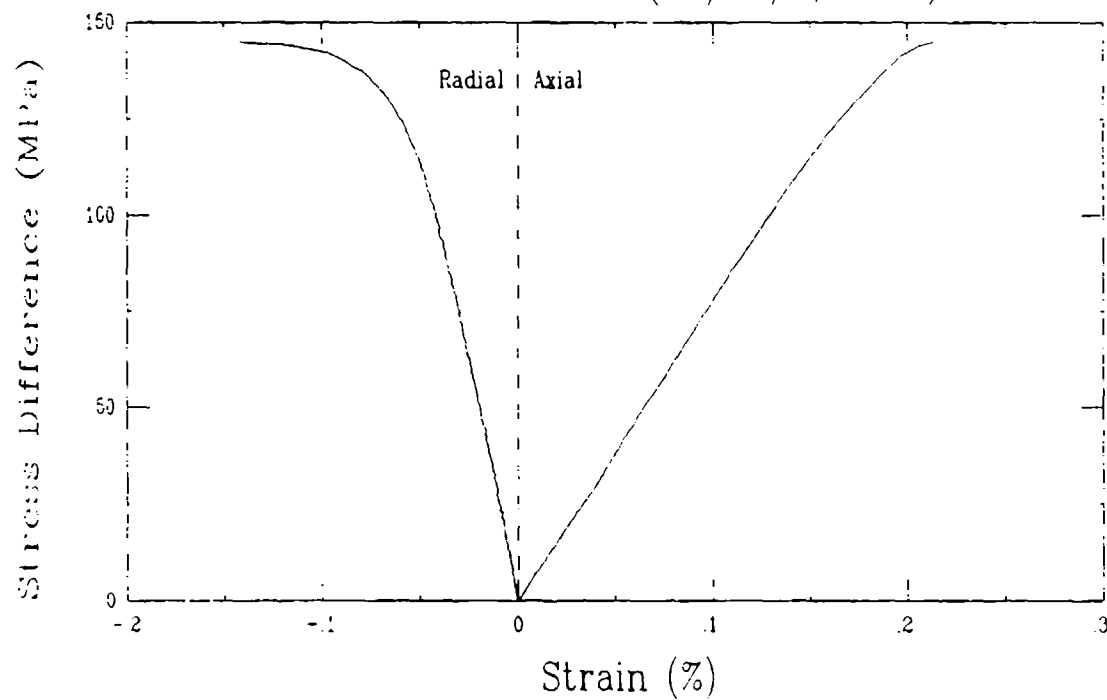
Unconfined Compression Test (G29C1)  
Tennessee Marble (TM/91/3/2-19B)



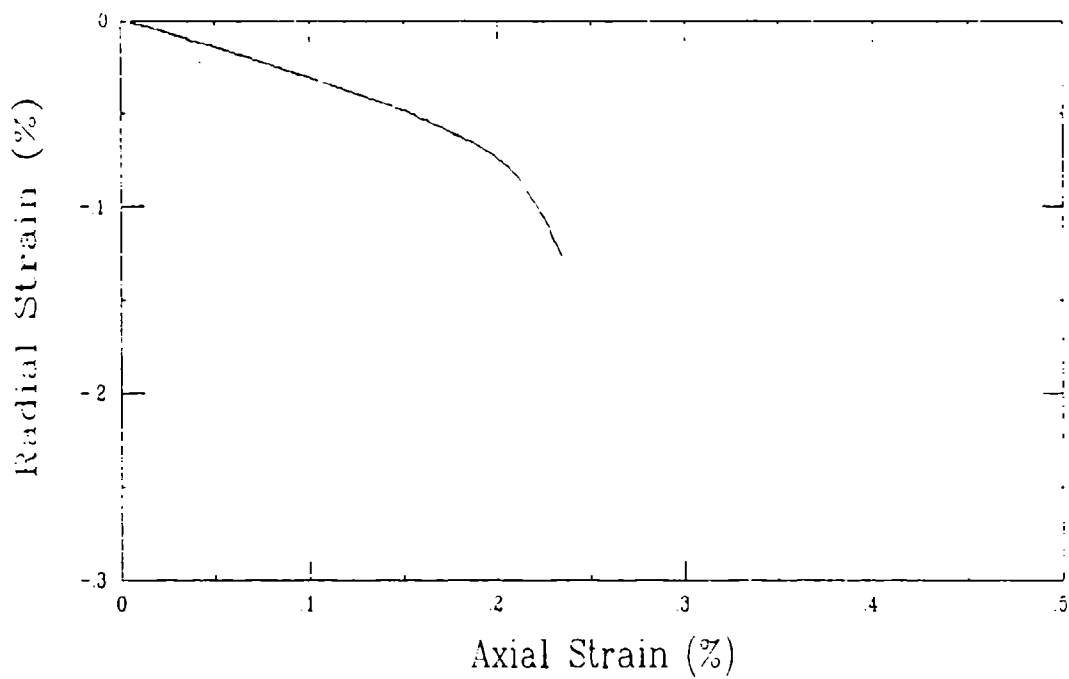
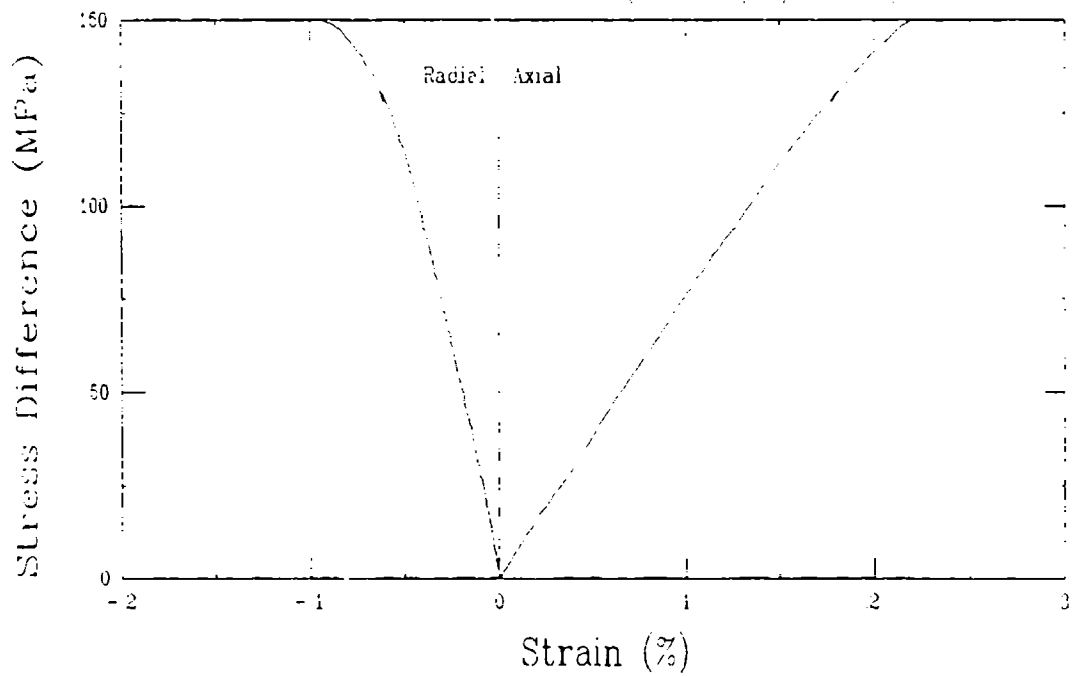
Unconfined Compression Test (G29E1)  
Tennessee Marble (TM/91/4/1-2B)



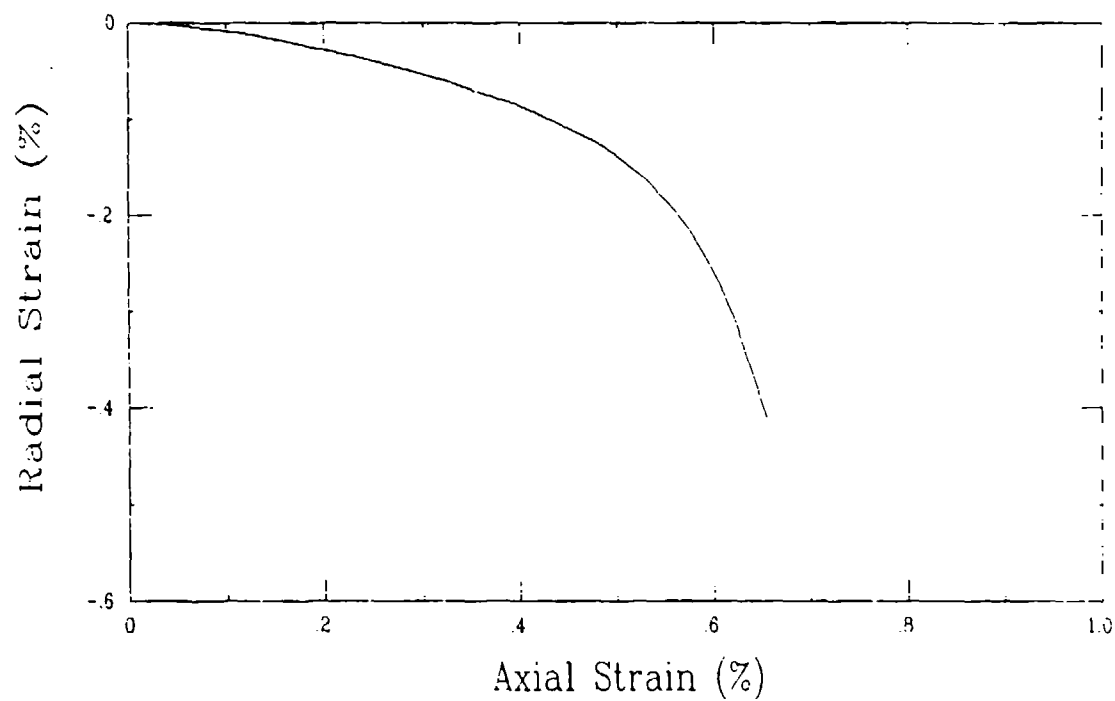
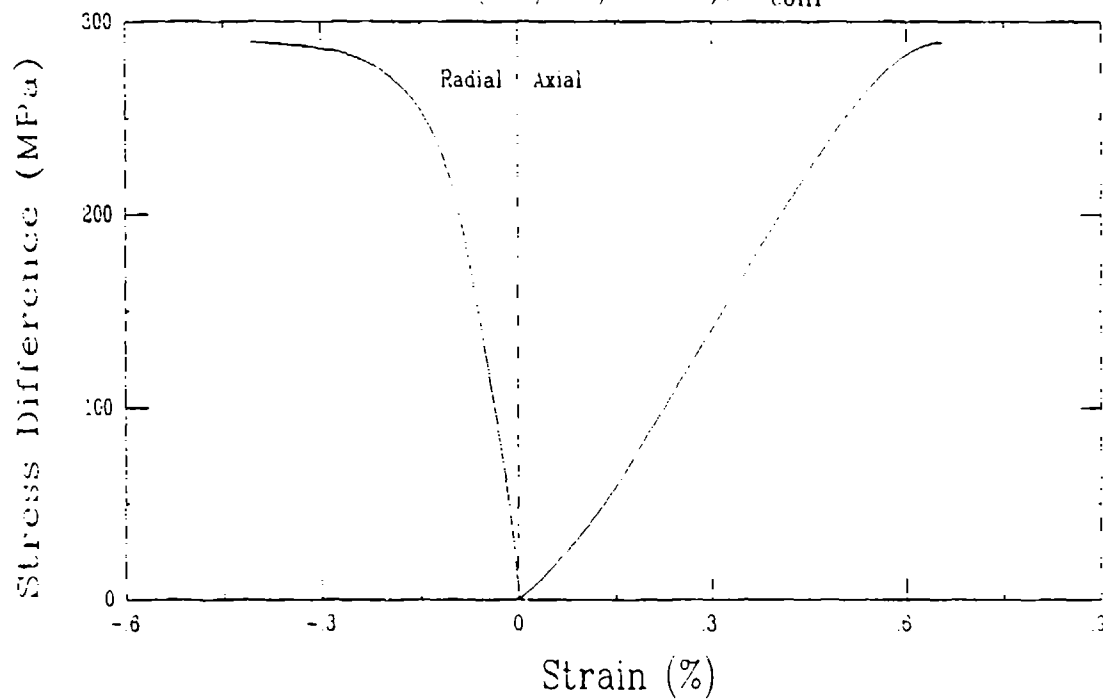
Unconfined Compression Test (G29D1)  
Tennessee Marble (TM/91/4/2-5B)



Unconfined Compression Test (G29B1)  
Tennessee Marble (TM/91/4/2-20)

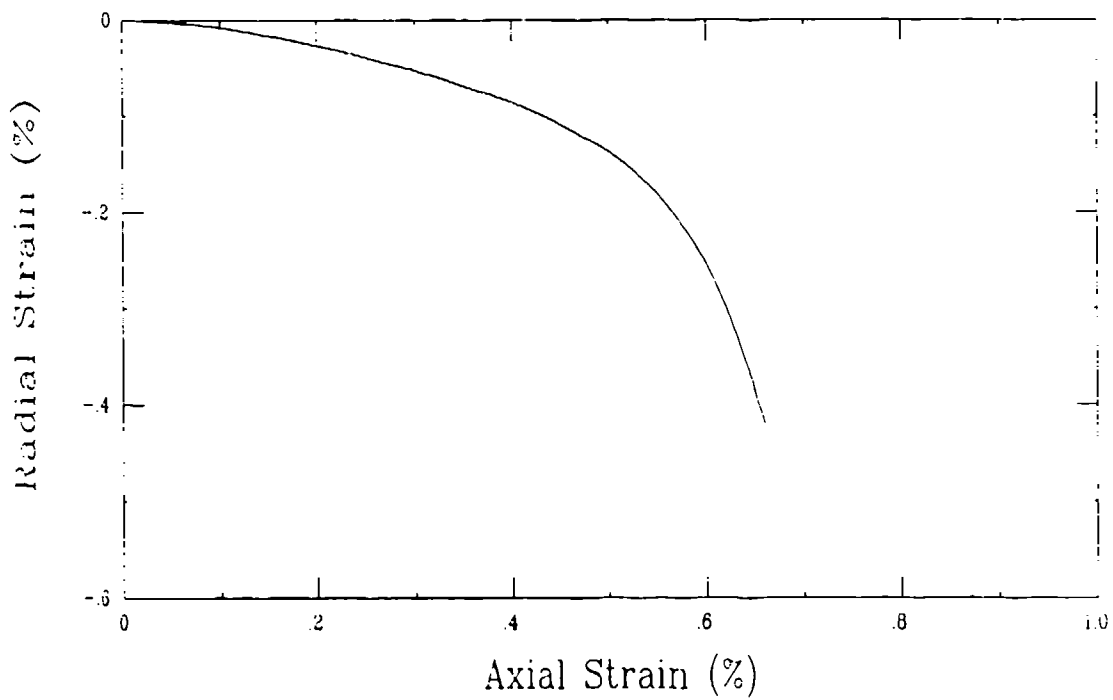
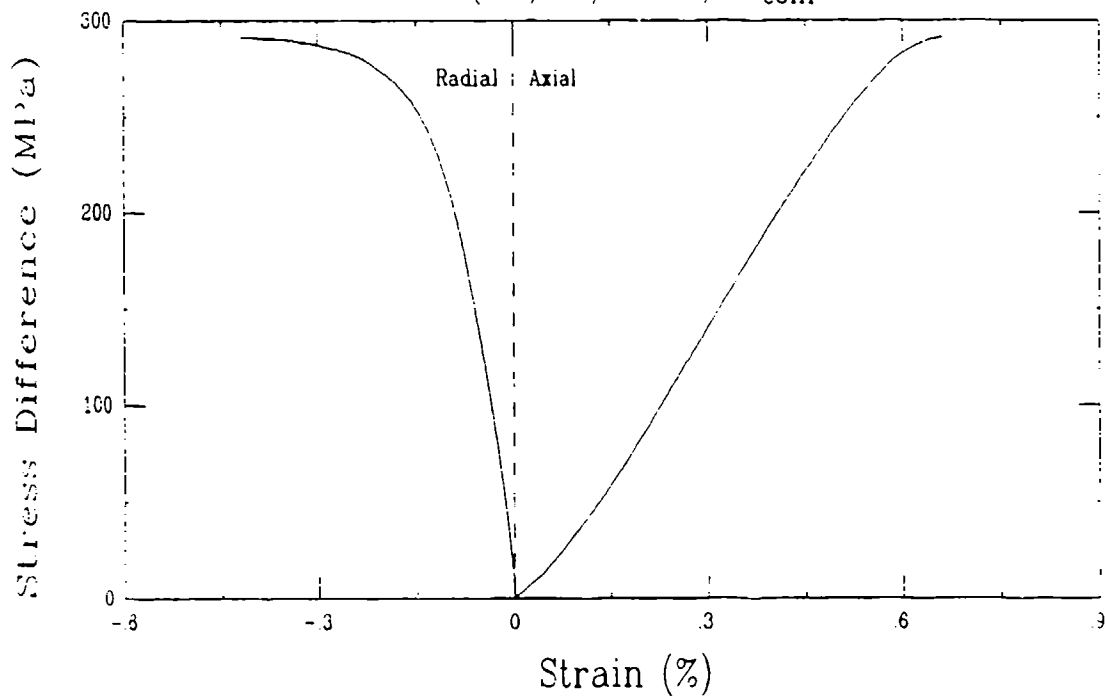


Triaxial Compression Test (U2E3)  
Barre Granite (BG/91/1-1B),  $\sigma_{\text{conf}} = 10 \text{ MPa}$

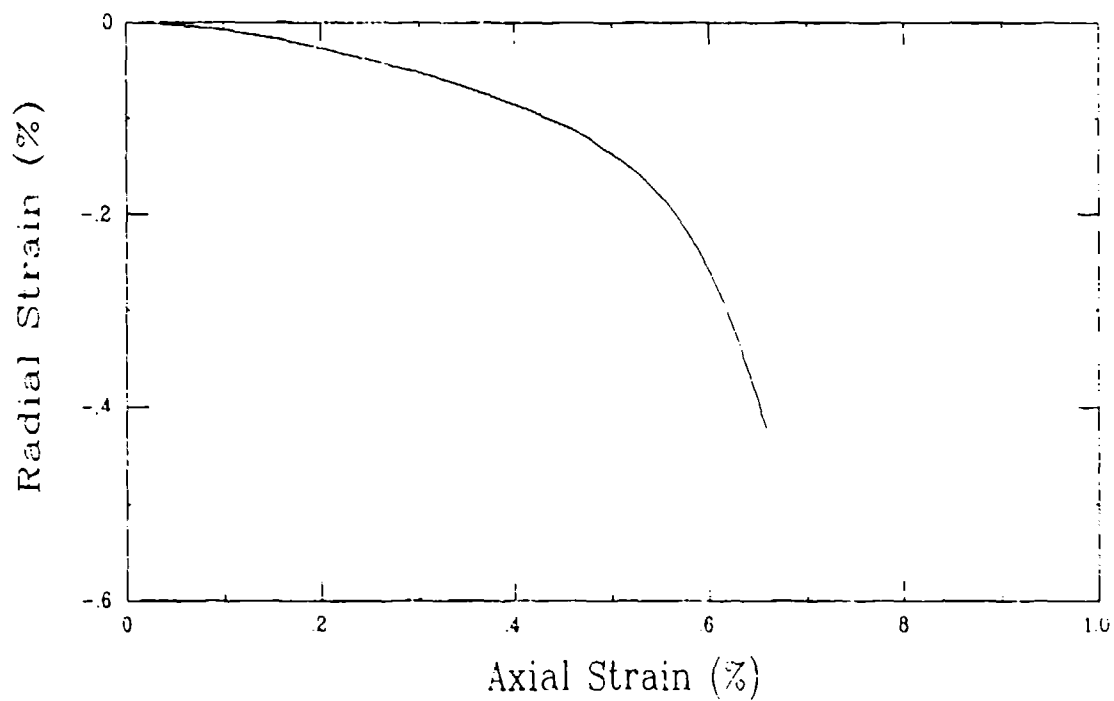
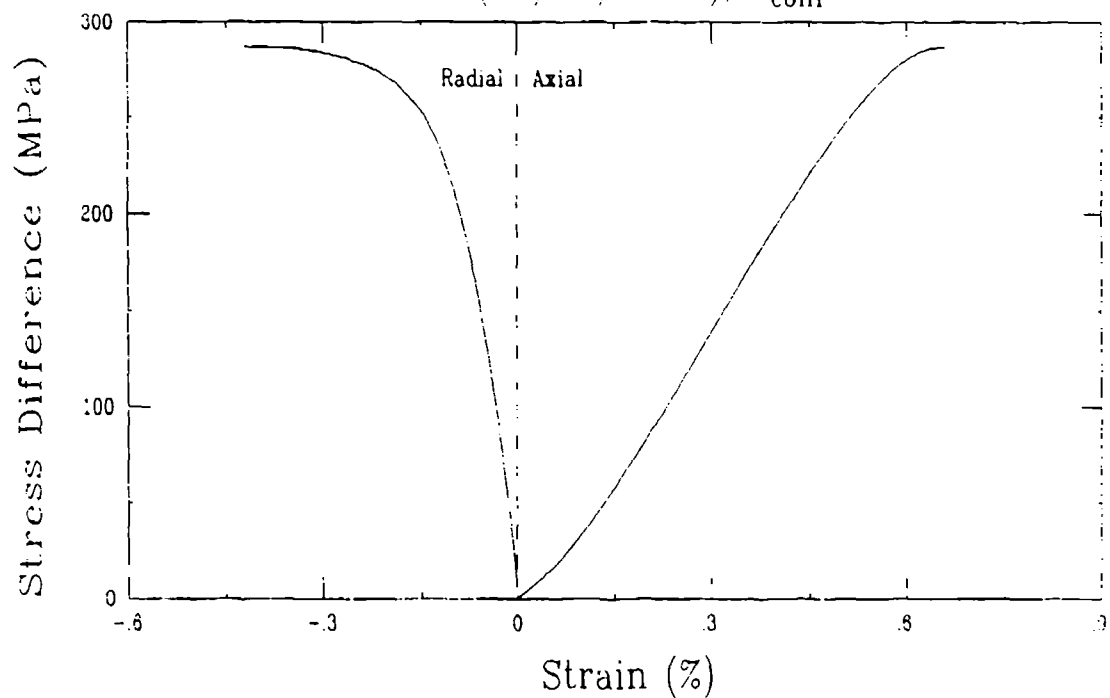




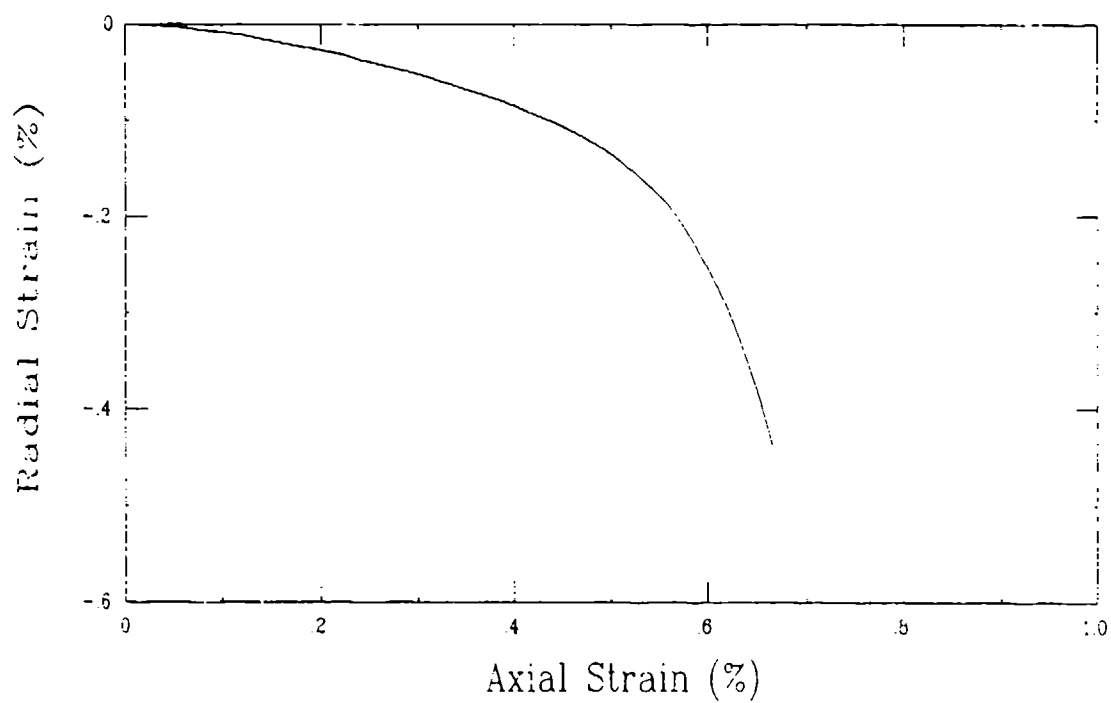
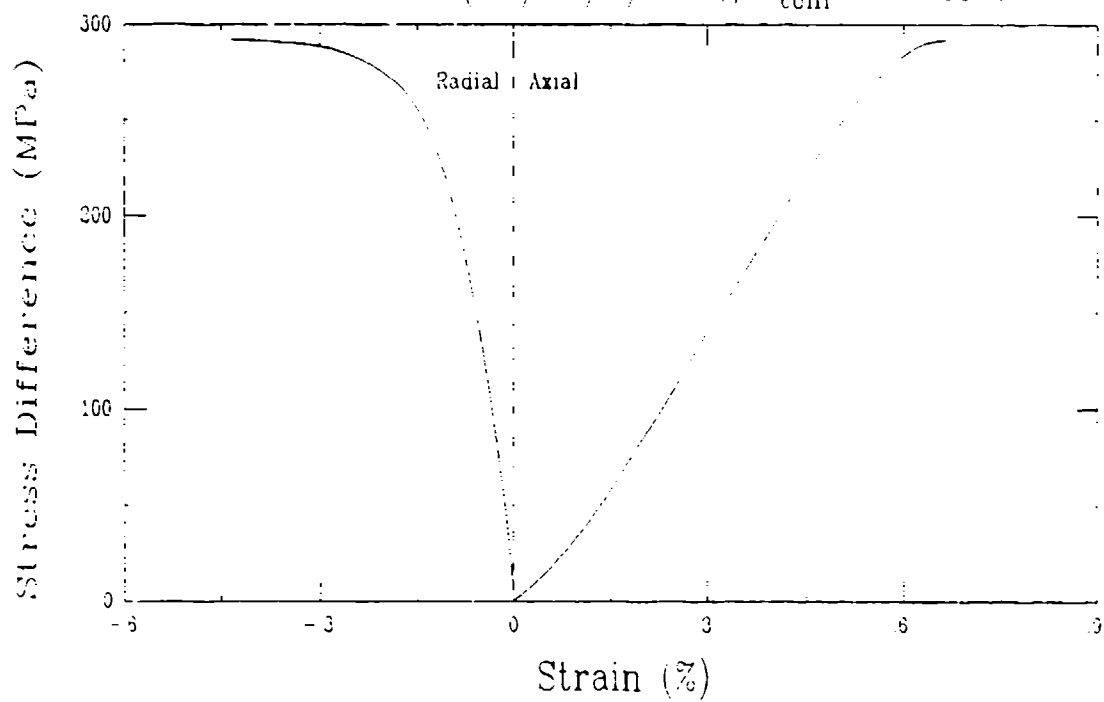
Triaxial Compression Test (U3B3)  
Barre Granite (BG/91/1-8T),  $\sigma_{\text{conf}} = 10 \text{ MPa}$



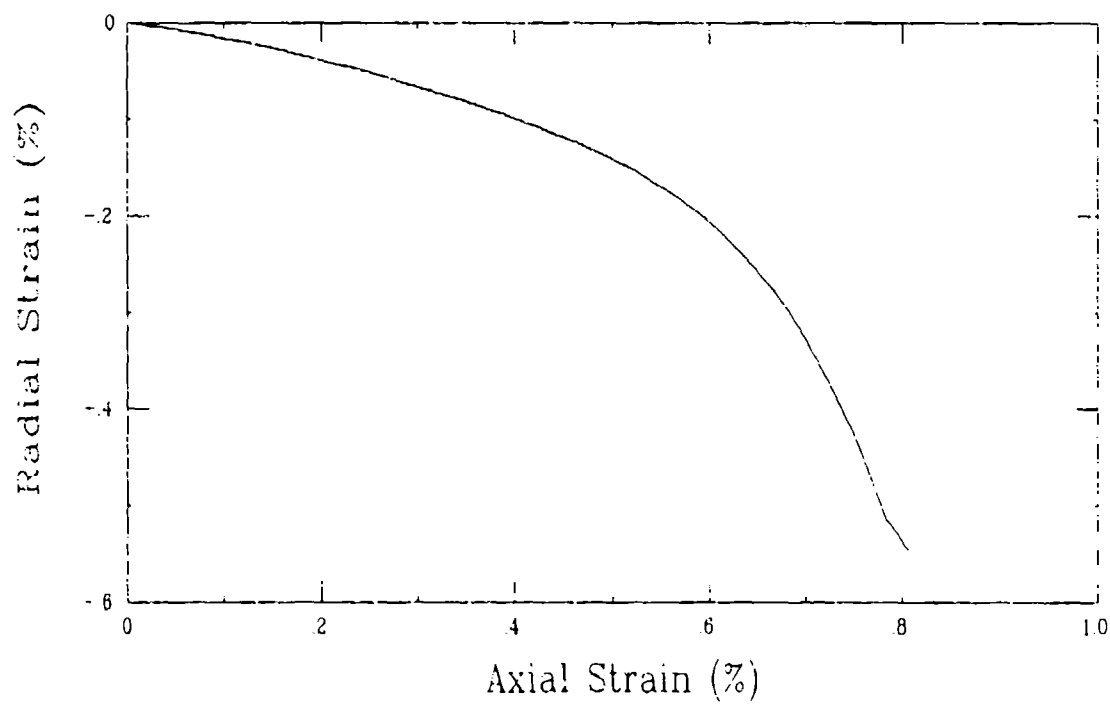
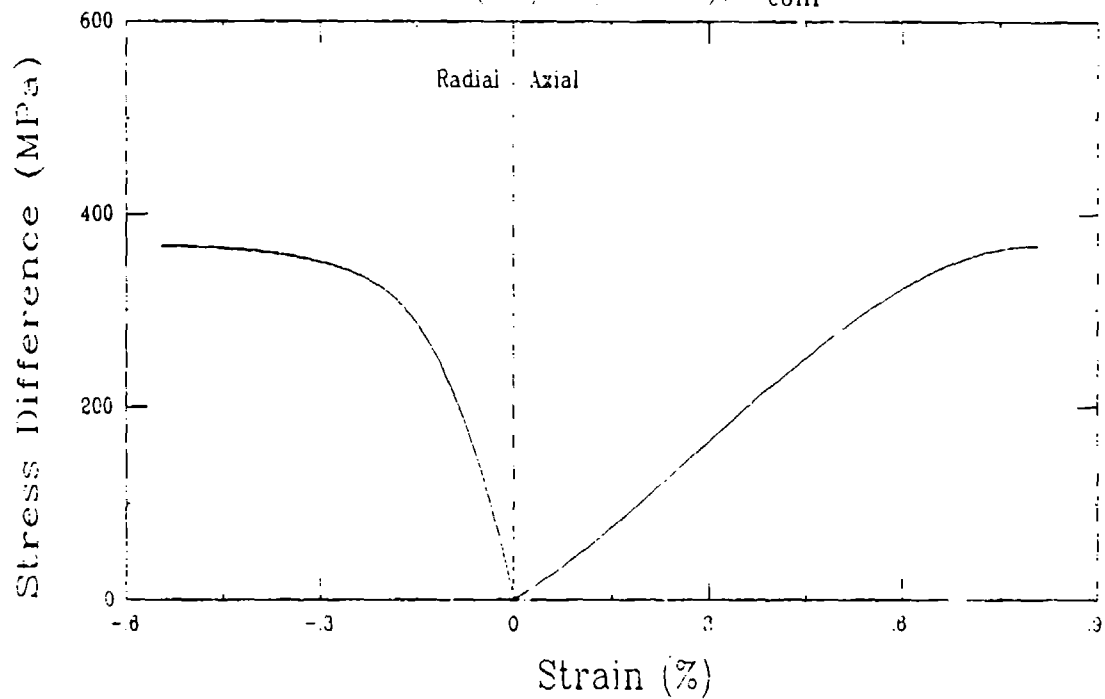
Triaxial Compression Test (U2F3)  
Barre Granite (BG/91/3-1B),  $\sigma_{\text{conf}} = 10 \text{ MPa}$



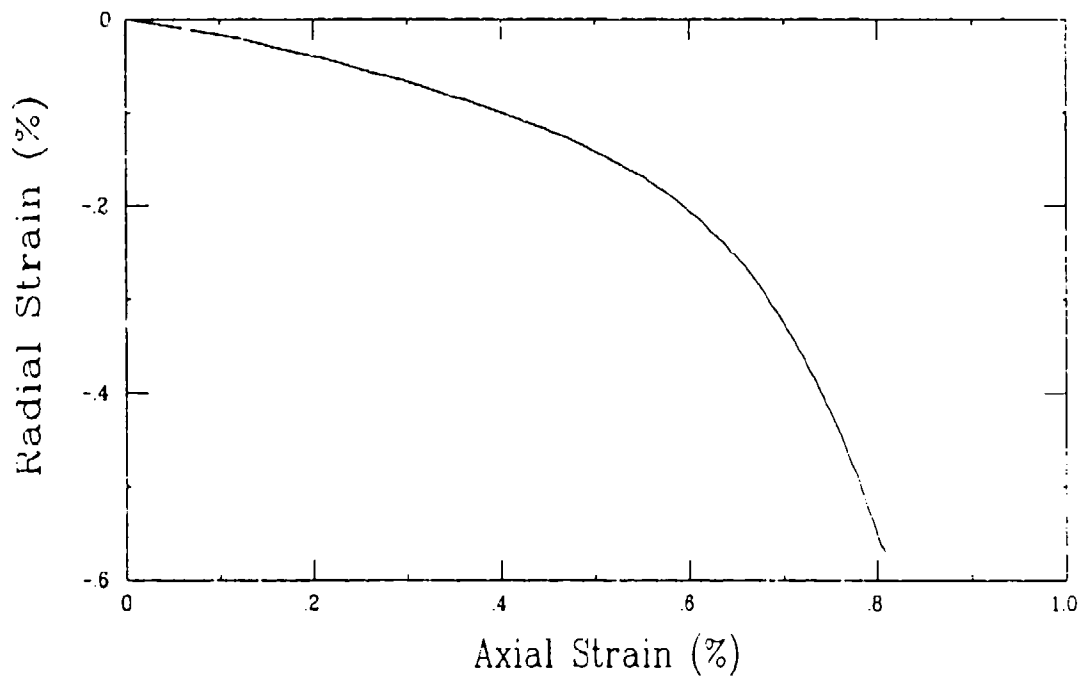
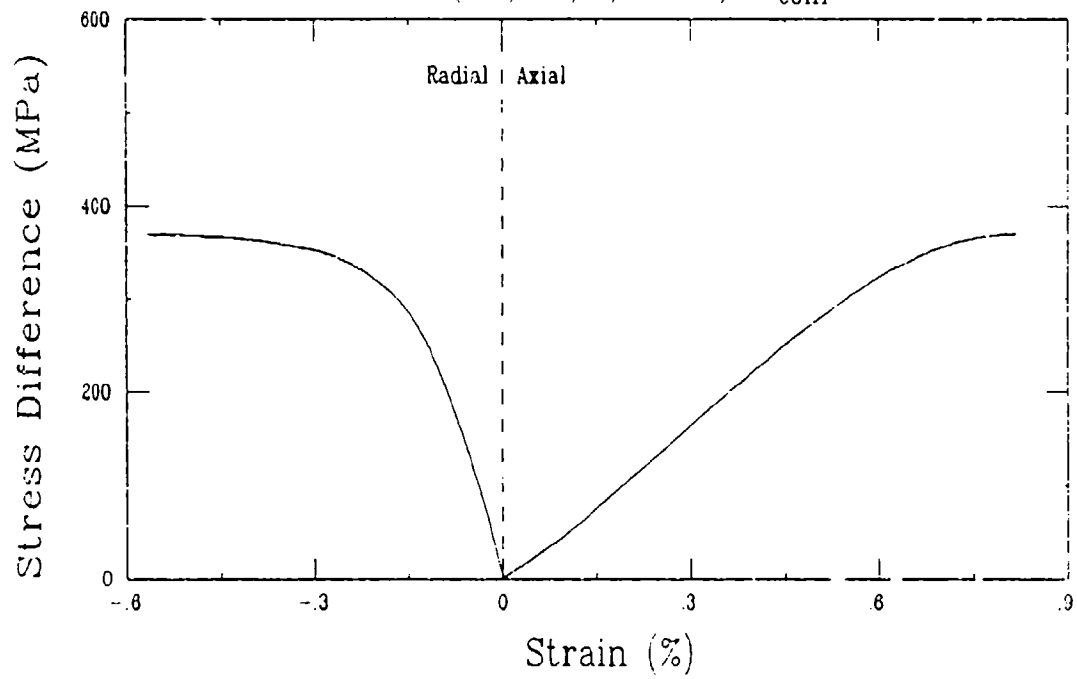
# Triaxial Compression Test (U3A3) Barre Granite (BG/92/1/1-3), $\sigma_{conf} = 10$ MPa



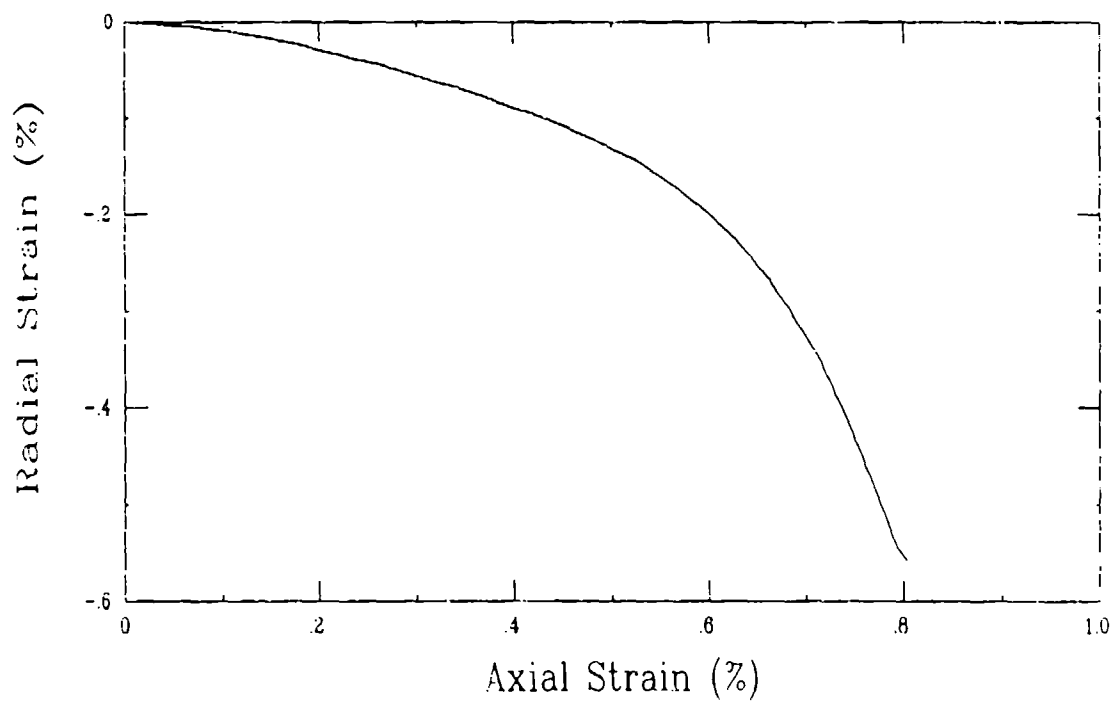
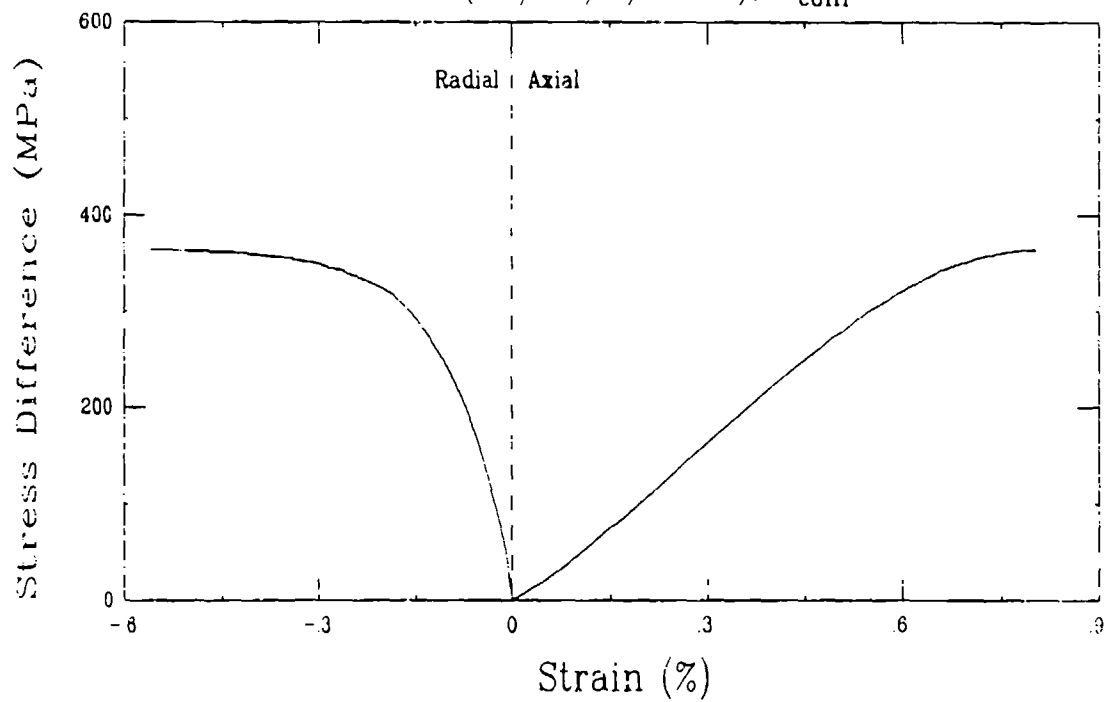
Triaxial Compression Test (U3E3)  
Barre Granite (BG/91/1-4B),  $\sigma_{\text{conf}} = 25 \text{ MPa}$



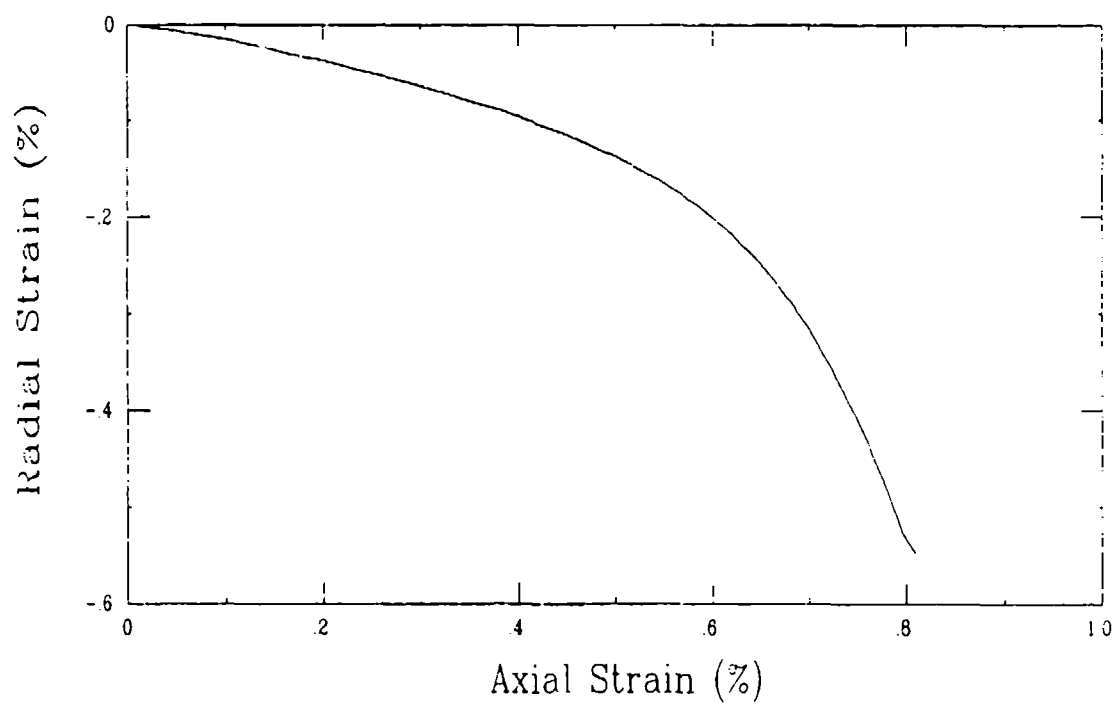
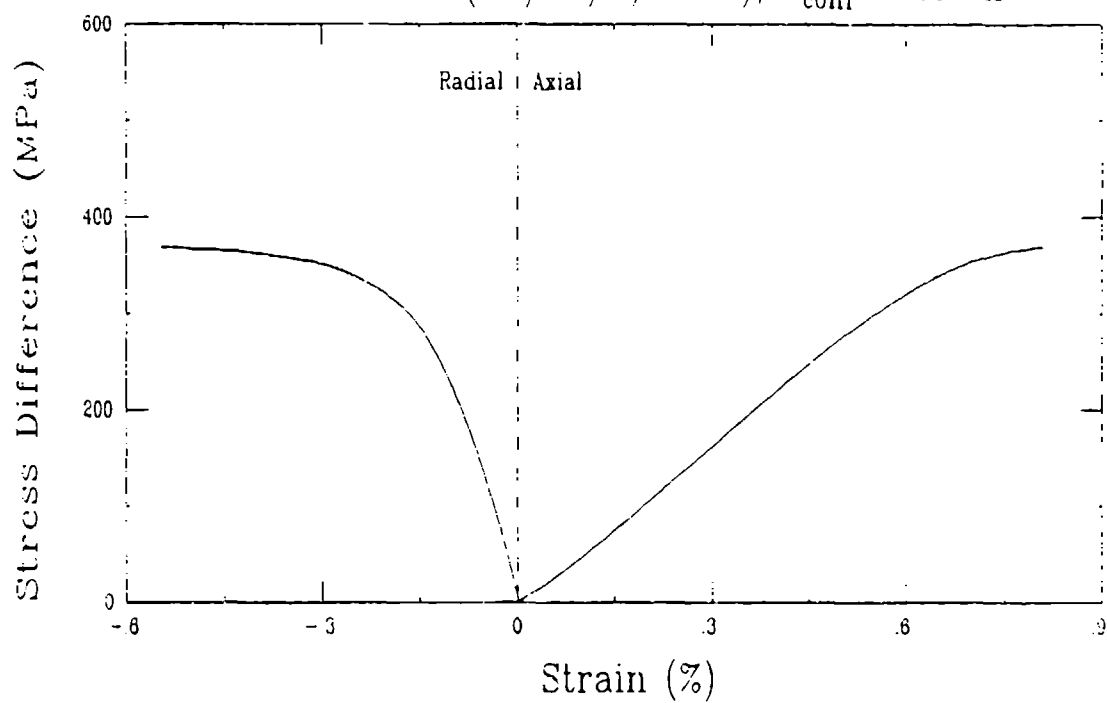
Triaxial Compression Test (U3C3)  
Barre Granite (BG/92/1/1-24),  $\sigma_{\text{conf}} = 25 \text{ MPa}$



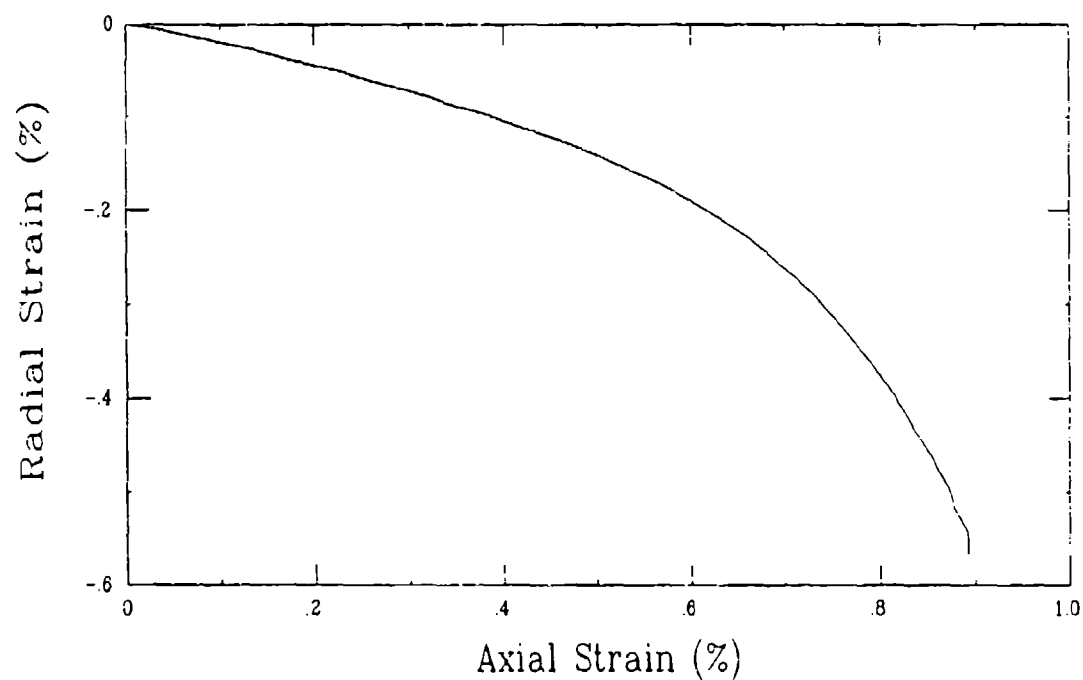
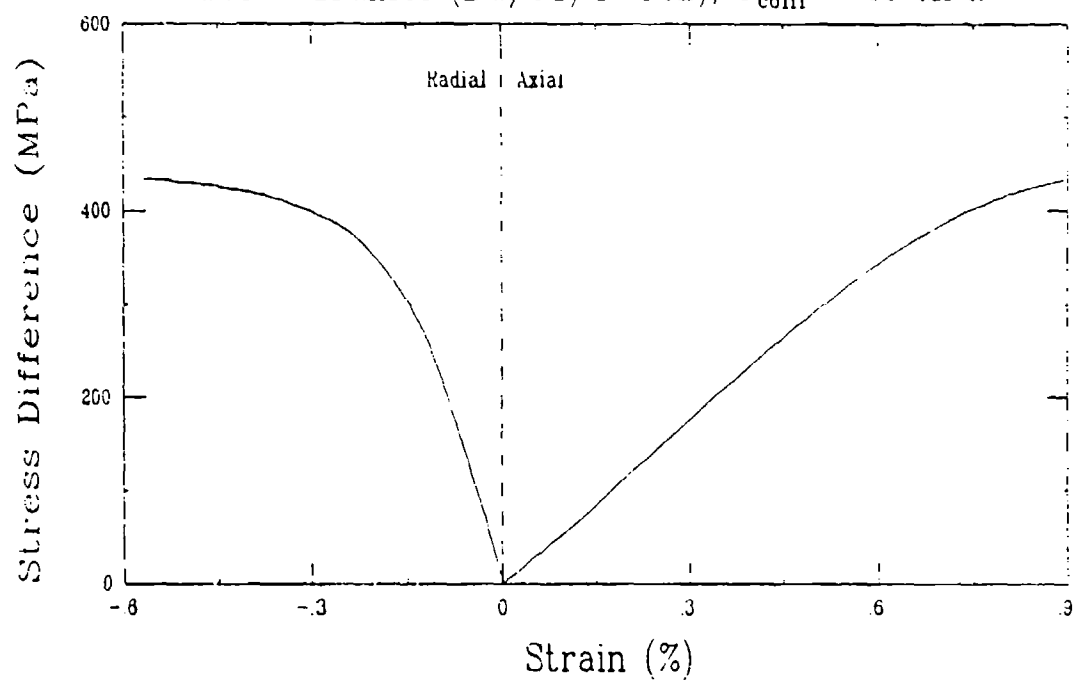
Triaxial Compression Test (U3D3)  
Barre Granite (BG/92/1/1-27),  $\sigma_{\text{conf}} = 25 \text{ MPa}$



Triaxial Compression Test (U4A3)  
Barre Granite (BG/92/1/2-13),  $\sigma_{\text{conf}} = 25 \text{ MPa}$

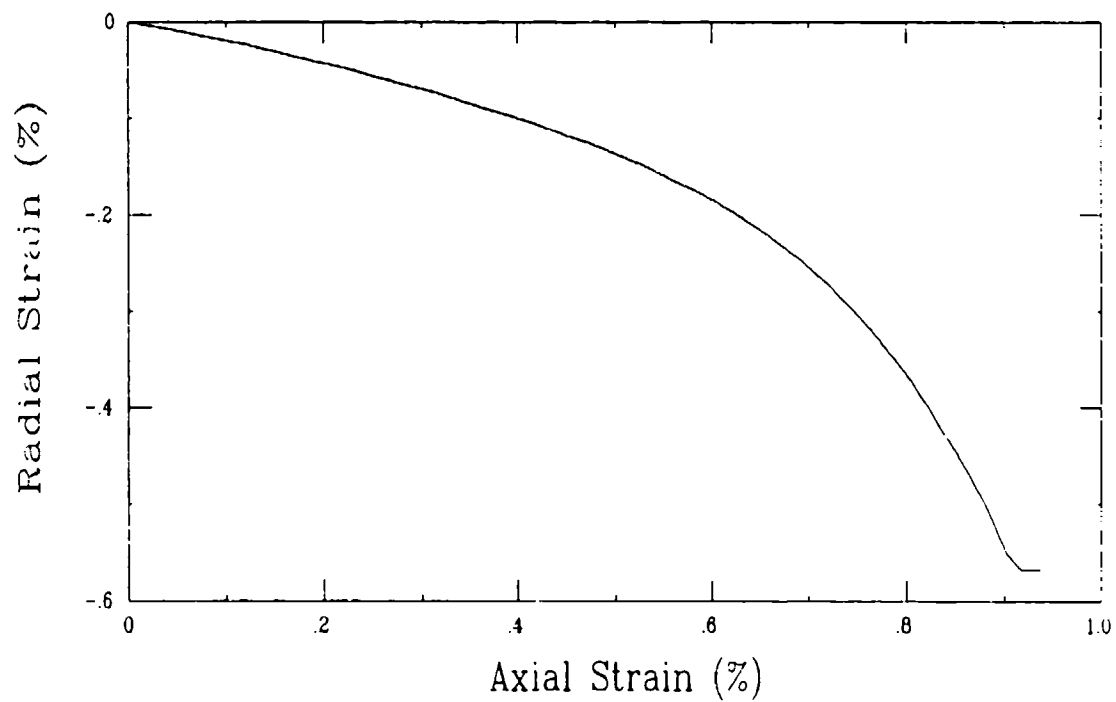
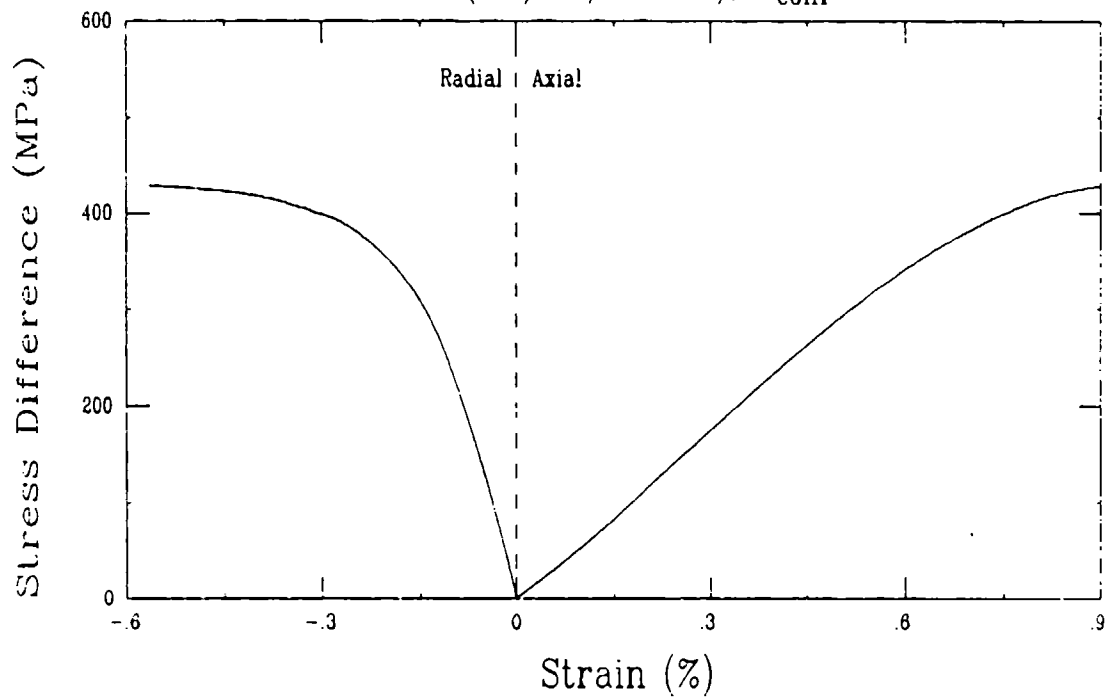


Triaxial Compression Test (U4B3)  
Barre Granite (BG/91/1-12B),  $\sigma_{\text{conf}} = 40 \text{ MPa}$

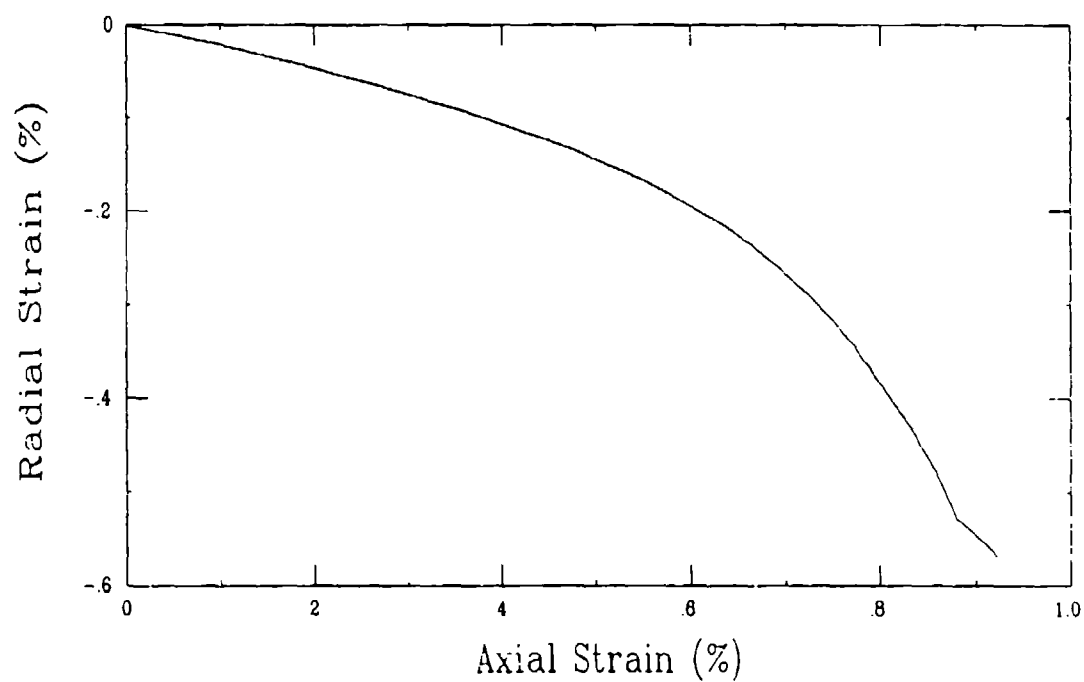
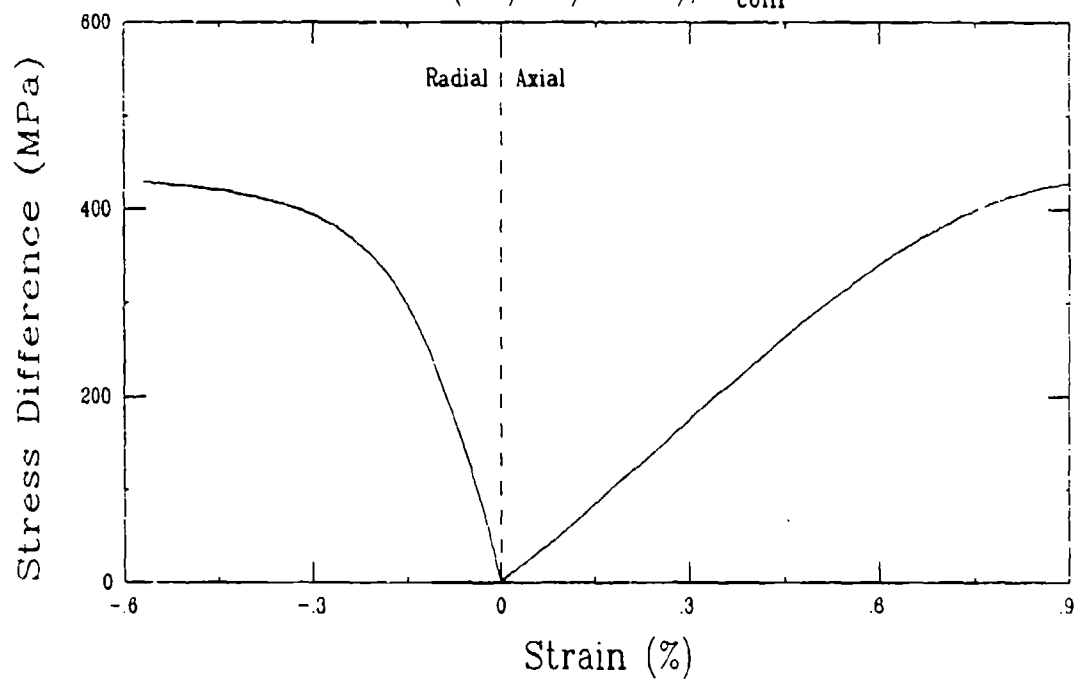




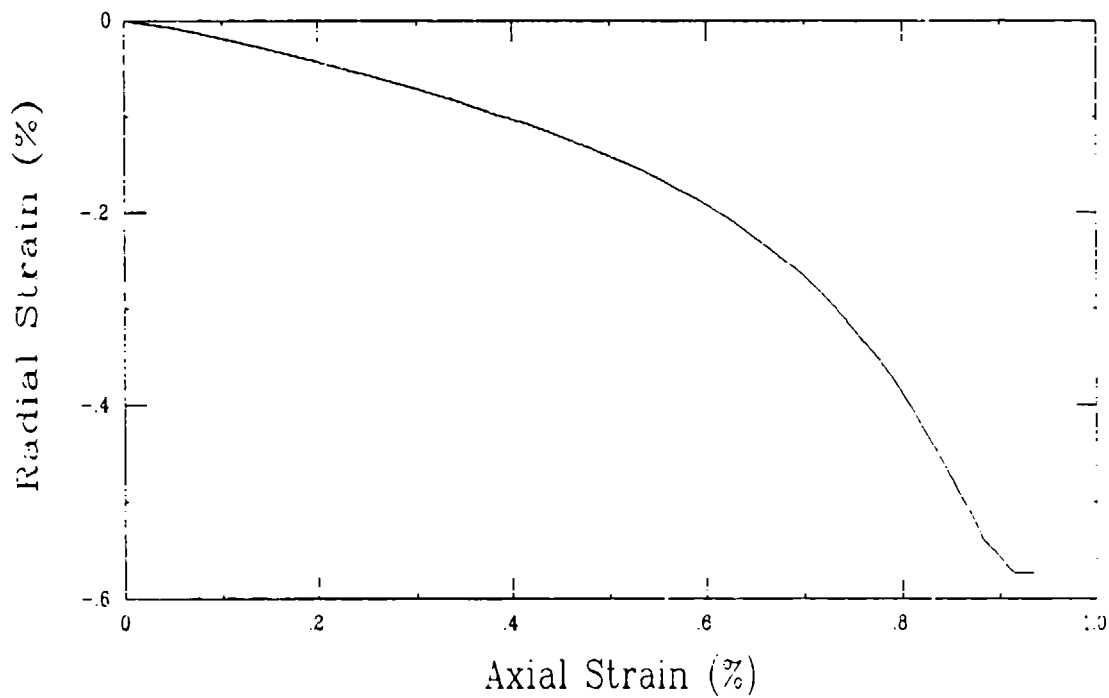
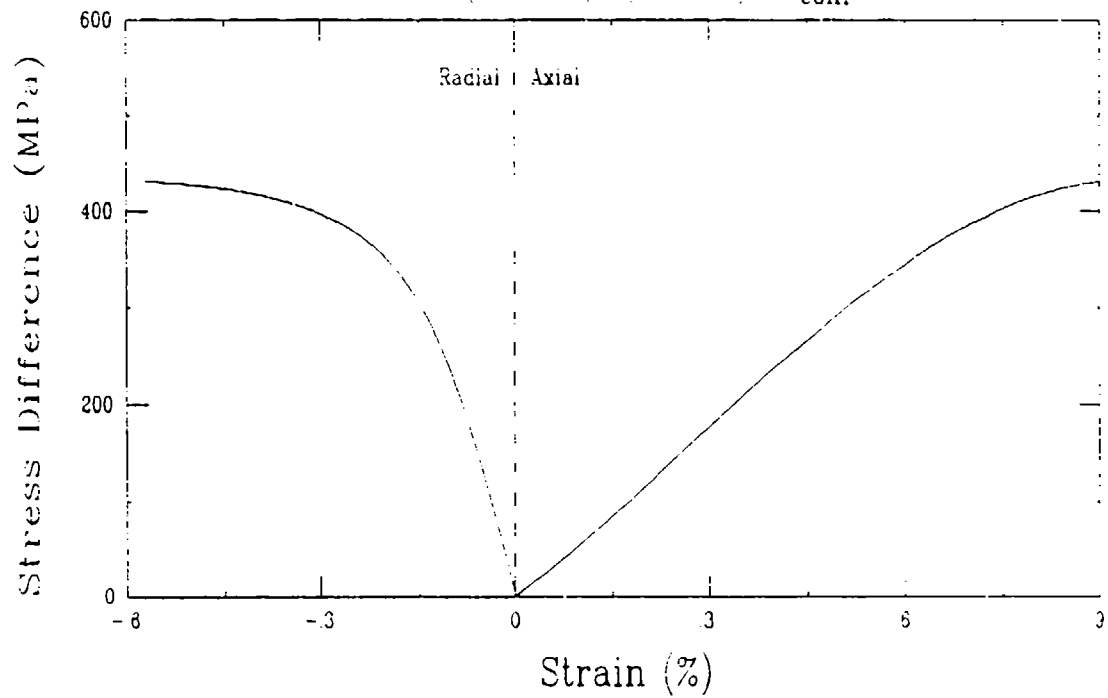
Triaxial Compression Test (U4E3)  
Barre Granite (BG/91/2-17T),  $\sigma_{\text{conf}} = 40 \text{ MPa}$



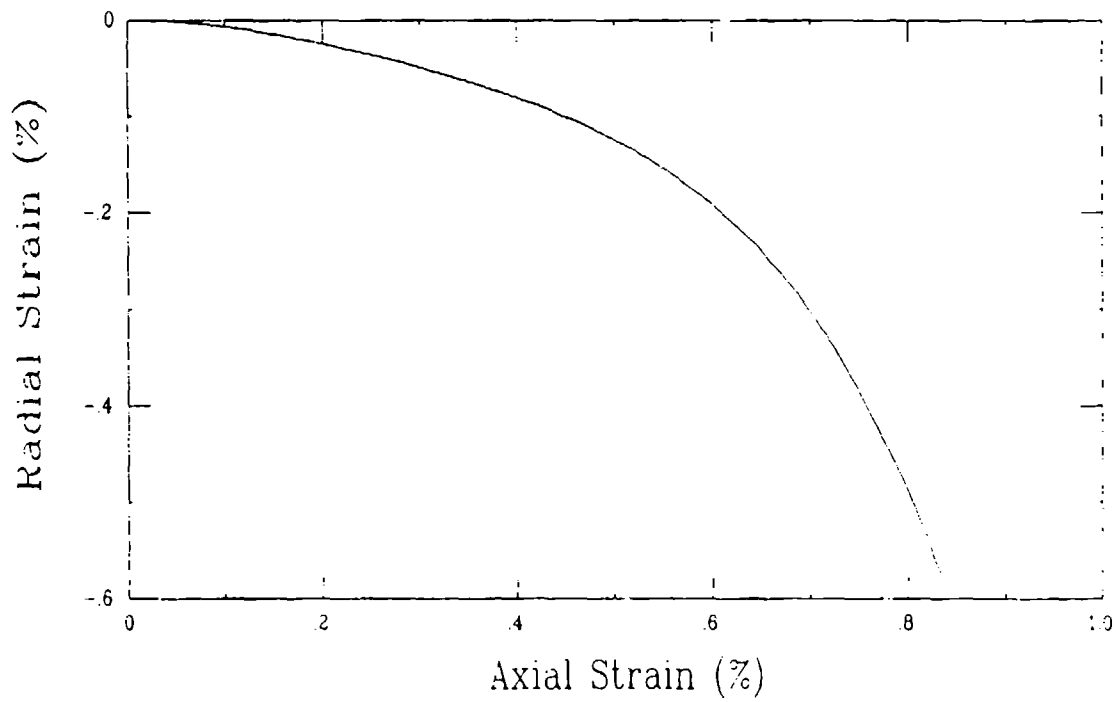
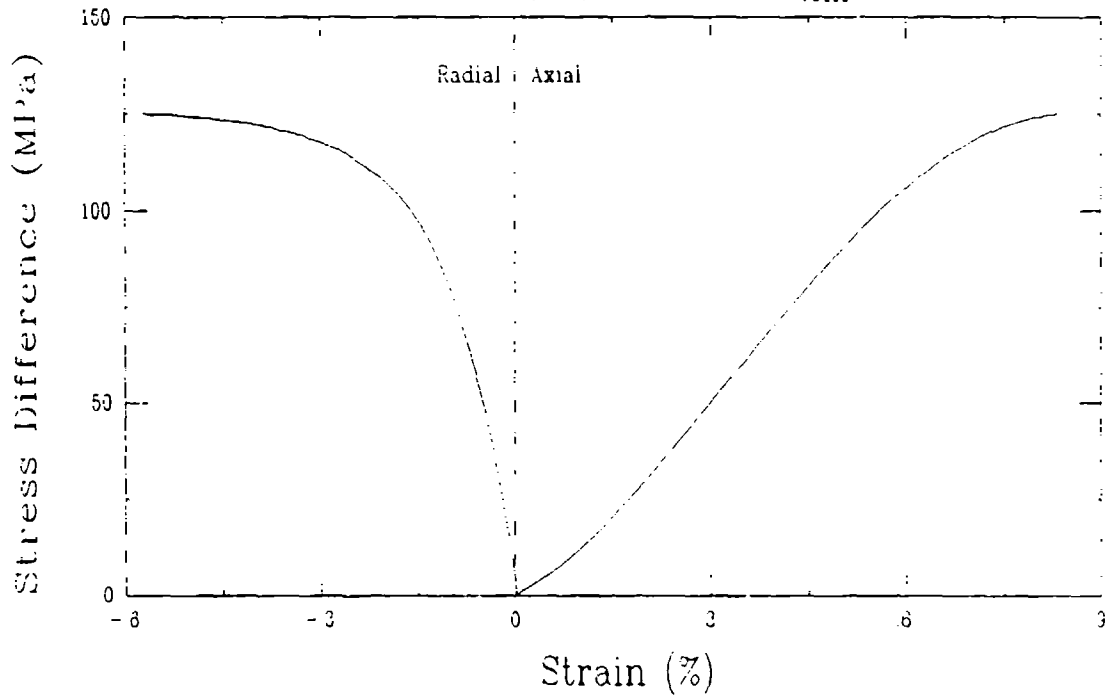
Triaxial Compression Test (U4C3)  
Barre Granite (BG/91/6-4T),  $\sigma_{\text{conf}} = 40 \text{ MPa}$



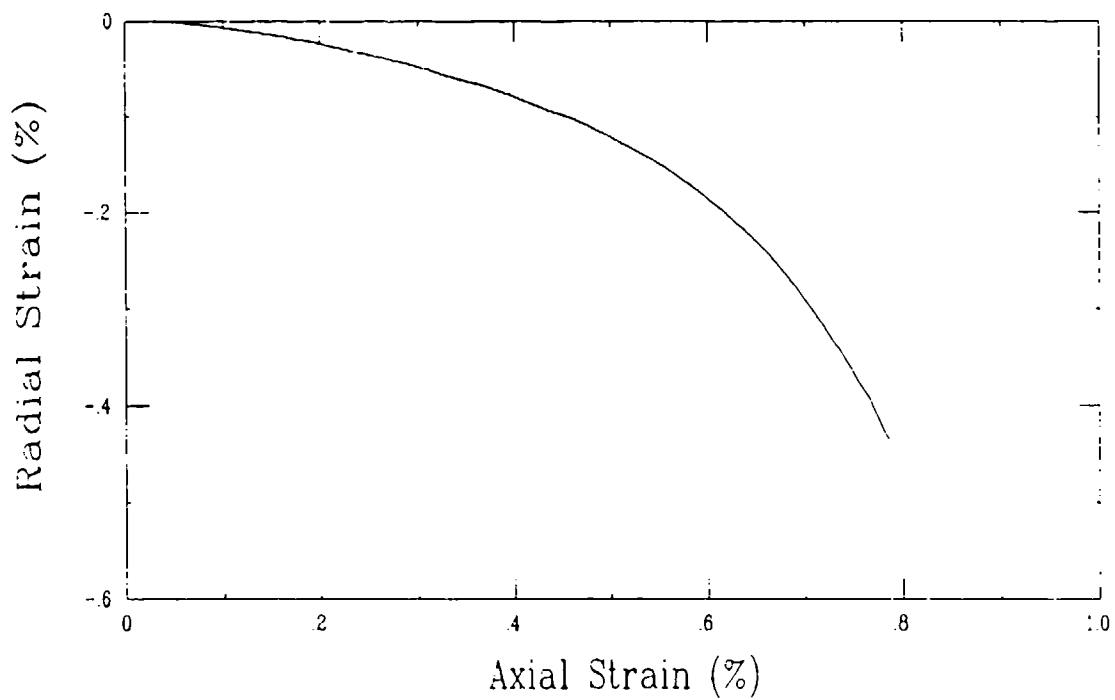
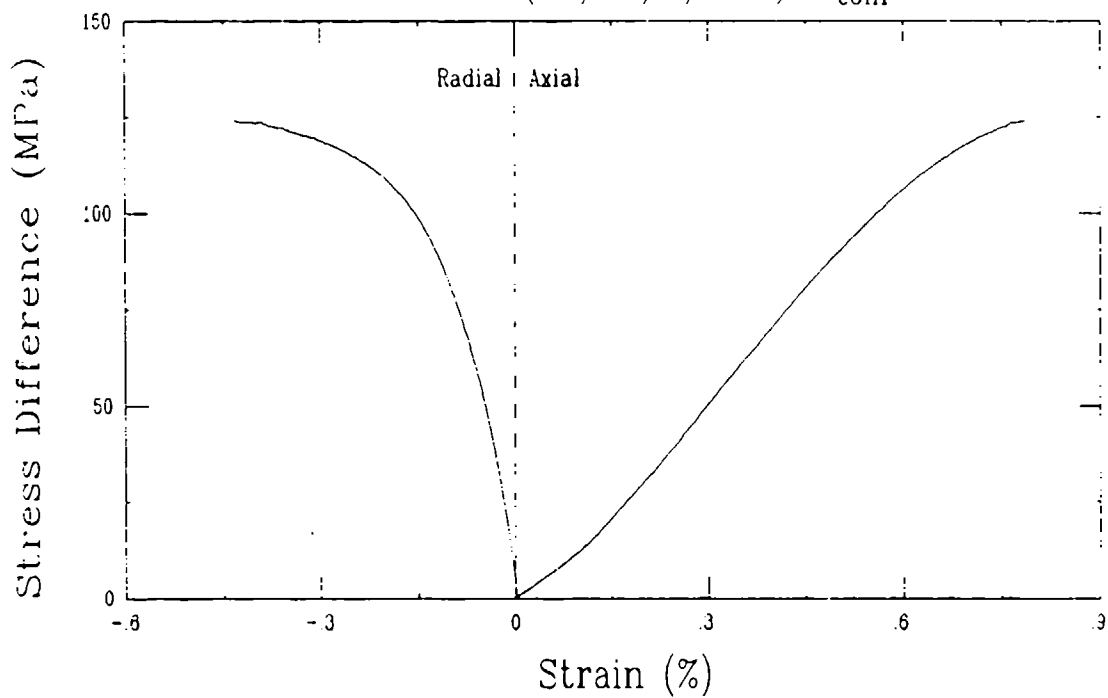
# Triaxial Compression Test (U4D3) Barre Granite (BG/92/1/1-30), $\sigma_{\text{conf}} = 40 \text{ MPa}$



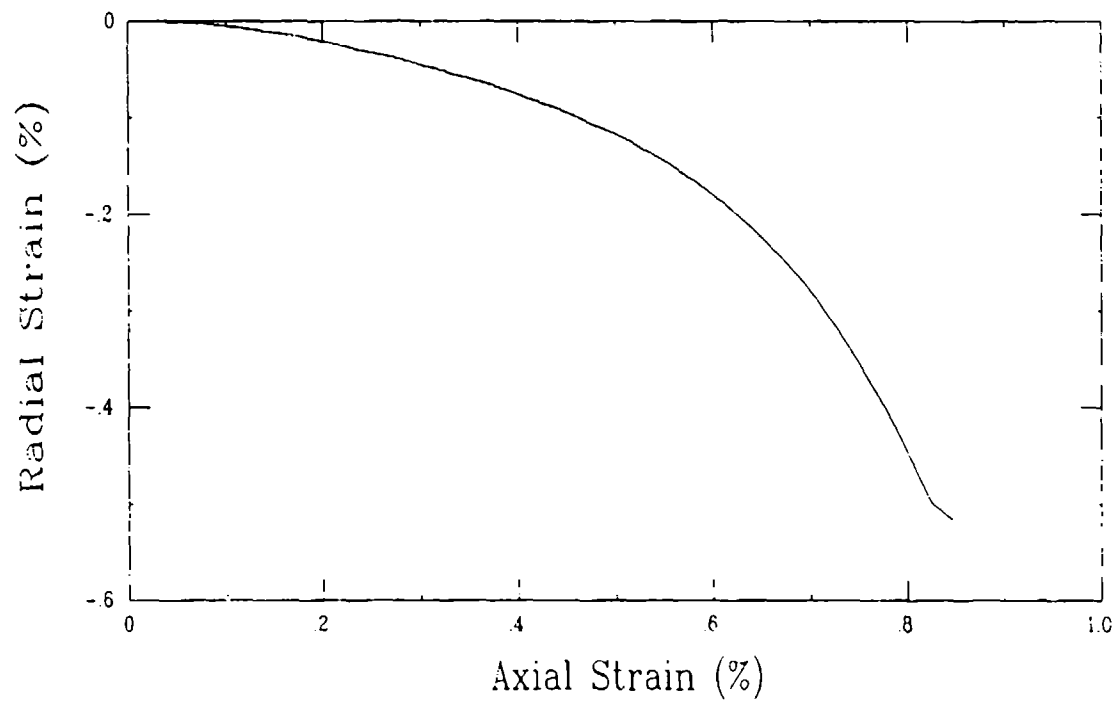
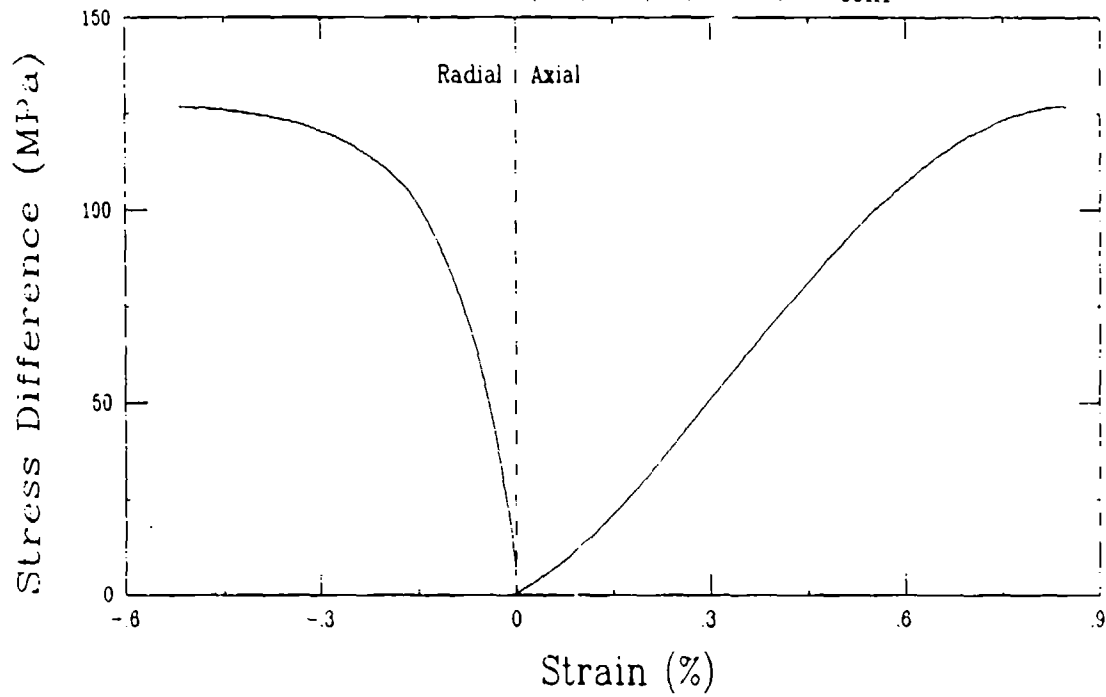
Triaxial Compression Test (Y26C3)  
Berea Sandstone (BS/91/1-1),  $\sigma_{\text{conf}} = 10 \text{ MPa}$



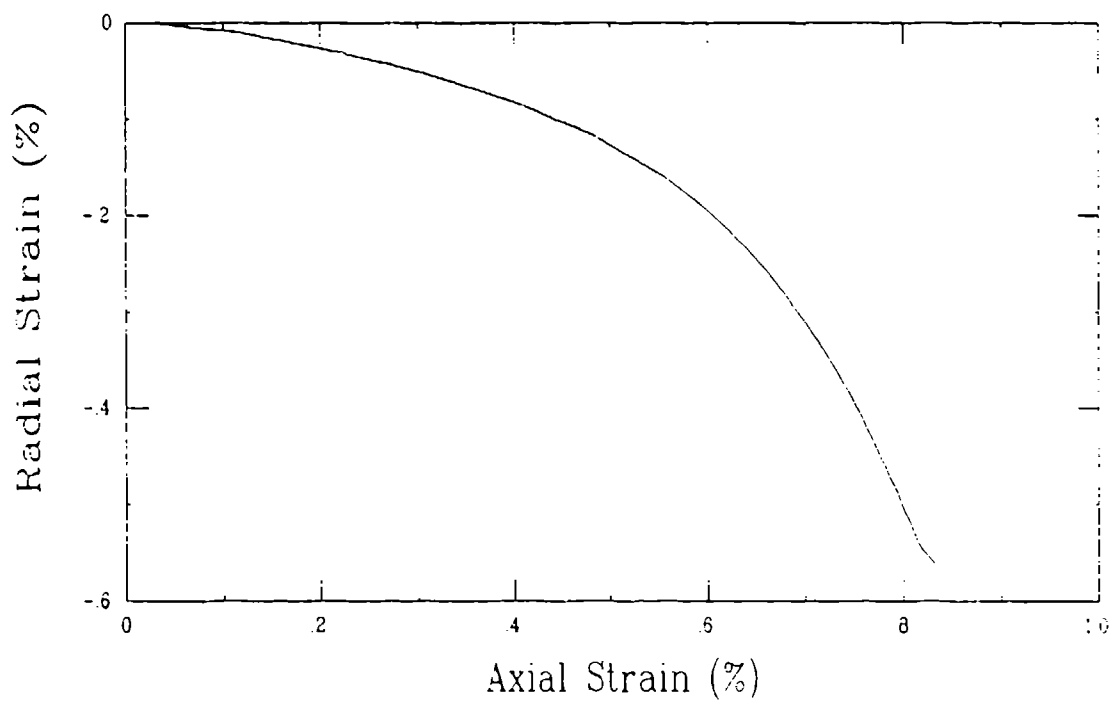
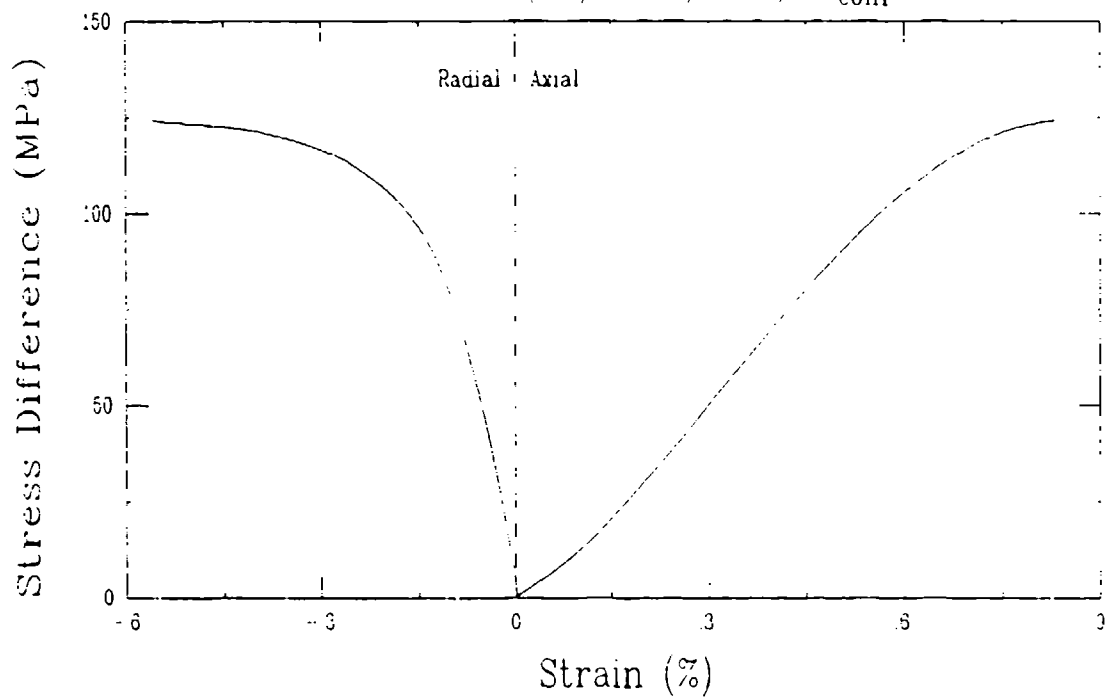
Triaxial Compression Test (Y26D3)  
Berea Sandstone (BS/92/7/3-3),  $\sigma_{\text{conf}} = 10 \text{ MPa}$



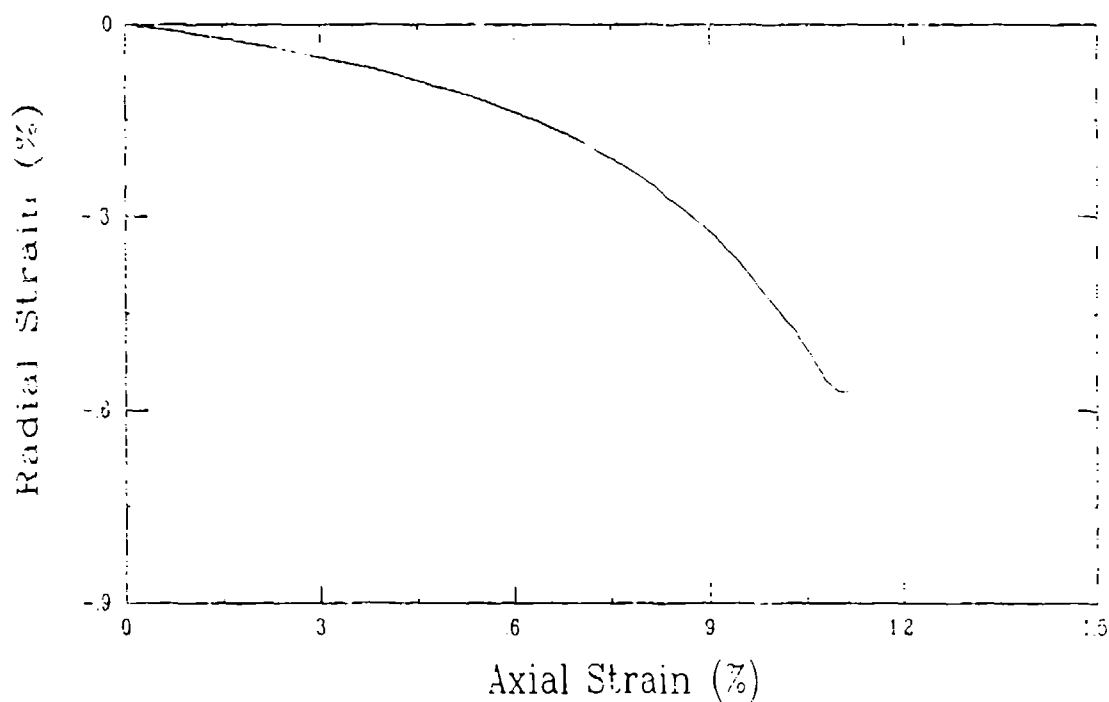
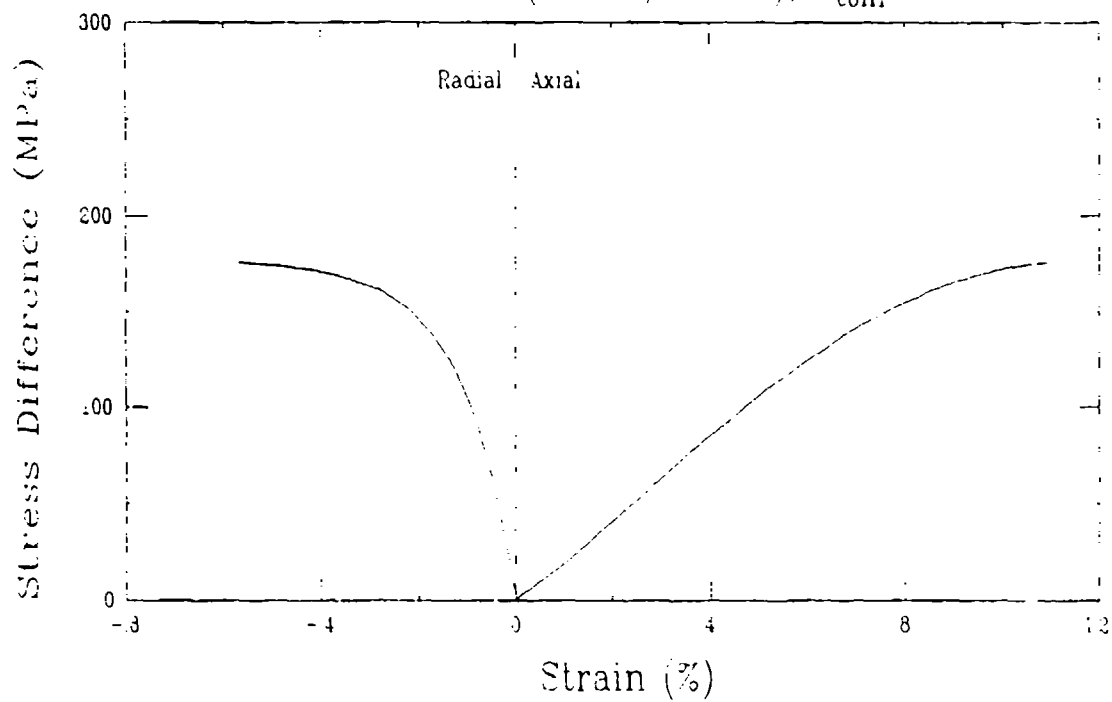
Triaxial Compression Test (Y26A3)  
Berea Sandstone (BS/92/7/3-8),  $\sigma_{\text{conf}} = 10 \text{ MPa}$



Triaxial Compression Test (Y26B3)  
Berea Sandstone (BS/92/8/1-3),  $\sigma_{\text{conf}} = 10 \text{ MPa}$

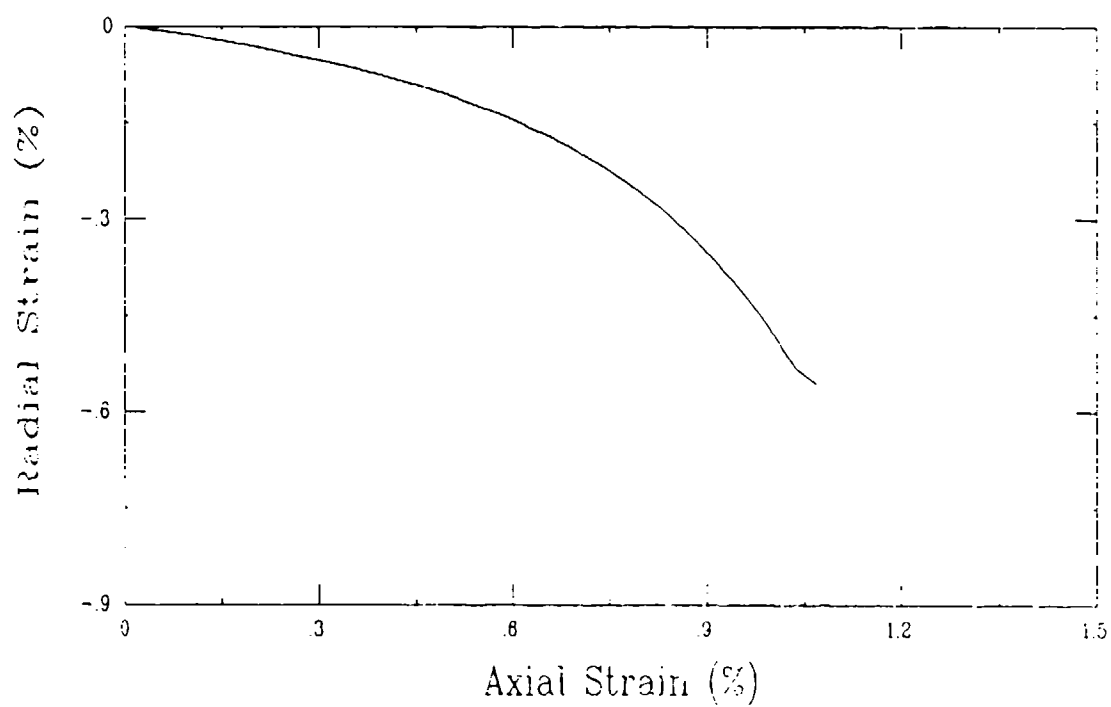
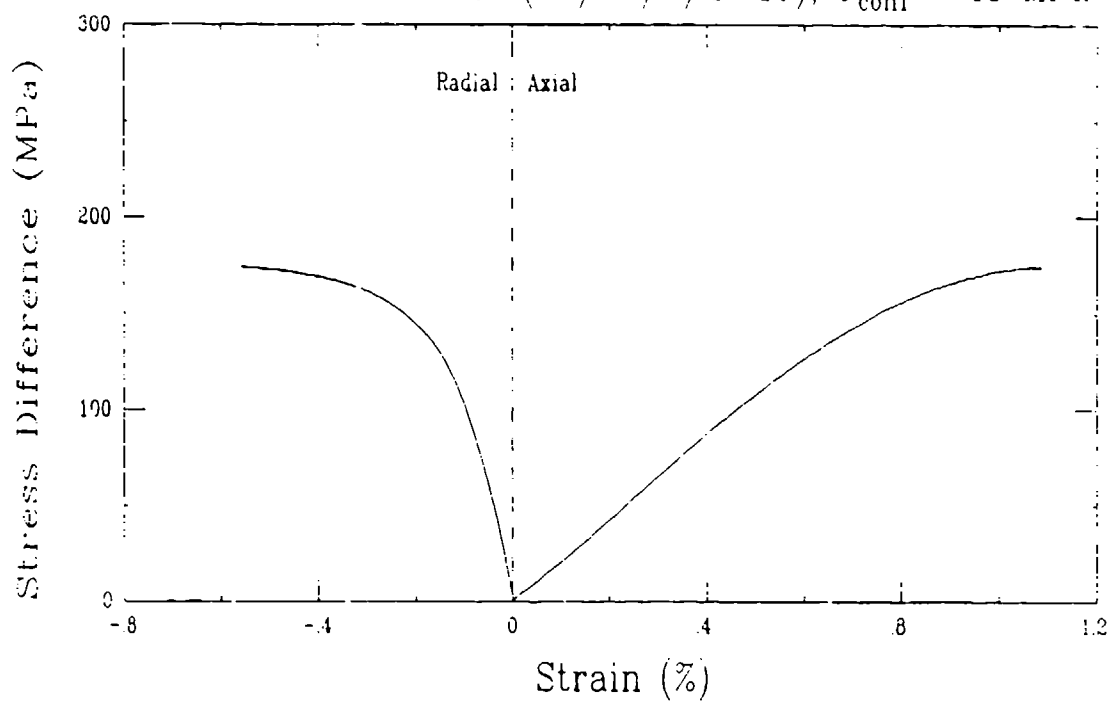


# Triaxial Compression Test (Y27A3) Berea Sandstone (BS/91/3-19T), $\sigma_{conf} = 25$ MPa

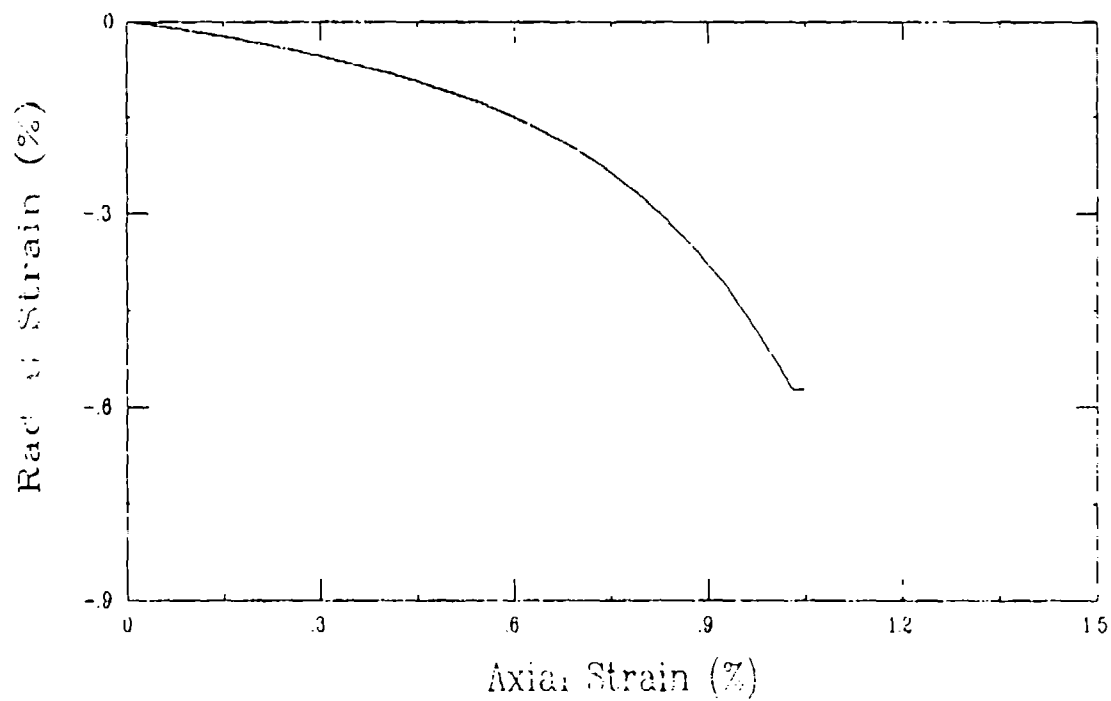
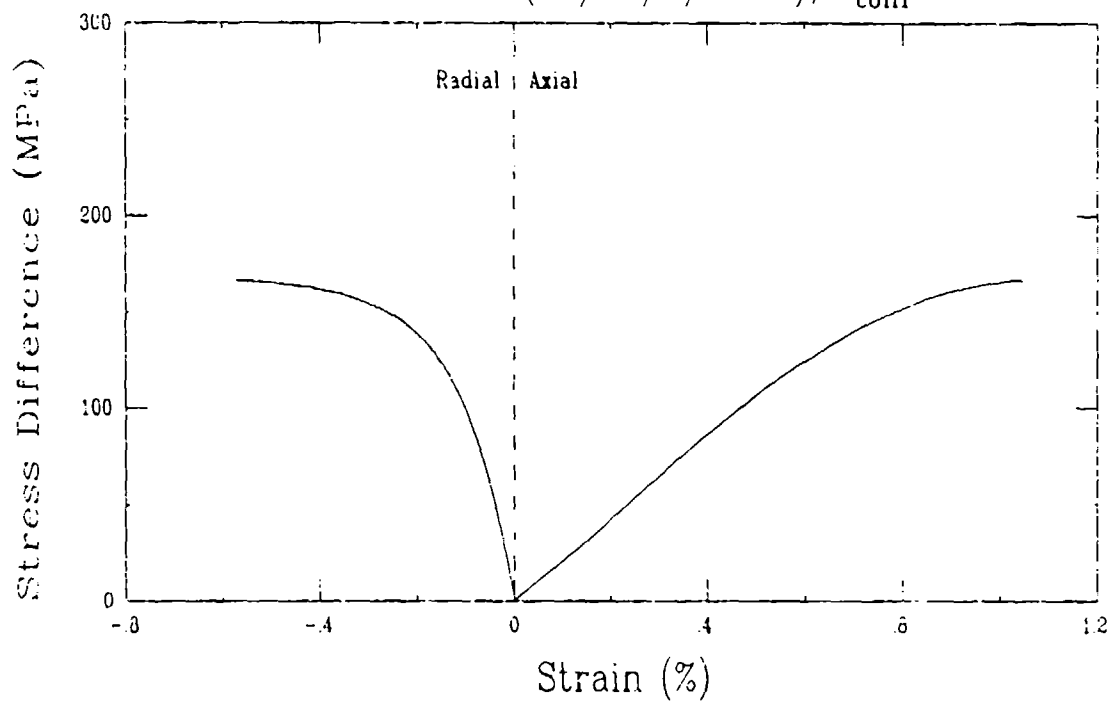




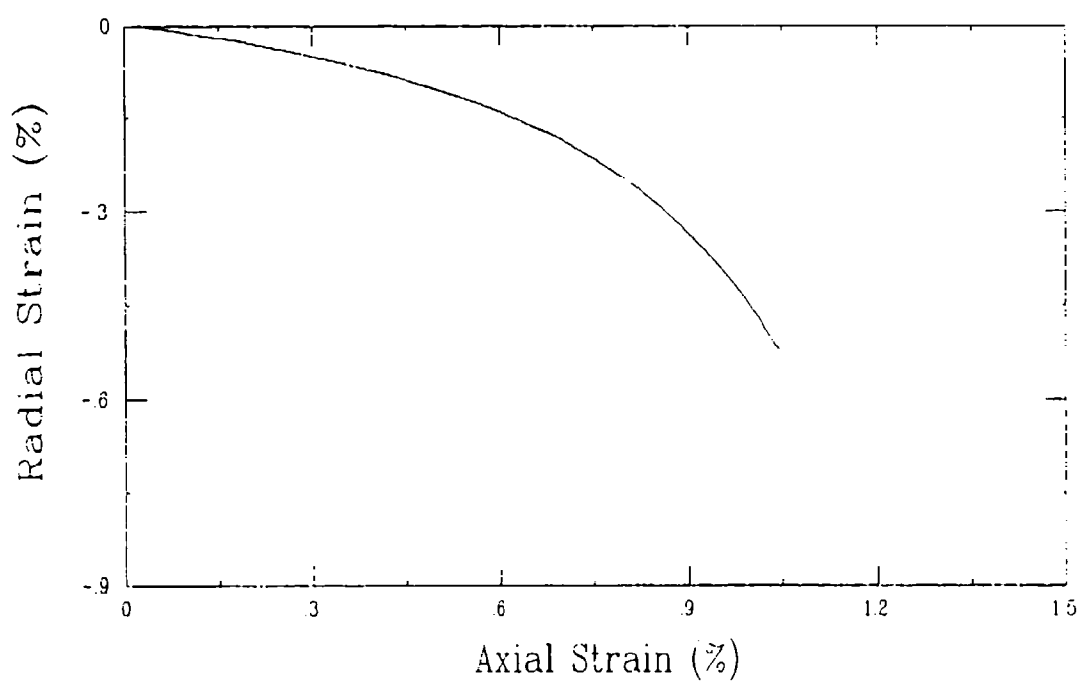
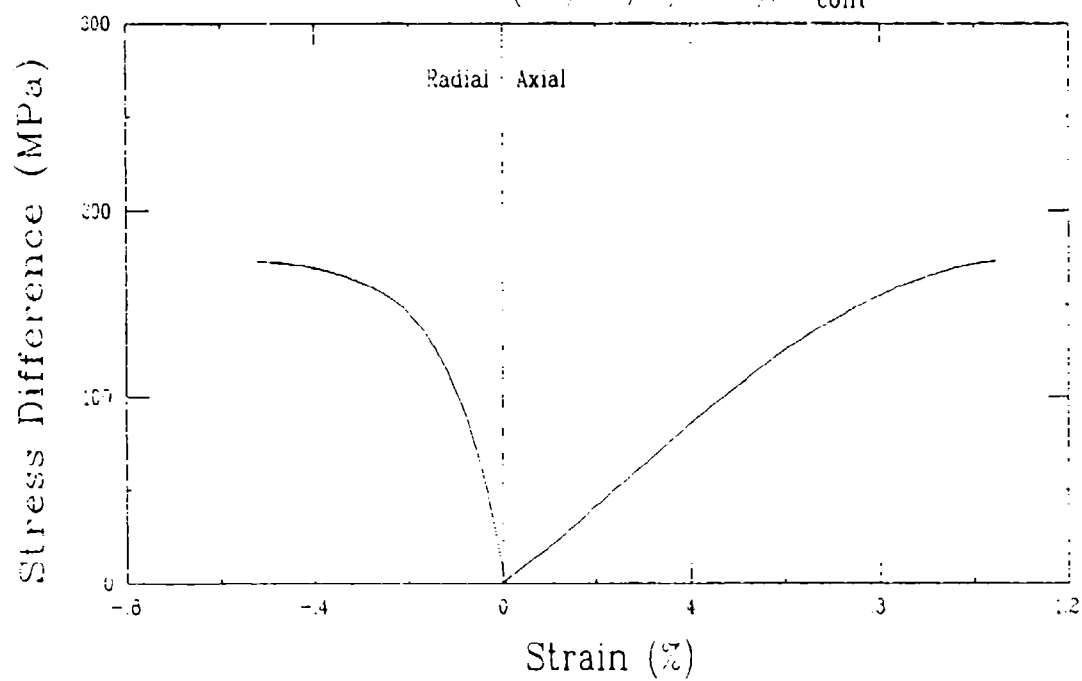
Triaxial Compression Test (Y26E3)  
Berea Sandstone (BS/92/7/1-10),  $\sigma_{\text{conf}} = 25 \text{ MPa}$



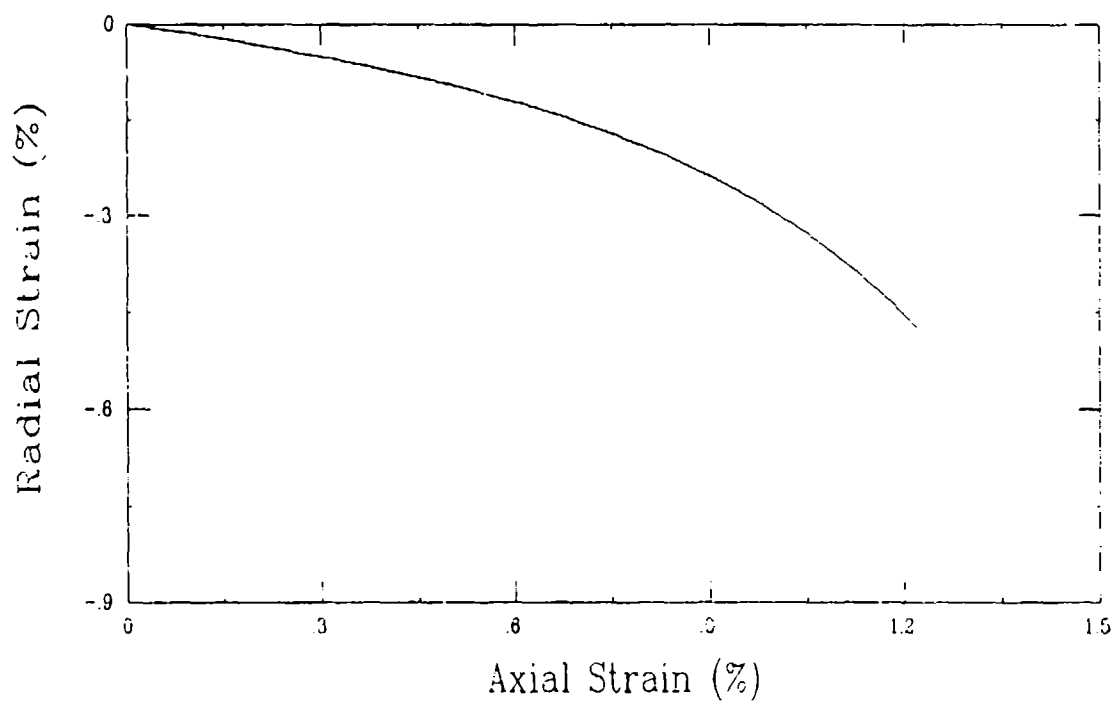
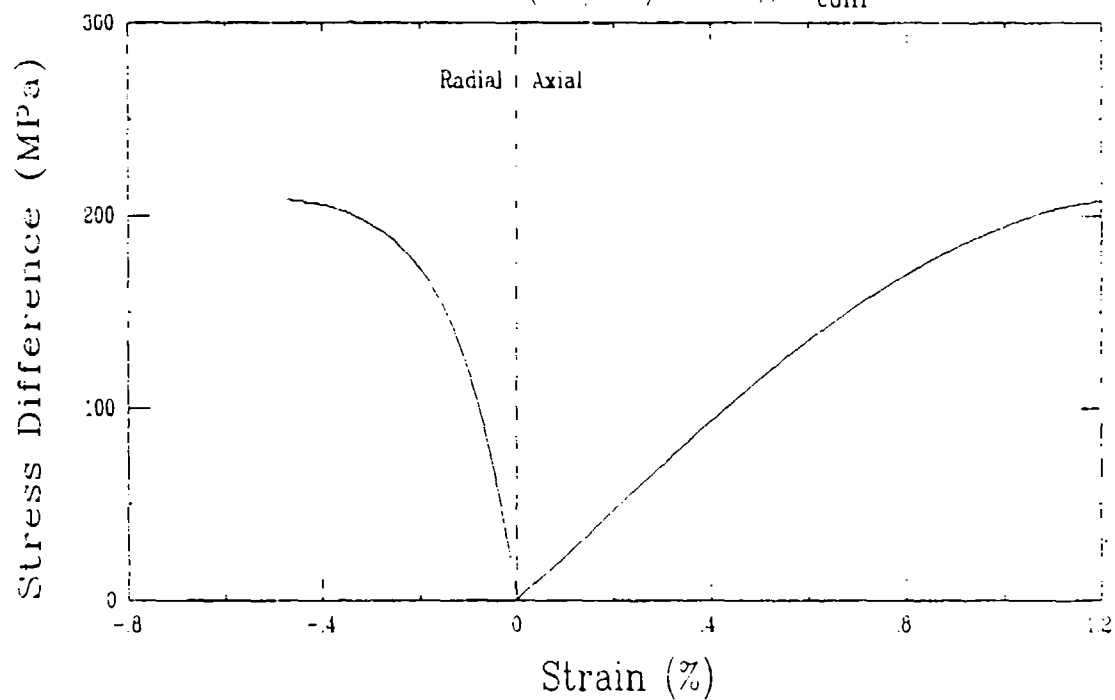
# Triaxial Compression Test (Y27B3) Berea Sandstone (BS/92/7/2-18), $\sigma_{\text{conf}} = 25 \text{ MPa}$



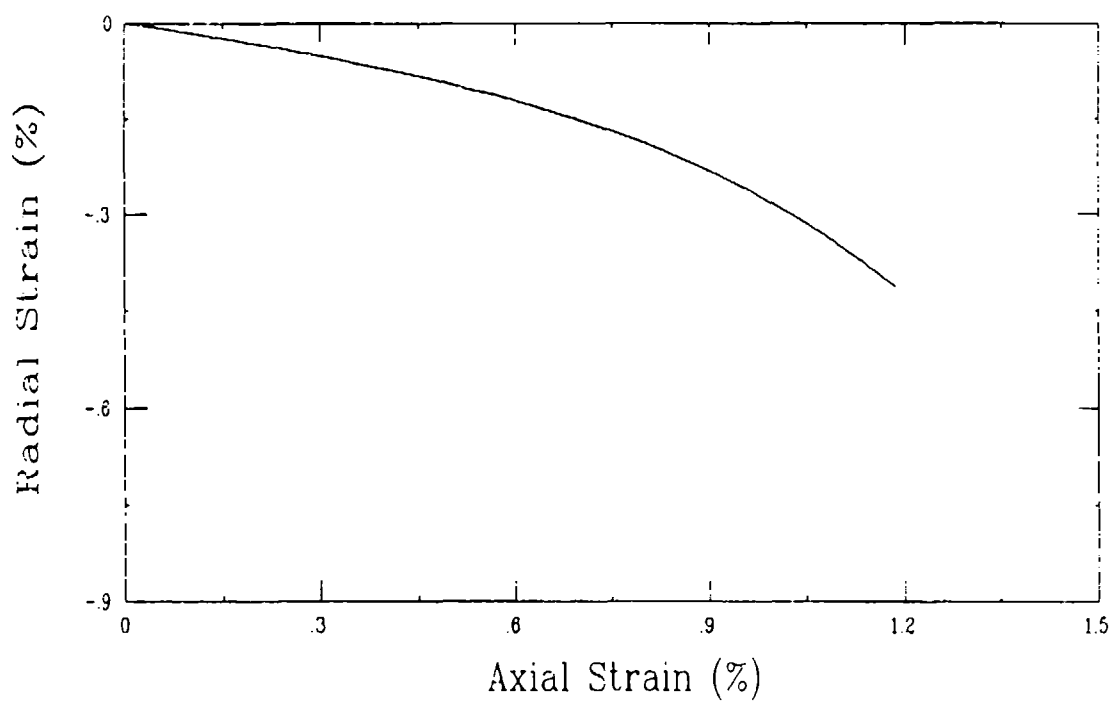
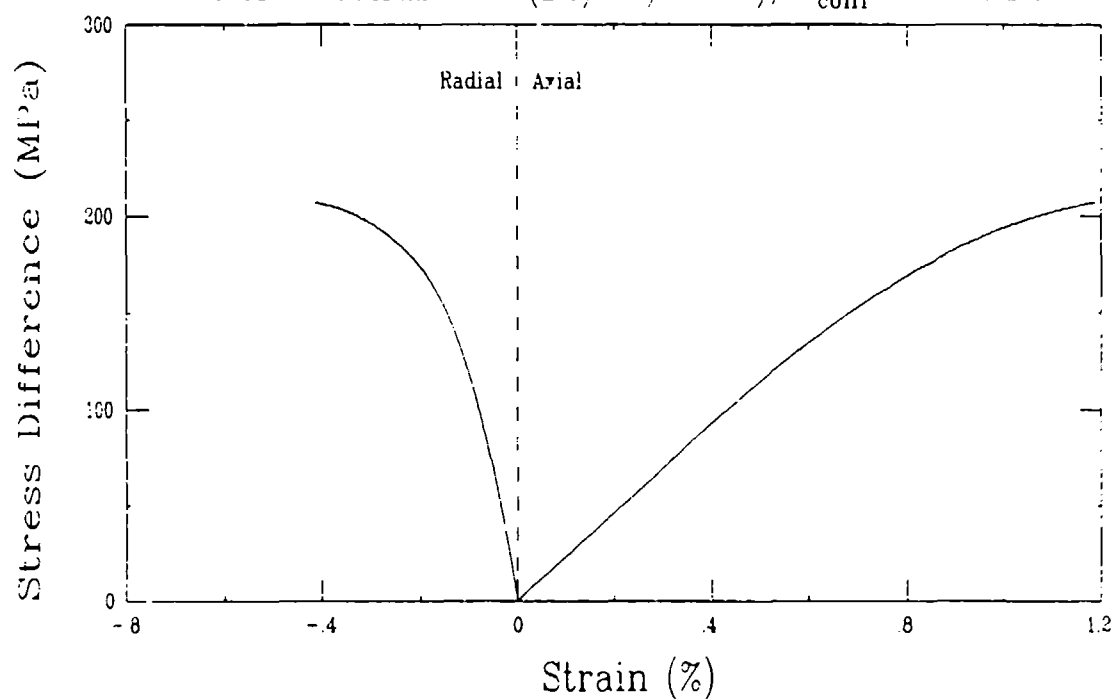
# Triaxial Compression Test (Y27C3) Berea Sandstone (BS/92/7/3-6), $\sigma_{\text{conf}} = 25 \text{ MPa}$



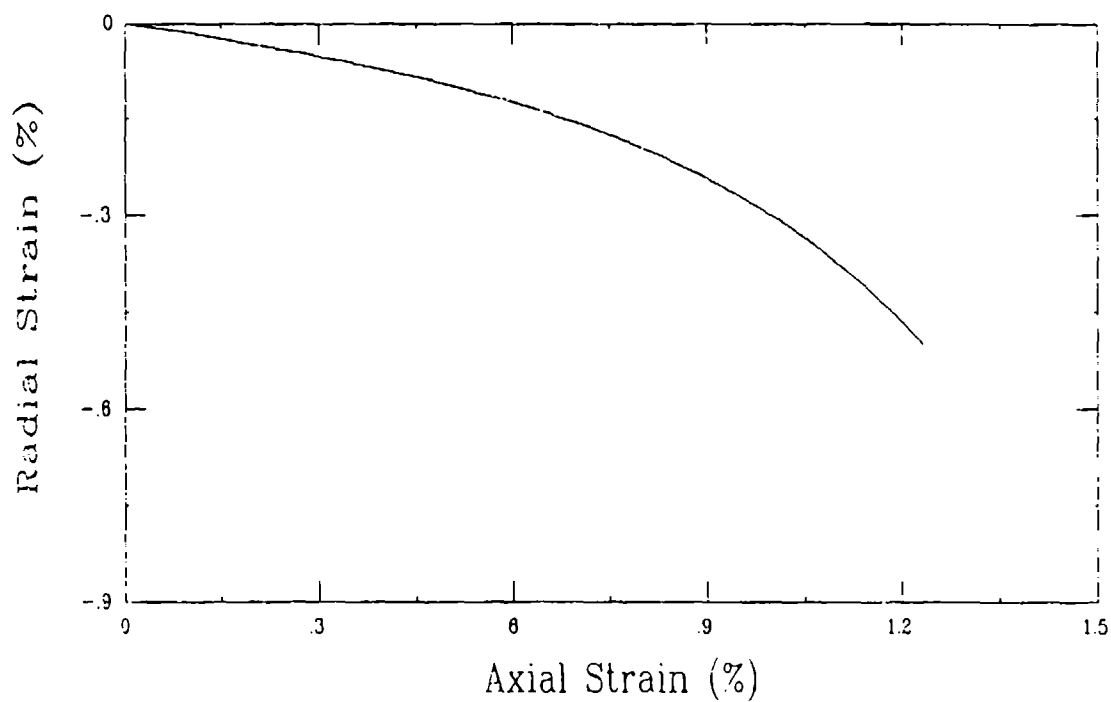
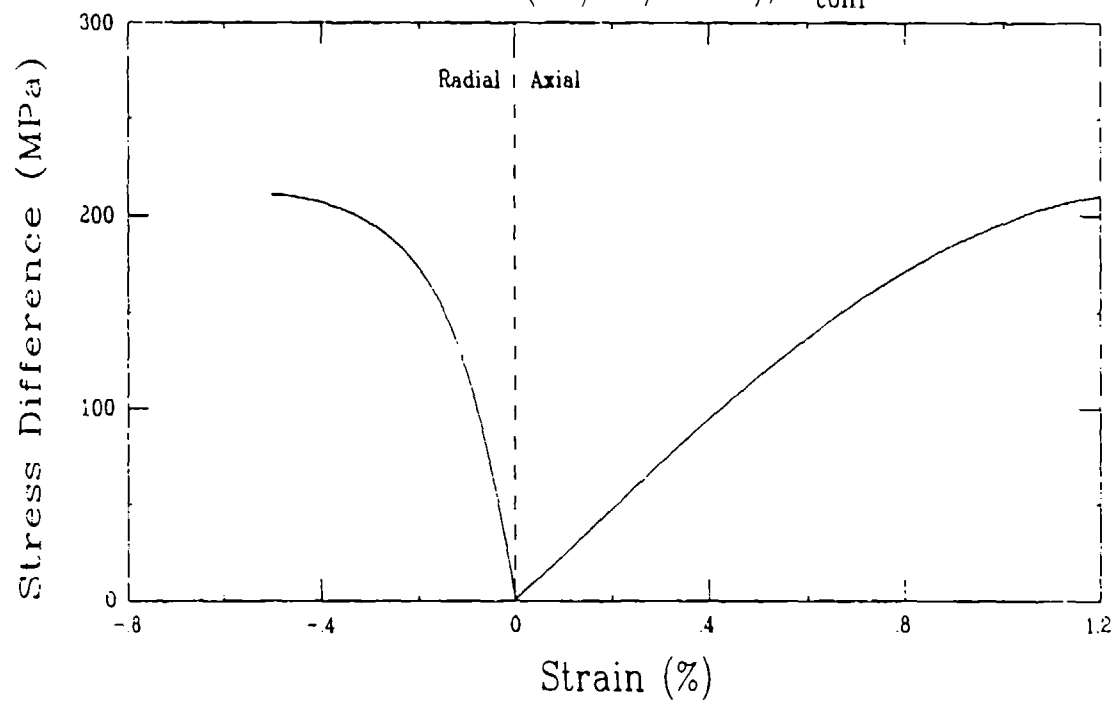
Triaxial Compression Test (Y27E3)  
Berea Sandstone (BS/91/1-8T),  $\sigma_{\text{conf}} = 40 \text{ MPa}$



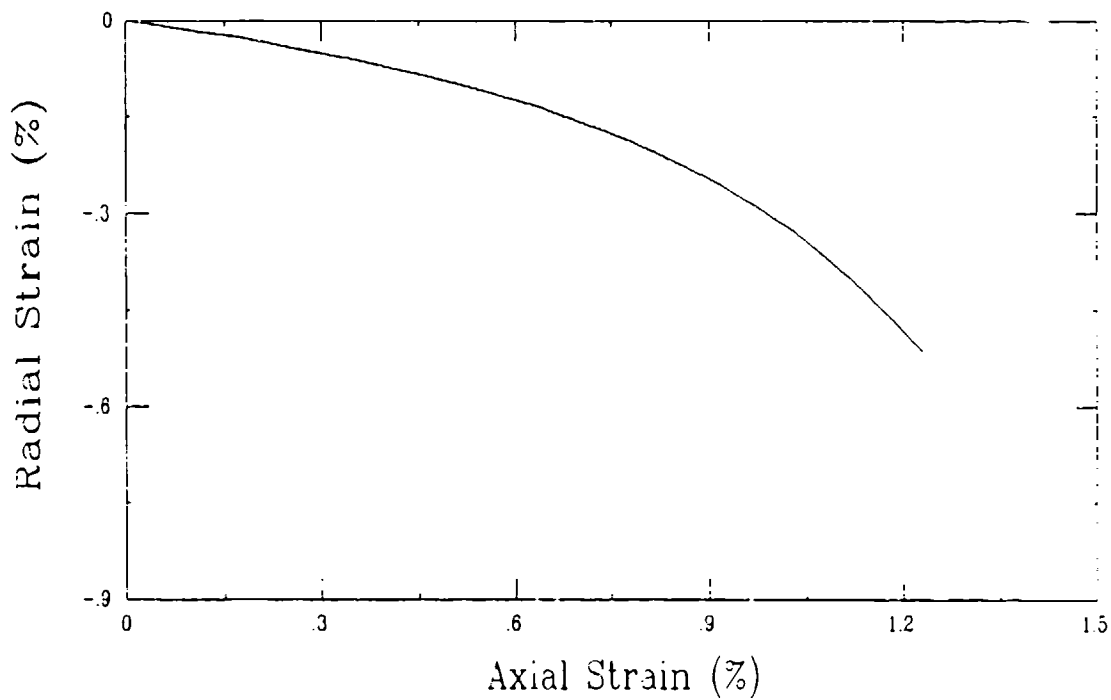
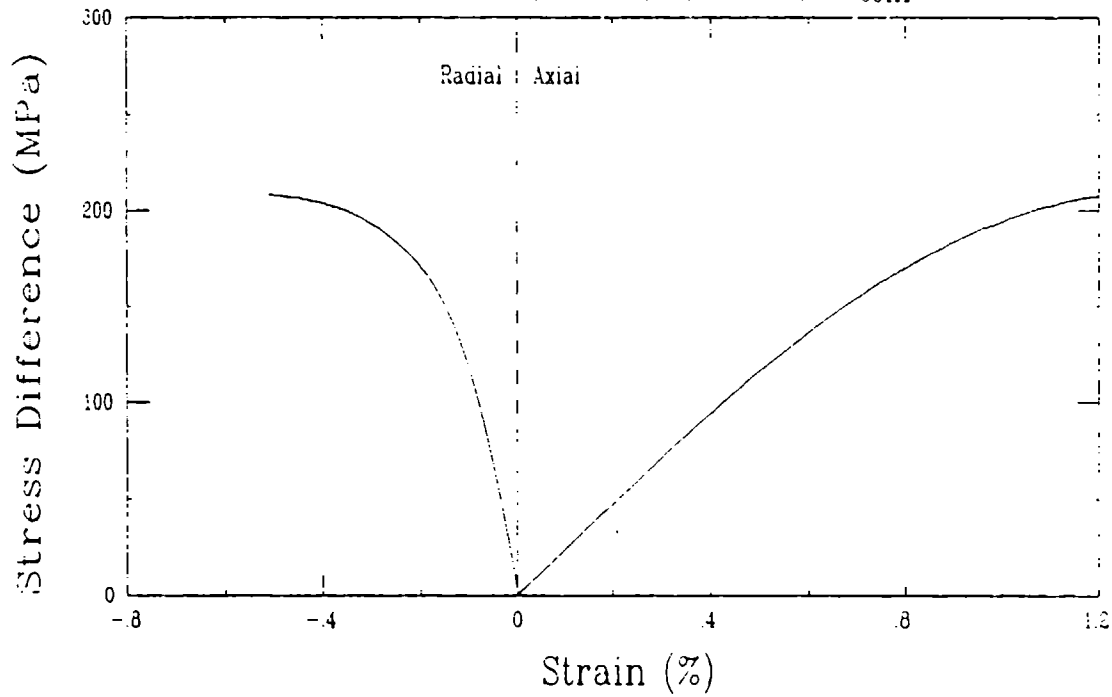
Triaxial Compression Test (Y27D3)  
Berea Sandstone (BS/92/4-2T),  $\sigma_{\text{conf}} = 40 \text{ MPa}$



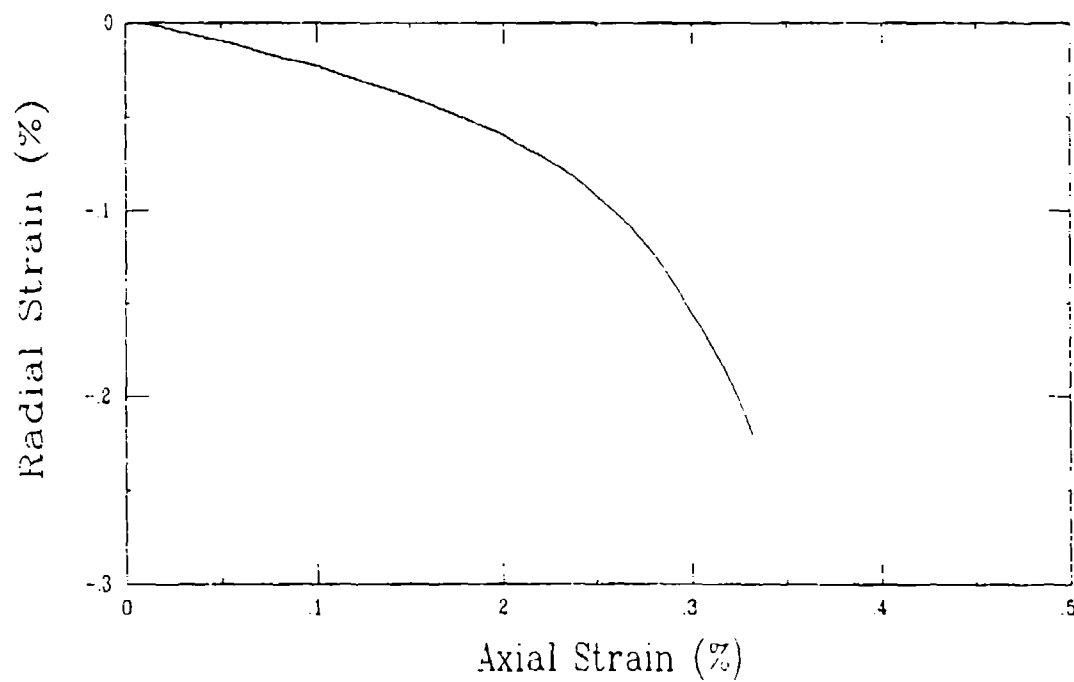
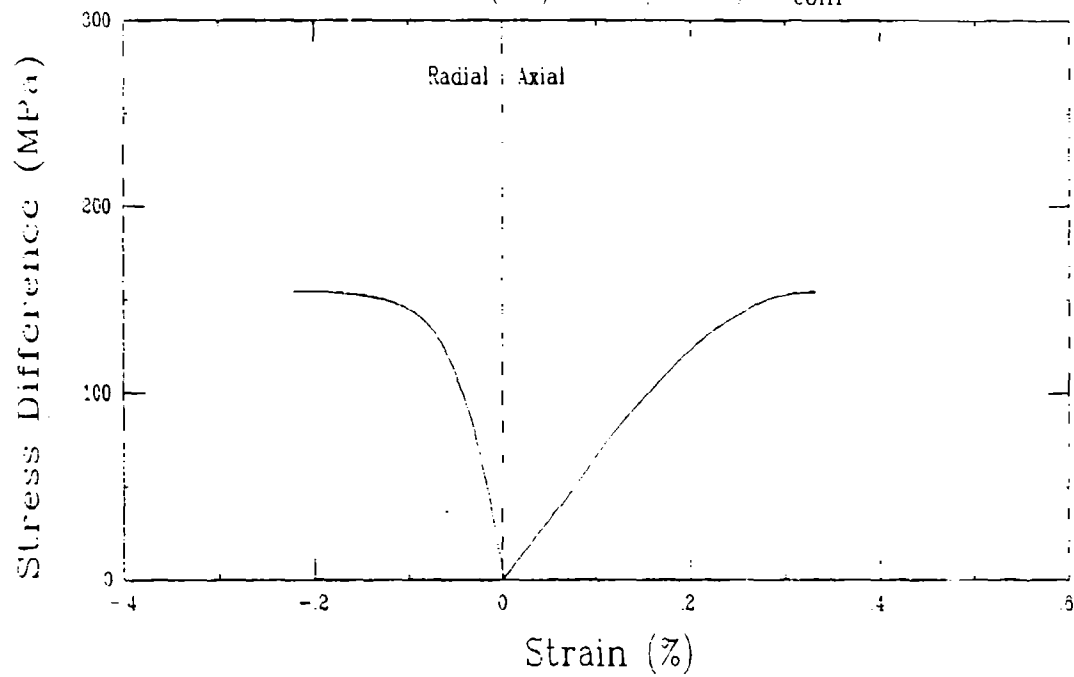
Triaxial Compression Test (Y28A3)  
Berea Sandstone (BS/91/4-4T),  $\sigma_{conf} = 40$  MPa



# Triaxial Compression Test (Y27F3) Berea Sandstone (BS/92/7/1-14), $\sigma_{\text{conf}} = 40 \text{ MPa}$

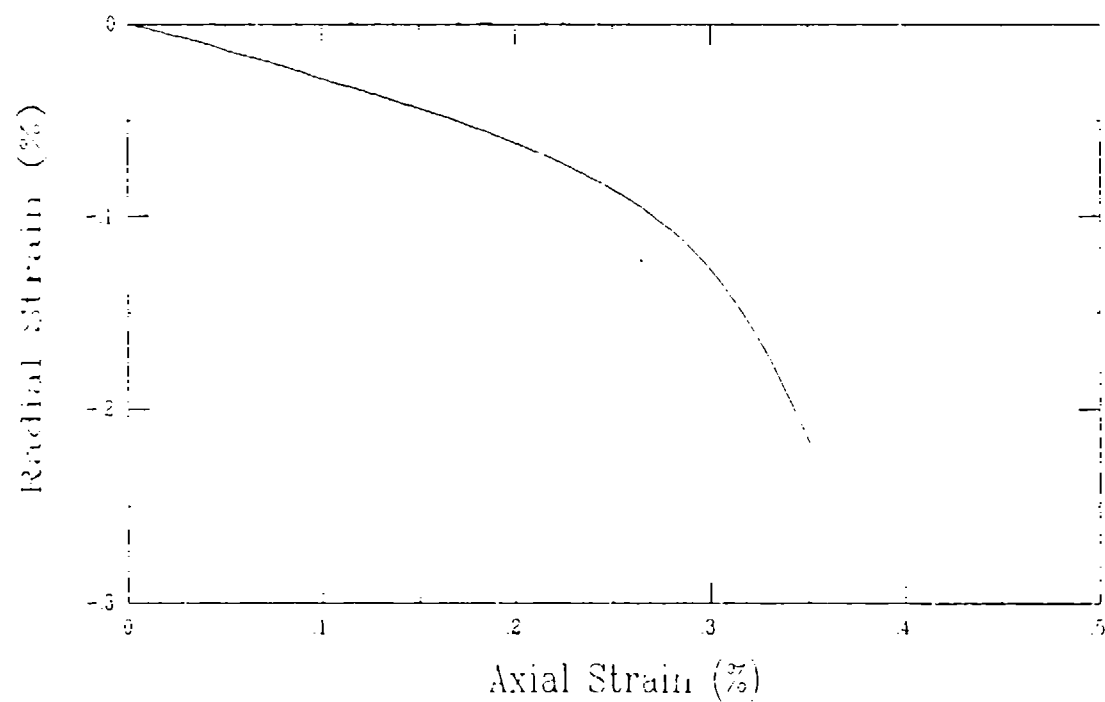
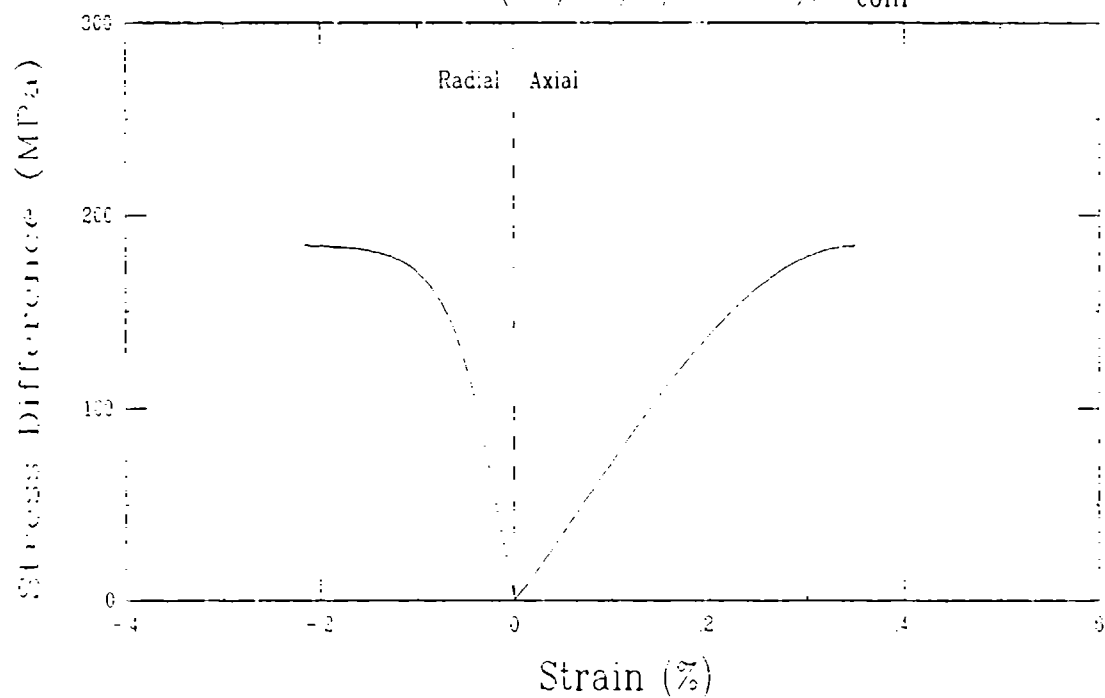


Triaxial Compression Test (Y28D3)  
Tennessee Marble (TM/91/1/1-4),  $\sigma_{conf} = 10$  MPa

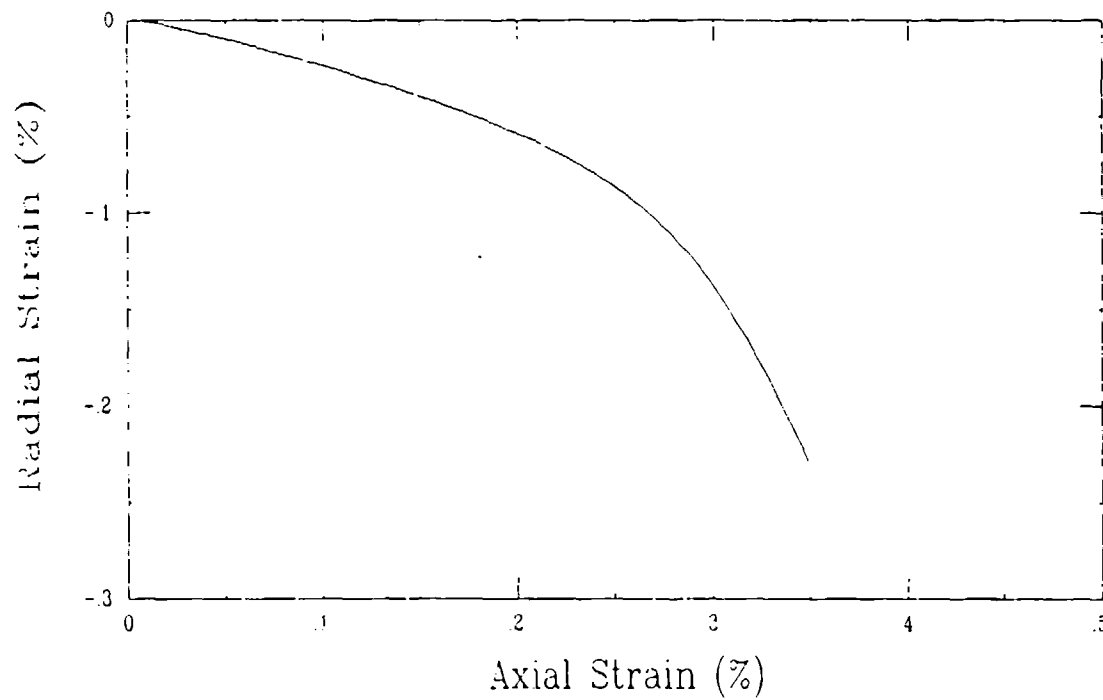
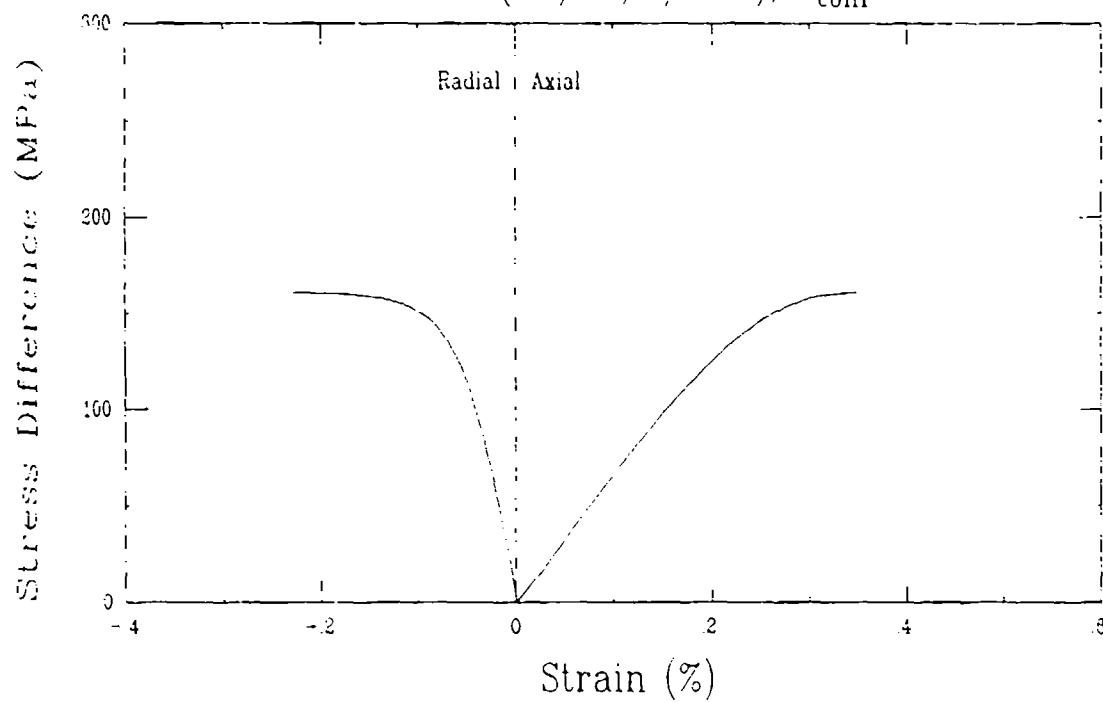




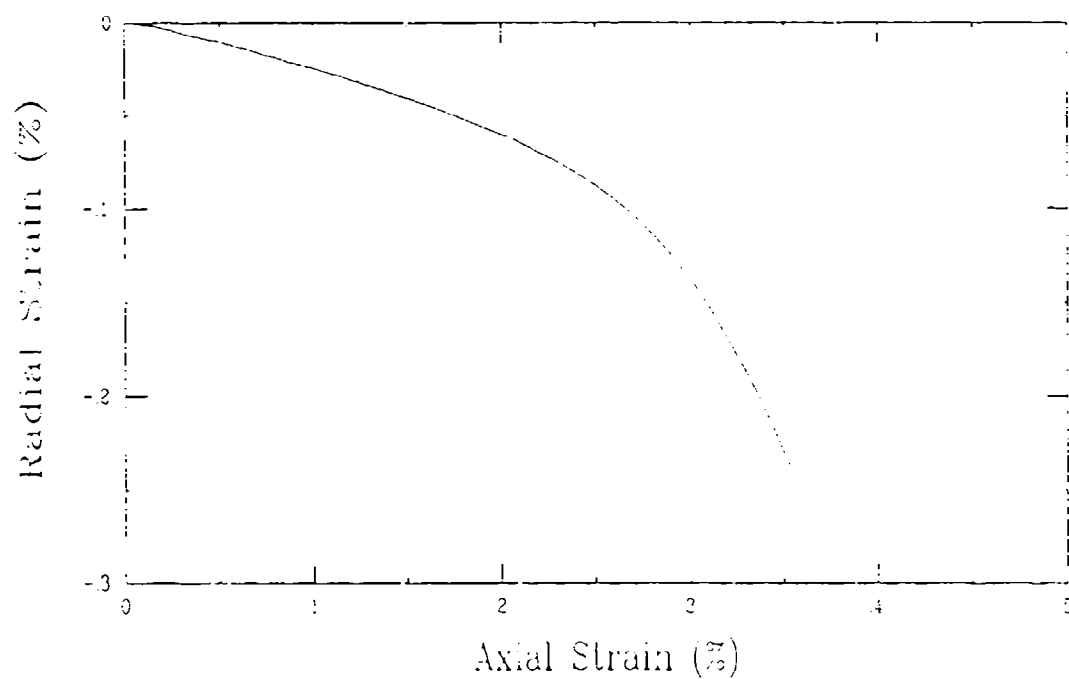
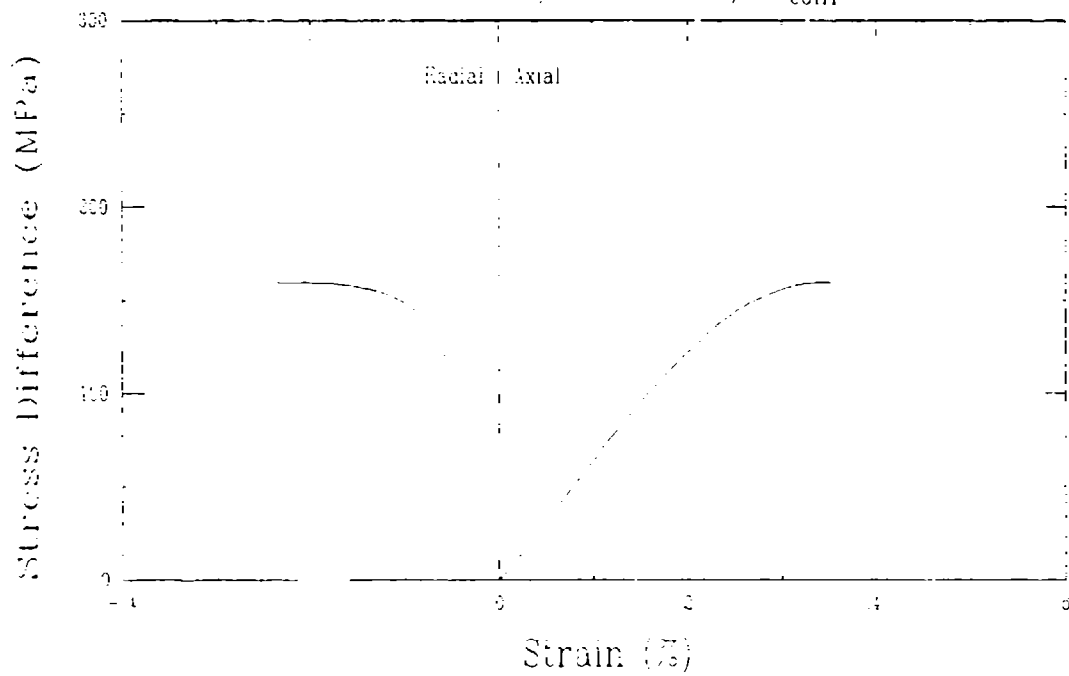
Triaxial Compression Test (Y28B3)  
Tennessee Marble (TM/91/2/2-22B),  $\sigma_{\text{conf}} = 10 \text{ MPa}$



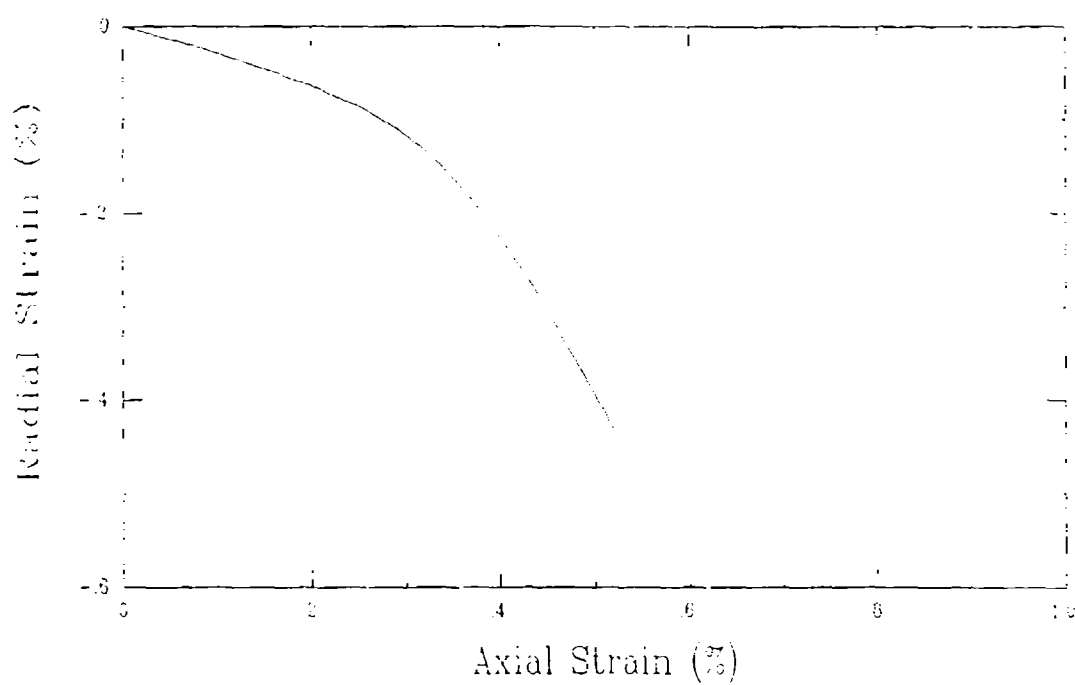
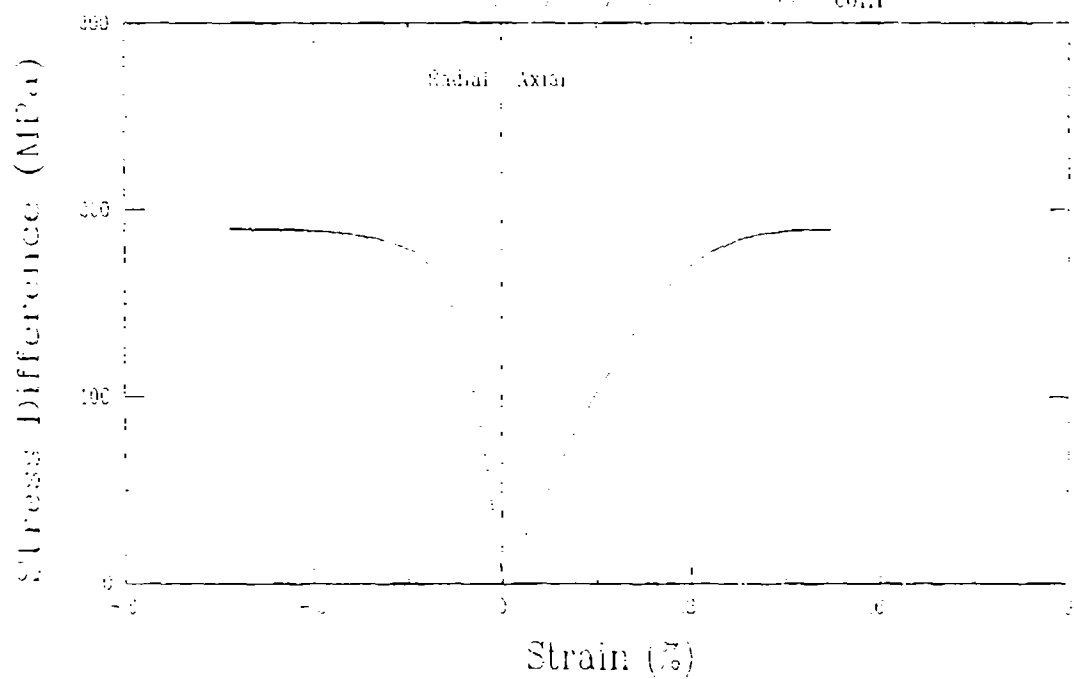
Triaxial Compression Test (Y28C3)  
Tennessee Marble (TM/92/5/2-2),  $\sigma_{\text{conf}} = 10 \text{ MPa}$



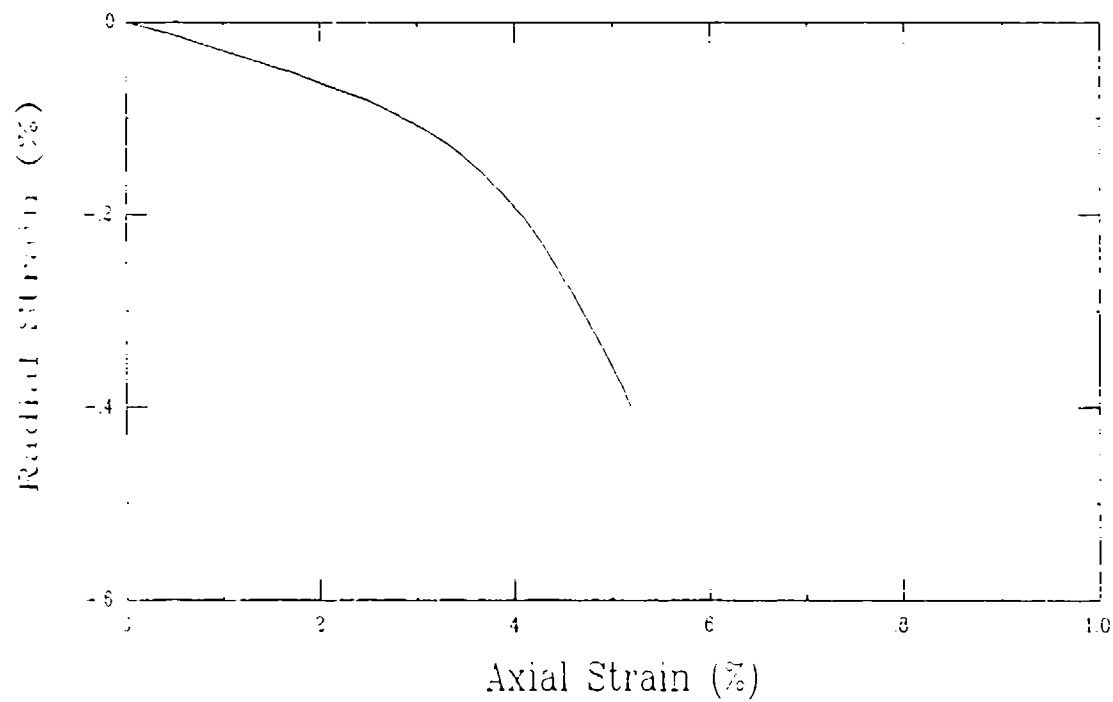
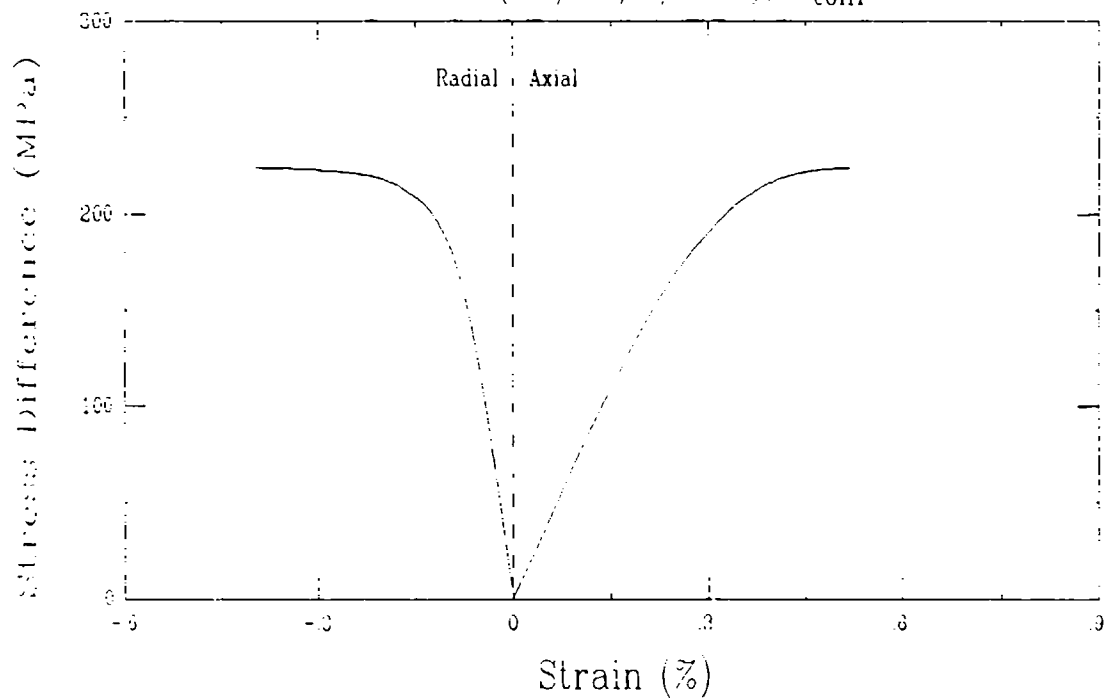
# Triaxial Compression Test (U1A3) Tennessee Marble (TM 92.5 4-5), $\sigma_{conf} = 10$ MPa



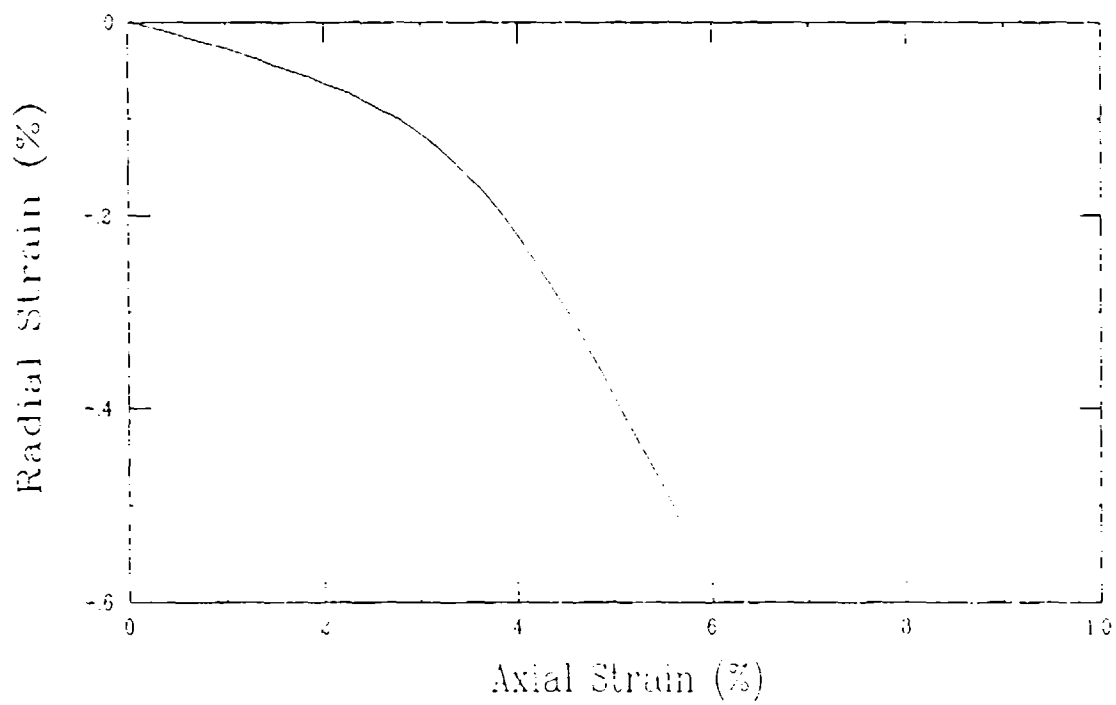
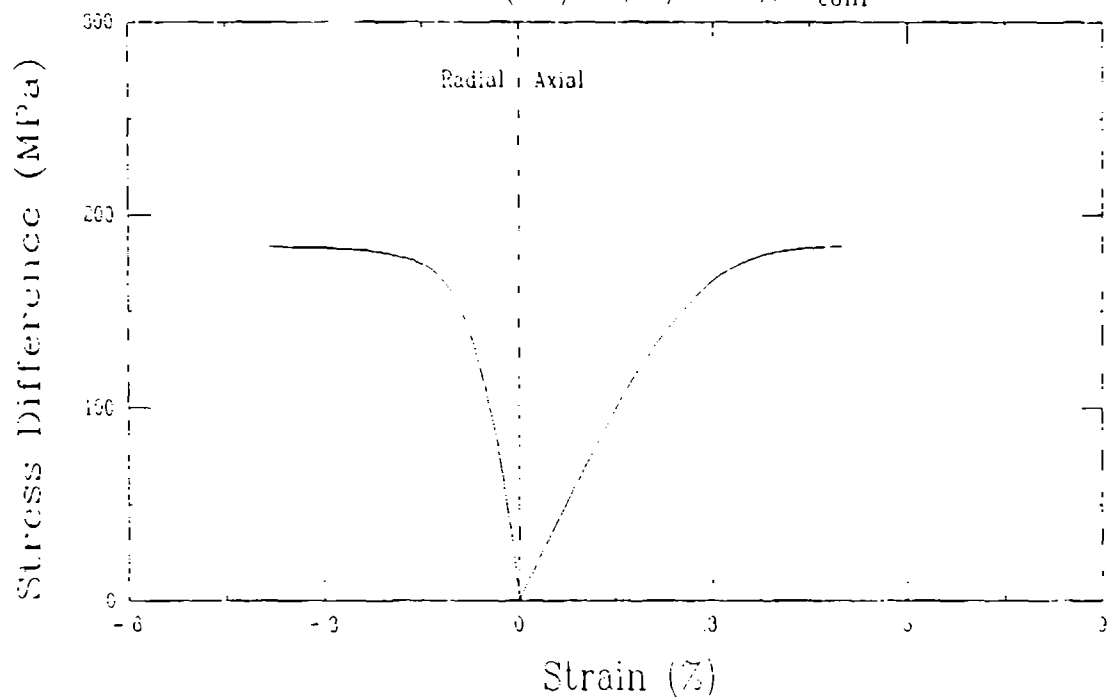
# Triaxial Compression Test (U1B3) Tennessee Marble (TM/91, 1, 2-23B), $\sigma_{conf} = 25 \text{ MPa}$



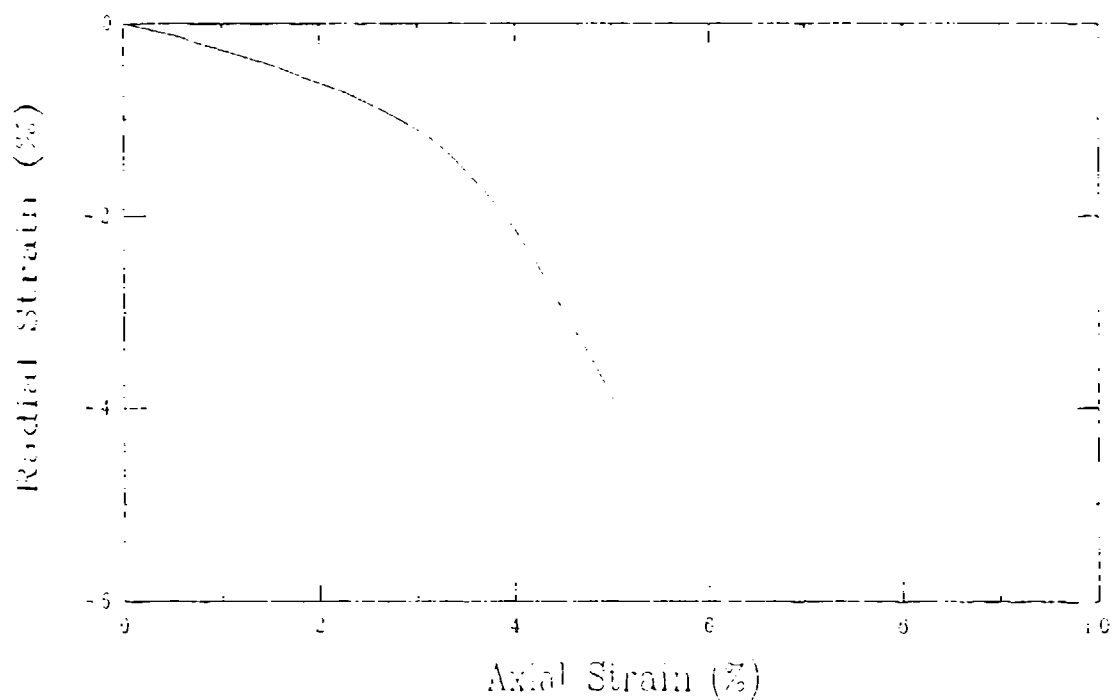
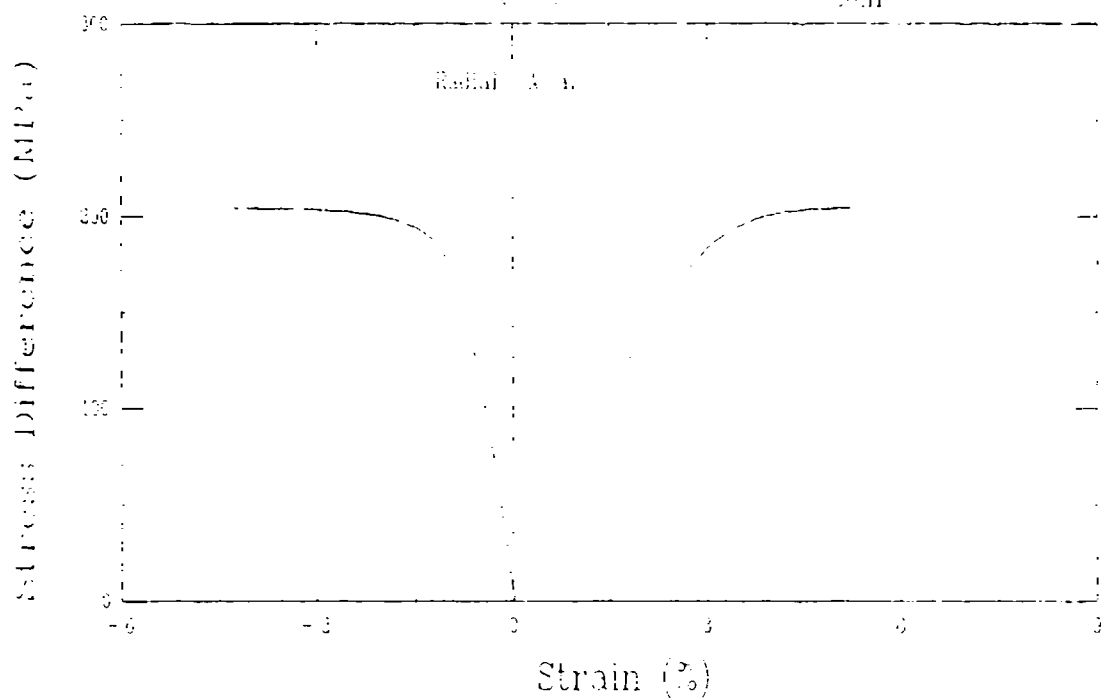
# Triaxial Compression Test (U1E3) Tennessee Marble (TM/91/2/1-2), $\sigma_{\text{conf}} = 25 \text{ MPa}$



# Triaxial Compression Test (U1C3) Tennessee Marble (TM/92/5/1-2), $\sigma_{\text{conf}} = 25 \text{ MPa}$

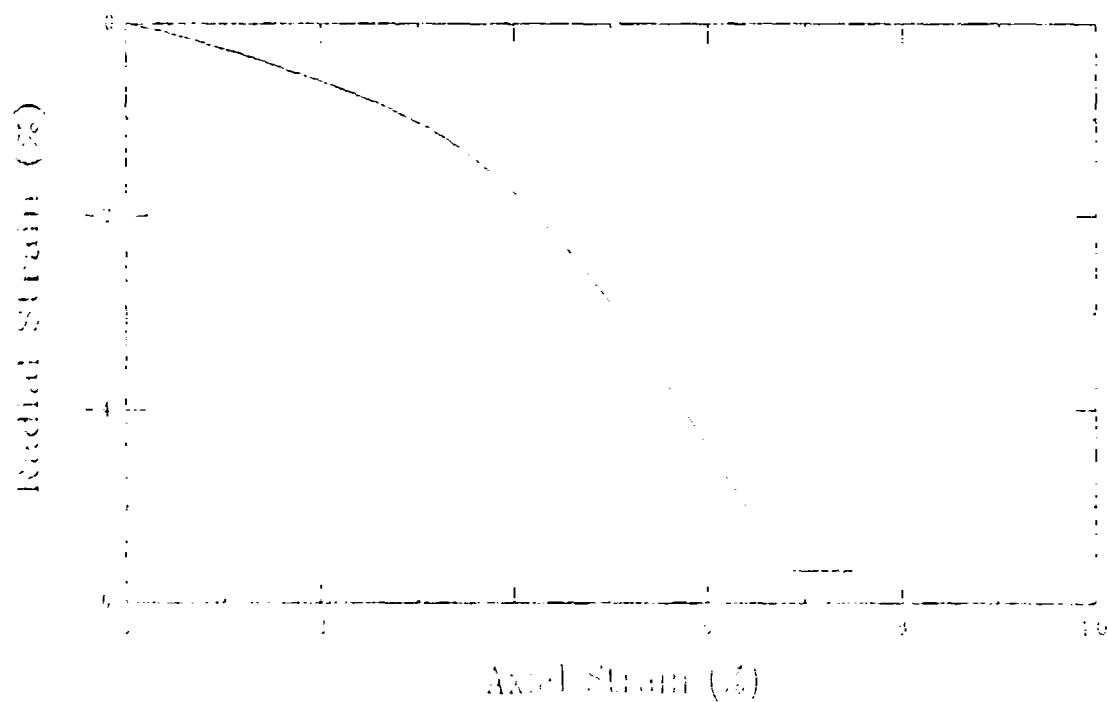
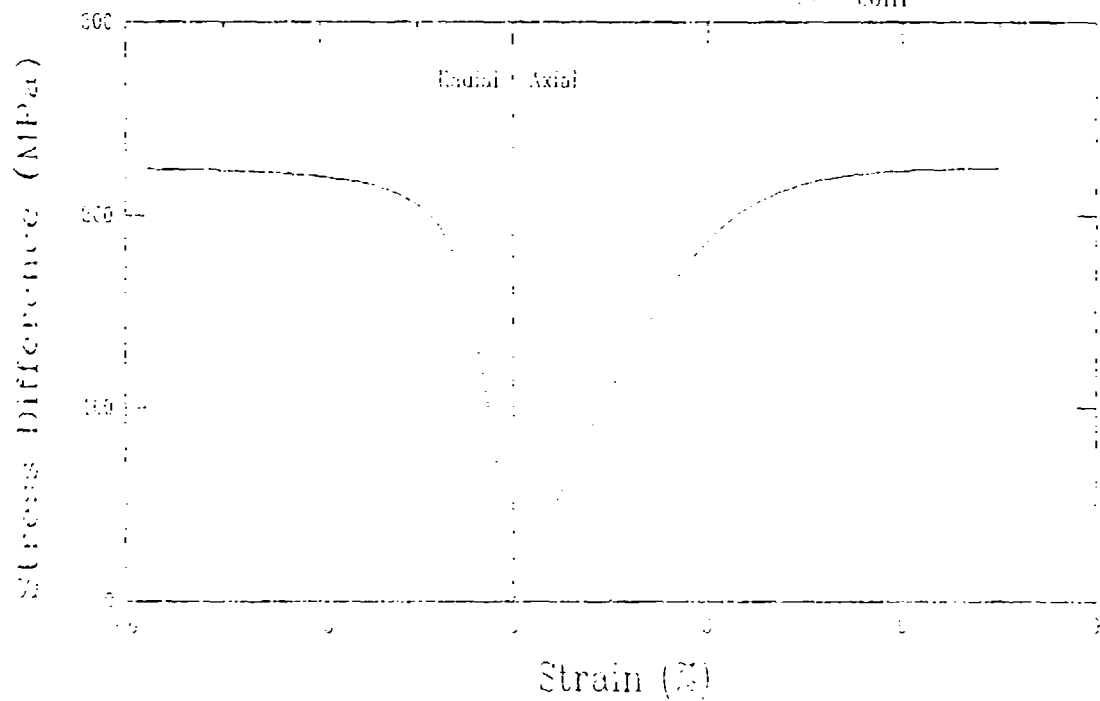


# Triaxial Compression Test (LID3) Tennessee Marble (TM 92 5.2-18), $\sigma_{\text{total}} = 35 \text{ MPa}$



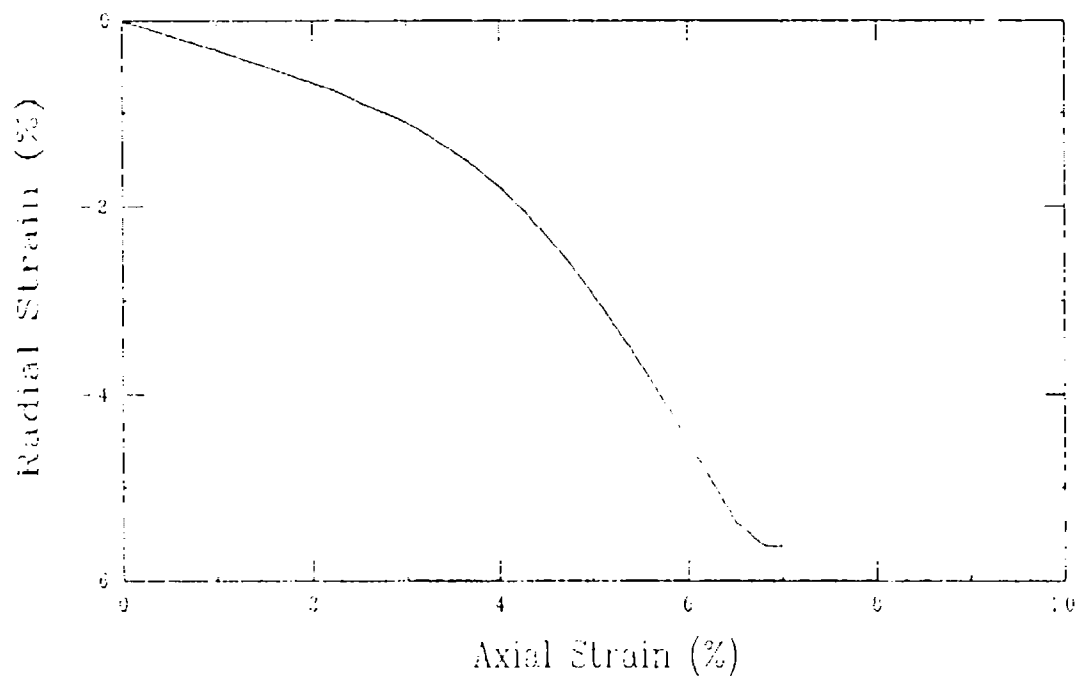
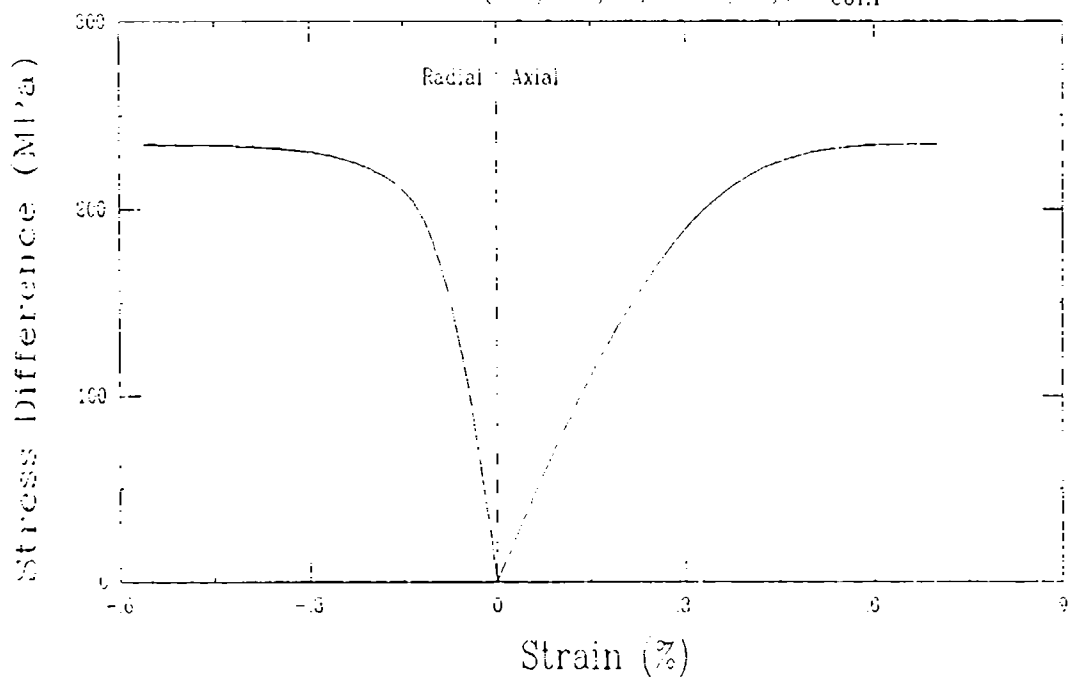
# Triaxial Compression Test (U3C3)

Tennessee Marble (TM 91, 1-2-15B),  $\sigma_{conf} = 10 \text{ MPa}$

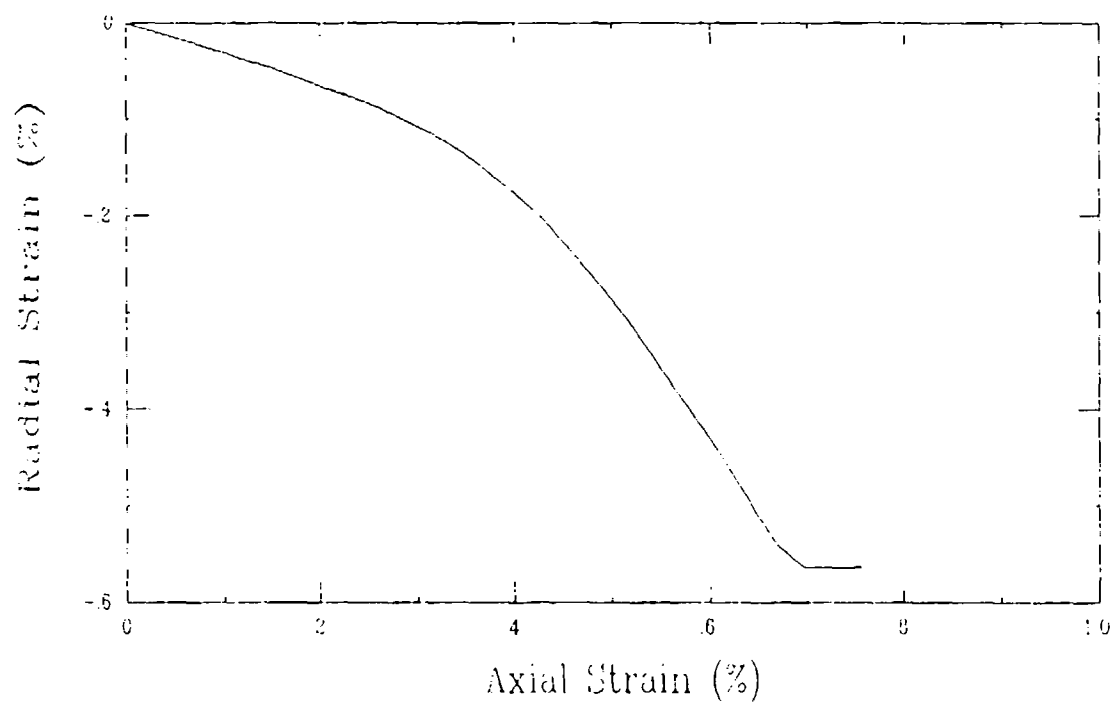
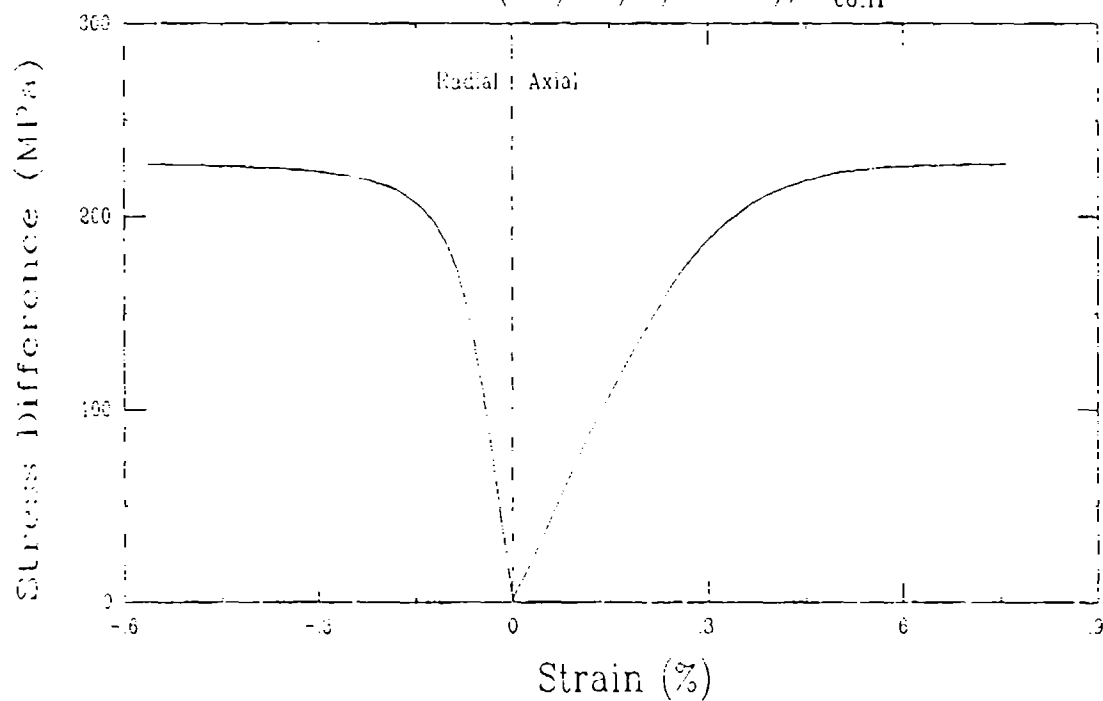




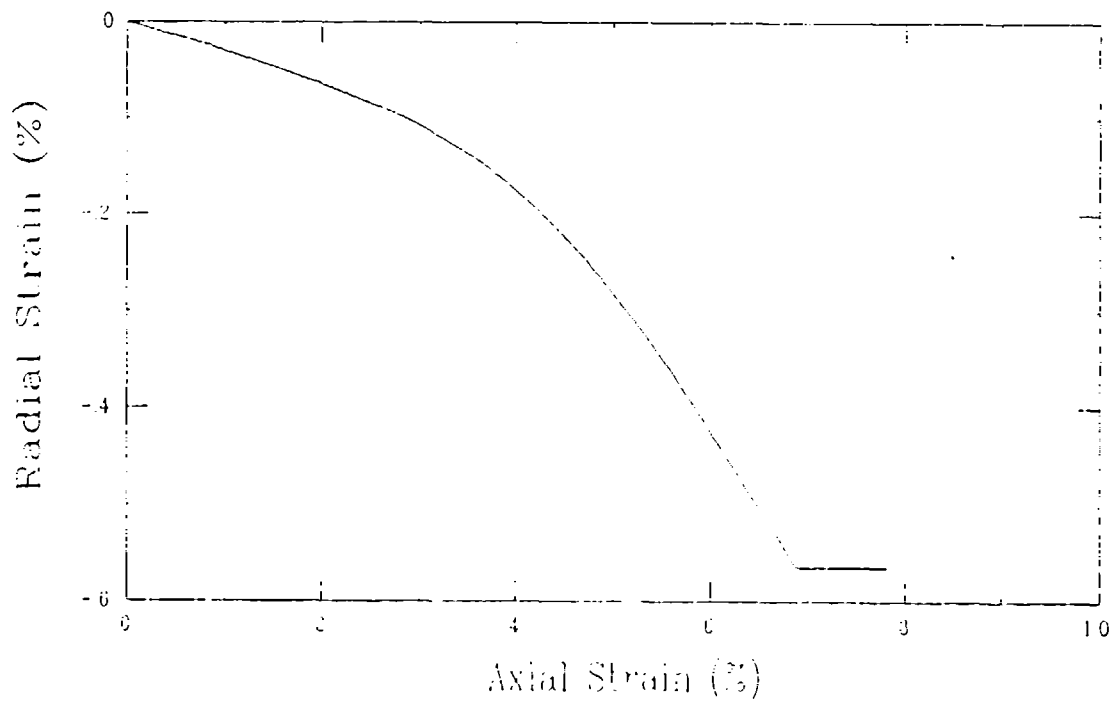
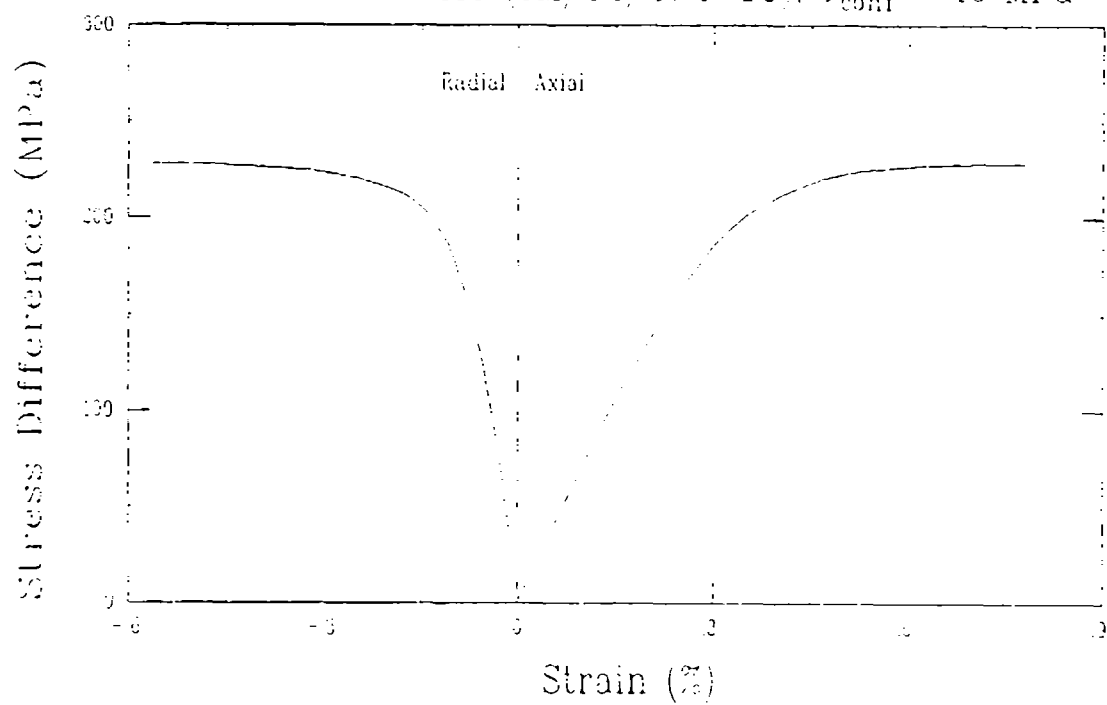
# Triaxial Compression Test (U2A3) Tennessee Marble (TM/91/4/8-6/B), $\sigma_{conf} = 40$ MPa



# Triaxial Compression Test (U2D3) Tennessee Marble (TM/92/5/2-10), $\sigma_{conf} = 40$ MPa



# Triaxial Compression Test (U2B2) Tennessee Marble (TM/92/5.2-15), $\sigma_{conf} = 40 \text{ MPa}$



## DISTRIBUTION LIST

DNA-TR-93-63

### DEPARTMENT OF DEFENSE

ADVANCED RESEARCH PROJECT AGENCY  
ATTN: DEFENSE SCIENCES OFFICE

ASSISTANT TO THE SECRETARY OF DEFENSE  
ATTN: EXECUTIVE ASSISTANT

DEFENSE INTELLIGENCE AGENCY  
ATTN: DB-6E2 J DOPERALSKI  
ATTN: DIW-4

DEFENSE NUCLEAR AGENCY  
ATTN: OPNA  
ATTN: SPSC  
ATTN: SPSC P SENSENY  
2 CY ATTN: TITL

DEFENSE TECHNICAL INFORMATION CENTER  
2 CY ATTN: DTIC/CC

DNA PACOM LIAISON OFFICE  
ATTN: DNALO

FIELD COMMAND DEFENSE NUCLEAR AGENCY  
ATTN: FCTO  
ATTN: FCTOH  
ATTN: FCTTG BALADI  
ATTN: W SUMMA

### DEPARTMENT OF THE ARMY

U S ARMY CORPS OF ENGINEERS  
ATTN: CERD-L

U S ARMY ENGINEER DIST OMAHA  
ATTN: MROED-S H GAUBE

U S ARMY ENGR WATERWAYS EXPER STATION  
ATTN: C D NORMAN  
ATTN: CEWES J K INGRAM  
ATTN: CEWES-SD DR J G JACKSON JR  
ATTN: CEWES-SE MR L K DAVIS  
ATTN: DR D BANKS CEWES-GS  
ATTN: G ALBRITTON  
ATTN: J BALSARA CEWES-SS-R  
ATTN: J WARRINER WESGR-M  
ATTN: RESEARCH LIBRARY  
ATTN: W MILLER

### DEPARTMENT OF THE AIR FORCE

AIR FORCE CTR FOR STUDIES & ANALYSIS  
ATTN: AFSAA-SAI

AIR UNIVERSITY LIBRARY  
ATTN: AUL-LSE

### DEPARTMENT OF ENERGY

LOS ALAMOS NATIONAL LABORATORY  
ATTN: REPORT LIBRARY

SANDIA NATIONAL LABORATORIES  
ATTN: DIV 9311 L R HILL  
ATTN: TECH LB 3141  
ATTN: 9311 C W SMITH

### OTHER GOVERNMENT

CENTRAL INTELLIGENCE AGENCY  
ATTN: OSWR NED

DEPARTMENT OF THE INTERIOR  
ATTN: P SANDS

### DEPARTMENT OF DEFENSE CONTRACTORS

AEROSPACE CORP  
ATTN: LIBRARY ACQUISITION

ANALYTIC SERVICES, INC LANSER  
ATTN: K BAKER

APPLIED RESEARCH ASSOCIATES, INC  
ATTN: C J HIGGINS

APPLIED RESEARCH ASSOCIATES, INC  
2 CY ATTN: D CHITTY  
2 CY ATTN: S BLOUIN  
2 CY ATTN: K KIM  
2 CY ATTN: X SUN

APPLIED RESEARCH ASSOCIATES, INC  
ATTN: R FRANK

BDM ENGINEERING SERVICES CO  
ATTN: D BURGESS

BOEING TECHNICAL & MANAGEMENT SVCS, INC  
ATTN: W M LEAVENS  
ATTN: A W SPENCER  
ATTN: ROSS J WOOD

CALIFORNIA RESEARCH & TECHNOLOGY, INC  
ATTN: J THOMSEN  
ATTN: K KREYENHAGEN

IIT RESEARCH INSTITUTE  
ATTN: DOCUMENTS LIBRARY  
ATTN: M JOHNSON

INSTITUTE FOR DEFENSE ANALYSES  
ATTN: CLASSIFIED LIBRARY

JAYCOR  
ATTN: CYRUS P KNOWLES

KAMAN SCIENCES CORP  
ATTN: RICHARD KEEFFE

KAMAN SCIENCES CORP  
ATTN: DASAC

KAMAN SCIENCES CORPORATION  
ATTN: DASAC

DNA-TR-93-63 (DL CONTINUED)

LACHEL AND ASSOCIATES, INC  
ATTN: C LINAMEN  
ATTN: J BECK

LOGICON R & D ASSOCIATES  
ATTN: LIBRARY

LOGICON R & D ASSOCIATES  
ATTN: J WALTON

LOGICON R & D ASSOCIATES  
ATTN: D PIEFENBURG

NTS ENGINEERING  
ATTN: R KENNEDY  
ATTN: S SHORT

PACIFIC-SIERRA RESEARCH CORP  
ATTN: H BRODE

PACIFIC-SIERRA RESEARCH CORP  
ATTN: D GORMLEY

S-CUBED  
ATTN: K D PYATT JR

SCIENCE APPLICATIONS INTL CORP  
ATTN: DR M MCKAY  
ATTN: H PRATT  
ATTN: TECHNICAL REPORT SYSTEM

SCIENCE APPLICATIONS INTL CORP  
ATTN: W LAYSON

SOUTHWEST RESEARCH INSTITUTE  
ATTN: A FOSSUM  
ATTN: B THACKER

SRI INTERNATIONAL  
ATTN: J GRAN

TITAN CORPORATION (THE  
ATTN: LIBRARY  
ATTN: S SCHUSTER  
ATTN: Y MITO

TRW SPACE & DEFENSE SECTOR  
ATTN: W WAMPLER

UTC, INC  
ATTN: E FOSTER

WEIDLINGER ASSOC, INC  
ATTN: H LEVINE

WEIDLINGER ASSOCIATES, INC  
ATTN: I SANDLER  
ATTN: M BARON